DOT/FAA/RD-93/40,. III

Research and Development
Service
Washington, D.C. 20591

Synthetic Vision Technology Demonstration

Volume 3 of 4
Flight Tests

Malcolm A. Burgess, FAA
Terence Chang, TRW
Dale E. Dunford, USAF
Roger H. Hoh, Hoh Aeronautics
Walter F. Horne, GTRI
Richard F. Tucker, TRW
J. Allen Zak, Hughes-STX

Synthetic Vision Program Office
Federal Aviation Administration

December 1993

Final Report

U.S. Department of Transportation
Federal Aviation Administration

U.S. Department of Defense

NOTICE

Technical Report Documentation Page

1. Report No.	2. Government Accession No.	3. Recipient's Catalog No.
DOT/FAA/RD-93/40,III		

4. Title and Subtitle	5. Report Date
SYNTHETIC VISION TECHNOLOGY DEMONSTRATION (4 VOLUMES) Volume III - Flight Tests	DECEMBER 1993
	6. Performing Organization Code ARD-100
7. Author(s) M. Burgess, T. Chang, D. Dunford, R. Hoh, W. Horne, R. Tucker, J. Allen Zak	8. Performing Organization Report No.
9. Performing Organization Name and Address SYNTHETIC VISION PROGRAM OFFICE FEDERAL AVIATION ADMINISTRATION 800 Independence Avenue, S. W. Washington, DC 20591	10. Work Unit No. (TRAIS)
	11. Contract or Grant No.
12. Sponsoring Agency Name and Address RESEARCH AND DEVELOPMENT SERVICES FEDERAL AVIATION ADMINISTRATION 800 Independence Avenue, S.W. Washington, DC 20591	13. Type of Report and Period Covered FINAL REPORT
	14. Sponsoring Agency Code ARD-1

15. Supplementary Notes

CO SPONSER: Control Systems Division
USAF Wright Laboratory
Wright-Patterson AFB, OHIO 45433-7521

16. Abstract

This report contains the description and results of a Synthetic Vision technology demonstration program conducted jointly by the Federal Aviation Administration, the Department of Defense and industry. The relevant technologies including millimeter wave radar sensors, infrared sensors, head-up displays, and computer processing were developed and tested in static tower tests and in flight tests in which the weather conditions were carefully measured and documented. The purpose of the program was to evaluate and demonstrate the performance of the imaging sensors and of the complete imaging system during aircraft approaches and landings in low-visibility conditions.

The static tower test facility used was the Avionics Tower Test Facility, located at Wright Patterson AFB, in which candidate sensors were set up at approximately 260 feet overlooking a nearby runway. The runway scene imaged by the sensors was instrumented to carefully measure the characteristics of fog, rain and snow as those conditions occurred in 1991-1992. Sensor performance and phenomenology was then fully characterized to provide a basis for further sensor development and for selection of sensors with which to proceed to flight test.

The test aircraft used was a Gulfstream II configured with a comprehensive data collection system and instrumentation to permit measurement of fog and precipitation through which the aircraft was flown as well as system and pilot performance during those operations. Millimeter wave sensors and an infrared sensor were used to provide an electronic image of the runway on both head-up and head-down displays during approach, landing and takeoff. Test and demonstration flights were flown into 27 difference airports in a wide variety of rain, fog and snow conditions during the period of May through December, 1992.

17. Key Words	18. Distribution Statement
SYNTHETIC VISION FLIGHT TEST MMW RADAR	Document of available to the public through the National Technical Information Service, Springfield, VA 22161

19. Security Classif. (of this report)	20. Security Classif. (of this page)	21. No. of Pages	22. Price
Unclassified	Unclassified	297	

Form DOT F 1700.7 (8-72) Reproduction of completed page authorized

TABLE OF CONTENTS

Section	Title	Page
1.	INTRODUCTION	1
1.1.	Overview of Flight Test Program	1
1.2.	Objectives	2
1.3.	Approach	2
1.4.	Scope	7
1.5.	Organization and Responsibilities	8
1.6.	Final Report Organization	11
2.	TASK MANAGEMENT	13
2.1.	Management Process	13
2.2.	Engineering Process	15
3.	DESCRIPTION OF FACILITIES	22
3.1.	Experimental System	22
3.1.1.	Sensors	22
3.1.1.1.	35 GHz MMW	22
3.1.1.2.	94 GHz MMW	23
3.1.1.3.	3 - 5 Micron FLIR	23
3.1.2.	Head-Up Display	24
3.1.2.1.	Hardware Description, Registration Issues and Calibration Procedures	24
3.1.2.2.	Head-Up Display Symbols and Flight Director	24
3.1.3.	Weather Sensors	27
3.1.4.	Aircraft Instrumentation	28
3.1.5.	Data Acquisition System	32
3.2	Description of Airports	34
3.3	Ground-Based Simulation	34
4.	FLIGHT TEST METHODS AND PROCEDURES	37
4.1.	Test Plan and Priorities	37
4.2.	Evaluation Pilot Background and Training	39
4.3.	SVS Instrument Approach Procedures	40
4.4.	Sensor Performance Measurement Methodology	42
4.4.1	Radar Phenomenology	42
4.4.1.1.1	Surface Reflectivity	43
4.4.1.1.2	Meteorological Effects	44
4.4.1.2	Radar Performance Issues	47
4.4.1.3	Synthetic Vision Figures of Merit	49
4.4.2	Radar Evaluation Methodology	58
4.4.2.1	Data Sources	59
4.4.2.1.1	Radar Data	59
4.4.2.1.2	Flight Profile Data	62
4.4.2.1.3	Weather Data	62
4.4.2.1.4	Ground-Truth Data	64
4.4.2.1.4.1	Airport Surveys	64
4.4.2.1.4.2	Other Ground Truth Data	65
4.4.2.2	Data Acquisition Problems	67
4.4.2.2.1	Range Bin Misalignment	67
4.4.2.2.2	Loss of Data	67
4.4.2.2.3	Data Synchronization Problems	68

TABLE OF CONTENTS (CONTINUED)

4.4.2.2.3.1	Effect on Image Quality Analyses	69
4.4.2.2.3.2	Effect on Analyses of Surface Reflectivities	70
4.4.2.2.3.3	Effect on Analyses of Attenuations and Volumetric Reflectivities	71
4.4.2.3	Radar Data Reduction	71
4.4.2.3.1	Software Description	72
4.4.2.3.1.1	SUN-Based Software	72
4.4.2.3.1.1.1	Data Format	72
4.4.2.3.1.1.2	Display Formats	74
4.4.2.3.1.1.3	Range Bin Misalignment	78
4.4.2.3.1.1.4	Estimating Received Power	78
4.4.2.3.1.2	Image Macros	86
4.4.2.3.1.2.1	Importing Radar Data for Display	88
4.4.2.3.1.2.2	Importing Floating Point Data	88
4.4.2.3.1.2.3	Exporting a ROI	88
4.4.2.3.1.2.4	Computation of Average Received Power for a ROI	90
4.4.2.3.1.2.5	Horizontal and Vertical Antenna Patterns	90
4.4.2.3.1.2.6	RCS and Normalized RCS	94
4.4.2.3.1.2.7	Volumetric Backscatter and Attenuation	96
4.4.2.3.1.3	MATLAB M-files	98
4.4.2.3.1.3.1	Regions of Interest	98
4.4.2.3.1.3.2	Contrast	104
4.4.2.3.1.3.3	Sharpness	104
4.4.2.3.1.3.4	Variability	107
4.4.2.3.1.4	Data Storage	109
4.4.2.3.2	Data Reduction Process	109
4.4.2.3.2.1	Data Selection, Transfer and Pre-Processing	110
4.4.2.3.2.2	Contrast, Sharpness, and Variability Processing	113
4.4.2.3.2.3	Radar Cross Section Processing	126
4.4.2.3.2.4	Attenuation and Volumetric Reflectivity Processing	130
4.4.2.3.2.5	Data Base of Reduction Products	131
4.4.2.3.3	Weather Data Reduction	131
4.4.2.3.3.1	Processing of JTD Supplied Data	131
4.4.2.3.3.2	Contents of files supplied by JTD	132
4.4.2.3.3.3	Conversion of JTD Files to Spreadsheet Files	133
4.4.2.3.3.4	Converted JTD Data	134
4.4.2.3.3.5	Temperature Deviations And Corrections	134
4.4.3	System Calibration	136
4.4.3.1	Data Acquisition Transfer Function	136
4.4.3.2	Absolute System Calibration	138
4.4.3.2.1	Radar Scene Modeling	139
4.4.3.2.2	Arcata, CA Calibration	152
4.4.3.2.4	Santa Barbara, CA Calibration	180
4.4.3.2.5	Santa Maria, CA Calibration	197
4.4.3.2.6	Summary	209
4.5.	Image Quality Analyses Methods	210
4.5.1	Raster Image Quality Metrics	211
4.5.1.1	Contrast	212
4.5.1.2	Variability	215
4.5.3	Image Registration With HUD and Outside Scene	215
4.5.3.1	Through-The-HUD Measurements	216
4.5.3.2	Known Target Calibration	216

TABLE OF CONTENTS (CONTINUED)

4.5.4	Video Raster Data Preparation	217
4.5.5	Image Calibration	219
5.	PILOT SYSTEM PERFORMANCE RESULTS	221
5.1.	Pilot Performance And Opinion	222
5.1.1.	Experimental System (35 GHz MMW Sensor) Performance in Terms of Range and Altitude Where Pilot Called Runway Image	223 223
5.1.1.1	Variation Between and Within Pilots	223
5.1.1.2	Effect of Fog	223
5.1.1.3	Effect of Airport Surface	225
5.1.1.4	Effect of Rain	230
5.1.1.5	Effect of Snow	233
5.1.2.	Subjective Pilot Ratings and Opinion	233
5.1.2.1	Subjective Pilot Ratings for Simulated IMC	238
5.1.2.2	Runway Surface and Limited Range Problems at SAN	240
5.1.2.3	Non-Precision and No-Navaid Approaches	240
5.1.2.4	Approaches to Simulated Cat IIIc (0/0) Minimums	243
5.1.2.5	Takeoffs in Simulated Cat IIIc (0/0) Conditions	244
5.1.2.6	Simulated Runway Intrusion Cases	245
5.1.2.7	Approaches Using the Head Down Display	245
5.1.2.8	Approaches in Actual Cat II and Cat IIIa Conditions	246
5.1.3	Summary Comments Regarding Pilot Performance	250
5.1.4	Summary of Pilot Commentary	253
5.2.	Tracking Performance	255
6.	SENSOR PERFORMANCE RESULTS	264
6.1.	Radar Performance	264
6.1.1	Basic Phenomenological Measures	264
6.1.1.1	Surface Reflectivities	264
6.1.1.2	Vehicle Reflectivity	280
6.1.1.3	Atmospheric Effects	282
6.1.1.3.1	Attenuation	282
6.1.1.3.1.1	Attenuation References	283
6.1.1.3.1.2	Attenuation Measurements	288
6.1.1.3.2	Volumetric Reflectivity	291
6.1.1.3.2.1	Volumetric Reflectivity References	293
6.1.1.3.2.2	Volumetric Reflectivity Measurements	293
6.1.2	Image Quality Metrics	296
6.1.2.1	Contrast Results	296
6.1.2.1.1	Measured Contrast as a Function of Weather	297
6.1.2.1.1.1	Contrast in Clear Weather	298
6.1.2.1.1.2	Contrast in Fog	304
6.1.2.1.1.3	Contrast in Rain	313
6.1.2.1.1.4	Contrast in Snow	317
6.1.2.1.2	Summary of Contrast Results	325
6.1.2.2	Sharpness	326
6.1.2.2.1	Flight Tests	327
6.1.2.2.2	Tower Tests	332
6.1.2.2.3	Conclusion	334
6.1.2.3	Signal-to-Variability Ratio	337

TABLE OF CONTENTS (CONTINUED)

6.1.2.3.1	Flight Tests	339
6.1.2.3.2	Tower Tests	349
6.1.2.3.3	Summary	353
6.1.2.4	Other Potential Image Quality Metrics	354
7.	IMAGE QUALITY PERFORMANCE	359
7.1	Contrast	359
7.2	Sharpness	376
7.3	Variability	376
8.	LESSONS LEARNED SUMMARY	377
9.	CONCLUSIONS	382

LIST OF ILLUSTRATIONS

Figure	Title	Page
1.1-1	Flight Test Methodology	4
1.1-2	Gulfstream II Flight Test Aircraft	6
1.1-5	SIED Project Team	9
2.2-1	FPSVS Block Diagram	16
3.3-1	Head-Up Display Symbology Used in Test Aircraft	26
4.3-1	Approach Procedures Used in Flight Test Program	41
4.4.1-1	Radar scattering from airport surfaces	43
4.4.1-2	Meteorological effects on MMW radar	45
4.4.1-3	Illustration of Basic Radar Signature for Runway-Terrain Scenario	50
4.4.1-4	Illustration of Simple Gutter Plot with Basic Image Quality Metrics Indicated	51
4.4.1-5	Illustration of relationship between contrast and terrain-to-runway ratio	52
4.4.2-1	Honeywell raw data file format	73
4.4.2-2	Example of Honeywell Radar Image displayed in Three different formats	76
4.4.2-3	Geometry for Converting from B-Scope to C-Scope formats	77
4.4.2-4	Illustration of B-Scope to PPI transformation	77
4.4.2-5	Illustration of Range Bin Misalignment and Correction	78
4.4.2-6	Block Diagram of the Honeywell Data Acquisition System	79
4.4.2-8	Measured and Calculated Data Acquisition System Transfer	83
4.4.2-9	Measured and Calculated Data Acquisition System Transfer	87
4.4.2-10	Illustration of Relationship between Display Fixed-Point PPI Image and Parallel Floating-Point Data Structure	89
4.4.2-11	Illustration of Selecting a Region of Interest (ROI) Via IMAGE	91
4.4.2-12	Example of Automated Calculation of Average Received Power and RCS for a ROI	92
4.4.2-13	Illustration of Honeywell Antenna Mounting	93
4.4.2-14	Range Cells used in computing volumetric backscatter	98
4.4.2-15	Example ROI Selected for Export to MATLAB	100
4.4.2-16	Example ROI Imported from IMAGE into MATLAB	101
4.4.2-17	Example Gutter Profile Created in MATLAB	102
4.4.2-18	Illustration of Gutter Profile Partitioned into Runway and Terrain Regions in MATLAB	103
4.4.2-19	Illustration of Contrast Computation	105
4.4.2-20	Illustration of Sharpness Computation	106
4.4.2-21	Illustration of Variability Computation	108
4.4.2-22	Positions of the Aircraft Corresponding to Snapshots of Interest	111
4.4.2-23	Four Nominal Refions of Interest Along the Runway	112
4.4.2-24	Example PPI Snapshot Image From Arcata, CA Taken In Fog On 8/28/92	114
4.4.2-25	Three Dimensional, Linear-Amplitude Presentation of Radar Data from Box 1 of Figure 4.4.2-24	117
4.4.2-26	Three Dimensional, Linear-Amplitude Presentation of Radar Data from Box 2 of Figure 4.4.2-24	118
4.4.2-27	Three Dimensional, Linear-Amplitude Presentation of Radar Data from Box 3 of Figure 4.4.2-24	119
4.4.2-28	Example PPI Snapshot Image form Huntington, WV Taken In Fog On 9/28/92	121
4.4.2-29	Gutter Plot Corresponding to Box 1 in Figure 4.4.2-28	122

LIST OF ILLUSTRATIONS (CONTINUED)

4.4.2-30	Gutter Plot Corresponding to Box 2 in Figure 4.4.2-28	124
4.4.2-31	Gutter Plot Corresponding to Box 3 in Figure 4.4.2-28	125
4.4.2-32	Example of Rectangle Placement for Computation of Normalized RCS Values for Runway and Terrain	129
4.4.2-33	JTD Original Plot (Top) Compared With GTRI Optimized Plots (Bottom)	135
4.4.3-1	Data Acquisition Transfer Function	137
4.4.2-2	Example Flight Test Geometry	139
4.4.3-3	Illustration of Multipath Geometry for Flight Test Scene	140
4.4.3-4	Computer Model of 23 dBsm (at 35 GHz) Bruderhedral Calibration Reflector	141
4.4.3-5	Bistatic Pattern of a 23 dBsm (35 GHz) Bruderhedral Calibration Target for Circular Polarization	142
4.4.3-6	Multipath Scenario to Examine Terrain Roughness Effects on Lobing Pattern	146
4.4.3-7	Computed Multipath Lobing Pattern at 3000 Meter Ground Range, for Flat Dielectric Terrain with Permittivity = 4.863 + j 4.290 Circular Polarization and 35 GHz Frequency Assumed	146
4.4.3-8	Computed Multipath Lobing Pattern at 3000 Meter Ground Range, for Flat Dielectric Terrain with Permittivity = 4.863 + j 4.290, RMS Roughness = 0.01 m, and RMS Slope = 0.12 Radian. Circular Polarization and 35 GHz Frequency Assumed	147
4.4.3-9	Computed Multipath Lobing Pattern at 3000 Meter Ground Range, for Flat Dielectric Terrain with Permittivity = 4.863 + j 4.290, RMS Roughness = 0.025 m, and RMS Slope = 0.12 Radian. Circular Polarization and 35 GHz Frequency Assumed	148
4.4.3-10	Computed Multipath Lobing Pattern at 1000 Meter Ground Range, for Flat Dielectric Terrain with Permittivity = 4.863 + j 4.290, Circular Polarization and 35 GHz Frequency Assumed	149
4.4.3-11	Computed Multipath Lobing Pattern at 1000 Meter Ground Range, for Flat Dielectric Terrain with Permittivity = 4.863 + j 4.290, RMS Roughness = 0.01 m, and RMS Slope = 0.12 Radian. Circular Polarization and 35 GHz Frequency Assumed	150
4.4.3-12	Computed Multipath Lobing Pattern at 1000 Meter Ground Range, for Flat Dielectric Terrain with Permittivity = 4.863 + j 4.290, RMS Roughness = 0.025 m, and RMS Slope = 0.12 Radian. Circular Polarization and 35 GHz Frequency Assumed	150
4.4.3-13	Plot of Measured and Predicted RCS Versus Altitude for the 23.0 dBsm Bruderhedral at Arcata, CA on August 27, 1992 (Approach 2A). Both the Measured Peak RCS and the Sum RCS are Indicated. The Predicted RCS is Based on an Assumed RMS Surface Roughness of 0.025M	158
4.4.3-14	Plot of Measured RCS Sum Values After Adjustment as Well as Corresponding Predicted RCS Values Used to Compute Adjustment. Data are for the 23.0 dBsm Bruderhedral at Arcata, CA on August 27, 1992 (Approach 2A)	159
4.4.3-15	Plot of Measured and Predicted RCS Versus Altitude for the 18.7 dBsm Bruderhedral at Arcata, CA on August 27, 1992 (August 2A). Both the Measured Peak RCS and the Sum RCS are Indicated. The Predicted RCS is Based on an Assumed TMS Surface Roughness of 0.025M	160

LIST OF ILLUSTRATIONS (CONTINUED)

4.4.3-16	Plot of Measured TCS Sum Values After Adjustment as Well as Corresponding Predicted RCS Values used to Compute Adjustment. Data are for the 18.7 dBsm Bruderhedral at Arcata, CA on August 27, 1992 (Approach 2A)	161
4.4.3-17	Plot of Measured and Predicted RCS Versus Altitude for the 23.0 dBsm Bruderhedral at Arcata, CA on August 27, 1992 (Approach 2C). Both the Measured Peak RCS and the Sum RCS are Indicated. The Predicted RCS is based on an Assumed RMS Surface Roughness of 0.025m	162
4.4.3-18	Plot of Measured RCS Sum Values After Adjustment as Well as Corresponding Predicted RCS Values Used to Compute Adjustment. Data are for the 23.0 dBsm Bruderhedral at Arcata, CA on August 27, 1992 (Approach 2C)	163
4.4.3-19	Plot of measured and Predicted RCS Versus Altitude for the 18.7 dBsm Bruderhedral at Arcata, CA on August 27, 1992 (Approach 2C). Both the Measured Peak RCS and the Sum RCS are Indicated. The Predicted RCS is Based on an Assumed RMS Surface Roughness of 0.025m	164
4.4.3-20	Plot of Measured RCS Sum Values After Adjustment as Well as Corresponding Predicted RCS Values Used to Compute Adjustment. Data are for the 18.7 dBsm Bruderhedral at Arcata, CA on August 27, 1992 (Approach 2C)	165
4.4.3-21	Illustration of flight test snapshop geometry	166
4.4.3-22	Plot of Measured and Predicted RCS Versus Altitude for the 23.0 dBsm Bruderhedral at Vandenburg Air Force Base, CA on August 19, 1992 (Approach 2C). Predicted RCVS Values are computed for Three Assumed RMS Surface Roughness as Indicated	170
4.4.3-23	Plot of measured RCS Sum Values after adjustment as Well as Corresponding Predicted RCS Values Used to Compute Adjustment. Data are for the 23.0 dBsm Bruderhedral at Vandenburg Air Force Base, CA on August 19, 1992 (Approach 2C)	171
4.4.3-24	Plot of Measured RCS Versus Altitude for the 18.7 dBsm Bruderhedral at Vandenburg Air Force BAse, CA on August 19, 1992 (Approach 2C). Predicted RCS Values are Computed for Three Assumed RMS Surface Roughness as Indicated	172
4.4.3-25	Plot of Measured RCS Sum Values After Adjustment as Well as Corresponding Predicted RCS Values Used to Compute Adjustment. Data are for the 18.7 dBsm Bruderhedral at Vandenburg Air Force Base, CA on August 19, 1992 (Approach 2C)	173
4.4.3-26	Plot of Measured RCS Versus Altitude for the 23.0 dBsm Bruderhedral at Vandenburg Air Forced Base, CA on August 19, 1992 (Approach 2D). Predicted RCS Values are Computed for Three Assumed RMS Surface Roughness as Indicated	174
4.4.3-27	Plot of Measured RCS Sum Values After Adjustment as Well as Corresponding Predicted RCS Values used to Compute Adjustment. Data are for the 23.0 dBsm Bruderhedral at Vandenburg Air Force Base, CA on August 19, 1992 (Approach 2D)	175

LIST OF ILLUSTRATIONS (CONTINUED)

4.4.3-28 Plot of Measure RCS Versus Altitude for the 18.7 dBsm Bruderhedral at Vandenburg Air Force Base, CA on August 19, 1992 (Approach 2D). Predicted RCS Values are Computed for Three Assumed RMS Surface Roughness as Indicated 176

4.4.3-29 Plot of Measured RCS Sum Values After Adjustment as Well as Corresponding Predicted RCS Values Used To Compute Adjustment. Data are for the 18.7 dBsm Bruderhedral at Vandenburg Air Force Base, CA on August 19, 1992 (Approach 2D) 177

4.4.3-30 Plot of Measured and Predicted RCS Versus Altitude for the 23.0 dBsm Bruderhedral at Santa Barbara, CA on August 19, 1992 (Approach 1B). Predicted RCS Values are computed for Three Assumed RMS Surface Roughness as Indicated 184

4.4.3-31 Plot of Mearsured RCS Sum Values After Adjustment as Well as Corresponding Predicted RCS Values Used to Compute Adjustment. Data are for the 23.0 dBsm Bruderhedral at Santa Barbara, CA on August 19, 1992 (Approach 1B) 185

4.4.3-32 Plot of Measured and Predicted RCS Versus Altitude for the 18.7 dBsm Bruderhedral at Santa Barbara, CA on August 19,1992 (Approach 1B). Predicted RCS Values are Computed for Three Assumed RMS Surface Roughness as Indicated 186

4.4.3-33 Plot of Measured RCS Sum Values After Adjustment as Well as Corresponding Predicted RCS Values Used to Compute Adjustment. Data are for the 18.7 dBsm Bruderhedral at Santa Barbara, CA on August 19, 1992 (Approach 1B) 187

4.4.3-34 Plot of Measured and Predicted RCS Versus Altitude for the 23.0 dBsm Bruderhedral at Santa Barbara, CA on August 19, 1992 (Approach 1C). Predicted RCS Values are Computed for Three Assumed RMS Surface Roughness as Indicated 188

4.4.3-35 Plot of Measured RCS Sum Values After Adjustment as Well as Corresponding Predicted RCS Values Used to Compute Adjustment. Data are for the 23.0 dBsm Bruderhedral at Santa Barbara, CA on August 19, 1992 (Approach 1C) 189

4.4.3-36 Plot of Measured and Predicted RCS Versus Altitude for the 18.7 dBsm Bruderhedral at Santa Barbara, CA on August 19, 1992 (Approach 1C). Predicted RCS Values are Computed for Three Assumed RMS Surface Roughness as Indicated 190

4.4.3-37 Plot of Measured RCS Sum Values After Adjustment as Well as Corresponding Predicted RCS Values Used to Compute Adjustment. Data are for the 18.7 dBsm Bruderhedral at Santa Barbara, CA on August 19, 1992 (Approach 1C) 191

4.4.3-38 Plot of Measured and Predicted RCS Versus Altitude for the 23.0 dBsm Bruderhedral at Santa Barbara, CA on August 19, 1992 (Approach 1D). Predicted RCS Values are Computed for Three Assumed RMS Surface Roughness as Indicated 192

4.4.3-39 Plot of Measured RCS Sum Values After Adjustment as Well as Corresponding Predicted RCS Values Used to Compute Adjustment. Data are for the 23.0 dBsm Bruderhedral at Santa Barbara, CA on August 19, 1992 (Approach 1D) 193

LIST OF ILLUSTRATIONS (CONTINUED)

4.4.3-40	Plot of Measured and Predicted RCS Versus Altitude for the 18.7 dBsm Bruderhedral at Santa Barbara, CA on August 19, 1992 (Approach 1D). Predicted RCS Values are Computed for Three Assumed RMS Surface Roughness as Indicated	194
4.4.3-41	Plot of Measured RCS Sum Values After Adjustment as Well as Corresponding Predicted RCS Values Used to Compute Adjustment. Data are for the 18.7 dBsm Bruderhedral at Santa Barbara, CA on August 19, 1992 (Approach 1D)	195
4.4.3-42	Plot of Measured and Predicted RCS Versus Altitude for the 23.0 dBsm Bruderhedral at Santa Barbara, CA on August 19, 1992 (Approach 1B). Predicted RCS Values are computed for Three Assumed RMS Surface Roughness as Indicated	201
4.4.3-43	Plot of Measured RCS Sum Values After Adjustment as Well as Corresponding Predicted RCS Values Used to Compute Adjustment. Data are for the 23.0 dBsm Bruderhedral at Santa Barbara, CA on August 19, 1992 (Approach 1B)	202
4.4.3-44	Plot of Measured and Predicted RCS Versus Altitude for the 18.7 dBsm Bruderhedral at Santa Barbara, CA on August 19, 1992 (Approach 1B). Predicted RCS Values are computed for Three Assumed RMS Surface Roughness as Indicated	203
4.4.3-45	Plot of Measured RCS Sum Values After Adjustment as Well as Corresponding Predicted RCS Values Used to Compute Adjustment. Data are for the 18.7 dBsm Bruderhedral at Santa Barbara, CA on August 19, 1992 (Approach 1B)	204
4.4.3-46	Plot of Measured and Predicted RCS Versus Altitude for the 23.0 dBsm Bruderhedral at Santa Barbara, CA on August 19, 1992 (Approach 1B). Predicted RCS Values are computed for Three Assumed RMS Surface Roughness as Indicated	205
4.4.3-47	Plot of Measured RCS Sum Values After Adjustment as Well as Corresponding Predicted RCS Values Used to Compute Adjustment. Data are for the 23.0 dBsm Bruderhedral at Santa Barbara, CA on August 19, 1992 (Approach 1C)	206
4.4.3-48	Plot of Measured and Predicted RCS Versus Altitude for the 23.0 dBsm Bruderhedral at Santa Barbara, CA on August 19, 1992 (Approach 1C). Predicted RCS Values are computed for Three Assumed RMS Surfa204	207
4.4.3-49	Plot of Measured RCS Sum Values After Adjustment as Well as Corresponding Predicted RCS Values Used to Compute Adjustment. Data are for the 18.7 dBsm Bruderhedral at Santa Barbara, CA on August 19, 1992 (Approach 1C)	208
4.5-1	Diagram of Video Output, Pilot Displays and Recording Equipment	213
4.5-2	Image Quality Metrics	214
5.1-1	Variation of Runway Image Call Altitude and Range Between and Within Pilots	224
5.1-2	Variation of Runway Image Call Altitude and Range with Fog	225
5.1-3	Variation of Runway Image Call Altitude and Range Between and Within Airports	227
5.1-4	Rain-Rate Versus Range Where Pilot Called Runway Image	231
5.1-5	Rain-Rate Profile for Three Selected Runs From Figure 5.1-4	238

LIST OF ILLUSTRATIONS (CONTINUED)

5.1-6	Cooper Harper Handling Qualities Rating (HQR) Scale	235
5.1-7	Modified Cooper Harper Workload Rating Scale (MCH)	236
5.1-8	Pilot Questionnaire	237
5.1-9	Correlation Between Workload Ratings and Acceptability for Normal Operations	237
5.1-10	Frequency Distribution of Pilot Workload Rating Data for Simulating CAT IIIa and CAT IIIc Approaches	239
5.1-11	Observed Problem Descending to Low Minimums Without Vertical Guidance	241
5.1-12	Illustration of Near-Range Problem experienced With 35-GHz MMW During Flare and Rollout	244
5.1-13	Frequency Distribution of Pilot Workload Rating Data for Actual CAT II and CAT IIIa Approaches	248
5.1-14	Observed Beam Bend Problem at SMX - Actual CAT IIIc Conditions	249
5.1-15	Workload Ratings for All CAT I, CAT II, and CAT IIIa Approaches	251
5.2-1	Glideslope Deviation Values	256
5.2-2	Glideslope Deviation Histogram	257
5.2-3	Localizer Deviation Values	258
5.2-4	Localizer Deviation Histogram	259
5.2-5	Sink Rate Values	262
5.2-6	Sink Rate Histogram	263
6.1-1	Plot of Normalized RCS Versus Depression Angle for Both Runway and Terrain At Arcata, CA, on August 27, 1992 (Approach 2A)	267
6.1-2	Plot of Normalized RCS Versus Depression Angle for Both Runway and Terrain At Vandenburg Air Force Base, CA, on August 19, 1992 (Approach 2C)	268
6.1-3	Plot of Normalized RCS Versus Depression Angle for Both Runway and Terrain At Santa Maria, CA, on August 20, 1992 (Approach 1A)	269
6.1-4	Plot of Normalized RCS Versus Depression Angle for Both Runway and Terrain At Santa Barbara, CA, on August 20, 1992 (Approach 1C)	270
6.1-5	Plot of Normalized RCS Versus Depression Angle for Both Runway and Terrain and Noise Floor Estimates at Santa Barbara, CA. Data Correspond to an Altitude of 47.95m During Approach 1C on August 19, 1992	271
6.1-6	Image Displaying A/D Counts and Corresponding Received Power File in RAM	272
6.1-7	Plot of Normalized RCS Versus Depression Angle for Runway, Terrain and Noise Floor Estimates at Santa Barbara, CA. Data Correspond to an Altitude of 47.95m During Approach 1C on August 19, 1992 Data Excluded Due to Noise-Floor Limits Are Circled	274
6.1-8	Plot of Normalized RCS Versus Depression Angle for Runway, Terrain and Noise Floor Estimates at Santa Barbara, CA. Data Correspond to an Altitude of 35.16m During Approach 1C on August 19, 1992 Data Excluded Due to Noise-Floor Limits Are Circled	275

LIST OF ILLUSTRATIONS (CONTINUED)

6.1-9 Plot of Normalized RCS Versus Depression Angle for Runway, Terrain and Noise Floor Estimates at Santa Barbara, CA. Data Correspond to an Altitude of 17.92m During Approach 1C on August 19, 1992 Data Excluded Due to Noise-Floor Limits Are Circled 276

6.1-10 Plot of Normalized RCS Versus Depression Angle for Runway, Terrain, at Santa Barbara, CA. on August 19, 1992 (Approach 1C)..... 277

6.1-11 Summary of Normalized RCS Versus Depression Angle Plots for the Four Airports..... 279

6.1-12 Total Atmospheric Attenuation Due to Both Water and Oxygen For Several Different Relative Humidities..... 284

6.1-13 Atmospheric Attenuation in Fog at Four Different Radar Frequencies..... 285

6.1-14 Typical Raindrop Size Distribution at 5.3 mm/hr Rain Rate, From Tower Measurements 286

6.1-15 Measured Attenuation in Rain From 35 GHz Tower Tests..... 292

6.1-16 Measured Volumetric RCS in Rain From 35 GHz Tower Tests..... 295

6.1-17 Plot of Contrast Versus Range to Region of Interest for Clear Weather at Vandenburg Air Force Base on August 19, 1992 (Approach 2A-2D)..... 299

6.1-18 Plot of Contrast LMSE Linear Fit Versus Range to Region of Interest for Twelve Clear Weather Airports. Different Line Symbols are used for each Runway Composition Type..... 302

6.1-19 Plot of Contrast Versus Range to Region of Interest for Twelve Clear Weather Approaches. Approximate Contrast Levels Corresponding to Pilot Detection Ranges are Indicated 303

6.1-20 Plot of Contrast Versus Range to Region of Interest for Fog Approaches at Arcata, CA on August 28, 1992. Data are taken from snapshots with an Integrated LWC of 0.00 to 0.09 g/m^3 306

6.1-21 Plot of Contrast Versus Range to Region of Interest for Fog Approaches at Arcata, CA on August 28, 1992. Data are taken from snapshots with an Integrated LWC of 0.09 to 0.13 g/m^3 307

6.1-22 Plot of Contrast Versus Range to Region of Interest for Fog Approaches at Arcata, CA on August 28, 1992. Data are taken from snapshots with an Integrated LWC of 0.13 to 0.20 g/m^3 308

6.1-23 Plot of Contrast Versus Range to Region of Interest for Fog Approaches at Arcata, CA on August 28, 1992. Data are presented as the :MSE Lines Fitted to the Measured Values for each LWC Interval 309

6.1-24 Plot of Contrast Versus Range to Region of Interest for Fog Approaches at Vandenburg Air Force Base, CA on August 11, 1992. Data are Presented as the LMSE Lines Fitted to the Measured Values for Each LWC Interval.... 311

6.1-25 Plot of Contrast Versus Range to Region of Interest for Fog Approaches at Vandenburg Air Force Base, CA on August 11, 1992. Data are Presented as the LMSE Lines Fitted to the Measured Values for Each LWC Interval.... 312

6.1-26 Plot of Measured Contrast Versus Range for the Honeywell Radar for Three Rain Rates at the Tower..... 316

6.1-27 Plot of Contrast Versus Range to Region of Interest for Snow Approached at Pueblo, CO on November 20, 1992. The Runway and Terrain were covered with snow 318

6.1-28 Plot of Measured Contrast Versus Range for the Honeywell Radar in Clear Weather, Fog, and Snow at the Tower 320

LIST OF ILLUSTRATIONS (CONTINUED)

6.1-29 Plot of Contrast Versus Range to Region of Interest for Snow Approaches at Pueblo, CO, on November 21, 1992. The Runway had been Plowed, but Patches of Snow and Ice Remained 322

6.1-30 Plot of Contrast Versus Range to Region of Interest for Snow Approaches at Pueblo, CO, on November 21, 1992. The Runway had been Plowed 323

6.1-31 Plot of Contrast Versus Range to Region of Interest for Snow Approaches at Pueblo, CO, on November 21, 1992. Data are Presented as the LMSE Lines Fitted to the Measured Values for each Sortie 324

6.1-32 Plot of Sharpness (In Inverse Degrees) Versus Range to Region of Interest for Fog Approaches at Arcata, CA on August 28, 1992. Data are Taken from Snapshots with an Integrated LWC of 0.00 to 0.09 g/m^3 328

6.1-33 Plot of Sharpness (In Pixels) Versus Range to Region of Interest for Fog Approaches at Arcata, CA on August 28, 1992. Data are Taken from Snapshots with an Integrated LWC of 0.00 to 0.09 g/m^3 329

6.1-34 Plot of Sharpness (In Pixels) Versus Range to Region of Interest for Fog Approaches at Arcata, CA on August 28, 1992. Data are Taken from Snapshots with an Integrated LWC of 0.09 to 0.13 g/m^3 330

6.1-35 Plot of Sharpness (In Pixels) Versus Range to Region of Interest for Fog Approaches at Arcata, CA on August 28, 1992. Data are Taken from Snapshots with an Integrated LWC of 0.13 to 0.19 g/m^3 331

6.1-36 Plot of Sharpness (In Pixels) Versus Range to Region of Interest for Snow Approaches at Pueblo, CO and Colorado Springs, CO on November 20, 21, 1992 333

6.1-37 Illustration of Normal Transitioin-Point Selection in Sample Gutter Plot 335

6.1-38 Illustration of Alternative Transition-Point Selection in Sample Gutter Plot 336

6.1-39 Illustration of Sharpness "Penalty" for High-Contrast Scenes 338

6.1-40 Plot of Signal-To-Variability Ratio Versus Range to Region of Interest for Fog Runs at Arcata, CA on August 28, 1992. Data are Taken From Snapshops With An Integrated LWC of 0.00 to 0.09 g/m^3 340

6.1-41 Plot of Signal-To-Variability Ratio Versus Range to Region of Interest for Fog Runs at Arcata, CA on August 28, 1992. Data are Taken From Snapshops With An Integrated LWC of 0.09 to 0.13 g/m^3 341

6.1-42 Plot of Signal-To-Variability Ratio Versus Range to Region of Interest for Fog Runs at Arcata, CA on August 28, 1992. Data are Taken From Snapshops With An Integrated LWC of 0.13 to 0.20 g/m^3 342

6.1-43 Plot of Signal-To-Variability Ratio Versus Range to Region of Interest for Snow Runs at Pueblo, CO and Colorado Springs, CO on August 20, 21, 1992 343

6.1-44 Plot of Signal Versus Range to Tegion of Interest for all Fog Runs at Arcata, CA on August 28, 1992 344

6.1-45 Plot of Terrain Variablity Versus Range to Region of Interest for all Fog Runs at Arcata, CA on August 28, 1992 345

6.1-46 Plot of Runway Variability Versus Range to Region of Interest for all Fog Runs at Arcata, CA on August 28, 1992 346

6.1-47 Conceptual Illustration of Gutter Plot and PPI Display for Low and High SVR Scenarios 349

LIST OF ILLUSTRATIONS (CONTINUED)

6.1-48 Plot of Signal-To-Variability Ratio Versus Range for Honeywell Tower Test Data in Clear Weather, Fog and Snow 351
6.1-49 Plot of Signal-To-Variability Ratio Versus Range for Honeywell Tower Test Data for Rain Rates of 1.2, 5.3, and 12.9 mm/hr 352
6.1-50 Magnified Portion of PPI Image from Vandenburg Air Force Base, CA 357
7.1 Contrast - August 18, 1992-2B (NTD at 2.5 KM) 361
7.2 Contrast - August 18, 1992-2B (NTD at 200' AGL) 361
7.3 Contrast - August 18, 1992-2B (NTD at 50' AGL) 362
7.4 Contrast - August 18, 1992-2B (NTD at Pilot Confirms Runway) 362
7.5 Contrast - August 18, 1992-2B (NTD at Pilot Confirms Runway) 363
7.6 Contrast - August 18, 1992-2B (NTD at Pilot Confirms Runway) 363
7.7 Contrast - August 18, 1992-2B (NTD at Pilot Confirms Runway) 364
7.8 Contrast - August 18, 1992-2B (NTD at Pilot Confirms Runway) 364
7.9 Contrast - August 28, 1992-1A (ACV at Pilot Confirms Runway) 365
7.10 Contrast - August 28, 1992-1A (ACV at Pilot Confirms Runway) 365
7.11 Contrast - August 28, 1992-1C (ACV at Pilot Confirms Runway) 366
7.12 Contrast - August 28, 1992-1D (ACV at Pilot Confirms Runway) 366
7.13 Contrast - August 28, 1992-1E (ACV at Pilot Confirms Runway) 367
7.14 Contrast - August 28, 1992-1F (ACV at Pilot Confirms Runway) 367
7.15 Contrast - August 28, 1992-1G (ACV at Pilot Confirms Runway) 368
7.16 Contrast - August 28, 1992-1H (ACV at Pilot Confirms Runway) 368
7.17 Contrast - September 25, 1992-1B (LFI at Pilot Confirms Runway) 369
7.18 Contrast - September 25, 1992-1B (LFI at Pilot Confirms Runway) 369
7.19 Contrast - September 25, 1992-1D (NHK at Pilot Confirms Runway) 370
7.20 Contrast - September 27, 1992-1C (NHK at Pilot Confirms Runway) 370
7.21 Contrast - September 27, 1992-1E (NHK at Pilot Confirms Runway) 371
7.22 Contrast - September 27, 1992-1B (MIV at Pilot Confirms Runway) 371
7.23 Contrast - September 25, 1992-1I (ACY at Pilot Confirms Runway) 372
7.24 Contrast - September 27, 1992-1A (ACY at Pilot Confirms Runway) 372
7.25 Contrast - September 26, 1992-2A (ORH at Pilot Confirms Runway) 373
7.26 Contrast - September 26, 1992-2B (ORH at Pilot Confirms Runway) 373
7.27 Contrast - September 26, 1992-2C (ORH at Pilot Confirms Runway) 374
7.28 Contrast - September 28, 1992-1B (HTS at Pilot Confirms Runway) 374

LIST OF TABLES

Table	Title	Page
3.1-1	Aircraft Avionics	28
3.2.1	Description of Primary Test Airports	35
4.1.1	Summary of Project Objectives and Accomplishments	38
4.4.1-1	Selected Radar Characteristics Important for Synthetic Vision	55
4.4.2-1	Summary of Raw Data Available from Flight Test of the Honeywell 35GHz Radar System	61
4.4.2-2	List of Primary Aircraft	64
4.4.2-3	Desired Ground-Truth Data From Airport Sites	65
4.4.2-4	Honeywell File Header Format	74
4.4.2-5	Measured receiver response	82
4.4.2-6	Average Recorded A/D Count Values for Selected Injected Power Levels and Gain/Bais Settings	85
4.4.2-7	Fixed Honeywell System Parameters Used to Compute RCS	95
4.4.2-8	Honeywell System Parameters Used in Computing Illuminated Area	96
4.4.2-9	Altitudes for Snapshots of Interest	111
4.4.2-10	Azimuth Width Versus Range for 10dB and 15 dB Beamwidths	127
4.4.3-1	Summary of Measured RCS Values For Both Bruderhedral Reflectors at Arcata, CA on August 27, 1992 (Approach 2A). All Angles Are In Degrees and All Reflector Values Are in DBSM	153
4.4.3-2	Summary of Measured RCS Values for Both Bruderhedral Reflectorsat Arcata, CA on August 27, 1992 (Approach 2C). All Angles Are in Degrees and All Reflector Values are in DBSM	157
4.4.3-3	Summary of Absolute Calibration Data From Arcata, California on 8/27/92	166
4.4.3-4	Summary of Measures RCS Values for Both Bruderhedral Reflectors at Vandenburg Air Force Base, CA on August 19, 1992 (Approach 2C). All Angles are in Degrees and All Reflector Values Are in dBsm	168
4.4.3-4	Summary of Measures RCS Values for Both Bruderhedral Reflectors at Vandenburg Air Force Base, CA on August 19, 1992 (Approach 2C). All Angles are in Degrees and All Reflector Values Are in dBsm	169
4.4.3-6	Summary of Absolute Calibration Data from Vandenburg AFB, California on 8/19/92	178
4.4.3-7	Summary of Measures RCS Values for Both Bruderhedral Reflectors at Santa Barbara, CA on August 19, 1992 (Approach 1B). All Angles are in Degrees and All Reflector Values Are in dBsm	181
4.4.3-8	Summary of Measures RCS Values for Both Bruderhedral Reflectors at Santa Barbara, CA on August 19, 1992 (Approach 1C). All Angles are in Degrees and All Reflector Values Are in dBsm	182
4.4.3-9	Summary of Measures RCS Values for Both Bruderhedral Reflectors at Santa Barbara, CA on August 19, 1992 (Approach 1D). All Angles are in Degrees and All Reflector Values Are in DBsm	183
4.4.3-10	Summary of Absolute Calibration Data from Santa Barbara, California on 8/19/92	197
4.4.3-11	Summary of Measures RCS Values for Both Bruderhedral Reflectors at Santa Maria, CA on August 19, 1992 (Approach 1B). All Angles are in Degrees and All Reflector Values Are in dBsm	199
4.4.3-12	Summary of Measures RCS Values for Both Bruderhedral Reflectors at Santa Maria, CA on August 19, 1992 (Approach 1C). All Angles are in Degrees and All Reflector Values Are in dBsm	200

LIST OF TABLES (CONTINUED)

4.4.3-13	Summary of Absolute Calibration Data from Santa Maria, California on 8/20/92	209
4.4.3-14	Summary of Absolute Calibration Results From Four Airports	210
5.1-1	Estimated Probability of a Missed Approach Because Pilot Could Not Call Runway Image Prior to 250 feet Above The Runway	226
5.1-2	Runway Image Call Data for Primary Test Airports	228
5.1-3	Runway Image Call Data for Each Evaluation Pilot	229
5.1-4	Performance Standards	238
5.1-5	Required Range From Runway Threshold for an MMW Radar Used for Non-Precision Approaches	243
5.1-6	Results of Pilot Questionnaire	252
5.2-1	Localizer and Glideslope RMS Deviations	260
5.2-2	Localizer and Glideslope RMS Deviations Without ILS for Two Pilots	260
6.1-1	Measured RCS Values for GMC Suburban at Pt. Mugu, CA on 8/18/92	280
6.1-2	Measured One-Way Fog Attenuation and Volumetric Reflectivity at 35 GHZ for Approach 1A at Arcata on 8/28/92	289
6.1-3	Measured One-Way Fog Attenuation and Volumetric Reflectivity at 35 GHZ For Approach 1F at VANDENBURG AFB, CA on 8/27/92	289
6.1-4	35 GHZ Attenuation in dB/km as a Function of Snow Concentration -g/m3 (Equivalent Rain Rate - mm/hr)	318
7.1	Summary of Contrast Metric Correlation to Runway Detection	375

SECTION 1.

INTRODUCTION

1.1. Overview of Flight Test Program

The Joint FAA/DoD/Industry Synthetic Vision System Technology Demonstration Program issued TRW, Inc. a Contractual Engineering Task (CET) for the System Integration, Evaluation and Demonstration (SIED) of a functional prototype synthetic vision system in an executive class aircraft. The USAF Sacramento Air Logistics Center (SMALC) provided the Contractual Engineering Task (ET) contracting vehicle through it's Micro Technology Support Program (MTSP).

TRW then organized a team of experts within industry through a series of subcontracts and, in conjunction with the Synthetic Vision Program Office (SVPO), managed the integration, installation and operation of an experimental functional prototype synthetic vision system on-board a Gulfstream II aircraft and both evaluated and demonstrated its capabilities. This SIED team managed three simultaneous activity threads to meet the schedule and resource constraints.

First, the SIED team developed a functional prototype synthetic vision system (FPSVS) that could accommodate multiple millimeter wavelength sensors and a full time infra-red sensor. Display capability on both head-up and head-down devices was provided along with television viewing of the out-the-window scene. Control law and mode selection options were installed to allow the pilot to explore low visibility approaches both with and without ILS based flight director guidance assistance. This experimental system was required to perform the essential functions of a synthetic vision system, hence it was designated a Functional Prototype Synthetic Vision System (FPSP).

Second, the SIED team designed and implemented a data acquisition system which supported complete documentation of the flight results in quantitative terms as well as qualitative data reduction and analysis. This system also included extensive real time measurement of the actual weather conditions through which the aircraft flew during approach, landing, taxi and takeoff operations at selected airports.

Third, the SIED team designed the necessary experiments and carried out a full program for the demonstration and evaluation of the experimental system's capabilities. This

included the development of the overall program plan and specifications for all system elements, management of all subcontracts, and the development and operation of the data acquisition system and data reduction system. The effort included the preparation of the safety and operational analysis required to obtain FAA waivers to conduct actual weather operations below the G-II's Category I certification down to Category IIIa minimums.

Key to the success in accomplishing the task was the team work as well as the individual efforts of the multi-disciplined team of TRW personnel, members of the SVS Program Office, subcontractors, and consultants which provided the broad base of technical and operational expertise.

The SIED Task commenced on 11 March 1991 and was completed on 28 February 1993.

1.2. Objectives

The objectives of the SIED task were to implement, demonstrate and document the capabilities of a functional prototype synthetic vision system using existing technologies on-board an executive class aircraft. MMW and FLIR sensor data were to be collected, along with measured weather data, aircraft performance data and pilot performance data for analyses and documentation. This was to be accomplished under varying weather conditions and at a variety of airports for approach, landing and ground operations.

1.3. Approach

An experimental design, capable of achieving the program objectives, was developed that would:

- Empirically measure the achieved performance of the integrated pilot/synthetic vision system during low visibility operations.
- Assess the pilots capabilities and workload when using the functional prototype synthetic vision system
- Determine the operational characteristics of the imaging sensor used in the functional prototype synthetic vision system in terms of the airport environment and actual weather encountered.
    - Measure the physical phenomena of millimeter wavelength radar imaging of airport scenes at low grazing angles.
    - Measure performance of the millimeter wavelength radar and its image processing under operational conditions.
    - Measure performance of the forward looking infra-red sensor under operational conditions.

- Measure the actual weather conditions that the aircraft encounters when measuring the above phenomena and sensor performance.

- Determine, document, and correlate the actual weather conditions existing between the aircraft and the runway for all approaches in actual weather.
- Determine the image quality in a manner that can be correlated to achieved performance and is transferable to future synthetic vision systems.

Figure 1.1-1 presents the operational approach used in making the evaluation measurements listed above. They included :

- Manually flown precision approaches through the end of roll out or missed approach point.
- Manually flown non-precision approaches through the end of roll out or missed approach point.
- Manually flown non-precision approaches with a no-navaid final segment.
- Ground operations including taxi, roll out and takeoff.

Simulation was used to determine the symbology to be displayed on the head-up and head-down displays and the pilot interface with the appropriate controls. Simulation was also used to develop the necessary crew procedures for normal and abnormal operations in actual IMC flights in the G-II aircraft.

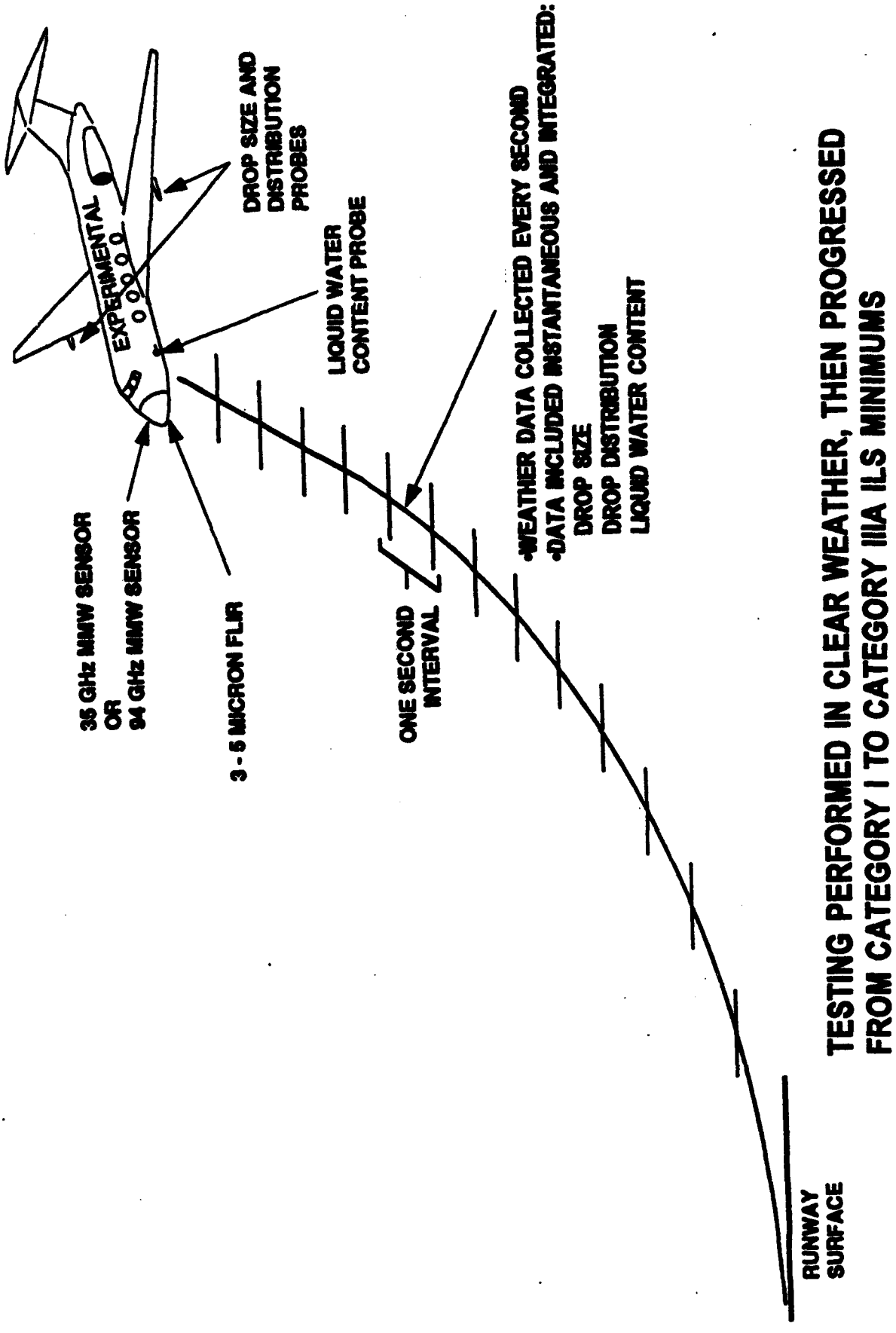

Figure 1.1-1 Flight Test Methodology

The major program milestones defined as part of the Program Plan were:

Requirements Study Complete
Simulation Task Complete
Preliminary Design Review
Critical Design Review
Flight Test Plan
Safety Plan and Hazard Analysis
Flight Readiness Reviews
Suitability Flights
Waiver to go below CAT 1 minimums
Evaluation and Demonstration Flights

The Honeywell 35 GHz. MMW sensor was designated by the SVPO as the primary MMW sensor and was delivered in April of 1992 for hot bench integration and test. It was installed in the aircraft and began flight test (suitability) in June of 1992.

The Lear Astronics 94 GHz. MMW radar became available in October of 1992 and was flown in November 1992. The Kodak 3-5 micron FLIR was delivered in the same time period as the Honeywell sensor and flew throughout the flight test program to document FLIR capability in weather.

Each MMW sensor (Honeywell or Lear) had its own data collection system which was accommodated by and interfaced to the TRW system installed in the test aircraft (See Figure 1.1-2). The raw data collected by these MMW sensors were analyzed by Georgia Tech Research Institute (GTRI) as both proprietary and non-proprietary data. The proprietary data has been documented by GTRI and supplied to the government as a separate proprietary report. The non-proprietary results were supplied by GTRI for incorporation in this report.

To further define and document how these objectives were to be achieved, the SVSTD/SIED Program Plan was created (Plan is provided in Volume 4 of this Final Report). Volume 1 of the Program Plan defined the methodology, tasks, responsible personnel and schedules to ensure program success within the budget and schedule limitations. Volume 2 of the Program Plan defined the experimental design of the flight evaluation phase of the SIED including the prioritized test matrix.

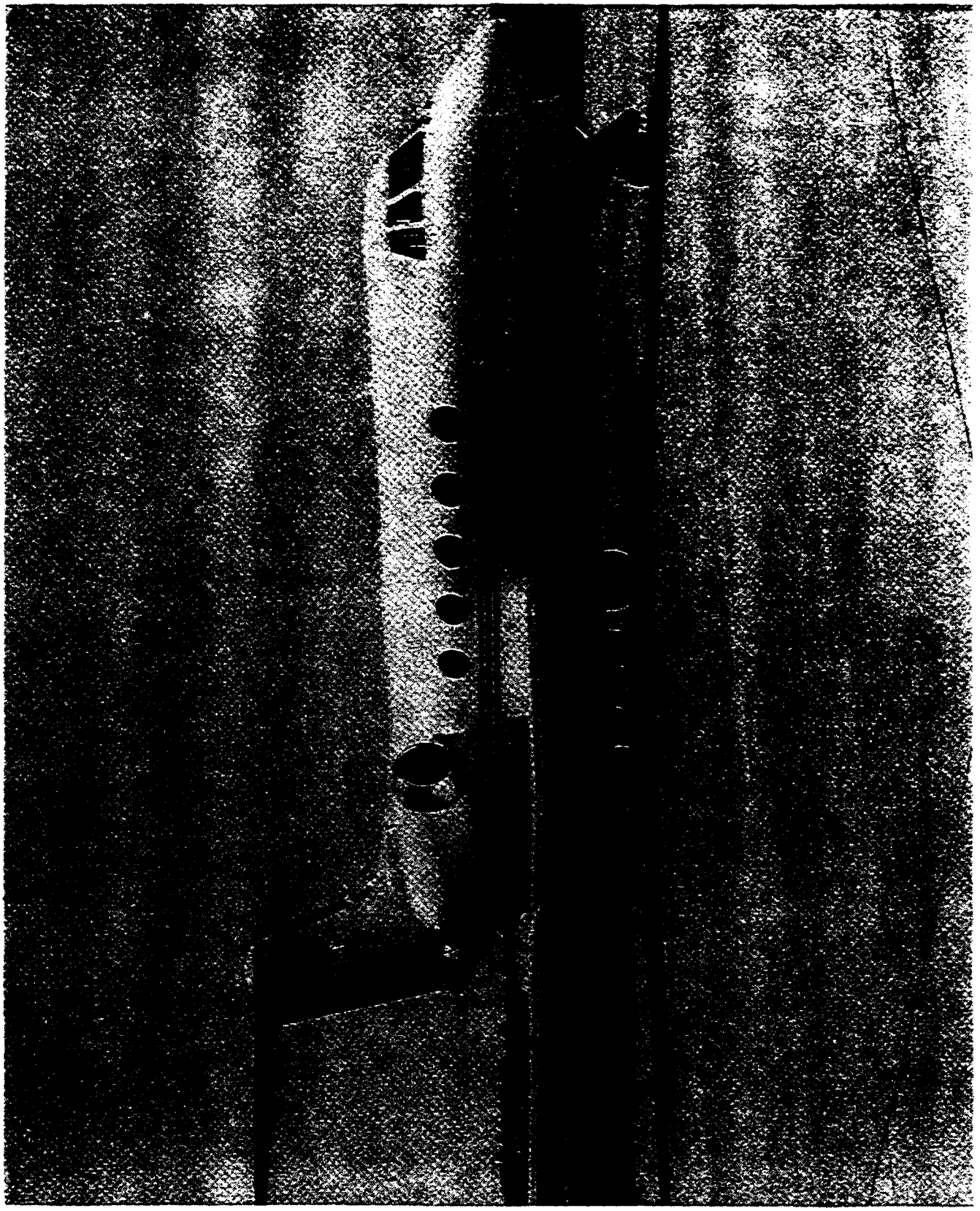

Figure 1.1-2. Gulfstream II Flight Test Aircraft

1.4. Scope

The SIED effort was divided into the following three major areas:

System Design:

System design included definition of experiments and scenarios, test methodology, flight test matrixes, Functional Prototype SVS performance requirements, data analyses to be performed, requirements and methods for simulation, data elements/source requirements, and the safety plan.

To reduce risk to the SVS design and implementation, a simulation effort was accomplished using the McDonnell Douglas Aircraft (DAC) MD-11 fixed base simulator in Long Beach, California. The simulator employed a head-up display (HUD) provided by GEC that projected both stroke and raster to the combiner. DAC provided simulated raster superimposed on the GEC stroke symbology. The simulator was essential for pilot familiarization and for developing the crew safety procedures.

The functional prototype and its implementation and integration consisted of the definition and development of the sensors, HUD, cockpit controls, interfaces, data acquisition and data reduction system and the test and observer stations. Also included was the generation of detailed requirements and specifications, integration and test plans, and configuration management required to successfully integrate the SVS system.

A ground-based "Hot Bench" was used to integrate and test the sensors, HUD, and aircraft interfaces prior to installation on the aircraft. This tool was invaluable in meeting the schedule, minimizing aircraft lease time and reducing costs. The "Hot Bench" used a cable harness that was a duplicate of the harness built for the aircraft.

Aircraft Preparation

Aircraft preparation consisted of the selection and acquisition of a Gulfstream aircraft, and the engineering and modifications necessary to support the SVS flight tests. This included the following tasks:

- Design and fabrication of both a 35 and 94 GHz. radome that supports the operation of the FLIR.
- Mounting pylons on the wings for the weather pods and probes.
- Mounting for the head-up display and head-down display.
- Cockpit controls.
- Cockpit mounted windshield TV camera.

- Cabin modifications for the data acquisition racks.
- Wire harness fabrication and installation.
- Additional power sources.
- The associated analyses and flight safety tests.

These efforts provided an experimental category Gulfstream II aircraft suitable for supporting the flight test portion of the program.

Flight Operations

The flight operations effort consisted of the flight planning phase to establish the flight parameters such as base of operations, scheduling, and deployment. Such factors as weather forecasting, experimental flight approval and restrictions, flight procedures, mission rules, and data handling procedures were elements of the planning.

Scheduling of the aircraft was based on the development of a prioritized test matrix. This test matrix considered the parameters of the airport type, the weather and the type of flight operation including approach and ground tests.

Suitability flights of the Honeywell 35 GHz. radar were flown to determine the suitability of the sensor to operate in weather with acceptable performance. A waiver was requested and received from the FAA to operate down to CAT IIIa minimums at specified TYPE I ILS airports based on the performance of the sensor and HUD and the Flight Readiness Review results.

Evaluation flights were flown initially in visual weather conditions using a windshield cover on the evaluation pilot's side of the cockpit to simulate IMC. Flights were then conducted in actual weather conditions to CAT I minimums and progressing, as crew experience and proficiency permitted, to CAT IIIa minimums. Data were collected at both the sensor and system level for selected analyses.

1.5. Organization and Responsibilities

TRW, as prime contractor, selected key subcontractors to provide the necessary expertise and cap-abilities to help develop, integrate, install and operate the SVS (see Figure 1.5-1). In addition, TRW hired specific consultants to support various activities and provide the necessary expert guidance for program success.

Project Team

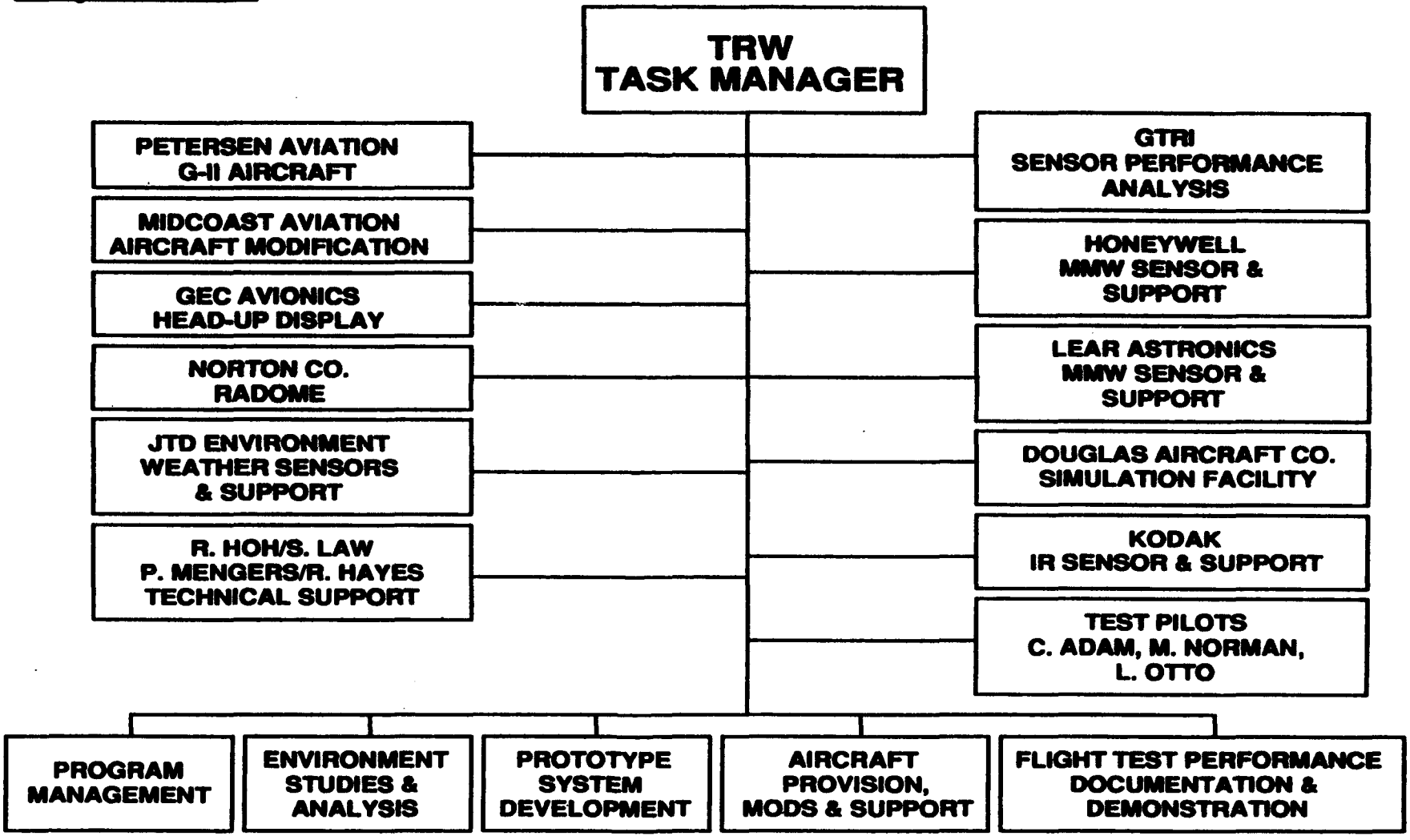

Figure 1.1-5. SIED Project Team

The team consisted of:

TRW	Prime Contractor responsible to the SVPO for the management of the task.
Petersen Aviation	Subcontractor for the Gulfstream II aircraft and its operation.
Mid-Coast Aviation	Subcontractor for the aircraft engineering and modifications.
GEC Avionics	Subcontractor for the Head-up Display and its operation including hardware and software
Honeywell Inc.	Associate team member for the 35 GHz. MMW sensor hardware and support of its operation.
Lear Astronics	Subcontractor for the 94 GHz. MMW sensor hardware and support of its operation.
Eastman Kodak	Subcontractor for the FLIR and support of its operation.
Georgia Tech Research Institute	Subcontractor for the raw radar data analysis
Norton Company	Subcontractor for the modified radomes for both MMW sensors and FLIR.
JTD, Inc.	Subcontractor for the weather sensors and analysis.
Douglas Aircraft Company	Subcontractor for simulation support
Roger Hoh	Flight test director and consultant for flight test and simulation design and analyses
Stuart W. Law	Consultant for program support and test analysis.
Robert D. Hayes	Consultant for radar analysis.
Paul Mengers	Consultant for video image quality analysis.

The SIED Contractor, TRW, developed a Work Breakdown Structure (WBS) that identified all the tasks necessary for meeting the program contractual commitments. The WBS included all subcontractor and consultant tasks and was used as the basis for the Resource Allocation Plan (RAP).

The RAP was used to measure the task costs on a monthly basis and to allow reassessment of any task based on efforts versus cost. In this way the tasks could be modified when necessary to optimize the total effort required for success of the task and the effects on SIED task costs could be clearly understood and managed.

1.6. Final Report Organization

This volume, Volume 3 of the Synthetic Vision System Technology Demonstration Program Final Report, describes the efforts carried out in the System Integration, Evaluation and Documentation(SIED) Task and the results.

Following the Introduction (Section 1) and a brief description of the management of the SIED Task (Section 2), a brief description of the facilities used for the SIED Task is presented including a description of the experimental system (Section 3). The MMW sensors are described in detail as to their method of operation, unique features and other non-proprietary characteristics. The FLIR sensor is described relative to its operation in the test program. Also described is the Head-Up Display (HUD) and its operation. This includes descriptions of the hardware, registration issues and calibration procedures. The HUD symbology is discussed as to its origin and modifications for this program. A brief description is provided of the Weather Sensors addressing the hardware, software and implementation. This section also describes the Data Acquisition and Data Reduction systems and the aircraft interfaces to the sensors. A description of the airports that were used for the program is presented in this section. Lastly, a description of the Ground-Based Simulator is presented with an overview of its implementation, operation and usefulness to the system development and flight test program.

Flight Test Methods and Procedures are then described (Section 4) in which test objectives and accomplishments are summarized, the backgrounds of the pilots are outlined, flight procedures in low visibilities are described, and the methodology and procedures used for measuring sensor performance are and image quality is described. A significant effort was undertaken in this SIED Task to develop useful techniques for measuring the performance of such imaging systems for use in future efforts; a substantial amount of information is incorporated in this section as a result.

The results of the SIED Task are presented (Section 5) in terms of the system and pilot performance. The description of the results includes the effects on system and pilot performance of the various weather conditions that affect visibility including rain, fog and snow. The effects of various airport surface materials and weather conditions both on the ground and in the atmosphere on specific metrics such as radar contrast, sharpness and variability are addressed.

System performance is discussed relative to image quality and its correlation to the MMW radar performance metrics. Pilot and system performance results are summarized for

clear air, fog, rain and snow conditions and include such analyses as the correlation of when the pilot identified the runway image and the quality of the image at that time. Landing system guidance tracking performance is discussed as is the pilot's opinion of the workload during the approach. Pilot performance is also compared to pilot opinion of system performance for various aircraft operations.

Sensor performance is then described (Section 6); the presentation consists of analyses performed by GTRI of the performance of the 35 GHz radar during the flight tests of the experimental synthetic vision system. Specific metrics such as radar contrast, sharpness and variability are used in the examination of the effects of surface materials and weather conditions both on the ground and in the atmosphere. Also included for selected airports is documentation of such absolute measures as volumetric backscatter and scene radar cross section. The performance of the 94 GHz radar and of the 3-5 micron FLIR sensor are also discussed at the sensor system level.

A brief summary of the quality of the image produced by the sensor system is provided (Section 7). System issues addressed include sensor range, resolution and sharpness. Also addressed are the HUD design , radar minimum range, display registration, and system latency improvements needed. Other issues addressed include image enhancement, runway intrusion detection, and unwanted image artifacts.

The report provides a summary of the lessons learned (Section 8) by the SIED team in the course of carrying out this flight test program, and then ends with a statement of the conclusions (Section 9).

SECTION II

TASK MANAGEMENT

Management and system engineering processes were tailored specifically to the SIED Task to ensure that the objectives were simple and clearly understood by all, that the resources available for the task were clearly visible and carefully managed, and that adequate planning was undertaken to minimize the number and magnitude of surprises.

The management process established the work breakdown structure and responsibilities which derived directly from the objectives. The engineering process provided the technical approach that began with the objectives, progressed to functional and system requirements and continued through system design trade-off studies, system design, implementation, and flight test.

2.1. Management Process

The management process started with the generation of the Program Plan (Appendix A) that identified the scope of the program and the goals, objectives and methods. An experimental design was defined that in turn determined the program efforts and operational scenarios. Flight experiments were established in terms of priorities and conditions that would provide the basic phenomenology data to be collected and analyzed. These flight experiments also supported an assessment of the functional prototype sensor performance and provided data permitting extrapolation to the performance of future systems.

As part of the program plan, a management approach was adopted that identified individual responsibilities and all aspects of the SIED tasks to be completed. TRW developed a Work Breakdown Structure which defined the tasks and schedules that needed to be performed. A team of subcontractors and consultants was established along with TRW internal personnel to accomplish the associated tasks. Subcontract Statements Of Work were generated for each vendor for both competitive and single source solicitations. The appropriate vendors were selected and subcontracts established for their participation on the program. The same was true for consultants and agreements established between TRW and the consultants selected for participation.

TRW, the SVPO, the subcontractors and the consultants organized the pertinent milestones into a single collection of schedules and tasks for determining and tracking progress.

A task dependency network was developed showing both critical and near-critical paths across all team members. A resource allocation plan that included tracking mechanisms operating on a monthly basis as well as on key decisions was established to assure that project resources were properly distributed to permit achievement of the goals and objectives on schedule within contract requirements.

The SVPO and TRW established an open forum environment to allow all team members to not only be made aware of their individual responsibilities, but also how their work was to contribute to the overall effort. Inputs, suggestions, and criticisms from all participants were encouraged, both individually and collectively, through project management meetings and Technical Interchange Meetings (TIM's). Frequent communications through these TIM's and the telephone ensured that the work maintained schedule performance in addition to meeting the SIED task commitments.

Planned project reviews consisting of the Preliminary and Critical Design Reviews along with Flight Readiness Reviews assured that the program requirements were met and that the SIED team operated as a single entity in the design and integration process.

Major Milestones. The following major milestones were established and accomplished during the program.

Program Milestones	
Milestone	**Date**
Task Accomplishment Plan	April 1991
Head-up Display Selection	April 1991
Radome Specification	May 1991
FPSVS Requirements Study	June 1991
Simulation Requirements	June 1991
Aircraft Selection	July 1991
Preliminary Design Review	July 1991
Critical Design Review	Nov/Dec 1991
Program Plan	February 1992
35 GHz. Radome Available	February 1992
Hot Bench I&T	February 1992
Flight Test Plan	March 1992
Safety Plan	March 1992
FAA Experimental Certificate	March 1992
Flight Readiness Review No. 1	April 1992
Suitability Flights (35 GHz.)	May 1992
Evaluation Flights (35 GHz.)	July 1992
Flight Readiness Review No. 2	August 1992
FAA Waiver To CAT IIIa	August 1992
Suitability Flights (94 GHz,)	October 1992
Continue Eval. Flights (35 GHz.)	November 1992
Final CIST conference Meeting	January 1993
Final Report	February 1993

2.2. Engineering Process

To accomplish the goal of the Synthetic Vision System Integration and Evaluation Development Task to demonstrate and evaluate existing sensor, display and computer processing technologies on a flying test bed, a SV System had to be developed and integrated into an aircraft for the flight test. The experimental system would consist of the sensors, pilot displays, data acquisition system, and appropriate cabin displays for the test engineers. The flight tests would also require a test crew, test pilots and safety pilots.

The Functional Prototype System is diagrammed in Figure 2.2-1, Functional Prototype System Block Diagram. There are two independent MMW sensors and a FLIR sensor. These sensors produced a video image, RS-170. This signal was routed to the Pilot displays, cabin displays, and Data Recorders (VCR). The HUD, based on existing avionics data, produced

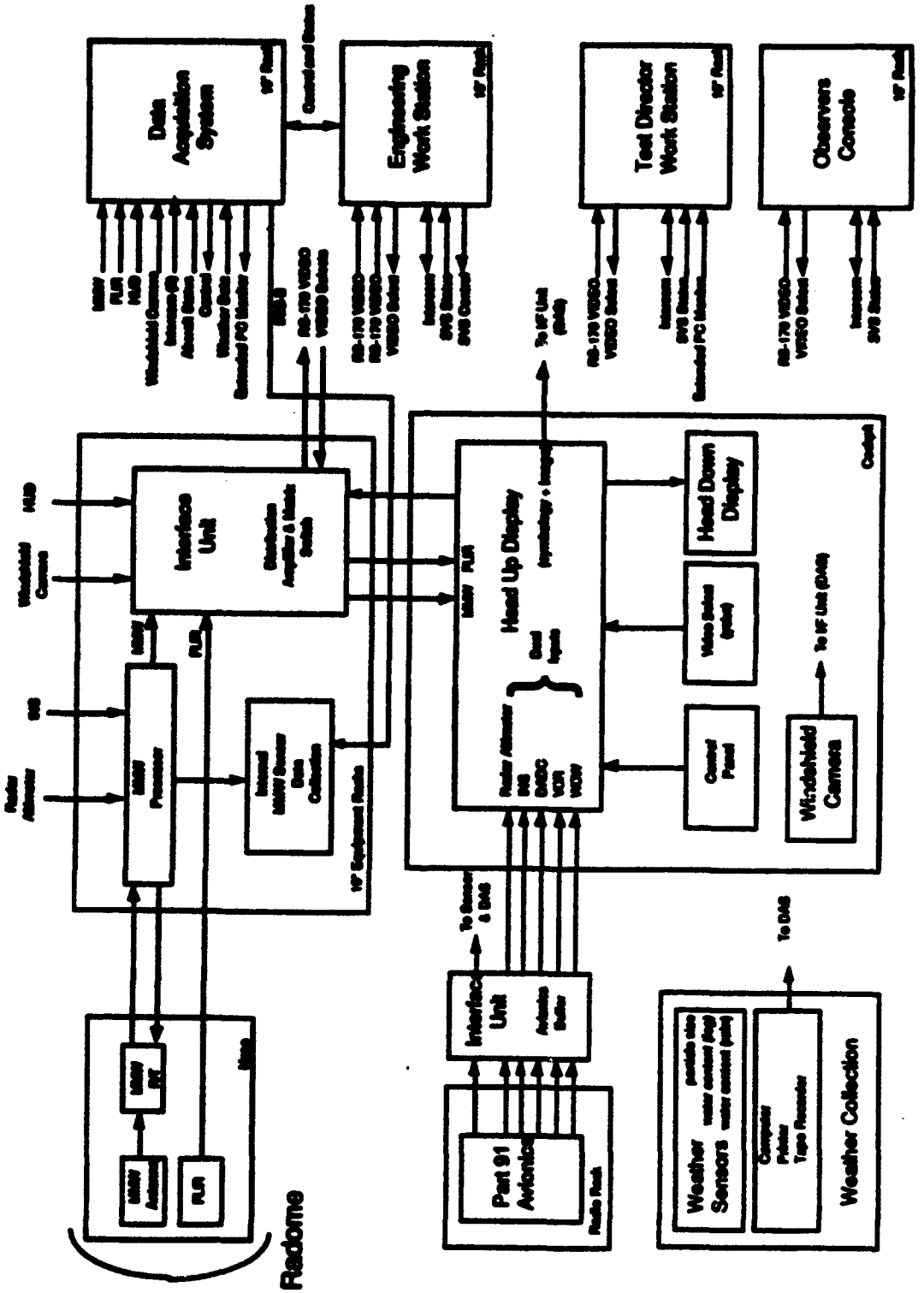

Figure 2.2-1. FPSVS Block Diagram

symbology (situation awareness, flight guidance, and flare guidance). A complete Data Acquisition System recorded aircraft avionics data, video image data, and weather data

The methodology for developing the Functional Prototype System was based on a top down flow down of requirements. The following sequence of events occurred (some of which occurred in parallel).

System and subsystem Specifications
Vendor search and award Subcontracts
Subsystem Development
HUD Symbology Simulation
Hotbench Test and Integration
Aircraft Modification and SVS Installation and Test
Sensor Flights (Primary MMW and FLIR)
Sensor Flights (Backup MMW and FLIR)
Sensor Flights (Primary MMW and FLIR)

System and Subsystem Specifications. The generation of system level specifications were key to the development of the SVS Functional Prototype System. A PERT chart was developed which contained the major program tasks and their interdependencies. A key task in the PERT chart was the development of the Functional Prototype System Specification. The requirements in this specification were imposed based on the technical and operational requirements but were also very dependent on the capability/limitations of the existing MMW and FLIR sensors. Once written, the system level requirements were used as the basis for the subsystem specifications. The following is a list of the specifications written for the FP System:

Doc Number	Specification
SR4-5012	SVS System Requirements
EQ4-5001	HUD Specification
EQ4-5003	DAS Specification
EQ4-5004	Work Stations Specification
EQ4-5005	Radome, 94 GHz
EQ4-5006	A/C Modification Specification
EQ4-5007	Radome, 35 GHz
EQ4-5010	FLIR Window

Vendor Search and Subcontract Awards. Subsystem specifications were prepared and used to query companies for proposals. Technical and cost evaluations and fact finding was performed prior to award of the subcontracts. The following is a list of participating companies and their respective responsibilities:

Company	Responsibility
TRW	System Integration, Video and Digital Data Acq, and Analyses
Honeywell	Primary MMW Sensor
Lear	Backup MMW Sensor
Kodak	FLIR Camera
GEC Avionics	Stroke/Raster HUD
JTD Environment	Weather Acquisition
Norton	Radomes
Petersen Aviation	G-II Aircraft and Safety Pilots
Midcoast Aviation	Aircraft Modification
GTRI	MMW Analysis

Subsystem Development, The individual hardware functions were designed and tested based on the appropriate specification. These subsystems were stand-alone, but consisted of multiple boxes which resided in several aircraft locations. This required a complex aircraft wire harness (defined as the group A cable).

Key to the successful development of the hardware and software were the Interface Control Documents (ICD). The two System ICD's, Group A (aircraft) and Group B (racks), defined every interconnect in the SVS equipment. These documents were developed based on the individual function ICD written by each vendor. Other key mechanical installation definitions were placed in the two Installation documents. Of key importance were the 3D drawings used to determine the placement of the 35 GHz and 94 GHz antenna and FLIR within the GII radome space. To accomplish this the existing aircraft Localizer and Glideslope antenna were moved, the weather radar antenna was changed (to a smaller 12" version) and moved up), and the bottom of the radome was modified to accept an IR window for the FLIR. The installation documents and ICDs are listed below.

Document Number	Specification	Responsibility
DI-6011	Cabin Installation	TRW
DI-6012	Sensor Installation	TRW
DI-6013	MMW (Lear) ICD	Lear
DI-6015	FLIR ICD	Kodak
DI-6016	Weather ICD	JTD
DI-6051	HUD ICD	GEC Avionics
DI-6052	MMW (Honeywell) ICD	Honeywell
IF1-7000	System ICD Group A	TRW
IF1-7001	System ICD Group B	TRW

HUD Symbology Simulation. A Flight Test Simulator was used to 1) work out the HUD symbology interface with the raster image, 2) work out crew procedures for approach and landing operations in very low visibilities, and 3) provide a simulator as a training vehicle for the test pilots and demonstration pilots.

A Douglas fixed platform MD-11 simulator was used. Enhancements to the simulator included the installation of a GEC Stroke/Raster HUD. This HUD ran the same software found in the GII HUD, but used RS-232 drivers rather than the aircraft ARINC-429 drivers. The simulator image generator was also programmed to produce a MMW image (VFR and FLIR imaging capabilities already existed).

Hotbench Test and Integration, A Hot Bench Test set was developed to reduce technical risk during aircraft integration. The Hot Bench was a test set which 1) could generate all the avionics signals dynamically to exercise SVS interconnect and functionality, 2) used a replicated group A aircraft cable, 3) used actual racks and group B cables, 4) provided all AC and DC power (28 VDC, 115 VAC 60 Hz, 15 VAC 400 Hz single phase, and 115 VAC 400 Hz triple phase), and 5) resembled the layout of the aircraft.

The computer was a Colorado Data Systems 386 based unit. The unit had the capability to drive ARINC-429, analog, and discrete signals. The test software was written to emulate approaches and provide specific test cases to test the SVS equipment. Data streams from the INS, DME, ADC, Radar Altimeter could be emulated. Other discretes and audio tones were generated by means of switches and standard test equipment.

Each of the subsystems were designed built and tested as stand alone units by their respective manufacturer. The units were delivered to TRW and installed into the 19" racks. A pre-planned build up of tests were performed to insure functionality and safety. These tests were done first as stand-alone units then as a system.

A reduced Hot Bench test was also performed at Midcoast (test set was located near the aircraft). This provided three benefits; 1) damage due to shipping was identified, 2) tested any software modifications performed since the last test, and 3) aided in the installation of the equipment into the aircraft.

Aircraft Modification and Installation and Test. Integration on the aircraft was accomplished in two phases; 1) aircraft modification and 2) SVS installation and test. These tasks were performed at Midcoast Aviation in St. Louis.

The first phase, aircraft modification, included removal of the interior and decorative panels, installation of the support equipment such as power supplies, monitor points, intercom, the relocation and installation of special antennas, the sensor brackets, pressure bulkhead and wing wiring, and the development and installation of the two wing pylons.

SVS equipment installation began with the installation of the group "A" cable. This cable was a rack to rack cable which interconnected the nine SVS equipment racks located in the cabin and the sensors in the nose, cockpit displays, and power supplies located in the rear of the cabin. Installation of the loaded racks followed. Again, as was done in the Hot Bench, a pre-planned build up of tests were performed to insure functionality and safety. These tests were accomplished first as stand-alone units then as a system. Testing the SVS equipment on the aircraft was initially accomplished with the use of the Hot Bench Computer. Rather than drive the system with the on-board avionics (much of which required special test equipment to generate useful data; since the aircraft was in a hangar) the Hot Bench Computer was used to exercise the SVS System.

Initial testing then continued using special test equipment which forced the avionics to produce meaningful data . Ground test, MMW calibrations and HUD alignments were performed by placing the aircraft on a ramp overlooking a field with crossing runways and taxiways. Final ground testing was done in a taxi mode. Flight tests were performed in a pre-planned fashion; initially to test air worthiness then SVS equipment (see System Integration Test Plan for details).

Sensor Suitability Flights Upon completion of the integration testing and shake-down flights, the aircraft was flown to Van Nuys California and based at Petersen Aviation. The first series of flights were sensor suitability tests. These flights were designed to confirm suitability and provided a period to improve the performance of the MMW and FLIR sensors during the appropriate approach to landing, taxi and takeoff phases.

Functional Prototype SVS Evaluation and Demonstration Flights. These flights were designed to test the performance of the Functional Prototype System (MMW and FLIR) under various weather conditions and at different facilities. The tests included approach to landing, runway intrusions, and taxi and takeoff. The weather conditions included a range of rain (up to 22 mm/hr), fog (down to CAT IIIA, 1/16 mile RVR), and snow.

Sensor Suitability Flights (Backup MMW). Upon satisfactorily passing a performance3 acceptance test in the Tower Test Facility, and as soon as it was made available for flight testing, the Lear Astronics 94 GHz backup MMW sensor was integrated and tested on the aircraft. Aircraft integration tests were performed on the Hotbench. Upon successfully completing these tests, and at a logical point in the testing of the primary sensor, the 94 GHz sensor was installed and tested in the aircraft. Suitability flights then followed. As with the primary sensor, these flights were designed to confirm suitability and provided a period to improve the performance of the sensor during the appropriate approach to landing, taxi and takeoff phases. After a series of flights, the backup MMW sensor failed to pass the acceptance test and was deemed to be unsuitable as a sensor with which to continue evaluation of the experimental SV system. It was then removed from the aircraft. The primary sensor was reinstalled in the aircraft, suitability for further testing confirmed, and the remaining evaluation and demonstration flights were completed.

SECTION 3.

DESCRIPTION OF FACILITIES

3.1. Experimental System

The experimental Functional Prototype System consisted of 1) MMW and FLIR Sensors, 2) Head Up Display, 3) Weather Acquisition Sensors, 4) Aircraft, and 5) Data Acquisition System.

3.1.1. Sensors

The experimental system used three sensors; the Honeywell 35 GHz MMW Sensor, the Lear 94 GHz MMW Sensor, and the Kodak 3-5 micron FLIR. These sensors provided an opportunity to examine a wide range of sensor technology.

3.1.1.1. 35 GHz MMW

Primary MMW Sensor (Honeywell). A Honeywell MMW Sensor was used to generate a electronic image of the runway and surrounding terrain. The sensor and its processor produced a conformal "C-scope" image based on reflected 35 GHz power. The image was displayed on the pilots Head Up Combiner Display (right seat) and the Head Down Video display (centrally located in on the cockpit panel).

The Honeywell sensor system was developed specifically for this SVS Technology Demonstration Program using an existing receiver/transmitter unit developed several years earlier for another application. An electro-mechanical scanning antenna was developed specifically for the SVS application by the Malibu Research Incorporated. A shaped reflector was used to achieve a vertical fan-beam pattern of approximately 26 degrees with cosecant squared rolloff, and an azimuthal beamwidth of 0.8 degrees. Based on an "Eagle Scanner" technique, a dielectric slug was used to change the phase velocity of the waveguide feed, scanning 30 degrees in the horizontal plane at approximately 10 Hz . An image processor performed the trigonometric conversion from range-azimuth to elevation-azimuth to produce the conformal image. Conformality was also maintained during platform motion. Platform altitude, pitch, and roll information were required by the processor to perform the conversion and stabilization.

Further description of the Honeywell MMW Sensor is provided in Appendix B Honeywell MMW Sensor.

3.1.1.2. 94 GHz MMW

The Lear Astronics 94 GHz MMW sensor system was built specifically for the SVS Technology Demonstration Program, as a 94 GHz imaging sensor had not been developed previously for this purpose. The design was selected from competing designs and technologies in a competitive design study conducted within industry and then built and subjected to initial static testing within the Synthetic Vision Program as an effort separate from the SIED Task. Because of delays in its development and acceptance testing resulting in late availability to the SIED effort, this sensor became the backup to the 35 GHz sensor system.

The Lear Astronics sensor produced a conformal "C-scope" image based on reflected 94 GHz power. The image was displayed on the pilots Head Up Combiner Display (right seat) and the Head Down Video display (centrally located in on the cockpit panel).

Range data was obtained by means of the chirped frequency. The sensor used a narrow vertical fan beam antenna in which range data was obtained for a given horizontal position. The fan beam was mechanically swept horizontally to fill in the remaining azimuth locations. The Lear antenna incorporated pitch stabilization enabling the antenna to maintain the correct pointing angle down the glidepath aimed at the touchdown point during an established approach.

An image processor performed the trigonometric conversion from range-azimuth to elevation-azimuth to produce the conformal image. Conformality was also maintained during platform motion. Platform altitude, pitch, and roll were required by the processor to perform the conversion and stabilization.

Key specifications for the Lear MMW Sensor are provided in Appendix B Lear MMW Sensor.

3.1.1.3. 3 - 5 Micron FLIR

FLIR Camera (Kodak). A Kodak FLIR Camera, model KIR-310 series 200, was used to produce an IR image. This sensor was also designed as a part of the competitive design study carried out separately from the SIED Task. This design was then built by Kodak for another

customer and for other purposes but was subsequently provided by Kodak for use in the SIED Task.

The sensor used a platinum silicide staring array, which was sensitive in the 1-6 micron wavelength range. An internal bandpass filter limited operation to the 3-5 micron range. The array had excellent resolution, 640 x 486 pixels, and very good thermal performance.

The FLIR contained both a manual mode, requiring a dedicated human to constantly optimize the settings, and an auto brightness and contrast mode for hands-off operation. This automatic feature was very important when operating under varying dynamic conditions, approach, touchdown and taxi. The platinum silicide detector provided 12 bits of dynamic range. The auto brightness/contrast histogrammed the pixels in the scene and set the 8 bit RS-170 (video) levels appropriately. The net result was very good hands off operation under a variety of conditions.

Further description of the Kodak FLIR Camera is provided in Appendix B Kodak FLIR Sensor.

3.1.2. Head Up Display

3.1.2.1. Hardware Description, Registration Issues and Calibration Procedures

Head Up Display (GEC Avionics). The GEC Avionics HUD projected both stroke symbology and raster image. Symbols were produced by controlling the X-Y deflection coils during the fly back time of the raster image. This resulted in very bright crisp symbols, overlaid upon "normal" TV raster image. Symbol generation was based upon data from existing on-board avionics. A computer received, interpreted, and generated text and symbols (i.e.. text - airspeed, ground speed, Barometric Alt, Radar Alt,... symbols - heading tape, pitch ladder, flight director, flare guidance cue, ..) The HUD also produced a RS-170 combined symbology image signal. This signal was used to drive the central HDD video display and was recorded on the data acquisition VCR.

3.1.2.2. Head-Up Display Symbols and Flight Director

An illustration of the stroke symbology used on the GEC head-up display (HUD) is shown in Figure 3.1-1. The symbol layout was patterned after that used on a HUD manufactured by

Flight Dynamics, Inc. That HUD is currently certified for Cat IIIa approaches in a Boeing 727 aircraft to runways with Cat IIIa equipment (3 transmissometers, a Type II ILS, and an ALSF approach lighting system with touchdown zone and centerline lights). The FDI HUD has been successfully used in Cat IIIa conditions by Alaska Airlines for several years. The symbology layout was used in this program because it was a known reference . The concept was to start from this reference and add the synthetic vision image, varying from the established layout only as required for the SIED Task. The symbols in Figure 3.1-1 depart from the certified symbol set based on recommendations from an SAE subcommittee on HUD symbology, and on opinions of engineers at GEC. The variations are as follows: the numbers for groundspeed, airspeed, barometric altitude, and radar altitude are larger, a ground pointer instead of a sky pointer was used, the ILS raw data is referenced to the flight path marker instead of the center of the display, the radar altitude is in a different place, and the mode annunciator is different.

The flight director guidance laws were developed by Hoh Aeronautics, Inc., under contract to TRW. These control laws were adequate to accomplish the approach task in significant winds and wind shear and provide flare guidance that was considered adequate by the pilots. However, the laws would have to be further refined before they could be certified for flight in all operational conditions, especially for the localizer and glideslope capture functions.

Further description of the GEC Avionics HUD is provided in Appendix C GEC Head Up Display.

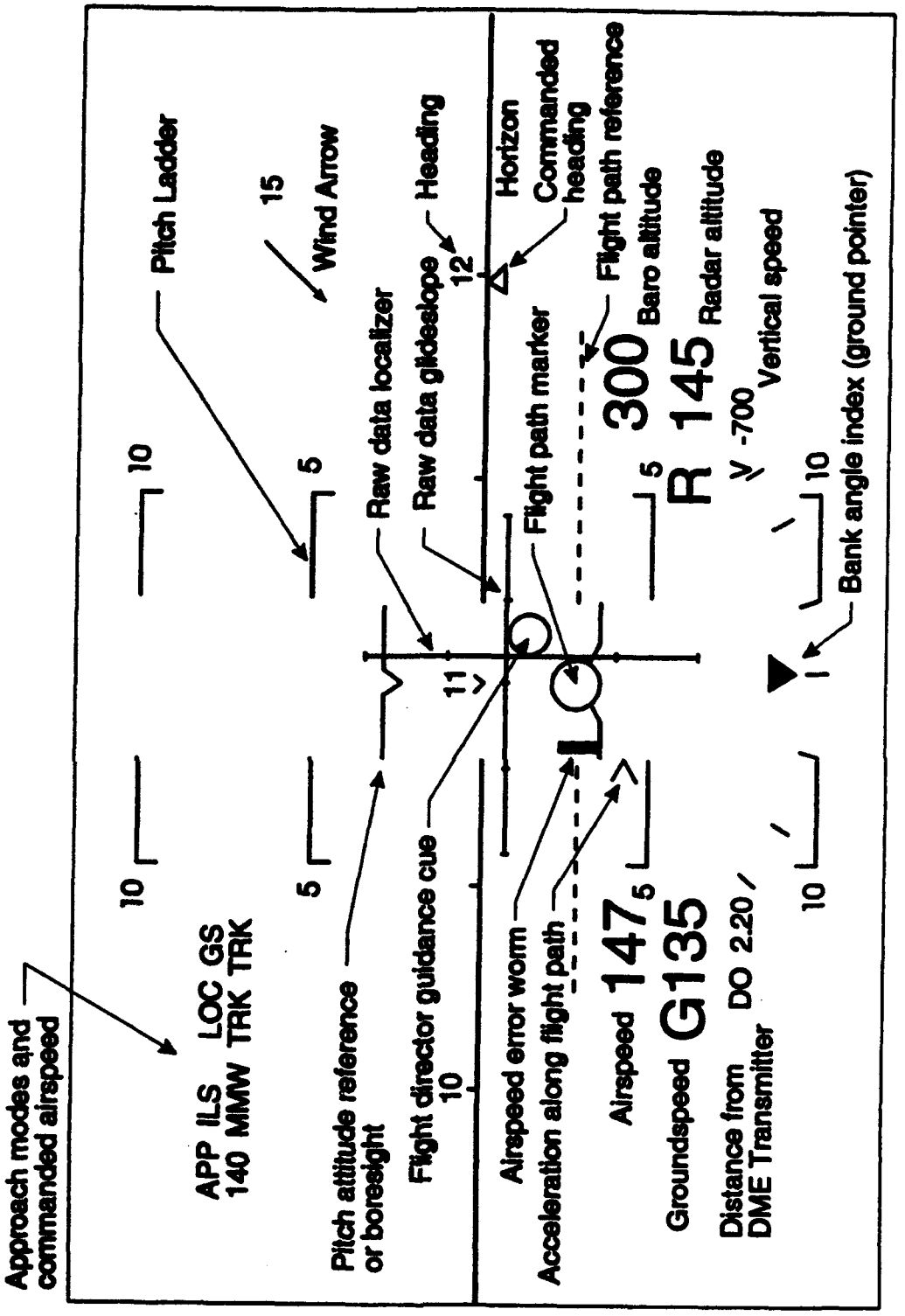

Figure 3.3-1. Head-Up Display Symbology Used in Test Aircraft

Calibration Procedures. The HUD Combiner Assembly underwent a critical boresighting procedure with the aircraft at Midcoast Aviation, St. Louis. The alignment procedure aligned both the left and right HUD Overhead Trays to within the required location. The GEC HUD was designed to be placed in an overhead tray. The tray held the HUD Overhead Combiner Assembly in place; moving the HUD to the other seat required 10 minutes to remove and install the HUD into the other tray. Two trays were installed and aligned in the GII aircraft. This permitted a technician to quickly move the HUD to the other cockpit seat while maintaining proper alignment of the HUD.

Each tray was aligned using a GEC alignment tool (telescopic lens assembly held in the tray). Each tray was shimmed and locked into place using the alignment tool and a pre-positioned target. The target was two cross-hairs (left and right seat) properly boresighted and positioned. To establish the position of the targets, the aircraft was leveled on jack stands and the target positioned on a scaffold using a theodolite.

3.1.3. Weather Sensors

The aircraft was equipped with three weather sensors; two wing mounted probes and one fuselage mounted probe. The wing mounted pods could carry interchangeable PMS particle measurement laser probes. The fuselage probe measured liquid water content. The laser probes available covered a wide range of particle sizes including those of water droplets found in fog, cloud and precipitation.

Prior to each flight a standard calibration was performed. The FSSP probe had a spray check for probe functionality and a size check using three standard size calibrated glass beads. The OAP probe also had a spray check and size check using a calibration rod. The LWCP, Liquid Water Content Probe, was checked using a Calibration Box. These checks were done to insure that the probes were functioning to the manufacturer's standards. The PMS probes were cleaned periodically to insure proper function and sizing.

In-flight quality control was maintained by monitoring real time data. The data was compared to expected ranges and levels. Post-flight inspection was also performed prior to data reduction to also confirm proper operation and sizing of the instruments.

Measurement accuracy was based on the manufacturer's calibration standards. The PMS FSSP-fog probe had an accuracy of +/- 3 microns (measurement range set to 2.0 - 47 microns). The OAP-Cloud had an accuracy to +/- 20 microns (measurement range set to 20 - 300 microns),

and the OAP-Precipitation had and accuracy of +/- 300 microns (measurement range set to 300 - 4500 microns). The LWCP had an accuracy of +/- 0.05 grams/meter^3.

3.1.4. Aircraft Instrumentation

A Gulfstream-II business class jet, tail number N65ST, was used as the flying platform. The aircraft was modified to support the SVS Equipment. Modifications included structural (wing pylons), electrical (power busses, power converters, Intercom,...), and installation of the SVS racks and workstations. The aircraft was flown in the experimental category.

The aircraft avionics complement is described in Table 3.1-1. The existing avionics package provided the safety pilot (left seat) with standard part 91 equipment.

Table 3.1-1 Aircraft Avionics

1	Weather Radar System; one Honeywell WC-650 (15" antenna replaced by 12" antenna)
2	Electronic Flight Instrument System; one Honeywell 5 tube EFIS
3	Air Data Computer System; one Honeywell AZ-800
4	Altimeter Indicators
5	Vertical Speed Indicators
6	VHF Communications System; triple Collins VHF-20
7	HF Radio; two King KHF-950 w/ Motorola NA-135 SELCAL
8	VHF Navigation System, two Collins VIR-30
9	Avionics Power Switching
10	Inertial Navigation System; two Litton LTN-92
11	VLF/Omega; one Universal UNS-1Jr
12	Distance Measurement Equipment System; one Collins DME-42 and one DME-40
13	Automatic Direction Finder System; two Collins ADF-60A
14	Flight Director System; two Honeywell FZ-500
15	Transponders; two Collins TDR-90
16	Radio Altimeter System, one Collins ALT-55B
17	Cockpit Voice Recorder; Fairchild A-100
18	Flight Phone; Wolfsberg Flitefone VI
19	Angle of Attack; Teledyne AOA
20	GPS; Marconi

Special SVS Aircraft Features

The aircraft was modified to accommodate the following features designed specifically for the SVS Functional Prototype System:

Special Antennas. The MMW and FLIR sensors required more space than was originally available. Several modifications had to be performed to the nose area. The ILS glideslope antenna was replaced with a conformal antenna and relocated at the bottom of the radome., the ILS localizer antenna was relocated to the fuselage, and the existing 15" Weather Radar Antenna was replaced with a smaller 12" model and moved up. The relative locations of each unit along with the MMW antenna and FLIR are provided in Sensor Installation Definition for FPSVS A/C Modifications (specification number D1-6012).

An external VHF Communications antenna was added to the rear bottom of the fuselage. The antenna was connected to a portable hand held radio located in the cabin at the Test Directors Work Station

The radio was operated in the cabin by the Test Engineer. Antenna Specifications can be found in appendix C VHF Communication Antenna.

Control Position Transducers. Position transducers were added to the test pilot's yoke (right seat). The transducers (pitch and roll) was designed to provide a resistance which was linearly proportional to the yoke position. This position data was recorded by the Data Acquisition System.

Sensor Selector. A left thumb switch was placed on the right seat yoke. The push button switch was used by the pilot to rotate between the MMW image, FLIR image, and no image on the HUD.

Event Marker. A right thumb switch was placed on the right seat yoke. The thumb switches was used by the pilot to record an Event Mark on the Data Acquisition System.

Dual-Circuit Intercom. The existing aircraft intercom and Public Address System was enhanced with a second cabin intercom loop. The enhanced intercom system provided each of the FPSVS Engineering crew (Test Director, Test Engineer, MMW Sensor Engineer, Host/Wx, and Observers (Qty 4)) with a headset and microphone. The intercom was based on a "Hot" Microphone. For safety, the installation was designed so that the pilot/copilot was able to address

the support crew over the existing PA system. Three audio outputs were routed to the DAS for audio recording.

Radome Air Purge. Pressurized dry cabin air was vented into the radome . The cabin air reduced the moisture content within the radome. The purpose of the vent was to prevent condensation on the FLIR window, waveguides, and the non-sealed FPSVS components. The vent remained open for altitudes below 10,000 feet.

Power Converters/Inverters The aircraft contained special power generators, converters /inverters, and transformer rectifiers. The Power Supplies provided clean regulated power to the FPSVS equipment.

Circuit Breakers The FPSVS Equipment contain a hierarchical 2-level circuit breaker system. The first level was located in the rear baggage compartment of the aircraft. This panel contained individual circuit breakers for each rack, and each type of power within each rack. These circuit breakers were rated slightly above the maximum required current. The next level circuit breakers were at the back of each rack. These breakers were rated at a higher current level but had a faster response time (short circuit protection). Power distribution and circuit breakers were installed per 1159-GER-38 Grumman Outfitters Interface Specification.

External Ground Power. Provisions were made to use an external AC power cart. The ground cart provided 3 phase 115 VAC 400 Hz power to the FPSVS. The input was connectorized and were easily accessible. Note: Ground DC power was used in conjunction with the AC Cart while on the ground. The DC cart was plugged into the normal connector located on the right side of the fuselage just aft of the front wheel well.

Monitor Points. Electronic interfaces to the existing aircraft avionics were installed and connectorized. This permitted connections to be made easily between the FP System and the avionics. These connectors also permitted the Hot Bench computer to bypass the aircraft avionics and emulate all the required signals for the FP System.

Sensor Mounting Bracket. A "Universal" Mounting bracket was installed on the forward bulkhead located within the radome space. Special signature brackets were designed for the Honeywell Sensor, Lear Sensor, and Kodak Sensor. The signature brackets held each sensor; and mounted directly to the universal bracket.

HUD Combiner Camera. A HUD Combiner video camera was developed to record the HUD Combiner image (as seen by the pilot). The camera was located between the combiner glass and the pilot's eye. As such the camera was able to see the HUD image and the outside world. This camera was used to record contrast shifts (due to ambient light), runway edge problems and image registration with the outside world.

Glareshield Camera. A glareshield video camera was mounted to provide an out the window view of the approaches and taxi. The color camera provided a real-time image of the approach. The image was available to the cabin monitors and was recorded on the VCR.

Equipment Racks. Nine 5 foot high 19" equipment racks were installed in the aircraft. These racks were used to hold the FP equipment.

Head Up Display. The HUD Overhead Unit was mounted above the right seat. A second tray was installed above the left seat (transfer between the trays required approximately 10 minutes).

Head Down Display. A Head Down Display was centrally installed on the cockpit panel. The display was mounted in place of the center tube of a 5-tube Honeywell EFIS system.

Wing Mounted Weather Pods. The aircraft was required to carry two weather probe pods in a free air stream. The two interchangeable pods, Particle Measurement System OAP and FSSP, was mounted on each wing and the probe.

Each pod was held stable beneath the wing using two dedicated pylons. These pylons were designed to carry a single pod each of approximately 45 lbs at a maximum aircraft speed. The pylon was designed to allow a quick removal and installation of the pod.

The pylons oriented the two pods forward at 0° azimuth and with an elevation angle of - 2°, with respect to the waterline of the aircraft. Pod elevation angles of + 2° through - 4° in 1° increments was accommodated in the pylons.

Fuselage Mounted Weather Probe. The aircraft was required to carry one weather probe in a free air stream. The probe, PMS Model LWH-1 Liquid Water Content Indicator, was mounted on the aircraft fuselage (left cheek panel).

3.1.5. Data Acquisition System

The Data Acquisition and Analysis equipment was used to record and analyze three distinct categories of data; 1) System level, 2) Weather, and 3) Sensor.

The Data Acquisition System was designed to record and reduce flight data for the evaluation flight test. The recorded information consisted of aircraft avionics, video, internal MMW, and weather parameters. There were four major airborne acquisition categories and three major ground analysis categories. See Appendix D for Data Sources and Data Elements.

Location	Purpose	Responsibility
Airborne (Acquisition)	System Data	TRW
	Weather	JTD
	MMW (Primary)	Honeywell
	MMW (Secondary)	Lear
Ground (Reduction/Analysis)	System Data	TRW
	Weather	JTD
	MMW (both)	GTRI

System Data Acquisition/Analysis (TRW). The airborne data acquisition system was required to record analog, digital, and video data. There were three major subsections; 1) Digital Recorder based on a Colorado Data Systems PC based computer, 2) Video Recorders, and 3) IRIG-B Time Base System (Datum 9700).

The computer system was implemented to interface with high and low speed ARINC-429 buses, multiple analog signals, discrete signals and audio tones. The computer provided the appropriate protocols, interpreted the data, recorded the data, and provided a real time display of key parameters on the Test Director Station Monitor. All data was converted to digital and stored on a high speed high capacity 8mm Cybernetics Tape Drive.

The video section consisted of a high bandwidth video distribution amplifier, video matrix switcher, FLIR video inverter, and four Hi 8mm VCRs. The Hi 8mm format was selected due to it's compact size and excellent resolution. See Appendix C in Volume 4 of this report for details. The four VCRs recorded HUD video, MMW Sensor video, FLIR video, Windshield Camera video, Pilot audio, co-Pilot audio, cabin intercom, and IRIG-B time. IRIG-B was recorded as a 1 KHz encoded sine wave (right audio channels on each VCR).

The Time Base was set to GMT standard time. This time was routed to the other acquisition equipment for data tagging.

The data analysis system was designed to support system level data reduction and analyses. This included pilot-in-the-loop aircraft deviations (such as centerline and glideslope deviations) and image quality analyses. The analysis equipment is configured to read the 8mm digital and Hi 8mm video tapes recorded during the flight test. The raw data recorded on the digital tapes are processed to produce plot and data (such as standard deviations and RMS errors). Video tapes can be viewed, digitized, and pixel levels extracted to produce Image Quality metrics.

The analysis station was built around a Macintosh IIci Computer. A 8mm tape drive was used to read the digital tapes recorded during the flights. LabView (software package) support analysis. Four Hi 8mm VCRs and monitors supported video viewing. A video frame grabber in the Macintosh supported digitization of the video. Enhance software was used for image analyses.

Weather Data Acquisition/Analysis (JTD Environment). The Weather Acquisition equipment was designed to determine key weather parameters which the aircraft experienced. The parameters could then be integrated to formulate the true weather conditions between the sensor and the airport at all instances of the approach.

To accomplish this the data from the PMS particle size measurement probes and the liquid water content probe was sent to a computer, where it was recorded on a digital cassette tape. The computer also interpreted and printed a real time snapshot of the collected data. Airspeed, Temperature, and Static and Pitot pressures were recorded.

MMW Sensor Data Acquisition (Honeywell). The Honeywell Data Acquisition System was implemented on a SUN Computer. This Computer also acted as the User Interface during setup and provided monitor functions. The SUN Computer controlled the large amount of data storage (> 0.5 Mbytes every 4 seconds of recording) within the Display Processor. See Appendix E for details on data sources, data elements, and data rates. To accommodate the large amount of data at a high speed, a double serial buffer was employed. The first was a smaller very high speed disk and the second was a much larger but slower hard disk.

Data transfer, at the end of a sortie, was accomplished using standard 1/4" cartridge tapes. The tapes were pre-processed at Honeywell and transferred to a 8mm format and sent to GTRI for analysis.

MMW Sensor Data Acquisition (Lear). The Lear Data Acquisition System was implemented on an IBM Computer. The IBM Computer controlled a large amount of data storage. See Appendix E for details on data sources, data elements, and data rates. To accommodate the large amount of data at a high speed, a double serial buffer was employed similar to that used with the Honeywell DAS.

MMW Sensor Data Analysis (GTRI). The GTRI Data Analysis System was implemented on a SUN SPARC II Computer and a Macintosh. The SUN Computer had a 8mm tape drive which was used to read the Honeywell data tapes. Initial formatting, mass storage, and Region of Interest extraction was performed on the SUN. Data was then transferred to the Macintosh via a Gator box. Image processing and statistical analyses were then performed. The Macintosh used IMAGE, MATLAB, and EXCEL software tools were used with the Macintosh.

3.2. Description of Airports

A description of the primary airports used during the testing is provided in Table II1.2-1. With the exception of San Diego, all of the runways were surrounded by grass. In some cases, the primary runway surface had a different texture than the sides, where the runway lights were installed. For example, Los Angles had a concrete runway with asphalt sides. In other cases, the sides of the asphalt runway were also asphalt, but the surface was not as well maintained as the runway itself, and had a rough appearance.

3.3. Ground-Based Simulation

A fixed-base simulation of the synthetic vision HUD display was developed by the Douglas Aircraft Company under contract to TRW. An existing MD-11 cockpit and math model was used as a starting point. A GEC HUD was installed in the cockpit in a configuration identical to that planned for the G-II flight test aircraft. This HUD was capable of providing superimposed stroke and raster information. The software supplied by GEC for the HUD was identical to that used in the flight test. The raster display on the HUD was capable of simulating a FLIR scene and a MMW scene. Since these were developed before the flight testing it was necessary to estimate the FLIR and MMW sensor performance characteristics. All the evaluation pilots agreed that the raster scene displayed during the simulation was reasonably representative of the results obtained during the subsequent flight testing. The MD-11 approach pitch attitude was found to be considerably

Table 3.2-1. Description of Primary Test Airports

Airport	Identifier	Runway Heading (mag)	Approach Lights	Centerline Lights	Touchdown Zone Light	Runway Lights	Trans-missometer	Surface	TDZ Elevation	Length	Width	Approach	DH or MDA	Minimums
Arcata	ACV	316.0	SSALR	Yes	Yes	HIRL	2	Asph-grb	218	5,998	150	ILS	200	1800 ft
Atlantic City	ACY	129.6	SSALR	No	No	HIRL	3	Asph - grooved	76	10,000	180	ILS	200	1800 ft
Colorado Spring	COS	349.2	ALSF-1	No	No	HIRL	None	Asph-grb	6075	11,021	150	ILS	200	1/2 mile
Paloomar	CRQ	245.0	MALSR	No	No	HIRL	None	Asph - grb	323	4,700	150	ILS	200	1/2 mile
Huntington	HTS	316.0	MALSR	No	No	HIRL	None	Asph-grooved	828	6,589	150	ILS	200	3/4 mile
Los Angeles	LAX	249.1	MALSR	Yes	Yes	HIRL	3	Concrete-grooved	121	10,285	150	ILS	200	1800 ft
Langley	LFI	77.5	ALSF-1	No	No	HIRL	None	Asph	9	10,000	150	ILS	200	1/2 mile
Millville	MIV	100.0	MALSR	No	No	HIRL	None	Concrete	74	6,000	150	ILS	200	1/2 mile
Patuxent River	NHK	59.3	ALSF-1	No	No	HIRL	None	Concrete	40	11,800	200	GCA	200	1/2 mile
Ft. Mogu	NTD	209.0	MALSR	No	No	HIRL	None	Asph	12	11,100	200	ILS	200	1/2 mile
Pueblo	PUB	77.6	SSALR	No	No	HIRL	None	Asph-grb	4668	10,496	150	ILS	200	1/2 mile
Worcester	ORH	109.1	MALSR	No	No	HIRL	None	Asph	981	6,999	150	ILS	200	1/2 mile
San Diego	SAN	272.5	MALSF	No	No	HIRL	1	Concrete-grooved	14	9,400	200	LOC	646	5000 ft
Santa Maria	SMX	121.1	MALSR	No	No	HIRL	None	Asph - grb	237	6,300	150	ILS	200	1/2 mile
Santa Barbara	SBA	74.3	MALSR	No	No	HIRL	1	Asph-grooved	10	6,049	150	ILS	200	2400 ft
Vandenberg	VBG	301.7	ALSF-2	No	No	HIRL	None	Concrete	367	15,000	200	ILS	200	1/2 mile
Van Nuys	VNY	161.5	MALSR	No	No	HIRL	None	Asph	790	6580	150	ILS	250	3/4 mile

higher than the G-II. This was compensated for by using a higher approach airspeed, and conducting all approaches in a 25-knot headwind.

The simulation included a Redifon camera-model type Visual Flight Attachment (VFA). The model runway was 10,400 feet long, 200 feet wide and included approach lights, strobes, runway end markers, threshold bars, touchdown zone, VASI, edge lights, and centerline lights. This VFA system was capable of simulating varying runway visual range and ceilings. It was set up to perform approach, landing and takeoff operations in Cat I, Cat II, Cat IIIa, and Cat IIIc conditions. Steady winds, wind-shears, crosswinds, and turbulence were simulated to assist in the development and evaluation of the flight director laws and to provide pilot training for the flight t est program. The cockpit was configured like an MD-11 with six across 8x8 inch fully operational CRT displays. The Electronic Display formats were modeled after the MD-11. The MD-11 autopilot was operational, and was frequently used for demonstration flights.

The objectives of the simulation were to:

- Evaluate and refine the HUD symbology and flight director guidance laws
- Familiarize the evaluation pilots with the HUD symbology and SVS procedures. Also develop SVS procedures where necessary
- Provide familiarization for demonstration pilots

Some changes were made to the HUD symbology as a result of the initial evaluations by the evaluation pilots. The primary change was in the flight director guidance laws. There were modified considerably from the initial configuration, and the simulation was used extensively to accomplish the necessary fine tuning. Even though the laws were tuned for the MD-11 aerodynamics, they were found to work acceptably well on the G-II without modification.

The evaluation pilots were requested to provide Cooper Harper and Workload subjective pilot ratings using the scales shown later in Figures 5.2-1 and 2. Once the initial training effects were accounted for the ratings all fell into the 2-3 range for the approach, flare and touchdown. Runs in moderate turbulence were sometimes rated an HQR of 4. This data was considered to be training only, and is not reported as results of the program in Section 5. Most of the runs were made to simulated Cat IIIa conditions.

A number of demonstration flights were also made to key members of government and industry. In most cases, the demonstration pilots were given a simulation session to gain familiarity with the HUD symbology.

SECTION 4.

FLIGHT TEST METHODS AND PROCEDURES

The methods and procedures employed to accomplish the flight test objectives are summarized in this section. The intent is to provide the reader with sufficient background information to interpret the results in Sections 5 (Pilot/System Performance) and 6 (Sensor Performance), and the Lessons Learned in Section 7.

4.1. Test Plan and Priorities

The detailed test plan used to guide the flight testing is included in Appendix F of this report. The waiver issued to the project by the FAA to permit descents to below CAT I minimums is also included in Appendix F. The five selected airports were Arcata, Santa Maria, Vandenberg AFB, Santa Barbara, and Point Mugu NAS, all in California. The test aircraft was operated out of Van Nuys, California within a reasonable flying time of the five approved airports. A list of prioritized test objectives from the test plan is given in Table 4.1-1, along with what was done to accomplish the objectives. The test objective priorities were established by the test team based on inputs from the Certification Issues Study Team.

Table 4.1-1. Summary of Project Objectives and Accomplishments

Priority	Objective	Accomplishment
1	Low visibility approaches to Cat IIIa minimums in actual Cat IIIa conditions.	37 approaches in actual Cat IIIa conditions of which 12 were to Cat IIIa minimums. Some approaches were not conducted to the Cat IIIa DH because the airport was not included in the waiver, or because the waiver had not yet been issued
2	Accomplish the above approaches in different types of fog	Approaches were made in coastal fog (Arcata, Santa Maria, and Vandenberg), in valley fog (Huntington WV), and in frontal fog (Worcester, MA).
3	Conduct approaches in rain with varying rain-rates	Approaches were made to five different airports in rain with rain-rates varying from 0.50 to 22 mm/hr.
4	Conduct approaches to different types of airport surfaces	Approaches were made to 27 different airports. Formal evaluations were made during approaches to 17 of these airports.
5	Conduct landings in simulated Cat IIIc conditions (i.e., simulated 0/0)	All three evaluation pilots successfully accomplished three simulated 0/0 landings and roll-outs. Simulated 0/0 takeoffs were also accomplished
6	Test ability to identify runway incursions using the MMW sensors	Six runs were made in simulated IMC conditions where runway and taxi way incursions were staged. The evaluation pilot did not know in advance when these incursions were to be staged
7	Test a second MMW radar at 94 GHz	The Lear 94 GHz MMW radar was installed, checked out, and 11 final suitability runs were made
8	Test an infrared sensor in actual weather	A Kodak 3-5 micron FLIR was installed and was operational in all actual weather runs.
9	Conduct approaches in snow conditions	Approaches were made to Pueblo Colorado in falling snow, with 1 to 2 inches of wet snow on the runway, and to Pueblo and Colorado Springs to a plowed runway
10	Test ability to conduct non-precision approaches to simulated Cat IIa minimums	Localizer approaches and no-navaid-final-segment approaches were flown to simulated Cat IIIa conditions

IMC conditions were simulated by inserting a cardboard shield between the HUD and windscreen. The shield was held in place with Velcro tape, and was removed by the Test Director at the appropriate decision height. In the case of simulated Cat IIIc (0/0) landings, the shield was not removed throughout the approach, landing, and rollout. The safety pilot typically took over control of the aircraft below 60 knots as he had control of the nosewheel steering. For some runs, the shield was removed at 50 feet altitude to simulate Cat IIIa, and was reinserted during the rollout to simulate a surprise fog bank encounter.

4.2. Evaluation Pilot Background and Training

Three evaluation pilots were used to take data during this program. The background of these pilots is summarized below.

- Pilot CA (Chip Adam)
  - FAA test pilot
  - Former U. S. Army aviator with extensive experience with cockpit vision aids (forward looking infrared or FLIR)
  - Graduate of U. S. Navy Test Pilot School
- Pilot MN (Michael Norman)
  - Douglas Test Pilot
  - Former Navy Aviator with extensive HUD experience in F-14 aircraft
  - Graduate of U. S. Navy Test Pilot School
- Pilot LO (Larry Otto)
  - Douglas Test Pilot
  - Former Air Force Aviator and United Airlines Test Pilot
  - Graduate of U. S. Navy Test Pilot School

All three of the evaluation pilots are type-rated in a number of transport category aircraft.

Training for the evaluations in the G-II aircraft was accomplished in two phases. First, all of the evaluation pilots attended simulation and ground training to qualify as second-in-command in the G-II aircraft at Simuflight in Dallas Texas. Second, a fixed-base simulator was modified by Douglas Aircraft to include the GEC HUD used for the SVS program. Models of the millimeter-wave radar and forward looking infrared sensors were included in the simulation, and were superimposed on the stroke symbology on the HUD. The simulation was used to optimize the HUD symbology, refine the flight director control laws, and to accomplish pilot training.

4.3. SVS Instrument Approach Procedures

For the most part, the instrument approach procedures used in the flight tests were conventional. Specialized procedures were employed to ensure safety, and to obtain data. The evaluation pilot was required to make three callouts unique to the SVS program.

- Radar Image - This callout indicated that the pilot could see a pattern on the HUD that signified that the radar was imaging the ground

- Runway Image - This was a highly significant call. It indicated that the evaluation pilot had an image of the landing runway, and that the quality of the image was sufficiently good to continue below Cat I minimums on a Type 1 beam, with no transmissometers (RVR data), and no touchdown zone or centerline lights. The safety pilot was required to execute a missed-approach if he did not hear the "runway image" call before reaching the published decision-height for the approach.

- Visual-Land - This was also a highly significant call in that it indicated that the pilot had a view of the runway environment that was sufficient to continue to landing without synthetic vision. The safety pilot was required to execute a missed approach if he did not hear the "visual land" call above the SVS DH for the five airports on the waiver, and the published DH for all other airports. The SVS DH was always 50 feet.

In addition to the above calls, the Test Director was required to monitor the radar and barometric altimeters approaching the Cat I decision-height. If the radar altimeter indicated the proper trends approaching DH, the test director called "altimeters verified". The safety pilot was required to execute a missed approach if he did not hear this call for approaches in weather below Cat I minimums. The purpose of this procedure was to limit the exposure time over which the single radar altimeter could fail with significant consequences. The probability of such a failure was calculated to be less than 10^{-6}, a value felt to be adequate for the test environment by the flight safety review board.

Three types of approaches were made during the flight test program; the normal ILS, a non-precision localizer approach, and a no-navaid-final-segment approach. These are illustrated in Figure 4.3-1. For the ILS approaches, the evaluation pilot tracked the flight director down to the Cat IIIa decision-height of 50 feet. The image was primarily used to monitor the approach, although it was common for the evaluation pilot to use the image for runway alignment when the integrity of the localizer was questionable. This is discussed in more detail in Section V. For the

non-precision localizer approach, the normal procedure was used for the descent to the minimum descent altitude (MDA). A descent below the MDA was initiated after the pilot made the "runway image" call. Lateral control was identical to the ILS whereas longitudinal flight path control depended on the image and the HUD symbology. The flight director guidance cue was in a mode to provide only altitude hold or vertical speed hold for non-precision approaches, and the raw-data glideslope information was not displayed on the HUD. The no-navaid-final-segment approach was conducted in an identical fashion to the localizer approach except that the test director detuned the ILS localizer frequency after hearing the pilot call "runway image". This required the evaluation pilot to rely only on the HUD image for outer-loop guidance (i.e., raw data). The safety pilot always had full ILS glideslope and localizer information on his displays.

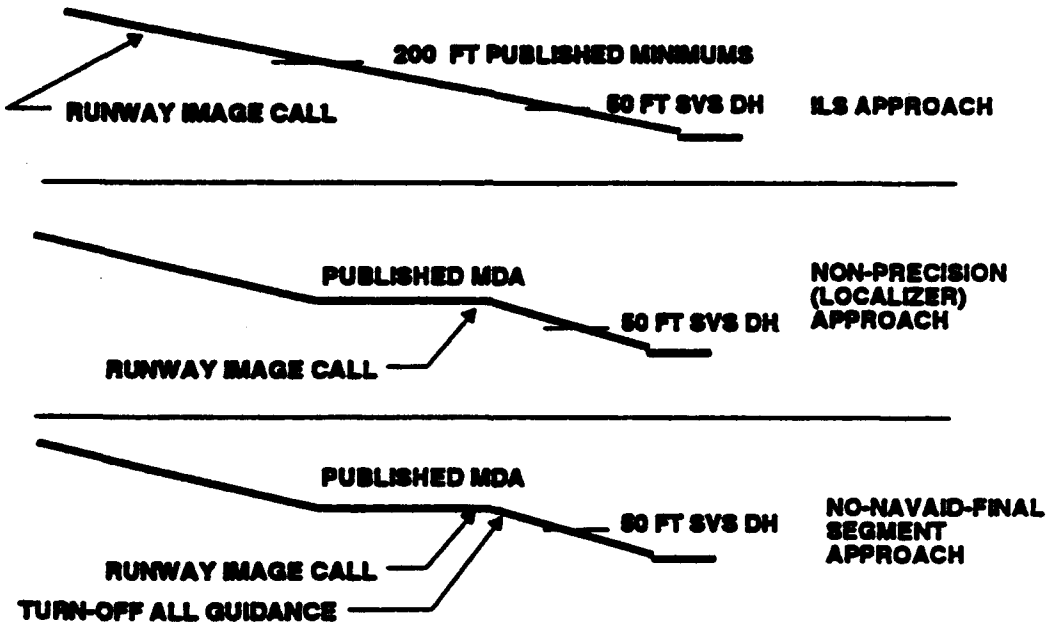

Figure 4.3-1. Approach Procedures Used in Flight Test Program

For most simulated IMC approaches the cardboard shield was in place in front of the HUD down to an altitude of 50 feet. A few ILS approaches were conducted to Cat IIIc (0/0) minimums, and a few were conducted to Cat II (100 ft DH) minimums.

4.4. SENSOR PERFORMANCE MEASUREMENT METHODOLOGY

4.4.1 Radar Phenomenology

Radar design parameters were established by Honeywell during sensor development to meet the SVSTD mission requirements. Tower and flight testing measured how well the radar sensor can perform that mission in a realistic operating environment. Measured performance is dependent on both the radar design parameters and the characteristics of the operating environment. Radar phenomenology is the formal description of a radar's interaction with the operating environment. Phenomenology includes radar backscatter from ground clutter and from the atmosphere (mainly from precipitation), plus the atmospheric propagation. The following section introduces the physics of radar scattering and atmospheric propagation, and how these phenomena affect radar sensor performance. Section 4.4.1.2 discusses radar performance issues that are most important to SVS imaging radar sensors.

4.4.1.1 Physics of Radar Scattering

A synthetic vision radar sensor exploits the difference in radar backscatter from adjacent airport surfaces-- that is, the pavement and bordering ground cover -- to develop display contrast between those surfaces in the processed image. Figure 4.4.1-1 depicts radar scattering from a section of airport runway bordered by grass. At the low radar beam grazing angles encountered during a typical approach, most of the transmitted radar energy striking the smooth pavement surfaces is forward-scattered. The remainder of the incident energy is diffused, so that very little power is scattered back toward the radar receiver. Thus, the runway appears as a dark area in the radar image. Bordering grass-covered areas are "rough" at millimeter wavelengths, so a larger portion of the incident energy is diffusely scattered. Therefore, more of the incident radar energy is backscattered toward the receiver, and these border areas appear brighter in the radar images. A radar calibration reflector, such as the segmented cylindrical corner used during the flight tests, is designed specifically to produce a strong, consistent radar target and thus is a good source of backscattered energy.

4.4.1.1.1 Surface Reflectivity

Smooth surface areas have very low radar backscatter at shallow viewing angles, while rougher surfaces have higher backscatter when viewed from such angles. The Rayleigh roughness criterion is a mathematical model for describing the roughness of an irregular surface to illuminating electromagnetic waves. The Rayleigh criterion states that a surface can be considered smooth when $\Delta h \sin \theta < \lambda/8$,

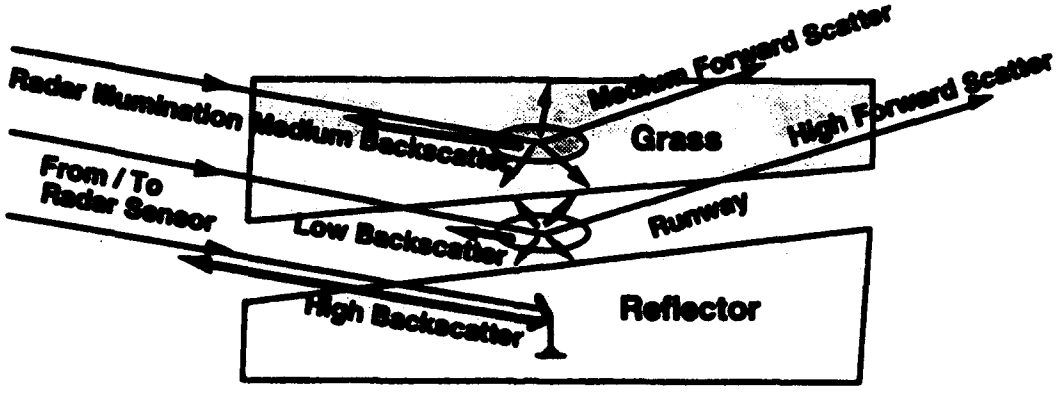

Figure 4.4.1-1. Radar scattering from airport surfaces.

where Δh is the root mean square (RMS) height of surface irregularities, θ is the viewing angle from the surface plane, and λ is the electromagnetic wavelength. Substituting an incident angle of 2.5° and an RF wavelength of 8.5 mm (at 35.3 GHz), and solving for Δh, a RMS roughness value of 24 mm is obtained. This would suggest that all the runways encountered during testing, including concrete, asphalt, and porous friction coated (PFC) asphalt, should be considered smooth at 35 GHz by the Rayleigh criterion. Even grooved concrete and asphalt runways probably have an RMS roughness of less than 24 mm.

Grass-covered terrain will usually be rough based on the Rayleigh criterion at millimeter wavelengths, so these surface areas have backscatter reflectivity coefficients significantly greater than pavement surfaces. Grass appears to the radar illumination as many randomly distributed scatterers that also absorb some of the incident energy. Since grass blades tend to be vertically oriented, a vertical polarized radar wave would likely produce greater reflectivity than a horizontally polarized wave. If scattering is more random due to randomly oriented reflecting surfaces, then the radar reflectivity would be relatively independent of the illuminating polarization. For dense grass cover, the illuminating energy does not strike the underlying dirt, and is reflected only by the grass. Thus, the grass reflectivity in this case is relatively

independent of grass height. Reflectivity does exhibit seasonal changes due to the grass freshness and density of growth.[0] The moisture content of the grass is also a key factor in determining its radar reflectivity.

Radar reflectivity of targets is expressed in square meters (m^2) of radar cross section (RCS), or in dB relative to a one-square-meter reference target (dBsm). The RCS of a ground clutter "patch" area, as determined by the radar resolution cell size, is also expressed in dBsm. Radar clutter is defined as radar backscatter from the illuminated area that is not attributable to a man-made target. Clutter RCS values are divided by resolution cell area to normalize the RCS to one square meter of surface area. Normalized clutter RCS is expressed as dBsm per square meter, or is simplified to dB by canceling the area units. The normalized RCS of smooth Rayleigh surfaces, such as a paved runway, is expected to be very low, and in the range of -50 dB. The bordering grass areas in an airport scene are rough by the Rayleigh criterion, and will have normalized RCS values in the range of -30 dB. This implies a possible 20 dB difference in RCS between runway pavement and bordering grass areas.

4.4.1.1.2 Meteorological Effects

The same meteorological conditions that justify deploying a synthetic vision MMW sensor will degrade the sensor's runway detection performance relative to that in clear weather conditions. Meteorological effects on a synthetic vision (SV) MMW radar are (1) atmospheric attenuation, (2) volumetric backscatter, and (3) reflectivity modification of surfaces, as shown in Figure 4.4.1-2.

---

0 M. W. Long, "Radar Reflectivity of Land and Sea," Lexington Books, Lexington, MA, 1975, pp. 145-156.

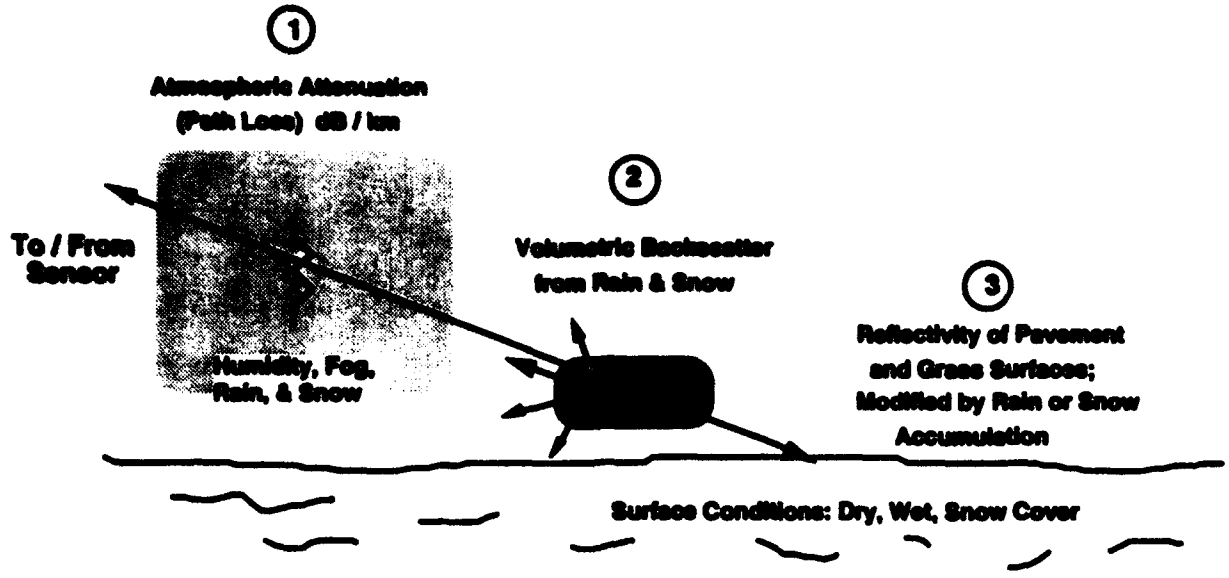

Figure 4.4.1-2. Meteorological effects on MMW radar.

Atmospheric attenuation is expressed in dB per kilometer (dB/km) over the propagation path of the radar energy. Total radar path attenuation is calculated over the transmit path plus the receive path lengths, or twice the slant range. The 35 GHz band (K_a) is in an atmospheric radio frequency (RF) transmission "window" that avoids the resonant frequencies of atmospheric gasses and water vapor. In clear conditions, the atmospheric attenuation at 35 GHz is very low, less than 0.1 dB per kilometer, even at 100% relative humidity. Attenuation in fog is a function of liquid water content per unit volume, and can be as high as 1 dB per km at 35 GHz for a very dense fog of 1 gram per cubic meter. RF attenuation in fog is due to the dielectric absorption and scattering of suspended water molecules, and the dielectric constant of the atmosphere which drives this process varies somewhat with temperature.

Rain attenuation is primarily a function of precipitation rate, but is also dependent on the size distribution of the droplets. The 3-4 dB/km attenuation measured at the Air Force Wright Laboratory Tower for a 10 mm/hr rain rate correlates well with the GTRI mathematical model of this phenomenon. Path attenuation for sleet and snow is a function of precipitation rate and of liquid water content, since frozen water has a much lower dielectric constant that does liquid water. Path attenuation at 35 GHz in even the heaviest snowfall rates is unlikely to exceed 2 dB/km. Atmospheric attenuation at 35 GHz from all contributors should vary somewhat depending on the transmitted polarization of the radar system.

Not only does the atmosphere attenuate the propagating radar wave; it reflects a portion of the incident energy back toward the radar. Since each volume of atmosphere delimited by the resolution cell size of the radar produces such backscatter, this phenomenon is termed volumetric reflectivity. Volumetric backscatter from precipitation is expressed as dBsm per cubic meter of illuminated volume. The illuminated volume is calculated from the radar resolution cell horizontal area projected through the antenna elevation beam pattern. Measured RCS from the cell volume is then divided by the illuminated volume for that resolution cell to normalize it to one cubic meter.

The radar receives combined clutter backscatter from ground surfaces and volumetric backscatter from the atmosphere within the same resolution cell, so the effects of each are not easily separated. The reflectivity of precipitation is typically modeled as the electromagnetic scattering from many small dielectric spheres, and varies with the distribution of droplet sizes and with temperature. Rain droplets are primarily single-bounce radar scatterers, so a radar with circular polarization can reject much of the rain backscatter since circular polarization is less sensitive to odd-bounce reflections than to even-bounce ones. Tower tests using the Honeywell 35 GHz radar with its circularly-polarized antenna have measured volumetric RCS of -50 $dBsm/m^3$ at a 10 mm/hr rain rate. Previous rain measurements made by GTRI at 35 GHz using vertical linear polarization show a volumetric RCS of -38 $dBsm/m^3$ at a 10 mm/hr rain rate.[1]. This indicates that the circularly polarized system has 12 dB less volumetric backscatter with which to contend in this case, and thus will provide significantly better rain penetration, all other factors being equal.

The reflectivity of terrain surfaces is modified by the presence of standing water or snow cover. Rain puddling on a paved runway makes the surface appear even smoother, so the radar backscatter is reduced below the already small value for dry conditions. Standing water in the grass border areas can reduce backscatter, but only if the grass areas become flooded. However, mere dampness on the grass, perhaps from dew or heavy fog, can increase the radar reflectivity. Fallen snow can more easily cover the grass, and effectively mask it from the radar. Freshly fallen snow behaves like a blotter to radar illumination, absorbing much of the incident energy, and causing low reflectivity. Snow cover will tend to equalize the reflectivity of runway and bordering surface areas. However, the observed radar effects of snow cover can vary greatly

---

1 N. C. Currie, F. B. Dyer, and R. D. Hayes, "Analysis of Radar Rain Return at Frequencies of 9.375, 35, 70, and 95 GHz," Georgia Institute of Technology, Atlanta, GA, Technical Report No. 2 under Contract DAAA25-73-C-0256, February 1975.

depending on the total water content, the free liquid water content, whether the snow is fresh or has thawed and then refrozen, as well as on other factors.[2]

4.4.1.2 Radar Performance Issues

A good synthetic vision (SV) radar sensor must offer a combination of performance features tailored to this application, including a rapid-scan antenna, high resolution, high average power, wide dynamic range, and high sensitivity. Existing airborne radars with surface search capability are typically optimized for coarse terrain mapping / terrain following applications, or for detecting important, high-threat military targets in clutter. On the other hand, a synthetic vision radar performs a different airborne sensor mission.

An SV radar must be capable of resolving the line of demarcation between two types of clutter: paved runways with very low backscatter, and bordering grass with higher backscatter. The principle SV requirement for traditional "hard" target detection is identification of runway intrusions, say, by taxing aircraft or ground support vehicles. Since there will be many man-made targets in the SV radar's field of view, the presence of these targets should not detract from the runway scene imaging performance of the radar.

The terrain-mapping resolution of an airborne radar with a real-aperture antenna is defined by the antenna azimuth beamwidth and the range resolution. The smallest terrain area resolvable by the radar is called a resolution cell. The depth of the resolution cell is determined by the range resolution of the system, and the cell width approximately equals the slant range times the tangent of the antenna azimuth beamwidth. An SV radar should offer high resolution to produce a clear, sharp image, and also a high antenna scan rate, so that the images presented to the pilot are updated quickly and without excessive latency.

Unfortunately, these two requirements compromise the detection of low-reflectivity clutter. A narrow-beam antenna scanning at a high rate does not dwell very long on each resolution cell, so little time is available to collect and integrate the backscatter return from a given resolution cell before the antenna beam moves away to another one. Broadening the antenna beamwidth would degrade the resolution, and allowing the antenna to dwell longer at each scan position would reduce the rate at which updated images are presented to the pilot. One available option is

---

2 N. C. Currie, R. D. Hayes, R. N. Trebits, *Millimeter-Wave Radar Clutter,* Artech House, Boston, 1992, pp. 145-152.

to increase the pulse repetition frequency (PRF) of the radar so that more pulses are generated during each period the radar dwells on a particular region in the scene. Radar returns from more pulses could then be integrated to produce a larger radar signal without "smearing" the azimuth resolution of the image.

Radar imaging of low RCS clutter at longer ranges requires methods that provide the maximum received power from the clutter backscatter. The radar range equation indicates the factors that contribute to received power, and states that the power received by the radar (P_r) is given by:

$$P_r = \frac{P_t G^2 \lambda^2 \sigma}{(4\pi)^3 R^4 L \alpha_a} \qquad (4.4.1\text{-}1)$$

where				
	P_t	=	radar peak transmit power	(watts)
	G	=	radar antenna power gain	(unit-less)
	λ	=	wavelength	(meters)
	σ	=	clutter radar cross section	(square.meters)
	R	=	slant range	(meters)
	L	=	system losses	(unit-less)
	α_a	=	total atmospheric attenuation	(unit-less)

The RCS of a clutter resolution cell, sigma (σ), equals the normalized clutter RCS, denoted sigma zero (σ_0), times the area of the cell. Sigma zero is not controllable, but the resolution cell area can be increased by lengthening the transmitted pulsewidth, or broadening the antenna beamwidth. The latter change is undesirable, since resolution and antenna gain will be decreased also. Increasing the antenna gain by decreasing the beamwidth is not practical, given the scan dwell time restrictions presented above and the fixed aperture typically available.

Received power increases directly with the peak transmit power. Thus, the reflected energy from the clutter can be increased by increasing the power transmitted by the radar. Furthermore, as indicated in Equation 4.4.1-1 above, reducing system losses can achieve the same benefit. The capability of the radar engineer to increase the transmitted power and/or reduce system losses is largely determined by the performance of available, newest-generation RF hardware components.

4.4.1.3 Synthetic Vision Figures of Merit

Figure 4.4.1-1 presented previously illustrates the basic radar phenomenology which supports runway detection in the synthetic vision application. This figure shows a hypothetical runway surface and the surrounding terrain, as a radar might view them. The runway surface is typically flat and smooth, and is viewed from roughly a 3 to 4 degree angle with respect to horizontal on approach. This angle is referred to as the depression angle. Thus, the great majority of the radar energy impinging on the runway surface is forward-scattered, away from the radar. The amount of energy scattered back toward the radar is very small.

The terrain surrounding the runway, on the other hand, tends to be more textured, and hence rougher, than the pavement surface. Surface debris, such as rocks or gravel, and surface vegetation both contribute to this overall roughness. This rougher surface tends to reflect a significant portion of the incident radar energy back toward the radar, which results in a larger-amplitude received radar signal from these areas.

Figure 4.4.1-3 illustrates the radar signature expected for the runway-terrain scenario. The oval in this figure contains seven constant-range cross-sections from the return signal a radar might receive when viewing the airport scene. Note the left and right transitions in the signals corresponding to the boundaries between the higher-amplitude terrain returns and those of lower-amplitude from the runway. If the seven constant-range cross-sections of Figure 4.4.1-3 were to be averaged (along each azimuth line), a composite waveform would be derived which could be analyzed as illustrated in Figure 4.4.1-4. Based on its general shape, the plot of this waveform is referred to as a "gutter" plot.

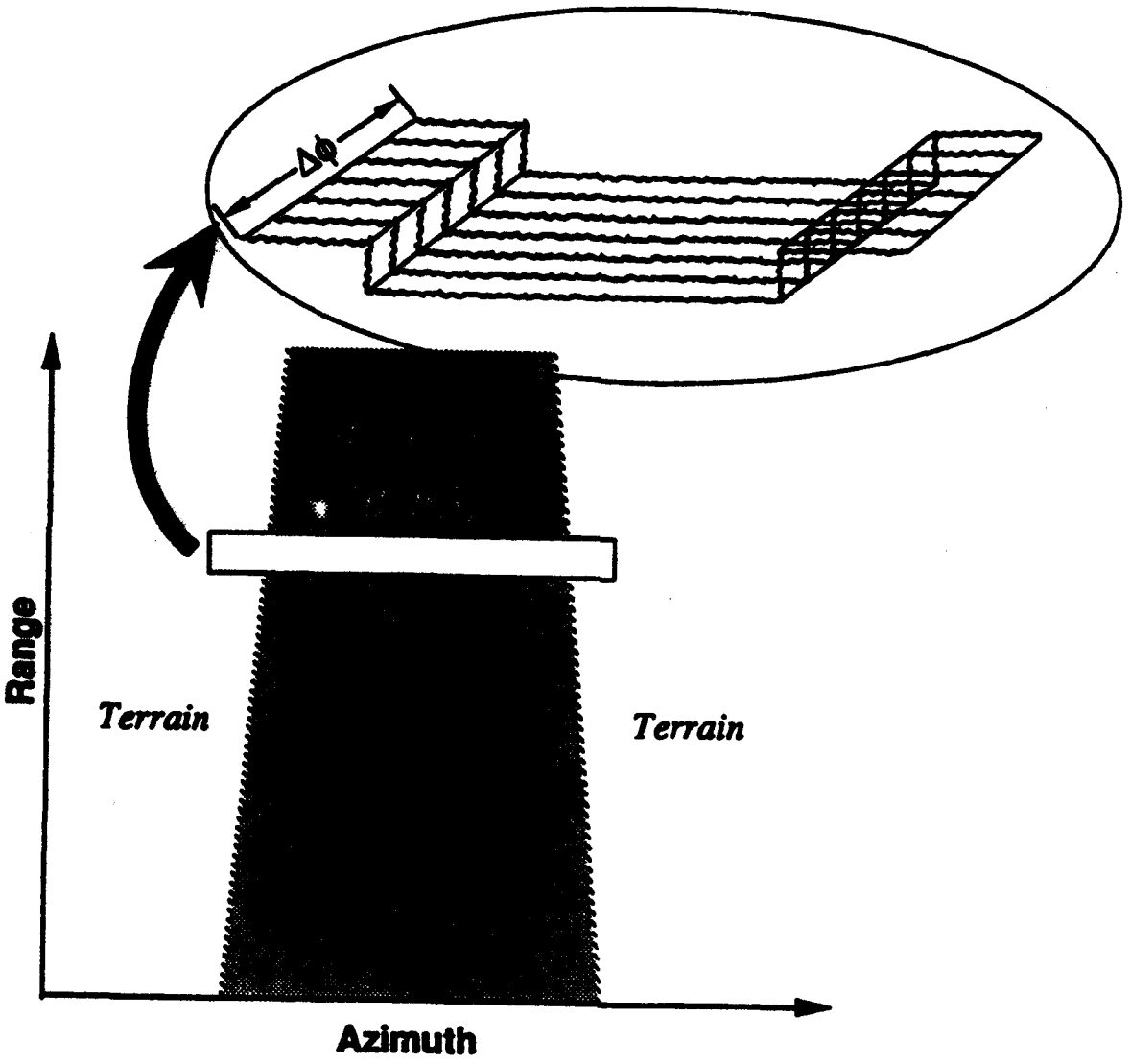

Figure 4.4.1-3. Illustration of Basic Radar Signature for Runway-Terrain Scenario

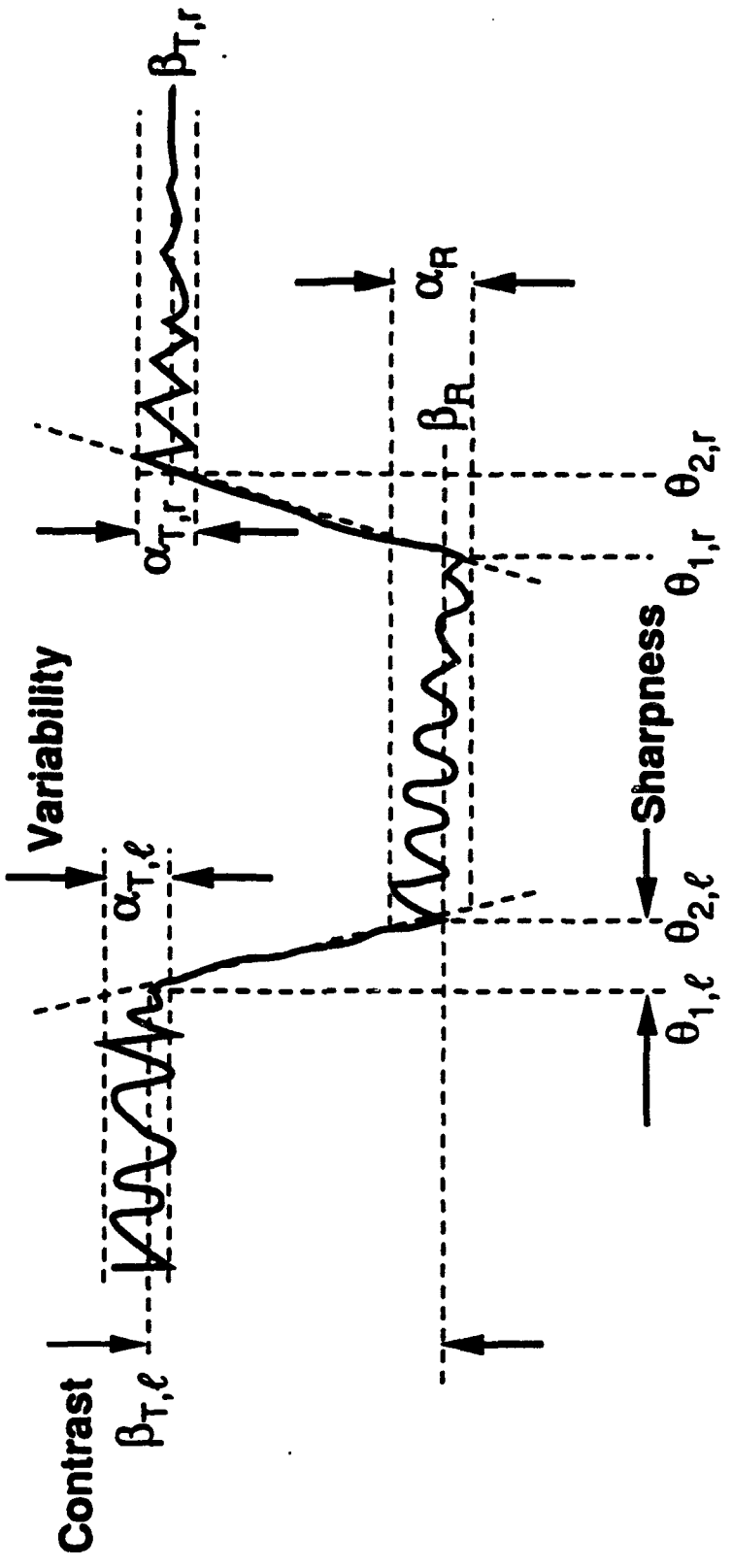

Figure 4.4.1-4. Illustration of Simple Gutter Plot with Basic Image Quality Metrics Indicated

Based on this gutter plot, three parameters can be defined which are indicative of how well the runway can be distinguished from the surrounding terrain. First, there is contrast which is a function of the average signal level received from the runway relative to that received from the surrounding terrain. The actual equation for the contrast, C, of the left-hand transition in Figure 4.4.1-4 is given by

$$C = \frac{\beta_R - \beta_{T,l}}{\beta_{T,l}} \qquad (4.4.1\text{-}2)$$

where the "brightness" levels β_R and $\beta_{T,l}$ are the average levels indicated in Figure 4.4.1-4.

Intuitively from Figure 4.4.1-4, the contrast improves as the terrain brightness becomes increasingly larger than the runway brightness. When this occurs, the contrast computed in Equation 4.4.1-2 above approaches -1. On the other hand, if the amplitude of the received signal from the runway is about the same as that from the surrounding terrain, then the contrast will be roughly zero. Thus, a radar contrast of -1 is the best which can be achieved, whereas a value of zero indicates no distinction at all between the two areas based on the received radar signal. Instead of a contrast metric which varies from -1 to 0, the radar engineer might prefer a runway-to-terrain ratio reported in dB. The relationship between these two metrics is illustrated in Figure 4.4.1-5.

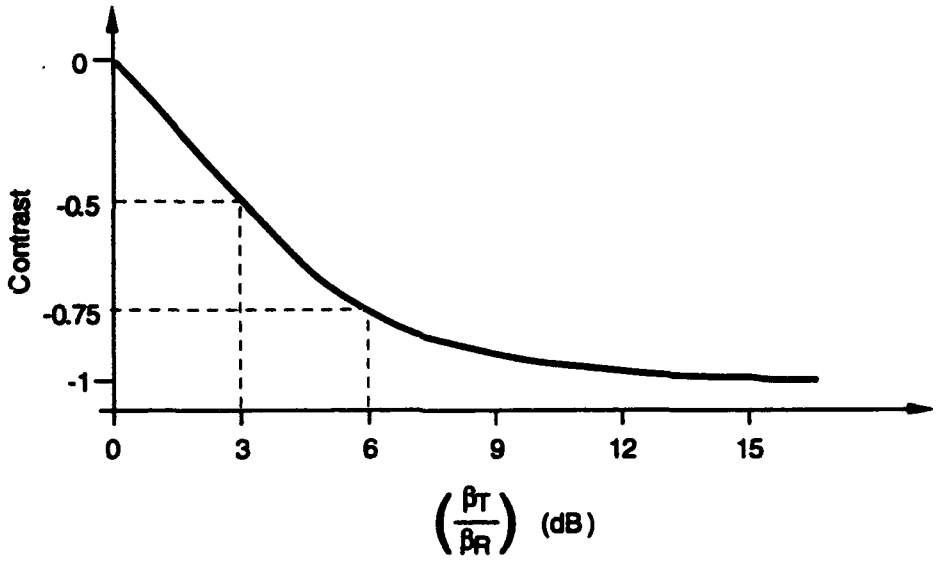

Figure 4.4.1-5. Illustration of relationship between contrast and terrain-to-runway ratio

The notion of sharpness is illustrated in Figure 4.4.1-4. Sharpness is defined as the inverse of the angular extent in azimuth over which the low-to-high or high-to-low transition occurs. The corresponding angular extents in Figure 4.4.1-4 are $(\theta_{2,l} - \theta_{1,l})$ and $(\theta_{2,r} - \theta_{1,r})$. If these angular extents are very small, then the transition will be clear and distinct and can be identified easily by the pilot. And since sharpness is inversely proportional to the angular transition, larger sharpness values are desirable.

The final parameter illustrated in Figure 4.4.1-4 is variability, which is a measure of the standard deviation of the radar signal amplitude. For a waveform such as that shown in Figure 4.4.1-4, there are three variability measures - one for each side of the terrain and one for the runway. Large variabilities correspond to "noisy" or "spiky" return signals which can mask actual surface transitions or be taken to falsely represent surface transitions not present in the scene.

This definition of variability is closely related to the term speckle noise, which is used to describe the ubiquitous, random variations seen in signals returned from nominally homogeneous areas, such as a section of asphalt pavement, or a patch of uniform grass. While large amounts of speckle noise within an image will certainly be distracting to the pilot, smaller amounts should be tolerable, and may even have the desirable effect of giving the image texture and facilitating depth perception by the pilot. In general, however, low speckle noise levels (small variability's) are desirable in the radar data.

In order to quantify small and large variabilities, the parameter actually measured under this program was the signal-to-variability ratio. This ratio was obtained by dividing the signal level difference between the terrain and the runway by the weighted average variability for the terrain and runway.

The image quality metrics defined above were computed for the data provided by the Honeywell radar at two points in the systems. First, the raw data output provided by the radar receiver was analyzed. These data were obtained prior to the B-to-C-scope conversion necessary for presenting these data to the HUD. The raw radar data were not recorded continuously, but a discrete image corresponding to a complete azimuth scan of the radar was captured roughly every four seconds during approach and roll-out. Each of these discrete raw radar data images is called a snapshot. The image quality analyses of these snapshots were performed by GTRI and are described in this report.

Second, the same image quality metrics were computed for the RS-170 video presentation of the radar data, just prior to display on the HUD. These video images were presented in standard C-scope format (elevation versus azimuth), and the update rate for these video images as provided by the radar was approximately 10 per second. The analyses of these RS-170 radar video data are documented in Sections 4.5. and 7.

One of the objectives of the synthetic vision data analysis efforts was to apply identical metrics to identical regions within the raw radar data (snapshots) and the RS-170 radar image data available for display on the HUD. Based on this concept, the metrics computed from the raw data would represent the potential for runway detection and recognition offered by the radar. Those computed from the processed RS-170 data would indicate how well the Honeywell image processing methodology took advantage of this potential, as well as what, if any, degradations were introduced by formatting the data for presentation on the HUD.

Thus, the use of identical image quality metrics for the two processes was essential. The three described above - contrast, sharpness, and signal-to-variability ratio - were suitable for both applications and were thus agreed upon at the outset of the analysis efforts.

Other image quality parameters could have been defined to measure the quality of the runway image. At first glance, it may seem that the runway detection problem is one of detecting two straight lines in the data - one corresponding to the right edge of the runway, the other representing the left. Some have proposed convolving an edge-detecting kernel with the data to determine how closely any transitions within the data match an ideal edge. Such operations are commonly encountered in image enhancement applications.

This later section will also point out that application of an equivalent convolution operation to the radar data in its various presentation formats is not straightforward. Whereas the two runway edges appear as parallel lines in the plan position indicator (PPI) display used in the raw data analysis, the two lines are in general not parallel in the corresponding C-scope display used in the RS-170 image data analysis, and are curved in the B-scope display of the same data (which was used in the tower tests).

The point to be made is that while other image quality parameters could be envisioned, these three were selected because they were appropriate to the synthetic vision imaging application; they were well-known and simple to understand and compute; and they could be

readily applied to the radar data in its various formats. Since the results of the image quality analyses are discussed in Section 7, comments are made there regarding the interpretation and usefulness of these metrics for the synthetic vision application.

The three image quality parameters described above are just some of the radar characteristics which are important in the SV application. Table 4.4.1-1 below lists these and others. For each characteristic, the associated units are indicated, as well as the significance of the characteristic and the source of the measurement. Some analyses could best be performed at the tower; whereas others were performed both at the tower and during the flight tests. In addition, two of the characteristics were assessed only in the flight tests and were evaluated based on subjective pilot opinion, rather than on pilot-independent analysis of the raw data. These characteristics are so noted in Table 4.4.1-1.

Table 4.4.1-1. Selected Radar Characteristics Important for Synthetic Vision

Characteristics	Units	Significance	Assessment Source
Contrast	-	Runway Detection & ID	Tower, Flight
Sharpness	degrees-1	Runway Detection & ID	Tower, Flight
Variability	-	Runway Detection & ID	Tower, Flight
Pt Scatterer Range Response	-	Range Resolution	Tower
Pt Scatterer Angle Response	-	Azimuth Resolution	Tower
Geometric Distortion	-	Runway Detection and ID	Subj. Pilot Assessment
Field of View	deg x deg	Sensor Coverage	Tower
Sensor Update Rate	frames/sec	Image Continuity	Subj. Pilot Assessment
Radar Cross Section*	dBsm	Detection vs. Range	Tower, Flight
Reflectivity (σ°)*	dB	Detection vs. Range	Tower, Flight
Volumetric Reflectivity*	dBm	Detection vs. Range	Tower, Flight
Path Attenuation*	dB/km	Detection vs. Range	Tower, Flight

Note: * indicates measurement requires fully calibrated data.

The first three characteristics in Table 4.4.1-1, as described above, are all relative-amplitude based and thus do not require absolute calibration of the radar sensor. The next two radar characteristics - the point-scatterer range response and the point-scatterer angle response - address the fundamental spatial resolution offered by the sensor. The better the resolution, the finer the details which the sensor can distinguish in the image. Due to the ease of positioning

calibrated radar reflectors in the scene as well as the static sensor-scene geometry there, these measurements were performed at the tower only.

Likewise, measurement of the instrumented sensor field of view was made only at the tower. This sensor field of view represents the two-dimensional (azimuth versus range) extent covered by the sensor in a normal scan. This parameter was measured at the tower since the sensor-scene geometry is fixed in this case and calibrated reflectors could be conveniently placed in the scene being imaged.

The sensor update rate represents the rate at which new images are presented by the sensor to the pilot. Like the field of view, it is a design parameter and can be easily verified. However, in this case, determining the specific update rate was not the final goal. Rather, determining whether the sensor update rate is adequate for the pilot was the real issue of interest. Increasing the update rate beyond the point at which it is deemed acceptable is not typically cost-effective. Thus, evaluation of whether the update rate is acceptable or not was done as part of the flight test subject pilot evaluations.

The geometric distortion introduced by the radar sensor is also assessed during the subjective pilot evaluations. Due to the relatively poor azimuth resolution of MMW radar sensors (compared with the human eye) and the lack of height resolution with the radars tested, these sensors will distort the scene relative to our visual perception. However, defining a single figure of merit that reflects this distortion and is meaningful in all situations is difficult to do. Also, the key issue is not one of computing this distortion for a given sensor, but rather one of determining the pilot's response to this distortion. This latter, subjective assessment was obtained when appropriate via the pilots' evaluations.

The last four parameters in Table 4.4.1-1 quantify the basic radar phenomenology for the SV scenario. The radar cross section (RCS) of a particular region of the ground is a measure of the equivalent radar scattering area of that region. RCS has been discussed previously in Section 4.4.1.1.1. This radar cross-sectional area should not be confused with the physical area of the region of interest. For a constant-area patch on the ground, the RCS is a function of the specific surface roughness, composition (grass, concrete, dirt, etc.), and viewing angle, among others. RCS values are typically reported in units of decibels relative to a square meter (dBsm).

For surface scattering regions, such as patches on the ground, the RCS is often normalized to yield the radar cross section per unit area illuminated. The resulting reflectivity is typically

reported in decibels (= dBsm per square meter). Since the radar actually measures RCS, the reflectivity is derived from this measurement by computing the illuminated area on the ground surface (based on the scenario geometry as well as the antenna pattern and waveform characteristics of the radar), and dividing the measured RCS by this value.

As the radar energy propagates from the radar to the illuminated region of the ground and back to the radar, the intervening atmosphere affects that energy. First, this atmosphere is characterized by a reflectivity since it reflects some of the incident energy back toward the radar. In clear weather at 35 GHz, this reflectivity is relatively small, but it can become a severe limitation in heavy precipitation. Since this atmospheric reflectivity is a volume-based rather than area-based phenomena, it is referred to as volumetric reflectivity and is typically reported in units of decibels with respect to a square meter per meter cubed(= $dBsm/m^3$).

The second primary effect of the atmosphere for SV applications is attenuation. As the radar energy travels through the atmosphere, a portion of this energy is absorbed by water droplets or vapor, atmospheric gases, suspended particulate matter, etc. The attenuation of the radar energy as it travels through the atmosphere is typically reported in units of dB per kilometer (dB/km).

As indicated above, surface reflectivity (and RCS), volumetric reflectivity, and atmospheric attenuation are all fundamental phenomenological parameters. The accurate measurement of these parameters requires that the radar be fully calibrated so that absolute received power levels are known. This calibration process typically requires that a standard radar reflector of known RCS be placed in the scene so that measured power levels can be associated with specific RCS values. Typically, two or more such standard reflectors are used to improve the accuracy of the calibration process.

These four "calibrated" parameters define the basic phenomenology that determines how well the radar can image the airport scene of interest. However, for any given approach, they are not essential for quantifying the observed sensor performance. The observed contrast, sharpness, etc. *define* that performance. Nonetheless, the phenomenological parameters help *explain* the observed performance.

Not only are these parameters important in explaining sensor performance in a given scenario, they also are critical to extrapolation of the observed performance in one scenario to some other, different scenario. The contrast observable between a concrete runway and surrounding grass can be predicted based on the measured contrast for asphalt runway surrounded by grass, and knowledge of the respective reflectivities of concrete and asphalt.

4.4.2 RADAR EVALUATION METHODOLOGY

The flight test methodology was carefully designed to provide a cost-effective, yet thorough synthetic vision technology demonstration and assessment. This methodology was based on a top-down approach whereby program objectives were analyzed to determine flight test requirements, which in turn, led to a definition of the test "observables" to be quantified. The data analyses required to quantify these observables were then defined, and finally, the test data which must be acquired to support these analyses were specified.

This disciplined, goal-oriented approach ensured that the key issues of the SVSTD program were systematically addressed and that all required data were gathered, without resorting to the costly process of recording everything conceivably needed and sorting it all out later. The decision of whether specific data should be collected and analyzed was based on the value of these data in addressing program objectives.

Two types of analyses were performed. First, there were system analyses which measured the performance of the pilot while using the synthetic vision system. Second, there were radar sensor analyses which provided an objective assessment of the SV sensors themselves. This report addresses those analyses applied to the raw data acquired with the Honeywell radar sensor. These analyses are critical since the performance of the sensor bounds the ultimate performance which can be achieved using the overall SV system. The quality of the synthetic vision images available to the pilot is determined by (1) the raw sensor data quality, (2) the enhancements (or degradations) introduced by the signal and/or image processing systems, and (3) the fidelity of the image presentation system (the HUD). In addition, some of the image processing functions (for example, the C-scope conversion) depend on aircraft attitude and flight inputs, so the accuracy's of these latter data are important as well.

If the quality of the raw sensor data is high (implying the sensor is well-suited to the airport synthetic vision task), then relatively straightforward downstream signal/image processing

techniques may be adequate to provide the needed SV performance. On the other hand, if the raw sensor data quality is poor, the particular sensor is not well-matched to the SV mission, and even the most sophisticated downstream processing techniques will not produce an acceptable image. Only by analyzing the raw sensor data can this assessment be made. These analyses for the Honeywell radar sensor are documented in the current report.

4.4.2.1 DATA SOURCES

In order to assess the performance of the Honeywell radar, several fundamental characteristics were analyzed for a variety of approaches during the flight tests. These characteristics have been discussed previously in Section 4.4.1.3 and are listed in Table 4.4.1-1 above. In order to perform these analyses, data were required from several sources. The paragraphs which follow describe each of these data sources.

4.4.2.1.1 Radar Data

In order to perform the necessary radar system analyses, data from the radar must be acquired. Fortunately, in order to assess the flight test parameters indicated in Table 4.4.1-1 (not including the two addressed via subjective pilot assessment), continuous radar data are not required. Rather, each of these "static" parameters can be measured from individual "snapshots" of the radar data. Each of these snapshots presents a single image of the airport scene, and corresponds to one full azimuth scan of the antenna.

The use of discrete data snapshots rather than continuous data provided at the full update rate of the sensor greatly simplified data acquisition system requirements and cost. Based on a desired 500 meter maximum spacing of the snapshots in slant range and the typical 72 m/sec (140 knot) ground approach speed of the Gulfstream II, one radar data snapshot should be taken every 6.94 seconds. The Honeywell data acquisition system generated a radar data snapshot approximately every four seconds, and thus more than satisfied this requirement. The actual format of the radar data in each snapshot is described in Section 4.4.2.3.1.1.1 below.

Table 4.4.2-1 below summarizes the raw radar data available from the flight tests of the Honeywell 35 GHz radar sensor. This list includes airports, dates, and general weather conditions for each set of approaches. Table 4.4.2-1 includes only those approaches which include at least one of three fixed snapshots typically examined. 'Snapshots correspond to a 50 ft altitude

Table 4.4.2-1. Summary of Raw DataAvailable from Flight Tests of the Honeywell 35 GHz Radar System

Airport	Date (1992)	Approaches	Weather	Comments
Arcata, CA (ACV)	8/27	3	Clear	Calibration
	8/28	10	Fog	
Atlantic City, NJ (ACY)	9/27	1	Clear	
Colorado Springs, CA (COS)	11/21	2	Snow	
Carlsbad/Palomar, CA (CRQ)	8/18	3	Clear	
Huntington, WV (HTS)	9/28	4	Fog	
Los Angeles, CA (LAX)	8/18	3	Clear	
Langley AFB, VA (LFI)	9/27	1	Clear	
Millville, NJ (MIV)	9/27	1	Clear	
Patuxent River NAS, MD (NHK)	9/27	1	Clear	
Point Mugu NAS, CA (NTD)	8/4	1	Clear	
	8/13	5	Clear	
	8/18	6	Clear	Cal & Runway Intrusion
	11/27	6	Clear	Calibration
Pueblo, CO (PUB)	11/20	4	Snow	
	11/21	2	Snow	
San Diego, CA (SAN)	8/18	2	Clear	
Santa Barbara, CA (SBA)	8/19	4	Clear	Calibration
Santa Maria, CA (SMX)	8/20	3	Clear	Calibration
Vandenburg AFB, CA (VBG)	8/8	7	Fog	
	8/11	8	Fog	
	8/13	6	Fog	
	8/19	4	Clear	Calibration
	8/27	6	Fog	
Van Nuys, CA (VNY)	8/13	1	Clear	
	11/27	1	Clear	
McGuire AFB, NJ (WRI)	9/26	1	Rain	Refuel Stop only

of the aircraft (roughly the flare point), a 200 ft aircraft altitude (the decision height), and a 2500 meter slant range from the aircraft to the touchdown target. Appendix G includes a much more detailed list of the raw data available and notes which specific snapshots were selected for analysis.

As can be seen from Table 4.4.2-1, raw radar data are available for 96 total approaches at a total of 17 airport facilities. Of these 96 approaches, 46 were made in clear weather, 41 in fog, 8 in snow (or with snow on the ground), and 1 was made in rain. However, the single rain approach was actually a refueling stop and no weather data are available to correlate with the

observed radar performance. Thus, for purposes of GTRI's analysis, no radar data in known rain conditions are available from the flight tests. Fortunately, Honeywell radar data in rain are available from the tower.

4.4.2.1.2 Flight Profile Data

In addition to the recorded radar data, information describing the flight profile was also needed. However, since only discrete raw radar data snapshots were captured for analysis; discrete, static descriptions of the aircraft position and orientation at each snapshot location were sufficient for the GTRI analyses. Thus, recording continuous flight profile data was not necessary.

The approach adopted by Honeywell for capturing the flight profile data was to record them as part of a header for each radar data snapshot file. Included in this header were aircraft attitude and position as provided via the ARINC data bus by the on-board inertial navigation system (INS) and radar altimeter. Aircraft attitude data included roll, pitch, and heading; these were used in the analysis for scene registration and for antenna gain calculations. The term scene registration denotes the process whereby the image provided by the radar sensor is associated with a physical area on the earth's surface. Aircraft position data included latitude, longitude, and altitude. Both barometric and radar altimeter data were available. These aircraft position data were used by GTRI in scene registration and in computing depression angles to various regions of interest on the ground. The raw radar data itself was used to determine slant ranges to regions of interest in the image. The 7.5 meter range accuracy of the Honeywell radar was felt to be far better than that which could be derived based on differential latitude, longitude, and altitude calculations.

4.4.2.1.3 Weather Data

Weather data for each approach were provided by a pair of probes, one mounted under each wing of the Gulfstream II aircraft. These probes were supplied by JTD Environmental Services, Inc. of Pasadena, California under subcontract to TRW. JTD personnel collected data from the probes, reduced these data and provided them in electronic format to GTRI. These weather data were subsequently processed by GTRI as described in Section 4.4.2.3.3 below. The equipment

supplied by JTD included a JW Liquid Water Content Probe (JW-LWC), a temperature probe, a pressure transducer, and two aerosol particle probes to measure cloud and rain drop size spectra.

The particle probes were the Forward Scatter Spectrometer Probe (FSSP-100), capable of measuring fog particles from 2 μm to 47 μm, and three optical array spectrometers, the OAP-200X, OAP-200Y, and OAP-200N sensors, capable of measuring larger drops. The OAP-200X can measure cloud and rain drops from 20 μm to 300 μm. The OAP-200Y can measure particles from 300 μm to 4500 μm (4.5 mm). The OAP-200N, also called the "Narrow Arm Precipitation Probe" in JTD material, can measure particles from 140 μm to 2100 μm (2.1 μm). Only one of the OAP sensors was placed in service at a time, and the selection was based on the expected precipitation particle sizes for the upcoming flights.

JTD provided calibration and processing for the data recorded during the flights. The original raw data sets were converted into engineering units useful in calculating meteorological parameters of interest. Essential derived quantities were calculated from the in-flight data sets and included in the ASCII data sets provided to GTRI. These derived quantities included height above the surface, pressure within the layer, temperature (T), liquid water content (LWC), water vapor density (D_v), rainfall rate (RR), and number concentrations for the two particle probes used during the flight. Several other derived quantities were calculated by JTD and presented only in graphical form. These graphed quantities included total particle number concentration (N_t), median particle radius (R_0), and calculated slant visual range (VR). A description of the algorithms used to produce these derived quantities is provided in Appendix H.

National Weather Service surface hourly observations from the airports used in the tests were also obtained to verify the JTD data sets. These reports were especially useful in applying corrections to the temperature readings recorded in-flight. A summary of the nature of the deviations between the in-flight temperatures and the observed surface temperature, as well as the suggested remedy for the discrepancies is reported in Section 4.4.2.3.2.5.

On each approach, the wing-mounted probes measured continuously the water drop-size distributions and other meteorological parameters encountered along the glidepath. Then, following completion of the approach, these measured distributions and data were effectively integrated along the approach path and further analyzed to compute the weather metrics used in the radar performance analyses. These metrics were liquid water content (in gm/m^3) for fog,

rainfall rate (in mm/hr) for rain, and equivalent rainfall rate (mm/hr) for any other precipitation, such as snow.

4.4.2.1.4 Ground-Truth Data

Basically two types of ground truth data were obtained during the program. First, pre-flight airport surveys were conducted at six California airports designated as primary. These airport surveys are discussed in the following section. Second, additional information was obtained as needed either post-flight or near-simultaneous with the flights. This information is discussed in Section 4.4.2.1.4.2.

4.4.2.1.4.1 Airport Surveys

Before flight tests could be conducted, suitable airports had to be identified at which the Gulfstream II experimental SV aircraft could be operated. Several airports were identified as suitable candidates for the flight tests based on airport facilities available, probability of encountering weather conditions of interest, logistics concerns, as well as runway surface type. The Gulfstream II aircraft actually made approaches at all of these airports.

The six airports listed in Table 4.4.2-2 were designated primary, largely based on the probabilities of encountering weather conditions of interest at these facilities as well as the fact that they are all within a 70-mile radius of Van Nuys, California, which served as the home base of the Gulfstream II test aircraft. Provided the desired weather events were present at these airports, they were used most frequently during the flight test program to minimize transit times and costs.

Table 4.4.2-2. List of Primary Airports

Airport	Latitude/Longitude	Elev. (ft)	Run-ways	Length (ft)	Width (ft)	Surface	Precision Approach Aids
Arcata (Eureka) California	N 40° 58' 42"/ W 124° 06' 27"	218	14-32	5998	150	Asph-Pfc	ILS/DME 32 200-3/8 GS 3.0°
Pt Mugu NAS California	N 34° 07' 12"/ W 119° 07' 12"	12	03-21 09-27	11100 5500	200 200'	Asph Asph	PAR/ILS P- 03 100-1/4 GS 3.0° P- 21 100-1/2 GS 3.0° I- 21 200-1/2 GS 3.0°
Santa Barbara California	N 34° 25' 32"/ W 119° 52' 02"	10	07-25 15R-33L 15L-33R	6049 4183 4179	150 100 75	Asph-Grv Asph Asph	ILS 07 200-1/2 GS 3.0°

Santa Maria California	N 34° 53' 54"/ W 120° 27' 24"	259	12-30	6300	150	Asph-Pfc	ILS 12 200-1/2 GS 3.0°
Vandenburg AFB California	N 34° 43' 48"/ W 120° 34' 36"	367	12-30	15000	200	Conc	ILS/DME 1-12 100-1/2 GS 3.0° 30 200-1/2 GS 3.0°
Van Nuys California	N 34° 12' 35"/ W 118° 29' 21"	799	16R-34L 16L-34R	8001 4000	150 75	Asph-Conc Asph	ILS 16R 300-3/4 GS 3.9°

In order to accurately calibrate the Honeywell radar system, four Bruderhedral precision radar reflectors were provided to the program by GTRI. These Bruderhedrals can best be described as a portion of a top hat resting on a flat plate.[3] They are thus double-bounce reflectors well-suited for calibrating a circularly polarized radar such as the Honeywell system. During the course of the flight test program, a pair of these Bruderhedral reflectors was positioned at each of the six primary airports and several approaches made against them to obtain absolute radar calibration data. Calibration data for four of these airports have been analyzed, and the results of this analysis are presented in Section 4.4.3 to follow.

Due to the importance of these six airports, all six were visited and surveyed in May, 1992 in preparation for anticipated flight test operations. The primary purpose of these surveys was to obtain information regarding (1) airport geometry and terrain, (2) runway and surrounding border type and condition, and (3) any man-made structures which would likely contribute to the sensor image. In addition, appropriate points-of-contact were identified and briefed to facilitate subsequent flight test activities and data collection.

4.4.2.1.4.2 Other Ground Truth Data

Table 4.4.2-3 lists the airport data desired to support analysis of the synthetic vision radar data for each approach.

Table 4.4.2-3. Desired Ground-Truth Data From Airport Sites

Parameter	Usage
Runway Description	
Type	Scenario Definition
Condition and roughness	Data Segregation for Analysis
Surface Water (snow) depth and condition	
Percent free water content (snow only)	
Terrain Description	
Type	Scenario Definition

[3] N. C. Currie and C. E. Brown, ed., *Principles and Applications of Millimeter-Wave Radar*, Artech House, Norwood, MA, 1987, pp. 773 - 774

Condition and roughness	Data Segregation for Analysis
Surface Water (snow) depth and condition	
Percent free water content (snow only)	
General Information	
X,Y, and Z of Range Reference in Scene	Scene Registration
Lat, Long, and Alt of Calibration Reflectors in Scene	Range Computation
Lat, Long, and Alt of Significant objects along approach (Glideslope Tower, Localizer, etc.)	System Calibration Scenario Definition
Time-tagged record of runway and taxiway traffic during approach and landing	(ground structure and vehicle ID)

For the most part, the "General Information" indicated in Table 4.4.2-3 was obtained for the six primary airports as part of the pre-flight-test airport survey described above. Some of the "Runway" and "Terrain Description" data indicated in this table were also obtained during these airport surveys. In addition, site notes, including photographs, were recorded by GTRI at some of the primary airports during the course of deploying the Bruderhedral reflectors. This information was very important since it captured the actual condition of the terrain and runway surfaces (moisture conditions, height of vegetation, etc.) in the same time frame as when the radar data were actually acquired.

Even for airports not surveyed visually by test personnel, ground truth data were available. One source was the terminal charts contained in the United States Government Flight Information Publications. These were used to determine airport layout; airport latitude, longitude, and altitude above sea level; and relative position of key structures (control tower, etc.). Appropriate documents were also consulted to determine runway pavement type (concrete, asphalt, grooved, etc.).

In addition, surface weather observations from various airports were obtained covering the time period during which approaches were made at that airport. These could often be used to infer weather conditions on approach, and thus complemented the weather data supplied by the instrumentation on board the Gulfstream II. For example, the analyst knew that surfaces were wet if rain had been falling for some time prior to the approach. For approaches made in snow at Pueblo and Colorado Springs, CO, test personnel obtained data by visual inspection of the snow (fresh, wet, dry, etc.) and whether or not the runway had been recently plowed.

Obtaining a detailed record of runway and taxiway traffic was not practicable for the approaches. For many of the poor weather approaches, airport traffic was either very limited or even non-existent due to the weather conditions, so time-tagged traffic data were not needed.

However, for the specific set of approaches designed to assess the ability of the system to detect runway intrusions, the various locations of the ground vehicle used in this test were noted.

4.4.2.2 Data Acquisition Problems

Three data acquisition problems associated with the raw data snapshots were encountered during the course of the program and impacted subsequent data analysis activities. These are discussed in the paragraphs which follow.

4.4.2.2.1 Range Bin Misalignment

A range bin misalignment was found in the Honeywell raw radar data which caused the samples for the odd range bins along each azimuth line to be shifted up by two bins. Thus, the actual return for range bin 1 was stored in range bin 3, that for bin 3 was stored in bin 5, etc. The actual bin 1 return was lost, but this was not a problem in the raw radar analyses since this bin spans the first 7.5 meters, and ranges that close to the radar were not examined.

Once discovered, this range bin misalignment was easily fixed. Section 4.4.2.3.1.1.3 describes the range bin alignment correction implemented in the GTRI data import software to fix this problem. In order to avoid confusion, the misalignment was left in the Honeywell data acquisition system even after it was discovered, and GTRI agreed to correct the misalignment each time data were read for analysis. If the misalignment had been fixed midway through the program, then confusion could possibly arise as to which data should be fixed by GTRI and which had already been fixed by Honeywell.

4.4.2.2.2 Loss of Data

The second data acquisition problem was more severe than the first and unfortunately could not be rectified after the fact. The Honeywell data acquisition system sometimes encountered problems transferring radar snapshot data from random-access memory to the hard disk. These problems were reportedly associated with power supply "glitches" and the data acquisition system operator was not always aware of their occurrence. The result was that data were never recorded on hard disk for a significant number of approaches and were thus not available for

analysis. Table 4.4.2-1 above lists the approaches for which radar snapshot data are available, and Appendix G lists the specific snapshots analyzed.

4.4.2.2.3 Data Synchronization Problems

The third significant data acquisition problem involved the synchronization between the radar data collected in each snapshot and the associated IRIG time and inertial navigation system (INS) data also collected with that snapshot The Honeywell data acquisition software was reportedly interrupt-driven and the INS data update for each frame was not a relatively high priority. Thus, the INS data associated with any given snapshot were delayed with respect to the corresponding radar data.

Initial attempts to compensate for these synchronization problems were based on Honeywell estimates of the delay involved. Honeywell's initial estimate of this delay was 0.2 second, but was later revised to 0.5 second. In making these estimates, Honeywell noted that the interrupt processing was complex and accurate delay values were difficult to estimate. Although the mechanism of the delay was understood, the exact value was not known and was likely not constant for all snapshots.

To better quantify the delay, the IRIG time reported by Honeywell for a specific barometric altitude was compared with the IRIG time recorded by the TRW RS-170 data collection system for that same altitude. This comparison was made for four snapshots from approach 2A at Arcata, California on 8/28/92. The corresponding measured delays were 0.836, 1.751, 2.897, and 1.812 seconds for the Honeywell data acquisition system with respect to the TRW acquisition system. (Any relative data delays within the TRW system were believed to be insignificant, and thus data acquired with this system were used as a reference.) Note that this is the delay between the IRIG time and the INS data, as recorded by Honeywell. Unfortunately, no way could be found to measure the delay between the radar data and the INS data, which is the essential delay of interest.

Since gathering the radar data, the INS data, and the IRIG time were all different tasks with different interrupt priorities and thus different timings, the relative delay between the INS data and the radar data would be expected to be different than that between the INS data and the IRIG time information. Nonetheless, computing the latter gave a good indication of the general magnitudes of delays present in the system.

As indicated above, the relative delay between the INS data and the radar data could not be determined. Honeywell personnel did state that the delay was guaranteed to be no greater than the data snapshot spacing, based on the design of their data acquisition system. Thus, the delay for each snapshot was greater than 0 and less than 4 seconds, the latter being the approximate snapshot spacing. A 2 second delay was therefore assumed in the aircraft inertial data recorded for each snapshot. This assumed 2-second delay was used whenever accounting for and attempting to correct for this delay were appropriate based on the analysis being performed.

Based on a 3 to 4 meter/second descent rate on approach, a 2 second delay corresponds to a reported altitude that is too low by about 6 to 8 meters (20 to 26 feet). In addition, the pitch and roll angles used to compute antenna gain are also delayed with respect to the radar data and therefore invalid in a strict sense. The effects of these synchronization errors vary according to the specific radar analysis being performed.

4.4.2.2.3.1 Effect on Image Quality Analyses

First, consider the Image Quality (IQ) assessment which includes the contrast, sharpness, and signal-to-variability ratio metrics. The analyses of these IQ metrics as functions of slant range remain valid since slant range is determined from the radar return timing, independent of altitude. Even analyses of these IQ metrics as functions of depression angles are fairly sound at higher altitudes since depression angle changes little for a 6 to 8 meter error in this case. However, at lower altitudes, the depression angle error is more significant.

The primary impact for the IQ assessment is the registration error between the snapshot for which the raw radar analysis is applied by GTRI and the corresponding RS-170 radar image for which the image analysis is applied by TRW. One of the goals of this program was to compute identical IQ metrics for the same regions in the raw radar data as well as in the RS-170 image data produced by the Honeywell system. The method used to coordinate these two sets of analyses was based on the barometric altitudes provided for each snapshot selected for raw data analysis to those responsible for performing the RS-170 image analysis. The image analysts then selected the images corresponding to each of those altitudes for their processing. Unfortunately, the current synchronization problem means that the RS-170 image analyzed will lag the corresponding raw radar image by roughly 2 seconds.

4.4.2.2.3.2 Effect on Analyses of Surface Reflectivities

The goal of the second broad type of radar data analysis is the measurement of reflectivities of the runway surfaces and surrounding terrain. Because such data are most naturally reported as functions of depression angle, the contamination of depression angle by altitude errors is a concern. As noted above, these errors are relatively small at higher altitudes. However, lower altitude data were typically used for these analyses since at lower altitudes the runway radar return is more likely to be above the noise floor of the system, especially for shallower depression angles (1 - 3 degrees). This effect is due to the fact that the slant range to a runway region of interest at a given depression angle decreases as the altitude of the radar decreases.

Another impact of the altitude error concerns the multipath analyses performed for each snapshot to compute the effective radar cross section of the Bruderhedral for that specific image. (This analysis is described in Section 4.4.2.2.1 below.) Multipath is the term used to describe the interference between the direct target illumination by the radar and the indirect illumination caused by reflections from the ground. In order to accurately calibrate the radar (so that absolute reflectivities can then be compluted), this multipath should be quantified and appropriate correction factors applied.

A first-cut analysis indicates that, at a slant range of 2.8 km, the multipath effects go from a maximum to a minimum for an altitude change of 6 meters. Thus, altitude errors on the order of 6 to 8 meters are indeed significant for this effect.

Fortunately, the impact of these multipath errors can be mitigated somewhat. First, the real purpose of the multipath analysis for reflectivity computations is system calibration, not individual scene calibration. A calibration factor can be computed for the radar system for each of several snapshots, and these factors then averaged to get a better estimate of the final factor to actually apply to the system. The multipath estimate may be low for some snapshots and high for others, but the average should be reliable. This approach is valid provided the Honeywell system remains fairly stable over time

In addition, only the most reliable calibration data would be used; snapshots suspected of being highly contaminated by multipath can be discarded. Since multipath effects are dependent on geometry, and each calibrated scene has two reflectors in place, the calibration can be based on only one reflector when it is significantly less affected by multipath than the other.

Accurate analysis of reflectivities dictates that not only the radar (aircraft) altitude be known, but also radar attitude. This attitude information is used to compute the appropriate antenna gain applied to each cell in the raw radar image. The magnitude of the error in computing reflectivity's due to an error in aircraft attitude depends on the specific aircraft dynamics at the time the data are acquired; larger short-term changes in pitch and roll will produce larger errors in the reflectivity measurements. Fortunately, the baseline calibration approaches were made in clear weather, so that weather-induced aircraft attitude effects should be minimal.

4.4.2.2.3.3 Effect on Analyses of Attenuations and Volumetric Reflectivities

The analyses applied to each clear-weather snapshot to calibrate the radar system and compute surface reflectivities were very similar to those applied to each in-weather snapshot to measure the effects of weather. These weather effects are reported as attenuation and volumetric reflectivity. However, two factors magnify the impact of the data synchronization problems for the weather metrics. First, the weather runs were made in lower visibility conditions so aircraft attitude (roll and pitch) deviations can be expected to be greater than those for the clear weather approaches. And, as noted previously, the larger the deviations, the larger the errors in computing antenna gain, which translate directly into errors in computing volumetric reflectivity and attenuation.

Second, the weather for one snapshot differs from that for another, even along the same approach. Indeed, a key aspect of the experiments was that the weather be measured and quantified along the approach path so that the changes in the images could be correlated to specific weather conditions. This implies that the weather analysis involves a series of scene calibrations, as opposed to the overall system calibration needed for measuring the surface reflectivities. Thus the techniques of reducing the impact of multipath errors by averaging scene-to-scene will be less effective in this case.

4.4.2.3 Radar Data Reduction

This section gives a detailed description of the algorithms and tools used in the GTRI data reduction process. Radar data reduction was a multistep process which involved the use of a SUN SPARC II workstation and a Macintosh personal computer. The raw radar data files were extracted from 8mm tapes provided by Honeywell and stored on the SUN computer where

conversions to the appropriate display formats and data types were performed. Data files were then downloaded to the Macintoshes where different metrics such as RCS, contrast, and sharpness were computed and stored in spreadsheets for subsequent analysis. Spreadsheets were also available which contained airport, flight, and weather information which could be correlated with the metrics computed from the images.

4.4.2.3.1 Software Description

Software developed for data reduction was developed on either a SUN workstation or a Macintosh personal computer, depending on the requirements for each particular stage of the reduction process. A SUN SPARC II was used to extract and store data files, convert recorded A/D counts to received power, and to convert data files to B-scope, C-scope, and PPI display formats. Images and data files were then downloaded from the SUN to one of three Macintoshes connected over an Appletalk Network which permitted the sharing of data and executable code. Two commercial software packages (Microsoft MATLAB and EXCEL by The MathWorks, Inc.) and one shareware software package (IMAGE, developed by the National Institute of Health) were used on the Macintoshes to analyze data and compile results. IMAGE was used to display B-scope, C-scope, and PPI images for registration and analysis (such as computing received power values and RCSs for a selected region), and MATLAB was used to compute metrics such as contrast, sharpness, and variability from integrated gutter plots extracted from an image. EXCEL was used to develop a database for storing computed metrics and flight and weather information.

4.4.2.3.1.1 SUN-Based Software

The primary data storage device and host for pre-processing the Honeywell raw radar data files was a SUN SPARC II. The software developed on the SUN was written in C. The following sections discuss how the raw data files were interpreted and formatted for display and analysis.

4.4.2.3.1.1.1 Data Format

The Honeywell data acquisition system recorded raw data snapshots taken approximately four seconds apart and provided them to GTRI on 8mm cartridge tapes. The data files on these tapes were labeled with a date/time tag which consisted of day, hour, minute, and second fields.

An example of such a time-tag-based file name is 3330045.07. Where "333" represents the Julian day, "00" denotes the hour, "45" denotes the minutes, and "07," the seconds. All time values were expressed in terms of Greenwich mean time. Subsecond timing was extracted by GTRI from the header information contained in each file. This subsecond timing could be used to match specific raw data snapshots with corresponding RS-170 data.

The data files provided by Honeywell were divided into a header section containing flight profile information and a data section containing the raw radar data. This format is illustrated in Figure 4.4.2-1. The header was 80 bytes in length and contained the flight information given in Table 4.4.2-4.

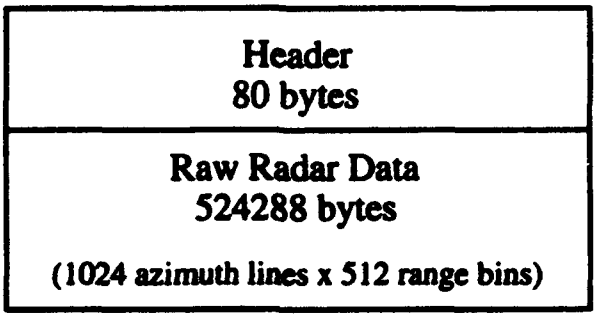

Figure 4.4.2-1. Honeywell raw data file format

The header information was extracted from the files using a program called "READ_HEADER.C" written by GTRI. This program reads in the first 80 bytes of a file and writes them out using the appropriate data type. An example of the program's output is:

```
file name: 2401535.09
time is 240 days 15 hours 35 minutes 09 seconds
subseconds = 0.921630
antennaTilt = 0X0
blendedAlt = 162.954697 ft (49.681310 m)
latitude = 0.606099
longitude = -2.104157
altitude = 488.000000 ft
roll = -0.823975 deg
pitch = 1.334840 deg
heading = -0.741009 deg
sensor Gain = 197
sensor Bias = 130
airport Altitude = 367 ft
radio altitude = 146.748047 ft
range mode = 1
```

Table 4.4.2-4. Honeywell file header format

	Number of Bytes	Data Type
Days (hundreds)	1	Character
Days (tens)	1	Character
Days (units)	1	Character
Hours (tens)	1	Character
Hours (units)	1	Character
Minutes (tens)	1	Character
Minutes (units)	1	Character
Seconds (tens)	1	Character
Seconds (units)	1	Character
Spare	1	Character
Subsecond Count	4	Character
Spare	4	Character
Frequency Error	4	Character
Spare	5	Character
Antenna Tilt	1	Character
Blended Altitude	8	Double
Latitude	4	Float
Longitude	4	Float
Altitude (barometric)	4	Float
Roll	4	Float
Pitch	4	Float
Heading	4	Float
Sensor Gain	4	Integer
Sensor Bias	4	Integer
Airport Altitude	4	Integer
Radio Altitude	4	Float
Range Mode	4	Integer

Following the 80 byte header in each file are 524,288 bytes of data which represent 512 range bins along each of 1024 azimuth lines. Each byte of data represents an 8-bit A/D count recorded for that range and azimuth bin.

4.4.2.3.1.1.2 Display Formats

The Honeywell raw radar data (8-bit A/D counts) can be displayed in three formats: PPI, B-scope, and C-scope. The files containing the data in these display formats are generated on the SUN and then transferred over a Gator Box interface to a Macintosh for display using IMAGE. IMAGE is a shareware product developed by the National Institute of Health for image processing and display.

A B-scope display represents the natural format in which data are produced by the radar. In a B-scope, the raw radar data are presented in a range/azimuth grid in x-y coordinates. The B-scope display file is generated using "B_SCOPE.C," a program written by GTRI. This program

reads in the raw data file and extracts the portion containing the A/D counts. The B-scope program then averages every four azimuth bins to create an azimuth/range array of dimension 256 x 512. Thus, the processed image contains 256 azimuth lines rather than the 1024 in the original data set. (This averaging process parallels a 4-azimuth-line average computed within the Honeywell system itself, before the data are displayed to the pilot.)

The resulting array is then written to a file with the same name as the input file but with the new extension ".b". The order in which the array is written to the file is determined by the input requirements of IMAGE which dictates that the data be read in starting with the upper left-hand pixel of the image and read a row at a time. An example B-scope radar data presentation displayed in IMAGE is shown in Figure 4.4.2-2.

In a C-scope display, the raw radar data are presented in an azimuth versus elevation angle coordinate system. This is the natural coordinate system for humans since it represents how we "see" the world around us. Thus, the Honeywell system performs a B-scope-to-C-scope conversion before passing the radar data to the HUD for display to the pilot. GTRI created the software module "C_SCOPE.C" to perform the transformation from azimuth/range (B-scope) to azimuth/elevation (C-scope) coordinates. This transformation was performed by summing the range bins, δR, contained in each constant elevation angle increment, $\delta\theta_{el}$, as shown in Figure 4.4.2-3.

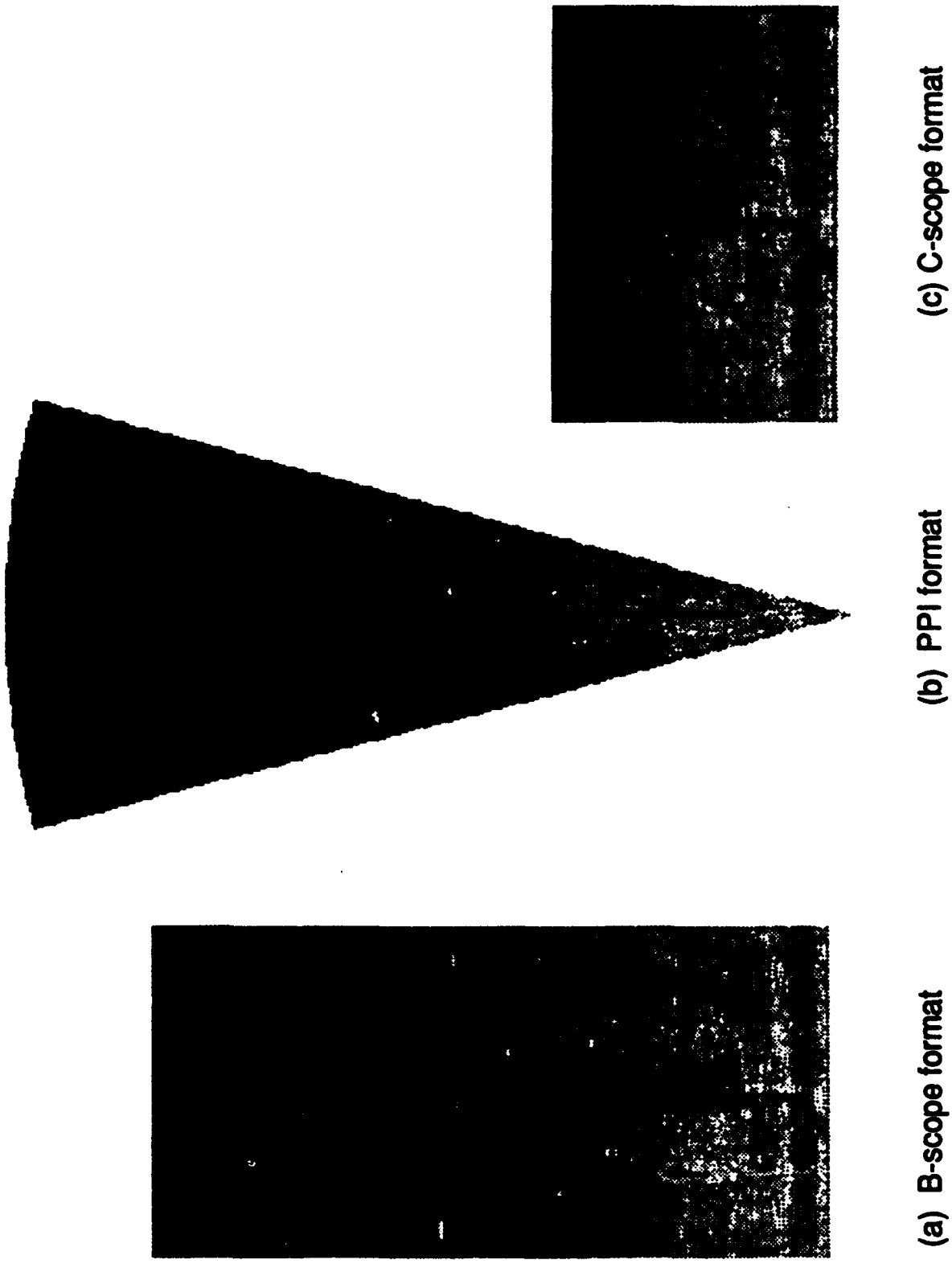

Figure 4.4.2-2. Example Honeywell Radar Image Displayed in Three Different Formats

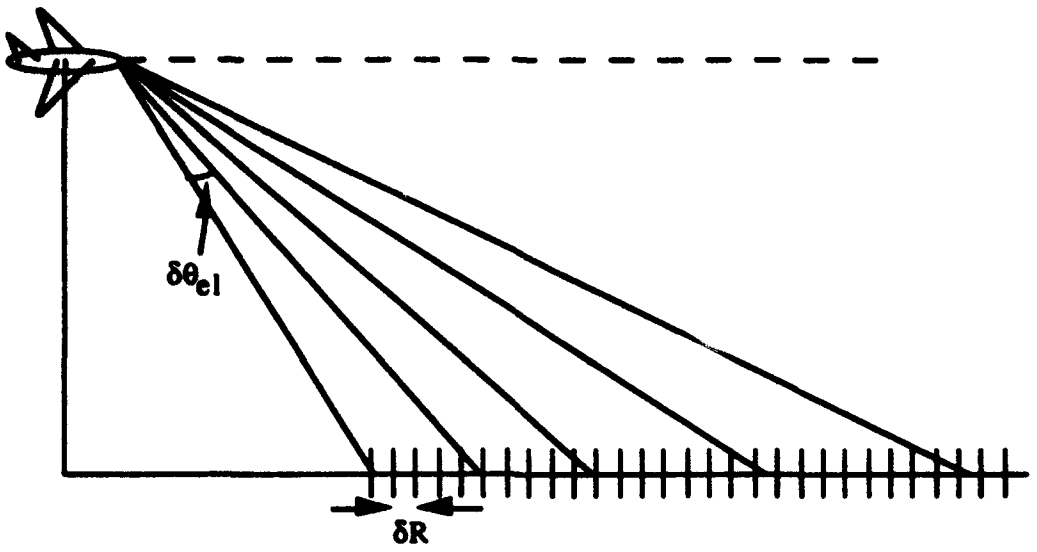

Figure 4.4.2-3. Geometry for Converting From B-scope to C-scope formats.

This C-scope transformation was performed after the azimuth/range data had been averaged in azimuth as described above for the B-scope display. The resulting array was written to a file with the appropriate IMAGE format and with the same file name as the input file but with the new extension ".c". An example of a C-scope image displayed in IMAGE is given in Figure 4.4.2-2(c). The PPI display was generated by converting from azimuth/range in x-y coordinates to polar coordinates, as illustrated in Figure 4.4.2-4. This conversion was performed using the program "MPPI.C" created by GTRI.

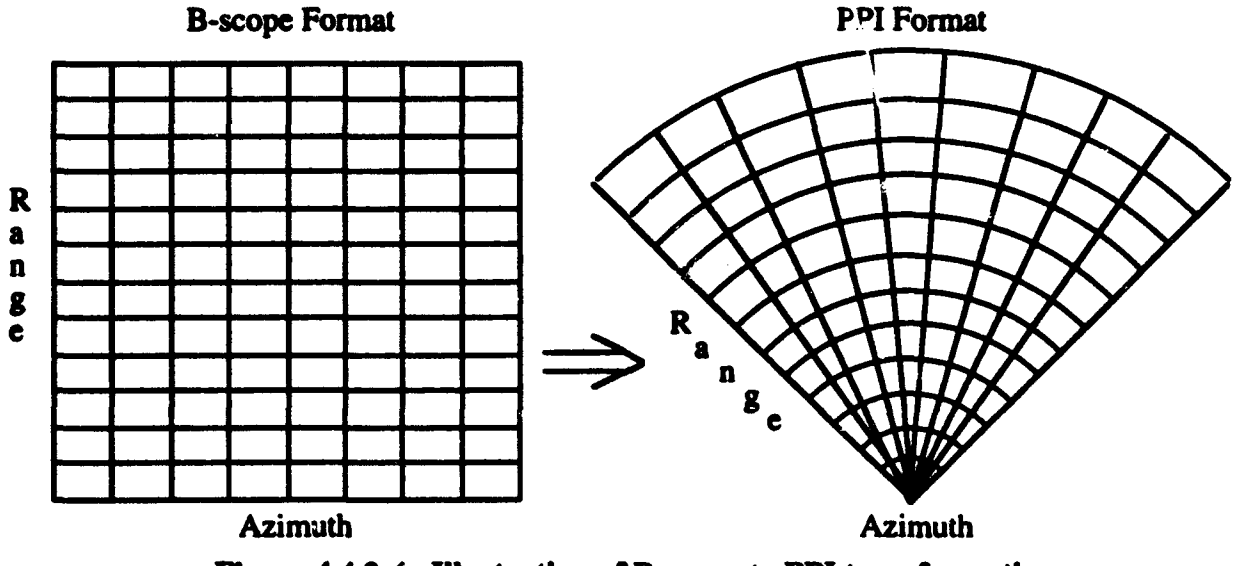

Figure 4.4.2-4. Illustration of B-scope to PPI transformation.

Again, as in the case of the C-scope, the data were averaged in azimuth before the conversion to polar coordinates and written to a file in the appropriate format for IMAGE. The output file name consisted of the input file name with the extension ".image". An example of a PPI displayed in IMAGE is given in Figure 4.4.2-2(b).

4.4.2.3.1.1.3 Range Bin Misalignment

As discussed in Section 4.4.2.2.1 above, there was a range bin misalignment in the Honeywell data. Specifically, the raw radar data files provided by Honeywell contained azimuth/range data for which the odd range bins (numbered 0 through 511) were shifted up by two ranges bins from their correct positions in the data files. Each of the display format programs described in the previous section corrected for this misalignment by shifting data in the odd range bins down by two bins. This process is illustrated in Figure 4.4.2-5.

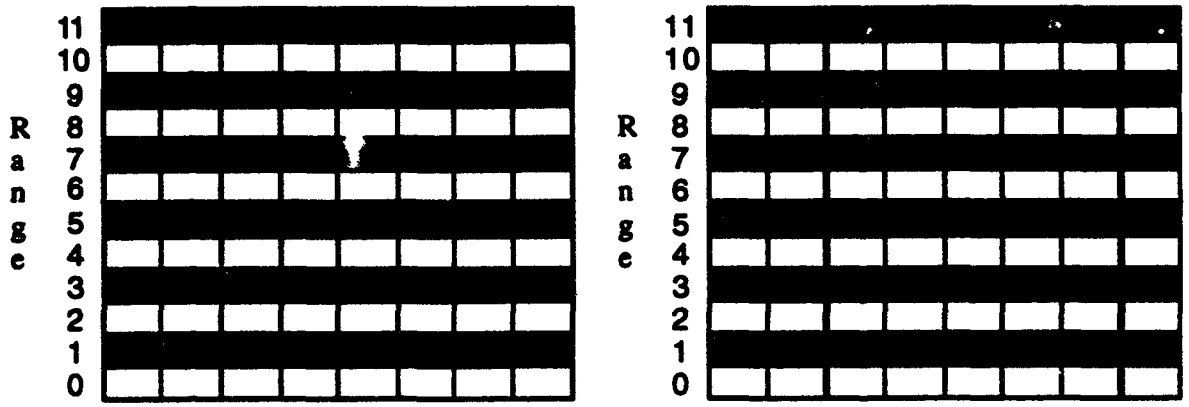

(a) Before misalignment correction. (b) After misalignment correction.

Figure 4.4.2-5. Illustration of Range Bin Misalignment and Correction.

4.4.2.3.1.1.4 Estimating Received Power

Figure 4.4.2-6 below illustrates the block diagram of the Honeywell data acquisition system. The data files provided by Honeywell contained A/D counts recorded at the output of the data acquisition system, denoted as point D in Figure 4.4.2-6. For calculations of RCS, contrast, sharpness, and other metrics defined under this program, a conversion from recorded A/D counts to received power was required. The power value of interest was that existing at the

input to the Honeywell receiver, denoted as point A in Figure 4.4.2-6. This A/D-count-to-input-power conversion was performed using the GTRI program "MPPI.C" which reads in an array of A/D counts in a B-scope format and writes out a PPI-formatted file containing the corresponding received power values.

Typically, the data acquisition system transfer function (the transfer function between points A and D in Figure 4.4.2-6) can be measured by injecting a series of known signals which span the

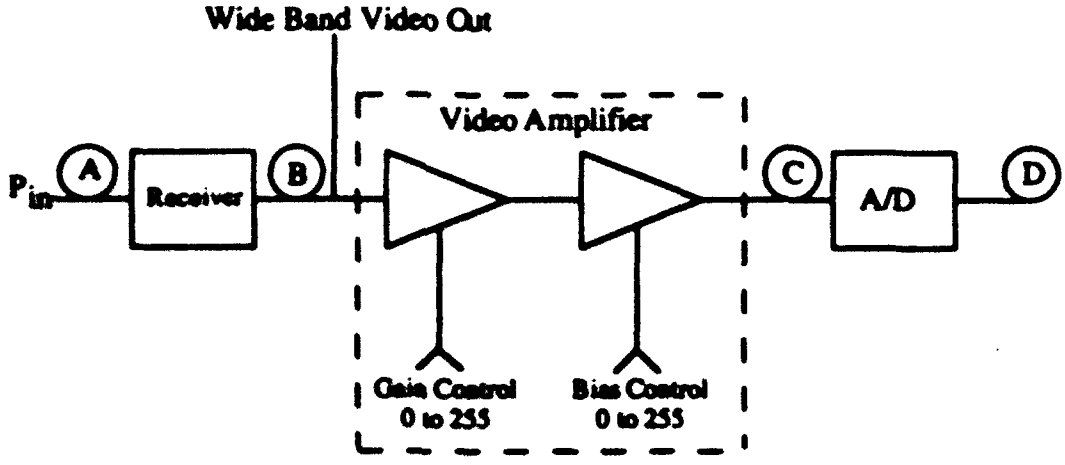

Figure 4.4.2-6. Block Diagram of the Honeywell Data Acquisition System.

operating range of the system. These signals are injected into the system at point A, and by measuring the output of the A/D, the desired transfer function can be determined. However, the variable gain and bias settings of the video amplifier in Figure 4.4.2-6 would normally require a measurement of the transfer function at every possible setting of the gain and bias controls.

To eliminate the need for 65,536 measured transfer functions corresponding to the 256 gain and 256 bias settings, Honeywell provided an analytic expression describing the transfer function for the video amplifier. The transfer function for the video amplifier provided to GTRI by Honeywell was

$$G_v = 1.78\left(10^{0.003634 G_D}\right) \tag{4.4.2-1}$$

$$\text{Bias} = -1.977 + \left(0.001986 B_D\right) \tag{4.4.2-2}$$

$$V_{out} = V_{in} G_v + \text{Bias} \tag{4.4.2-3}$$

where G_D is the gain control (0 - 255), B_D is the bias control (0 - 255), and V_{in} and V_{out} are the input and output voltage levels of the video amplifier (points B and C), respectively.

The other components needed to characterize the data acquisition transfer function are the transfer functions for the receiver and the A/D in Figure 4.4.2-6. The transfer function for the receiver was measured by Honeywell by injecting signals corresponding to discrete power levels at point A and recording the voltage at the output of the receiver at point B. The measured input and output values for the receiver transfer function are given in Table 4.4.2-5 and a graph of the corresponding receiver transfer curve (RTC) is given in Figure 4.4.2-7.

The transfer function for the 8-bit A/D which had an operating range of ± 1.75 volts was

$$V_{analog} = \frac{3.5}{255}\left(\text{Counts}_{A/D}\right) - 1.75 \qquad (4.4.2\text{-}4)$$

This function was based on manufacturer specifications. The term V_{analog} represents the input voltage at point C of Figure 4.4.2-6, and $\text{Counts}_{A/D}$ is obtained at point D.

Having obtained transfer functions for the A/D, the video amplifier, and the receiver; the received power corresponding to any recorded A/D count can be computed. The first step in this process is to convert A/D counts to voltage using Equation 4.4.2-4. This voltage represents the output of the video amplifier (point C) which can be used with Equations 4.4.2-1, 4.4.2-2, and 4.4.2-3 to find the voltage at the input to the amplifier given the gain and bias settings recorder in the header. The voltage at the input to the video amplifier (output of the receiver - point B) is then matched to the corresponding received power at the input to the receiver (point A) through linear interpolation of the RTC.

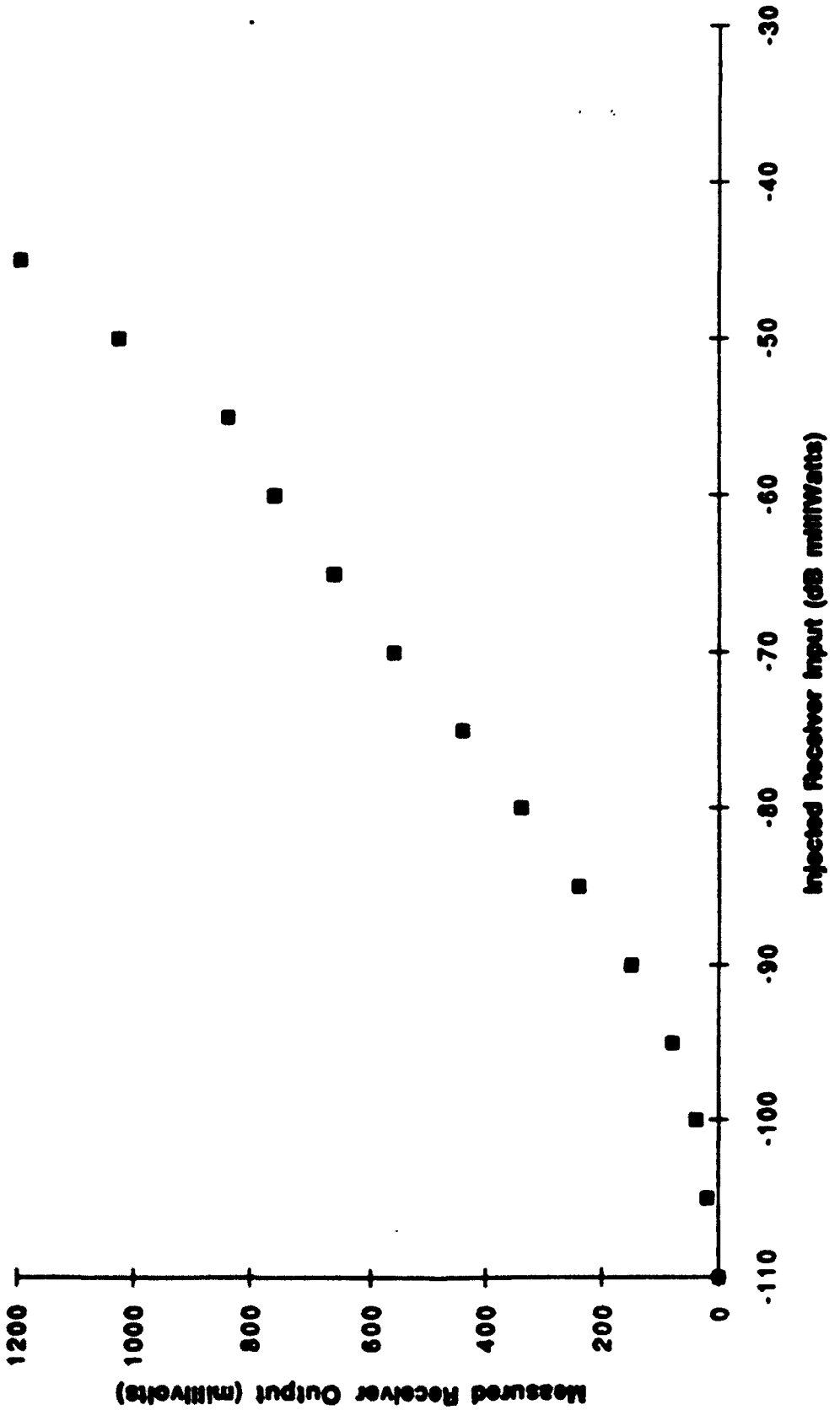

Figure 4.4.2-7. Measured Receiver Transfer Curve

Table 4.4.2-5. Measured receiver response

Power In	Wide Band Video Out
-110 dB mWatts	0 millivolts
-105 dB mWatts	20 millivolts
-100 dB mWatts	40 millivolts
-95 dB mWatts	80 millivolts
-90 dB mWatts	150 millivolts
-85 dB mWatts	240 millivolts
-80 dB mWatts	340 millivolts
-75 dB mWatts	440 millivolts
-70 dB mWatts	560 millivolts
-65 dB mWatts	660 millivolts
-60 dB mWatts	760 millivolts
-55 dB mWatts	840 millivolts
-50 dB mWatts	1030 millivolts
-45 dB mWatts	1200 millivolts

In order to validate and further refine, if needed, the overall data acquisition transfer function defined by the previous relations, Honeywell made measurements of the output of the A/D for a range of signal power levels injected into the receiver for selected gain/bias settings of the video amplifier. The output of the A/D was recorded over a single sweep while maintaining a constant input power and gain/bias setting. This process was repeated for the matrix of received power values and gain/bias setting given in Table 4.4.2-6. The A/D counts in Table 4.4.2-6 were averaged over a single sweep.

The third column from the left in Table 4.4.2-6 lists the average A/D count recorded for each injected power level for a Gain setting of 150 and a Bias of 120. Figure 4.4.2-8 plots these measured data points and also plots for comparison the calculated response based on the measured RTC and the transfer functions defined for the video amplifier and the A/D converter in Equations 4.4.2-1 through 4.4.2-4 above. As can be seen from Figure 4.4.2-8, there is a substantial deviation between the measured and calculated responses. Figures I-1 through I-11 of Appendix I present the same type of plot for each of the eleven gain bias combinations listed in Table 4.4.2-6. Substantial deviations between the measured and the calculated values are seen in each of the plots.

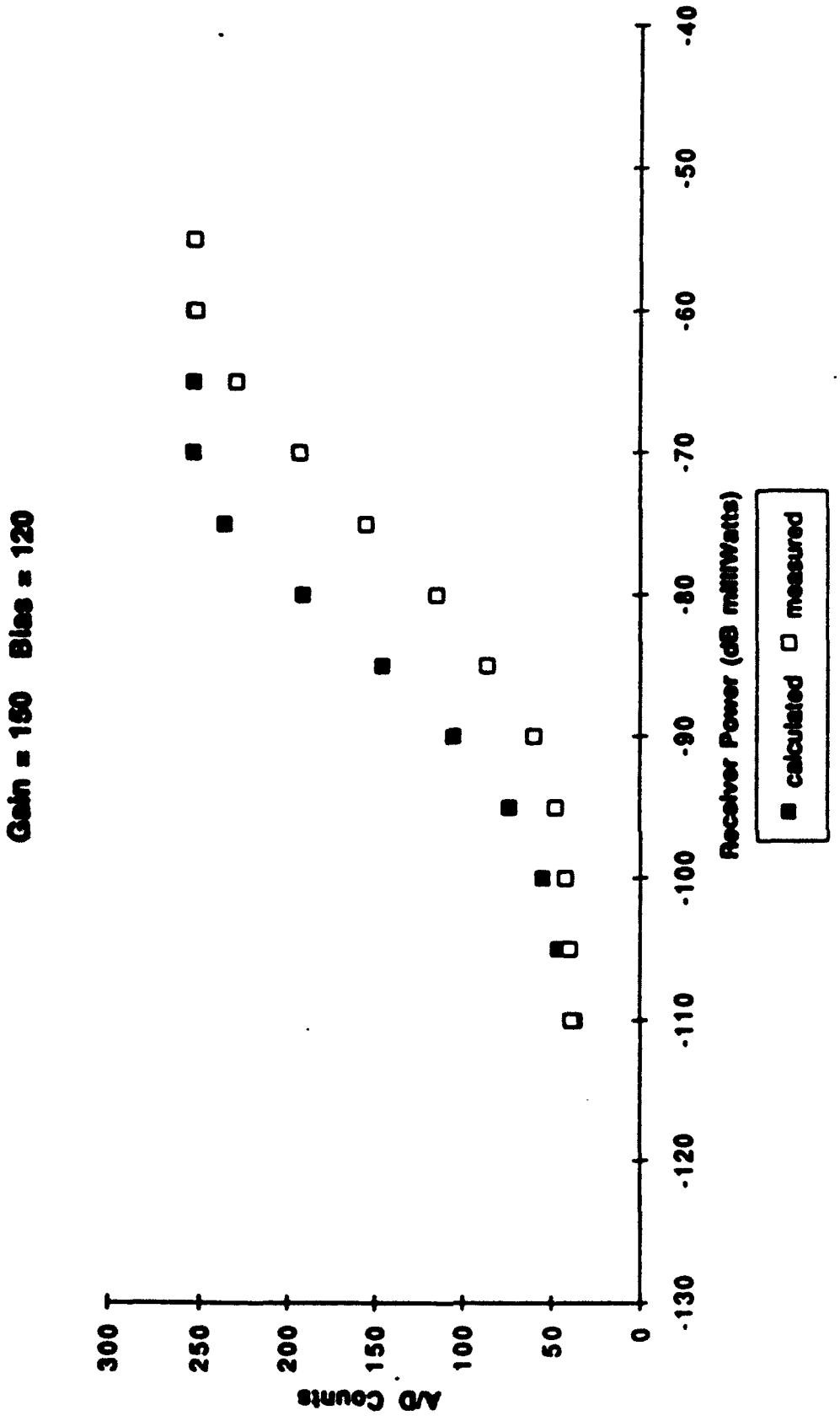

Figure 4.4.2-8. Measured and Calculated Data Acquisition System Transfer Function for a Gain/Bias Setting of 150/120. The Calculated Transfer Function is Based on Table 4.4.2-6 and Equations 4.4.2-1 Through 4.4.2-4

This page left blank intentionally.

Table 4.4.2-6. Average Recorded A/D Count Values for Selected Injected Power Levels and Gain/Bias settings

Gain/Bias Setting											
	140/	150/	160/	170/	180/	140/	150/	160/	170/	180/	180/
Pin (dBm)	120	120	120	120	120	150	150	150	150	150	180
-110	37.06	39.06	42.53	44.67	47.34	43.69	42.94	46.44	49.09	54.47	59.84
-105	36.97	39.94	42	43.22	49.25	43.38	45.25	47.5	52.47	55.22	60.62
-100	38.47	42.22	44.25	47.75	50.47	43.34	44.34	51.66	49.97	54.16	63.5
-95	44.5	47.72	50.12	55.97	58.09	47.12	51.66	54.19	57.94	62.41	67.69
-90	56.25	60.12	64.97	71.75	75.56	60.78	62.52	65.56	74.75	81.84	84.28
-85	80.66	86.5	93.25	101.62	107.97	84.34	91.75	98.5	106.19	113.51	114.66
-80	110.72	115.12	128.03	136.22	148.06	113.56	122.84	132.28	142.2	152.91	156.31
-75	144.53	155.94	169.38	180.64	197.06	147.94	158.62	172.25	187.58	200.1	204.12
-70	180.91	193.78	207.66	224.59	239.31	183.25	197.45	211.69	227.78	244.88	247.38
-65	214.55	230.63	246.31	253.94	255	217.97	233.94	248.28	254.53	255	255
-60	246.12	254.03	255	255	255	249.44	254.56	255	255	255	255
-55	254.91	255	255	255	255	255	255	255	255	255	255

Such deviations are not unreasonable, however, considering that the numeric constants in Equations 4.4.2-1 through 4.4.2-3 are nominal values computed based on specific parameters of components used in the video amplifier circuitry. There are no doubt deviations from these nominal values for the actual components used in the circuit. (For example, resistor values are typically quoted with a percentage tolerance over which actual values may range.) From this perspective, the numeric "constants" in these equations are not really constants at all, but might well vary from one amplifier to the next. With this in mind, these nominal constants were adjusted to obtain a better fit to the measured data. The adjusted versions of Equations 4.4.2-1 through 4.4.2-3 thus became:

$$G_v = 1.30\left(10^{0.0032G_D}\right) \tag{4.4.2-5}$$

$$\text{Bias} = -1.90 + \left(0.0019B_D\right) \tag{4.4.2-6}$$

$$V_{out} = V_{in}G_v + \text{Bias} \tag{4.4.2-7}$$

These new "constants" were determined through repeated empirical trials in an attempt to minimize the least-mean-square error (LMSE) between the measured and calculated data. Figure 4.4.2-9 is a plot of the measured transfer function versus the calculated response using Equations 4.4.2-5, 4.4.2-6, and 4.4.2-7 for the same gain/bias setting of 150/120 used in Figure 4.4.2-8. Note the much improved agreement between the measured and computed values in Figure 4.4.2-9 as compared with Figure 4.4.2-8. Figures I-12 through I-22 of Appendix I correspond to

Figures I-1 through I-11 described previously, except that the former set use Equations 4.4.2-5 though 4.4.2-7, while the later are based on Equations 4.4.2-1 through 4.4.2-3. Based on the good agreement observed in I-12 through I-22, Equations 4.4.2-5 through 4.4.2-7 were adopted by GTRI for all conversions between A/D counts and equivalent received power levels.

The GTRI software program "MPPI.C" used the RTC defined in Table 4.4.2-5, the video amplifier response defined by Equations 4.4.2-5, 4.4.2-6, and 4.4.2-7, and the A/D response in Equation 4.4.2-4 to convert A/D counts to the equivalent power received. Points not reported specifically in the RTC were computed through linear interpolation applied to the two nearest neighbors. The gain and bias inputs to the video amplifier for each snapshot were obtained from the header information extracted by "MPPI.C".

4.4.2.3.1.2 IMAGE Macros

At the outset of the program several commercial software packages offered powerful image display and analysis capabilities. Unfortunately, these packages typically were designed to operate on fixed-point (integer) data, rather than on floating-point (decimal) data.

Although the Honeywell raw data were provided in 8-bit fixed-point format, they were immediately processed by converting the samples to the corresponding received power values and averaging each four adjacent azimuth samples to generate a single value for each of 256 azimuth lines. This process generated inherently floating-point data, which could not be conveniently processed by typical off-the-shelf image processing software packages. However, rather than develop totally new software from scratch, GTRI adapted an existing commercial package to the tasks at hand to minimize costs. This overall software development approach was the foundation of the efforts described in the following paragraphs.

IMAGE is a public domain software package for the Macintosh developed by the National Institute of Health for image processing and analysis. IMAGE was used to display B-scope, C-scope, and PPI formatted data, to select regions of interest (ROI) for further analysis, to rotate images, to register scenes, and to perform statistical analysis on ROIs. IMAGE was written in PASCAL with sufficient "hooks" provided for user additions to the software. These hooks were exploited to expand its capabilities via custom software routines called macros. Some of the enhancements developed by GTRI were IMAGE subroutines to load a floating-point file into

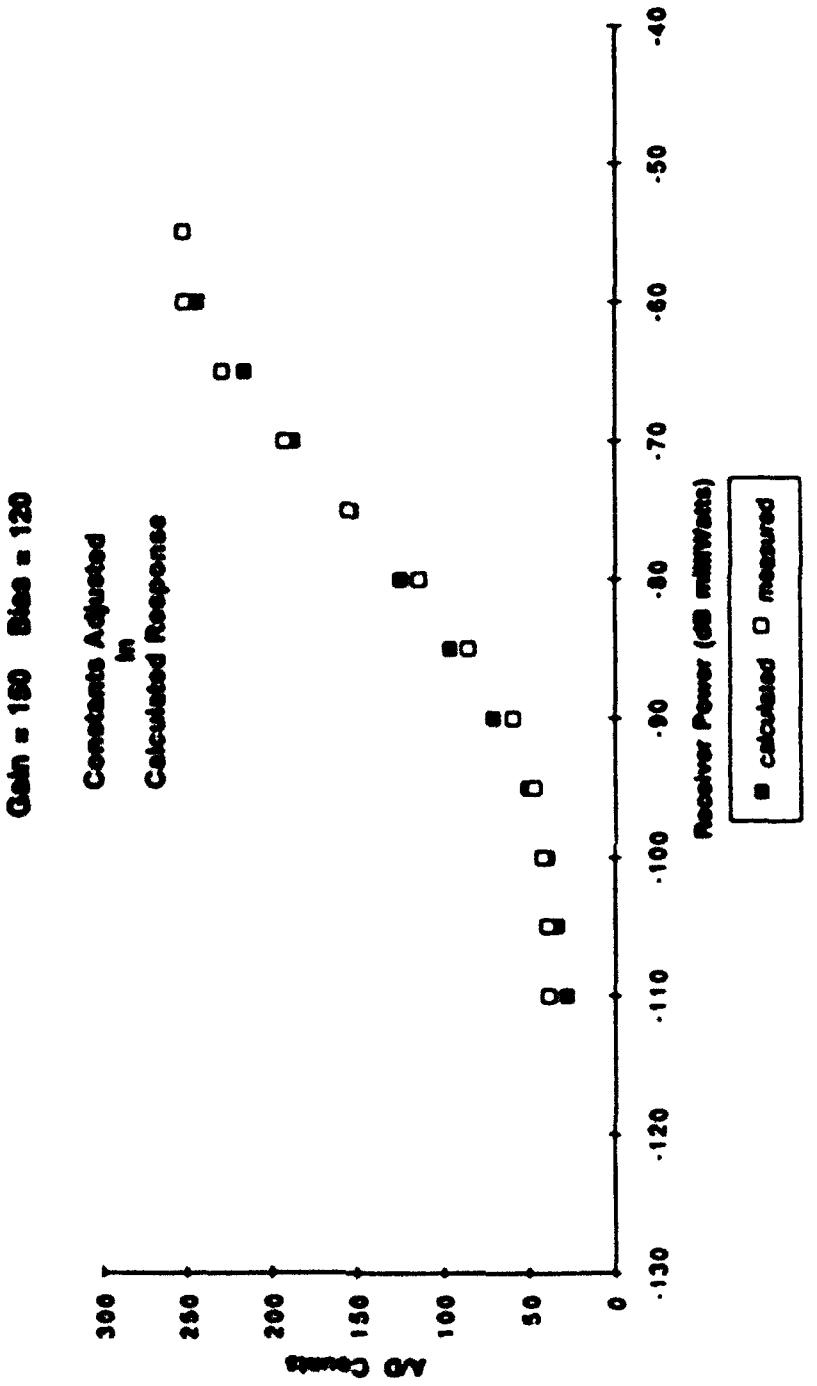

Figure 4.4.2-9. Measured and Calculated Data Acquisition System Transfer Function for a Gain/Bias Setting of 150/120. The Calculated Transfer Function is Based on Table 4.4.2-6 and Equations 4.4.2-1 Through 4.4.2-4 (Incorporates Adjusted Constants In Calculated Receiver Response)

memory and others mimicked operations naturally performed by IMAGE on fixed-point (display) files with parallel operations performed on the floating point files.

4.4.2.3.1.2.1 Importing Radar Data for Display

The IMAGE software package is capable of displaying and processing image data represented as an array of 8- or 16-bit unsigned integers. IMAGE was used to display B-scope, C-scope, and PPI formatted images developed on the SUN. These images were transferred across a Gator Box connection to a Macintosh computer with the proper file translation being performed by the Gator Box. Examples of these three display formats have been given previously in Figure 4.4.2-2.

4.4.2.3.1.2.2 Importing Floating Point Data

In order to select ROIs for calculation of RCS and to export ROIs for further analysis (calculation of contrast, sharpness, and variability in MATLAB), the data values expressed in terms of power received (generated from the corresponding A/D counts by the SUN) were loaded into RAM on the Macintosh by IMAGE subroutines developed by GTRI. These values were not displayed in IMAGE but formed a hidden data structure parallel to the corresponding fixed-point image which was displayed by IMAGE. Figure 4.4.2-10 illustrates the one-to-one relationship between the fixed-point image displayed and the corresponding floating-point data structure. When the operator instructed IMAGE to average four pixel values in the displayed image, for example, software routines developed by GTRI mimicked this operation by performing the corresponding averaging operation on the hidden floating-point data.

4.4.2.3.1.2.3 Exporting a ROI

Besides IMAGE, the suite of analysis tools chosen for this program included MATLAB, a commercial software package available from The MathWorks, Inc. MATLAB was used for calculating contrast, sharpness, and variability. These MATLAB operations will be discussed later in Section 4.4.2.3.1.3. The metrics calculated in MATLAB required data from a selected portion within the radar data image. Such a portion is called a region of interest (ROI) and is illustrated conceptually by the rectangle in Figure 4.4.1-3. Each ROI was selected by the user

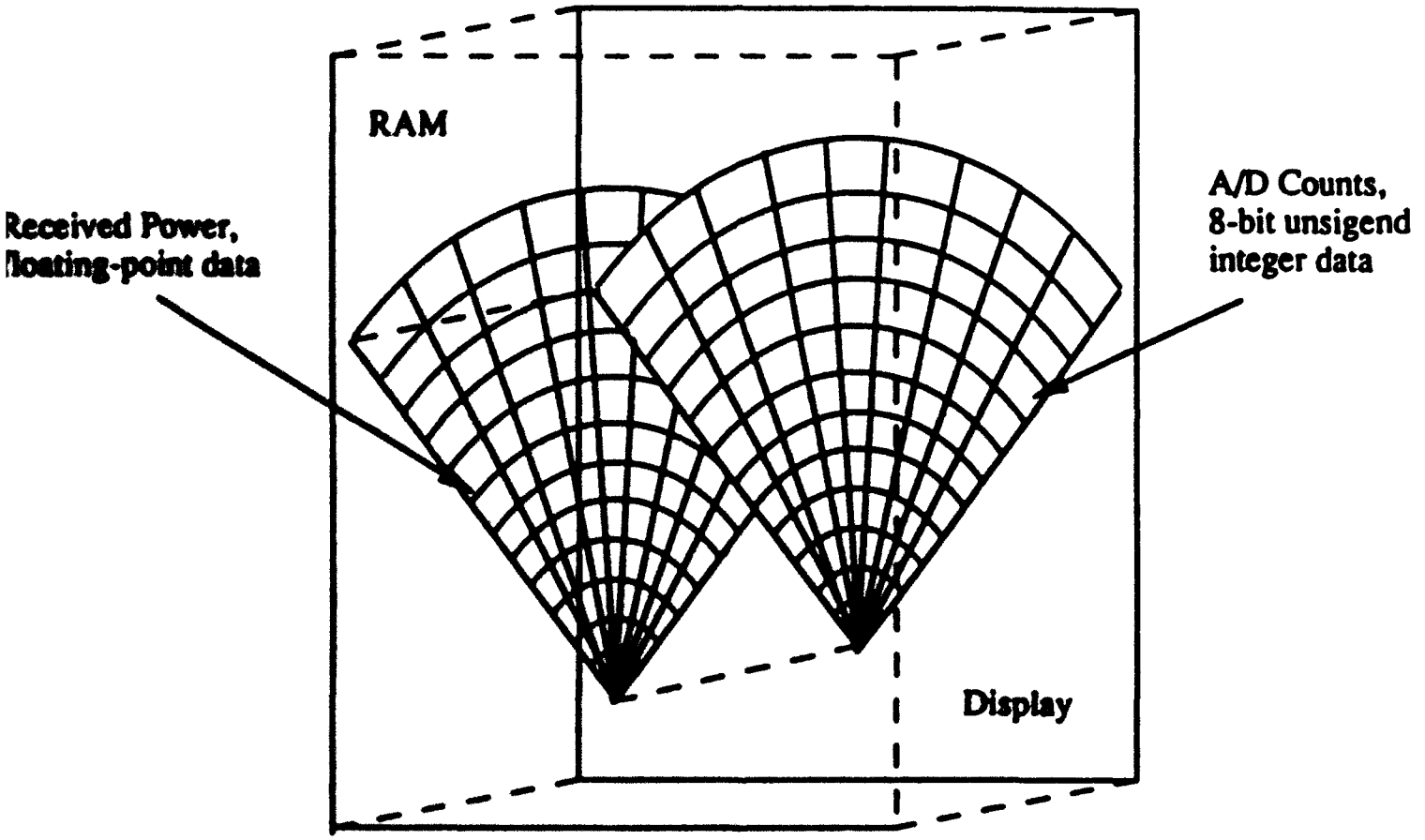

Figure 4.4.2-10. Illustration of Relationship Between Displayed Fixed-Point PPI Image and Parallel Floating-Point Data Structure

via IMAGE, and this process required the user to draw a rectangular box around the selected region in the image, as illustrated in Figure 4.4.2-11. When this was done, the corresponding region in the floating-point file was actually selected and could then be written to a file for export to MATLAB.

4.4.2.3.1.2.4 Computation of Average Received Power for a ROI

One of the capabilities implemented in IMAGE permitted the computation of average received power and reflectivity for a selected region of interest. Once the operator had designated the ROI via a mouse-controlled box superimposed on the data, the software computed the average received power for all samples (pixels) within the ROI box. The average power was computed in linear space based on the floating point values stored in the parallel data array. Thus, all logarithmic power values (expressed in dBW units) were first converted to Watts, the average Watt value computed, and then this average value was converted back to dBW units. The computation of average received power for a ROI is illustrated in Figure 4.4.2-12. The corresponding reflectivity's (RCS and normalized RCS) subsequently computed for this ROI based on the average received power are also indicated in this figure. The sections which follow describe how these reflectivity's were computed.

4.4.2.3.1.2.5 Horizontal and Vertical Antenna Patterns

In calculating RCS and other phenomenological parameters, the gain of the antenna in the direction of the patch being illuminated must be known. Honeywell supplied measured elevation and azimuth components of the antenna pattern. These patterns were used to estimate the antenna gain in the direction of a selected region given the vector from the aircraft to the patch as well as the aircraft pitch and roll. The vertical and horizontal antenna patterns are plotted in Appendix J. The measured vertical antenna pattern (shown in Figure J-1) was sampled every 1/3 of a degree to create a vertical gain look-up table to be used by the software. The horizontal antenna pattern was measured by electronically positioning the antenna at 1 degree increments over the 30 degree viewing sector and measuring at each position the pattern +/- 0.5 degree on either side of boresight. The corresponding pattern plot is shown in Figure J-2. An azimuth gain look-up table was created for use by the software by storing the relative peak gain for each 1° azimuth increment

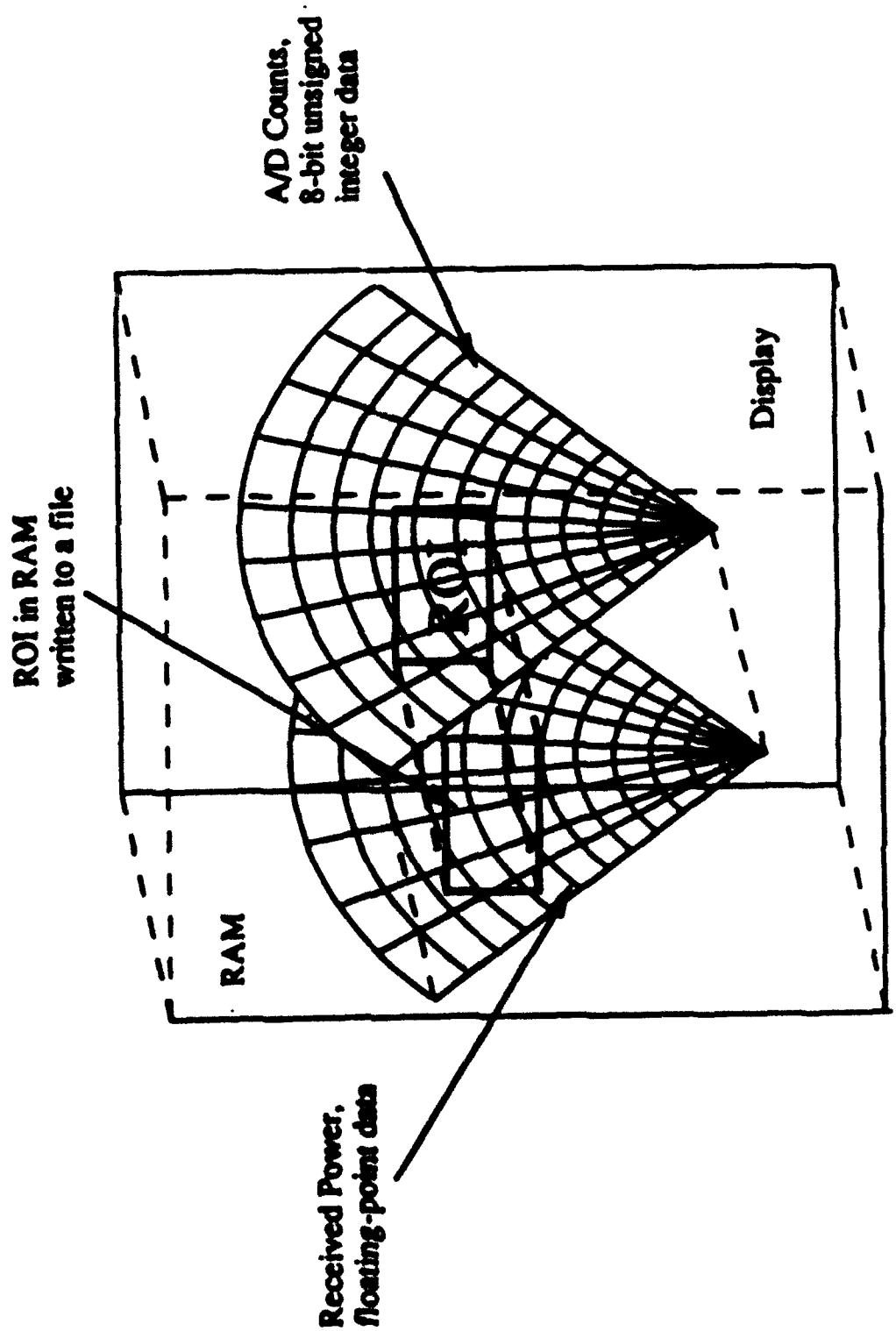

Figure 4.4.2-11. Illustration of Selecting a Region of Interest (ROI) Via IMAGE

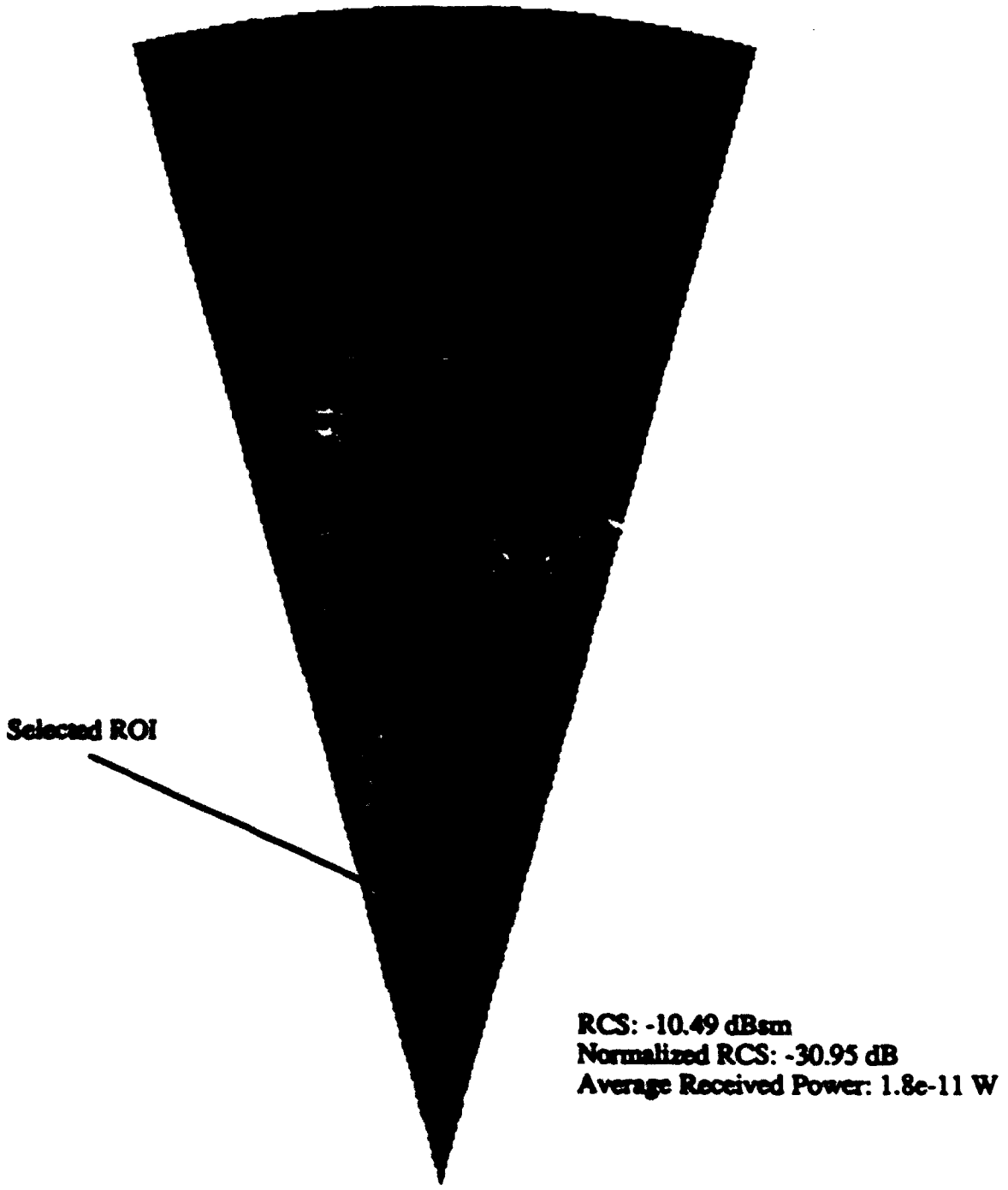

Figure 4.4.2-12. Example of Automated Calculation of Average Received Power and RCS for a ROI

based on the measured pattern. These two look-up tables were used by the IMAGE software to compute antenna gains where appropriate.

In order to define the exact antenna beam orientation with respect to the aircraft waterline, the specifications for the antenna's mounting on the aircraft were supplied by Honeywell. The antenna was mounted on a plate that is tilted upward at an angle of 6.6 degrees from a reference normal to the aircraft waterline. This is illustrated in Figure 4.4.2-13.

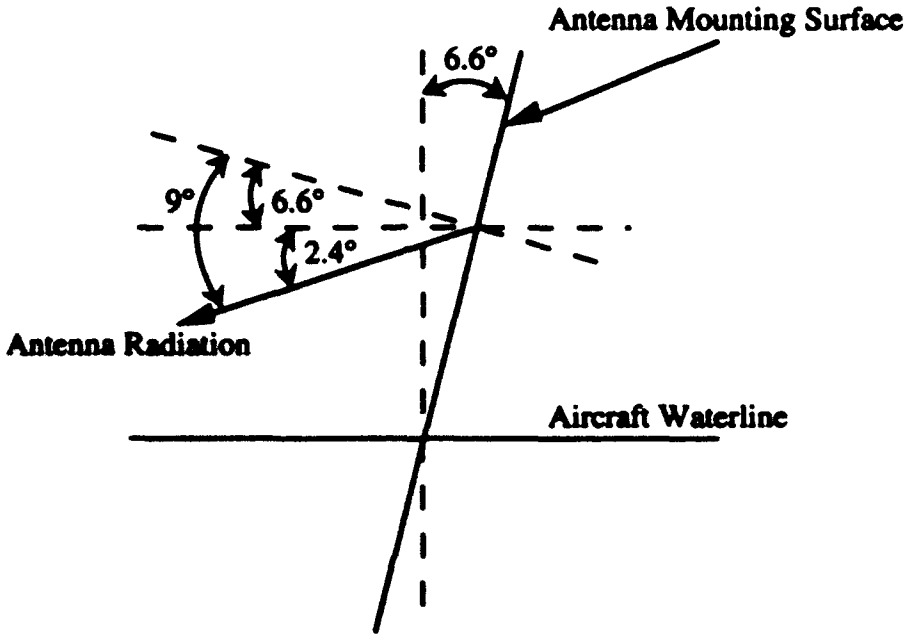

Figure 4.4.2-13. Illustration of Honeywell antenna mounting.

As indicated in Figure 4.4.2-13, the peak of the vertical antenna beam is nine degrees below the normal to the antenna mounting surface. Therefore, the peak of the antenna beam was pitched down 2.4 degrees (9 - 6.6) when the aircraft itself is level. This relative pitch was added to the pitch of the aircraft in order to define an absolute pitch with respect to horizontal for the antenna boresight.

Computing the appropriate antenna gain to use for each ROI was handled via a pair of table look-up operations, one for the horizontal pattern and the other for the vertical pattern. In general, the proper elevation and azimuth angles to use in accessing the antenna pattern look up tables were based on the pitch and roll of the aircraft as well as on the vector from the aircraft to the patch being illuminated. The transformation used to compensate for pitch and roll in an

xyz coordinate system was

$$\begin{bmatrix} x' \\ y' \\ z' \end{bmatrix} = \begin{bmatrix} \cos\phi_r & \sin\phi_r & 0 \\ -\sin\phi_r & \cos\phi_r & 0 \\ 0 & 0 & 1 \end{bmatrix} \begin{bmatrix} \cos\phi_p & 0 & \sin\phi_p \\ 0 & 1 & 0 \\ -\sin\phi_p & 0 & \cos\phi_p \end{bmatrix} \begin{bmatrix} \sin\delta \\ \cos\delta\sin\theta \\ \cos\delta\cos\theta \end{bmatrix} \quad (4.4.2\text{-}8)$$

where

$$\theta' = \tan^{-1}\left(\frac{y'}{z'}\right) \quad (4.4.2\text{-}9)$$

$$\delta' = \sin^{-1}(x') \quad (4.4.2\text{-}10)$$

ϕ_r is the roll angle, ϕ_p is the pitch angle, δ is the elevation angle, and θ is the azimuth angle based on the vector from the aircraft to the patch being illuminated. The corrected elevation angle, δ', and corrected azimuth angle, θ', were used in the antenna pattern look-up tables to obtain the correct antenna gain based on the scene geometry and the attitude of the aircraft.

4.4.2.3.1.2.6 RCS and Normalized RCS

The radar cross section (RCS) and normalized RCS (reflectivity) were calculated using subroutines developed by GTRI to run as part of IMAGE. The equation implemented to calculate RCS was

$$\sigma = \frac{P_{rec}(4\pi)^3 R^4 L_{radome} L_{prop} F_{calibration}}{P_{trans} G^2 \lambda^2} \quad (4.4.2\text{-}11)$$

where

P_{rec} is the average received power,

R is the slant range to the patch,

L_{radome} is the radome loss,

L_{prop} is the atmospheric attenuation,

$F_{calibration}$ is the calibration factor,

P_{trans} is the transmitted power,

G is the antenna gain, and

λ is the wavelength of the signal.

The values used for all fixed parameters in Equation 4.4.2-11 are given in Table 4.4.2-7

Table 4.4.2-7. FIXED Honeywell System Parameters USED to Compute RCS

Parameter	Value
P_{trans}	1.1 kW
L_{radome}	1 dB
L_{prop}[4]	0.05 dB/km
λ	8.5 millimeters

Since the actual radome used with the Honeywell radar system had not been previously characterized at 35 GHz, GTRI was tasked in May, 1992 to perform a ground test of the radar to assess radome effects. The report from this test is included as Appendix M. Based on the simple test performed, GTRI estimated the two-way attenuation through the radome to be 1 dB, with an uncertainty of -1 to +2 dB. Based on this estimate, the radome loss , L_{radome}, used in Equation 4.4.2-11 was set equal to 1 dB.

The normalized RCS in the pulse-length-limited case, which is appropriate for the shallow depression angles of the synthetic vision geometry, is defined as

$$\sigma^0 = \frac{\sigma}{A} \tag{4.4.2-12}$$

where the illuminated area, A, can be approximated by

$$A = R\, c\tau\, tan\left(\frac{\phi_{az}}{2\sqrt{\alpha}}\right) sec(\theta) \tag{4.4.2-13}$$

where

R is the slant range,

c is the speed of light,

τ is the pulse length,

α is the beamshape factor [5] $= 2 \ln 2 \approx 1.38$,

ϕ_{az} is the one-way azimuth beamwidth, and

---

4 Merrill I. Skolnik, *Introduction to Radar Systems*, McGraw-Hill, 1980, pp. 459-461.

5 J. R. Probert-Jones, "The Radar Equation in Meteorology," *Journal Royal Meteorological Society*, Vol. 88, 1962, pp. 485-495.

θ is the depression angle.

The Honeywell system parameters used to calculate the illuminated area are given in Table 4.4.2-8.

Table 4.4.2-8. Honeywell System Parameters Used in Computing Illuminated Area

Parameter	Value
ϕ_{az}	0.8 degree
τ	100 ns

4.4.2.3.1.2.7 Volumetric Backscatter and Attenuation

The volumetric backscatter due to precipitation and the associated attenuation were computed using RCS measurements from range cells above the earth's surface and range cells containing Bruderhedrals placed near the runways. The perceived RCS (RCS_1) for a three-dimensional resolution cell volume 100% above the earth's surface (not touching the ground) was modeled as a product of the actual RCS per unit volume, the volume of the range cell, and the attenuation due to precipitation expressed as

$$RCS_1 = V_{reflec} Vol_1 \left(10^{-0.1\alpha 2R_1}\right) \qquad (4.4.2\text{-}14)$$

where

V_{reflec} is the volumetric reflectivity,

Vol_1 is the volume of the cell being measured,

R_1 is the slant range to the cell in kilometers, and

α is the attenuation per kilometer.

The cell volume was approximated as

$$Vol = \frac{\pi}{4}\left(\frac{R^2 \phi_{az} \phi_{el}}{\alpha}\right)\frac{c\tau}{2} \qquad (4.4.2\text{-}15)$$

where

R is the range in meters,

α is the beamshape factor [6] ($\approx$ 1.38),

c is the speed of light in meters per second,

τ is the pulse length in seconds,

ϕ_{az} is the one-way azimuth beamwidth in radians, and

ϕ_{el} is the one-way elevation beamwidth in radians.

The cell chosen above the ground had a slant range less than the altitude of the aircraft in order to prevent ground returns received through the antenna sidelobes from contaminating the measurement. Equation 4.4.2-14 has two unknowns, the attenuation and the volumetric reflectivity. Therefore, a second equation was defined so that the two equations could be solved simultaneously for the two unknowns. This second equation

$$RCS_2 = \left(V_{reflec} Vol_2 + RCS_R\right)\left(10^{-0.1\alpha 2R_2}\right) \qquad (4.4.2\text{-}16)$$

defines the perceived RCS from a cell containing a calibration reflector on the ground at range R2 from the radar. In Equation 4.4.2-16, RCS_R is the known RCS of the reflector and RCS_2 is the measured RCS of the cell. The volume, Vol_2, containing the reflector, is weighted by the percentage of the volume above the ground, as illustrated in Figure 4.4.2-14.

---

6 J. R. Probert-Jones, "The Radar Equation in Meteorology," *Journal Royal Meteorological Society*, Vol. 88, 1962, p. 485.

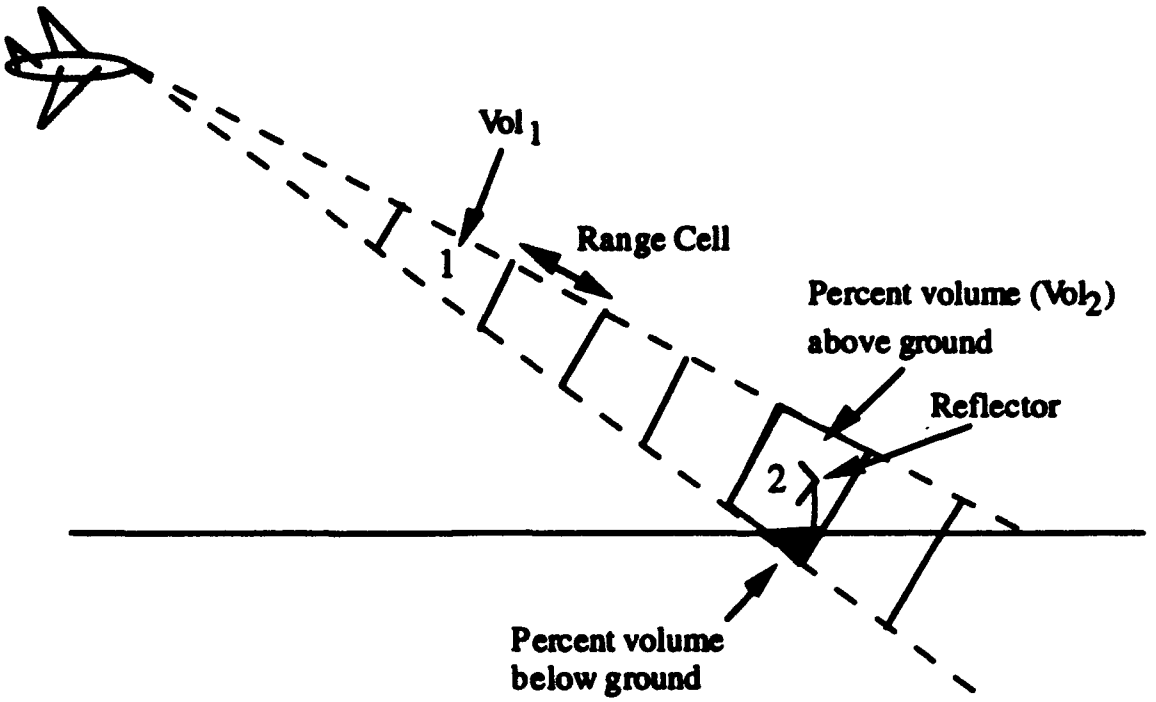

Figure 4.4.2-14. Range cells used in computing volumetric backscatter.

Measurements were made of RCS_1 and RCS_2 for a particular snapshot and then Equations 4.4.2-14 and 4.4.2-16 were solved simultaneously for the attenuation and volumetric reflectivity. This mathematical operation assumed that the normalized atmospheric reflectivities of the two volumes were the same, and that the attenuation per unit length along the two paths - one of length R_1 and the other of length R_2 - were the same.

4.4.2.3.1.3 MATLAB M-files

MATLAB is an interactive signal processing package distributed by The MathWorks Inc. MATLAB was chosen as an analysis tool under this program because of its interactive computation and plotting capabilities as well as its high-level language interface for developing analysis code to compute metrics such as contrast, sharpness, and variability.

4.4.2.3.1.3.1 Regions of Interest

Regions of interest were selected by the user in IMAGE for export to MATLAB for further analysis. Figure 4.4.2-15 shows an example of an ROI chosen for export to MATLAB. The

typical ROI is roughly centered on the runway and is defined to be seven range bins deep and forty azimuth pixels wide. An example of a selected ROI after importation into MATLAB is shown in Figure 4.4.2-16. This ROI was then averaged in range along each azimuth line to form the "gutter" profile shown in Figure 4.4.2-17.

The contrast, sharpness, and variability metrics compare statistical parameters computed for the runway and surrounding terrain. Figure 4.4.2-18 shows how a typical runway profile was partitioned into a runway region bordered by a pair of terrain plateaus for computation of these metrics. This interactive partitioning was developed in MATLAB to allow the analyst to select six points which define the different regions of the runway profile, as illustrated in Figure 4.4.2-18. The boundary for the runway was selected based on the width of the runway taken from airport maps as well as the general width of the runway in the overall PPI image. The surrounding terrain boundaries (1-2 and 5-6) were chosen so that they contain apparently homogeneous terrain and do not include non-terrain objects such as aircraft, aprons, taxiways or reflectors. Again, the relative position of man-made objects within the ROI was obtained from airport maps.

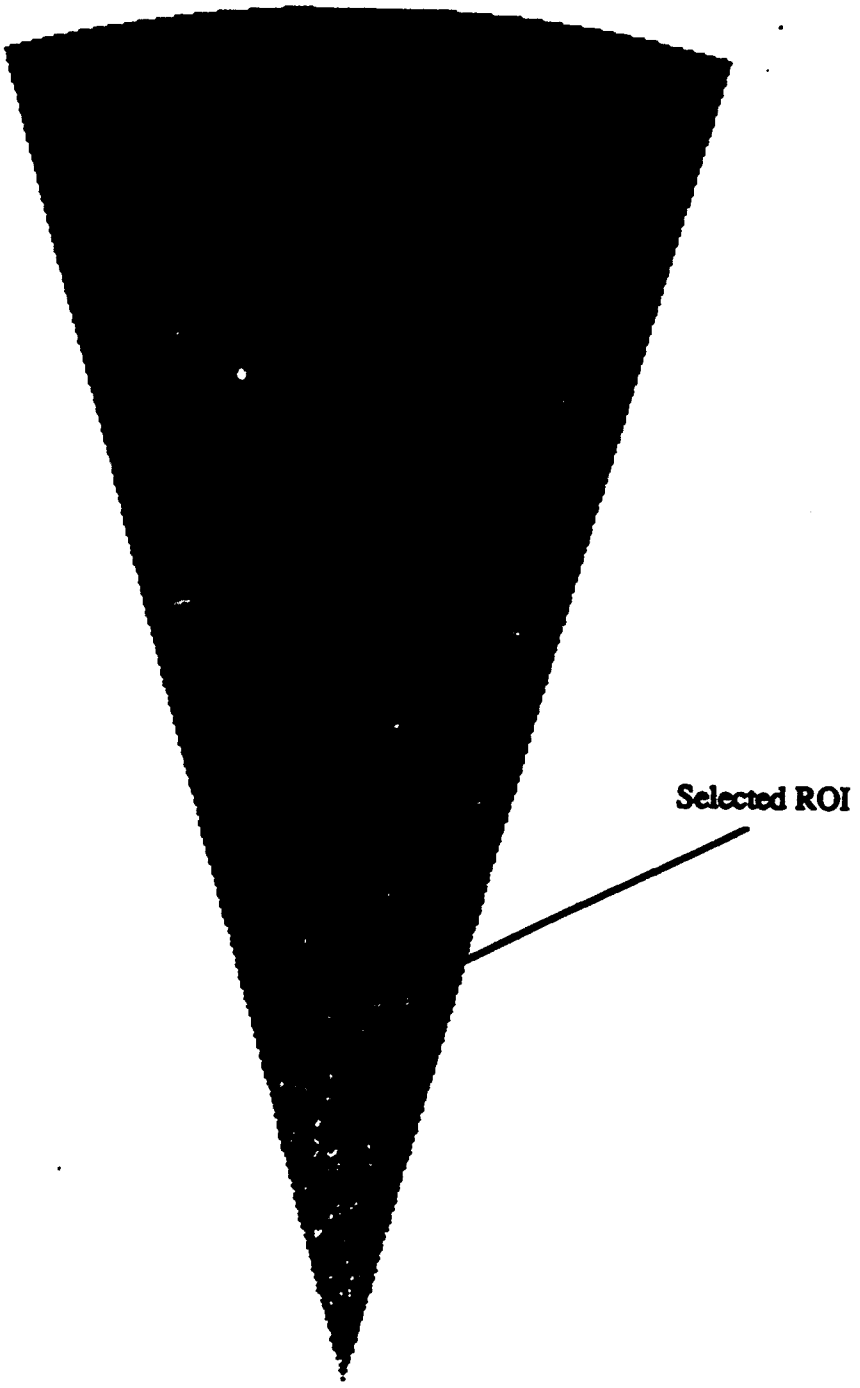

Figure 4.4.2-15. Example ROI Selected for Export to MATLAB

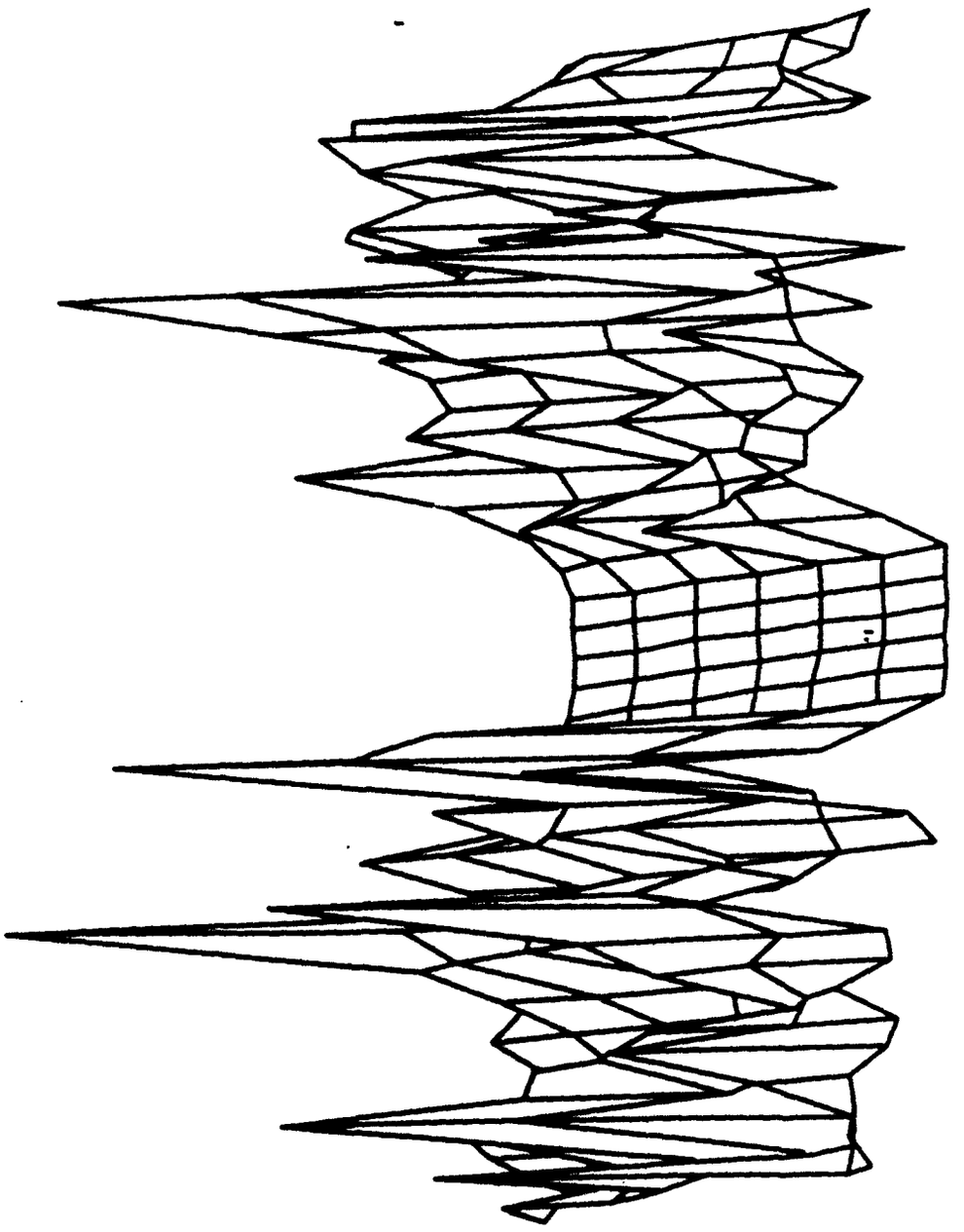

Figure 4.4.2-16. Example ROI Imported from IMAGE into MATLAB

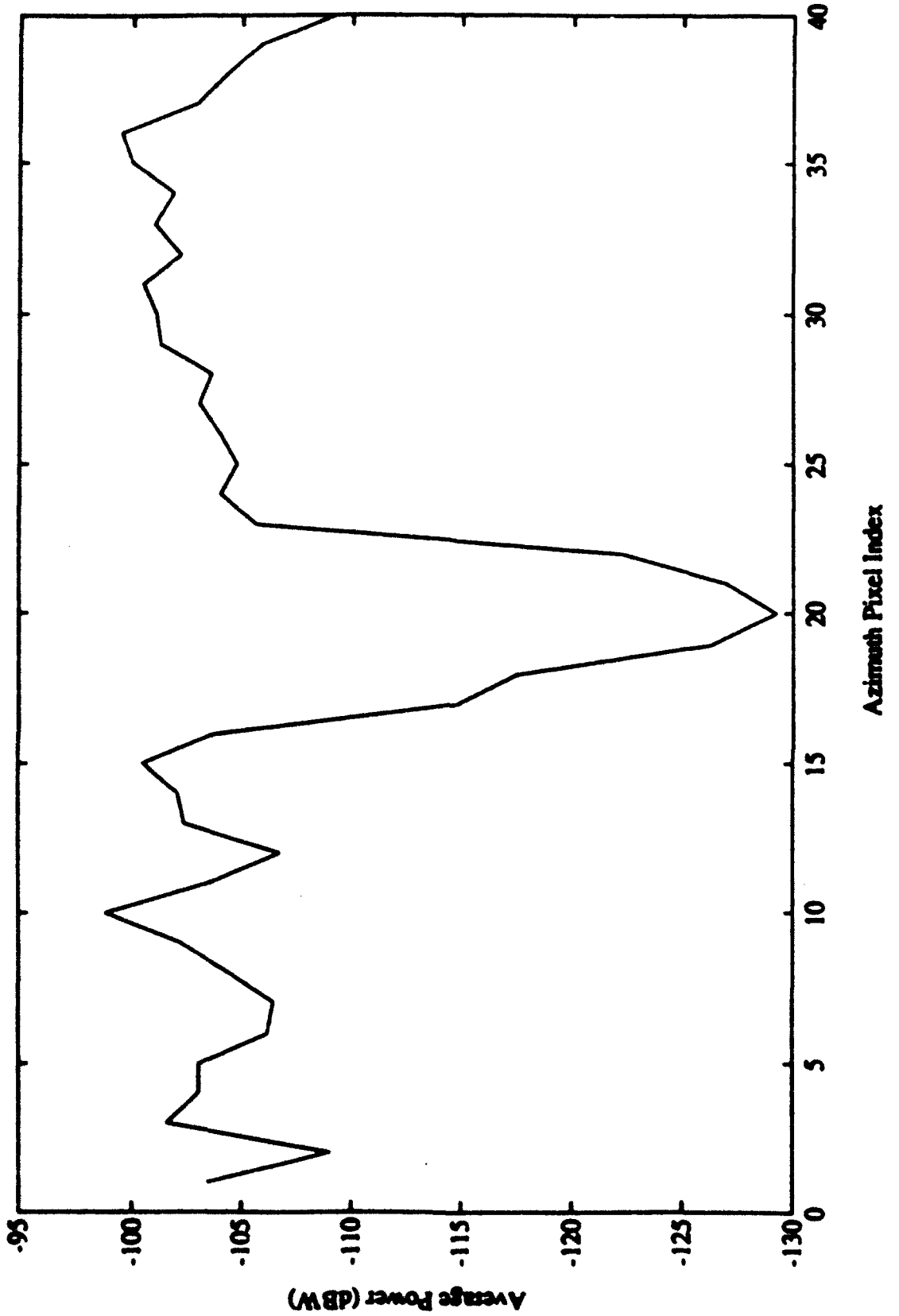

Figure 4.4.2-17. Example Gutter Profile Created in MATLAB

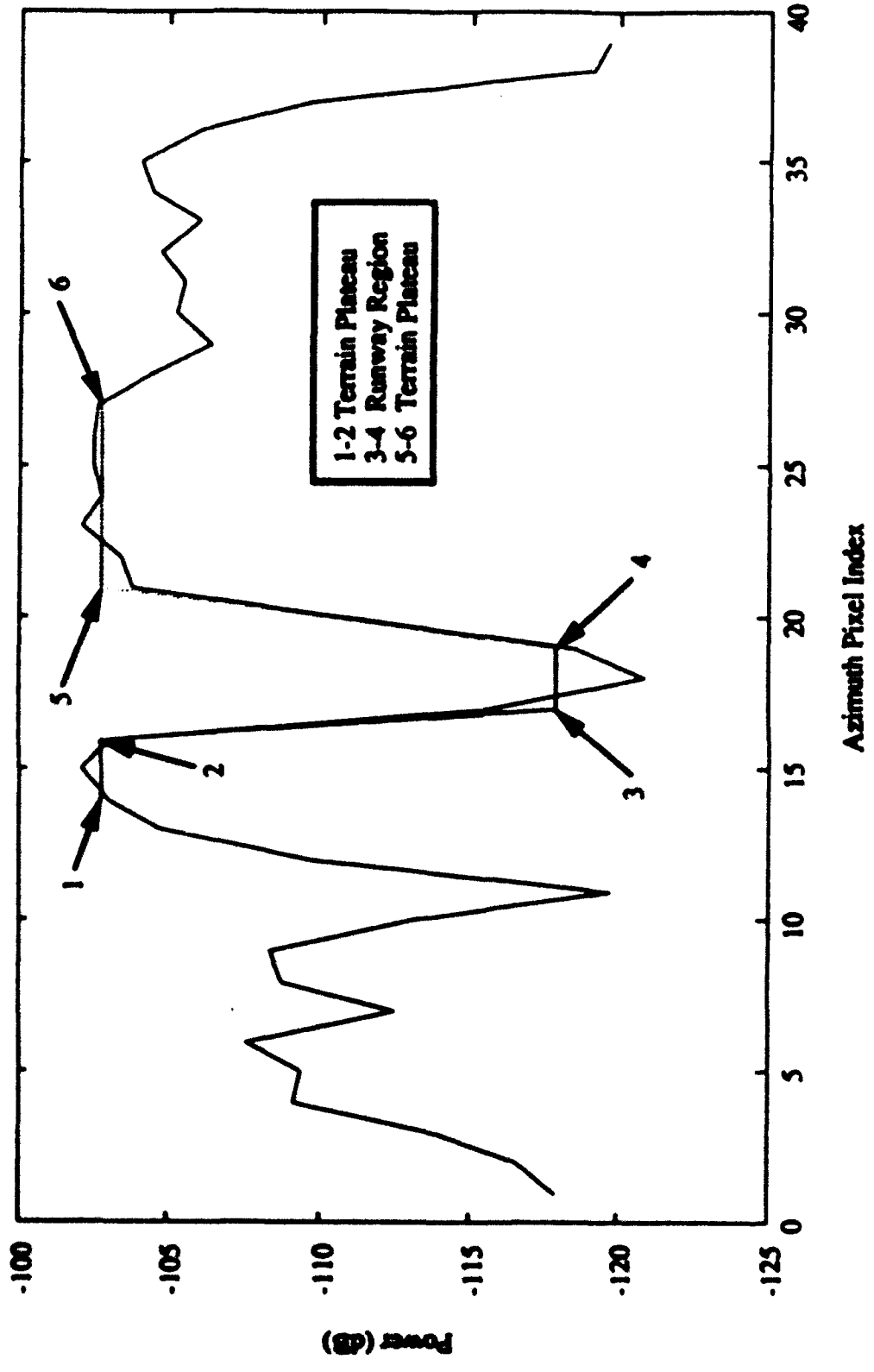

Figure 4.4.2-18. Illustration of Gutter Profile Partitioned Into Runway and Terrain Regions in MATLAB

4.4.2.3.1.3.2 Contrast

Contrast is a measure of the difference in mean received power levels between the runway and its surrounding terrain. This metric was computed in MATLAB using the average received power values supplied by IMAGE. The equations defining the contrast metric are

$$\beta_{\text{terrain left}} = \frac{1}{N_{\text{left}}} \sum_{i=1}^{N_{\text{left}}} x_i \tag{4.4.2-17}$$

$$\beta_{\text{terrain right}} = \frac{1}{N_{\text{right}}} \sum_{i=1}^{N_{\text{right}}} x_i \tag{4.4.2-18}$$

$$\beta_{\text{runway}} = \frac{1}{N_{\text{runway}}} \sum_{i=1}^{N_{\text{runway}}} x_i \tag{4.4.2-19}$$

$$\text{Contrast} = \frac{\left(\frac{\beta_{\text{runway}} - \beta_{\text{terrain left}}}{\beta_{\text{terrain left}}}\right) + \left(\frac{\beta_{\text{runway}} - \beta_{\text{terrain right}}}{\beta_{\text{terrain right}}}\right)}{2} \tag{4.4.2-20}$$

where x_i represents an individual average received power value within the ROI. The computation of contrast is illustrated in Figure 4.4.2-19.

4.4.2.3.1.3.3 Sharpness

Sharpness is a measure of the angular separation between the nominal valley in the radar return corresponding to the runway and the plateau corresponding to the surrounding terrain. The separation angles $\theta_{1,L}$, $\theta_{2,L}$, $\theta_{1,R}$, and $\theta_{2,R}$ in Figure 4.4.2-20 are computed in MATLAB based on the transition boundaries selected by the analyst (points 2, 3 ,4 and 5 in Figure 4.4.2-20). The sharpness metric is defined as follows:

$$\text{Sharpness} = \frac{1}{2}\left\{\frac{1}{|\theta_{1,L} - \theta_{2,L}|} + \frac{1}{|\theta_{1,R} - \theta_{2,R}|}\right\} \tag{4.4.2-21}$$

where all angles denoted by the θ symbols are in units of degrees. Thus, the sharpness value computed via Equation 4.4.2-21 has units of inverse degrees.

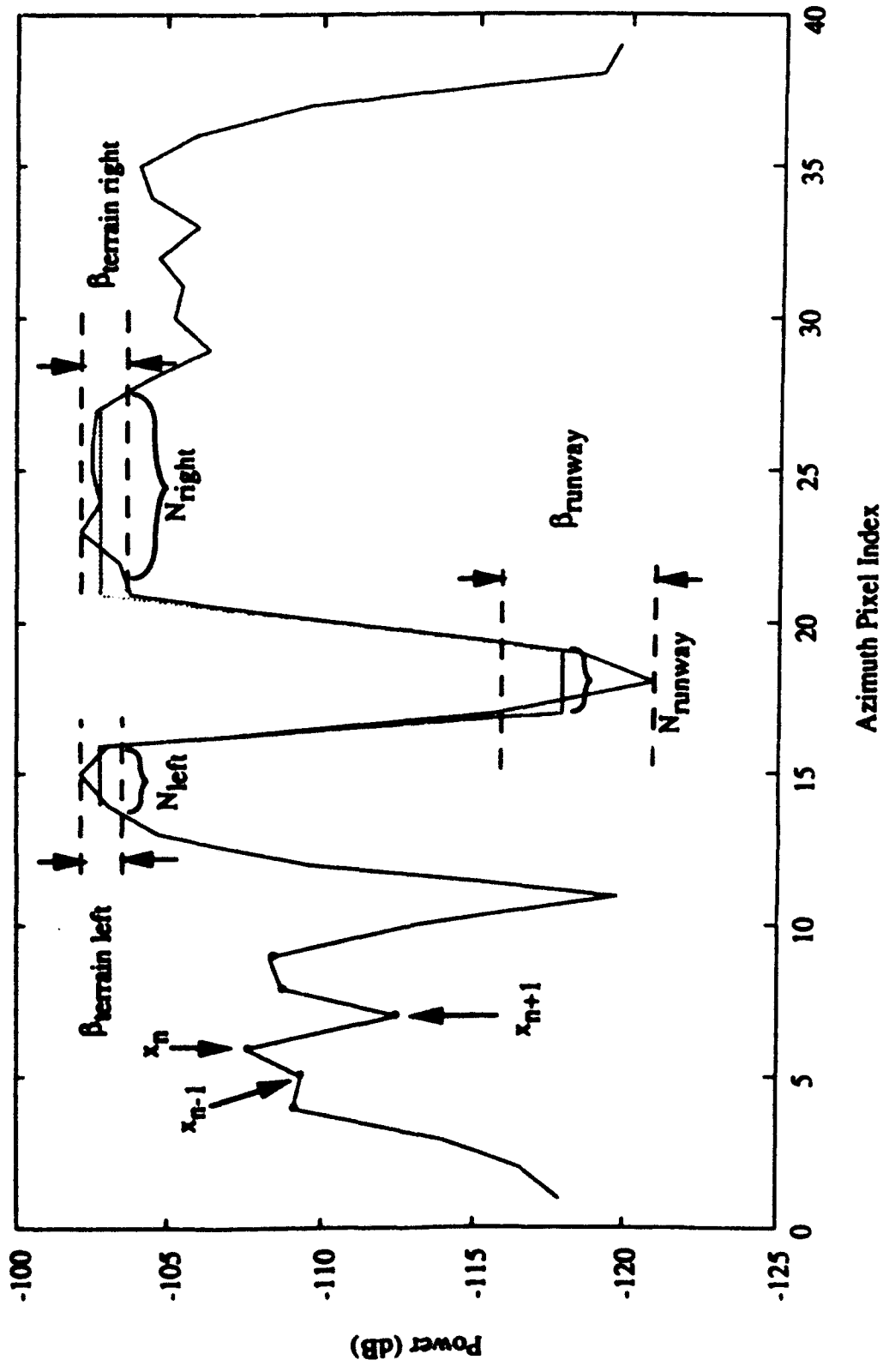

Figure 4.4.2-19, Illustration of Contrast Computation

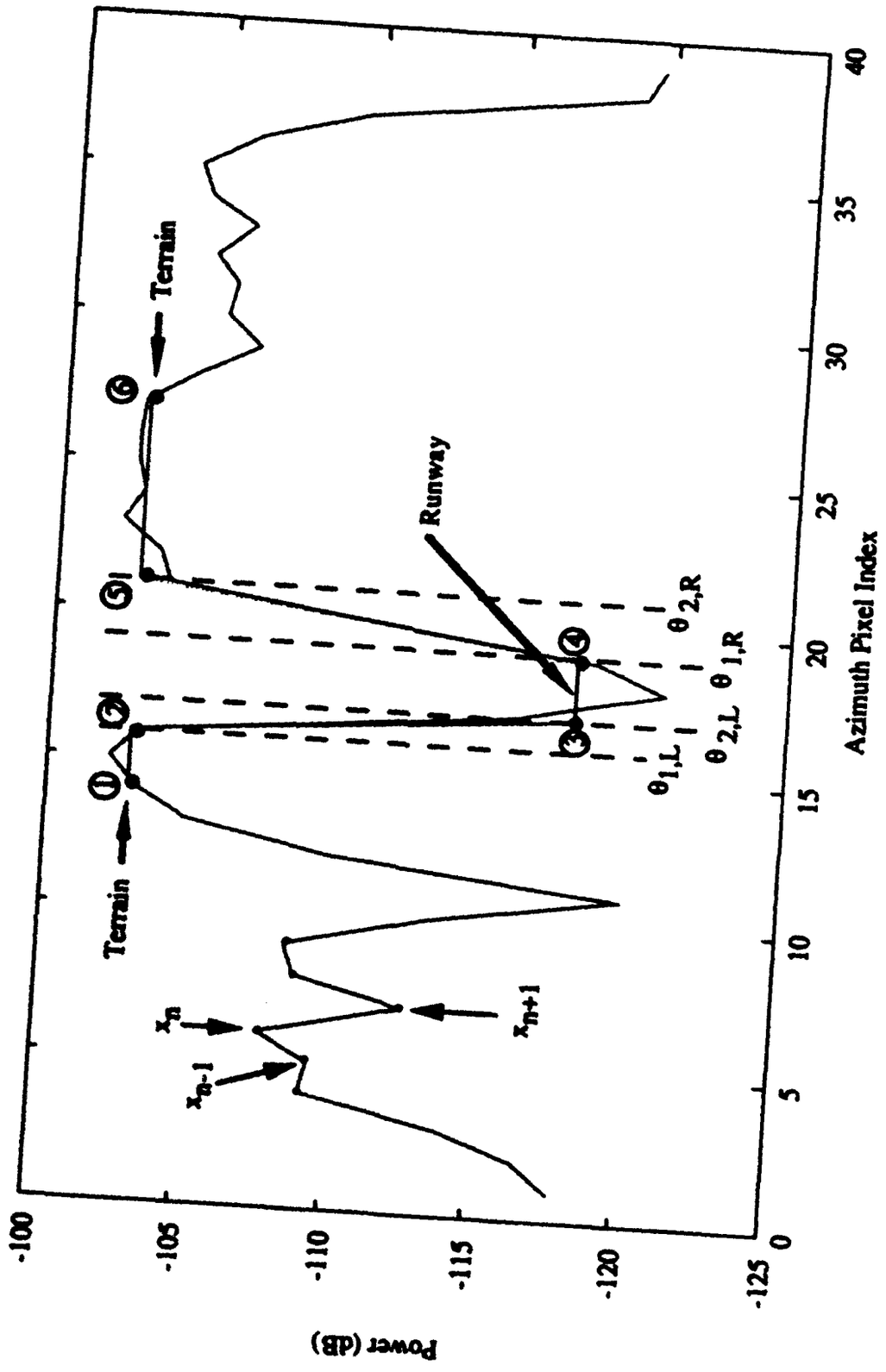

Figure 4.4.2-20. Illustration of Sharpness Computation

4.4.2.3.1.3.4 Variability

The variability for a given ROI was determined by the standard deviation of the received power values that lie along the corresponding gutter plot. This standard deviation was computed using the received power values expressed in dBW. The equations defining the variability as computed in MATLAB are

$$\alpha_{\text{terrain left}} = \sqrt{\frac{1}{N_{\text{left}}}\sum_{i=1}^{N_{\text{left}}} x_i^2 - \left(\frac{1}{N_{\text{left}}}\sum_{i=1}^{N_{\text{left}}} x_i\right)^2} \qquad (4.4.2\text{-}22)$$

$$\alpha_{\text{terrain right}} = \sqrt{\frac{1}{N_{\text{right}}}\sum_{i=1}^{N_{\text{right}}} x_i^2 - \left(\frac{1}{N_{\text{right}}}\sum_{i=1}^{N_{\text{right}}} x_i\right)^2} \qquad (4.4.2\text{-}23)$$

$$\text{Variability}_{\text{terrain}} = \frac{\alpha_{\text{terrain left}} + \alpha_{\text{terrain right}}}{2} \qquad (4.4.2\text{-}24)$$

$$\text{Variablility}_{\text{runway}} = \alpha_{\text{runway}} = \sqrt{\frac{1}{N_{\text{runway}}}\sum_{i=1}^{N_{\text{runway}}} x_i^2 - \left(\frac{1}{N_{\text{runway}}}\sum_{i=1}^{N_{\text{runway}}} x_i\right)^2} \qquad (4.4.2\text{-}25)$$

where x_i represents an individual average received power value (expressed in dBW) in the gutter plot. Note that a separate variability is computed for the terrain and for the runway, as indicated in Figure 4.4.2-21.

Often, the variability itself was less of interest than the relative size of the variability as compared to the runway-terrain transition the pilot must detect. Thus, the signal-to-variability ratio (SVR) was typically the reported metric. This SVR was computed as follows:

$$\text{SVR} = \frac{1}{2}\left\{\frac{\left|\beta_{\text{terrain left}} - \beta_{\text{runway}}\right|}{\frac{1}{2}\left[\alpha_{\text{terrain left}} + \alpha_{\text{runway}}\right]} + \frac{\left|\beta_{\text{terrain right}} - \beta_{\text{runway}}\right|}{\frac{1}{2}\left[\alpha_{\text{terrain right}} + \alpha_{\text{runway}}\right]}\right\} \qquad (4.4.2\text{-}26)$$

where the β's are defined in Equations 4.4.2-17 through 4.4.2-19, and the α's are defined in Equations 4.4.2-22, 4.4.2-23, and 4.4.2-25.

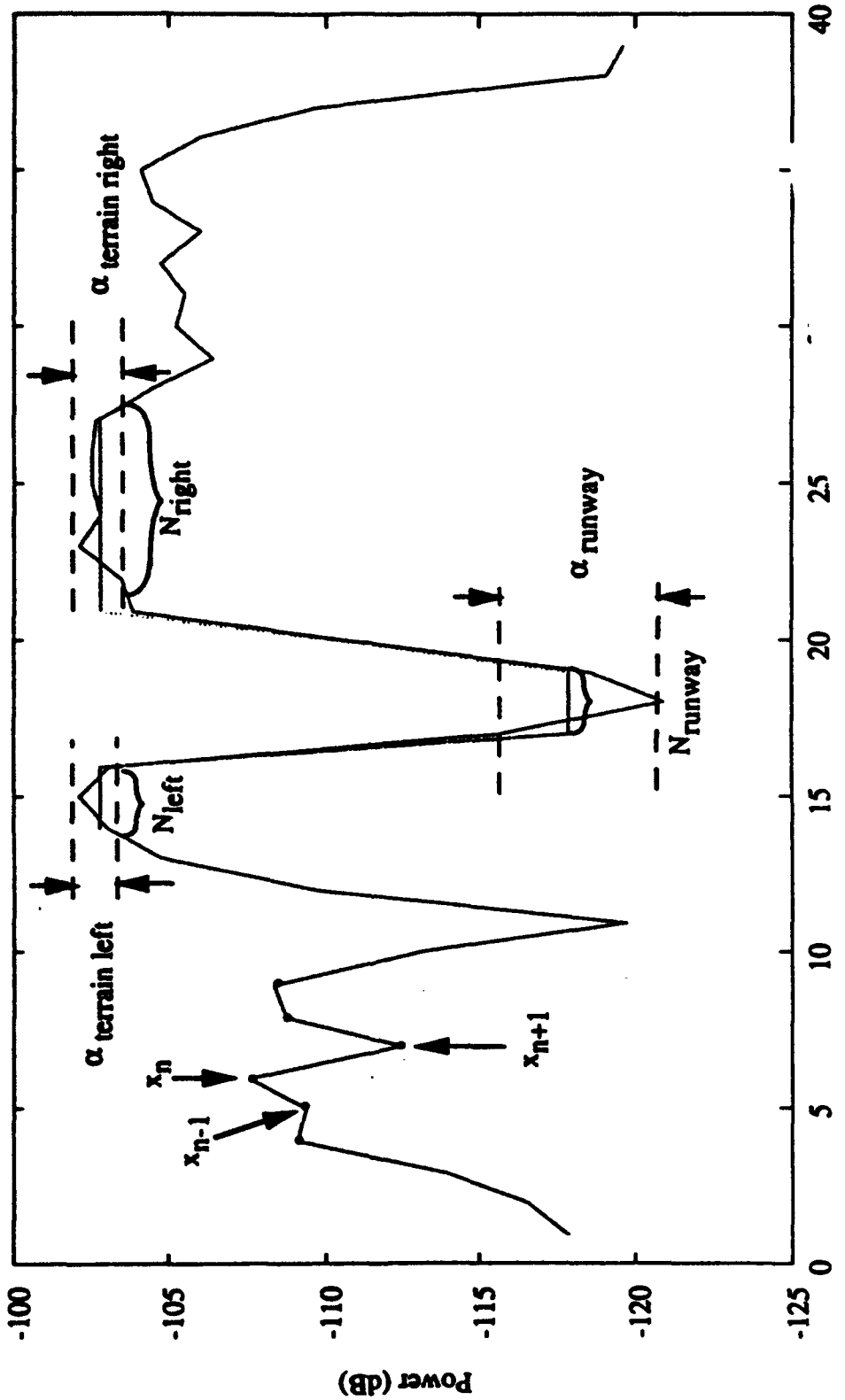

Figure 4.4.2-21. Illustration of Variability Computation

4.4.2. 3.1.4 Data Storage

Raw data files provided by Honeywell on 8mm tapes were given a number and cataloged upon receipt by GTRI. These tapes were then stored in a central location for tracking due to their proprietary nature. Files were downloaded to the SUN as needed using the UNIX "tar" command. The SUN served as a mass storage device for those files extracted from tape which needed to be accessed on a continual basis. Once the custom SUN software had preprocessed the data files, they were downloaded to a Macintosh computer for subsequent analysis.

The display files downloaded to the Macintosh from the SUN were only stored on the Macintosh temporarily due to the limited disk space available. Regions of interest from these files were extracted in IMAGE and written to an output file. These files containing data from the selected ROIs were stored permanently on the Macintosh and backed up on floppy disk. These files could thus be easily loaded into MATLAB at any time for further analysis. In addition, a hard copy of the each of the PPI display images downloaded from the SUN was made and filed for archive purposes. These hard copies served as references of where within each PPI image the ROIs were chosen.

The SUN also served as a backup platform for code and data developed on the Macintosh. Files and data were periodically uploaded to the SUN which was backed-up daily on 8 mm tapes.

.c.4.4.2.3.2 Reduction Process

The preceding paragraphs have outlined the software developed under this program to perform the necessary data reduction and analysis operations. The current section describes the data reduction process itself; it addresses how the software tools described above were used by the analysts in performing the required tasks.

The data reduction process involved choosing regions of interest within each selected snapshot and then computing metrics to describe certain properties within those ROIs. The first step in the process was to convert each raw data file to a PPI display format. The PPI images were then displayed using IMAGE so that regions of interest could be selected by the analyst. Metrics such as contrast, sharpness and RCS were then computed and stored in a spreadsheet for subsequent retrieval and analysis.

4.4.2.3.2.1 Data Selection, Transfer and Pre-Processing

The snapshot radar data and ancillary data described in Section 4.4.2.1 above were processed to assess the performance of the Honeywell radar sensor in each scenario of interest. These analyses were performed using the software tools described in Section 4.4.2.3.1 above. Selections of specific data to analyze were based on the importance of each approach in addressing the key sensor-performance issues of the program. Key factors considered include prevailing weather conditions and the specific airport approached, as well as others outlined in detail in the program Test Plan.

Once a specific approach had been selected for processing, the necessary radar data had to be made available to the analyst. Raw data files were received from Honeywell on 8mm cartridge tapes which were downloaded to the GTRI SUN. Each file was labeled with a date/time tag as defined in Section 4.4.2.3.1.1.1 above. These files, containing A/D counts, were converted from range/azimuth B-scope formats to PPI fixed-point (8-bit) images as discussed in Section 4.4.2.3.1.1.2. A corresponding floating-point PPI data structure, parallel to the PPI image, was also generated. This data structure contained received power values computed based on the measured A/D counts and the data acquisition transfer function discussed in Section 4.4.2.3.1.1.4. These two PPI-format files were then downloaded to the Macintosh for processing with IMAGE, as discussed in Section 4.4.2.3.1.2 above.

The snapshots were compared to maps of the subject airport to identify recognizable structures within each scene such as buildings, taxiways, and towers. By comparing the positions of these structures on the ground, with the locations of the corresponding radar returns in the image, the analyst was able to register the scene. Also, successive snapshots (which were spaced approximately four seconds apart) could be used to monitor the aircraft's approach toward the runway, which aided in referencing returns from objects in one snapshot with returns from those same objects in the next snapshot.

For contrast, sharpness, and variability processing, as many as four snapshots along each selected approach were analyzed. These snapshots corresponded approximately to the four points denoted in Table 4.4.2-9. The first two are fixed in altitude and correspond to the nominal flare point and decision height. The third snapshot is also fixed and corresponds to the point at which the slant range to the touchdown target is approximately 2,500 meters. The last snapshot represents the point at which the test pilot reports detection of the runway based on the real-time sensor image presented to him. Figure 4.4.2-22 illustrates the aircraft position corresponding to each of these for snapshots.

Table 4.4.2-9. Altitudes for snapshots of interest

Altitude	Range	Significance
50 ft	292 meters (approx.)	flare point
200 ft	1,165 meters (approx.)	decision height
429 ft (approx.)	2,500 meters	selected
variable	variable	pilot detection

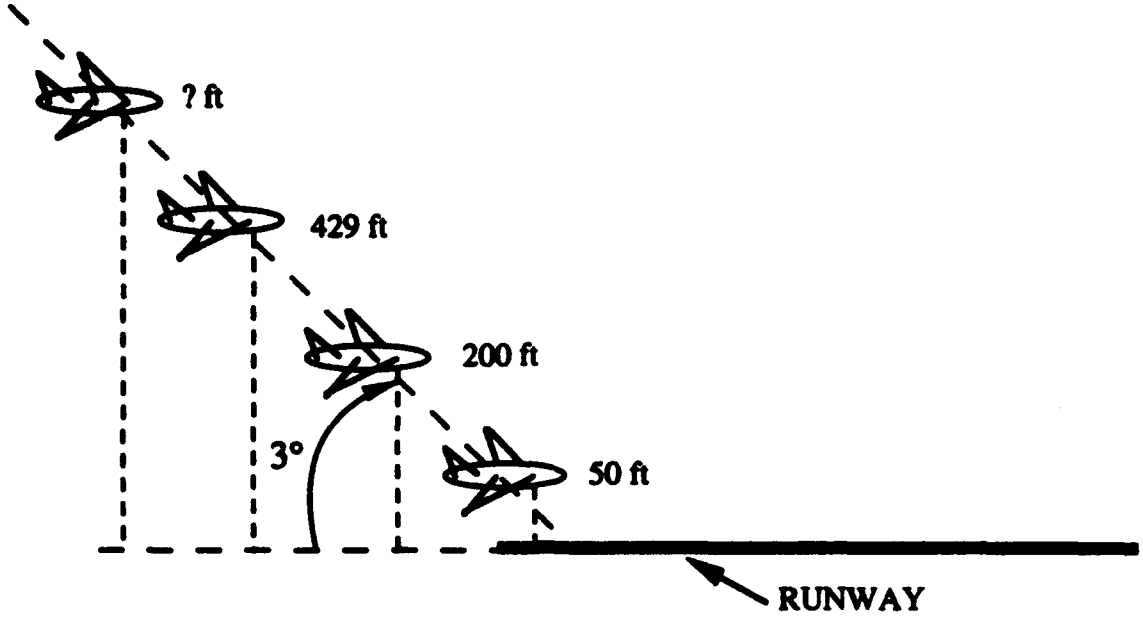

Figure 4.4.2-22. Positions of the Aircraft Corresponding to Snapshots of Interest.

The pilot detection point in Table 4.4.2-9 was recorded during each approach as the point at which the pilot first called detection of the runway. Therefore, the pilot detection altitude and range values varied from approach to approach.

For each of these four snapshots, as many as four regions within each snapshot were analyzed for contrast, sharpness, and signal-to-variability ratio. At least three regions were always analyzed. These were (1) the runway threshold, (2) the touchdown target, and (3) the furthest point at which the radar data analyst could distinguish the runway based on inspection of the radar data only (called the "radar vanishing point"). The fourth region was the very end of the runway pavement in the image. For this fourth region, the runway area at the very top of the PPI image (maximum range) was used for those cases in which the far end of the runway was not included in the image.

These four regions of interest are illustrated in Figure 4.4.2-23. Once each ROI was identified in the image, a rectangular patch of data, 40 azimuth lines wide by 7 range lines deep and centered on each ROI, was then extracted from the image for export to MATLAB.

Although this general method was used for selecting regions of interest within each snapshot, flexibility and judgment were used in deviating slightly from these guidelines as necessary. For example, if the region of interest was obviously contaminated by a spurious return, then the adjacent, uncontaminated region slightly further or closer in range was substituted in its place. For example, such substitutions were made at Point Mugu, CA, where the runway lights produced a distinct return which often dominated the edge-transition return the analyst was attempting to characterize. In these cases, the radar analysts were careful to pick regions of interest which did not include such runway light returns.

The radar phenomenological parameters - RCS, reflectivity, attenuation, and volumetric reflectivity - were computed only for a selected subset of the available approaches. These computations could be made only for approaches against airport scenes which contained the Bruderhedral reflectors described above since absolute calibration of the scene was necessary for the required computations. These analyses are described in Sections 4.4.2.3.2.3 and 4.4.2.3.2.4 below. First, however, the measurement process for the image quality metrics is described.

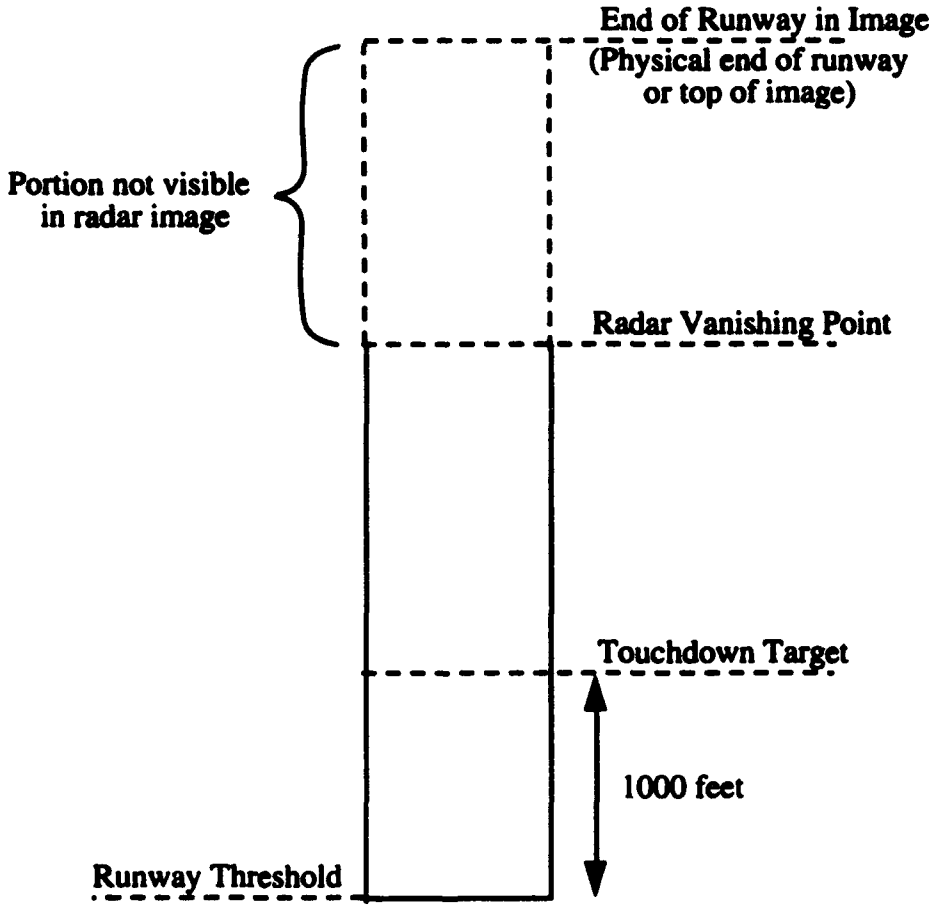

Figure 4.4.2-23. Four regions of interest along the runway.

4.4.2.3.2.2 Contrast, Sharpness, and Variability Processing

Section 4.4.2.3.1 above described the software tools created under this program to compute sharpness, contrast, and signal-to-variability ratio. These three parameters are collectively referred to as the image quality parameters. In addition, Section 4.4.2.3.2.1 discussed the four snapshots and the three or four regions within each for which the image quality parameters could be computed. The purpose of this section is to illustrate exactly how these analyses were performed.

Figure 4.4.2-24 presents the PPI display for a snapshot of the Arcata, CA airport taken from an altitude of about 216 feet. The radar data snapshot was taken on 8/28/92 in fog. Based on surface weather observations, the ceiling was indefinite with less than 100 feet vertical visibility, and runway visibility was 1/8 mile. Runways 32R-14L and the parallel "A" taxiway are evident just right of center in this snapshot. Runways 2-20 running diagonally across the PPI image can also be seen clearly. Three boxes are outlined in white superimposed on the data.

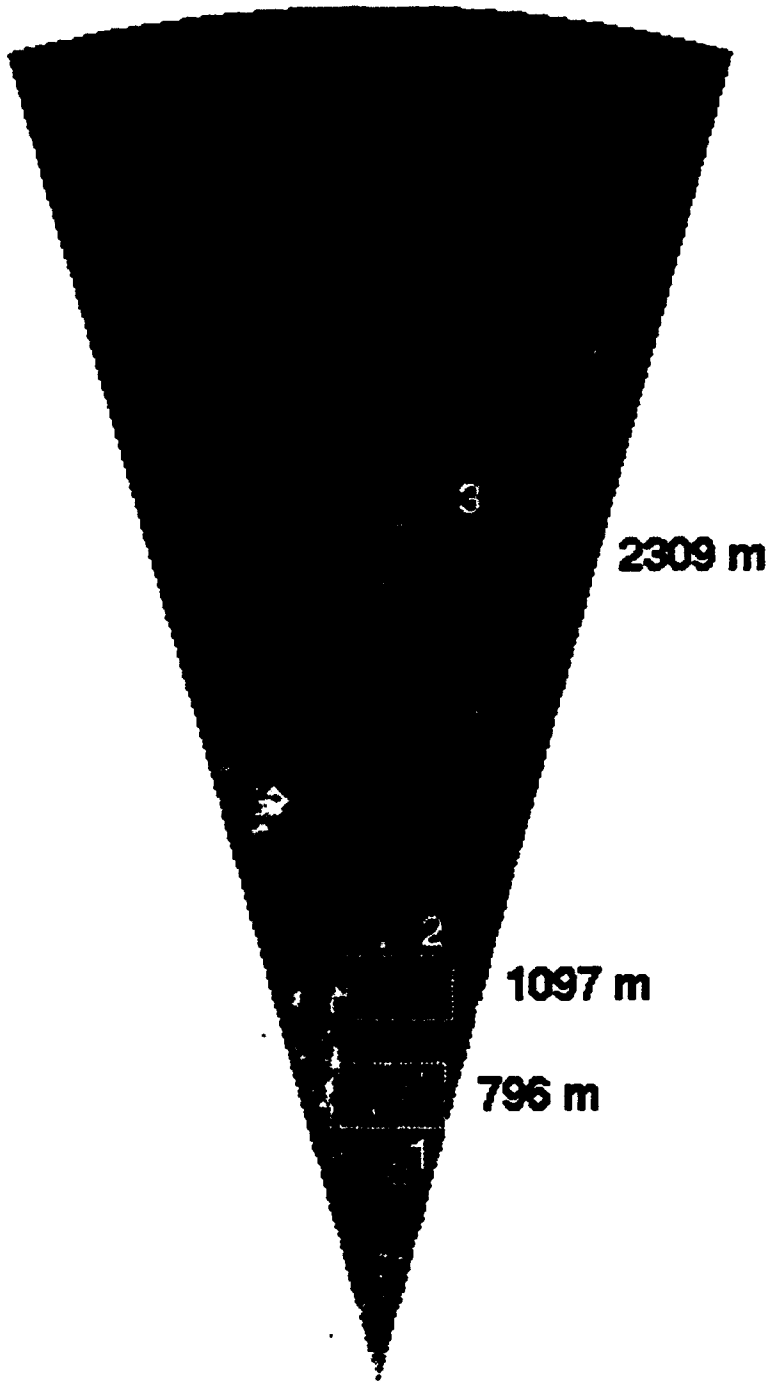

Figure 4.4.2-24. Example PPI Snapshot Image from Arcata, CA taken in Fog on August 28, 1992

The lowest box superimposed on the data, which is labeled "1," corresponds to the runway threshold. Box 2 corresponds to the touchdown target, and box 3 includes the radar vanishing point - the point beyond which the radar analyst could no longer distinguish the runway from the surrounding terrain. The numbers to the right of each box represent the slant range in meters to each respective region of interest in the image.

Figure 4.4.2-25 illustrates the three-dimensional nature of the radar data corresponding to box 1 in Figure 4.4.2-24. Azimuth is represented along the long edge of Figure 4.4.2-25, whereas range is represented as depth "into" the page. The amplitudes correspond to the linear received power levels in milliwatts for each range-azimuth cell. Note from Figure 4.4.2-24 that the left edge of Box 1 begins on an apron, and then extends right across taxiway A and then across runways 32R-14L.

In Figure 4.4.2-25, Runway 32R-14L is evident as the valley in the center of the plot, and the apron is also indicated as the valley to the far left of the plot. The "A" taxiway is visible as a very narrow valley between the apron and the runway 32R-14L. Figure 4.4.2-25 thus corroborates the observation based on Figure 4.4.2-24 that the runway is evident in the radar data.

Figures 4.4.2-26 and 4.4.2-27 are similar three-dimensional plots corresponding to boxes 2 and 3 in Figure 4.4.2-24, respectively. Note that in Figure 4.4.2-26, the runway, taxiway, and apron are still visible, and one can also see the "D" taxiway running perpendicular from the apron to the runway can also be seen. In Figure 4.4.2-27, which represents data over 2.3 km from the radar, the runway still can be seen in the middle of the plot, but the left boundary of the runway is not distinct. The "A" taxiway cannot be identified at all..

The purpose of the image quality metrics is to quantify, at least partially, how well the runway can be detected in the raw data images. In other words, they represent quantitative measures of how distinctly the runway stands out from the surrounding terrain in the radar image. Let us now walk through a sample analysis.

The first step in analyzing a given approach was snapshot selection. As noted previously, raw radar data snapshots were acquired approximately every four seconds. The analyst examined the snapshots available for the approach of interest and selected the one taken from the altitude nearest 50 feet, the one taken from the altitude nearest 200 feet, and the one for which the slant range to the touchdown target was nearest 2500 meters. These are the three fixed snapshots listed in Table 4.4.2-9. In addition, when available, the snapshot nearest the point of pilot detection was also selected.

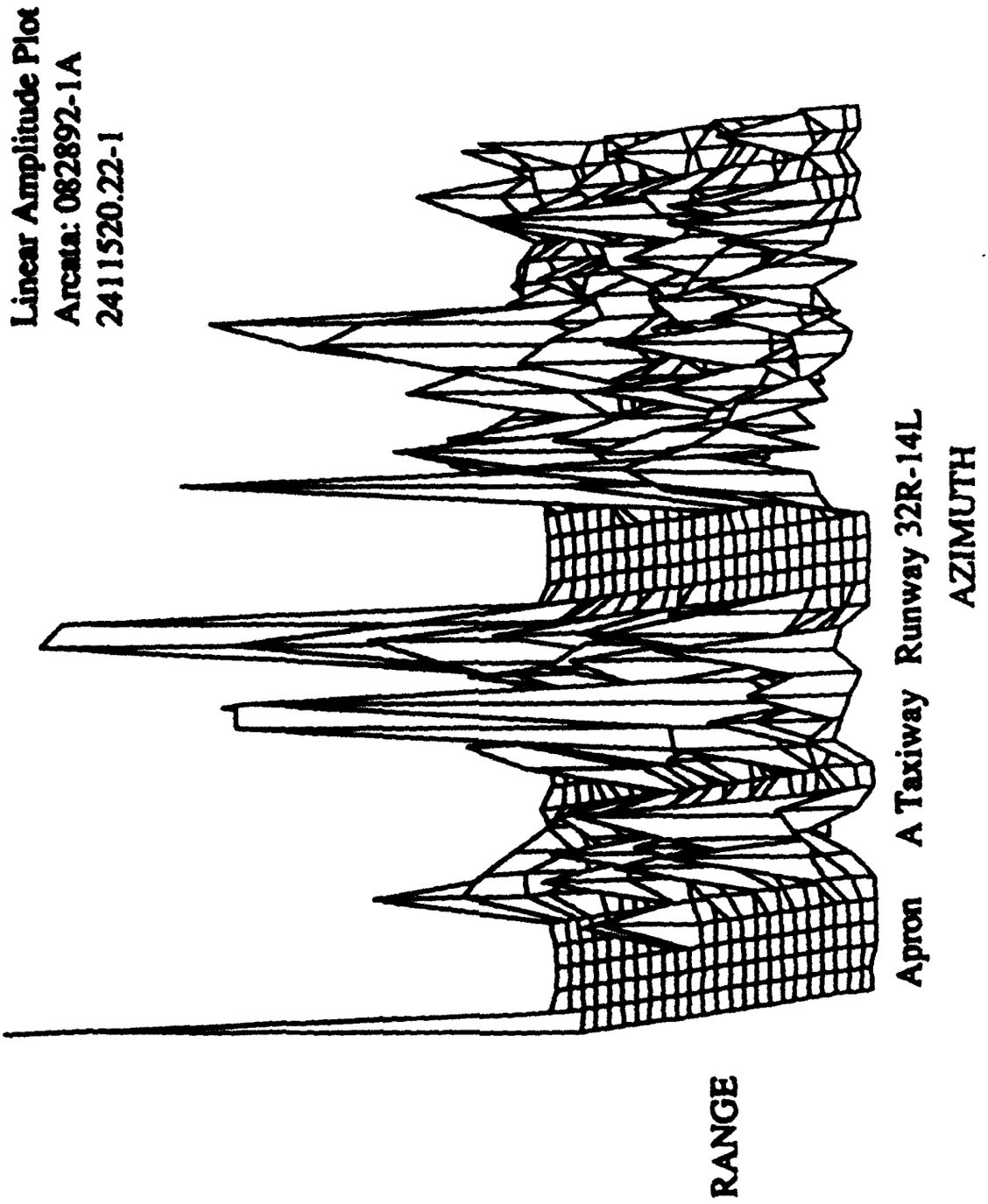

Figure 4.4.2-25. Three Dimensional, Linear-Amplitude Presentation of Radar Data From Box 1 of Figure 4.4.2-24

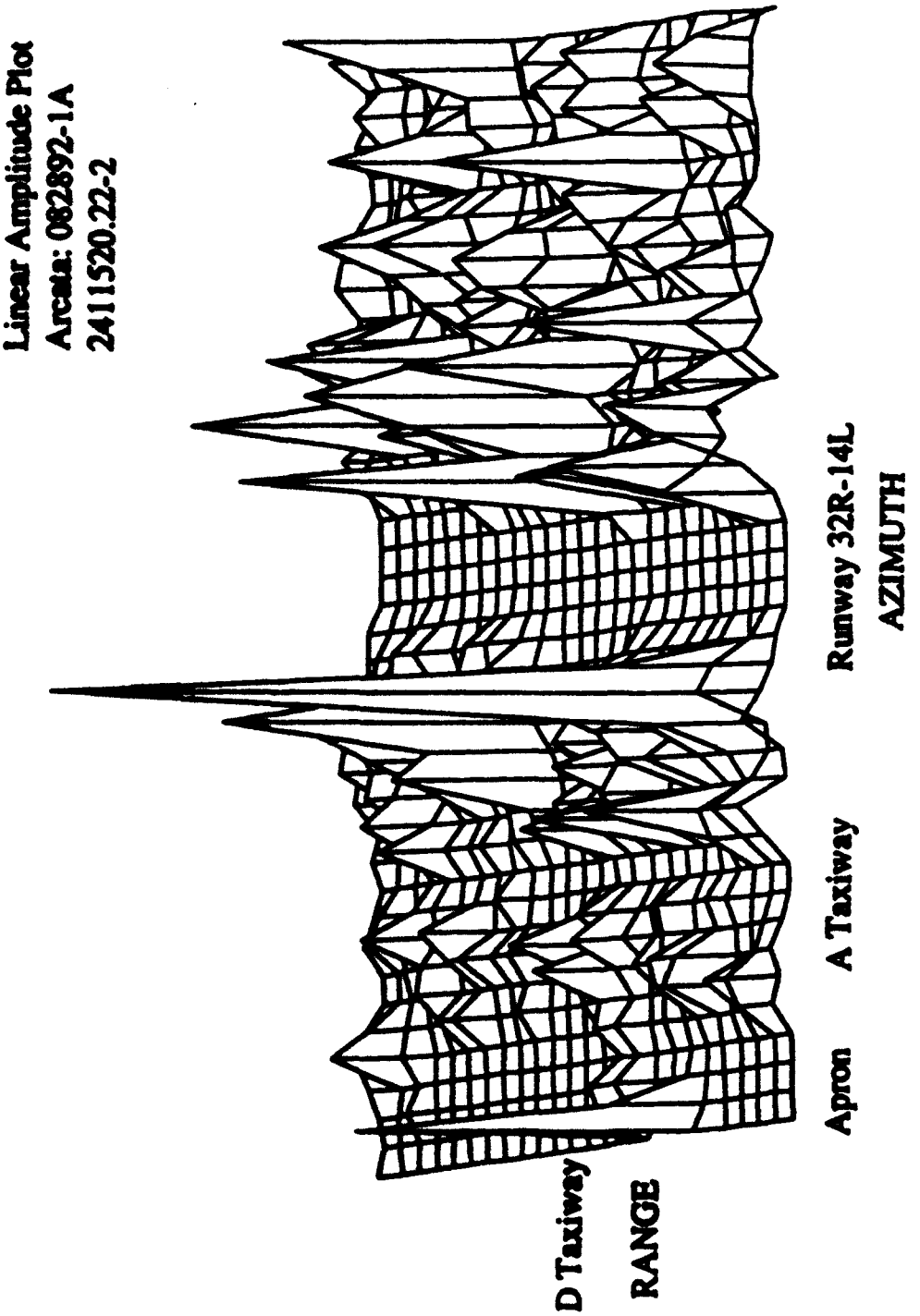

Figure 4.4.2-26. Three Dimensional, Linear-Amplitude Presentation of Radar Data From Box 2 of Figure 4.4.2-24

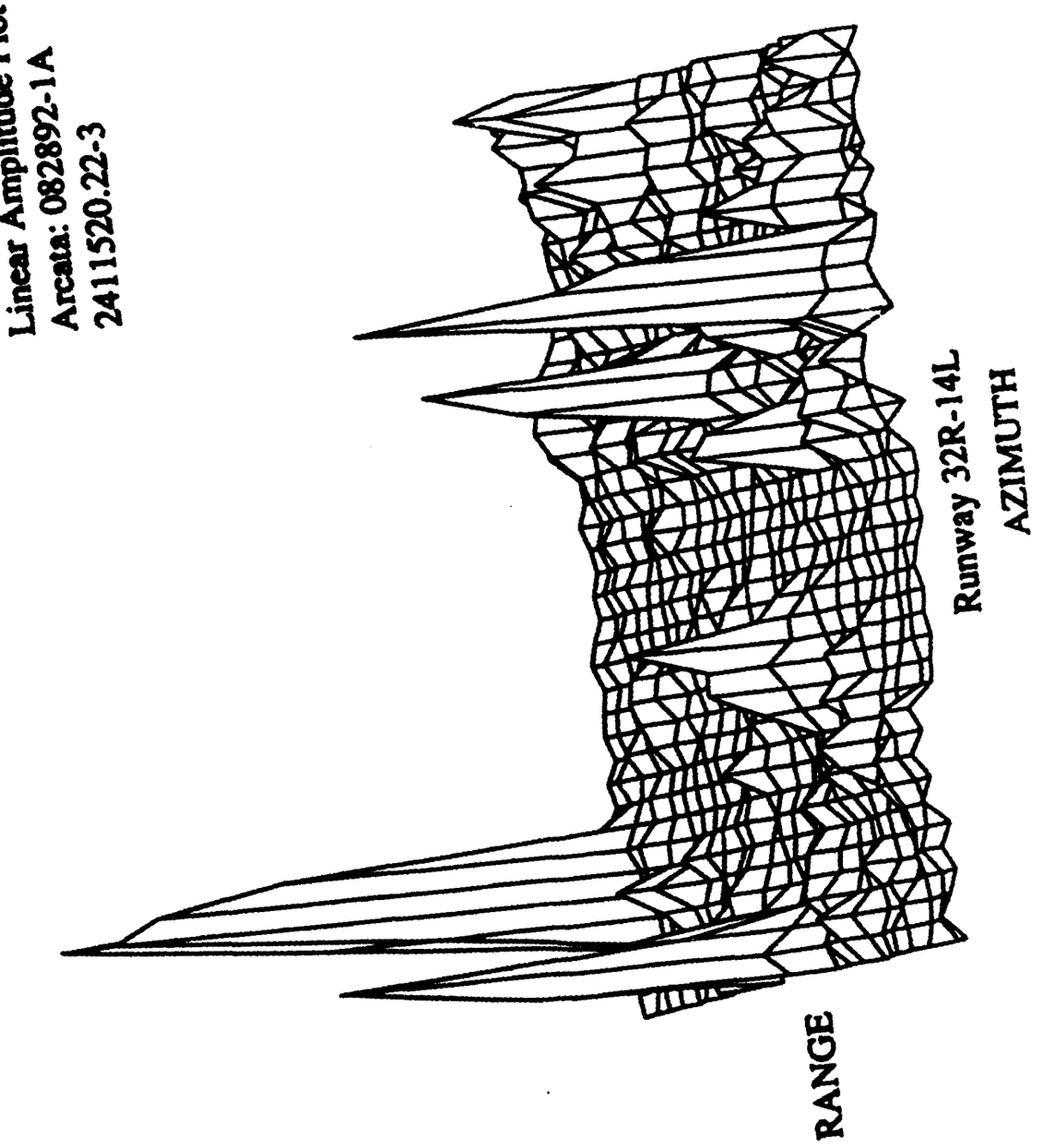

Figure 4.4.2-27. Three Dimensional, Linear-Amplitude Presentation of Radar Data From Box 3 of Figure 4.4.2-24

The blended altitude value was generated by the Honeywell system via a Kalman filter which has as its inputs the INS radar altimeter report and the barometric altimeter reading available over the ARINC data bus. The filter weights these inputs so that the barometric altitude more strongly impacts the blended altitude value at higher altitudes, whereas the radar altimeter dominates at lower altitudes.

Once these snapshots had been selected, the analyst proceeded to compute the image quality metrics for the various regions of interest. Figure 4.4.2-28 presents the PPI display for a snapshot of the Huntington, WV airport taken from an altitude of about 487 feet (corresponding to a slant range near 2.5 km). The snapshot was taken on 9/28/92 in fog, with runway visibility of 1/16 mile reported at the surface. The three boxes superimposed on the data correspond to the runway threshold (box 1), the touchdown target (box 2), and the end of the runway pavement in the image (box 3).

No radar vanishing point was determined for this snapshot, since the analyst could detect the runway all the way to the end of the image. (The reader should keep in mind that the radar data displays on the computer monitor are much clearer than the corresponding hardcopy PPI images included in this report.) To the right of boxes 1, 2, and 3 are the slant ranges in meters from the radar to each region of interest.

Each region of interest used in computing the image quality parameters was seven range cells deep. Thus, each box in Figure 4.4.2-28 includes seven range cells along each azimuth line. Once an appropriate region of interest had been identified, the first processing step involved averaging in range to produce a single two-dimensional waveform that represents average received power as a function of azimuth. Figure 4.4.2-29 plots the two-dimensional waveform corresponding to Box 1 in Figure 4.4.2-28. As noted previously, plots such as those of Figure 4.4.2-29 are called "gutter" plots.

Figure 4.4.2-29 plots power received by the radar in decibels with respect to a Watt versus azimuth pixel index. As can be seen, the gutter plot of Figure 4.4.2-29 spans 40 azimuth pixels in the PPI display. Each power value in the gutter plot is the average (computed in linear space) of the corresponding seven range cell values lying along a vertical line in Box 1 of Figure 4.4.2-28.

Once this two-dimensional gutter plot had been created, the analyst used MATLAB software procedures described previously in Section 4.4.2.3.1.3.1 to indicate six key boundary points. These six points are indicated in Figure 4.4.2-29 and represent the left terrain radar return edges (points 1 and 2), the runway edges (3 and 4), and the right terrain edges (5 and 6). MATLAB

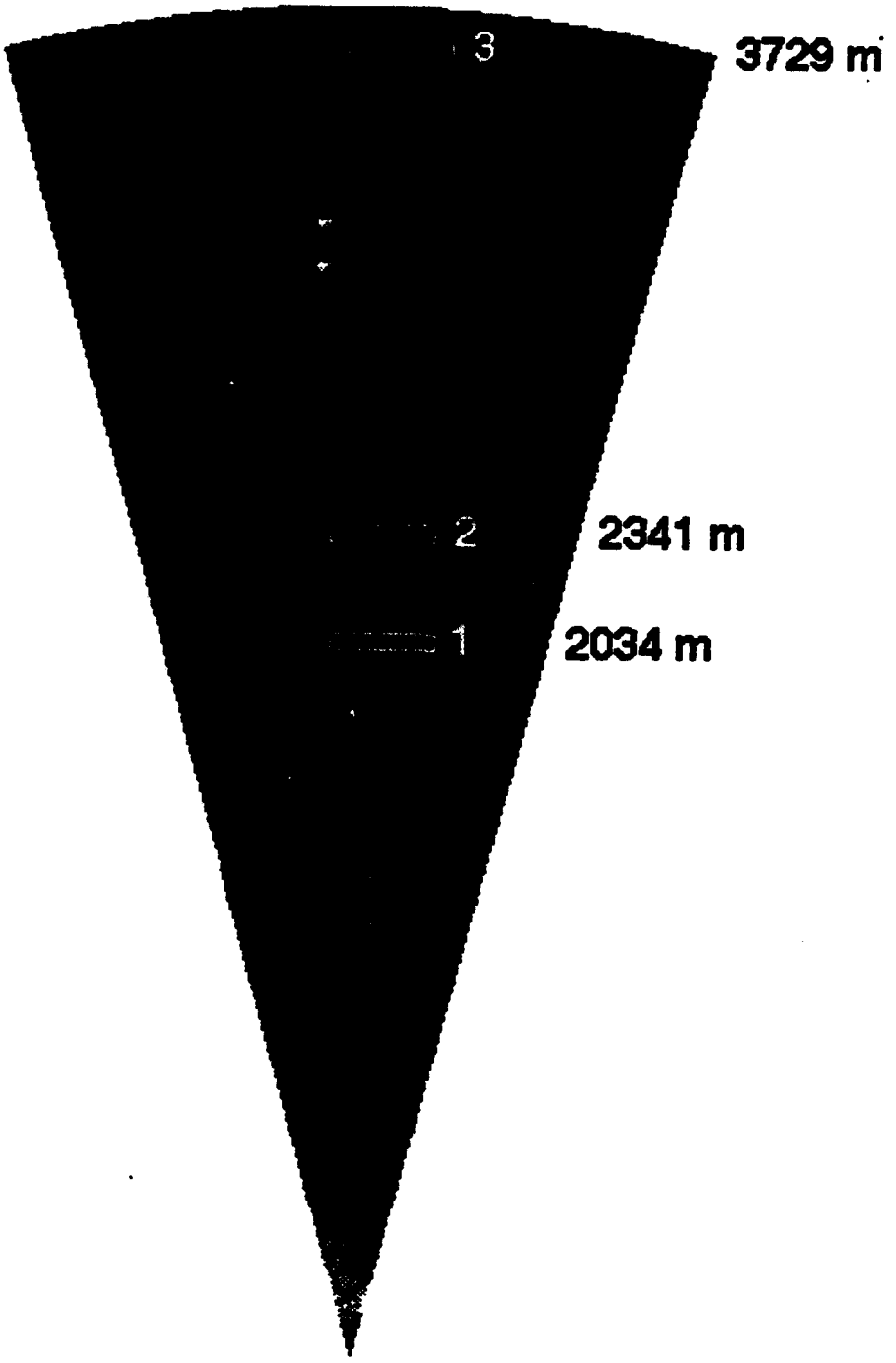

Figure 4.4.2-28. Example PPI Snapshot Image From Huntington, WV Taken in Fog September 28, 1992

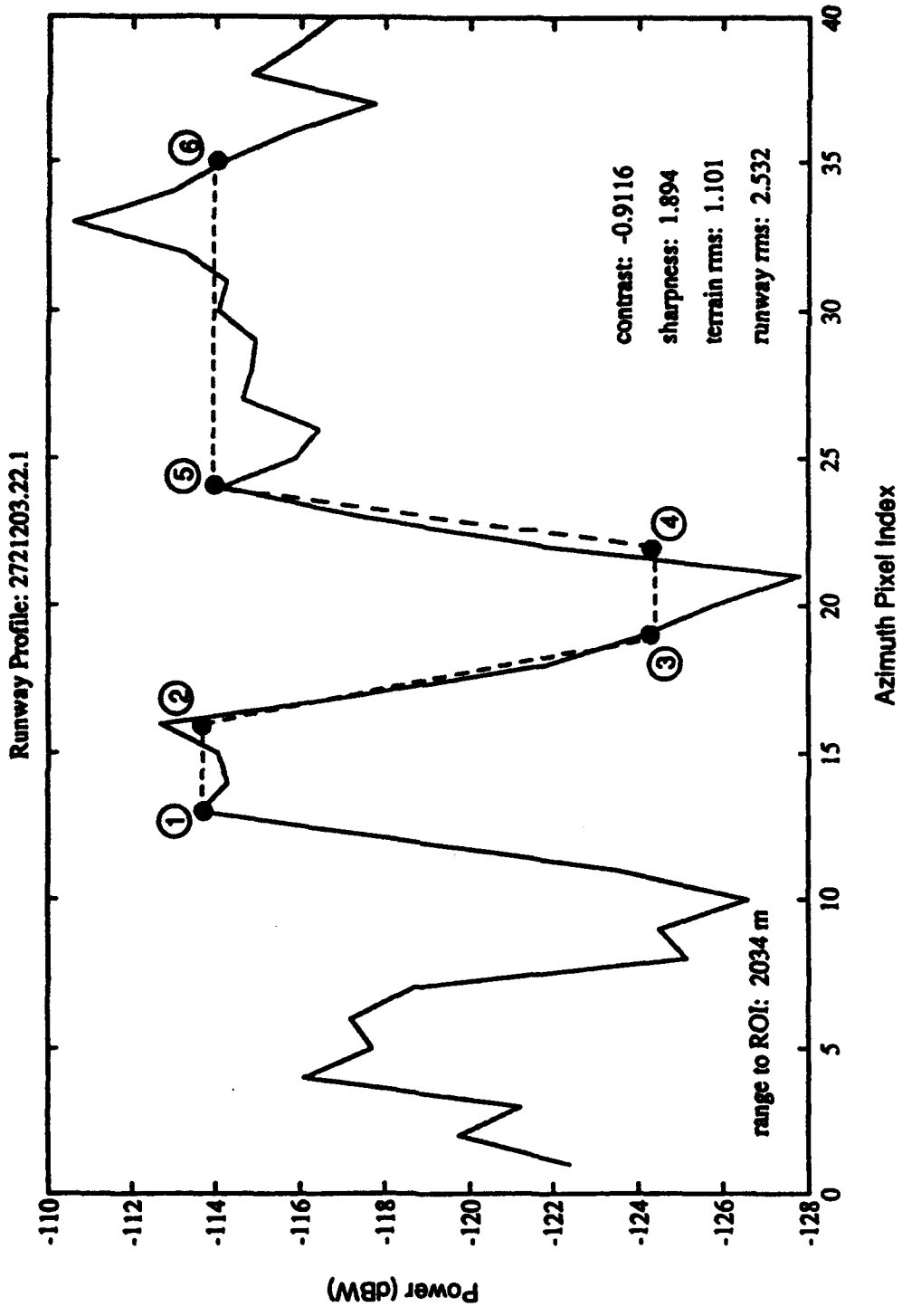

Figure 4.4.2-29. Gutter Plot Corresponding to Box 1 in Figure 4.4.2-28

procedure then averaged the power values between each pair of these points to arrive at the mean left terrain signal level, the mean runway signal level, and the mean right terrain signal level. These three levels are denoted by the three horizontal dashed lines in Figure 4.4.2-29. In addition, a line was drawn between each pair of points representing a terrain-runway transition (2 and 3, as well as 4 and 5).

As can be seen from Figure 4.4.2-29, there was some flexibility in selecting the six boundary points. For example, had point 6 been located closer to point 5 so that it did not span the "spike" evident in Figure 4.4.2-29, the average radar return level reported for the left terrain would have been a dB or so lower. However, the location of point 6 in Figure 4.4.2-29, while subjective, is not unreasonable. It was decided that permitting the analysts to use their judgment with each gutter plot in locating these boundary points was preferable to automating some arbitrary selection criteria which would not produce acceptable results in every case. The trained human eye is an excellent image processor and this analysis effort took advantage of this capability.

Nonetheless, even though the six point-selections were subjective to some extent, care was taken to maintain quality and consistency in the selection method. Airport diagrams were obtained for every airport of interest so that analysts were aware of parallel runways, taxiways, etc. Furthermore, each set of boundary point selections was documented via a hardcopy plot such as that shown in Figure 4.4.2-29.

The width of the runway region is indicated by the dashed line in Figure 4.4.2-29. If points 3 and 4 were co-located at the minimum level occurring at pixel #20, the runway return level would have been almost 4 dB lower than that measured in the figure. However, it can be seen from Figure 4.4.2-28 that the runway is more than one pixel wide. Typically, the runways were 3 to 5 pixels wide in the PPI displays. Boundary points 3 and 4 in the gutter plots were selected so that the corresponding runway "line" (between 3 and 4) was roughly the same width in pixels as it was in the PPI display.

Once the six boundary points had been designated by the operator, the MATLAB procedure automatically computed the contrast and the sharpness (in inverse degrees), as well as the terrain and runway variability parameters. The corresponding values for the gutter plot of Figure 4.4.2-29 are indicated in the lower right corner of the plot. Contrast and sharpness were computed as described in Sections 4.4.2.3.1.3.2 and 4.4.2.3.1.3.3, respectively. The signal-to-variability ratio (SVR) was computed from the average signal levels and the rms variability values as described in Section 4.4.2.3.1.3.4.

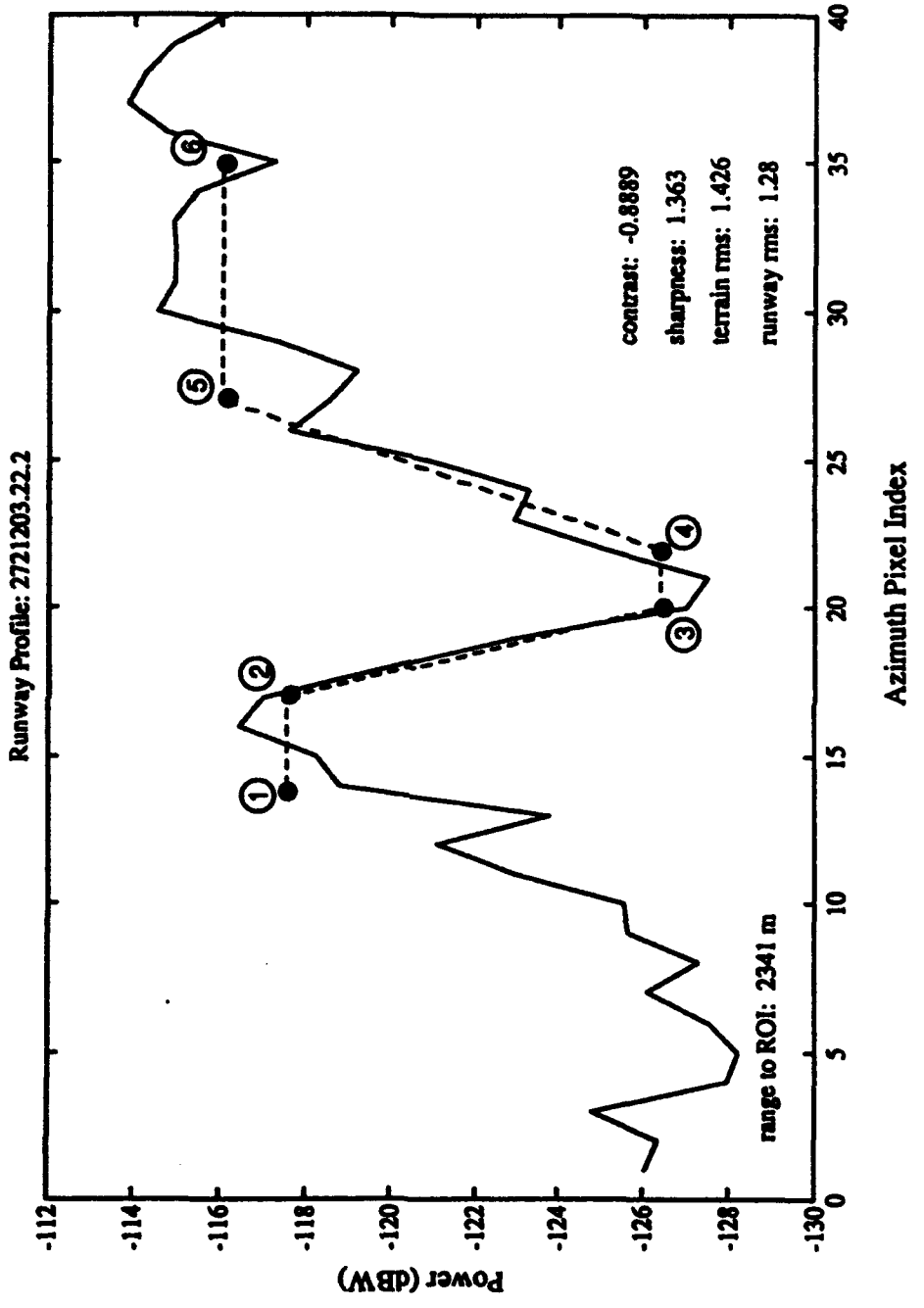

Figure 4.4.2-30. Gutter Plot Corresponding to Box 2 in Figure 4.4.2-28

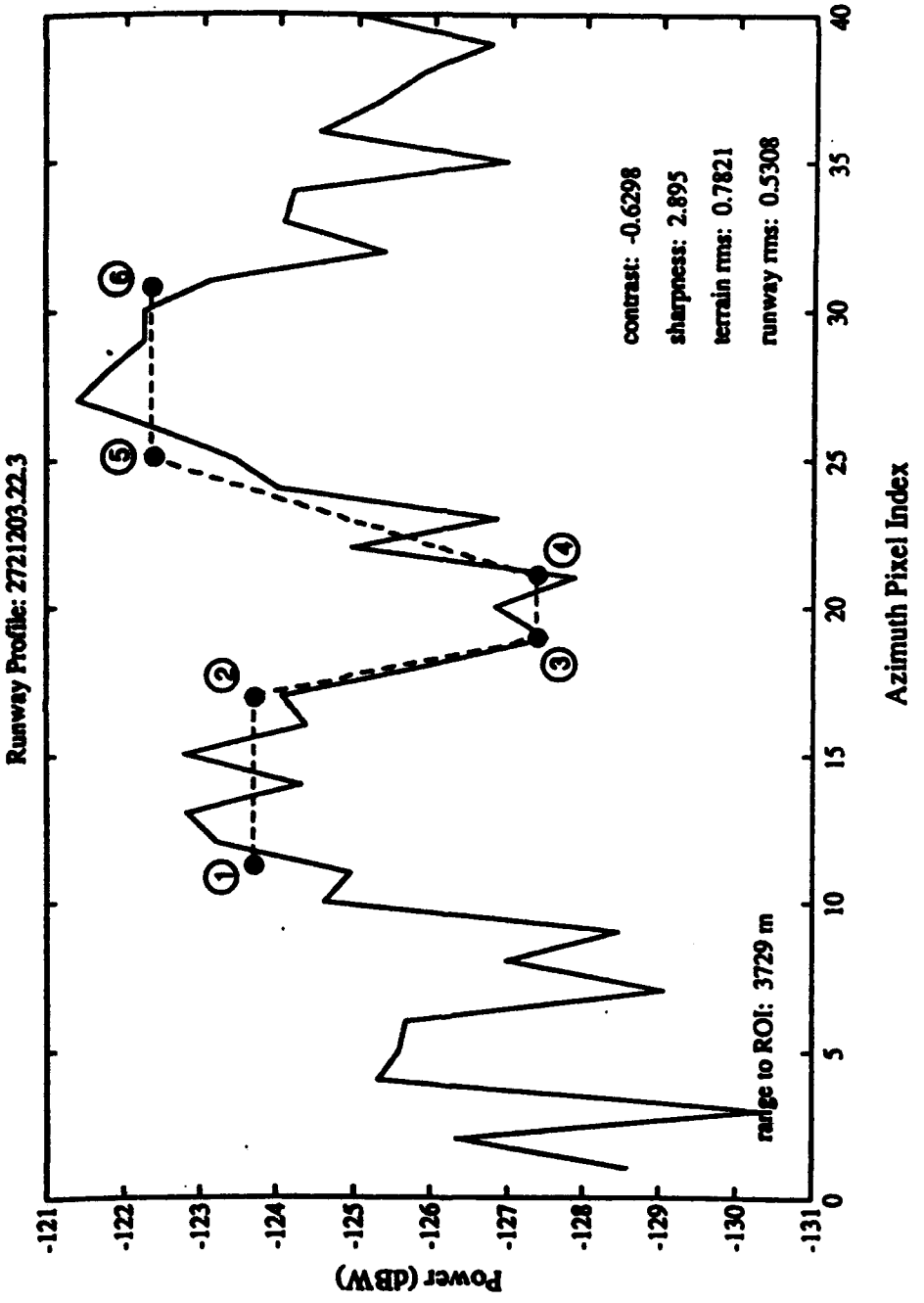

Figure 4.4.2-31. Gutter Plot Corresponding to Box 3 in Figure 4.4.2-28

Computing the image quality parameters for each region of interest within each snapshot involved the repetition of this process. Figure 4.4.2-30 presents the gutter plot for Box 2 (touchdown target) in Figure 4.4.2-28. Figure 4.4.2-31 presents the plot corresponding to Box 3 (end of runway in image). For Figures 4.4.2-29 through 4.4.2-31, the runway "gutters" are easy to find. However, this was not always the case. In fact, the runway-terrain transitions within the third (radar vanishing point) and fourth (end of pavement) regions were sometimes so difficult to determine that contrast, sharpness, and SVR parameters for these regions could not be reliably computed. In these cases, the parameters were not reported.

4.4.2.3.2.3 Radar Cross Section Processing

Measurements of radar cross section for the runway and surrounding terrain were made using the software tools developed in IMAGE by GTRI. RCS measurements were made of rectangular regions chosen along the center of the runway and also from the terrain bordering the runway. These rectangular regions were of constant area but were varied in shape in order to reduce the contamination of the runway RCS measurements by radar returns from the terrain received through the skirts of the antenna mainlobe. This potential contamination is due to the fact that the RCS of the terrain is much greater than that of the pavement. Even when the boresight of the antenna is positioned on the pavement, the terrain off to the side can generate a larger radar return provided the greater reflectivity of the terrain overcomes the lower antenna gain in the direction of the terrain.

Typically, the nominal beamwidth of an antenna is measured between the 3-dB points, and equals the total excursion between the points 3 dB below the peak gain, to the left and right of boresight. But, in general, the beamwidth of the antenna can be measured at any level with respect to the peak boresight gain. The full width of the radar beam in azimuth to a particular gain level on either side of boresight is given by

$$W = 2R \tan\left(\frac{\theta}{2}\right) \qquad (4.4.2\text{-}27)$$

where W is the width, R is the range, and θ is the beamwidth. For the Honeywell system, the 10 dB beamwidth in azimuth is about 1.7 degrees one-way and the one-way 15 dB beamwidth is approximately 2 degrees. These values were measured from the wider, left-hand full lobe in Figure J-2. Table 4.4.2-10 gives a comparison of azimuth width in feet for these 10 dB and 15 dB beamwidths at various ranges.

Table 4.4.2-10. Azimuth Width Versus Range for 10 dB and 15 dB Beamwidths

Range (meters)	10 dB Width (feet)	15 dB Width (feet)
100	10	11
200	19	23
500	49	57
800	78	92
1000	97	115
2000	195	229
3000	292	344
3840	374	440

Based on the values listed in Table 4.4.2-10, the width of the 10 dB beamwidth spans an entire 150-foot wide runway at a range of 2000 meters, and spills over 22.5 feet into the terrain on either side of the runway. Thus, if the terrain RCS was about 20 dB greater than that of the runway (which is a good rule-of-thumb for this case), these terrain strips would introduce contamination into an RCS measurement made of the runway at 2000 meters. (Keep in mind that the return from a region on the edge of the 10 dB beamwidth span is attenuated 20 dB with respect to the boresight region due to the 10 dB attenuation in each propagation direction.) This contamination would be present even if only the center pixel, which is centered on the runway, was used to make the RCS measurement.

The contamination would be worse if the terrain-to-runway RCS difference was greater. For example, if this difference was 30 dB, then the 30 dB beamwidth in Table 4.4.2-10 would be used and it could be seen that there would be contamination even for a 200-foot wide runway (14.5 feet of spill-over on each side). Care must be used in selecting pixels "on the runway" for RCS calculations. The widths of the runway regions used for RCS calculations were kept narrow, and RCS was computed at shorter ranges to reduce contamination effects.

The RCS computation process employed the usual PPI images generated on the SUN and downloaded into IMAGE on the Macintosh, along with the corresponding floating-point received power files (as discussed in Section 4.4.2.3.1.2.2). Two vertical arrays of rectangular regions including six pixels each were defined in the image. One set of rectangles was positioned down the center of the runway, and the other was positioned along the terrain at corresponding locations. The rectangles in each array were positioned approximately every 0.25-degree increment in elevation. An example layout of the rectangles is illustrated in Figure 4.4.2-32 with runway rectangles indicated in white and terrain rectangles shown to the right in black.

Each individual rectangle was either 3x2 (3 pixels wide and 2 pixels deep), 2x3, or 1x6. The widest rectangles (3x2) were used at the closest ranges, while the narrowest rectangles (1x6)

were used at the longest ranges. The normalized RCS for each rectangle was then computed using Equation 4.4.2-12 given previously.

Once the RCS values were computed for each rectangle, the resulting values had to be tested to ensure they were not significantly contaminated by noise. Fortunately, this noise test tended to exclude pavement RCS values computed at longer ranges, which were exactly those values most likely to be contaminated by adjacent terrain returns. In effect, all runway RCS values corresponding to a slant range greater than 800 meters were excluded from the data set used.

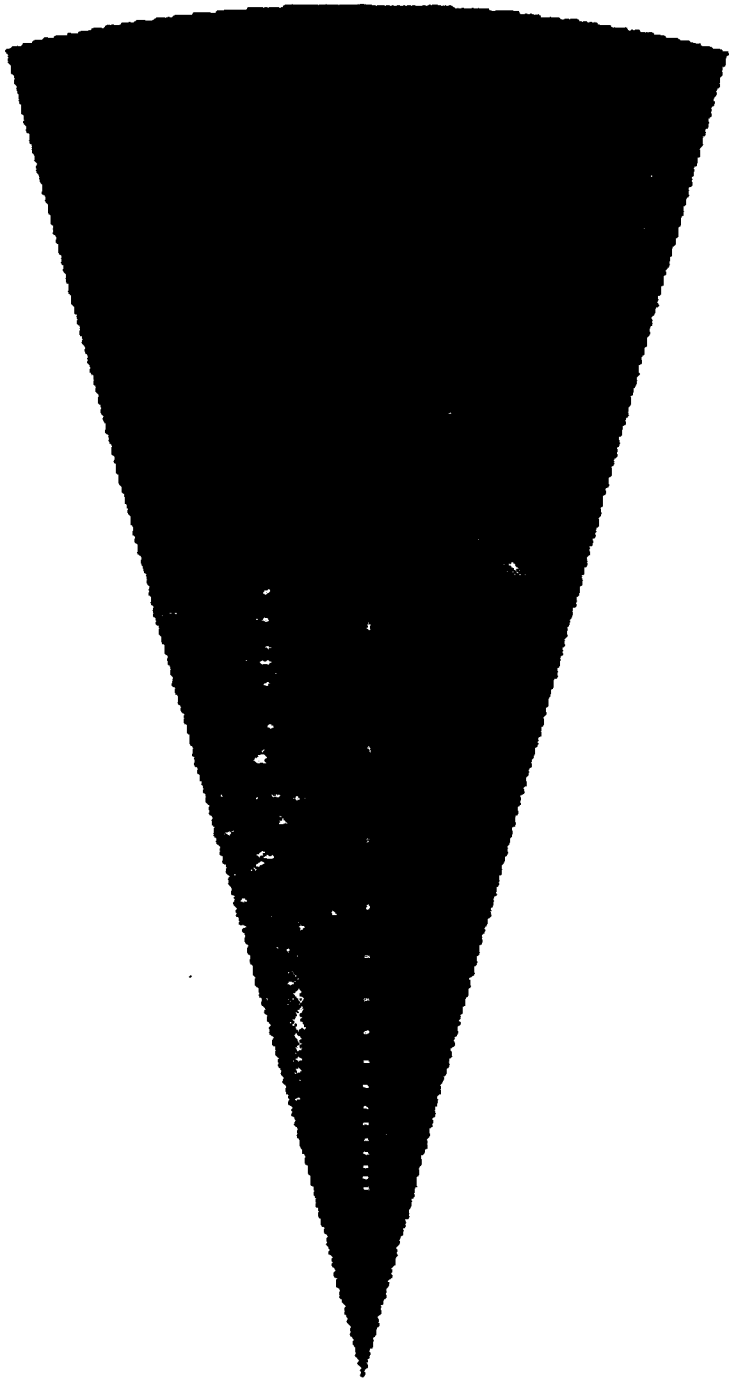

Figure 4.4.2-32. Example of Rectangle Placement for Computation of Normalized RCS Values for Runway and Terrain

4.4.2.3.2.4 Attenuation and Volumetric Reflectivity Processing

The attenuation and volumetric reflectivity equations were derived to calculate these quantities for approaches in fog, rain, or snow. However, due to the actual data set available (no rain data at all and no snow data at a "calibrated" airport), these parameters were computed for selected fog cases only. The purpose of the current section is to outline how these computations were made.

As indicated in Section 4.4.2.3.1.2.7 previously, the two unknowns, attenuation and volumetric reflectivity, were calculated by solving Equations 4.4.2-14 and 4.4.2-16 simultaneously. Meaningful results could only be obtained for approaches in weather against airports at which calibration reflectors were deployed. Clear weather approaches were not of interest since attenuation and volumetric reflectivity at 35 GHz for ranges of interest are known to be small and, in fact, virtually insignificant. Thus, approaches selected for this processing had to be in weather (fog in this case) and had to include calibration reflectors in the scene.

Once selected, the raw data on the SUN corresponding to that approach were processed to generate a PPI image and the parallel floating-point PPI data structure. These were then downloaded to the Macintosh computer. The two equations required that one range cell be chosen above the ground and at an altitude where sidelobe returns from the ground could not contaminate the measurement. This range cell was therefore selected by the analyst in the PPI image so that it had a slant range less than the altitude of the aircraft. Solving the two equations also required that the apparent radar cross section of a calibrated reflector in the scene be known. Thus, the second range cell selected by the operator contained one of the two Bruderhedral reflectors positioned in the scene.

The measured RCS values for these two cells represent the perceived radar cross sections of the two regions in fog. Thus, the measured RCS values were associated with RCS1 and RCS2 in Equations 4.4.2-14 and 4.4.2-16. Due to multipath effects, the parameter RCS_R in Equation 4.4.2-16 was not taken to equal the nominal RCS of the Bruderhedral reflector. Instead, a multipath model prediction of the perceived clear-weather RCS of that reflector was generated using the multipath model to be described later in 4.4.3.2.1. This predicted RCS value was actually used in Equation 4.4.2-16. By compensating for the expected multipath effects in this manner, a better estimate could be obtained of the true attenuation and volumetric reflectivity for each case examined.

4.4.2.3.2.5 Data Base of Reduction Products

The data analysis products discussed above for each approach were viewed as dependent variables. The corresponding independent variables on which they depended were the specific scenario and environmental parameters. Examples of these parameters are range to region of interest, type of runway surface, snowfall rate, and fog liquid water content, just to name a few.

To facilitate the accessibility and usefulness of these data in assessing overall radar performance and capabilities, these dependent and independent variables were stored in several Microsoft EXCEL spreadsheets. These spreadsheets enabled the analyst to selectively access the stored data based on specified criteria and also to plot one variable versus another for selected approaches. This spreadsheet tool proved to be a valuable asset in exploring data dependencies and generating standard plots for documentation.

All of the plots included in Sections 6 and 7 below were generated using Microsoft EXCEL. These spreadsheets can easily be expanded in the future to accommodate further analysis of the currently available data or parallel analyses applied to additional new data.

4.4.2.3.3 Weather Data Reduction

Three aspects of the meteorological data processing are discussed in this report. In the sections below, the contents of the initial data sets provided by JTD, the steps taken to improve the readability of the data products, and the processing required to incorporate those data sets into the sensor evaluation database will be discussed. In Appendix H.1, the derivation of various parameters provided in the JTD data sets and the assessed quality of these parameters are discussed. Several additional meteorological quantities were produced from the data sets by GTRI. The methods used to calculate these quantities and example data are provided in Appendix H.2.

4.4.2.3.3.1 Processing of JTD Supplied Data

The data sets provided by JTD consisted of ASCII files on diskettes readable by PC-compatible computers. The data for each flight typically consisted of two separate files, an archive file of the data taken at one-second intervals during each approach made during that flight, and a profile file in which the original archive data had been separated into 10-meter layers along the aircraft descent and then averaged within these layers. Several quantities derived from the original archive data sets were also calculated by JTD and included in the profile data sets. Plots of the profile data sets produced by JTD were provided along with the ASCII data files.

The first step in the processing of these data consisted of converting the ASCII files into a form which could be used by the spreadsheet programs used on the project. The data were replotted from these spreadsheet files to improve the readability of the initial data sets. The data could then be examined for quality and consistency and be combined with other sensor data for the performance analysis. The incorporation of the data into the spreadsheet format also permitted the derivation of the secondary data products provided in the profile data sets to be checked.

4.4.2.3.3.2 Contents of files supplied by JTD

Two data files were provided for each instrumented sortie or collection of approaches. Data were separated within these files into sections corresponding to each approach made during the sortie. The first data set consisted of data taken from the aircraft meteorological instruments at one-second intervals as it descended towards the runway. General descriptive information included in these "archive" data files included the sortie number; the year, month, and day; the total number of approaches for the sortie; a code to identify which of the three possible OAP sensors had been mounted for that particular flight; the nature of the precipitation encountered during the flight; and the diameter increments for the FSSP and secondary PMS probes (PMS2).

For each approach recorded for the sortie, general information recorded in the file included the approach number, the start and stop times of the approach, and the number of points from which the relationship between the radar altimeter and the pressure transducer reading was established. Data elements recorded to the file every second as the aircraft descended included the time, the state of two event switches, the static barometric pressure, the height above the runway as established by the barometric and radar altimeters, the static air temperature, the true air speed, the liquid water content (LWC) measured by the JW hot wire device, and the number densities recorded in the size channels of the FSSP and OAP particle probes.

The second set of data files provided by JTD for each flight, called "profile" data, consisted of averages of the archive data sets over each 10-meter level of descent for each approach. Typically, each 10-meter layer consisted of 2 or 3 individual values. The approaches attempted during each sortie were separated in these files also. Each profile data set began with the same flight information as was recorded in the archive data sets. The data recorded in the profiles for each approach within the sortie consisted of the approach number, the start and stop times of the approach, the heights of the top and bottom 10 m layers (in decameters), and a code indicating whether the height were determined solely by the radar altimeter or if it had been determined through other means.

For each 10 m layer within the approach, the data consisted of the layer height as well as average values of pressure, temperature, water vapor density, LWC derived from the JW hot wire device, LWC from each of the PMS probes, LWC calculated from a combination of the PMS probes data, and rainfall rate calculated from the PMS OAP sensor data. The number of one-second values averaged to produce the layer value was included. Finally, averaged particle number densities for the two PMS probes were written to the file for each layer. An integrated profile data set was appended to the end of the file after the data for each of the layers were written. In the integrated profile data, averages were taken over all the data between the current layer and the lowest layer. This integrated value attempted to characterize the average conditions along the path from the aircraft to the ground.

4.4.2.3.3.3 Conversion of JTD Files to Spreadsheet Files

The original ASCII files provided by JTD consisted of multiple lines of space-delimited numbers. The spreadsheet in use at GTRI was not capable of importing space-delimited numbers into separate cells of a spreadsheet file. An attempt was made to circumvent this problem by reading each line of numbers into a single spreadsheet cell and then parsing the individual components into separate cells. This attempt failed intermittently when the line length exceeded 255 characters. Two programs were written in C to solve this file conversion problem.

The first routine, "READACV.C," accepted a JTD archive file as input. The routine then parsed the individual elements within each line, applied some elementary logic, and output appropriate data items into one of three files. The READACV file produced a parameter file, with the same filename as the original file except that the file suffix was replaced with ".PAR". The parameter file contained all the data items not measured by either of the PMS particle probes. A second file produced by the READACV routine contained all the data recorded by the PMS FSSP-100 probe. This file was given a suffix of ".FSP". A third file contained all the data recorded by the OAP probe (PMS2). This final file was given a suffix of "PM2". Each of these files contained multiple data items separated by commas rather than spaces. Since the spreadsheet routine used at GTRI could directly import comma-delimited files, no problems were encountered with long lines of data elements.

A second routine, named "READPRO.C", acted in a similar fashion on the profile data sets. Again, the space delimited data were read in by this C routine and written out to three separate output files. These files were again given suffixes of ".PAR", ".FSP", and ".PM2".

4.4.2.3.3.4 Converted JTD Data

The conversion of the JTD space-delimited data files into comma-delimited files made it possible for these data sets to be imported into the spreadsheet programs in use at GTRI. This, in turn, permitted the data to be examined in more detail than was possible using the original ASCII files. The original plots supplied by JTD presented multiple parameters on each plot by using several x axes. This led to confusion as to which curves represented which data sets, as well as instances where the scales were not set over limits which made interpretation of the data sets difficult. An example of the original plots received from JTD and the optimized plots available from the output of the data converted to spreadsheet form are presented as Figure 4.4.2-33. The inclusion of these data into the spreadsheet format provided the basis for production of tables of parameters of interest to the analysis team and facilitated the location of data sets coincident with the selected radar snapshots of the runway scenes under analysis.

4.4.2.3.3.5 Temperature Deviations And Corrections

Significant deviations between the ambient air temperature recorded by the aircraft-mounted sensor and the air temperature recorded on the ground by independent means were noted by FAA program personnel during the flight tests. Resulting discussions with JTD indicated that the data received from the temperature probe used in the flight tests were probably subject to evaporative cooling as the aircraft descended through the fog and rain layers during approach. According to information from Rosemont, Inc., manufacturer of the probe, the aircraft-mounted probe is a resistive-temperature device located in a heated cavity. The cavity may undergo evaporative cooling when raindrops enter through the cavity orifice.

The degree of cooling is a function of the difference between the atmospheric wet bulb and ambient air temperatures. Determining the exact relationship between the measured and actual temperatures with the data available was not possible, as neither the temperature within the cavity or the number and sizes of the drops captured within the cavity were measured. If it is assumed that the trend of the temperatures was correct, and that a constant size distribution of drops entered the cavity, then the temperature correction with height would be constant. The difference

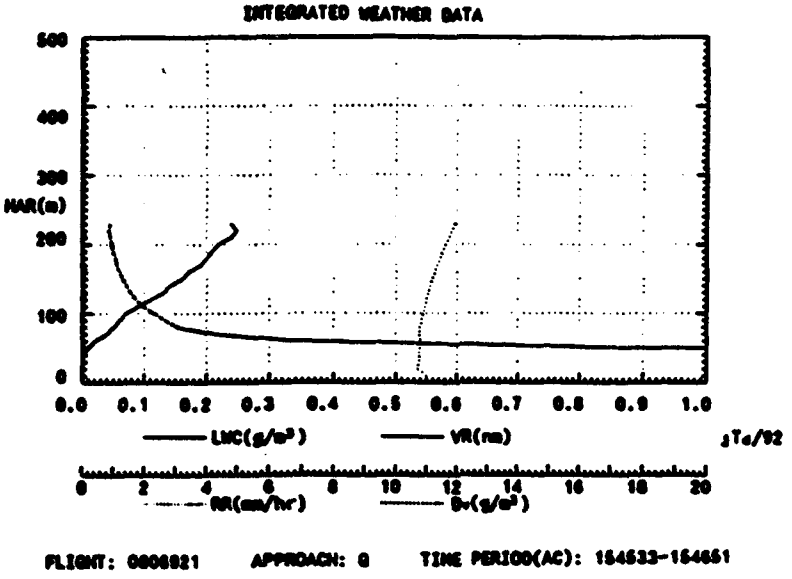

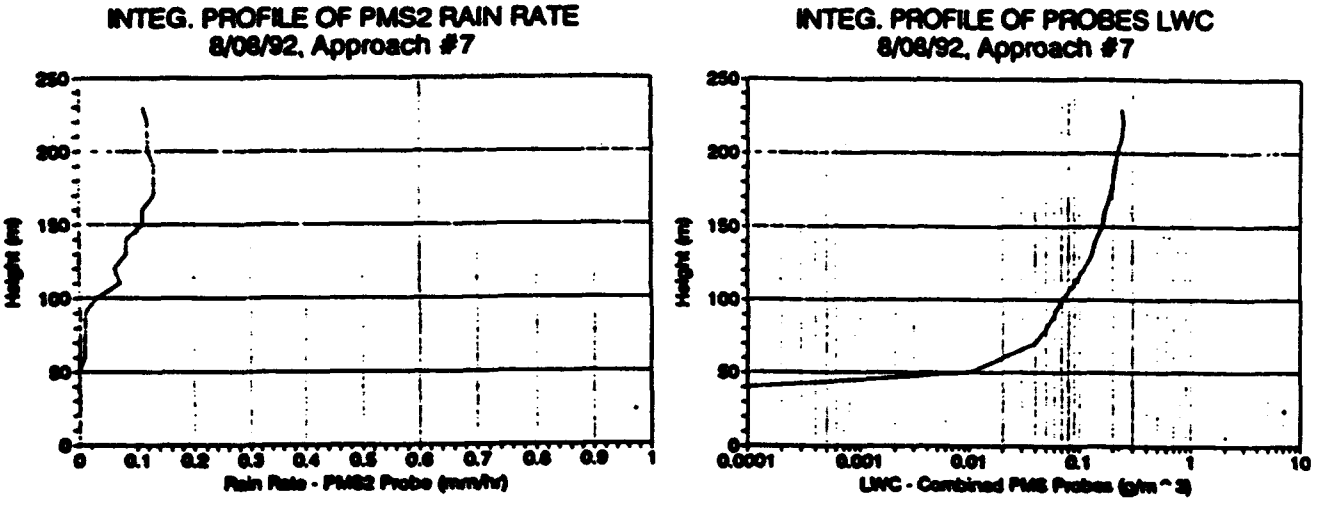

Figure 4.4.2-33. JTD Original Plot (Top) Compared With GTRI Optimized Plots (Bottom)

determined at the surface could then be applied to the portion of the approach containing near-uniform rain or fog drop distributions with some degree of accuracy. However, no attempt was made to actually adjust the reported JTD temperature values in this fashion.

4.4.3 SYSTEM CALIBRATION

Calibration of the Honeywell radar system involved two steps. First, the data acquisition transfer function was determined for all possible gain-offset settings as discussed in the following section. Second, the absolute calibration of the system was determined as described in Section 4.4.3.2.

4.4.3.1 Data Acquisition Transfer Function

The data acquisition transfer function of the Honeywell radar system relates each possible digital sample generated by the data acquisition system to the corresponding power level input to the receiver, as measured just beyond the antenna unit output. The raw radar data available to the analyst are a series of 8-bit numbers produced by the analog-to-digital converter (ADC) unit of the overall system. However, the analyses to be performed on these raw data are based on power levels sensed by the system. The data acquisition transfer function is the mechanism by which the recorded 8-bit ADC values can be related to the corresponding input power levels.

Figure 4.4.3-1 illustrates this process. The analyst has available the digital 8-bit values provided by the ADC at point B in Figure 4.4.3-1(a). However, the values really of interest are the corresponding input power values at point A in this figure. The specific mapping of ADC values to input power levels changes in general for different gain control and bias control values. A generic transfer function for a single gain and bias combination is shown in Figure 4.4.3-1(b). A family of such data acquisition transfer functions have been computed for the system corresponding to each possible gain-bias pair. Measured data representing a few of these functions are included in Appendix I.

Note that the receiver transfer curve (RTC) relates input power levels to the voltage output produced by the radar receiver. The data acquisition transfer function extends this functional dependence by taking into account the digital output of the ADC in response to the voltage output of the receiver. Thus, the data acquisition transfer function provides the overall mapping between input power level and ADC output values.

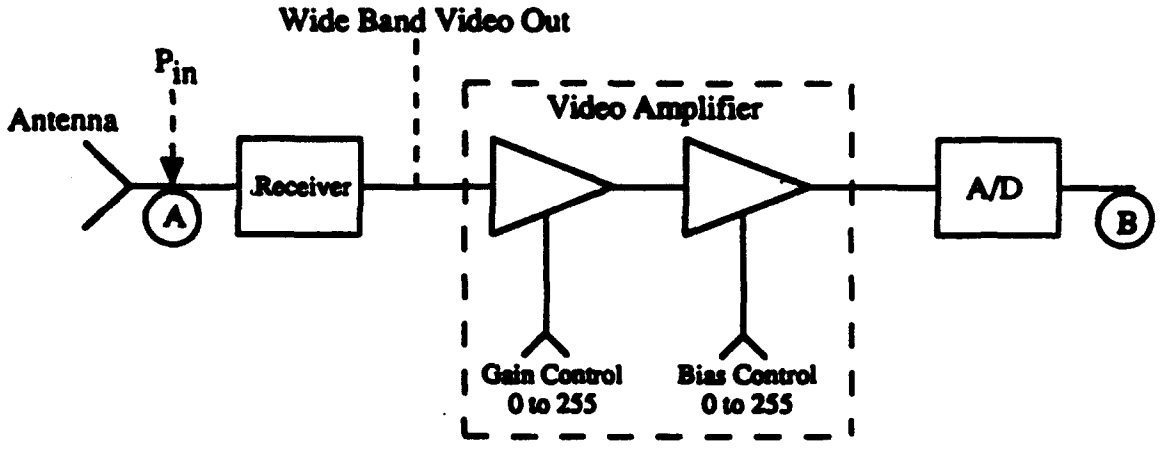

(a) Signal path and calibration points.

For a given Gain and Bias:

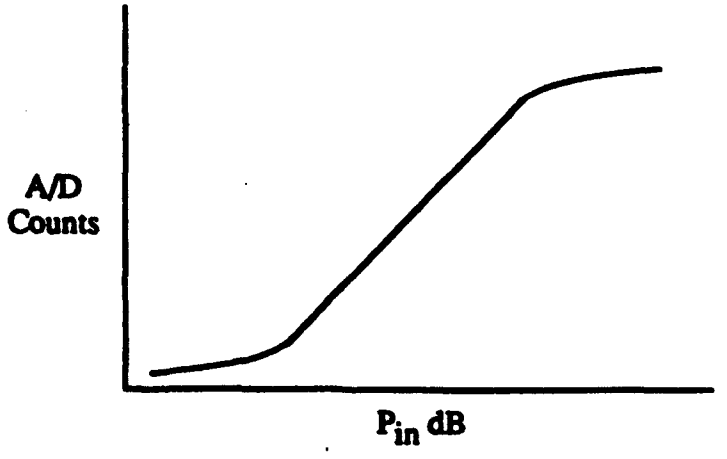

(b) Generic data acquisition transfer function plot.

Figure 4.4.3-1. Data Acquisition Transfer Function

4.4.3.2 Absolute System Calibration

The data acquisition transfer function described above is sufficient for many types of radar analyses. Based on it alone, relative power levels can be established as sensed by the radar system. Measures such as contrast can then be computed based solely on such relative power levels.

For other types of analyses, absolute rather than just relative power levels must be known. To compute the radar cross section of a particular object within the scene, the system must have been first absolutely calibrated. This absolute calibration process involves accounting for the specific gain characteristics of the antenna as well as the effects of the transmission media. This absolute calibration process is the subject of this section.

As discussed previously, Bruderhedral reflectors were placed at each of six California airports in order to absolutely calibrate the Honeywell radar. Approaches were then flown against these six airports in clear weather, and the resulting data were then available for calibration purposes. These data were used to compute the factor $F_{calibration}$ in Equation 4.4.3-1 below, which is identical to Equation 5-11 of Section 5.2.4.1.2.6.

$$\sigma = \frac{P_{rec}(4\pi)^3 R^4 L_{radome} L_{prop} F_{calibration}}{P_{trans} G^2 \lambda^2} \qquad (4.4.3\text{-}1)$$

Calibration data from four of the six airports were processed under this analysis effort. Each of these four airport calibrations is documented separately below. First, however, the following section details GTRI's radar scene modeling effort in support of these specific calibrations.

4.4.3.2.1 Radar Scene Modeling

TRACK [7], GTRI's RCS and radar tracking model, was used under this program to predict multipath and target reflections for calibration reflectors placed at selected airports during the flight tests. A typical flight test geometry is illustrated in Figure 4.4.3-2.

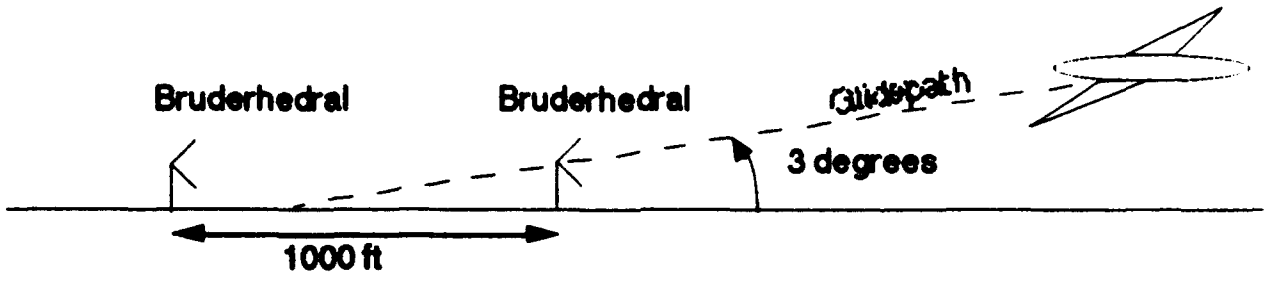

Figure 4.4.3-2: Example Flight Test Geometry.

Since the maximum instrumented range of the Honeywell radar was 3840 meters, effects due to curvature of the earth for this system are negligible, and flat earth approximations are appropriate. For the flat earth approximation, the direct path and the indirect path are parallel.[8] Based on the multipath geometry shown in Figure 4.4.3-3, the total electric field at the target, neglecting depolarization effects, is given by

$$\overline{E} = E_o \left[f(\theta_1)\, e^{-jkR_1} + \overline{\Gamma}\, f(\theta_2)\, e^{-jkR_2} \right], \qquad (4.4.3\text{-}2)$$

where

E_0 = magnitude of the free-space electric field at the target if the antenna boresight is pointed directly toward the target,

$f(\theta_1)$ = relative value of the antenna pattern for the direct ray,

$f(\theta_2)$ = relative value of the antenna pattern for the indirect ray,

$\overline{\Gamma}$ = overall reflection coefficient of the earth (includes a Fresnel reflection coefficient and a roughness factor),

---

7 J. L. Davis, G. J Bradley, R. B. Rakes, J. H. Andrews, M. T. Tuley, and P. A. Ryan, "TRACK 4.1 Radar Cross Section and Tracking Simulation User's Guide," Georgia Tech Research Institute, Georgia Institute of Technology, July 1990.

8 Eaves, J. L. and E. K. Reedy, ed., *Principles of Modern Radar,* Van Nostrand Reinhold, New York, 1987, p. 75.

R_1, R_2 =direct and indirect path lengths, and

$$k = \frac{2\pi}{\lambda}.$$

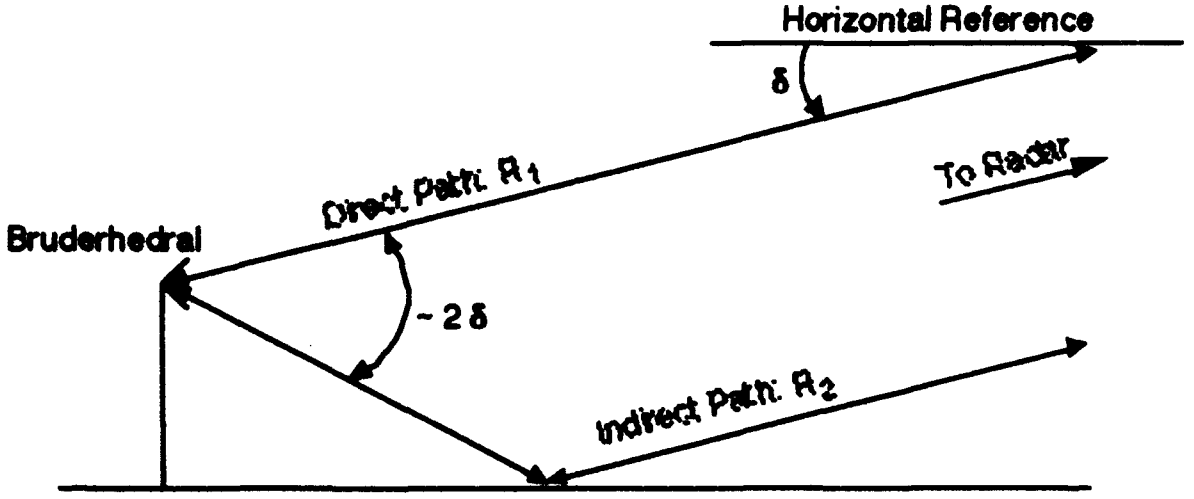

Figure 4.4.3-3. Illustration of Multipath Geometry for Flight Test Scene.

If the ground is assumed to be perfectly conducting, the overall reflection coefficient equals -1. For this case and neglecting antenna pattern effects, Equation 4.4.3-2 simplifies to

$$\overline{E} = E_o \left[e^{-jkR_1} + e^{-jkR_2} \right] = e^{-jkR} \left[1 + e^{-jk\Delta R} \right], \qquad (4.4.3\text{-}3)$$

where R is the slant range from the radar to the target. For a flat earth, ΔR is given by

$$\Delta R = \frac{2h_1h_2}{R} \qquad (4.4.3\text{-}4)$$

where h_1 is the altitude of the radar, and h_2 is the altitude of the target. The function

$$\left[1 + e^{-jk\Delta R} \right] \qquad (4.4.3\text{-}5)$$

defines the multipath lobing pattern for the scenario geometry. A half cycle (minimum to maximum) change in the multipath lobing pattern occurs when ΔR changes by one-half wavelength.

The Bruderhedral calibration target is modeled as a partial "top hat" scatterer. The computer model of this geometry is illustrated in Figure 4.4.3-4 and includes a partial frustum (part of a cylinder) and a flat plate. The curved, cylindrical surface in Figure 4.4.3-4 is shaded. The reflector illustrated in Figure 4.4.3-4 is a double-bounce scatterer, and is an appropriate choice for calibrating the Honeywell radar, since this latter system uses right-hand circular polarization for both transmitting and receiving.

TRACK models the radar return of the Bruderhedral based on a combination geometrical optics and physical optics solution. At MMW frequencies, the Bruderhedral is a vertically extensive target, and the multipath and direct path contributions over the length of the target must be coherently summed to obtain the total reflector RCS as seen by the radar. The TRACK model computes the Bruderhedral RCS by applying the far-field parallel-ray approximation and integrating all incident fields over the length of the target.

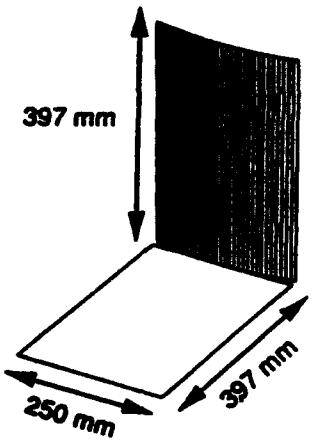

Figure 4.4.3-4. Computer Model of 23 dBsm (at 35 GHz) Bruderhedral Calibration Reflector

The main beam portion of the bistatic elevation-plane pattern of the Bruderhedral is shown in Figure 4.4.3-5. The narrow main beam (down at least 10 dB at +/- 1 degree from boresight) minimizes the effects of multipath for the typical flight test geometry. If it is assumed in Figure 4.4.3-3 that the boresight of the Bruderhedral is exactly aligned with the direct path, and that δ approximately equals the glidepath angle (about 3 degrees), then the indirect path makes an angle of 6 degrees with respect to the boresight of the reflector. Based on Figure 4.4.3-5, such a path is well off the main beam of the Bruderhedral. Thus, the indirect path is greatly attenuated with respect to the direct path.

Since Figure 4.4.3-5 indicates sidelobe levels roughly 20 dB below the main beam peak, the corresponding multipath return should be at least 20 dB below the direct-path return. Consequently, it might be concluded that the multipath is not an issue and should be ignored. However, it was decided to to model multipath nonetheless, since the two assumptions described above may not hold in all cases. First, the calibration was typically performed at longer ranges to avoid saturation of the receiver by the large signal produced by the Bruderhedral.

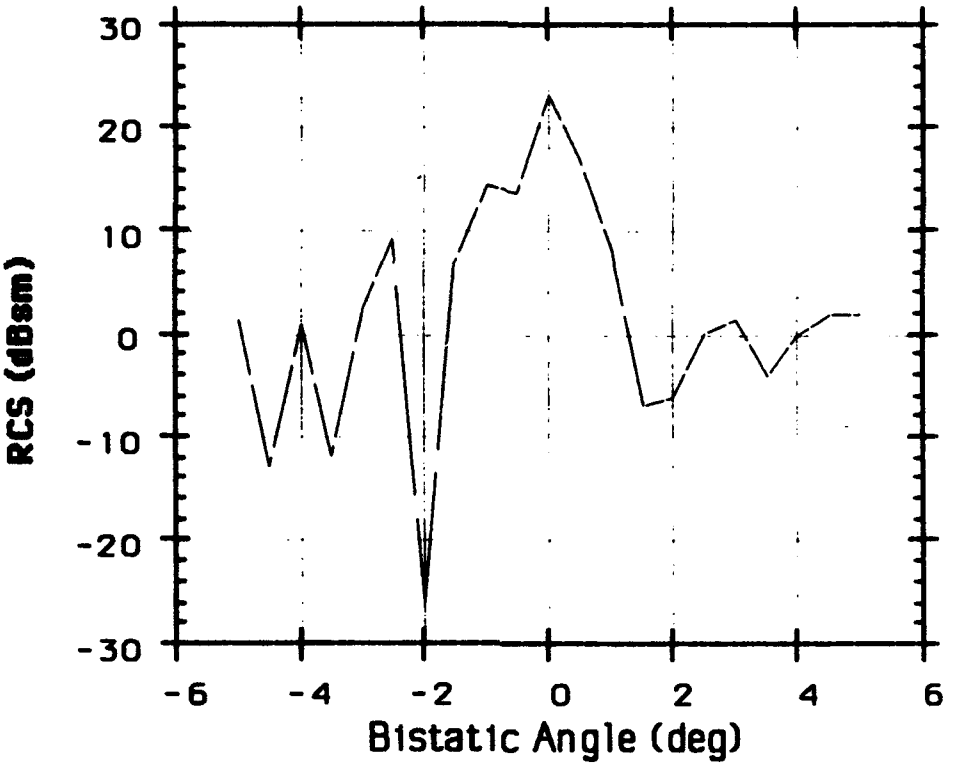

Figure 4.4.3-5. Bistatic Pattern of a 23 dBsm (35 GHz) Bruderhedral Calibration Target for Circular Polarization.

At these longer ranges, the vector from the aircraft to the Bruderhedral is likely more shallow than 3 degrees since the aircraft has not begun its descent. Thus, the angle δ is less than 3 degrees, and the angle off boresight of the indirect ray is less than 6 degrees.

Second, the Bruderhedral reflectors used during the flight tests were manually aimed by personnel on the ground during initial positioning of the reflectors. This aiming process used a specially constructed peep sight which enabled the aimer to optically align the reflector with aircraft on a typical approach. However, this aiming process was not without potential errors. First, there could be aiming errors due to the positioning and use of the peep site. Second, there would also be errors should the Gulfstream II deviate from the nominal glidepath used for reference in initially aligning the reflector. In light of these possible errors, multipath could become a significant issue. Thus, GTRI was tasked to model the multipath phenomenon to facilitate an accurate calibration of the Honeywell radar system.

This modeling effort produced significant benefits other than enabling the analysts to correct for multipath effects. It enabled them to explore and compensate for other scene geometry effects

in calibrating the system. For example, even with no multipath present, the radar return produced by the Bruderhedral would vary at different points along the approach path. One source of this variation is the monostatic gain pattern of the reflector, in both azimuth and elevation. The TRACK model employed under this effort made it possible to account for these effects as well as to predict the effective radar cross section of the Bruderhedrals for each snapshot analyzed.

The radar return from the reflector also varies with the gain of the radar antenna which applies to the angle from which the reflector is viewed. The TRACK model includes a user-defined antenna lookup table, and the Honeywell antenna patterns included in Appendix I were used in the TRACK scenario runs. The shape of the azimuth pattern was modeled as a $\left(\frac{\sin x}{x}\right)^2$ function with 15 dB sidelobes. The parameter x is a function of the wavelength, the sidelobe level, the aperture length, and the azimuth angle off boresight. The pitch angle of the aircraft and the depression angle from the aircraft to the target determined the elevation gain for target illumination.

In TRACK, the ground terrain is modeled with a single flat, dielectric, rough, ground plane. The dielectric constant and surface roughness parameters are chosen to best approximate the terrain being modeled. TRACK uses Fresnel reflection to model a terrain dielectric constant. A rough surface is modeled as a Gaussian-distributed surface with heights defined by a root-mean-square (RMS) surface roughness and a RMS surface slope. The physical optics integral for scattering from the surface is evaluated with an approximation developed by Barton for low-angle radar tracking.[9] The RMS surface roughness determines the amount by which the RCS magnitude is reduced compared to that of a completely smooth surface. The RMS surface slope determines the broadening of the main lobe of the scattering pattern as compared to the main lobe of the scattering pattern for a smooth surface.

The dielectric constant of grass and its relation to moisture content has been estimated to be [10]

$$\varepsilon = 2.5(1 - f)\varepsilon_w f \qquad (4.4.3\text{-}6)$$

where

f is the percentage moisture content of the grass by weight, and

---

9 D. K. Barton, "Low Angle Radar Tracking," *Proceedings of the IEEE,* Vol. 62, No. 6, June 1974, pp. 687-704.

10 R. L Cosgriff, W. H. Peake, and R. C. Taylor, "Terrain Scattering Properties for Sensor System Design," The Ohio State University, Columbus, Ohio, 1960.

ε_w is the dielectric constant of water.

The dielectric constant of water is given by

$$\varepsilon_W = 5 + \frac{75}{1 - j\frac{1.85}{\lambda}} \qquad \lambda \text{ in cm.} \qquad (4.4.3\text{-}7)$$

(In Equation 4.4.3-7, the sign of the imaginary term in the denominator is a matter of convention. Although, the sign used by many authors is positive, GTRI adopted the convention used by Cosgriff, et al [11] and used a negative sign.)

A moisture content of 15% was used for the flight test calibrations performed at each of the four California airports. Such a selection is reasonable since the terrain in these California regions was quite dry during the month of August when the calibration flights were made. However, to ensure that this moisture content assumption was reasonable, predictions were also run for assumed moisture contents of 5% and 40%. Based on these comparative runs and the known general dry conditions present, the 15% assumption was elected. The corresponding dielectric constant of grass for a 15% moisture content at 35 GHz is 4.863 + j 4.290, as computed by Equations 4.4.3-6 and 4.4.3-7 above.

Once the moisture content had been selected, the roughness of the surface had to be quantified. In general, the terrain at these California airports was relatively flat ground with sparse, clumpy grass coverage. Because of the difficulty in modeling an in-homogeneous terrain area as a single dielectric ground plane, proper selection of terrain roughness parameters was important. The first of these parameters is RMS surface slope. This surface slope for both land and sea is typically 0.05 radian to 0.25 radian.[12] A RMS surface slope above 0.2 radian represents an extremely rough surface while slopes between 0.1 and 0.15 represent slight to moderately rough surfaces. A RMS surface slope of 0.12 radian was used to model the terrain for the California airports.

---

11 R. L Cosgriff, W. H. Peake, and R. C. Taylor, "Terrain Scattering Properties for Sensor System Design," The Ohio State University, Columbus, Ohio, 1960.

12 R. L Cosgriff, W. H. Peake, and R. C. Taylor, "Terrain Scattering Properties for Sensor System Design," The Ohio State University, Columbus, Ohio, 1960.

The effect of the RMS surface roughness parameter on the multipath lobing pattern was examined for aircraft-to-ground ranges of about 3000 meters, and also closer in, at ranges around 1000 meters. The geometry shown in Figure 4.4.3-6 was used for the terrain roughness investigation. Reflector RCS, including multipath effects, was predicted for aircraft altitudes between 1 and 200 meters at ground ranges, R_g, of approximately 3000 meters and 1000 meters. With the ground range held constant, the slant range and depression angle both increase as the altitude increases.

Figure 4.4.3-7 shows the lobing pattern for the case of a flat terrain with 15% moisture content (dielectric constant = 4.863 + j4.290) at a 3000 meter ground range. The RCS value plotted is the apparent RCS of a 18.7 dBsm Bruderhedral as predicted based on multipath, radar antenna pattern, and Bruderhedral pattern effects. Since the slant range to the reflector and the altitude change with changing ground range, the predicted RCS is a function of both altitude and slant range. Although a plot of RCS versus depression angle reflects the dependence of RCS on both the slant range and altitude, plots of RCS versus altitude are shown to quantify multipath contributions due to measured aircraft glide path variations. Thus, it can be seen from Figure 4.4.3-7 that at an altitude of about 80 meters, roughly a 10 meter altitude deviation can cause the perceived reflector RCS to change over 20 dB for the flat terrain assumed.

For the case of a dielectric flat terrain at a range of 3000 meters, the amplitude of the multipath lobing pattern as shown in Figure 4.4.3-7, is approximately 18 dB, and the period of the lobing pattern is about 22 m. With measurements of aircraft altitude that are accurate to within 6 meters, the measured return can be expected to be accurate only to within 13 dB for this flat terrain assumption.

Figure 4.4.3-8 shows the lobing pattern for the same dielectric terrain with a RMS surface roughness of 0.01 meter and a RMS surface slope of 0.12 radian at the same 3000 meter ground range. Again, the predicted apparent RCS is plotted for a 18.7 dBsm Bruderhedral. A surface roughness of 0.01 meter has previously been used by GTRI to model radar clutter return from short mowed grass at MMW frequencies.[13] The multipath lobing pattern decreases in

---

13 P. A. Ryan, K. D. Vaughn, and J. T. Carpenter, "Aircraft Shelter Scene Images," Final Technical Report on Contract 658828, Georgia Institute of Technology, November 1989.

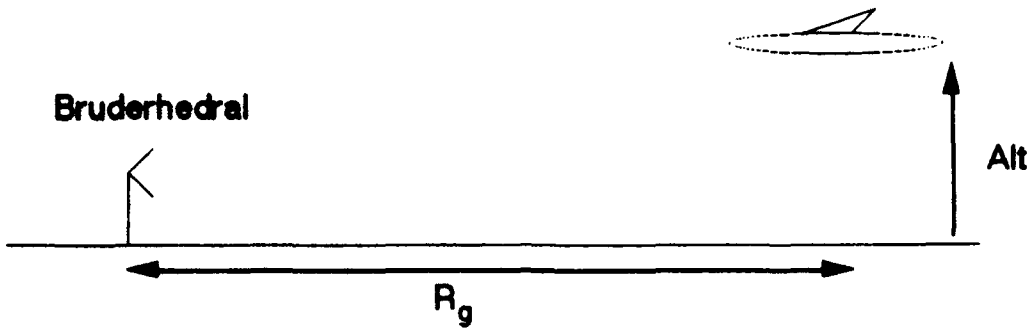

Figure 4.4.3-6. Multipath Scenario to Examine Terrain Roughness Effects on Lobing Pattern.

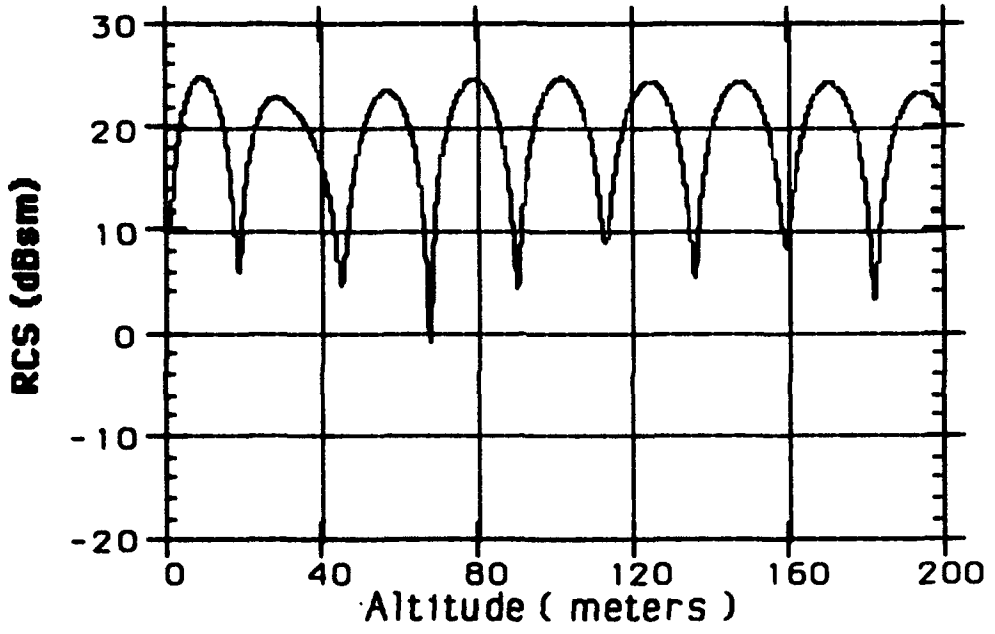

Figure 4.4.3-7. Computed Multipath Lobing Pattern at 3000 Meter Ground Range, for Flat Dielectric Terrain with Permittivity = 4.863 + j 4.290. Circular Polarization and 35 GHz Frequency Assumed.

amplitude as the altitude increases, but the period is approximately 22 meters as with the smooth surface case. Thus, a slightly rough surface has a dampening effect on the multipath lobing pattern as the slant range and depression angle increase.

In the flight tests, when the aircraft to reflector ground range is 3000 meters, a typical aircraft altitude is 150 meters, so the predicted RCS at altitudes around 150 meters gives an idea of the expected multipath problem for the flight tests. At an altitude of 150 meters, the amplitude of the lobing pattern is 7 dB in Figure 4.4.3-8. For the case of a slightly rough surface such as mowed grass, then, the measured return can be expected to be accurate to within +/- 3.5 dB.

The lobing pattern for the same dielectric terrain, except that the RMS surface roughness has been increased to 0.025 meter, at the same 3000 meter ground range is shown in Figure 4.4.3-9. The 0.025 meter surface roughness models longer grass and a moderately rough surface. Again the rough surface dampens the amplitude of the multipath lobing pattern. At an altitude of 150 meters, the amplitude of the lobing pattern is less than 1 dB. For the case of a moderately rough surface, then, the measured return should be virtually unaffected by multipath.

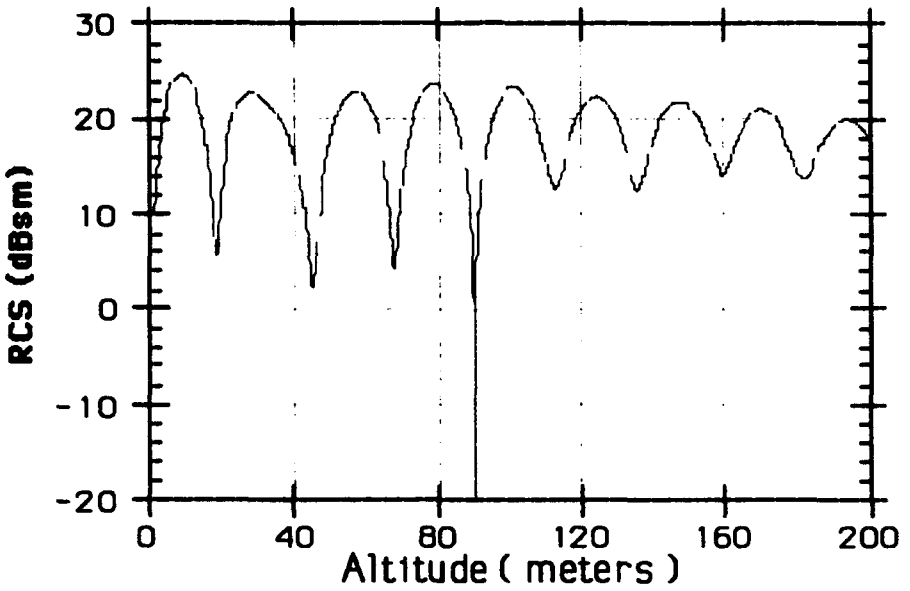

Figure 4.4.3-8. Computed Multipath Lobing Pattern at 3000 Meter Ground Range, for Flat Dielectric Terrain with Permittivity = 4.863 + j 4.290, RMS Roughness = 0.01 m, and RMS Slope = 0.12 Radian. Circular Polarization and 35 GHz Frequency Assumed.

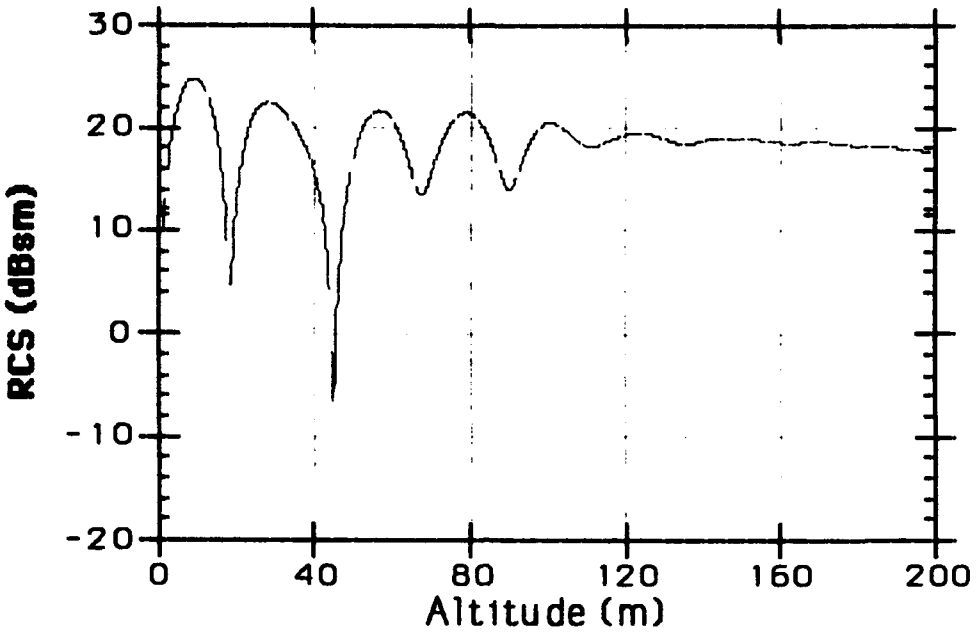

Figure 4.4.3-9. Computed Multipath Lobing Pattern at 3000 Meter Ground Range, for Flat Dielectric Terrain with Permittivity = 4.863 + j 4.290, RMS Roughness = 0.025 m, and RMS Slope = 0.12 Radian. Circular Polarization and 35 GHz Frequency Assumed.

Figures 4.4.3-10 through 4.4.3-12 illustrate the perceived RCS pattern of the Bruderhedral for the same set of assumed surface roughness at a ground range of 1000 meters. Note that at this closer range, the effect of the vertical pattern of the radar antenna becomes much more pronounced. The antenna for the Honeywell system is positioned so that the boresight is oriented downward 2.4 degrees with respect to the aircraft waterline. Thus, neglecting multipath effects, the reflector RCS would be perceived to be maximum at an altitude of about 42 meters for a 1000-meter ground range [1000 * tan(2.4) = 42]. As the altitude increases, the reflector moves increasingly off the antenna boresight so the perceived RCS of the reflector decreases (since antenna gain effects are not compensated for in computing perceived RCS).

Note from Figure 4.4.3-10 that at an altitude of 160 meters, the perceived RCS is reduced by about 24 dB from its maximum value. The 160-meter altitude corresponds to a depression angle of about 9.1 degrees, which is 6.7 degrees off the antenna boresight. The one-way antenna elevation gain at this point is about 10 dB down with respect to boresight.

Thus, based solely on the vertical pattern of the antenna, the perceived Bruderhedral RCS would be expected to be 20 dB (= 2 * 10 dB) lower than the nominal value for an altitude of 160 meters and a ground range of 1000 meters. The additional 4 dB reduction apparent in Figure

4.4.3-10 is likely due to off-boresight effects within the Bruderhedral pattern. The monostatic vertical pattern of the Bruderhedral is quite broad compared to the radar antenna pattern but still exhibits some roll-off as one moves off boresight.[14] A 2 dB reduction in the RCS of the

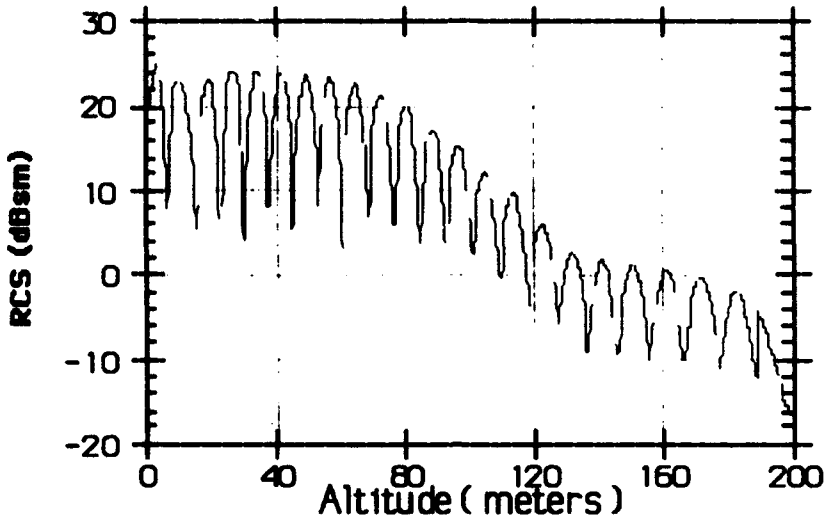

Figure 4.4.3-10. Computed Multipath Lobing Pattern at 1000 Meter Ground Range, for Flat Dielectric Terrain with Permittivity = 4.863 + j 4.290. Circular Polarization and 35 GHz Frequency Assumed.

14 N. C. Currie and C. E. Brown, ed., *Principles and Applications of Millimeter-Wave Radar*, Artech House, Norwood, MA, 1987, pp. 773 - 774.

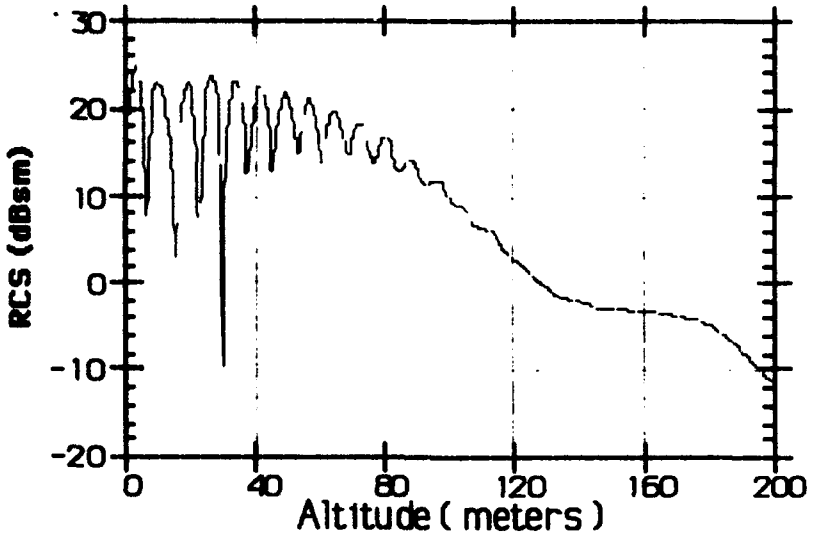

Figure 4.4.3-11.Computed Multipath Lobing Pattern at 1000 Meter Ground Range, for Flat Dielectric Terrain with Permittivity = 4.863 + j 4.290, RMS Roughness = 0.01 m, and RMS Slope = 0.12 Radian. Circular Polarization and 35 GHz Frequency Assumed.

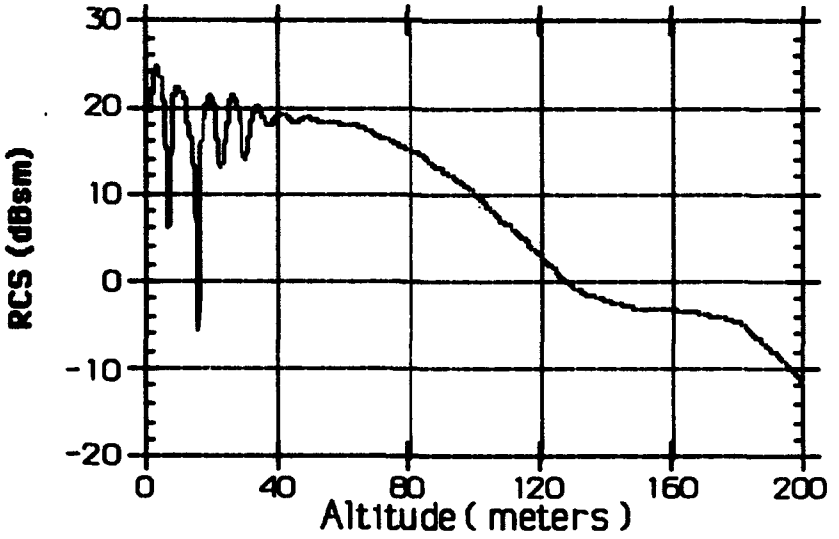

Figure 4.4.3-12. Computed Multipath Lobing Pattern at 1000 Meter Ground Range, for Flat Dielectric Terrain with Permittivity = 4.863 + j 4.290. RMS Roughness = 0.025 m, and RMS Slope = 0.12 Radian. Circular Polarization and 35 GHz Frequency Assumed.

Bruderhedral when viewed 6.7 degrees off boresight is reasonable and would account for the 4 dB discrepancy. The relatively broad monostatic elevation pattern of the Bruderhedral in this case is quite different from the very narrow bistatic elevation pattern plotted earlier in Figure 4.4.3-5.

For the dielectric flat terrain case shown in Figure 4.4.3-10, the amplitude of multipath oscillations decreases with increasing altitude, and the period of the multipath oscillations is 8 meters. The period of the multipath lobing pattern at a ground range of 1000 meters is about 40 percent of the period of the multipath lobing pattern at a ground range of 3000 meters. The period decreases at shorter range because the same altitude difference is a larger percentage of the aircraft to target range. Note that ΔR, defined in Equation 4.4.3-4, drives the period of multipath oscillations. At the shorter range, ΔR changes by half a wavelength over a smaller change in altitude.

As seen in Figure 4.4.3-10, the elevation antenna pattern defines the envelope of the multipath lobing pattern at the closer range. At a range of 3000 meters, a change in altitude from 1 to 200 meters corresponds to a change in depression angle from 0 to 4 degrees. At a range of 1000 meters, the same change in altitude from 1 to 200 meters corresponds to a change in depression angle from 0 to 10.5 degrees. In Figure 4.4.3-10, the target falls out of the antenna main beam at an altitude of 90 meters, which corresponds to a depression angle of 5.5 degrees.

For the flight tests, a typical altitude at a range of 1000 meters is 55 meters. For a flat dielectric terrain, the amplitude of multipath oscillations is 15 dB at an altitude of 55 meters. Assuming the INS measurement of aircraft altitude is accurate to within 6 meters, the measured return can only be accurate to within one-half the amplitude of the lobing pattern (+/-7.5 m), since the aircraft altitude error is greater that one-half the lobing pattern period. This is true, however, for a perfectly flat terrain only.

Figure 4.4.3-11 plots the multipath lobing structure for the same dielectric terrain with a RMS surface roughness of 0.01 meter and a RMS surface slope of 0.12 radian at the closer 1000-meter ground range. The slightly rough surfaces dampens the amplitude of the multipath lobing pattern as the altitude increases, but the period is 8 meters as with the flat terrain. At an altitude of 55 meters, the amplitude of the lobing pattern is 8 dB. Therefore, the measured reflector return will be accurate to within about +/- 4 dB of the RCS of the Bruderhedral with no multipath correction applied.

The multipath lobing structure for the same dielectric terrain with a RMS surface roughness of 0.025 meter and a RMS surface slope of 0.12 radian at a ground range of 1000 meters is shown in Figure 4.4.3-12. For this moderately rough surface, the amplitude of the multipath lobing pattern at a typical aircraft altitude is again less than 1 dB. Thus, the flight test measured return at the short range should also be unaffected by multipath if the terrain is moderately to severely rough.

The preceding analysis indicates that for the case of fairly smooth terrain (RMS roughness ≤ 0.010 meter), multipath is a potentially significant error source for flight test calibration approaches. Because the period of the multipath lobing structure increases with increasing range, the error caused by multipath is slightly less of a problem at the longer ranges than at the shorter ranges.

For the case of rough terrain (rms roughness > 0.010 meter), the multipath effects for the typical flight test geometry are small. However, this conclusion is based on the assumption that the antenna boresight remains aligned with the Bruderhedral throughout the approach. In the Honeywell system, the antenna is mounted on a rigid plate at a fixed 2.4 degree angle with respect to the aircraft waterline (horizontal). Thus, the antenna can not physically readjust as the aircraft pitches. Therefore, when the aircraft deviates significantly from the nominal 3 degree glidepath or pitches significantly, then the antenna mainbeam will no longer be approximately boresighted on the reflector.

In these cases, the antenna gain applied to the indirect path in Figure 4.4.3-3 may well increase relative to that applied along the direct path. Thus, the relative contribution of multipath may become significant, even for the case in which the terrain is rough. The knowledge and insight gained in exercising this computer-based multipath model were used in performing and assessing each of the four specific calibrations described below. For each airport calibration, the multipath scene model was employed to predict the apparent RCS of the reflectors for each specific snapshot geometry to obtain the most accurate radar system calibration possible.

4.4.3.2.2 Arcata, CA Calibration (8/27/92)

Suitable raw radar data were available for two calibration approaches made against the Arcata, CA airport on 8/27/92. These approaches were designated 2A and 2C. Table 4.4.3-1 presents key data for each of nine snapshots analyzed in approach 2A. The left-most three columns in Table 4.4.3-1 list the file designation, the slant range to the Bruderhedral reflector, and the corrected altitude for that particular snapshot. Both the range and the altitude are reported in meters. The reported altitudes are for the radar relative to the ground level where the Bruderhedral was positioned and have been adjusted to account for an assumed 2-second delay between the INS data and the radar data.

The fourth column from the left lists the depression angle in degrees with respect to horizontal for each snapshot. This depression angle is computed simply as the inverse sine of the corrected altitude divided by the slant range.

Table 4.4.3-1. Summary of Measured RCS Values For Both Bradderhedral Reflectors at Arcata, CA on August 27, 1992 (Approach 2A). All Angles Are In Degrees and All Reflector Values Are in DBSM

Airport: Arcata
Run: 082792-2A
Reflector: 23 dBsm

file	reflector range(m)	corrected alt. (m)	dep. angle	pitch angle	roll angle	elevation angle	azimuth angle	elevation gain	azimuth gain	reflector peak 1	reflector peak 2	reflector sum
2402205.05	n/a	228.07	n/a	-1.2195	0.8350	n/a	n/a	n/a	n/a	n/a	n/a	n/a
2402205.09	3787.7	205.60	3.11	0.0220	-1.7139	8.6638	0.6288	0.00	0.62	20.18	16.29	21.67
2402205.13	3487.8	192.12	3.16	1.5216	1.2250	10.2352	0.5215	-0.41	0.39	14.22	17.26	19.01
2402205.17	3187.9	177.98	3.20	1.0107	2.9169	9.7732	0.4447	-0.13	0.33	15.15	17.91	19.76
2402205.21	2902.5	162.57	3.21	1.3678	-0.5273	10.1916	-0.0539	-0.37	0.05	13.93	15.28	17.07
2402205.25	2617.7	149.65	3.28	0.4889	-0.7636	9.3605	-0.5317	-0.01	0.45	10.91	16.29	17.37
2402205.28	2340.6	137.26	3.36	0.2087	-1.1865	9.2058	-1.0940	0.00	0.83	14.32	6.53	14.99
2402205.33	2040.0	122.88	3.45	0.6042	3.2410	9.6698	-0.3415	-0.10	0.29	12.81	12.87	15.85
2402205.37	1755.4	106.72	3.49	0.8844	-0.9283	10.0085	-1.0636	-0.21	0.84	11.45	11.51	14.49

Airport: Arcata
Run: 082792-2A
Reflector: 18.7 dBsm

file	reflector range(m)	corrected alt. (m)	dep. angle	pitch angle	roll angle	elevation angle	azimuth angle	elevation gain	azimuth gain	reflector peak 1	reflector peak 2	reflector sum
2402205.05	3622.6	225.02	3.56	-1.2195	0.8350	7.7682	0.2409	-0.41	0.18	16.76	17.94	20.40
2402205.09	3322.6	202.55	3.49	0.0220	-1.7139	9.0982	0.6627	0.00	0.50	17.62	15.30	19.62
2402205.13	3022.6	189.07	3.59	1.5216	1.2250	10.7062	0.1970	-1.06	0.15	12.62	13.51	16.10
2402205.17	2722.9	174.93	3.66	1.0107	2.9169	10.3074	0.4204	-0.48	0.32	9.94	13.10	14.81
2402205.21	2437.5	159.52	3.75	1.3678	-0.5273	10.8091	-0.2534	-1.21	0.22	3.23	4.42	6.86
2402205.25	2152.8	146.60	3.90	0.4889	-0.7636	10.0707	-0.8640	-0.26	0.73	4.15	9.06	10.29
2402205.28	1875.7	134.22	4.10	0.2087	-1.1865	10.0493	-1.3950	-0.24	0.77	8.81	2.96	9.81
2402205.33	1575.0	119.81	4.36	0.6042	3.2410	10.6824	-0.6120	-1.02	0.52	6.44	9.20	11.05
2402205.37	1290.8	103.67	4.61	0.8844	-0.9283	11.2850	-1.8189	-1.93	0.69	9.81	5.97	11.31

The next two columns represent the pitch and roll angles of the aircraft reported in degrees for each snapshot. The corresponding elevation and azimuth angles in degrees with respect to the antenna

boresight are listed next. These angles are used to determine the appropriate antenna gain applied to the Bruderhedral coordinates. Next to these angles are the actual elevation and azimuth gain adjustments in dB with respect to the boresight gain of 33 dBi for the antenna.

Since antenna pattern data are available for only one azimuth cut and one elevation cut (see Appendix C), GTRI assumed that the antenna pattern is separable into independent azimuth and elevation components for this analysis. Since the gain of the Honeywell antenna is below the peak value when steered to the 0-degree azimuth pointing direction, the azimuth gain adjustments are typically positive.

The three rightmost columns in Table 4.4.3-1 are functions of the radar cross section (RCS) computed from the measured Bruderhedral return for each snapshot. The left two columns of this set list the RCS (in dB relative to a square meter) computed based on the first and second peak returns received from the Bruderhedral. With a 100 ns pulse width, the Honeywell system has a range resolution of 15 meters. However, the Honeywell data acquisition system effectively samples the radar return every 7.5 meters in range. The data acquisition system, therefore, produces 15-meter resolution samples spaced 7.5 meters on center. Thus, any point target within the instrumented range of the Honeywell radar will appear in at least two and sometimes three successive range cells.

In most cases, the Bruderhedral return was confined to two range cells. In some cases, it appeared in three, but even then, the returns in two of the cells were significantly larger than that in the third. The "peak" entries in Table 4.4.3-1 denote the computed RCS for the first (closer in range) peak and that computed for the second of these two dominant cells. These were both computed using Equation 4.4.3-1 with the factor $F_{calibration}$ set to zero.

In some of the lower altitude cases, the slant range to the Bruderhedral reflector was so small that the radar return from the Bruderhedral saturated the data acquisition system. In these cases, it is reasonable to expect the measured RCS of the Bruderhedral to be lower than the actual value that would have been observed had the data acquisition system limitations not contaminated the measurement. Such contaminated values are indicated by darker shading in the three rightmost columns of Table 4.4.3-1.

The rightmost column in Table 4.4.3-1 lists the sum of the two peak Bruderhedral returns, again expressed in dB with respect to a square meter. This sum is taken to be the actual measured Bruderhedral RCS for each particular snapshot. The rationale for this selection of the sum is that it is less sensitive to range sampling than is the peak return, and is thus a more accurate indicator of the true measured RCS value. When the Bruderhedral return "straddles" two adjacent range gates, the peak RCS return will be 3 dB lower than when it is centered in a single range cell. Such large deviations in the measured sum should not occur.

Table 4.4.3-2 presents similar information for calibration approach 2C. The significance of the columns is the same as for those described above for Table 4.4.3-1 (approach 2A). Figures 4.4.3-13 through 4.4.3-20 are plots generated based on the data in Tables 4.4.3-1 and 4.4.3-2 as well as on multipath predictions for Arcata.

Figure 4.4.3-13 plots the larger of the measured RCS peaks and the sum of the two for the 23 dBsm Bruderhedral as well as the RCS predicted for this standard reflector based on the radar scene model constructed for Arcata). The "measured sum" values in Figure 4.4.3-13 represent the actual measured RCS values used in the analysis; the "measured max" values are plotted only for reference.

Note that the two RCS values reported for each snapshot in Tables 4.4.3-1 and 4.4.3-2 are in dBsm (logarithmic) units. The peak summations are thus performed in linear space, and the result then converted back to dBsm units. Thus, the summed value will always be 0 to 3 dBsm larger than the maximum of the two values.

Both the measured RCS and the predicted RCS are plotted versus the corrected barometric altitude of the radar when the corresponding raw radar data snapshot was taken. Thus, it can be seen from Figure 4.4.3-13 that eight snapshots are available for approach 2A for which the RCS of the 23 dBsm Bruderhedral could be computed. These correspond to the eight rows listed in the upper half of Table 4.4.3-1. Two measured RCS values are denoted by an "x" as being saturated in Figure 4.4.3-13. These two values correspond to the two rows in the upper half of Table 4.4.3-1 for which the measured RCS values are shaded.

The predicted RCS values, denoted by the shaded diamonds in Figure 4.4.3-13, were computed using the multipath model described in Section 4.4.3.2.1 above. A 15% moisture content and a 2.5 cm root-mean-square (RMS) surface roughness were assumed for the terrain region at which the multipath reflection occurred on the ground. These values were felt to be reasonable based on photographs of the area where the Bruderhedral reflectors were placed as well

as the general dry conditions existing up to and including the day the calibration data were acquired.

However, to probe the dependencies of the predicted RCS values on these assumptions, predictions were made using other assumed values as well. The model was exercised with 40 % and 5 % moisture contents, as well as with RMS surface roughness of 0, 0.5, and 1 centimeter. The agreement between the measured and predicted RCS values was judged best for the 15% moisture content and the 2.5 cm RMS surface roughness values, and thus these values were used in the actual calibration process.

In examining Figure 4.4.3-13, a single multipath lobing pattern should not be visually superimposed, such as one of those shown in Section 4.4.3.2.1, which passes through each of the measured points. Each measured or computed value plotted in Figure 4.4.3-13 corresponds to a specific data snapshot acquired along the approach path. Since there was naturally some deviation by the pilot in following the exact glideslope, several factors changed from one snapshot to the next. Figure 4.4.3-21 depicts the flight test calibration geometry and illustrates this point.

The line drawn at a 3-degree incline in Figure 4.4.3-21 represents the nominal glidepath. The solid circles represent the various raw data snapshots taken along this nominal glidepath. Note that the aircraft altitude and the ground range to the reflector vary for each snapshot, whereas Figures 4.4.3-7 through 4.5.2-12 of the preceding section were created by varying the altitude only for a fixed ground range.

Furthermore, only one of the snapshot points illustrated in Figure 4.4.3-21 falls on the nominal 3-degree glide slope. The others correspond to glide paths which are smaller or larger than 3 degrees. Thus, even a theoretical lobing structure for which the altitude and the ground range varied, while maintaining a 3-degree glide path, cannot be validly superimposed on the measured data. Each measured value must be viewed separately from the others, since each corresponds to a separate snapshot taken in a changing scenario.

Figure 4.4.3-14 presented previously was constructed from 4.4.3-13 by neglecting the two saturated measured RCS sum values, and then adjusting the remaining six sum values by the constant offset that yielded the least-mean-square error (LMSE) when compared to the corresponding predicted RCS values. As indicated in Figure 4.4.3-14, the mean-square error is minimized when the six measured RCS sums are all increased by 1.23 dBsm. In other words, these six measured values, taken together, indicate that the factor $F_{calibration}$ in Equation 4.4.3-1 is actually 1.23 dB.

Table 4.4.3-2 Summary of Measured RCS Values for Both Bruderhedral Reflectorsat Arcata, CA on August 27, 1992 (Approach 2C). All Angles Are In Degrees and All Reflector Values are in DBSM

Airport: Arcata
Run: 082792-2C
Reflector: 23 dBsm

file	reflector range(m)	corrected alt. (m)	dep. angle	pitch angle	roll angle	elevation angle	azimuth angle	elevation gain	azimuth gain	reflector peak 1	reflector peak 2	reflector sum
2402304.33	n/a	215.90	n/a	-0.5328	-3.6584	n/a	n/a	n/a	n/a	n/a	n/a	n/a
2402304.37	3615.1	196.22	3.11	0.1978	-2.0544	8.7279	0.7915	0.00	0.59	12.02	23.18	23.50
2402304.41	3332.4	180.15	3.10	-0.0934	0.3900	8.5850	2.1334	-0.02	0.92	21.64	15.83	22.65
2402304.45	3039.9	165.73	3.13	0.0604	-0.1263	8.7143	2.2821	0.00	0.99	23.30	13.49	23.73
2402304.49	2753.2	151.60	3.16	-0.0055	1.7468	8.6036	0.9850	-0.02	0.74	18.20	11.31	19.01
2402304.53	2467.9	133.75	3.11	0.3516	4.1089	9.0793	0.3908	0.00	0.29	16.16	13.66	18.10
2402304.57	2183.0	120.17	3.16	0.3680	-1.0437	9.1360	-1.0147	0.00	0.85	7.24	10.33	12.06
2402305.01	1897.7	103.88	3.14	0.5603	1.1920	9.4452	0.7091	-0.03	0.53	10.05	10.12	13.10
2402305.04	1620.3	91.75	3.25	0.5823	-0.8899	9.5206	-0.9136	-0.06	0.78	8.90	8.97	11.95

Airport: Arcata
Run: 082792-2C
Reflector: 18.7 dBsm

file	reflector range(m)	corrected alt. (m)	dep. angle	pitch angle	roll angle	elevation angle	azimuth angle	elevation gain	azimuth gain	reflector peak 1	reflector peak 2	reflector sum
2402304.33	3443.0	212.85	3.54	-0.5328	-3.6584	8.4789	-0.4531	-0.06	0.39	14.49	18.71	20.10
2402304.37	3150.0	193.17	3.52	0.1978	-2.0544	9.1763	0.4686	0.00	0.35	12.70	17.23	18.54
2402304.41	2866.9	177.10	3.54	-0.0934	0.3900	9.0824	2.0361	0.00	0.87	14.48	11.17	16.14
2402304.45	2574.1	162.68	3.62	0.0604	-0.1263	9.2691	2.0246	0.00	0.86	16.84	8.11	17.39
2402304.49	2287.7	148.55	3.72	-0.0055	1.7468	9.1941	0.4689	0.00	0.35	12.11	4.50	12.80
2402304.53	2002.6	130.70	3.74	0.3516	4.1089	9.7644	-0.0622	-0.13	0.05	10.18	7.63	12.10
2402304.57	1718.1	117.12	3.91	0.3680	-1.0437	9.9946	-1.3189	-0.20	0.79	6.40	0.64	9.63
2402305.01	1432.5	100.83	4.04	0.5603	1.1920	10.4956	0.0797	-0.74	0.06	7.48	7.61	10.61
2402305.04	1155.4	88.70	4.40	0.5823	-0.8899	10.8666	-1.3201	-1.30	0.79	5.44	5.46	8.46

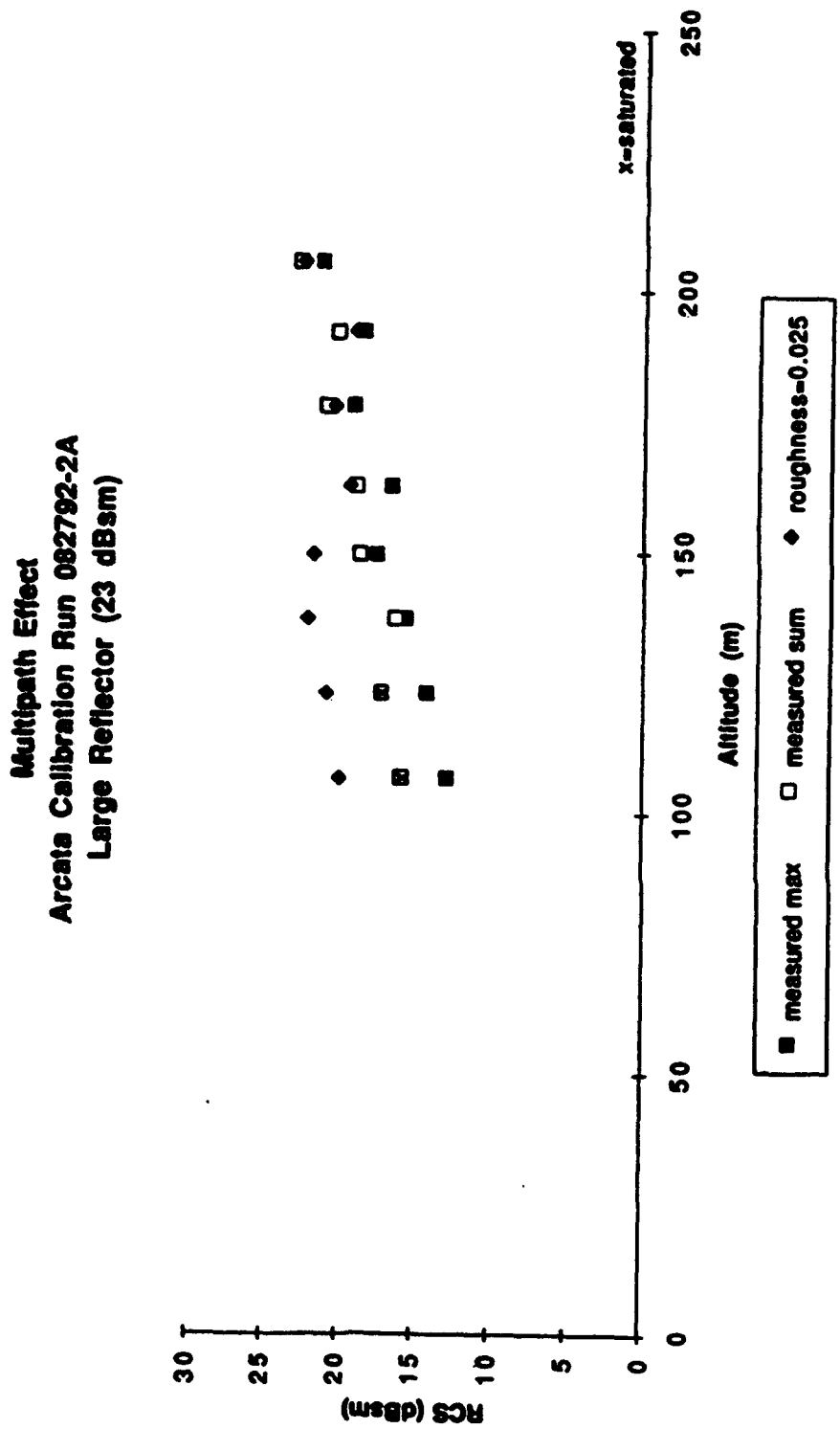

Figure 4.4.3-13. Plot of Measured and Predicted RCS Versus Altitude for the 23.0 dBsm Bruderhedral at Arcata, CA on August 27, 1992 (Approach 2A). Both the Measured Peak RCS and the Sum RCS Are Indicated. The Predicted RCS is Based on an Assumed RMS Surface Roughness of 0.025M

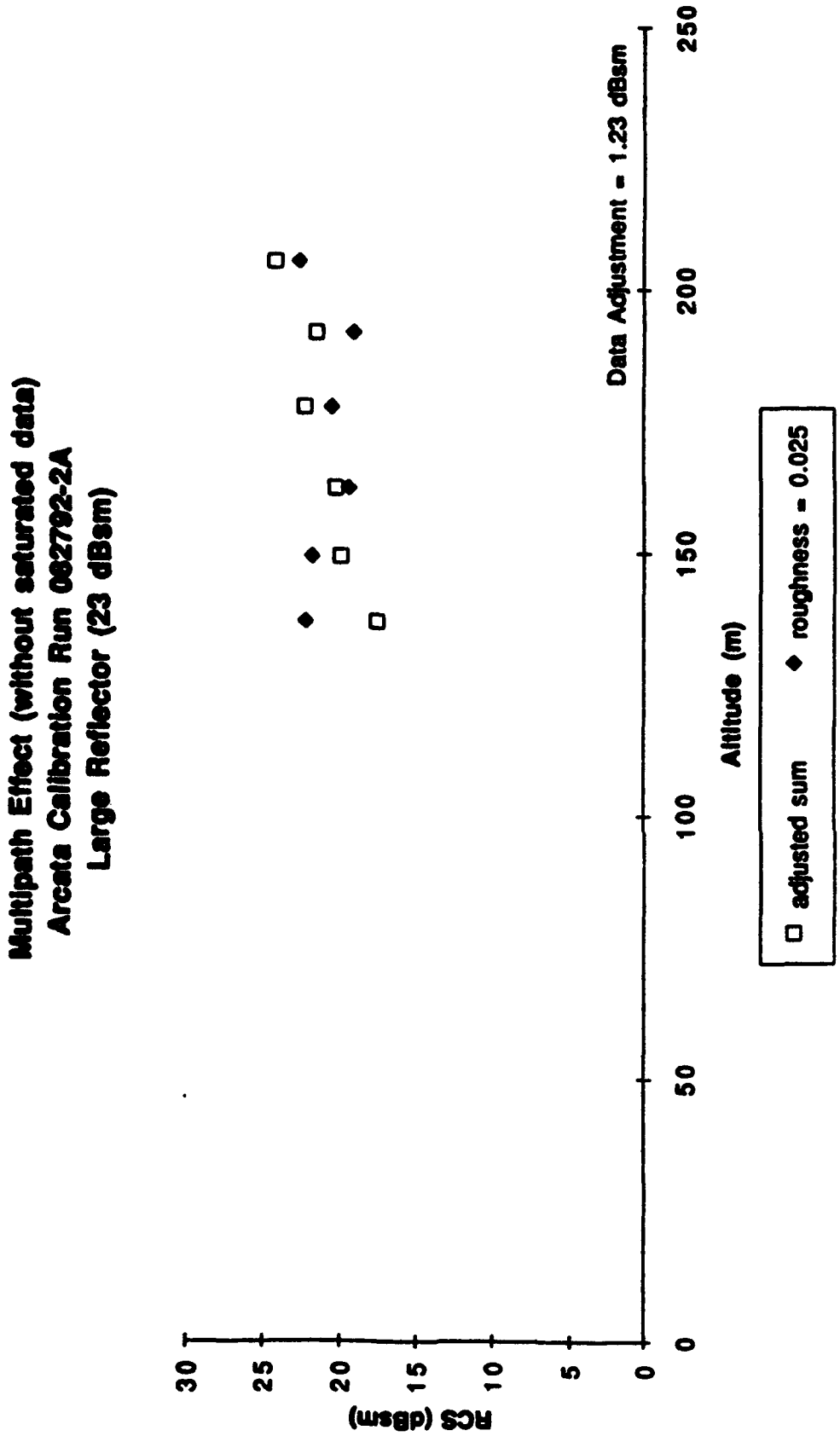

Figure 4.4.3-14. Plot of Measured RCS Sum Values After Adjustment as Well as Corresponding Predicted RCS Values Used to Compute Adjustment. Data are for the 23.0 dBsm Bruderhedral at Arcata, CA on August 27, 1992 (Approach 2A)

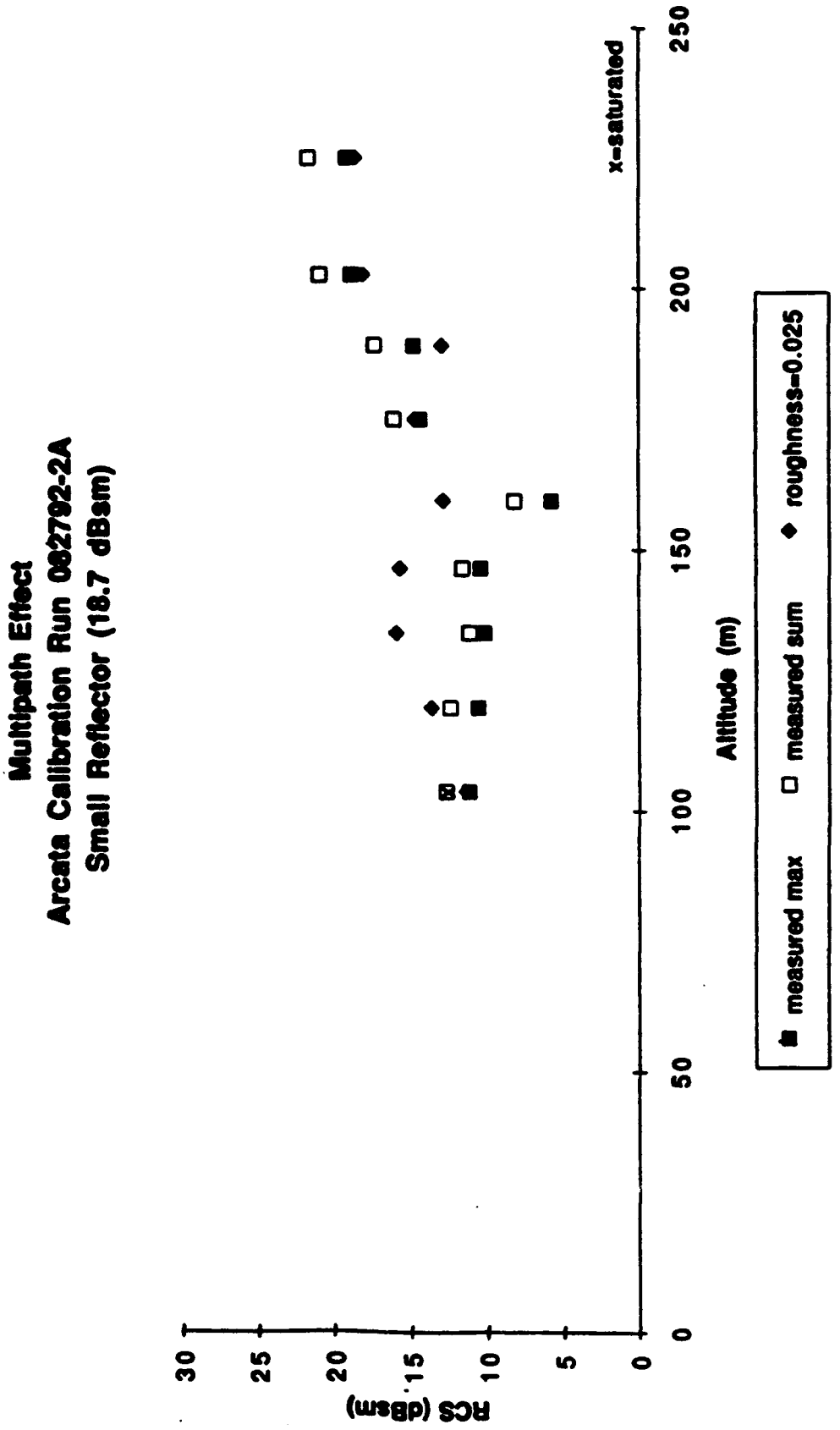

Figure 4.4.3-15. Plot of Measured and Predicted RCS Versus Altitude for the 18.7 dBsm Bruderhedral at Arcata, CA on August 27, 1992 (Approach 2A). Both the Measured Peak RCS and the Sum RCS are Indicated. The Predicted RCS is Based on an Assumed RMS Surface Roughness of 0.025M

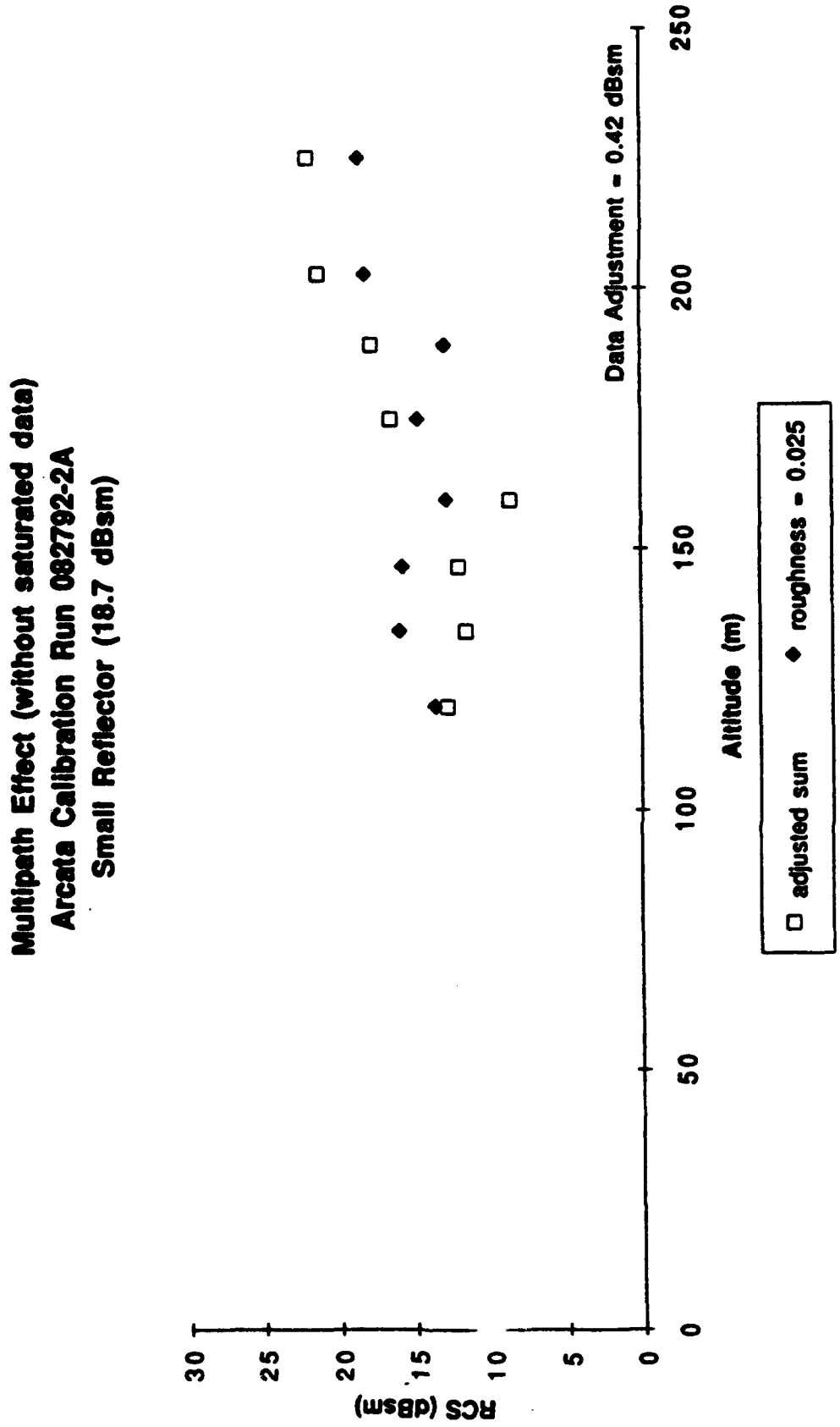

Figure 4.4.3-16. Plot of Measured RCS Sum Values After Adjustment as Well as Corresponding Predicted RCS Values Used to Compute Adjustment. Data are for the 18.7 dBsm Bruderhedral at Arcata, CA on August 27, 1992 (Approach 2A)

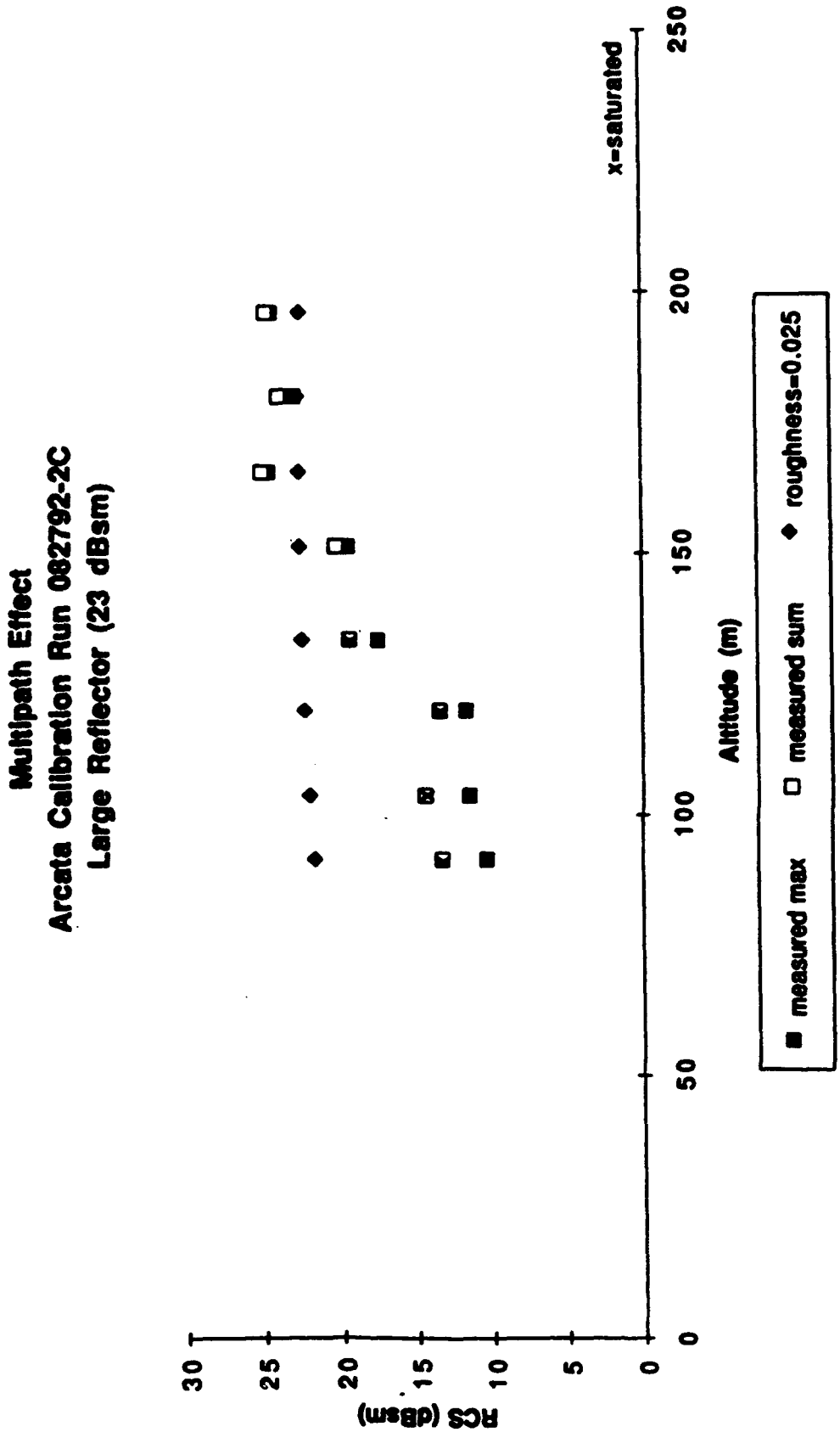

Figure 4.4.317. Plot of Measured and Predicted RCS Versus Altitude for the 23.0 dBsm Bruderhedral at Arcata, CA on August 27, 1992 (Approach 2C). Both the Measured Peak RCS and the Sum RCS are Indicated. The Predicted RCS is based on an Assumed RMS Surface Roughness of 0.025 m

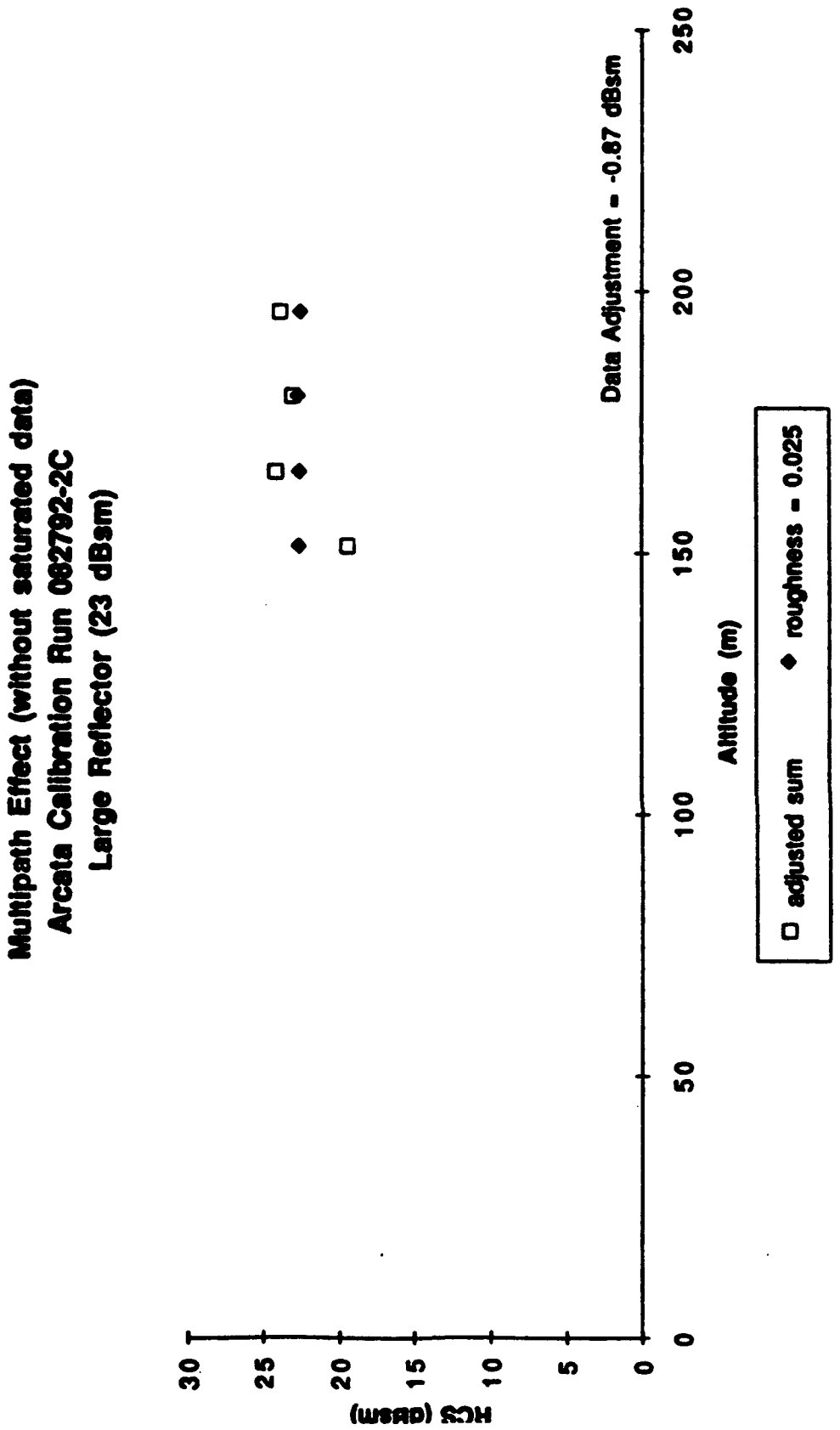

Figure 4.4.3-18. Plot of Measured RCS Sum Values After Adjustment as Well as Corresponding Predicted RCS Values Used to Compute Adjustment. Data are for the 23.0 dBsm Bruderhedral at Arcata, CA on August 27, 1992 (Approach 2C)

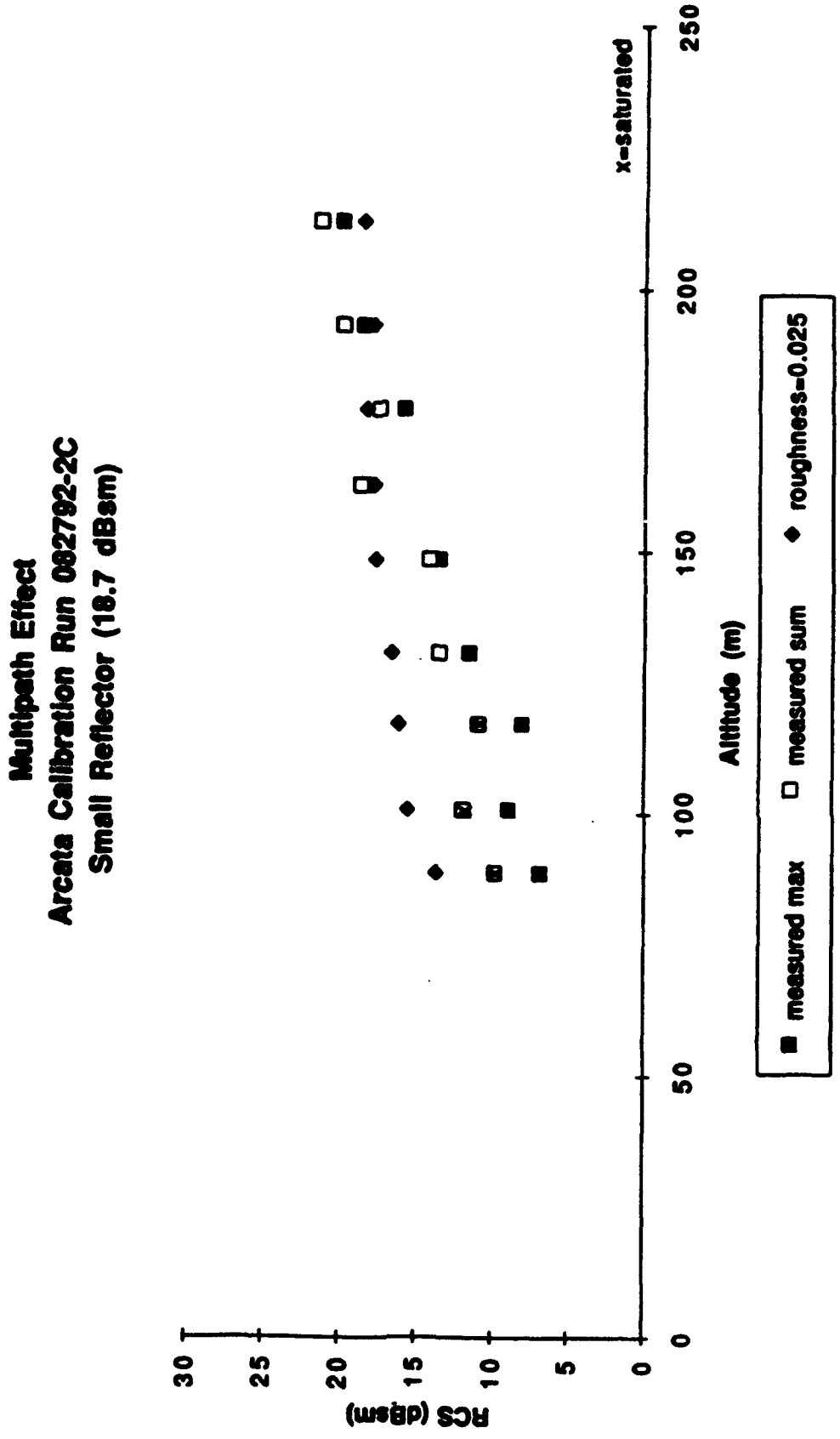

Figure 4.4.3-19. Plot of Measured and Predicted RCS Versus Altitude for the 18.7 dBsm Bruderhedral at Arcata, CA on August 27, 1992 (Approach 2C). Both the Measured Peak RCS and the Sum RCS are Indicated. The Predicted RCS is Based on an Assumed RMS Surface Roughness of 0.025 m

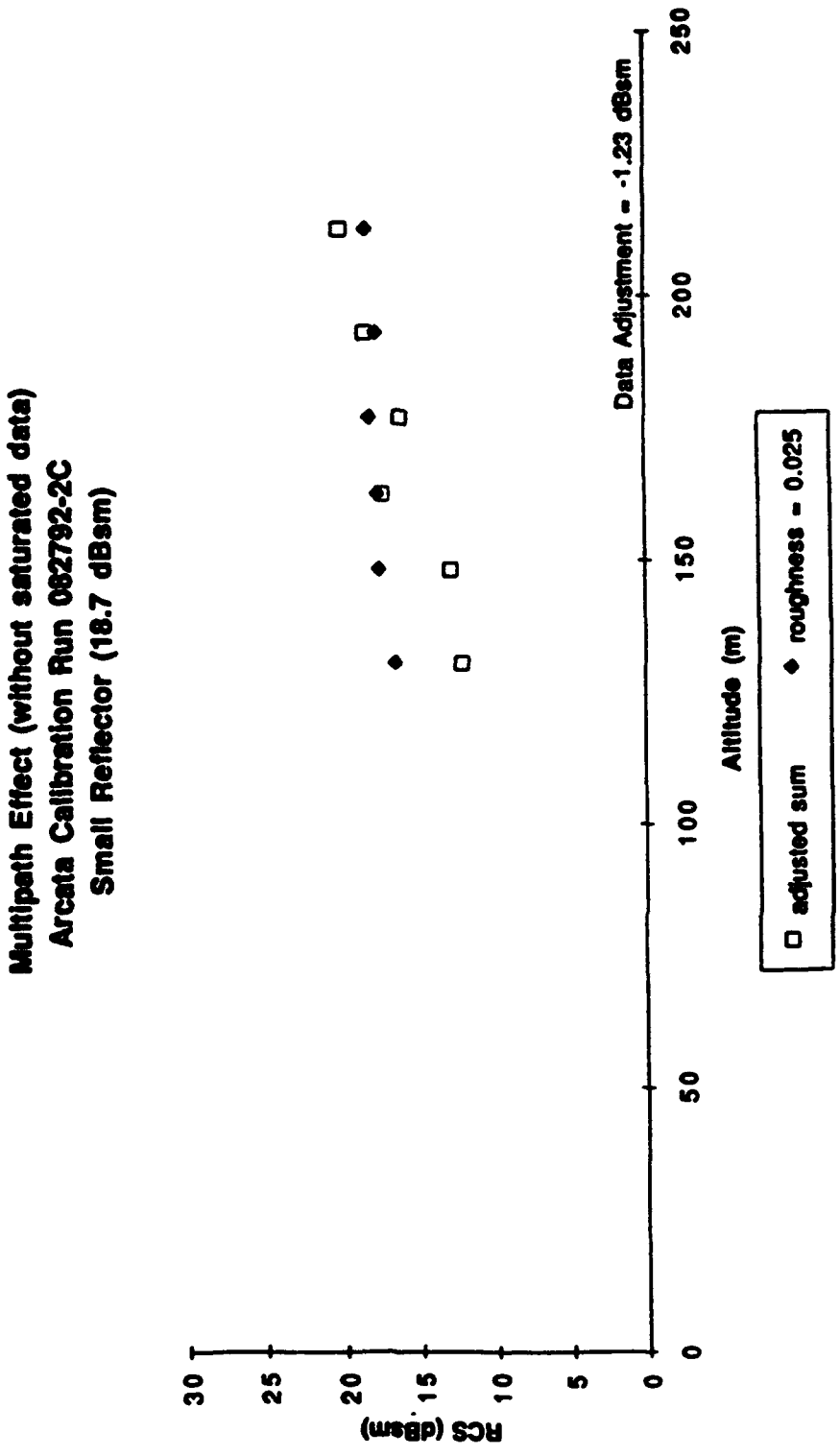

Figure 4.4.3-20. Plot of Measured RCS Sum Values After Adjustment as Well as Corresponding Predicted RCS Values Used to Compute Adjustment. Data Are For The 18.7 dBsm Bruderhedral at Arcata, CA on August 27, 1992 (Approach 2C)

Fortunately, there are other data which permit this estimate of $F_{calibration}$ to be refined. Figures 4.4.3-15 and 4.4.3-16 show the raw and adjusted calibration data, respectively, for the 18.7 dBsm Bruderhedral reflector for calibration approach 2A. They parallel Figures 4.4.3-13 and 4.4.3-14 just discussed, except they address the smaller reflector rather than the larger one. The RMS adjustment for this second data set is 0.42 dBsm, as indicated in Figure 4.4.3-16.

Figures 4.4.3-17 through 4.4.3-20 parallel Figures 4.4.3-13 through 4.4.3-16 just discussed, except that they pertain to calibration approach 2C rather than 2A. The data on which Figures 4.4.3-17 and 4.4.3-19 are based are contained in Table 4.4.3-2. The corresponding estimates of the factor $F_{calibration}$ are -0.87 dBsm (see Figure 4.4.3-18)

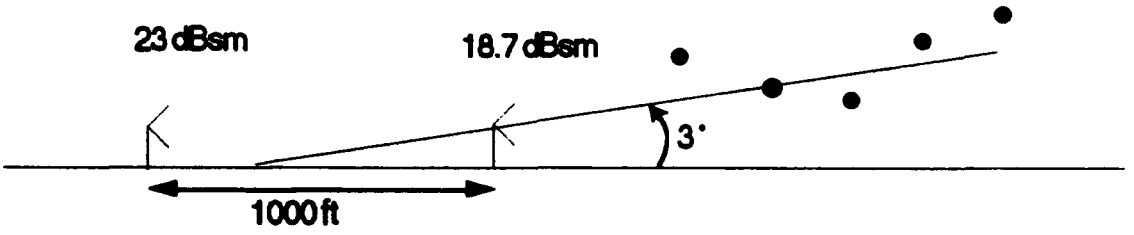

Figure 4.4.3-21: Illustration of flight test snapshot geometry.

and -1.23 dBsm (see Figure 4.4.3-20). Table 4.4.3-3 below summarizes the estimates of $F_{calibration}$ based on the available calibration data from Arcata.

Table 4.4.3-3. Summary of Absolute Calibration Data from Arcata, California on 8/27/92

Approach	Reflector	No. of Points	Average Adjustment
2A	23.0	6	1.23 dB
2A	18.7	8	0.42 dB
2C	23.0	4	-0.87 dB
2C	18.7	6	-1.23 dB

The overall estimate of $F_{calibration}$ for Aracata on 8/27 is computed based on a weighed average of the four individual estimates. This computation yields $F_{calibration}$ = 0.005 dB.

The consistency in the four data sets is fairly good, especially when the data synchronization problems described in Section 4.4.2.2 are considered. The maximum deviation between any pair of the four estimates of $F_{calibration}$ in Table 4.4.3-3 is 2.46 dB, and each individual estimate is within 1.23 dB of the weighted average. One factor which likely contributes to the good

agreement of the data is the relatively stable attitude of the aircraft during both approach 2A and 2C.

Note the pitch and roll angles (fifth and sixth columns from left) in Tables 4.4.3-1 and 4.4.3-2 how little each one tends to change from one snapshot to the next. The important result of this is the small changes in relative azimuth and elevation gains with respect to the boresight value as indicated in the ninth and tenth columns from the left. The data synchronization problem described previously means that there is some uncertainty in the correct roll and pitch angles associated with each snapshot. Thus, the elevation and azimuth relative gain values listed for each snapshot are likely not correct.

However, these relative gain values are typically quite small (magnitudes less than one dB), so the corresponding errors can be assumed to be small as well. Thus, the generally good agreement in the estimates of $F_{calibration}$ is reasonable. In addition, since the errors from one estimate to another are likely independent, it is anticipated that the averaging process will produce an overall estimate of $F_{calibration}$ which is even more accurate than any of the individual, component estimates.

4.4.3.2.3 Vandenburg AFB, CA Calibration (8/19/92)

Radar data were analyzed for two calibration approaches against the Vandenburg Air Force Base (AFB) runway on 8/19/92. These approaches are designated 2C and 2D. Table 4.4.3-4 presents key data for each of nine snapshots analyzed in approach 2C, and Table 4.4.3-5 presents the data for the nine snapshots along approach 2D. The format of these tables is the same as that for Tables 4.4.3-1 and 4.4.3-2 described above for the Arcata calibration.

As in the Arcata case, RCS values in shaded boxes saturated the data acquisition system and thus are likely smaller than the true values that would have been measured had not the acquisition system response been limited. While some measured RCS values that were not saturated are larger than others reported as saturated, a different gain and bias setting was used for each snapshot, so that the saturation point for each snapshot is different. Thus, a given value might saturate the data acquisition system in one snapshot and not in another.

Four pairs of plots for the Vandenburg calibration approaches are included as Figures 4.4.3-22 through 4.4.3-29. Figure 4.4.3-22 plots the measured RCS sum and three predicted RCS values versus radar altitude for the 23 dBsm Bruderhedral. The data correspond to eight snapshots

Table 4.4.3-4. Summary of Measures RCS Values for Both Bruderhedral Reflectors at Vandenburg Air Force Base, CA on August 19, 1992 (Approach 2C). All Angles are in Degrees and All Reflector Values Are in dBsm

Airport: Vandenburg
Run: 081992-2C
Reflector: 23 dBsm

file	reflector range(m)	corrected alt. (m)	dep. angle	pitch angle	roll angle	elevation angle	azimuth angle	elevation gain	azimuth gain	reflector peak 1	reflector peak 2	reflector sum
2322239.17	n/a	186.21	n/a	-2.2083	1.9006	n/a	n/a	n/a	n/a	n/a	n/a	n/a
2322239.22	3660.6	166.37	2.60	-2.1368	-0.1318	6.1600	1.0658	-3.16	0.76	25.34	22.99	27.33
2322239.26	3353.0	149.99	2.56	-1.3678	-0.2582	6.8176	1.0532	-1.83	0.76	18.34	24.61	25.69
2322239.30	3045.9	135.79	2.56	-0.7251	2.2247	7.3711	1.1217	-0.94	0.76	14.86	22.03	22.79
2322239.34	2738.5	117.69	2.44	-0.5328	-0.1593	7.4172	1.5881	-0.87	0.81	20.37	21.47	23.97
2322239.38	2431.7	105.21	2.48	-1.1700	-1.8677	6.5047	2.3297	-2.44	1.01	22.72	22.61	25.78
2322239.42	2133.0	88.12	2.37	-0.5823	2.3456	7.0741	2.7312	-1.39	1.22	19.78	13.12	20.69
2322239.46	1833.5	73.35	2.29	-1.2194	-1.7578	6.0193	3.0957	-3.46	1.42	23.59	22.70	26.66
2322239.50	1539.7	54.69	2.04	-0.4669	0.2417	6.6498	3.0403	-2.14	1.35	19.14	19.94	22.57

Airport: Vandenburg
Run: 081992-2C
Reflector: 18.7 dBsm

file	reflector range(m)	corrected alt. (m)	dep. angle	pitch angle	roll angle	elevation angle	azimuth angle	elevation gain	azimuth gain	reflector peak 1	reflector peak 2	reflector sum
2322239.17	3495.8	186.21	3.05	-2.2083	1.9006	6.5866	1.0042	-2.27	0.75	16.40	19.90	21.50
2322239.22	3188.2	166.37	2.99	-2.1368	-0.1318	6.5569	1.2220	-2.33	0.77	22.96	19.04	24.44
2322239.26	2880.8	149.99	2.98	-1.3678	-0.2582	7.2416	1.3712	-1.14	0.79	14.38	19.80	20.90
2322239.30	2573.6	135.79	3.02	-0.7251	2.2247	7.8253	1.3630	-0.36	0.79	13.02	17.45	18.79
2322239.34	2266.2	116.69	2.95	-0.5328	-0.1593	7.9101	1.9162	-0.28	0.84	11.48	16.90	18.00
2322239.38	1959.2	105.21	3.08	-1.1700	-1.8677	7.0129	2.6379	-1.48	1.17	16.01	16.77	18.42
2322239.42	1660.8	88.12	3.04	-0.5823	2.3456	7.6523	3.3075	-0.52	1.38	13.32	9.18	14.74
2322239.46	1361.0	73.35	3.09	-1.2194	-1.7578	6.6078	4.3022	-2.22	1.36	15.02	15.15	18.10
2322239.50	1075.7	54.69	2.91	-0.4669	0.2417	7.3016	4.3633	-1.05	1.34	11.38	11.53	14.47

Table 4.4.3-5. Summary of Measures RCS Values for Both Bruderhedral Reflectors at Vandenburg Air Force Base, CA on August 19, 1992 (Approach 2C). All Angles are in Degrees and All Reflector Values Are in dBsm

Airport: Vandenburg
Run: 081992-2D
Reflector: 23 dBsm

file	reflector range(m)	corrected alt. (m)	dep. angle	pitch angle	roll angle	elevation angle	azimuth angle	elevation gain	azimuth gain	reflector peak 1	reflector peak 2	reflector sum
2322304.02	n/a	193.87	n/a	-0.5713	-1.3566	n/a	n/a	n/a	n/a	n/a	n/a	n/a
2322304.06	n/a	176.20	n/a	-0.1318	-0.2032	n/a	n/a	n/a	n/a	n/a	n/a	n/a
2322304.10	3668.1	164.03	2.56	-0.3406	-1.1920	7.8143	1.2173	-0.37	0.77	19.26	19.55	22.42
2322304.13	3383.0	148.46	2.52	-0.7800	0.1209	7.4322	0.9986	-0.85	0.75	17.19	25.95	26.49
2322304.18	3099.0	136.15	2.52	-1.5656	1.1920	6.5412	1.6604	-2.36	0.82	20.76	22.72	24.86
2322304.22	2821.4	119.95	2.44	-0.4999	0.5658	7.3292	1.7532	-1.01	0.83	17.96	19.77	21.97
2322304.26	2542.6	102.29	2.31	0.6427	-1.6205	8.3135	0.7449	-0.11	0.56	15.30	17.81	19.74
2322304.30	2272.9	90.62	2.29	0.2032	0.4724	7.7748	1.0705	-0.40	0.76	14.46	10.89	16.06
2322304.34	1996.4	77.74	2.23	0.6537	-2.4829	8.0008	2.5073	-0.20	1.10	12.72	12.82	15.78

Airport: Vandenburg
Run: 081992-2D
Reflector: 18.7 dBsm

file	reflector range(m)	corrected alt. (m)	dep. angle	pitch angle	roll angle	elevation angle	azimuth angle	elevation gain	azimuth gain	reflector peak 1	reflector peak 2	reflector sum
2322304.02	3772.6	193.87	2.95	-0.5713	-1.3566	7.9528	0.5309	-0.24	0.40	13.83	15.88	17.99
2322304.06	3480.5	176.20	2.90	-0.1318	-0.2032	8.4344	1.0176	-0.07	0.75	5.05	10.13	11.30
2322304.10	3195.6	164.03	2.94	-0.3406	-1.1920	8.1980	1.2465	-0.14	0.77	13.25	15.78	17.71
2322304.13	2918.0	148.46	2.92	-0.7800	0.1209	7.8485	1.0124	-0.34	0.75	19.83	11.35	20.41
2322304.18	2626.8	136.15	2.97	-1.5656	1.1920	6.9880	1.9739	-1.52	0.85	11.38	17.80	18.69
2322304.22	2348.7	119.95	2.93	-0.4999	0.5658	7.7746	1.7500	-0.40	0.82	9.38	12.93	14.82
2322304.26	2070.2	102.29	2.83	0.6427	-1.6205	8.7782	1.0822	0.00	0.76	11.46	13.59	15.56
2322304.30	1793.1	90.62	2.90	0.2032	0.4724	8.2995	1.3703	-0.11	0.79	6.04	9.75	11.29
2322304.34	1524.7	77.74	2.92	0.6537	-2.4829	8.5272	3.4813	-0.04	1.40	7.09	7.19	10.15

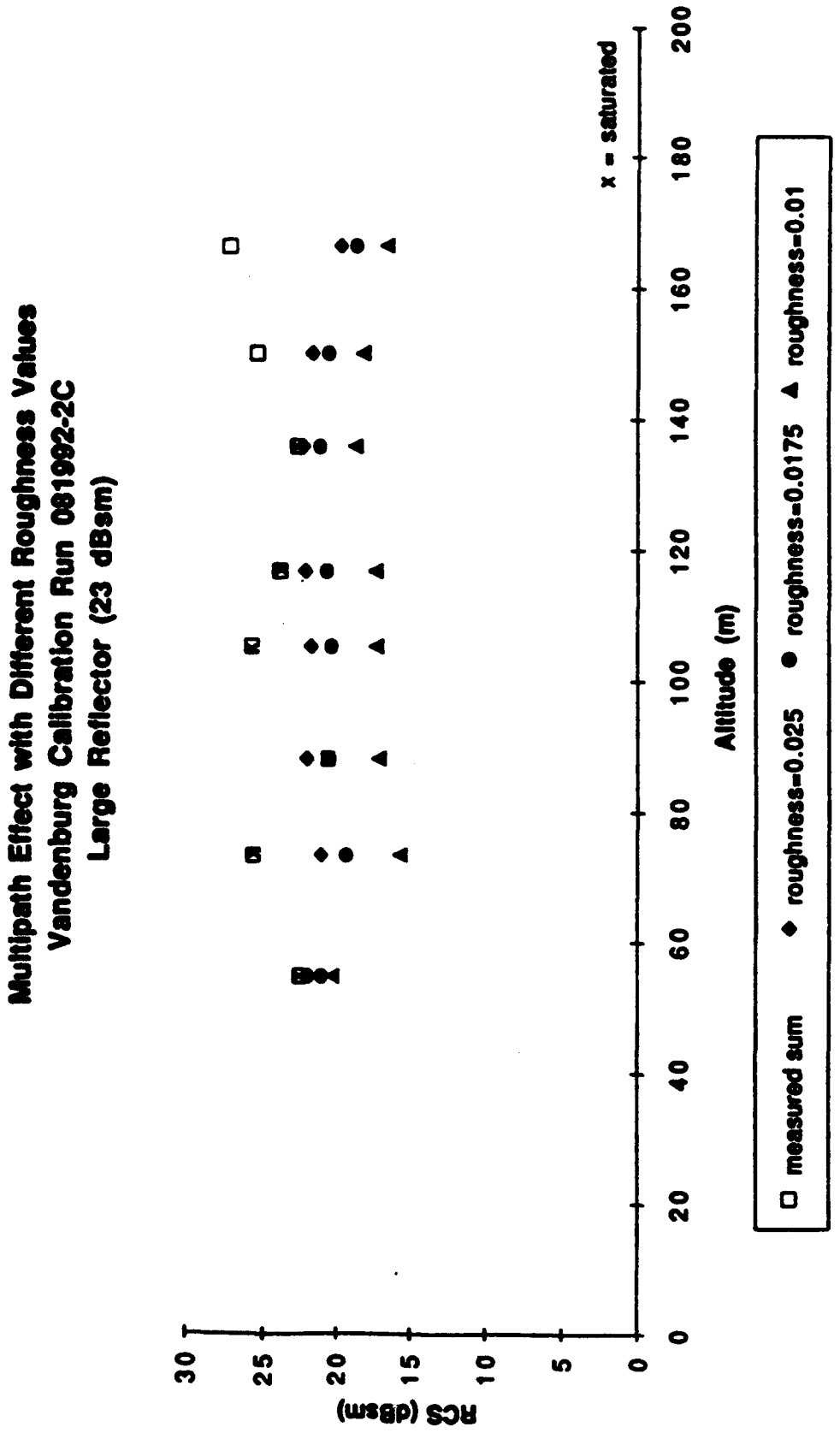

Figure 4.4.3-22. Plot of Measured and Predicted RCS Versus Altitude for the 23.0 dBsm Bruderhedral at Vandenburg Air Force Base, CA On August 19, 1992 (Approach 2C). Predicted RCVS Values are Computed For Three Assumed RMS Surface Roughness as Indicated

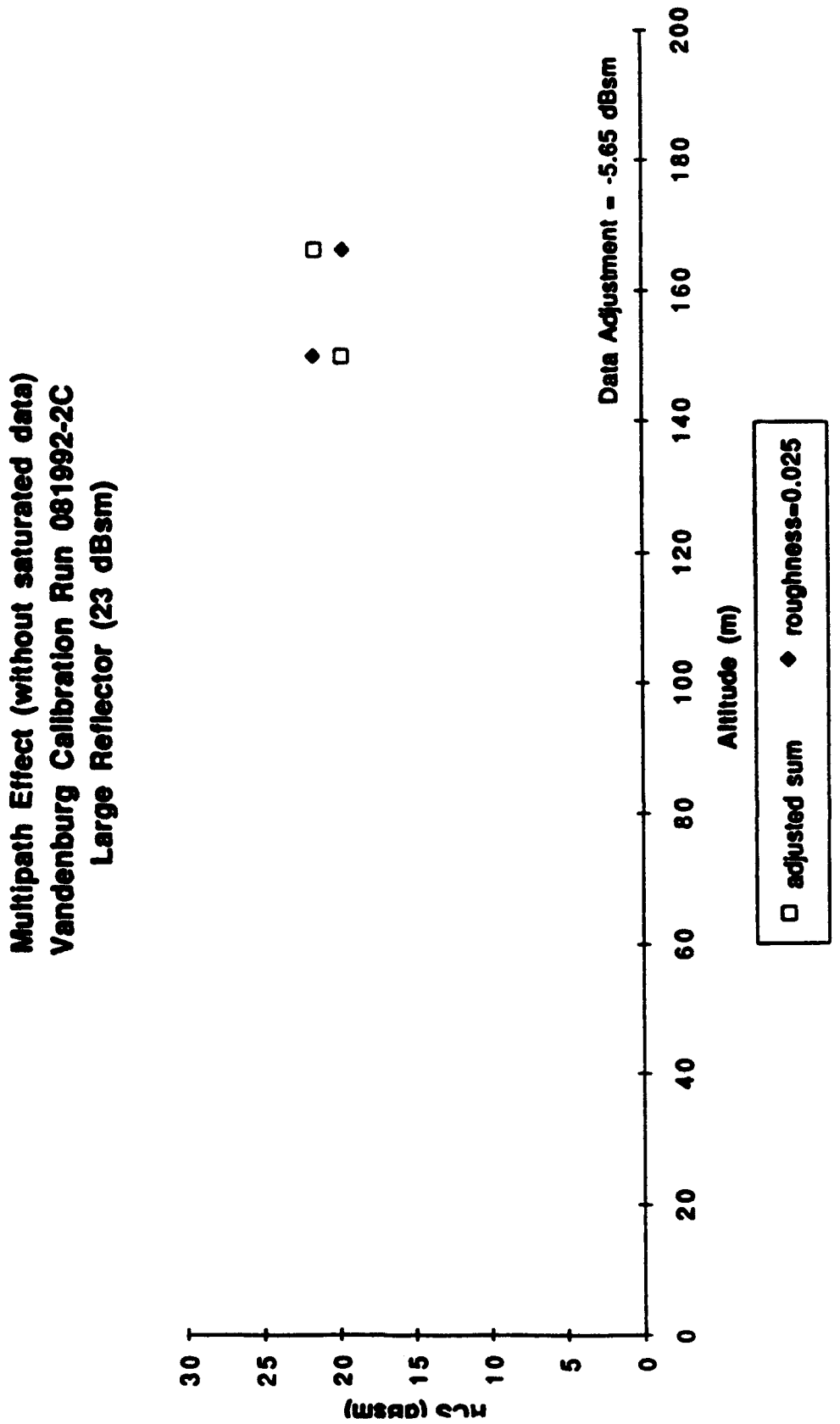

Figure 4.4.3-23. Plot of Measured RCS Sum Values After Adjustment as Well as Corresponding Predicted RCS Values Used to Compute Adjustment. Data are for the 23.0 dBsm Bruderhedral at Vandenburg Air Force Base, CA on August 19, 1992 (Approach 2C)

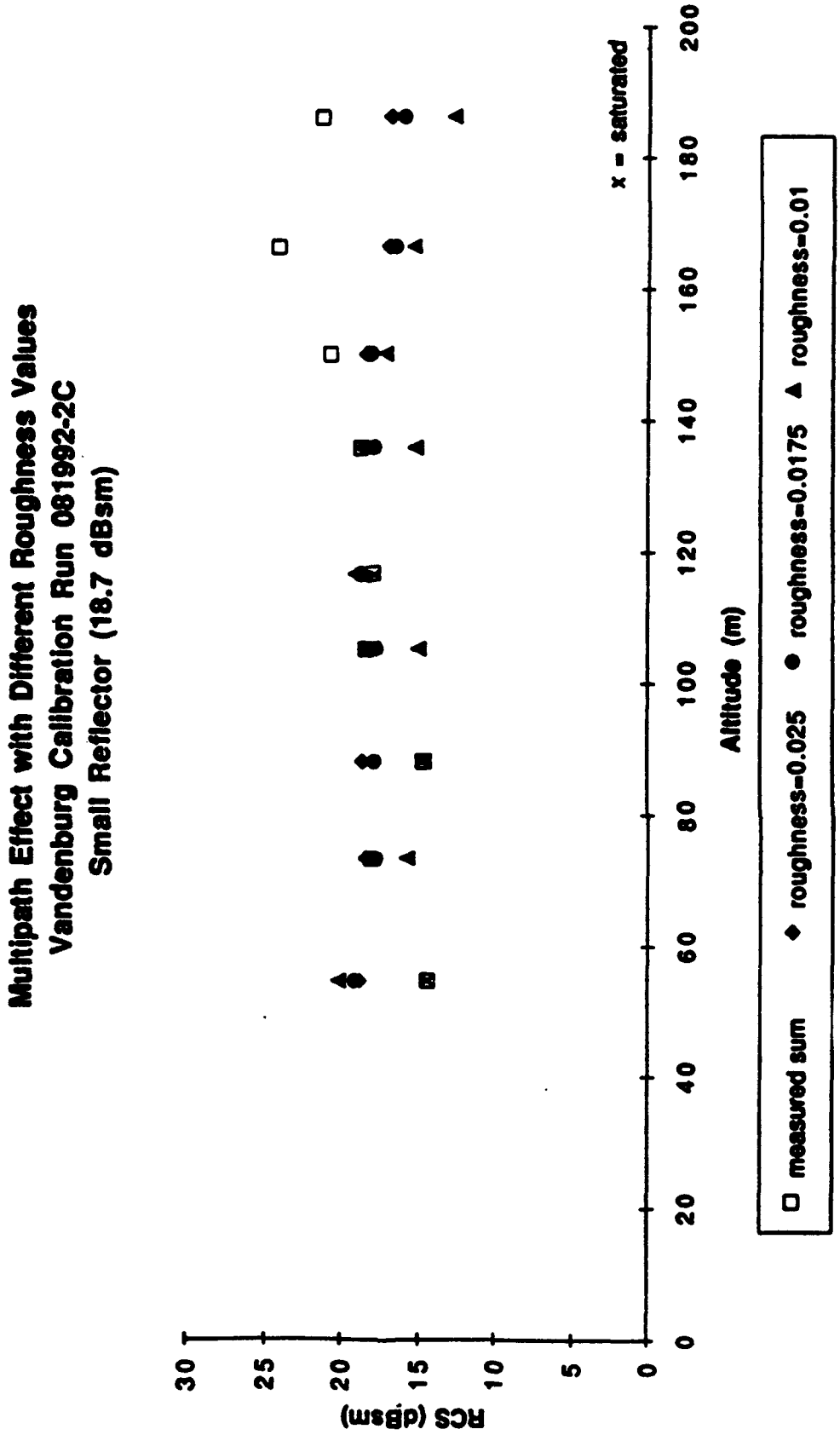

Figure 4.4.3-24. Plot of Measured RCS Versus Altitude for the 18.7 dBsm Bruderhedral at Vandenburg Air Forced Base, CA on August 19, 1992 (Approach 2C). Predicted RCS Values are Computed for Three Assumed RMS Surface Roughness as Indicated

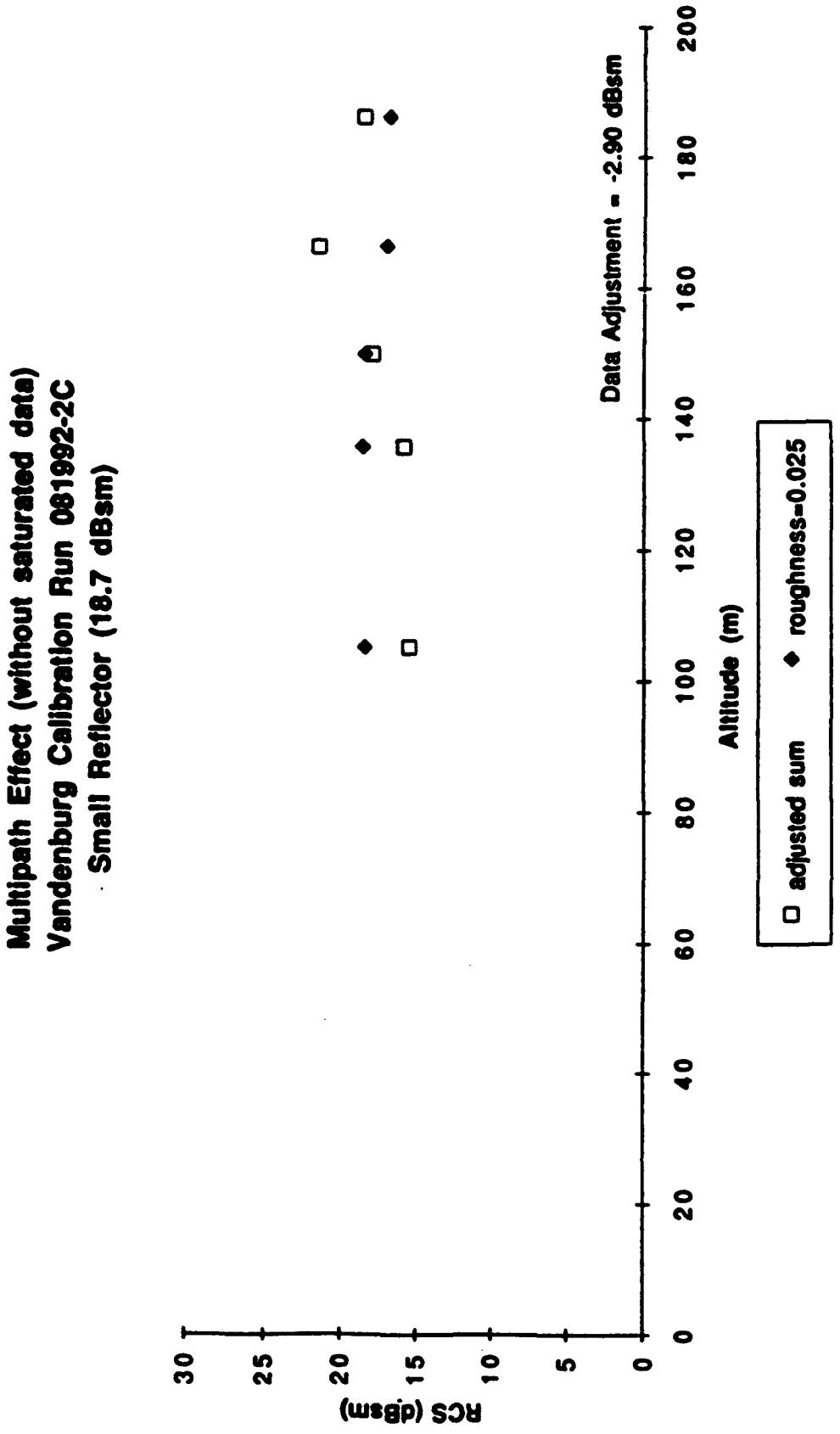

Figure 4.4.3-25. Plot of Measured RCS Sum Values After Adjustment as Well as Corresponding Predicted RCS Values Used to Compute Adjustment. Data are for the 18.7 dBsm Bruderhedral at Vandenburg Air Force Base, CA on August 19, 1992 (Approach 2C)

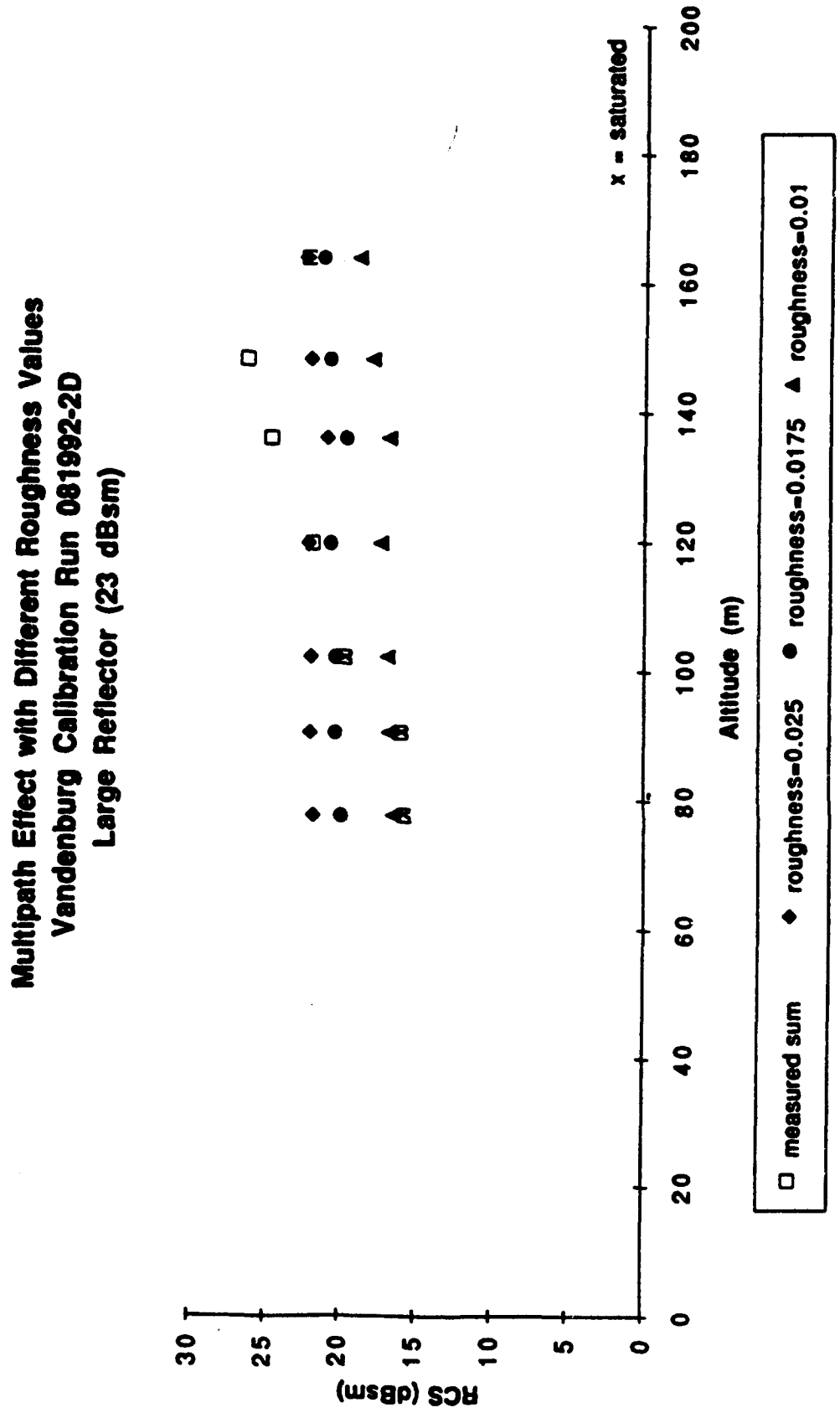

Figure 4.4.3-26 Plot of Measured RCS Versus Altitude for the 23.0 dBsm Bruderhedral at Vandenburg Air Forced Base, CA on August 19, 1992 (Approach 2D). Predicted RCS Values are Computed for Three Assumed RMS Surface Roughness as Indicated

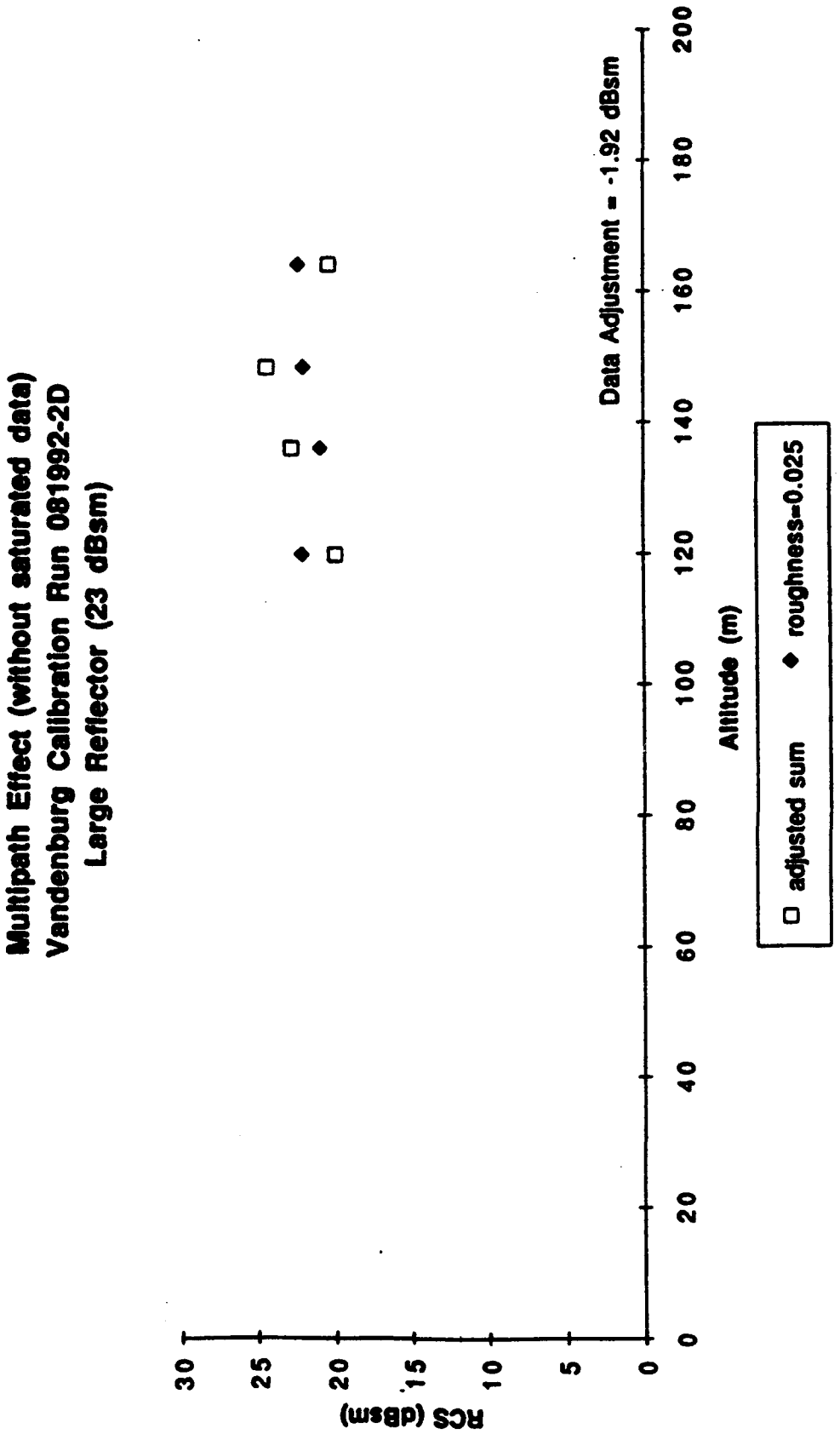

Figure 4.4.3-27 Plot of Measured RCS Sum Values After Adjustment as Well as Corresponding Predicted RCS Values Used to Compute Adjustment. Data are for the 23.0 dBsm Bruderhedral at Vandenburg Air Force Base, CA on August 19, 1992 (Approach 2D)

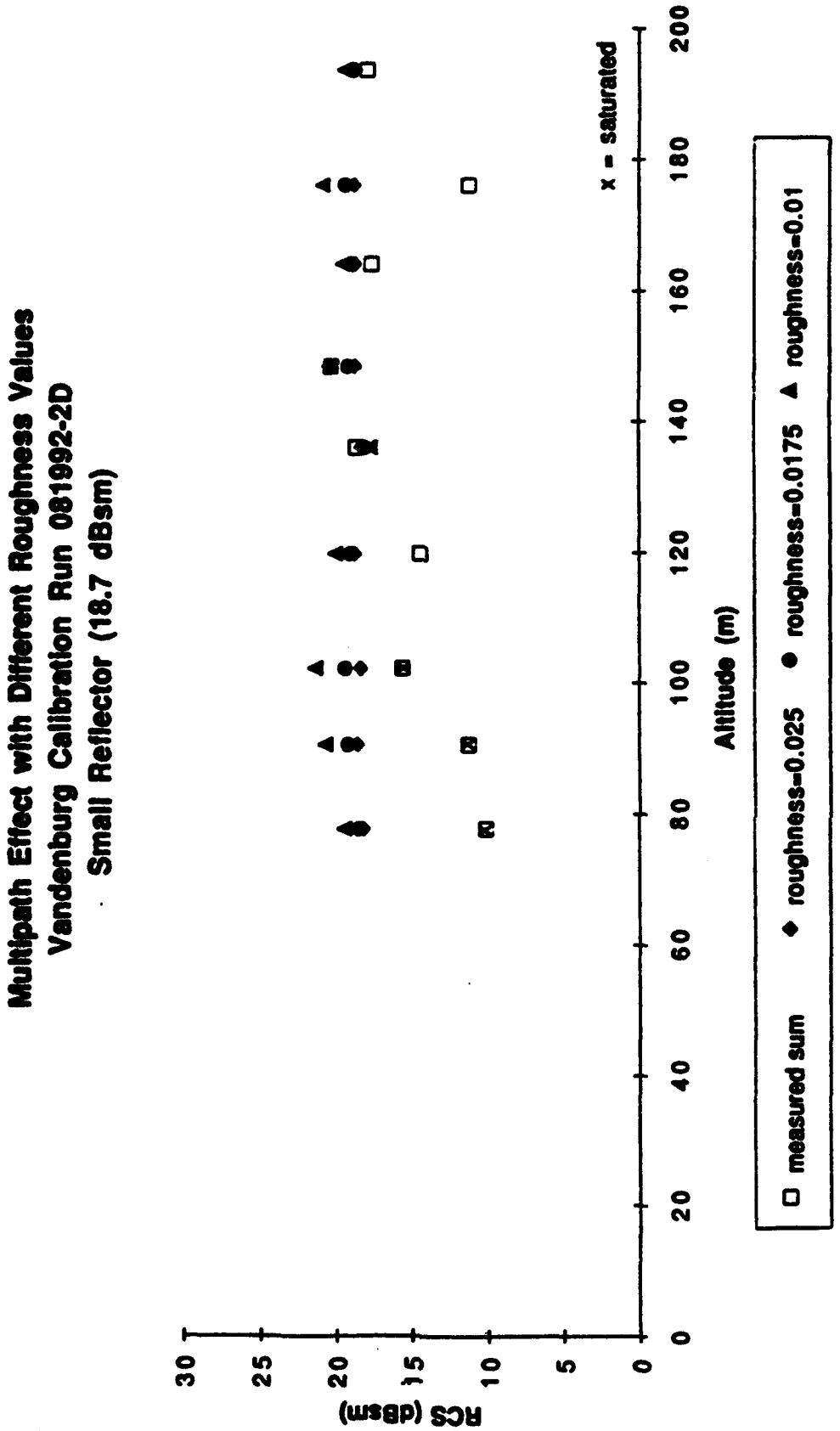

Figure 4.4.3-28. Plot of Measured RCS Versus Altitude for the 18.7 dBsm Bruderhedral at Vandenburg Air Force Base, CA on August 19, 1992 (Approach 2D). Predicted RCS Values are Computed for Three Assumed RMS Surface Roughness as Indicated

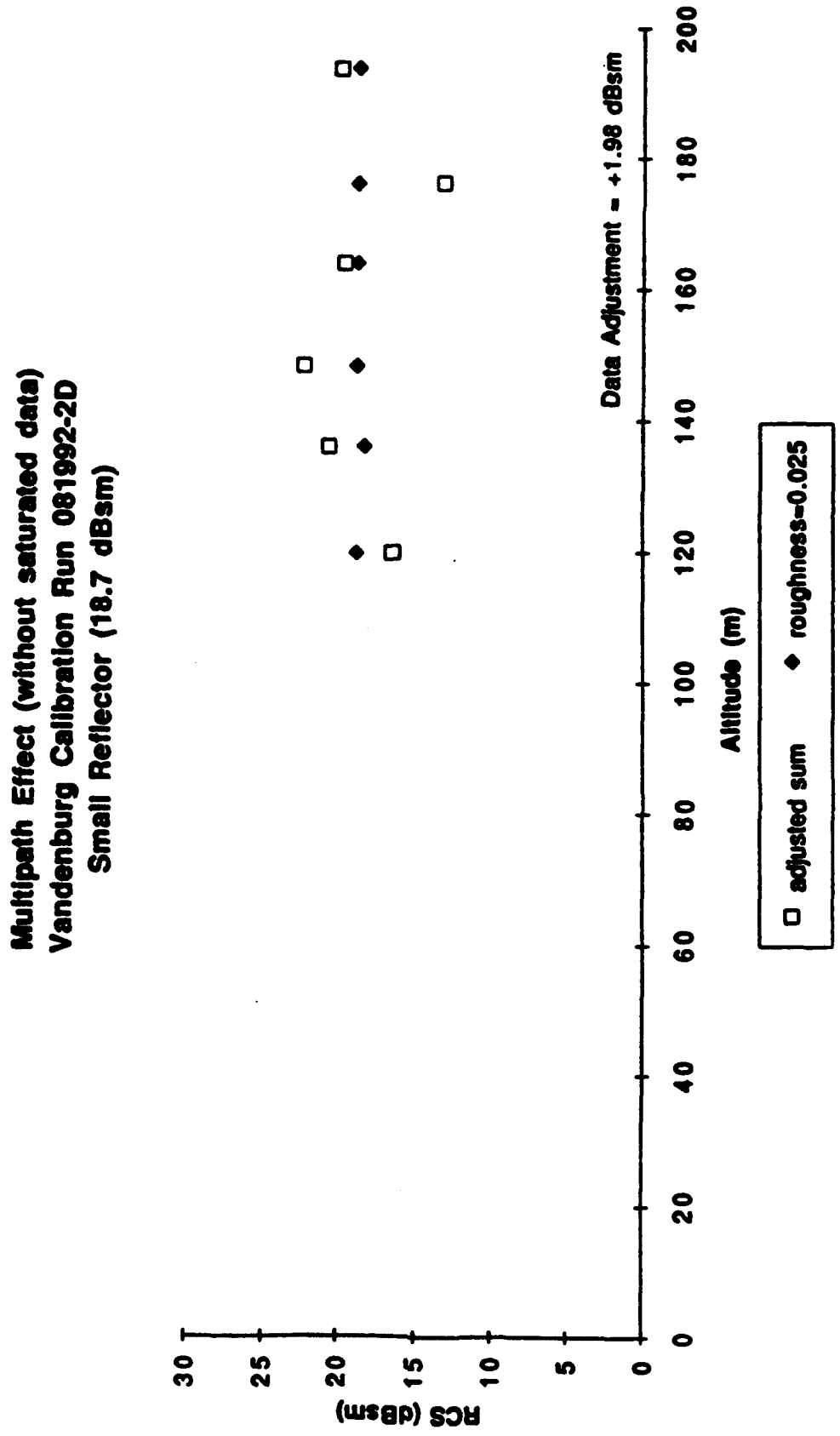

Figure 4.4.3-29. Plot of Measured RCS Sum Values After Adjustment as Well as Corresponding Predicted RCS Values Used to Compute Adjustment. Data are for the 18.7 dBsm Bruderhedral at Vandenburg Air Force Base, CA on August 19, 1992 (Approach 2D)

along approach 2C. (No data were available for this reflector in one of the nine snapshots for the approach.) As in the Arcata case, the predicted RCS is based on an assumed moisture content of 15 % for the terrain.

The three predicted values are denoted by solid symbols and correspond to assumed RMS terrain roughness of 1 cm (triangles), 1.75 cm (circles), and 2.5 cm (diamonds). When all data for both approaches were considered, the predicted values based on a 2.5 cm RMS roughness were selected as best matching the measured values. Thus, the 2.5 cm surface roughness assumption was made for all of the Vandenburg calibration data.

Figure 4.4.3-23 was constructed from 4.4.3-22 by neglecting the six saturated measured RCS values, and then adjusting the remaining two values by the constant offset that yielded the LMSE when compared to the corresponding predicted RCS values based on the assumed 2.5 cm RMS roughness. As indicated in Figure 4.4.3-23, the mean-square-error is minimized when the two measured RCS values are decreased by 5.65 dBsm. This pair of measured values indicate that the factor $F_{calibration}$ in Equation 4.5.2-1 is actually -5.65 dB for this approach.

In addition to the two values used in the calibration, there are three other data sets which can be used to refine the estimate of $F_{calibration}$ for this approach. Figures 4.4.3-24 and 4.4.3-25 present the raw and adjusted RCS values for the smaller 18.7 dBsm Bruderhedral reflector obtained during approach 2C. Based on the five non-saturated values, the corresponding estimate of $F_{calibration}$ is -2.90 dB.

Figures 4.4.3-26 through 4.4.3-29 parallel Figures 4.4.3-22 through 4.4.3-25 just discussed, except that they pertain to calibration approach 2D rather than 2C. The corresponding estimates of the factor $F_{calibration}$ are -1.92 dB (see Figure 4.4.3-27) and +1.98 dB (see Figure 4.4.3-29). Table 4.4.3-6 below summarizes the estimates of $F_{calibration}$ based on the available calibration data from Vandenburg AFB.

Table 4.4.3-6. Summary of Absolute Calibration Data from Vandenburg AFB, California on 8/19/92

Approach	Reflector	No. of Points	Average Adjustment
2C	23.0	2	-5.65 dB
2C	18.7	5	-2.90 dB
2D	23.0	4	-1.92 dB
2D	18.7	6	+1.98 dB

The overall estimate of $F_{calibration}$ for Vandenburg on 8/19/92 is computed based on a weighed average of the four individual estimates. This computation yields

$$F_{calibration} = \frac{2(-5.65) + 5(-2.90) + 4(-1.92) + 6(1.98)}{17} = -1.27 \text{ dB}$$

There is a considerable spread in the four data sets presented in Table 4.4.3-6. The overall variation in the four estimates of $F_{calibration}$ is over 7.5 dB. Contrast these results to the much better consistency in the Arcata data set summarized in Table 4.4.3-3 above. One possible explanation for the larger deviations in the Vandenburg data is the greater variations in aircraft attitude during the Vandenburg approaches.

Compare the pitch angles (fifth column from left) in Tables 4.4.3-4 and 4.4.3-5 for Vandenburg with those from Tables 4.4.3-1 and 4.4.3-2 for Arcata. The pitch angle variations tended to be significantly larger at Vandenburg, which resulted in larger off-boresight elevation antenna pattern gain corrections for each snapshot (see ninth column from left).

However, as explained in Section 4.4.2.2.3, the data synchronization problem means that there is some uncertainty in the correct roll and pitch angles associated with each snapshot. Thus, the elevation and azimuth relative gain values listed for each snapshot are likely not correct. If the relative gain corrections tend to be small and fairly consistent from one snapshot to the next, as in the Arcata case, then errors in these corrections also tend to be small. Thus, there is little deviation in the individual estimates of $F_{calibration}$ from the actual value.

However, in the Vandenburg case, the relative gain corrections tend to be larger than in the Arcata case and tend to deviate more from one snapshot to the next. Thus, the errors in these corrections due to the data synchronization problem will also tend to be larger. The result will be a tendency toward greater variations in the calibration factor estimates, as observed in the Vandenburg data.

4.4.3.2.4 Santa Barbara, CA Calibration (8/19/92)

Radar data were analyzed for three calibration approaches against the Santa Barbara, CA airport on 8/19/92. These approaches are designated 1B, 1C and 1D. Table 4.4.3-7 presents key data for each of nine snapshots analyzed in approach 1B. Tables 4.4.3-8 and 4.4.3-9 present data for the nine snapshots along approaches 1C and 1D, respectively. The format of these tables is the same as that for Tables 4.4.3-1 and 4.4.3-2 described in Section 4.4.3.2.2 above for the Arcata calibration.

Six pairs of plots for the Santa Barbara calibration approaches are included as Figures 4.4.3-30 through 4.4.3-41. Figure 4.4.3-30 plots the measured RCS and three predicted RCS values versus radar altitude for the 23 dBsm Bruderhedral. The data are taken from eight snapshots along approach 1B. (No data were available for this reflector in one of the nine snapshots from this approach.) As in the Arcata case, the predicted RCS is based on an assumed moisture content of 15% for the terrain.

Table 4.4.3-7. Summary of Measures RCS Values for Both Bruderhedral Reflectors at Santa Barbara, CA on August 19, 1992 (Approach 1B). All Angles are in Degrees and All Reflector Values Are in dBsm

Airport: Santa Barbara
Run: 081992-1B
Reflector: 23 dBsm

file	reflector range(m)	corrected alt. (m)	dep. angle	pitch angle	roll angle	elevation angle	azimuth angle	elevation gain	azimuth gain	reflector peak 1	reflector peak 2	reflector sum
2322024.48	n/a	198.61	n/a	0.9119	-1.1041	n/a	n/a	n/a	n/a	n/a	n/a	n/a
2322024.52	3787.6	184.97	2.80	1.0162	-1.2305	9.3415	-0.1390	0.00	0.12	7.29	9.46	11.52
2322024.56	3487.5	169.30	2.78	0.7581	0.7745	9.1204	-0.0009	0.00	0.00	17.55	10.50	18.33
2322025.00	3180.0	155.87	2.81	0.8075	-0.1318	9.1861	-0.1141	0.00	0.10	13.23	14.90	17.16
2322025.04	2873.0	142.76	2.85	0.8514	0.3571	9.1461	0.9920	0.00	0.74	18.31	18.52	21.43
2322025.08	2565.1	124.08	2.77	-0.0165	0.1868	8.2897	0.4753	-0.11	0.36	24.58	22.95	26.85
2322025.11	2252.7	109.11	2.78	-0.6812	-1.4832	7.4917	-0.5653	-0.76	0.48	20.64	13.96	21.47
2322025.16	1935.0	88.64	2.63	0.5164	0.8734	8.6142	0.0901	-0.02	0.07	20.21	16.15	21.65
2322025.20	1620.3	73.80	2.61	1.3019	-3.4937	9.1614	1.6306	0.00	0.81	13.77	11.23	15.69

Airport: Santa Barbara
Run: 081992-1B
Reflector: 18.7 dBsm

file	reflector range(m)	corrected alt. (m)	dep. angle	pitch angle	roll angle	elevation angle	azimuth angle	elevation gain	azimuth gain	reflector peak 1	reflector peak 2	reflector sum
2322024.48	3630.0	198.22	3.15	0.9119	-1.1041	9.5610	0.0567	-0.07	0.04	17.07	11.37	18.11
2322024.52	3322.5	185.58	3.20	1.0162	-1.2305	9.7109	0.2106	-0.11	0.16	8.80	13.90	15.07
2322024.56	3022.5	169.91	3.22	0.7581	0.7745	9.5477	0.1547	-0.06	0.12	19.95	12.46	20.66
2322025.00	2715.0	156.47	3.30	0.8075	-0.1318	9.8621	0.0224	-0.10	0.02	16.44	19.40	21.18
2322025.04	2408.1	143.37	3.41	0.8514	0.3571	9.6669	1.1916	-0.10	0.77	15.24	15.22	18.24
2322025.08	2100.2	124.69	3.40	-0.0165	0.1868	8.8900	0.7892	0.00	0.59	15.32	16.31	18.85
2322025.11	1792.5	109.72	3.51	-0.6812	-1.4832	8.1418	-0.0271	-0.16	0.02	8.52	5.51	10.28
2322025.16	1470.2	89.45	3.49	0.5164	0.8734	9.4138	0.7335	-0.02	0.55	12.16	6.51	13.22
2322025.20	1155.6	74.41	3.69	1.3019	-3.4937	10.0529	2.4900	-0.25	1.09	12.81	10.16	14.69

Table 4.4.3-8. Summary of Measures RCS Values for Both Bruderhedral Reflectors at Santa Barbara, CA on August 19, 1992 (Approach 1C). All Angles are in Degrees and All Reflector Values Are in dBsm

Airport: Santa Barbara
Run: 081992-1C
Reflector: 23 dBsm

file	reflector range(m)	corrected alt. (m)	dep. angle	pitch angle	roll angle	elevation angle	azimuth angle	elevation gain	azimuth gain	reflector peak 1	reflector peak 2	reflector sum
2322036.16	n/a	n/a	n/a	0.2197	2.1808	n/a	n/a	n/a	n/a	n/a	n/a	n/a
2322036.20	3795.4	191.99	2.90	0.2911	-0.1593	8.8323	0.8174	-0.01	0.61	20.01	10.67	20.49
2322036.24	3472.6	173.39	2.86	-0.3131	0.4120	8.0447	0.4364	-0.19	0.33	21.81	19.64	23.87
2322036.28	3150.0	157.45	2.87	-0.7251	0.1263	7.6011	-0.1630	-0.60	0.13	7.78	14.15	15.05
2322036.32	2828.0	137.62	2.79	-1.3129	-0.5878	7.0022	-0.9883	-1.50	0.84	11.98	21.42	21.89
2322036.36	2505.1	119.99	2.75	-1.7413	0.1373	6.4488	-0.5281	-2.56	0.45	15.81	21.04	22.18
2322036.40	2182.5	101.20	2.66	0.9668	-4.5154	8.9452	0.7122	0.00	0.53	26.42	12.72	26.60
2322036.44	1853.0	86.81	2.69	1.3019	-2.6532	9.2037	1.8279	0.00	0.83	11.63	19.68	20.31
2322036.48	1530.9	73.89	2.77	-0.2747	-2.3236	7.6167	2.2763	-0.57	0.99	13.24	23.40	23.80

Airport: Santa Barbara
Run: 081992-1C
Reflector: 18.7 dBsm

file	reflector range(m)	corrected alt. (m)	dep. angle	pitch angle	roll angle	elevation angle	azimuth angle	elevation gain	azimuth gain	reflector peak 1	reflector peak 2	reflector sum
2322036.16	3645.0	203.08	3.19	0.2197	2.1808	8.9166	-0.2243	0.00	0.19	17.56	12.14	18.66
2322036.20	3330.4	192.59	3.32	0.2911	-0.1593	9.0153	0.9292	0.00	0.70	15.49	7.00	16.07
2322036.24	3007.7	174.00	3.32	-0.3131	0.4120	8.4724	0.6524	-0.06	0.49	16.19	13.73	18.14
2322036.28	2692.5	158.05	3.37	-0.7251	0.1263	8.0651	-0.0179	-0.18	0.02	19.63	5.52	19.80
2322036.32	2370.1	138.23	3.34	-1.3129	-0.5878	7.5196	-0.4646	-0.72	0.39	11.46	2.51	11.98
2322036.36	2040.0	120.59	3.39	-1.7413	0.1373	7.0414	-0.0170	-1.44	0.01	13.91	16.02	18.10
2322036.40	1717.5	101.81	3.40	0.9668	-4.5154	9.5952	0.7649	-0.08	0.57	18.44	6.51	18.71
2322036.44	1388.0	87.42	3.61	1.3019	-2.6532	9.9925	2.0233	-0.20	0.86	6.97	14.06	14.84
2322036.48	1066.7	74.50	4.00	-0.2747	-2.3236	8.6008	3.5758	-0.02	1.41	10.50	15.91	17.01

Table 4.4.3-9. Summary of Measures RCS Values for Both Bruderhedral Reflectors at Santa Barbara, CA on August 19, 1992 (Approach 1D). All Angles are in Degrees and All Reflector Values Are in dBsm

Airport: Santa Barbara
Run: 081992-1D
Reflector: 23 dBsm

file	reflector range(m)	corrected alt. (m)	dep. angle	pitch angle	roll angle	elevation angle	azimuth angle	elevation gain	azimuth gain	reflector peak 1	reflector peak 2	reflector sum
2322047.12	n/a	206.43	n/a	-0.2582	1.4447	n/a	n/a	n/a	n/a	n/a	n/a	n/a
2322047.16	n/a	193.05	n/a	0.6427	2.3346	n/a	n/a	n/a	n/a	n/a	n/a	n/a
2322047.20	3548.1	177.58	2.87	0.7690	1.1371	9.1065	-1.2748	0.00	0.80	19.73	15.42	21.10
2322047.24	3233.6	164.17	2.91	0.3955	-0.6812	8.7607	-1.3587	0.00	0.78	14.64	7.64	15.43
2322047.28	2911.2	148.62	2.93	-0.8624	-1.7853	7.5138	-1.3859	-0.73	0.77	12.26	20.35	20.98
2322047.32	2596.8	129.21	2.85	-1.1426	-3.8232	7.2769	-1.8621	-1.06	0.72	17.53	12.47	18.71
2322047.35	2265.0	114.37	2.89	0.0055	-1.0437	8.1619	-0.2298	-0.15	0.20	-0.88	7.92	8.46
2322047.40	1935.0	95.28	2.82	0.5823	-4.6362	8.6876	0.9331	0.00	0.70	7.87	12.36	13.68
2322047.44	1621.1	87.10	3.08	0.5438	0.0385	8.5613	2.1182	-0.03	0.91	23.29	11.97	23.60

Airport: Santa Barbara
Run: 081992-1D
Reflector: 18.7 dBsm

file	reflector range(m)	corrected alt. (m)	dep. angle	pitch angle	roll angle	elevation angle	azimuth angle	elevation gain	azimuth gain	reflector peak 1	reflector peak 2	reflector sum
2322047.12	3713.8	207.03	3.20	-0.2582	1.4447	8.4927	1.2881	-0.05	0.78	15.85	15.81	16.84
2322047.16	3398.3	193.66	3.27	0.6427	2.3346	9.3545	0.8832	-0.01	0.66	14.69	13.03	16.95
2322047.20	3082.9	178.19	3.31	0.7690	1.1371	9.5257	-1.1689	-0.06	0.82	12.23	4.41	12.89
2322047.24	2768.3	164.78	3.41	0.3955	-0.6812	9.2223	-1.2882	0.00	0.79	10.62	2.28	11.21
2322047.28	2445.9	149.22	3.50	-0.8624	-1.7853	8.0318	-1.3267	-0.19	0.78	10.29	16.63	17.54
2322047.32	2131.1	129.81	3.49	-1.1426	-3.8232	7.8418	-1.2868	-0.34	0.79	19.81	12.08	20.49
2322047.35	1807.5	114.98	3.65	0.0055	-1.0437	8.8013	0.1616	0.00	0.12	15.93	4.58	16.24
2322047.40	1470.1	95.88	3.74	0.5823	-4.6362	9.4634	1.3620	-0.04	0.79	1.11	8.38	9.13
2322047.44	1156.6	87.71	4.35	0.5438	0.0385	9.5331	2.9719	-0.06	0.34	16.56	8.29	17.16

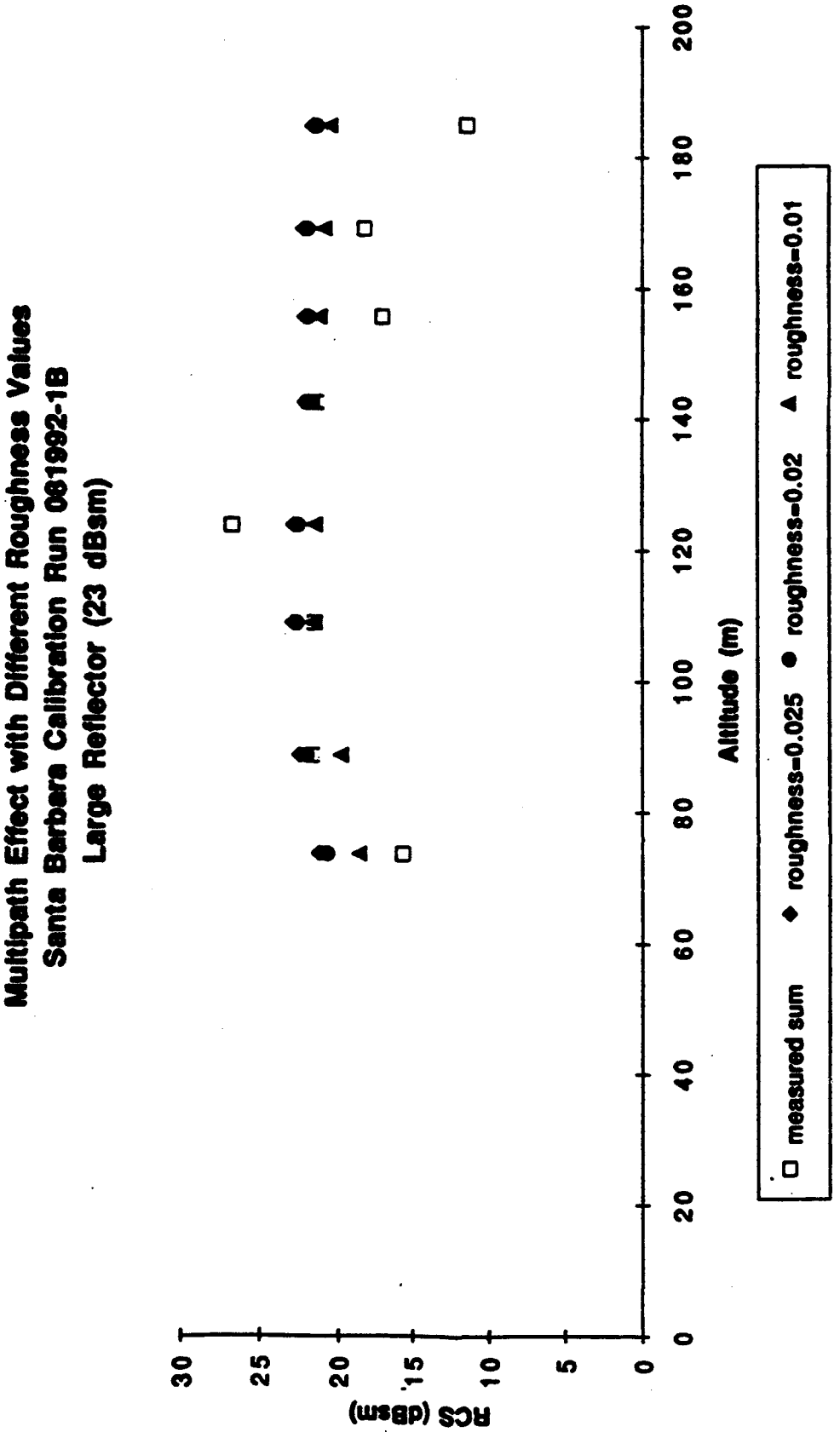

Figure 4.4.3-30. Plot of Measured and Predicted RCS Versus Altitude for the 23.0 dBsm Bruderhedral at Santa Barbara, CA on August 19, 1992 (Approach 1B). Predicted RCS Values are computed for Three Assumed RMS Surface Roughness as Indicated

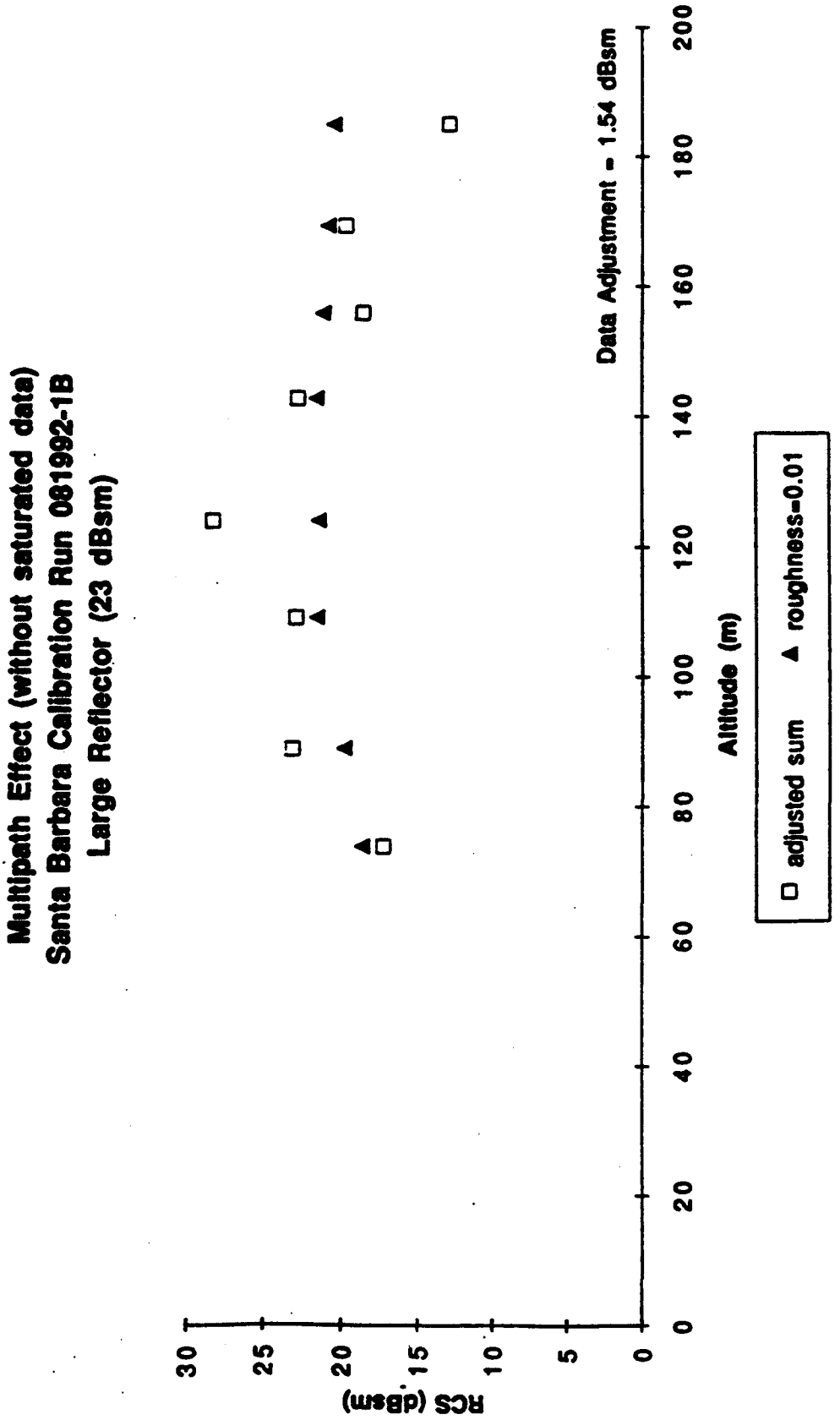

Figure 4.4.3-31. Plot of Measured RCS Sum Values After Adjustment as Well as Corresponding Predicted RCS Values Used to Compute Adjustment. Data are for the 23.0 dBsm Bruderhedral at Santa Barbara, CA on August 19, 1992 (Approach 1B)

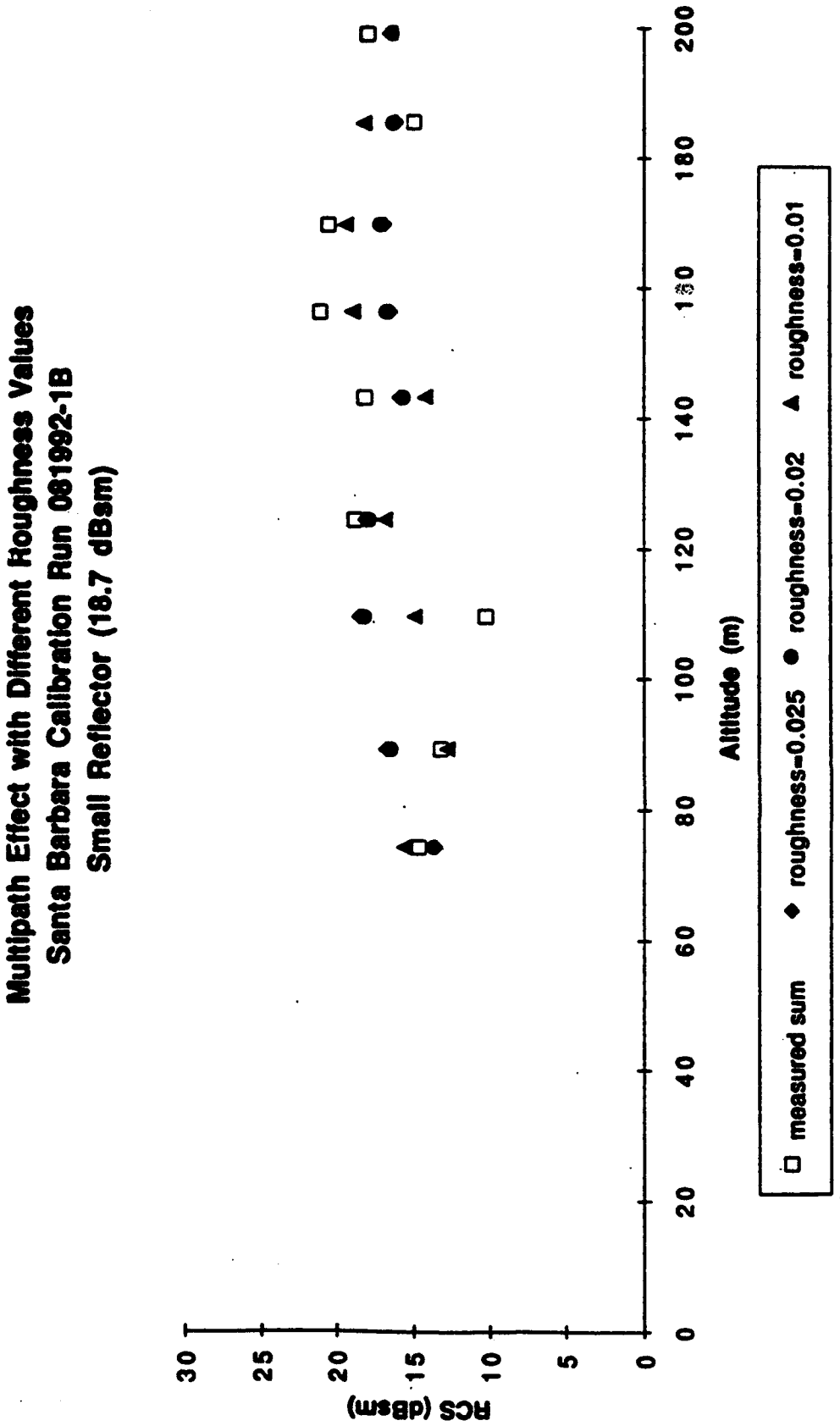

Figure 4.4.3-32. Plot of Measured and Predicted RCS Versus Altitude for the 18.7 dBsm Bruderhedral at Santa Barbara, CA on August 19, 1992 (Approach 1B). Predicted RCS Values are Computed for Three Assumed RMS Surface Roughness as Indicated

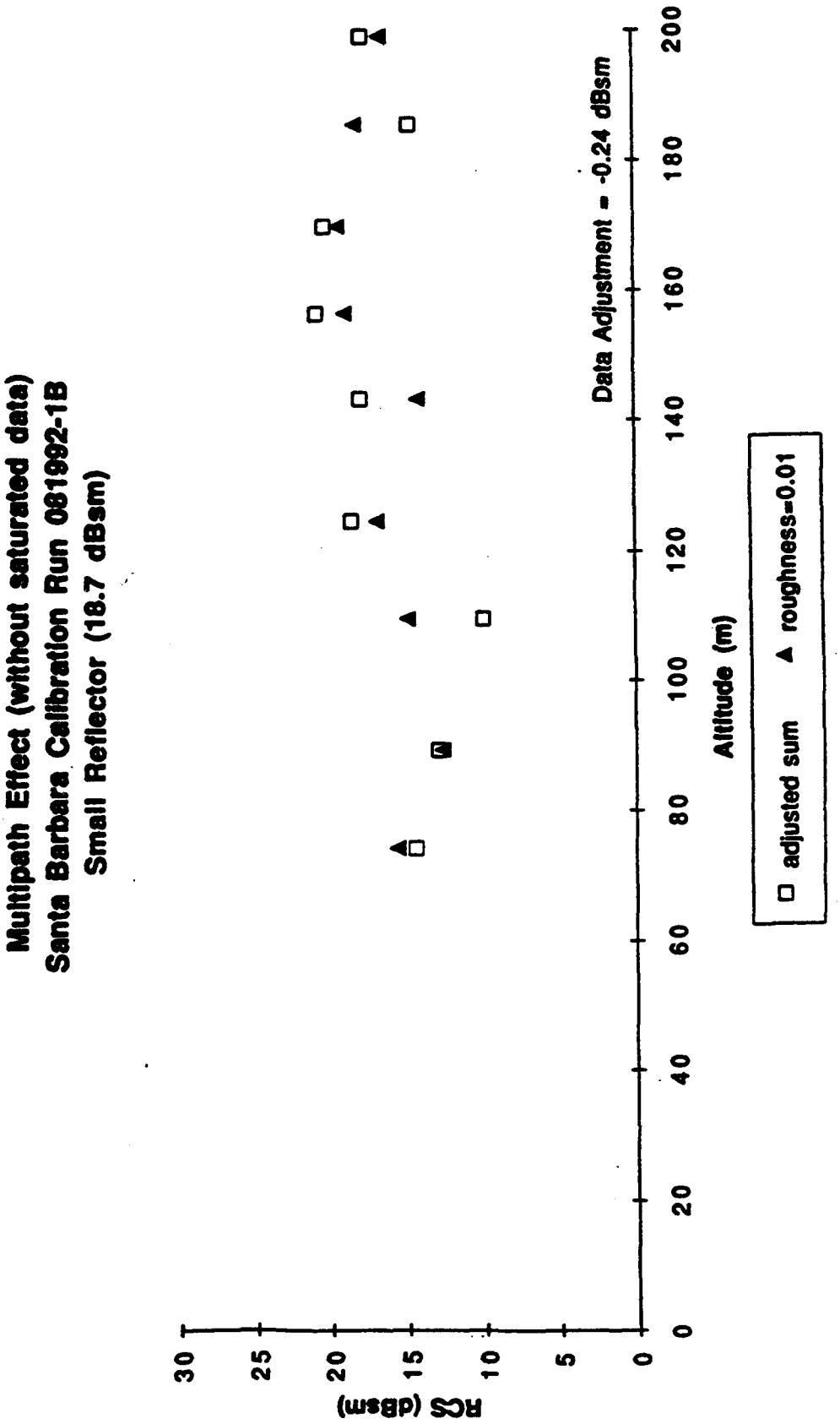

Figure 4.4.3-33. Plot of Measured RCS Sum Values After Adjustment as Well as Corresponding Predicted RCS Values Used to Compute Adjustment. Data are for the 18.7 dBsm Bruderhedral at Santa Barbara, CA on August 19, 1992 (Approach 1B)

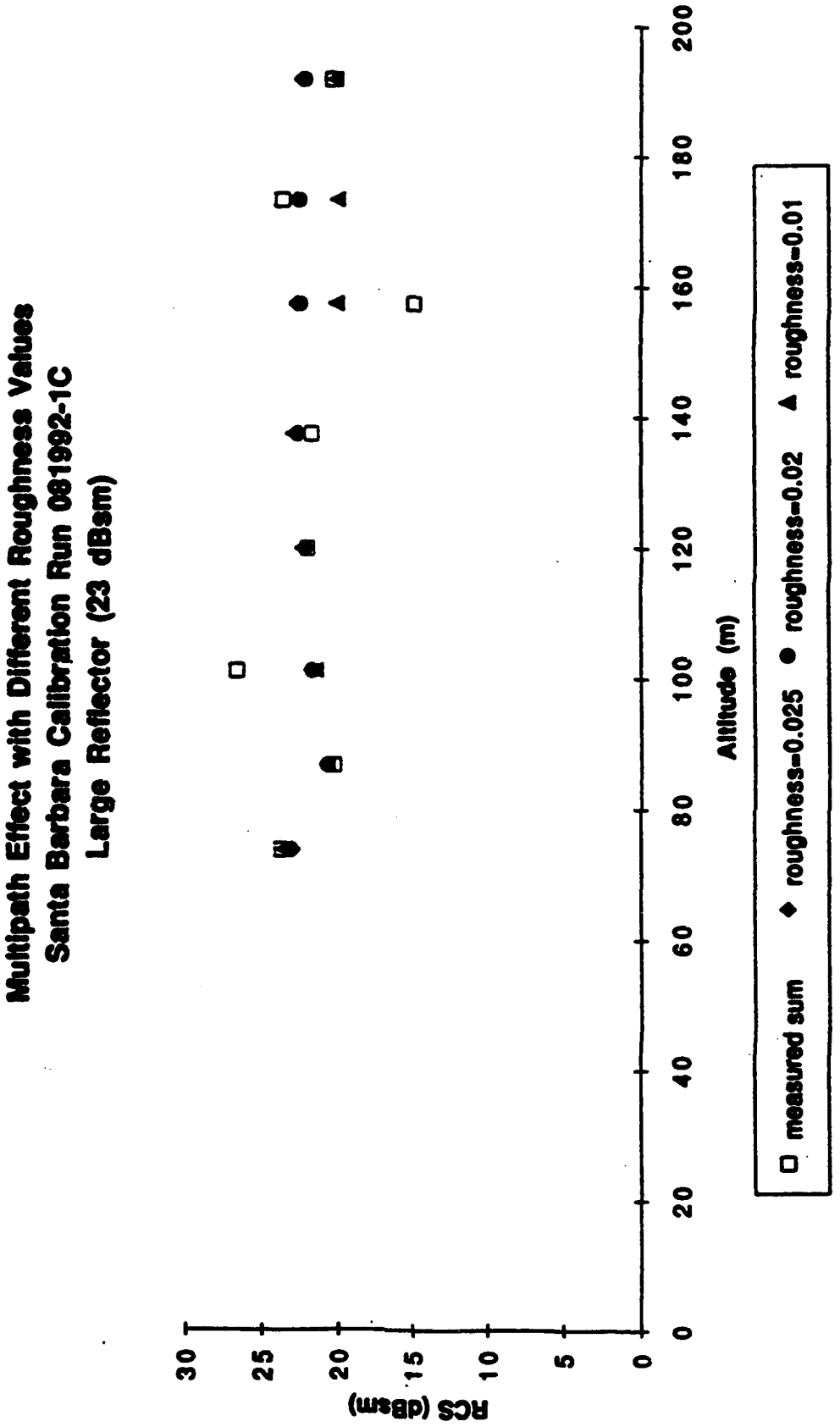

Figure 4.4.3-34. Plot of Measured and Predicted RCS Versus Altitude for the 23.0 dBsm Bruderhedral at Santa Barbara, CA on August 19, 1992 (Approach 1C). Predicted RCS Values are Computed for Three Assumed RMS Surface Roughness as Indicated

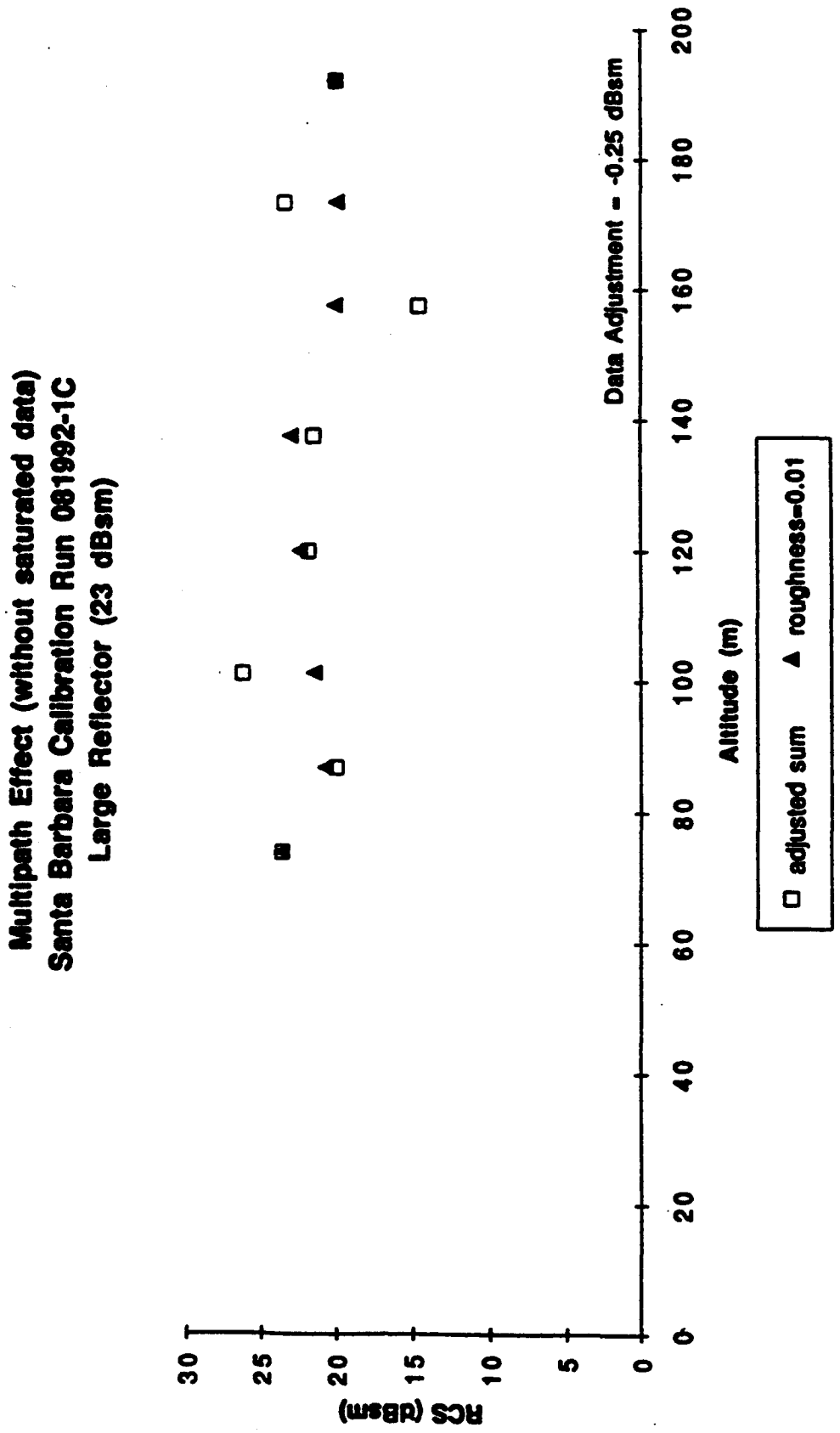

Figure 4.4.3-35. Plot of Measured RCS Sum Values After Adjustment as Well as Corresponding Predicted RCS Values Used to Compute Adjustment. Data are for the 23.0 dBsm Bruderhedral at Santa Barbara, CA on August 19, 1992 (Approach 1C)

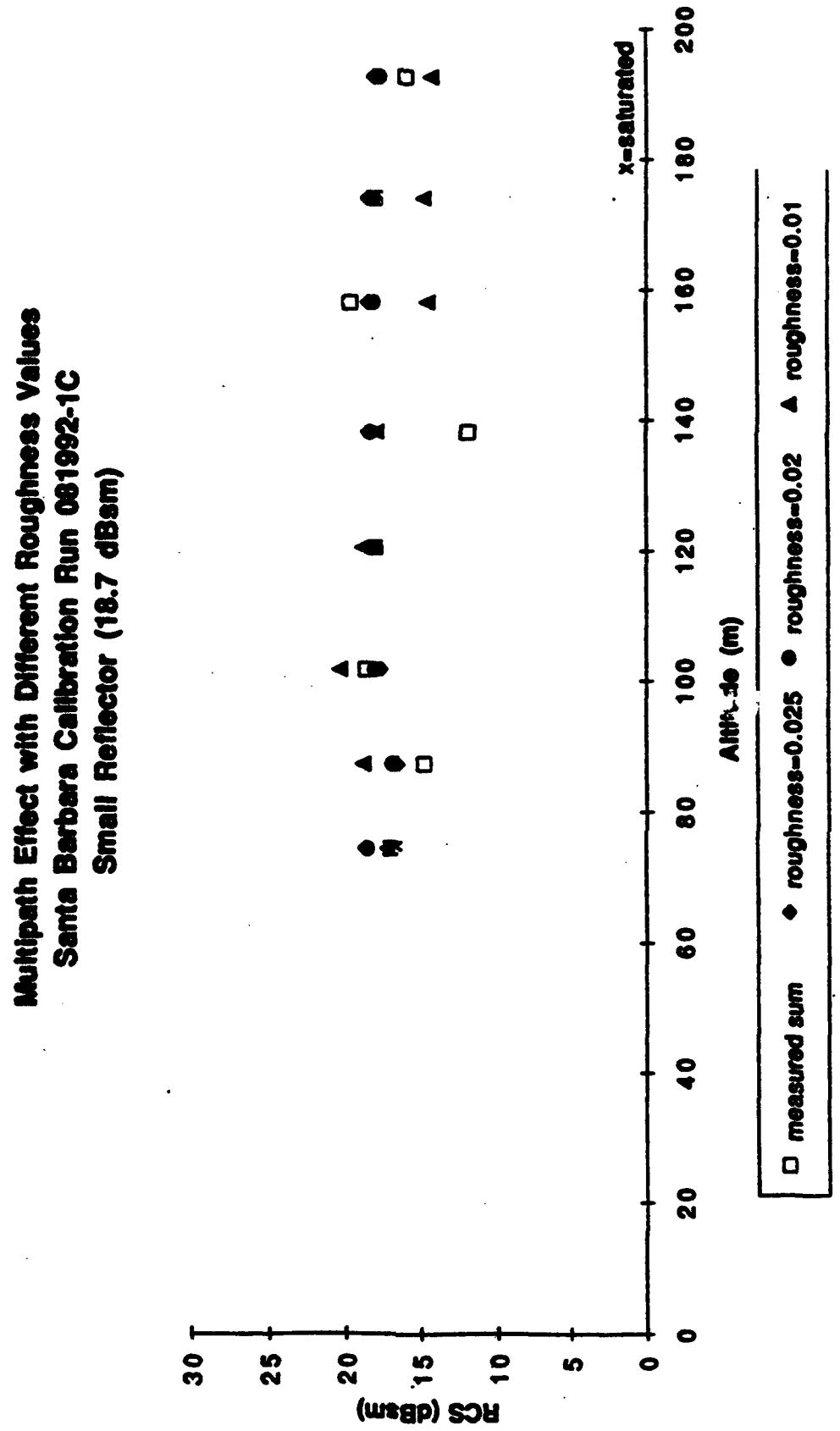

Figure 4.4.3-36. Plot of Measured and Predicted RCS Versus Altitude for the 18.7 dBsm Bruderhedral at Santa Barbara, CA on August 19, 1992 (Approach 1C). Predicted RCS Values are Computed for Three Assumed RMS Surface Roughness as Indicated

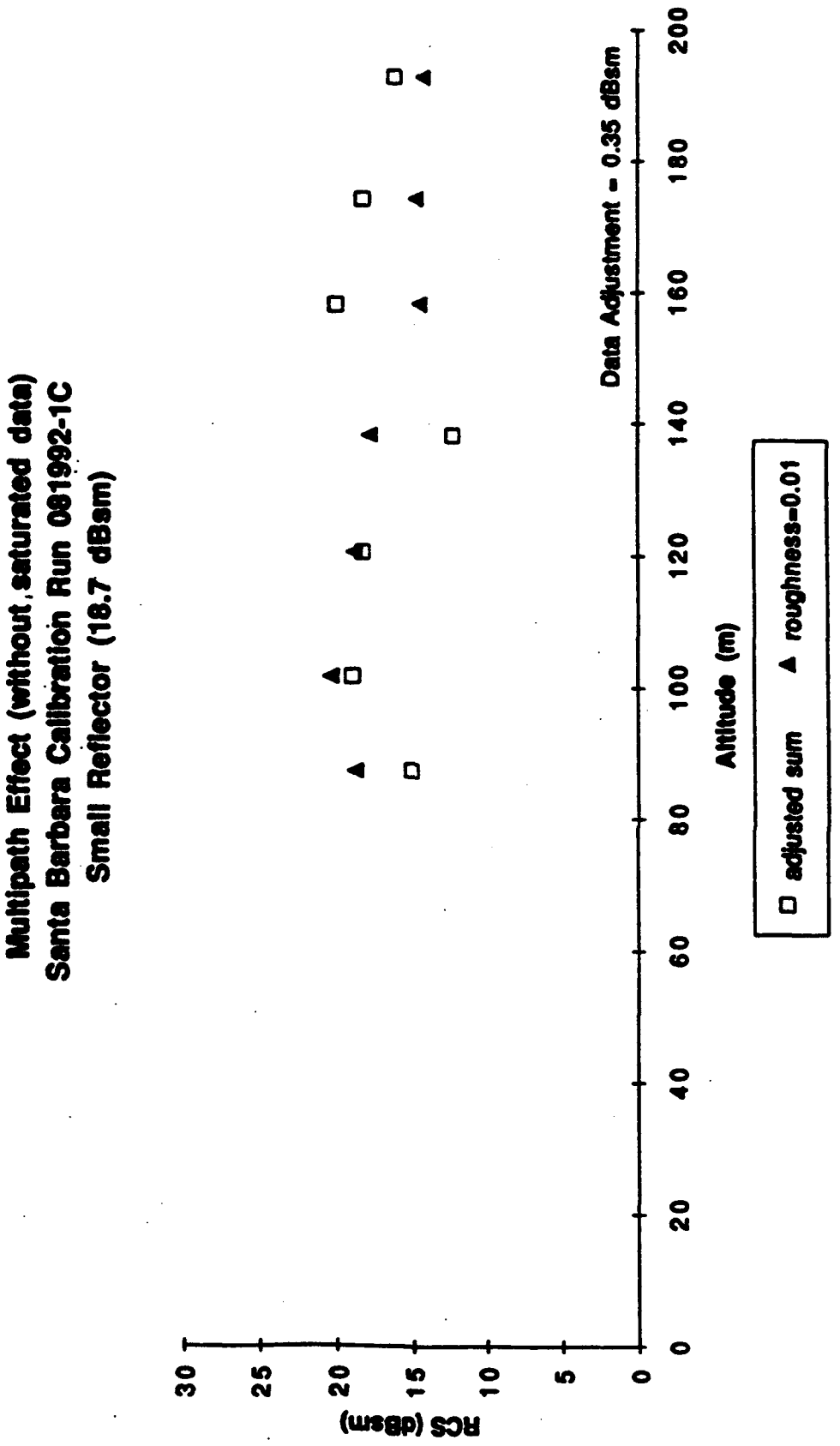

Figure 4.4.3-37. Plot of Measured RCS Sum Values After Adjustment as Well as Corresponding Predicted RCS Values Used to Compute Adjustment. Data are for the 18.7 dBsm Bruderhedral at Santa Barbara, CA on August 19, 1992 (Approach 1C)

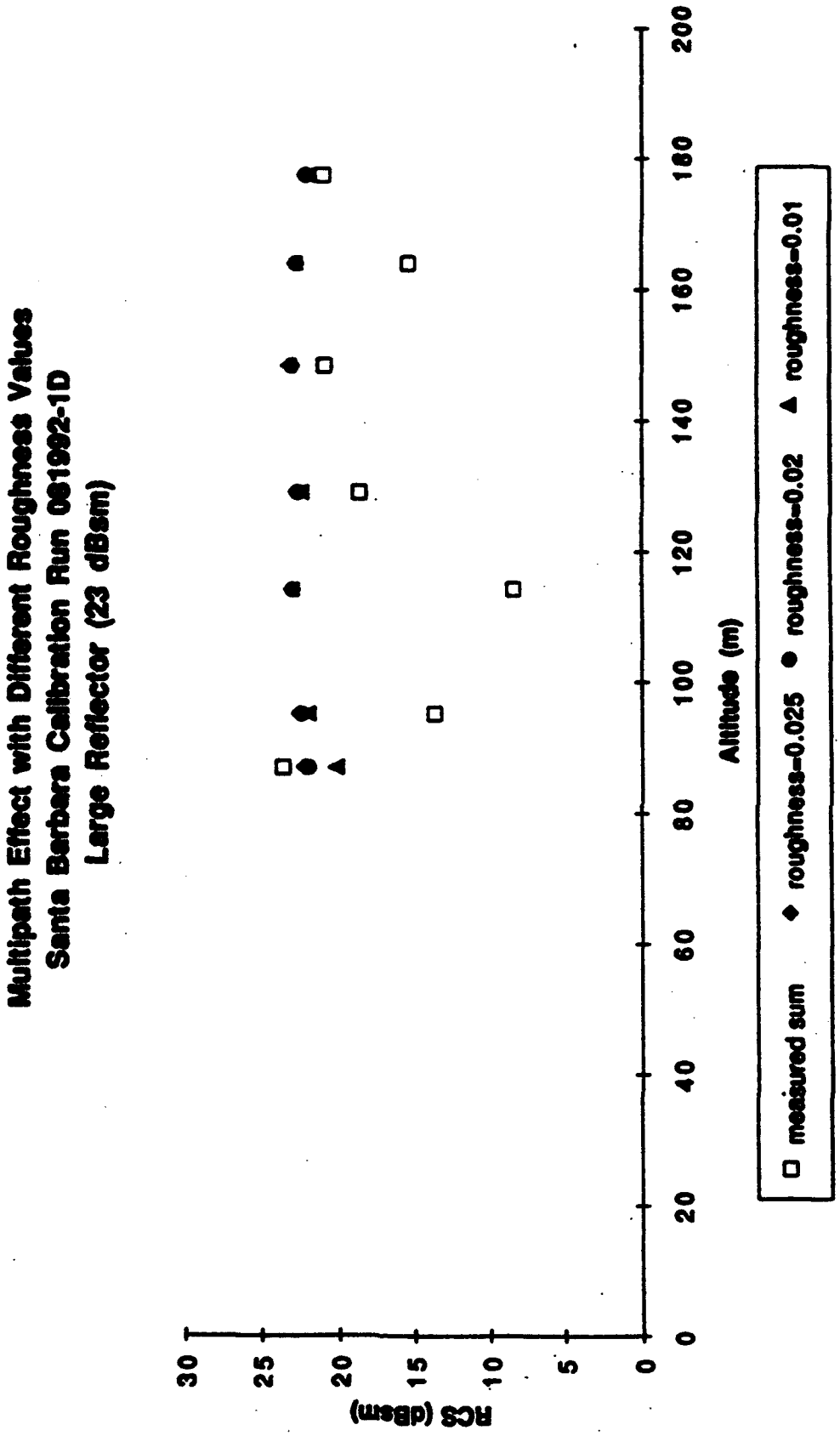

Figure 4.4.3-38. Plot of Measured and Predicted RCS Versus Altitude for the 23.0 dBsm Bruderhedral at Santa Barbara, CA on August 19, 1992 (Approach 1D). Predicted RCS Values are Computed for Three Assumed RMS Surface Roughness as Indicated

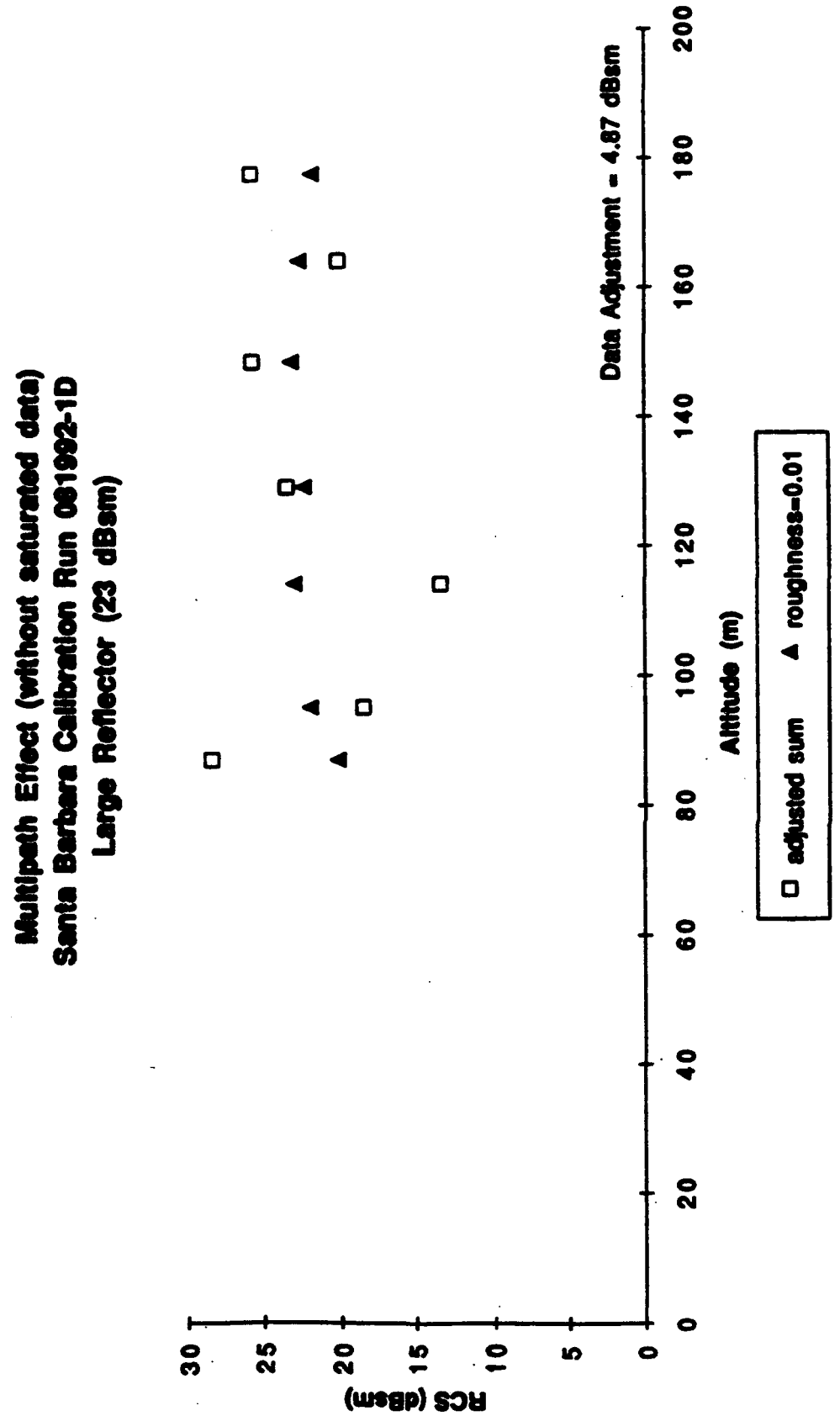

Figure 4.4.3-39. Plot of Measured RCS Sum Values After Adjustment as Well as Corresponding Predicted RCS Values Used to Compute Adjustment. Data are for the 23.0 dBsm Bruderhedral at Santa Barbara, CA on August 19, 1992 (Approach 1D)

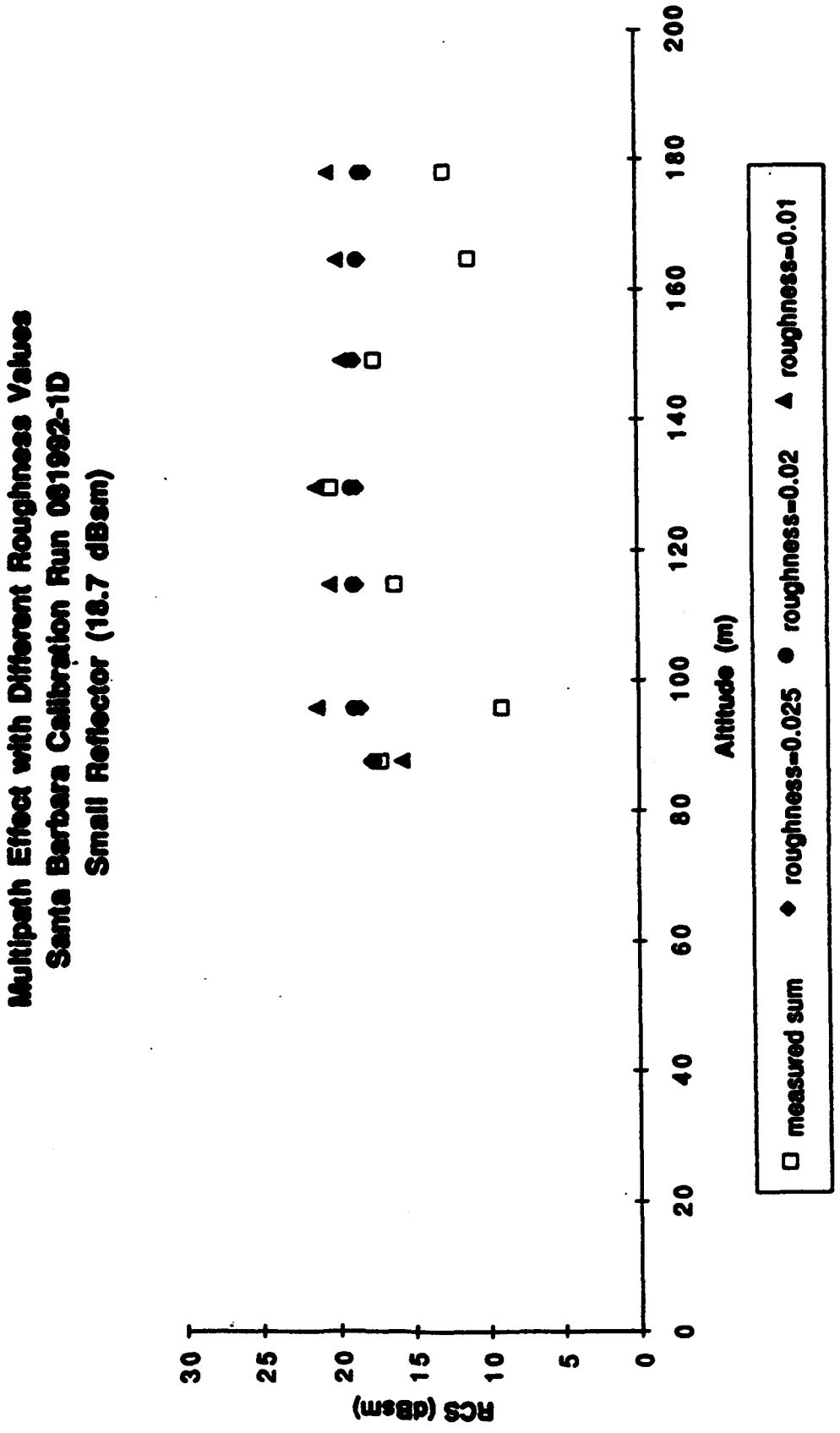

Figure 4.4.3-40 Plot of Measured and Predicted RCS Versus Altitude for the 18.7 dBsm Bruderhedral at Santa Barbara, CA on August 19, 1992 (Approach 1D). Predicted RCS Values are Computed for Three Assumed RMS Surface Roughness as Indicated

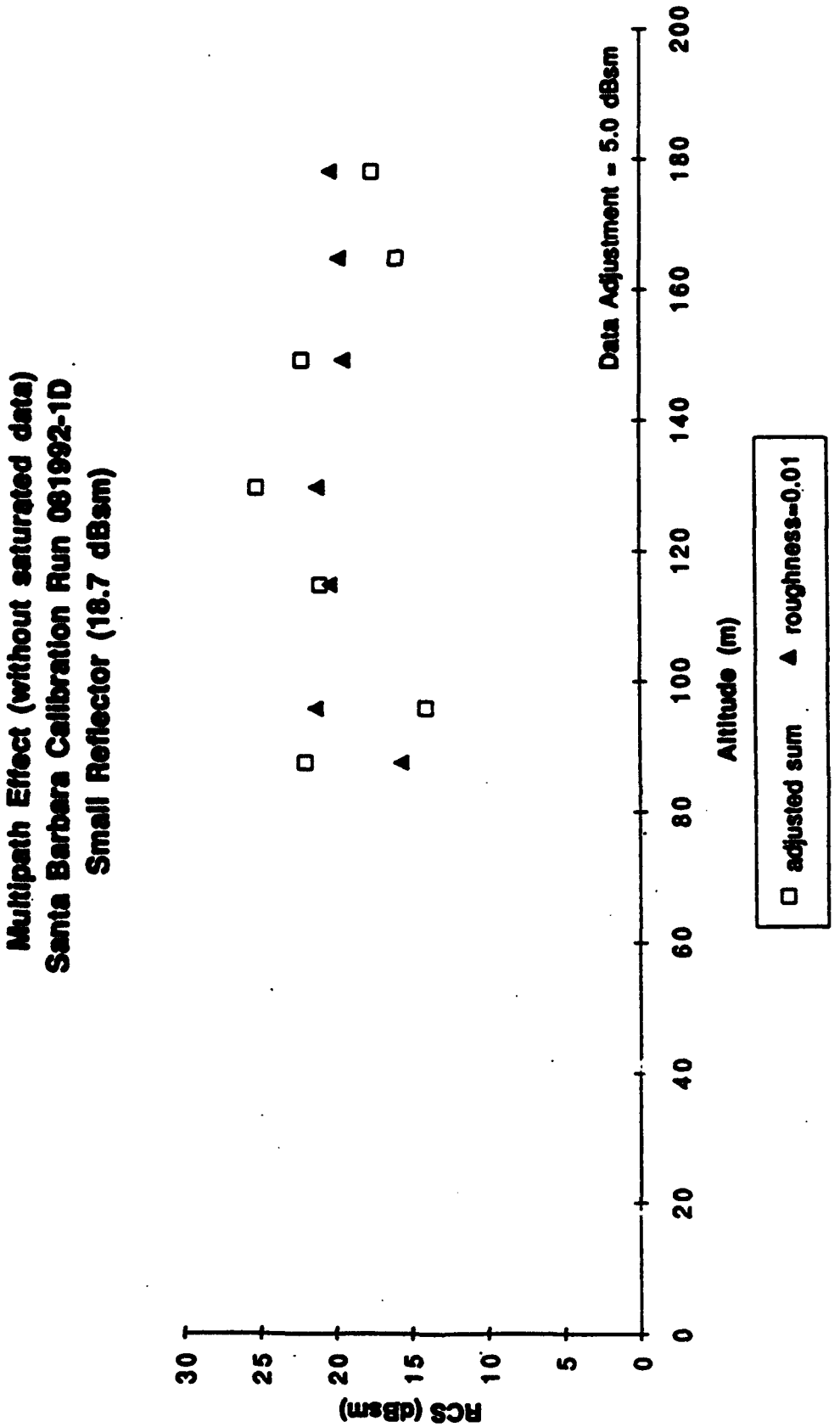

Figure 4.4.3-41. Plot of Measured RCS Sum Values After Adjustment as Well as Corresponding Predicted RCS Values Used to Compute Adjustment. Data are for the 18.7 dBsm Bruderhedral at Santa Barbara, CA on August 19, 1992 (Approach 1D)

The three predicted values are denoted by solid symbols and correspond to assumed RMS terrain roughness of 1 cm (triangles), 2 cm (circles), and 2.5 cm (diamonds). Based on this plot alone, the RCS predictions based on a 1 cm RMS roughness assumption appear to best match the measured data, although the preference is weak at best. A review of all calibration data for all three approaches led to the conclusion that the 1 cm RMS roughness predictions matched the measured data slightly better than the 2.5 cm predicted data. Thus, the 1 cm surface roughness assumption was made for all of the Santa Barbara calibration data.

Figure 4.4.3-31 was constructed from 4.4.3-30 by adjusting the eight measured RCS values by that constant offset which yielded the least mean-square-error when compared to the corresponding predicted RCS values. Note that none of the measured values in Figure 4.4.3-30 were saturated and thus none were excluded from Figure 4.4.3-31. As indicated in this latter figure, the mean-square-error is minimized when the eight measured RCS values are all increased by 1.54 dBsm. In other words, this set of measured values indicate that the factor $F_{calibration}$ in Equation 4.4.3-1 is actually 1.54 dB.

Figures 4.4.3-32 and 4.4.3-33 are similar to Figures 4.4.3-30 and 4.4.3-31, except that the former pertain to the smaller (18.7 dBsm) reflector, whereas the latter address the larger (23.0 dBsm) reflector. The estimate of $F_{calibration}$ based on the smaller reflector in approach 1B is -0.24 dB.

Figures 4.4.3-34 through 4.4.3-41 parallel Figures 4.4.3-30 through 4.4.3-33 just discussed, except that they pertain to calibration approaches 1C and 1D, respectively. The corresponding estimates of the factor $F_{calibration}$ are -0.25 dB (see Figure 4.4.3-35), 0.35 dB (Figure 4.4.3-37), 4.87 dB (Figure 4.4.3-39), and 5.00 dB (Figure 4.4.3-41). Table 4.4.3-10 below summarizes the estimates of $F_{calibration}$ based on the available calibration data from Santa Barbara.

The overall estimate of $F_{calibration}$ for Santa Barbara on 8/19/92 is computed based on a weighed average of the six individual estimates. This computation yields $F_{calibration}$ = 1.73 dB. For comparison purposes, the entire analysis outlined above was repeated using the RCS predictions based on an assumed RMS surface roughness of 2.5 cm. The overall estimate of $F_{calibration}$ which resulted is 2.13 dB. This result increases one's confidence in the computed calibration factor since the results do not appear overly sensitive to the surface roughness assumption in this case.

Table 4.4.3-10. Summary of Absolute Calibration Data from Santa Barbara, California on 8/19/92

Approach	Reflector	No. of Points	Average Adjustment
1B	23.0	8	1.54 dB
1B	18.7	9	-0.24 dB
1C	23.0	8	-0.25 dB
1C	18.7	7	0.35 dB
1D	23.0	7	4.87 dB
1D	18.7	7	5.00 dB

4.4.3.2.5 Santa Maria, CA Calibration (8/20/92)

Radar data were analyzed for two calibration approaches against the Santa Maria, CA airport on 8/20/92. These approaches are designated 1B and 1C. Table 4.4.3-11 presents key data for each of nine snapshots analyzed in approach 1B. Table 4.4.3-12 presents data for the nine snapshots along approach 1C. The format of these tables is the same as that for Tables 4.4.31 and 4.4.3-2 described in Section 4.4.3.2.2 above for the Arcata calibration.

Four pairs of plots for the Santa Maria calibration approaches are included as Figures 4.4.3-42 through 4.4.3-49. Figure 4.4.3-42 plots the measured RCS and three predicted RCS values versus radar altitude for the 23 dBsm Bruderhedral. The data are taken from eight snapshots along approach 1B. (No data were available for this reflector in one snapshot for this approach.) As in the Arcata case, the predicted RCS is based on an assumed moisture content of 15% for the terrain.

The three predicted values are denoted by solid symbols and correspond to assumed RMS terrain roughness of 1 cm (triangles), 1.75 cm (circles), and 2.5 cm (diamonds). When all data for both approaches were considered, the predicted values based on a 2.5 cm RMS roughness were selected as best matching the measured values. Thus, the 2.5 cm surface roughness assumption was made for all of the Santa Maria calibration data.

Figure 4.4.3-43 was constructed from 4.4.3-42 by adjusting the six non-saturated measured RCS values by that constant offset which yielded the LMSE when compared to the corresponding predicted RCS values based on the 2.5 cm RMS roughness assumption. Note that two of the measured values in Figure 4.4.3-42 were saturated and thus were excluded from Figure 4.4.3-43. As indicated in this latter figure, the mean-square error is minimized when the eight measured RCS

values are all decreased by 1.85 dBsm. In other words, this set of measured values indicates that the factor $F_{calibration}$ in Equation 4.4.3-1 is actually -1.85 dB.

Figures 4.4.3-44 and 4.4.3-45 are similar to Figures 4.4.3-42 and 4.4.3-43, except that the former pertain to the smaller (18.7 dBsm) reflector, whereas the latter address the larger (23.0 dBsm) reflector. The estimate of $F_{calibration}$ based on the smaller reflector in approach 1B is -1.25 dB.

Figures 4.4.3-46 through 4.4.3-49 parallel Figures 4.4.3-42 through 4.4.3-45 just discussed, except that they pertain to calibration approach 1C. The corresponding estimates of the factor $F_{calibration}$ are -4.00 dB (see Figure 4.4.3-47) and -1.05 dB (Figure 4.4.3-49). Table 4.4.3-13 below summarizes the estimates of $F_{calibration}$ based on the available calibration data from Santa Maria.

Table 4.4.3-11. Summary of Measures RCS Values for Both Bruderhedral Reflectors at Santa Maria, CA on August 19, 1992 (Approach 1B). All Angles are in Degrees and All Reflector Values Are in dBsm

Airport: Santa Maria
Run: 082092-1B
Reflector: 23 dBsm

file	reflector range(m)	corrected alt. (m)	dep. angle	pitch angle	roll angle	elevation angle	azimuth angle	elevation gain	azimuth gain	reflector peak 1	reflector peak 2	reflector sum
2331856.54	n/a	174.07	n/a	0.6317	0.6317	n/a	n/a	n/a	n/a	n/a	n/a	n/a
2331856.58	3638.3	158.03	2.49	0.4614	0.9503	8.6778	-1.3278	0.00	0.78	11.95	21.50	22.0
2331857.02	3323.7	144.51	2.49	0.9338	0.0659	9.1872	-1.5662	0.00	0.74	20.89	20.70	23.8
2331857.06	3000.5	132.20	2.53	1.2964	2.1918	9.4939	-1.3735	-0.05	0.78	20.81	18.54	22.8
2331857.10	2689.2	116.17	2.48	1.6534	1.2469	9.8545	-3.4294	-0.16	0.59	17.40	15.96	19.7
2331857.14	2374.7	103.59	2.50	1.2799	-1.5765	9.5950	-3.3694	-0.08	0.57	24.17	19.49	25.4
2331857.18	2051.0	87.18	2.44	0.7636	0.5493	8.7860	-3.4457	0.00	0.59	25.61	18.58	26.4
2331857.22	1731.5	68.60	2.27	-0.5933	-0.3900	7.3664	-4.9127	-0.95	0.75	27.03	19.45	27.7
2331857.26	1401.5	51.20	2.09	0.3241	-2.2907	8.2117	-5.2070	-0.14	0.69	23.30	23.38	26.4

Airport: Santa Maria
Run: 082092-1B
Reflector: 18.7 dBsm

file	reflector range(m)	corrected alt. (m)	dep. angle	pitch angle	roll angle	elevation angle	azimuth angle	elevation gain	azimuth gain	reflector peak 1	reflector peak 2	reflector sum
2331856.54	3496.2	178.62	2.93	0.6317	0.6317	9.1827	-1.5798	0.00	0.73	9.61	15.77	16.7
2331856.58	3180.9	162.57	2.93	0.4614	0.9503	9.0545	-1.5044	0.00	0.75	17.06	11.87	18.2
2331857.02	2859.2	149.06	2.99	0.9338	0.0659	9.6184	-1.9705	-0.09	0.66	12.75	20.56	21.2
2331857.06	2535.9	136.74	3.09	1.2964	2.1918	9.9579	-1.9170	-0.19	0.67	12.25	18.61	19.5
2331857.10	2223.7	120.71	3.11	1.6534	1.2469	10.4130	-3.5328	-0.62	0.61	8.62	14.44	15.4
2331857.14	1909.8	108.13	3.25	1.2799	-1.5765	10.2449	-3.7860	-0.42	0.66	15.87	19.23	20.9
2331857.18	1586.5	91.73	3.31	0.7636	0.5493	9.4983	-4.1669	-0.05	0.71	8.69	15.66	16.5
2331857.22	1266.4	73.14	3.31	-0.5933	-0.3900	8.2268	-5.7132	-0.13	0.54	20.17	20.42	23.3
2331857.26	929.3	55.74	3.44	0.3241	-2.2907	9.3218	-6.5912	0.00	0.75	3.43	15.00	15.3

Table 4.4.3-12. Summary of Measures RCS Values for Both Bruderhedral Reflectors at Santa Maria, CA on August 19, 1992 (Approach 1C). All Angles are in Degrees and All Reflector Values Are in dBsm

Airport: Santa Maria
Run: 062092-1C
Reflector: 23 dBsm

file	reflector range(m)	corrected alt. (m)	dep. angle	pitch angle	roll angle	elevation angle	azimuth angle	elevation gain	azimuth gain	reflector peak 1	reflector peak 2	reflector sum
2331907.06	n/a	174.29	n/a	1.3623	0.0275	n/a	n/a	n/a	n/a	n/a	n/a	n/a
2331907.10	3758.8	163.30	2.49	1.6260	1.2579	9.9999	-1.7184	-0.20	0.71	10.77	20.87	21.3
2331907.14	3452.6	149.65	2.40	0.6702	0.0385	9.1363	-2.2511	0.00	0.61	24.35	23.58	27.0
2331907.18	3136.1	137.85	2.52	0.3900	0.4285	8.7334	-1.5748	0.00	0.74	14.76	15.08	17.9
2331907.22	2818.3	118.42	2.41	-0.0110	1.8732	8.1784	-3.9325	-0.15	0.69	17.59	23.42	24.4
2331907.26	2495.5	103.18	2.37	0.2802	0.3076	8.5533	-3.8401	-0.03	0.67	21.84	22.67	25.3
2331907.30	2173.8	85.79	2.26	-0.3351	-1.8512	8.0868	-4.0895	-0.17	0.70	26.98	17.19	27.4
2331907.34	1843.0	73.18	2.28	-2.1533	-1.1096	6.0962	-4.2965	-3.30	0.71	22.64	28.05	29.1
2331907.38	1521.0	53.68	2.02	-1.4392	-4.3890	6.7156	-4.5754	-2.01	0.73	27.60	17.38	28.0

Airport: Santa Maria
Run: 062092-1C
Reflector: 18.7 dBsm

file	reflector range(m)	corrected alt. (m)	dep. angle	pitch angle	roll angle	elevation angle	azimuth angle	elevation gain	azimuth gain	reflector peak 1	reflector peak 2	reflector sum
2331907.06	3612.4	178.84	2.84	1.3623	0.0275	10.0726	-2.9919	-0.27	0.50	12.61	17.47	18.7
2331907.10	3301.4	167.84	2.91	1.6260	1.2579	10.3847	-1.9314	-0.58	0.66	16.18	10.33	17.2
2331907.14	2987.4	154.19	2.96	0.6702	0.0385	9.5833	-2.3130	-0.07	0.60	10.61	20.61	21.0
2331907.18	2671.3	142.39	3.06	0.3900	0.4285	9.2112	-1.8412	0.00	0.68	9.68	11.89	13.9
2331907.22	2360.8	122.96	2.99	-0.0110	1.8732	8.6932	-4.2956	0.00	0.71	20.11	13.50	21.0
2331907.26	2030.5	107.72	3.04	0.2802	0.3076	9.1682	-4.2893	0.00	0.71	5.80	19.99	20.2
2331907.30	1709.1	90.33	3.03	-0.3351	-1.8512	8.8394	-4.7462	0.00	0.74	18.45	14.86	20.0
2331907.34	1385.9	77.73	3.22	-2.1533	-1.1096	6.9597	-5.1172	-1.57	0.71	23.11	13.95	23.0
2331907.38	1056.0	58.22	3.16	-1.4392	-4.3890	7.7534	-5.5163	-0.42	0.60	16.64	17.21	19.9

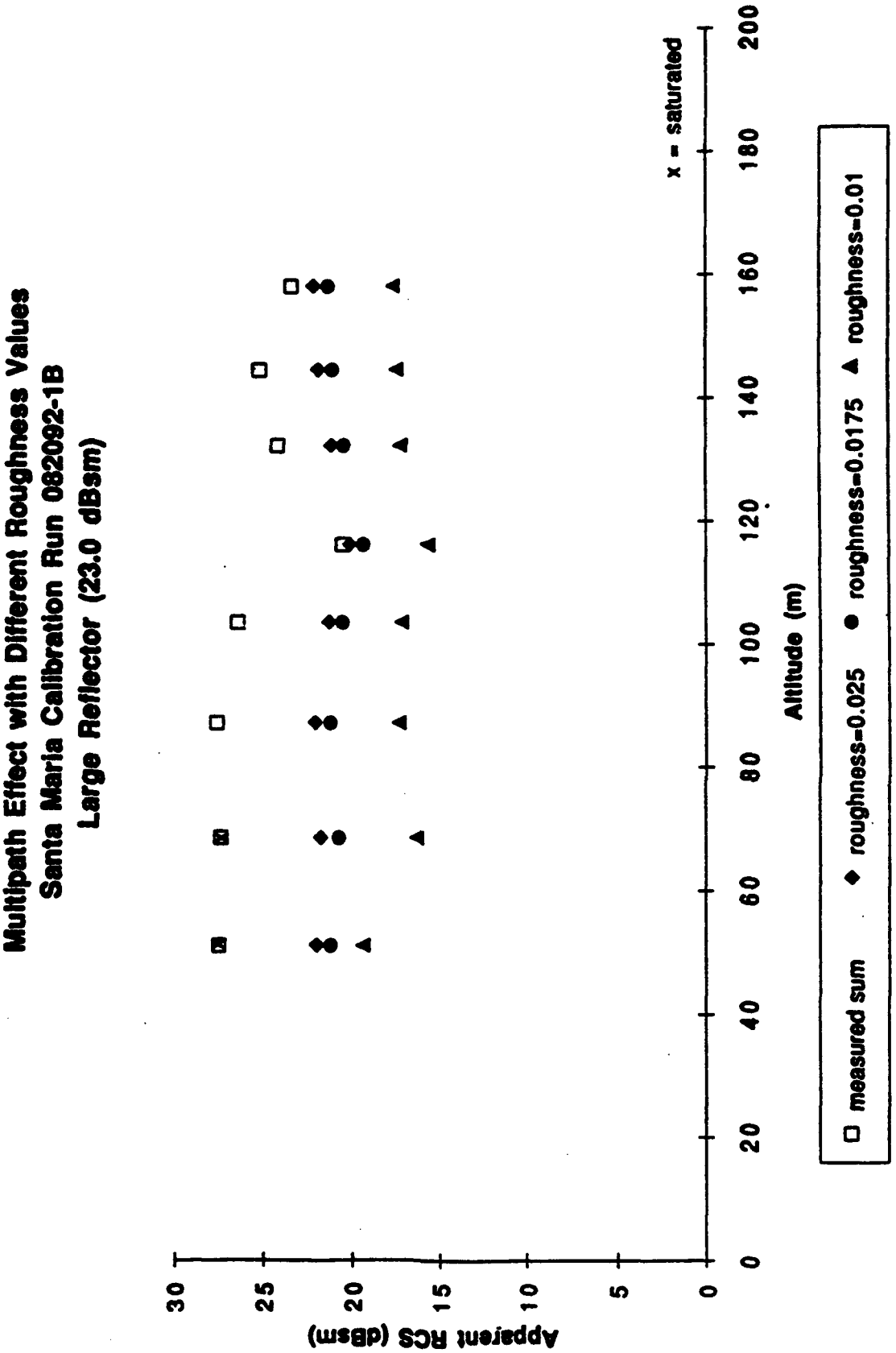

Figure 4.4.3-42. Plot of Measured and Predicted RCS Versus Altitude for the 23.0 dBsm Bruderhedral at Santa Maria, CA on August 19, 1992 (Approach 1B). Predicted RCS Values are computed for Three Assumed RMS Surface Roughness as Indicated

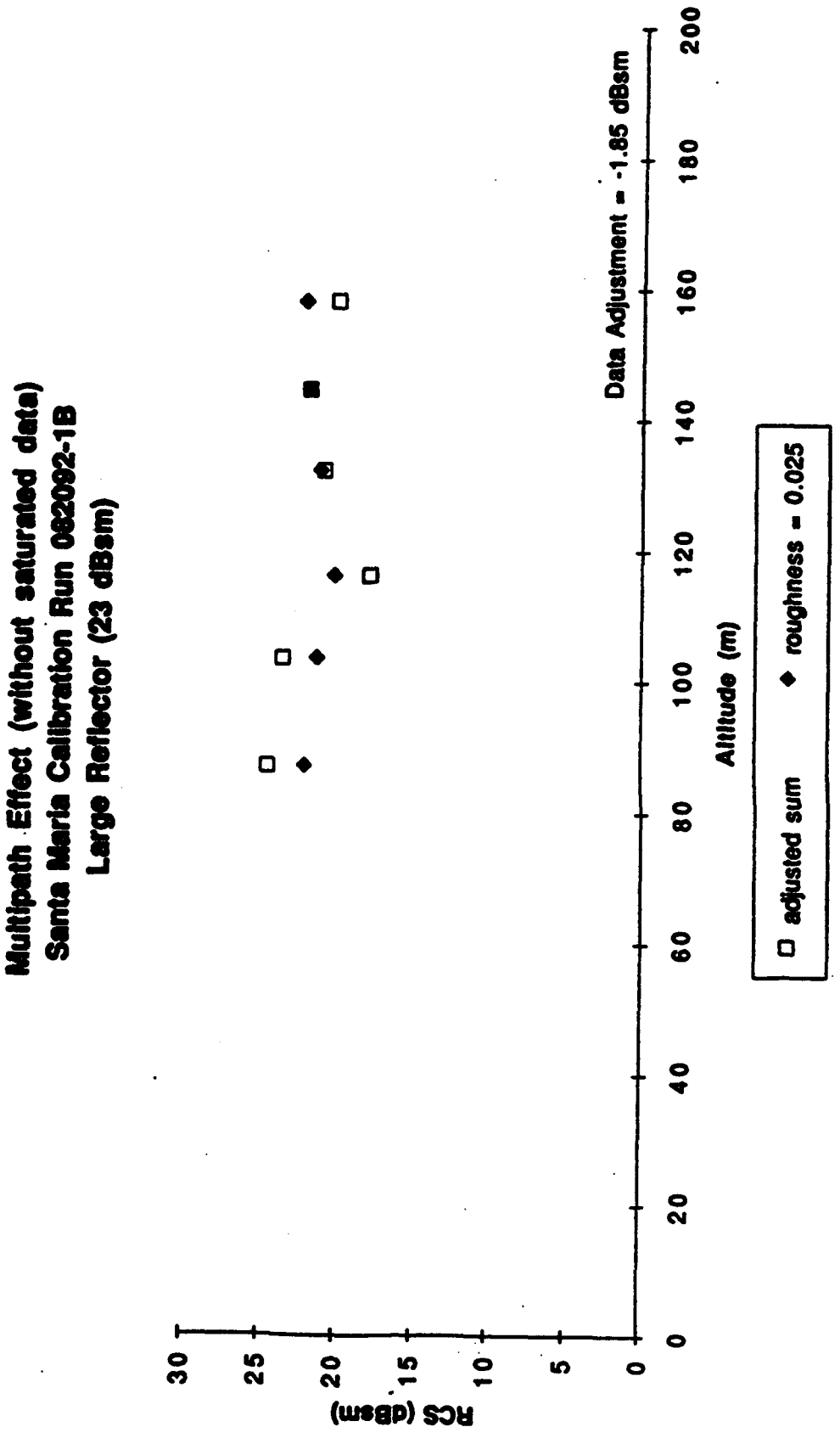

Figure 4.4.3-43. Plot of Measured RCS Sum Values After Adjustment as Well as Corresponding Predicted RCS Values Used to Compute Adjustment. Data are for the 23.0 dBsm Bruderhedral at Santa Maria, CA on August 19, 1992 (Approach 1B)

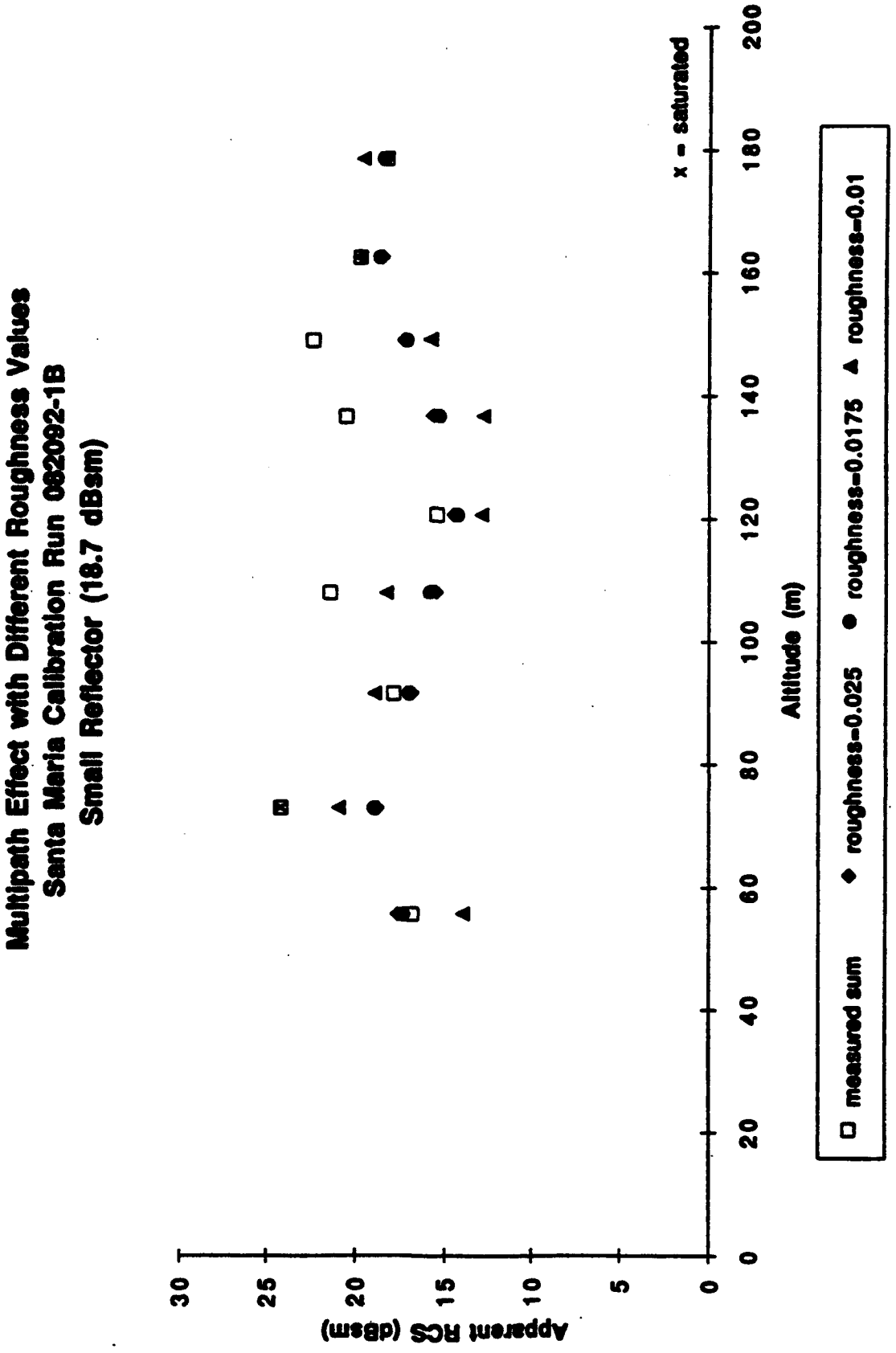

Figure 4.4.3-44. Plot of Measured and Predicted RCS Versus Altitude for the 18.7 dBsm Bruderhedral at Santa Maria, CA on August 19, 1992 (Approach 1B). Predicted RCS Values are Computed for Three Assumed RMS Surface Roughness as Indicated

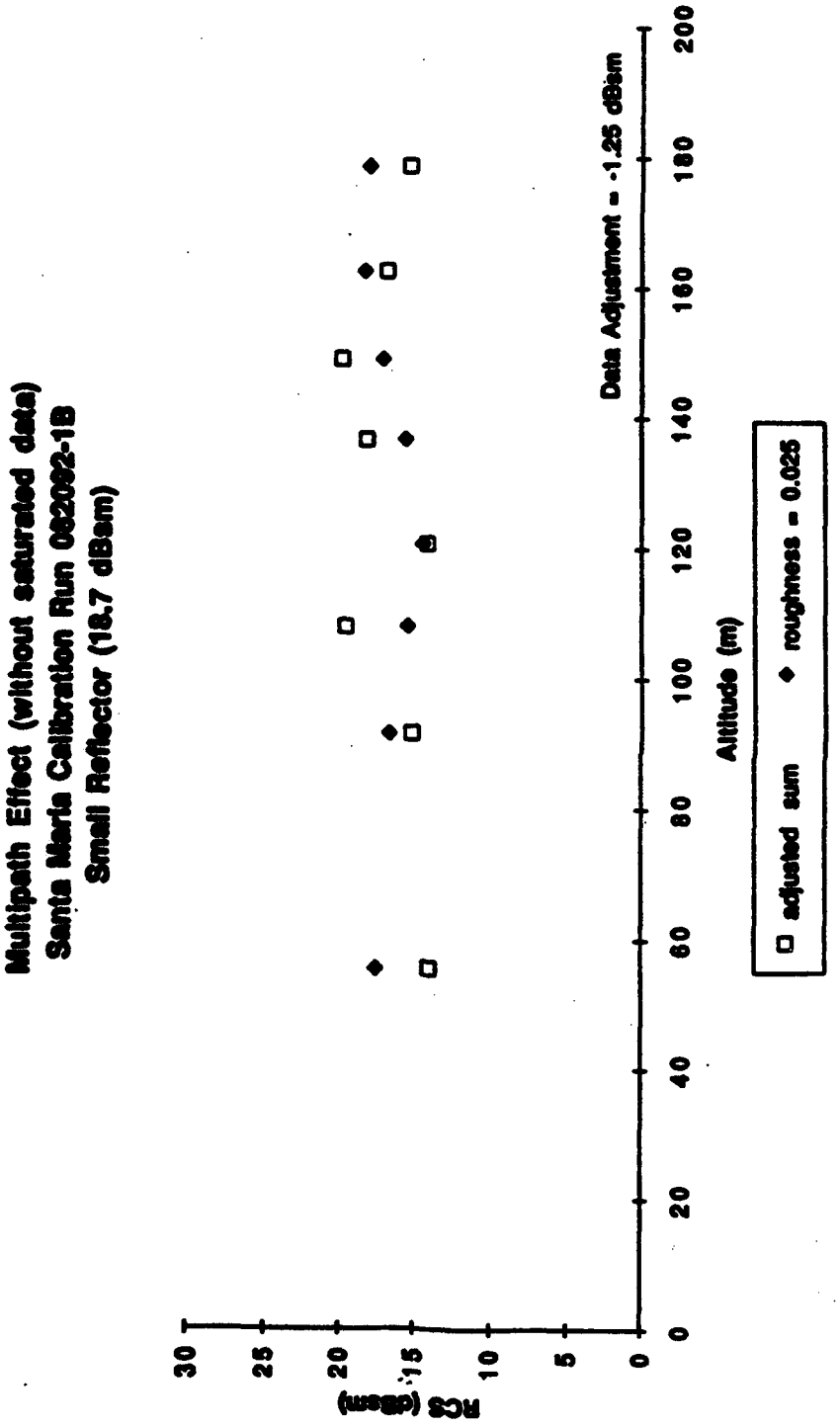

Figure 4.4.3-45. Plot of Measured RCS Sum Values After Adjustment as Well as Corresponding Predicted RCS Values Used to Compute Adjustment. Data are for the 18.7 dBsm Bruderhedral at Santa Maria, CA on August 19, 1992 (Approach 1B)

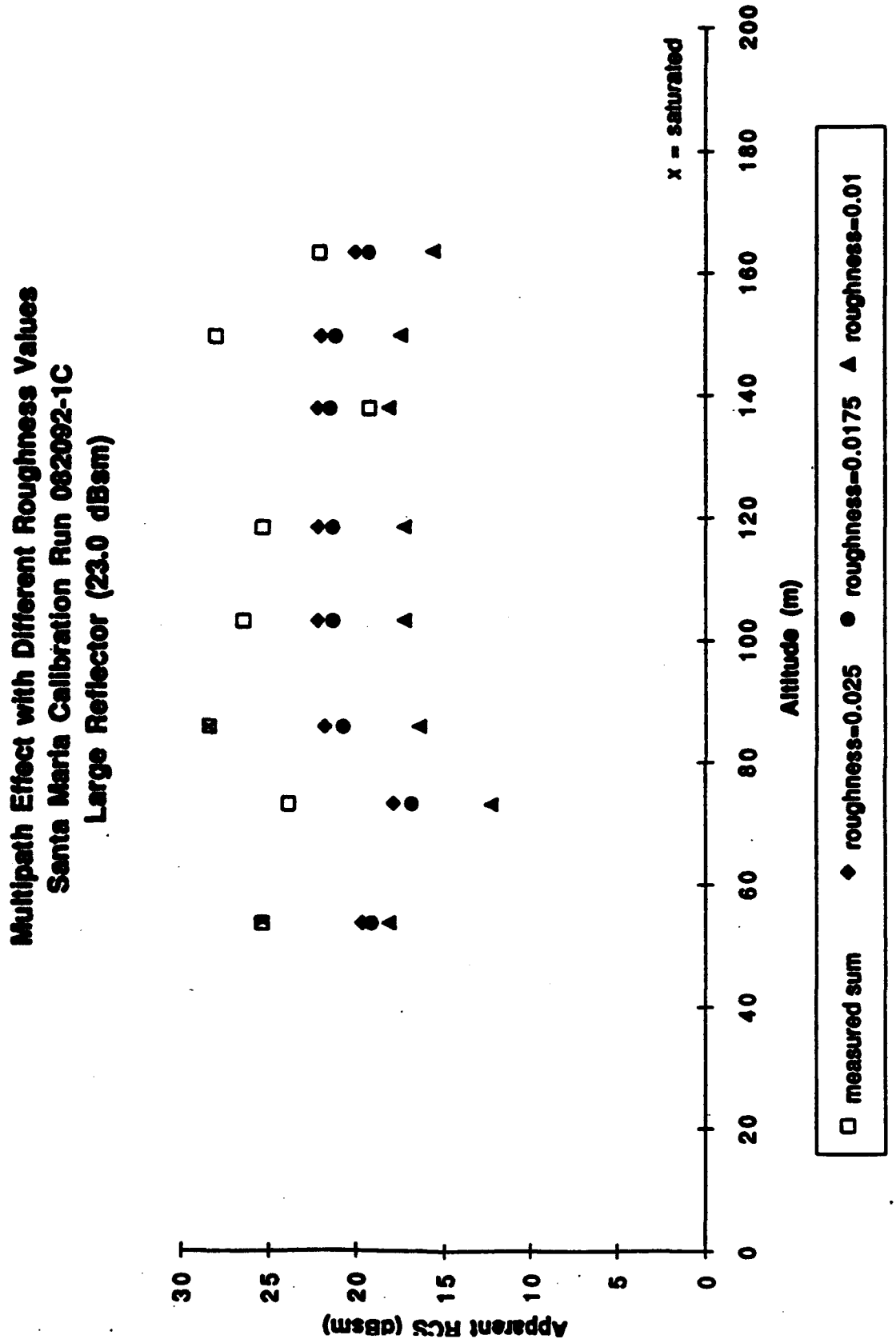

Figure 4.4.3-46. Plot of Measured and Predicted RCS Versus Altitude for the 23.0 dBsm Bruderhedral at Santa Maria, CA on August 19, 1992 (Approach 1C). Predicted RCS Values are Computed for Three Assumed RMS Surface Roughness as Indicated

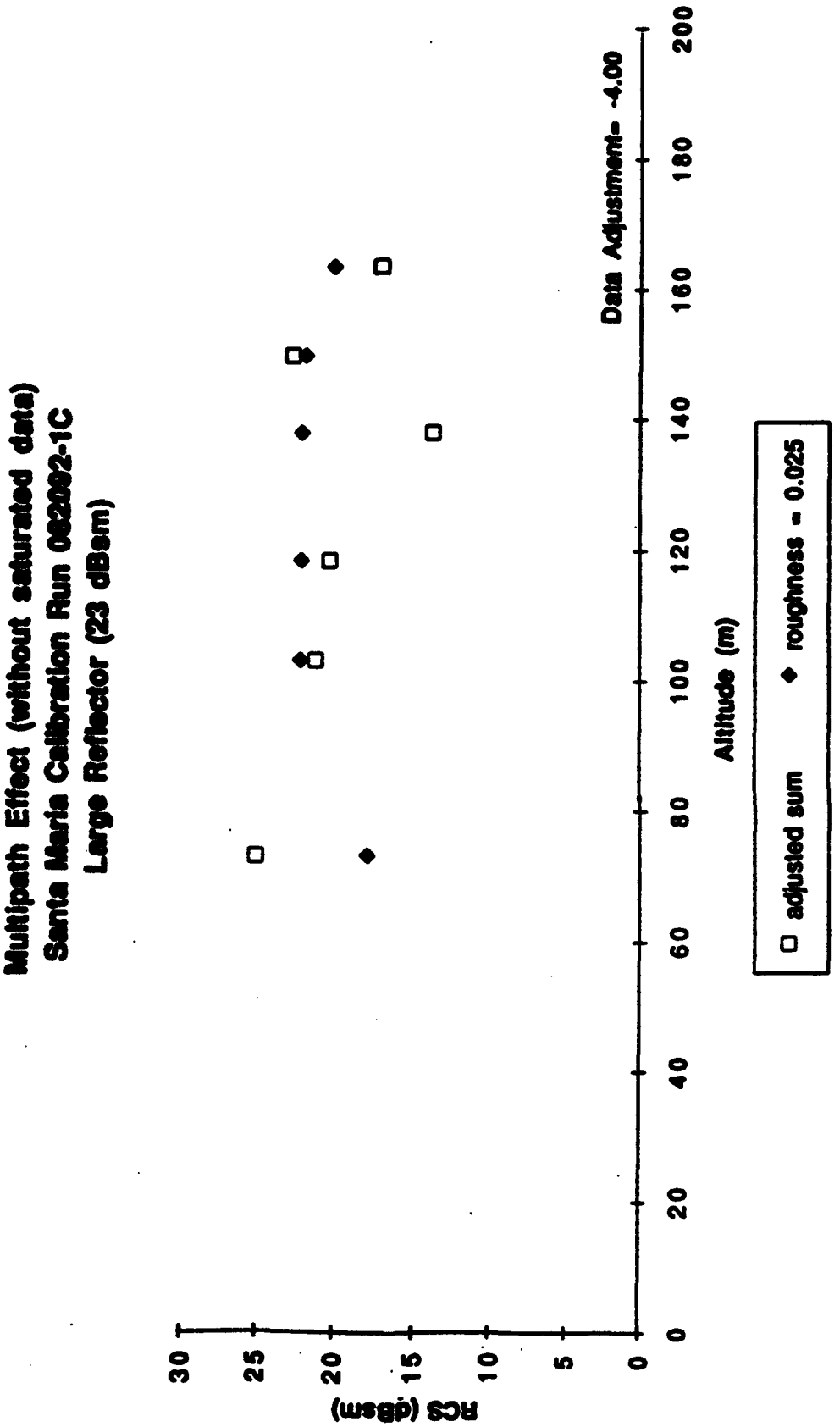

Figure 4.4.3-47. Plot of Measured RCS Sum Values After Adjustment as Well as Corresponding Predicted RCS Values Used to Compute Adjustment. Data are for the 23.0 dBsm Bruderhedral at Santa Maria, CA on August 19, 1992 (Approach 1C)

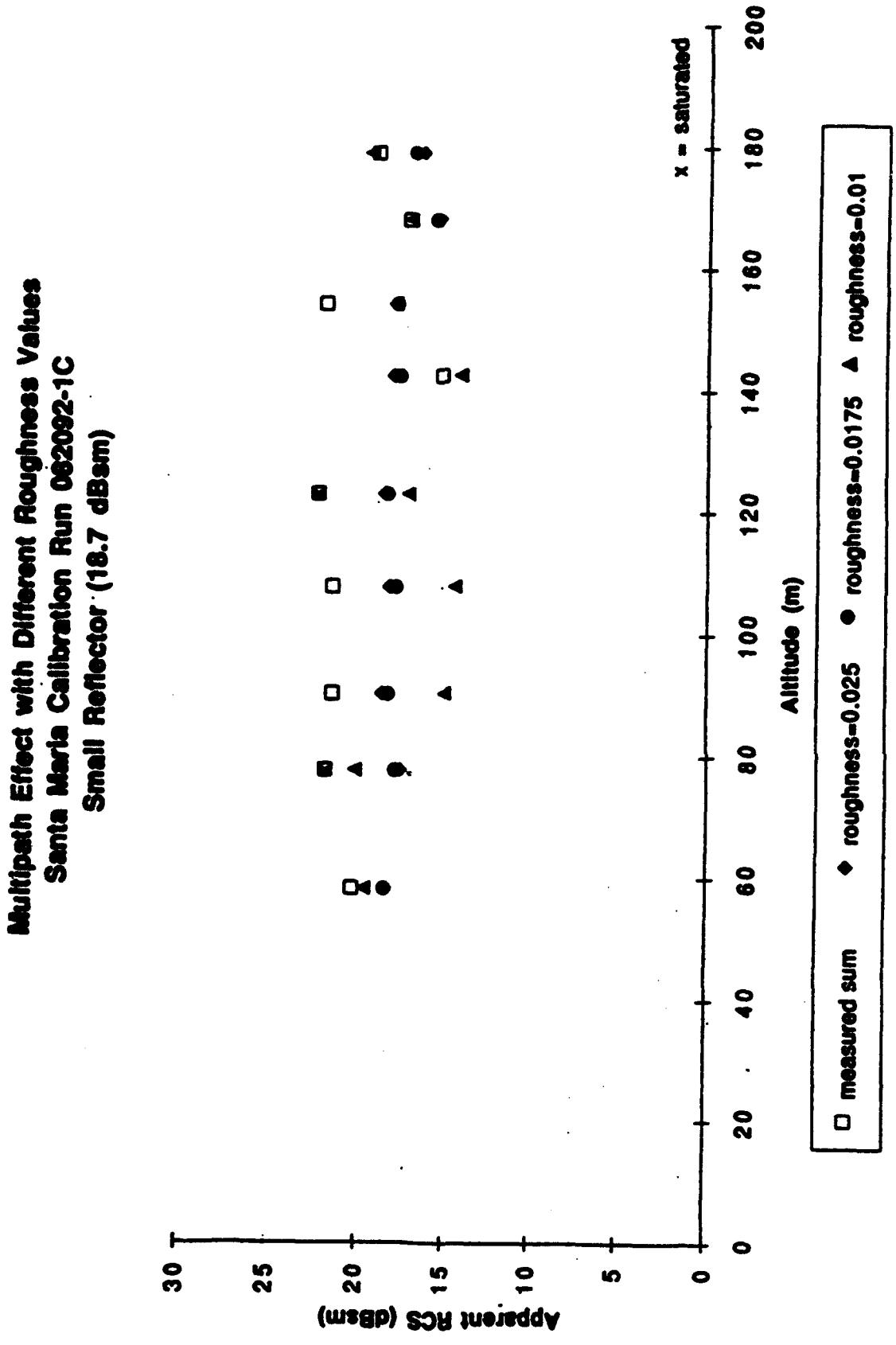

Figure 4.4.3-48. Plot of Measured and Predicted RCS Versus Altitude for the 18.7 dBsm Bruderhedral at Santa Maria, CA on August 19, 1992 (Approach 1C). Predicted RCS Values are Computed for Three Assumed RMS Surface Roughness as Indicated

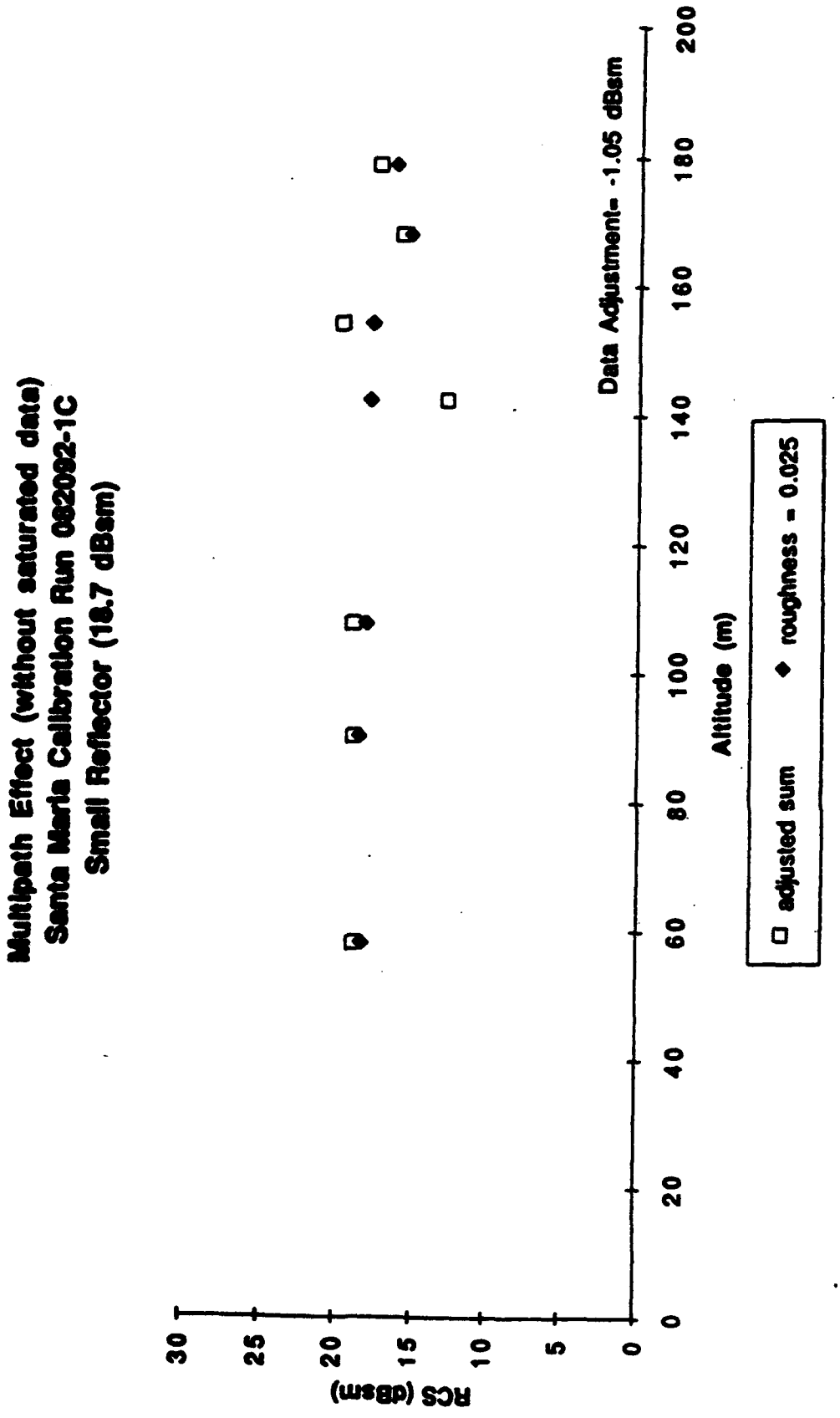

Figure 4.4.3-49. Plot of Measured RCS Sum Values After Adjustment as Well as Corresponding Predicted RCS Values Used to Compute Adjustment. Data are for the 18.7 dBsm Bruderhedral at Santa Maria, CA on August 19, 1992 (Approach 1C)

Table 4.4.3-13. Summary of Absolute Calibration Data from Santa Maria, California on 8/20/92

Approach	Reflector	No. of Points	Average Adjustment
1B	23.0	6	-1.85 dB
1B	18.7	8	-1.25 dB
1C	23.0	6	-4.00 dB
1C	18.7	7	-1.05 dB

The overall estimate of $F_{calibration}$ for Santa Maria on 8/20/92 is computed based on a weighed average of the four individual estimates. This computation yields $F_{calibration}$ = -1.94 dB.

4.4.3.2.6 Summary

Table 4.4.3-14 below summarizes the calibration results from each of the four airports. There are variations in the computed calibration values, however, a total span of roughly +/- 2 dB is reasonable and acceptable for an airborne measurements program such as this. Also note that the average of the four computed values is very small (-0.37 dB). Ideally, if all of the components of the radar system and the atmosphere had been properly characterized, then $F_{calibration}$ would be zero. The fact that the average value is so close to zero is very heartening, but is more likely due to error sources in the theoretical system characterization that tended to cancel rather than the absence of any significant errors.

Given the data in Table 4.4.3-14, GTRI elected to use both the four individual $F_{calibration}$ estimates as well as the overall -0.37 dB average. The four individual data sets noted in Table 4.4.3-14 were used to compute surface radar cross section (RCS) values in addition to serving as absolute calibration data. Since the very same data set was used for both analyses, GTRI used the estimate of $F_{calibration}$ computed for each airport in computing the corresponding RCS values for that airport. Thus, a calibration factor of 0.00 dB was used for all 8/27 Arcata RCS data, a factor of -1.27 dB was used for 8/19 Vandenburg data, etc.

Table 4.4.3-14. Summary of Absolute Calibration Results From Four Airports

Date	Airport	Assumed RMS Roughness	Total Snapshots	Computed $F_{calibration}$
8/27	Arcata	2.5 cm	24	0.00 dB
8/19	Vandenburg	2.5 cm	17	-1.27 dB
8/19	Santa Barbara	1.0 cm	46	1.73 dB
8/20	Santa Maria	2.5 cm	27	-1.94 dB
			TOTAL = 114	AVG = -0.37 dB

All of the calibration and RCS data reported above were obtained in clear weather at four different airports on three separate days. However, in order to compute attenuation and volumetric reflectivity in weather such as fog, other approaches were analyzed. For all these other analyses, the average $F_{calibration}$ value of -0.37 dB was used in calibrating the system.

4.5. IMAGE QUALITY ANALYSES METHODS

The synthetic vision raster image must be combined with the HUD symbology and with the outside view in such a way that the total scene can be assimilated by the pilot and provide him information needed for operation of the airplane. This section identifies those elements of the raster image which were expected to be important to this process and describes the methods used to characterize them.

The following elements contribute to the total image quality:

- The ability to detect the runway and supporting airport features in the raster image. For synthetic vision this is a very complex area of human pattern recognition involving both the two dimensional scene content and the dynamic changes to the scene over short and long periods time.

- Ability of the pilot to detect the runway and supporting features when the raster information is mixed with the outside scene in the Head Up Display. Daytime environments are especially important in the mixing process since the outside scene brightness may affect the ability of the pilot to see the raster and/or discern the gray shades of the raster image.

- The ability of the pilot to assimilate the raster scene information with the HUD symbology to provide increased situational awareness. This requires that the raster image be conformal with the outside scene which is also the reference for the HUD symbology. This process, called scene registration, has the following major elements:

  - Conversion of the imaged scene to the perspective view coordinate system used by the pilot to view the natural outside scene. For active radars such as were used in the

SVSTD, the slant-range based coordinate system must be converted to the perspective coordinate vertical axis using a process known as C-Scan Conversion. All of the sensors used on the SVSTD used the perspective coordinate system for azimuth data so no conversion was required in that axis.

- Placement of the raster image in the HUD display so that the boresight and field of view coincide with the pilot's view through the HUD. A particularly difficult portion of this task is related to the parallax distortions contributed by differing mounting locations of the sensors relative to the pilot's eyes.

- The dynamic response of the raster image during aircraft maneuvers and flight profile towards the runway landing point.

- The ability of the pilot to discern the outside (real) image when it comes into view and transition to it from the synthetic raster image.

Early in the SVSTD/SIED Task it was recognized that insufficient resources existed to study all of these image quality elements. Limited efforts were undertaken to explore the applicability of selected image quality elements. Additionally, significant effort was given to documentation that would support independent studies.

4.5.1 Raster Image Quality Metrics

Image quality metrics were calculated for the raster video data. Accordingly, the data acquisition system was designed to acquire the video data at the output of the individual FLIR and MMW imaging sensors. Two additional video sources and data recordings were provided. The first documented the out-the-window scene with a standard color video camera; the second recorded a special channel in the HUD computer which overlaid the raster image data with a rasterized version of the stroke symbology. The available video data is illustrated in Figure 4.5.1. Note that the settings of the pilot's HUD Raster Brightness and HUD Raster Contrast controls did not affect any of the recorded raster data.

None of the imaging systems delivered to the airplane incorporated significant image enhancement between the raw data and the raster video output, nor did the vendors impose restrictions on availability of GTRI results regarding image detection. This has made the raster video image detection analysis a confirming effort to the results of the GTRI raw data analysis.

The parameters chosen for use in analyses of the radar performance and raster video image quality are identical in principle, but differ slightly in implementation due to the effects of the C-Scan conversion in compressing multiple lines of radar data into a single line of raster as the range

increases. This compression makes it very difficult to choose a single scan line which has a pure runway / surrounding terrain interface. The analyses of video image quality used three trapezoids; one defining the runway, and the other two defining the terrain areas left and right of the runway. The metrics were then computed for all scan lines passing through the runway trapezoid and the results regressed into a ``metric versus range'' plot. This process is described fully in the Image Calibration discussion below and the metrics are illustrated in Figure 4.5-2.

A qualitative measurement of runway image detection in sensor video data was also used for selected approaches. In a post-flight setting, each of the imaging sensor video outputs (MMW, FLIR, and Window Camera) were reviewed and a call made when the data analyst was first able to detect and then confirm the runway. The time-stamped video was used, permitting correlation of these events with all data recorded by the data acquisition system.

4.5.1.1 Contrast

The analysis of raster image quality computed contrast between the runway and surrounding environment using the same equations used by GTRI in the analysis of radar performance.

$$\text{Contrast} = \frac{\left(\frac{\beta_{\text{runway}} - \beta_{\text{terrain left}}}{\beta_{\text{terrain left}}}\right) + \left(\frac{\beta_{\text{runway}} - \beta_{\text{terrain right}}}{\beta_{\text{terrain right}}}\right)}{2}$$

where β_{runway} the average brightness of the runway and β_{terrain} left/right is the average brightness of the terrain left and right of the runway.

When contrast is plotted against range (or equivalently by scan line), each point is the same as one or more GTRI points. The straight line fit is considered a good average of the contrast.

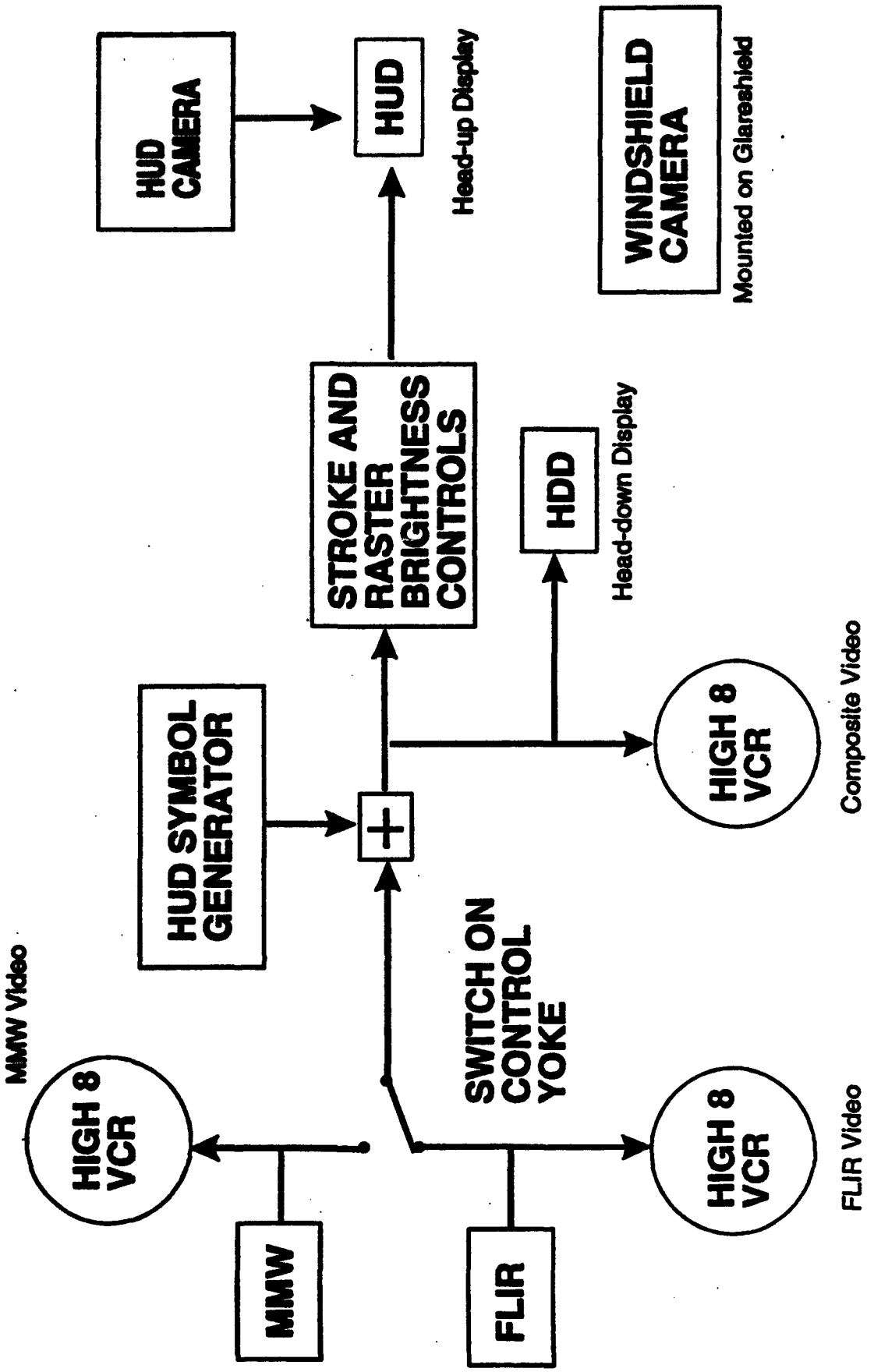

Figure 4.5-1. Diagram of Video Output, Pilot Displays and Recording Equipment

- β_t = Average Brightness of Terrain
- β_r = Average Brightness of Runway
- C = CONTRAST = $(\beta_r - \beta_t)/\beta_t$
- $\alpha_{t,r}$ = Variability of Terrain, Runway (noise)
- $\Delta\theta$ = Transition Angle for Sharpness
- S = Sharpness = $1/\Delta\theta$

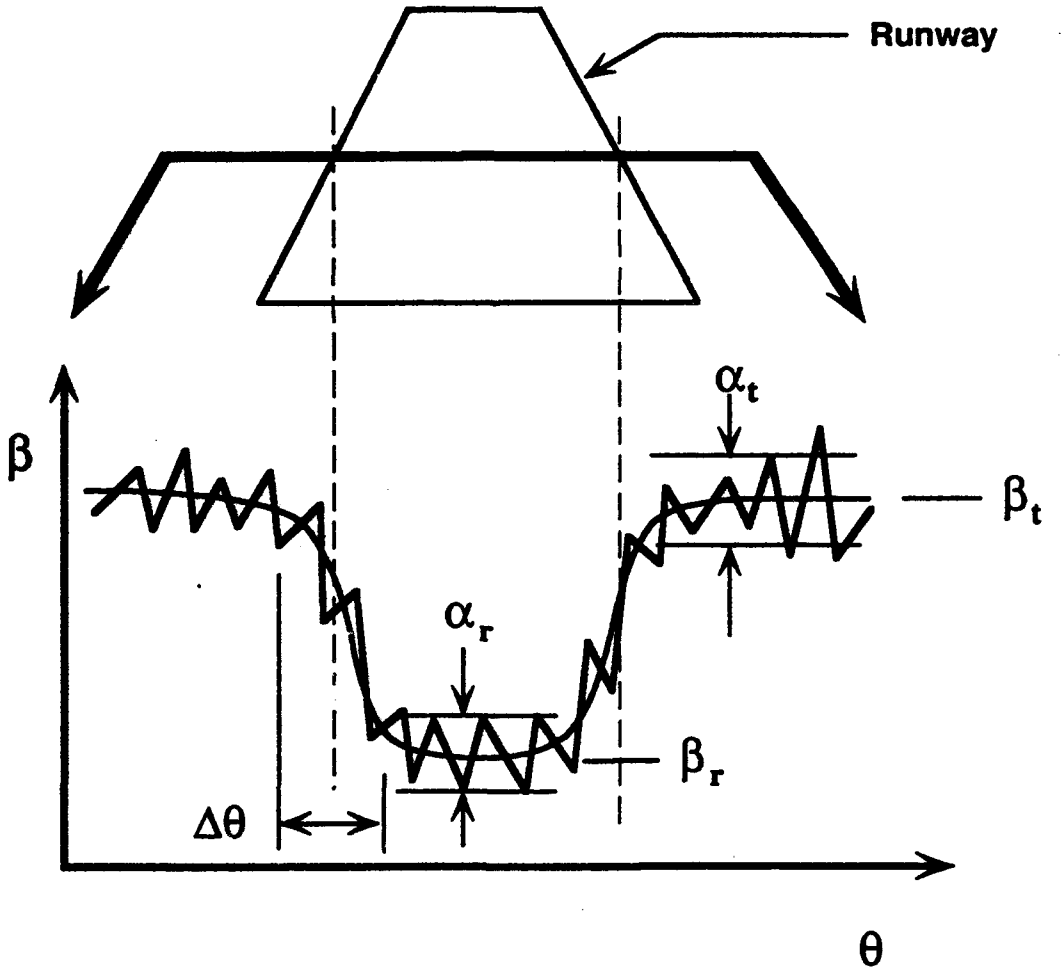

Figure 4.5-2. Image Quality Metrics

4.5.1.2 Variability.

Variability, expressed as a signal to variability ratio, was explored as another factor for characterizing the quality of an image of the runway. The equation used for Variability was:

$$\text{Signal Variability Ratio} = \frac{\left(\frac{\beta_{\text{terrain left}} - \beta_{\text{runway}}}{\frac{1}{2}\alpha_{\text{terrain left}} + \alpha_{\text{runway}}}\right) + \left(\frac{\beta_{\text{terrain right}} - \beta_{\text{runway}}}{\frac{1}{2}\alpha_{\text{terrain right}} + \alpha_{\text{runway}}}\right)}{2}$$

where β_{area} is the average brightness of the runway or terrain area, and α_{area} is the root-mean-square brightness of the runway or terrain area.

4.5.2 Pilot Use Of Raster Information

The information contained in the imaging sensor raster video was combined with the symbology and the outside scene in the Head Up Display. The pilot could adjust the raster brightness, raster contrast, symbology brightness, and control the use of a sun shade to reduce outside scene brightness. Each of these parameters could significantly change the quality of the image observed by the pilot from that recorded on the sensor video or sensor/symbology combined video data sources.

Qualitative documentation of the usefulness of the image was obtained by having the pilot call out when he was able to positively recognize the runway. The times of these call-outs were then determined by reviewing the call-outs on the time stamped video recordings. The recorded times permitted correlation of the event with all other data recorded by the data acquisition system.

Towards the end of the flight tests, quantitative documentation of the raster information was attained through the use of a borescope camera which looked through the HUD, recording the same integrated scene as viewed by the pilot. When used, this borescope camera's video was recorded by the data acquisition system. The data acquisition system recorded the external brightness measured by the Head Up Display and the settings of the HUD raster brightness and contrast controls. The HUD electronics were capable of generating a calibrated test pattern which could be used to establish reference settings for these controls.

4.5.3 Image Registration With Hud And Outside Scene

In approaches where precision guidance is not available, correct registration of the raster runway image with the HUD symbology is required to correctly fly a given glideslope consistently to a selected point on the runway. Even in precision approaches the presence of miss-registration can cause the integrated raster image and HUD symbology scene to contradict the commands of the flight director and result in possible confusion.

4.5.3.1 Through-The-HUD Measurements

Measurement of raster scene alignment was accomplished initially in the flight test program by comparing the relative placement of objects in the electronic image and in the real world image as they were viewed through the HUD . This method worked reasonably well using large objects such as taxiway intersections, runway ends, and vehicles. Late in the flight program, however, it became apparent during the analyses of the results of the flying that a more accurate and comprehensive alignment calibration technique was needed to achieve the degree of alignment required. The calibration procedures described below were developed and errors between the raster image and real image of the same object could be established in pixel distances and converted directly to angular errors. Some HUD symbology elements could also be checked using the same techniques.

4.5.3.2 Known Target Calibration

This second calibration technique was devised to handle targets which could not be easily seen visually at approach distances, such as radar reflectors, light bars, VASI installations, etc. Selected airport/runway features were located accurately in terms of airport map coordinates and then converted to latitude/longitude coordinates that would be compatible with the aircraft navigation system parameters recorded on the data acquisition system. At any given time in an approach, the position and attitude of the aircraft could be determined and used to calculate the position of the surveyed objects in the perspective coordinate system. These theoretical positions could then be compared against actual measurements in the video raster data, bypassing the need to see through the HUD. Note that this method could only determine the accuracy of the imaging sensor and not any manipulation of the scene by the HUD. Primary uses for this technique include:

- Measuring the alignment of imaging sensors.
- Measurement of field of view and deflection gains of imaging sensors.

- Measurement of C-Scan conversion errors. Linearity and gain measurements of the C-Scan conversion could be made by comparing the measured angles of features in the raster image (i.e. taxiway intersections with the main runway) with the theoretical values computed from several points along the approach trajectory.
- Recognition of errors during dynamic maneuvers by measuring the error changes between maneuvering and non-maneuvering periods.

To support this analysis, three airports (Arcata, Point Mugu, and Vandenburg) were surveyed using detailed facility maps and the results converted to the correct coordinate system, tabulated, and verified.

4.5.4 Video Raster Data Preparation

The following describes the process used in the preparation of raster video data for analyses. The in-flight video tape recordings of the sensor raster outputs and combined HUD symbology/raster have a ``IRIG-B'' time stamp supplied by the aircraft data acquisition system on one of the two audio channels. The second audio channel records cockpit and cabin communications. The time stamp was not made part of the video image to prevent inadvertent contamination of flight data.

Post-flight processing of the raster video included making a second generation copy of the original, but with the IRIG-B time stamp converted to a visual imprint located at the top right of the each video frame. The time stamp was made to the nearest 0.1 second which permitted up to 6 video frames (3 TV fields) to have the same time stamp. The dubbing process used the wide bandwidth capabilities of the Sony Hi-8 video system, resulting in negligible losses to the black-and-white recordings and only very small losses to the color window camera data.

Using flight logs, audio recordings of cockpit conversation, and the flight data shown on the combined HUD/raster image recording; the times of occurrence for all events to be analyzed were determined. When both raw radar data and video data was analyzed for the same run, GTRI provided the times for the events since their data was limited to one sample every 4 seconds compared to the raster video sampling of 60 samples per second.

The video data at the desired time was digitized as a full (16.2 million) color target image by a Cardinal Technologies SnapPlus ``video frame grabber'' and stored as a graphic computer file. The frame grabber included controls for brightness and contrast processing of the video prior to its digitization. Brightness was set at 50% and contrast to 80% to use the full 256 brightness levels available for each color. Since only black-and-white data existed in the FLIR and MMW images,

these files were converted to a 256 level black-and-white tiff image with an identifying title manually added to the upper left corner. The tiff format can be directly viewed on the computer screen using most popular paint and/or graphic programs and can be manipulated as data with the use of software utilities.

For all distances except those around 50' AGL or lower the actual image of the runway consumes only a small portion of the recorded scene. As a method of minimizing the data to be put into spreadsheets for manipulation, a second copy of the image file was made, but documentation of the cropping points assured that the cropped file lost none of the functionality of the full image. Since all of the data were then in a digital format, these additional copies were not degraded from the initial frame grabber graphic file in any way.

``Tiff'' file manipulation utilities (tiffcp and tiffinfo from the public domain tifflib distribution) were used to delog the contents of the graphic file to a standard ASCII character file containing the brightness value of each pixel. These ASCII files were loaded as data into the Wingz computer spreadsheet where the actual processing of the image to determine the image quality parameters was performed.

For each MMW raster image processed, a second raster image was also processed for the same time using the combined HUD symbology/raster video recording. The processing to acquire and archive this image was identical to that described above except that the runway was not cropped into a separate image. Since the raster image was identical in both scenes, the relationship of the raster image with the symbology in the combined video permitted a number of measurement to be made of the relationship of the raster image to the real world. image.

In many cases additional images were processed for the same time from the FLIR and Window cameras to permit visual comparison or to assist in identifying objects of interest in the MMW scene.

4.5.5 Image Calibration

Key to extracting the maximum amount of information from the images analyzed was the process of calibrating the raster video image to the real world. The calibration process used the combined HUD symbology/raster video output from the Head Up Display processor. To achieve scene calibration the following was determined for each digitized image time slice:

- The pixel coordinates of HUD symbols with known angular spacing in both pitch and azimuth axis. Vertical axis references included the 5 degree pitch up marker and the 5 or 10 degree pitch down markers. Azimuth axis references were the heading markers located every 5 degrees along the horizon line.
- The pixel location of the boresight symbol which provided the aircraft fuselage attitude
- The vertical pixel value of the horizon line's center point which provided the reference for local level (Euler) pitch measurements.
- Pixel coordinates for left and right horizon line ends (or heading markers on the horizon line) for computation of roll angle.
- Pixel location of the center of the perceived MMW horizon line. This point marked the C-Scan conversion's conclusion of the relationship between maximum slant range processed by the radar (12,467 feet for the Honeywell 35 GHz radar) and the vertical angle.
- The corner point locations of three trapezoids:
  - Describing the runway four corners, but located inside of any runway edge transitions.
  - Describing the terrain to the left and along the runway but outside of any runway edge transitions.
  - Describing the terrain to the right and along the runway but outside of any runway edge transitions.

  These points were used to define the boundaries used to compute contrast and variability, and were the starting point for sharpness determinations.
- Elevation of the aircraft using both barometric and radio altimeter sources.
- Runway approach end (touchdown zone) elevation. This parameter was usually derived from the ILS approach plate for the runway and was not always the same value as field elevation.

These parameters were manually entered into the image spreadsheet program which then computed the following:

- A scale factor of pixels per degree generated for both the pitch and azimuth axis of the image.

- The actual field of view of the image calculated by applying the scale factors to the image size in pixels.
- A correction factor for vertical errors encompassing C-Scan conversion and/or raster alignment relative to the symbology computed by comparing the measured angle between the HUD horizon and the maximum MMW processing range (MMW perceived horizon) and comparing it to the theoretical value for that altitude. This correction factor was then used to correct all vertical displacement measurements involving MMW raster objects.
- The depression angle of every scan line relative to the local level horizon.
- The slant range of every scan line in the image to its intercept with a ``flat earth'' terrain.
- The azimuth angle of every pixel (column) location relative to the aircraft boresight.

This process should be considered a close approximation since the electronic implementation of the combined raster/HUD symbology video signal was not guaranteed to be exactly that of the time multiplexed raster and stroked symbology presented to the pilot on the HUD display.

SECTION 5

PILOT/SYSTEM PERFORMANCE

The performance of the experimental Synthetic Vision System and of the pilots in using it is reported in the form of aircraft trajectory and attitude states, and the subjective opinions of the pilots who used it. These data reflect the ability of the pilots to interpret and use several sources of information including, 1) the image provided by the SVS sensor, 2) the flight guidance cue, and 3) the HUD symbology. The image provided on the HUD was used by the pilots as the primary source of information upon which to base the decision to go below Cat I minimums on a Type I ILS beam, and to continue the approach between Cat I and Cat IIIa minimums. The altitude and range at which the pilot called "runway image" is an important measure of the sensor performance, and are analyzed in detail in the first part of this section. This is followed by subjective pilot rating data and a summary and interpretation of the supporting pilot commentary taken during the conduct of the flight tests. Quantitative data related to image quality and aircraft tracking performance are presented in the remainder of the section. These data serve to quantify and expand on the results of the piloted evaluations.

The reported results are confined to the flight tests in which the Honeywell 35 GHz MMW radar sensor was used as the source of the HUD raster image. Suitability tests with the 94 GHz sensor indicated a substantial range limitation. The reasons for this limitation are not understood but are believed to be associated with the radome, the limited power of the transmitter and limitations in the processing of the radar data. Because the runway image call altitude was consistently below 200 feet (Cat I decision-height), a decision was made not to conduct formal testing with the Lear 94 GHz MMW radar. Data obtained during suitability testing indicated that the average runway image call altitude was 168 feet (standard deviation 26 feet) and the range was 0.50 nm (standard deviation .08 nm). Another shortcoming of the 94 GHz MMW was substantial noise in the foreground at altitudes below 100 feet above the runway. This noise interfered with the pilot's ability to see the stroke symbology including the flight director. There were indications that the resolution of the 94 GHz sensor would be quite good in the absence of the above problems. For example it was possible to identify runway lights and the runway edges were better defined than with the 35 GHz sensor.

The Kodak 3 - 5 micron forward looking infrared (FLIR) sensor provided excellent image quality in conditions without measurable moisture. The performance of the FLIR sensor deteriorated in conditions of measurable moisture to the point that it did not provide a useful image.

This was determined early in the program when the FLIR sensor was used as the primary sensor on alternating approaches in actual Cat II and Cat IIIa conditions. After consistent results in actual Cat II and Cat IIIa conditions indicated the FLIR sensor did not produce a usable image at the Cat I decision height (resulting in a missed approach), it was decided to abandon those approaches remaining in the test matrix using that sensor. However, in all actual weather, the FLIR image was monitored by the test engineer, and recorded on High-8 video tape. Any instances in which it appeared that the FLIR might provide a usable image were followed by an approach with the pilot using the FLIR image on the HUD. The results were invariably consistent; the FLIR sensor did not provide a useful image in measurable moisture.

5.1. PILOT PERFORMANCE AND OPINION

The image provided on the HUD was used by the pilots as the primary source of information upon which to base the decision to go below Cat I minimums on Type I ILS guidance. The "runway-image" call made by the evaluation pilot was highly significant because it indicated that he had an image of the landing runway that was sufficiently good to continue below Cat I minimums, on a Type 1 beam, with no transmissometers (RVR data), and no touchdown zone or centerline lights. The safety pilot was required to execute a missed-approach if he did not hear the "runway image" call before reaching the published decision height for approaches in actual Cat II or Cat IIIa conditions. Pilot commentary indicated that pattern recognition of the runway(s) and taxiway(s) played an important role in the pilot decision to call "runway image".

Runway image call data for flights conducted in fog were plotted separately from flights in clear air. Flights in fog were defined as occurring when the visibility was equal to or less than 1/2 mile, and/or a ceiling less than 400 feet. The runway image call data for flights in rain and snow are presented separately. Conditions where the rain-rate was less than 1 mm/hr were classified as fog. The range and altitude where the pilot called "runway image" is analyzed in detail in the following section.

5.1.1. Experimental System (35 GHz MMW Sensor) Performance in Terms of Range and Altitude Where Pilot Called Runway Image

5.1.1.1 Variation Between and Within Pilots.

The variability of the runway image call between pilots and the repeatability of the call for each pilot are significant because they are measures of the confidence the pilots had in identifying the airport pattern (taxiways, runways, etc.) and the landing runway. A large variability would indicate that the call is highly subjective, and would be indicative of a low level of confidence. Figure 5.1-1 indicates that the average range for the runway image call was 1.5 nm in clear air and 1.2 nm in fog. The average altitude above the runway for the call was 500 feet in clear air and 385 feet in fog. The standard deviation was approximately 1/4 nm in range and 100 feet in altitude, both in fog and in clear air. An inspection of Figure 5.1-1 indicates that these trends were reasonably consistent across all three of the evaluation pilots. Pilot commentary indicated that the runway image call was made only after it was possible to identify the landing runway with a high level of certainty. They also noted that the image tended to "pop into the field-of-view" suddenly and with reasonable quality as opposed to a more gradual improvement from poor to good image quality. This may explain why the image call ranges and altitudes were quite repeatable within each pilot, and were consistent between pilots.

5.1.1.2. Effect of Fog.

A comparison of the effect of fog compared to clear air on the range and altitude for the runway image call is shown in Figure 5.1-2. The range of the sensor is distinctly affected, but the degradation was not significant operationally. In fact, the pilots were not aware that there was a measurable degradation until the data was plotted.

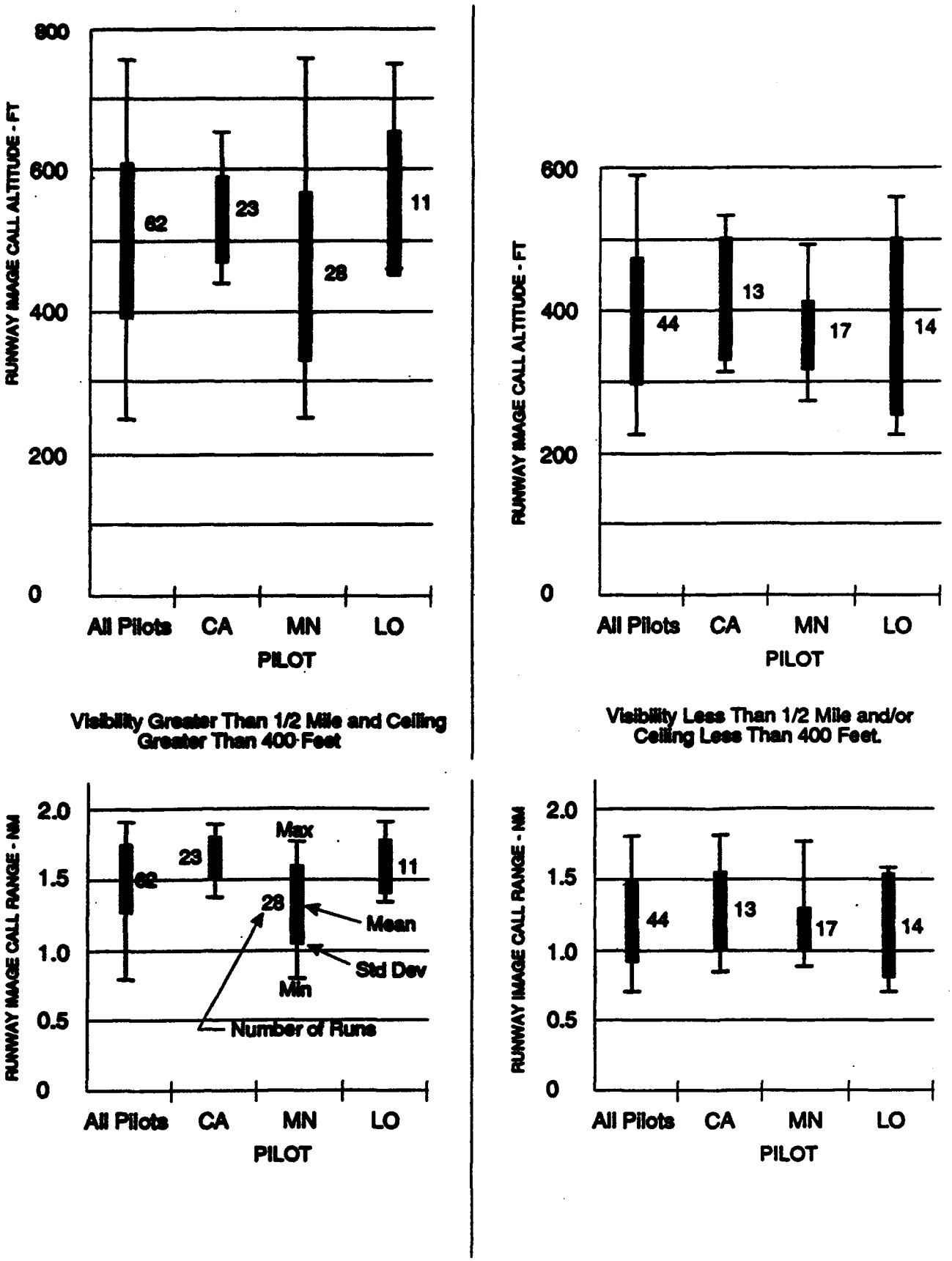

Figure 5.1-1. Variation of Runway Image Call Altitude and Range Between and Within Pilots

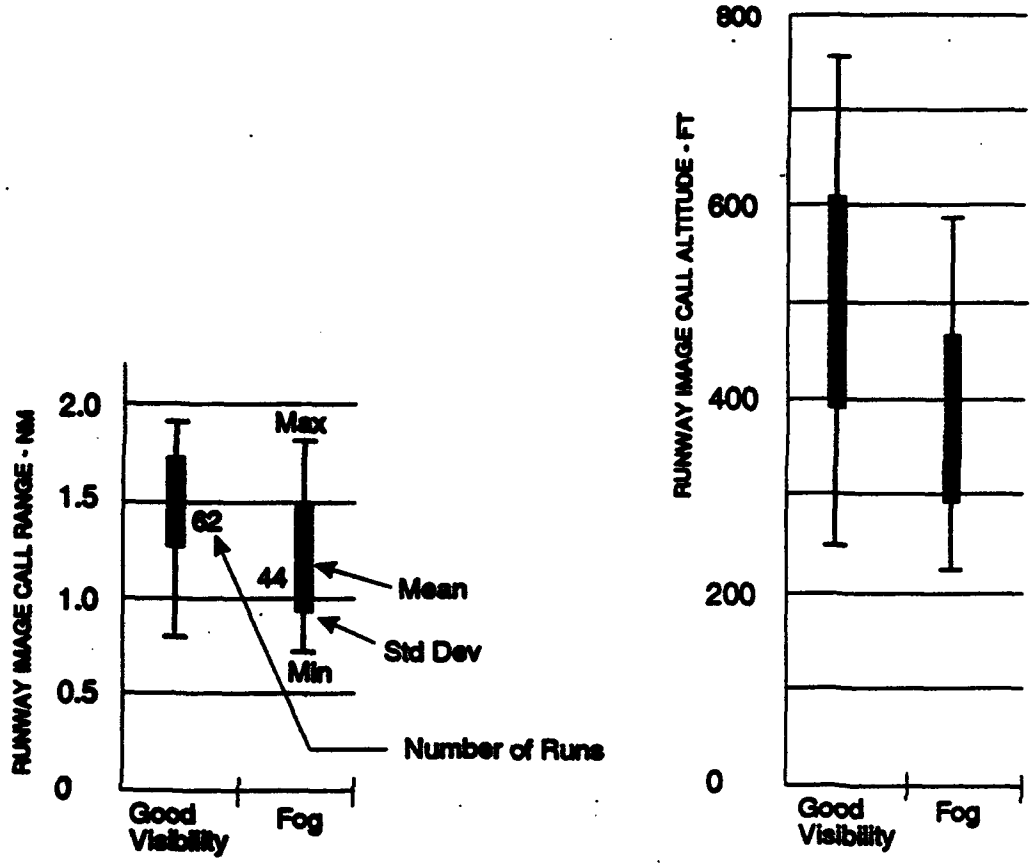

Notes:

Good Visibility - Visibility greater than 1/2 mile and ceiling greater than 400 feet

Fog - Visibility less than 1/2 mile and/or ceiling less than 400 feet

Figure 5.1-2. Variation of Runway Image Call Altitude and Range with Fog

5.1.1.3 Effect of Airport Surface.

The effect of different airport surfaces on the runway image call altitude and range is plotted in Figure 5.1-3. These data indicate that the airport surfaces had an important effect on the radar performance. San Diego is not plotted because the runway image was identified by one pilot and not by the other. That airport surface consisted of an asphalt runway on a large area of concrete. Subjectively, the image was judged to be poor. In general, a good image results when the sides of the runways and taxiways provide a high radar reflectivity and the runway and taxiway surfaces do not.

The significance of the standard deviation in Figures 5.1-1,2, and 3 is that it forms the basis for predicting the probability of calling runway image at a specified altitude, assuming that the runway image calls occur as a normal distribution over a large number of approaches. For the purpose of attaining physical insight into the data, assume that a missed approach would occur if the runway image call was not made by 250 feet, i.e., at least 50 feet above and approximately 4 seconds before DH. The probability of a missed approach prior to DH is estimated in Table 5.1-1, based on the data in actual fog conditions in Figure 5.1-3 (right side). Airports with less than four approaches are not included because of the unreliability of the standard deviation calculation.

Table 5.1-1 Estimated Probability of a Missed Approach Because Pilot Could Not Call Runway Image Prior to 250 feet Above The Runway

Airport	Probability of Missed Approach
VBG	.004
ACV	.022
ORH	$< 3x10^{-5}$
HTS	.0027

With the exception of Arcata (ACV), the probability of a missed approach, because the runway image call was not possible at or above 250 feet, is seen to be extremely low. More work is necessary to determine the margin above the 200 foot DH that is required. As will be discussed in the next section, there is evidence that a margin as low as 50 feet is acceptable for a nominal approach, but that an additional margin may be required in the presence of anomalies such as a beam bend combined with a marginally short runway. It is not fully understood why the standard deviation for the runway image call was higher at Arcata. Three important considerations were that the actual Cat IIIa approaches made to ACV occurred early in the program, the runway was marginally short for a G-II (6000 feet), and there was a slight quartering tailwind on the approach. The data in Figures 5.1-1, 2, and 3 are tabulated in Tables 5.1-2 and 3.

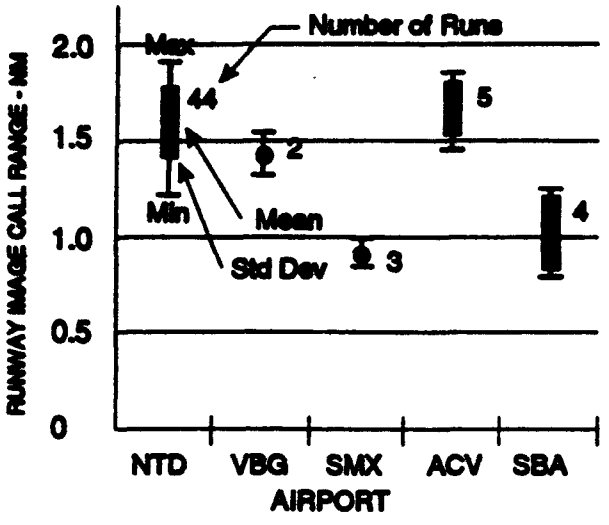

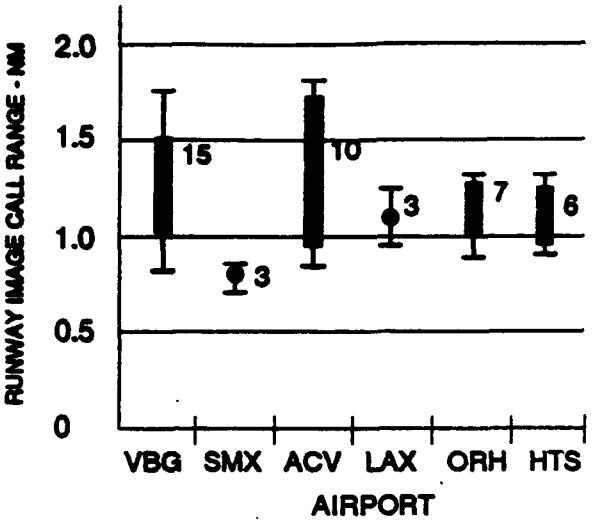

Note: The Standard Deviation is not shown for cases where there are less than four runs

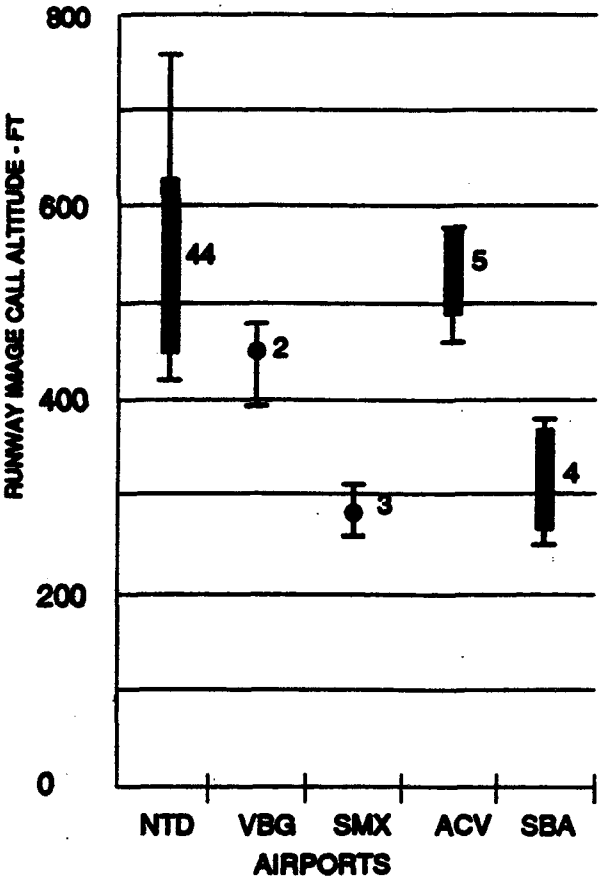

Visibility Greater Than 1/2 Mile and Ceiling Greater Than 400 Feet

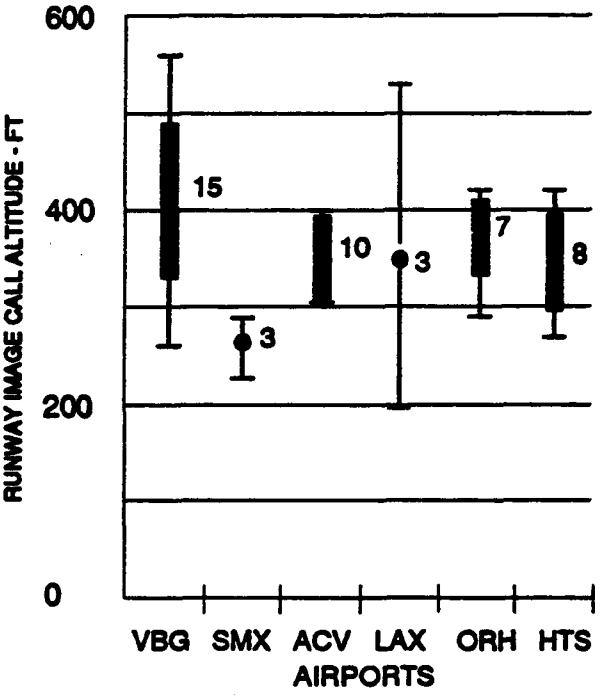

Visibility Less Than 1/2 Mile and/or Ceiling Less Than 400 Feet.

Figure 5.1-3. Variation of Runway Image Call Altitude and Range Between and Within Airports

Table 5.1-2. Runway Image Call Data for Primary Test Airports

	NTD			VBG			BUK			ACV			BBA			LAX			ORH			HTS		
	RUNWAY IMAGE CALL RANGE	RUNWAY IMAGE CALL ALTITUD		RUNWAY IMAGE CALL RANGE	RUNWAY IMAGE CALL ALTITUD		RUNWAY IMAGE CALL RANGE	RUNWAY IMAGE CALL ALTITUD		RUNWAY IMAGE CALL RANGE	RUNWAY IMAGE CALL ALTITUD		RUNWAY IMAGE CALL RANGE	RUNWAY IMAGE CALL ALTITUD		RUNWAY IMAGE CALL RANGE	RUNWAY IMAGE CALL ALTITUD		RUNWAY IMAGE CALL RANGE	RUNWAY IMAGE CALL ALTITUD		RUNWAY IMAGE CALL RANGE	RUNWAY IMAGE CALL ALTITUD	
	NM	FT		NM	FT		NM	FT		NM	FT		NM	FT		NM	FT		NM	FT		NM	FT	
	VISIBILITY GREATER THAN 1/2 MILE OR CEILING GREATER THAN 400 FEET - 35 GHz MMW																							
MEDIAN	1.59	500		1.42	450		0.90	290		1.67	550		1.04	320										
AVERAGE	1.40	540		1.42	450		0.91	298		1.67	534		1.02	318										
SIGMA	0.18	91		0.13	42		0.07	15		0.14	45		0.19	54										
MAX	1.91	760		1.51	480		0.99	310		1.85	590		1.24	380										
MIN	1.21	420		1.32	420		0.85	290		1.46	460		0.79	250										
COUNT	44	44		2	2		3	3		5	5		4	4										
	VISIBILITY LESS THAN 1/2 MILE AND/OR CEILING LESS THAN 400 FEET - 35 GHz MMW																							
MEDIAN			1.20		405	0.83		275	1.48		455				1.04		350	1.16		370	1.09		345	
AVERAGE			1.28		412	0.80		263	1.33		424				1.10		353	1.15		370	1.10		345	
SIGMA			0.26		80	0.08		34	0.39		127				0.15		45	0.13		40	0.14		52	
MAX			1.76		560	0.96		290	1.81		590				1.26		400	1.31		420	1.31		420	
MIN			0.82		260	0.71		225	0.83		260				0.93		310	0.89		290	0.90		270	
COUNT			15		15	3		3	10		10				3		3	7		7	6		6	

Table 5.1-3. Runway Image Call Data for Each Evaluation Pilot

	ALL PILOTS		PILOT CA		PILOT MN		PILOT LO		PILOT RH	
	RUNWAY IMAGE CALL RANGE	RUNWAY IMAGE CALL ALTITUDE	RUNWAY IMAGE CALL RANGE	RUNWAY IMAGE CALL ALTITUDE	RUNWAY IMAGE CALL RANGE	RUNWAY IMAGE CALL ALTITUDE	RUNWAY IMAGE CALL RANGE	RUNWAY IMAGE CALL ALTITUDE	RUNWAY IMAGE CALL RANGE	RUNWAY IMAGE CALL ALTITUDE
	NM	FT	NM	FT	NM	FT	NM	FT	NM	FT
	VISIBILITY GREATER THAN 1/2 MILE OR CEILING GREATER THAN 400 FEET - 35 GHz MMW									
MEDIAN	1.53	490	1.69	540	1.39	450	1.57	500		
AVERAGE	1.50	500	1.66	534	1.33	450	1.60	555		
STD DEV	0.26	109	0.15	61	0.27	121	0.19	106		
MAX	1.91	760	1.89	650	1.78	760	1.91	750		
MIN	0.79	250	1.38	440	0.79	250	1.34	460		
COUNT	62	62	23	23	28	28	11	11		
	VISIBILITY LESS THAN 1/ 2 MILE AND/OR CEILING LESS THAN 400 FEET - 35 GHz MMW									
MEDIAN	1.16	370	1.20	405	1.16	370	1.07	340		
AVERAGE	1.20	385	1.28	415	1.15	366	1.18	379		
STD DEV	0.28	90	0.29	88	0.14	48	0.38	124		
MAX	1.81	590	1.81	590	1.45	460	1.76	560		
MIN	0.71	225	0.85	290	0.89	270	0.71	225		
COUNT	44	44	13	13	17	17	14	14		
	VISIBILITY GREATER THAN 1/2 MILE OR CEILING GREATER THAN 400 FEET - 94 GHz MMW									
MEDIAN	0.51	170	0.51	150					0.50	170
AVERAGE	0.50	168	0.53	157					0.49	173
STD DEV	0.06	27	0.05	12					0.06	30
MAX	0.59	220	0.59	170					0.59	220
MIN	0.40	130	0.50	150					0.40	130
COUNT	11	11	3	3					8	8

5.1.1.4. Effect of Rain.

Increasing rain-rate had a significant effect on the 35 GHz MMW and FLIR sensors. The effect of rain on the 35 GHz sensor is shown in Figure 5.1-4, where it is seen that increasing rain-rate significantly reduced the range where the pilot called runway image. The data points at zero rain-rate were taken on dry runways. The rain-rate data is the averaged value from an altitude of 70 meters (230 feet) to touchdown. The variation between Atlantic City (ACY) and Millville (MIV) is potentially due to at least three factors. These are, 1) the airport surface at ACY does not produce a good image, even in dry conditions, 2) the average rain-rate is not representative of the effect of rain on the radar performance, and 3) the drop sizes were significantly different. An investigation of the weather sensor data indicated that the drop sizes at MIV were slightly larger than at ACY. Hence, drop size does not explain why the MMW degraded more rapidly at ACY than at MIV. The rain-rate profiles for the rain runs in Figure 5.1-4 are plotted in Figure 5.1-5. The total average rain rate plotted in Figure 5.1-4 was obtained by averaging the rain-rate at each of the 7 altitude slices from 70 meters to touchdown. The data presented in Figure 5.1-5 was averaged across 10 meter slices of altitude.

For the run at ACY where the average rain-rate was 5 mm/hr (total average from 70 meters to touchdown), there is a peak of 14 mm/hr between 30 and 40 meters of altitude (98 and 131 feet). This would indicate that there was a rain cell on the final approach course that is not well represented by the average rain-rate number. Once below 100 feet, the pilot no longer considered making the runway image call, but a review of the data indicates that there was an image below 100 feet for this approach. Considering the magnitude of the rain-rates at MIV, it is surprising that there was an image call at 148 feet (45 meters), which was just prior to the 38 mm/hr peak rain-rate. A review of the data shows that the image was poor, and tended to fade in and out as evidenced by the video, and by pilot callouts of "poor image" and "lost it". This is probably due to the large variability in rain-rate that occurred as the aircraft progressed down the glidepath.

The effect of rain on image quality is complex due to the variability of the rain activity as the aircraft approaches the runway (rain-rate tends to be a function of time and position). While the details are not well understood, the important finding is that moderate rain had a definite adverse effect on the image. The use of radar reflectors to improve the image quality in moderate and heavy rain should be studied as a means to overcome this deficiency.

It is notable that in all conditions where the rain-rate was high enough to degrade the radar image, the tower-reported visibility was well above Cat I minimums, see Figure 5.1-4. This

experimental result should be expanded by investigating statistics on visibility as a function of rain-rate and drop size distribution. If the visibility is only reduced to below Cat I minimums in very heavy rain, it could be argued that there is not a critical need for SVS in such conditions. Additionally, very heavy rain tends to occur in short intervals so that it may be possible to circumvent the problem by delaying the approach during the low-probability short-duration heavy-rain events.

The rain data was taken on a trip to the east coast to intercept a tropical storm. This storm resulted in very strong winds out of the north, and most of the runways to which approaches were flown were oriented east/west. As a result there were very strong crosswinds (up to 30 knots) and significant turbulence on some approaches. Pilot workload and Cooper-Harper rating data was not taken because the very high workload consisted primarily of controlling the G-II. In addition, the flight director sometimes disappeared from the HUD in very large crosswinds, forcing the pilot to resort to head-down information for flight director guidance. Finally, the visibility was always greater than two miles so it would have been necessary to install the HUD-shield to simulate IMC conditions below Cat I minimums. This was felt to be unsafe by the cockpit crew in these high wind conditions, and with the above noted flight director problem. As a result of these considerations, the SVS aircraft was used as a test bed for the sensors in varying rain conditions, without the benefit of subjective pilot rating data.

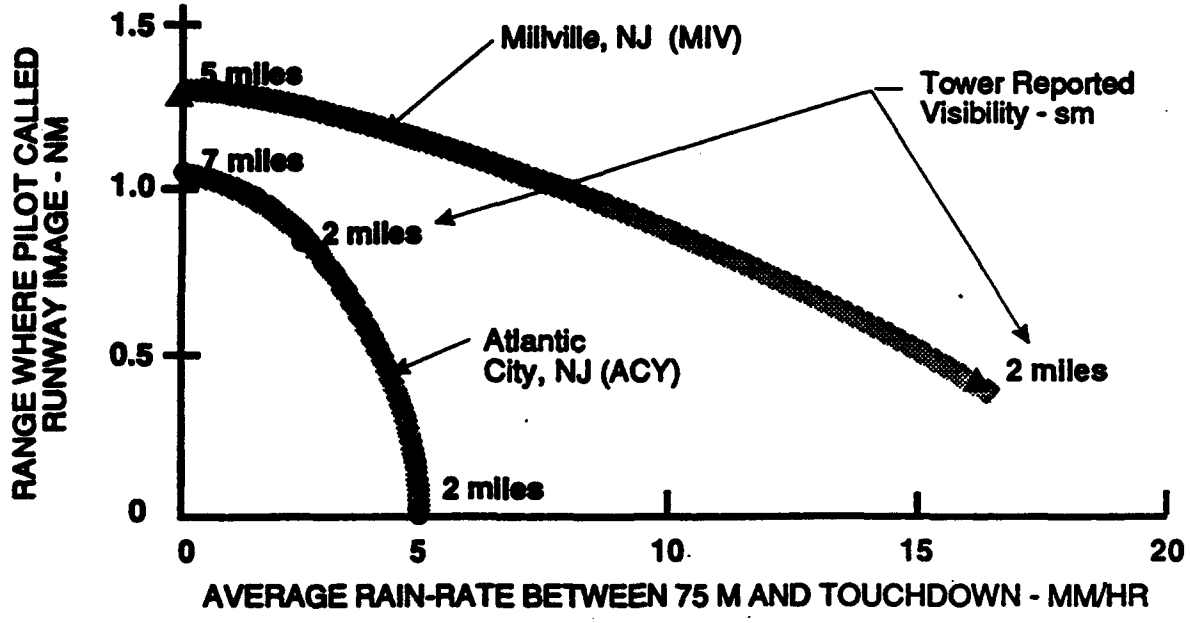

Figure 5.1-4. Rain-Rate Versus Range Where Pilot Called Runway Image

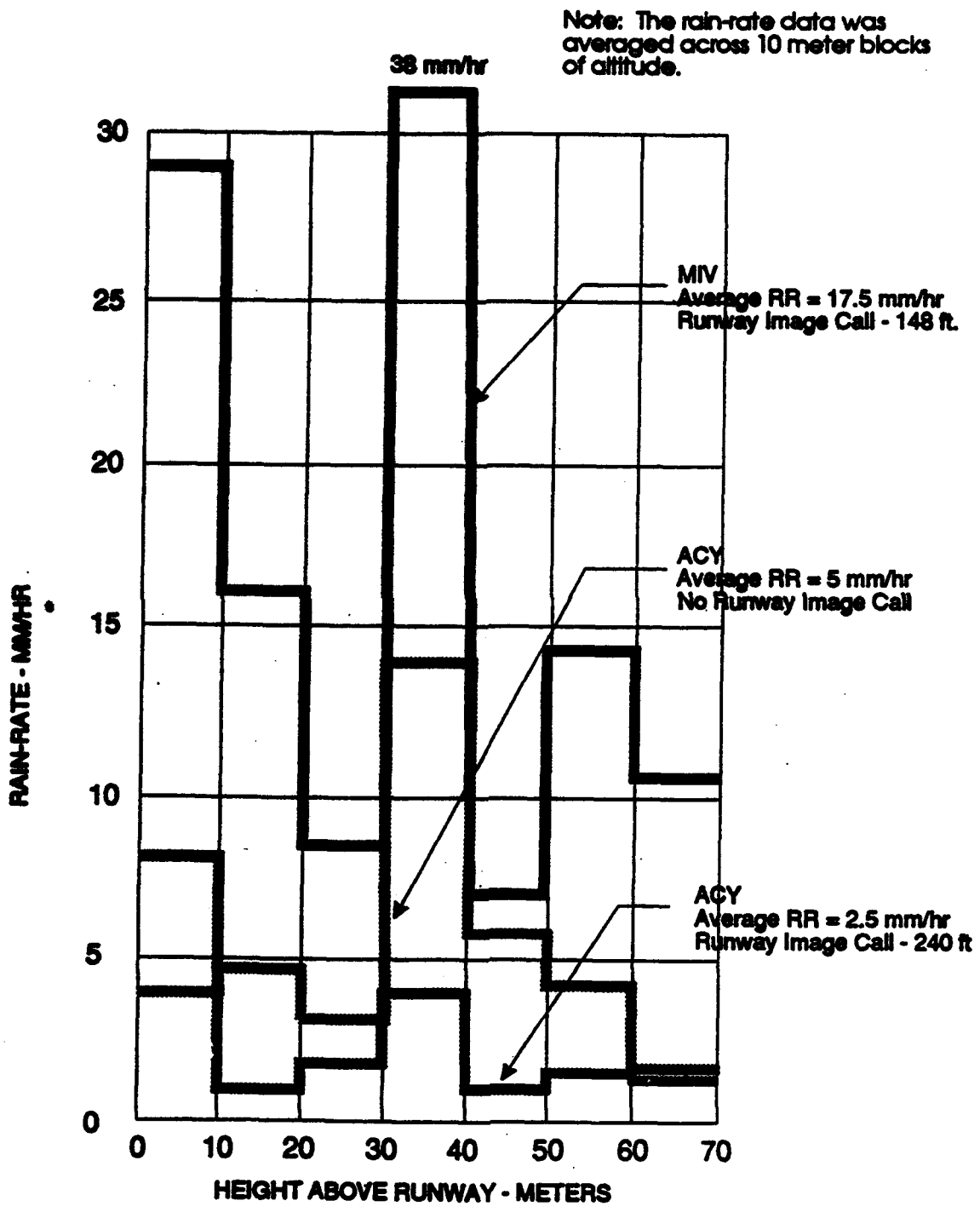

Figure 5.1-5. Rain-Rate Profile For Three Selected Runs From Figure 5.1-4

5.1.1.5 Effect of Snow.

Four approaches were made to Pueblo Colorado (PUB) with light-to-moderate snow falling This was officially reported as light snow, but the tower noted that it was moderate on some approaches. There was approximately 1 to 2 inches of very wet snow (almost slush) on the runway and surrounding areas. The tower reported visibility was 3/4 miles in fog and visual acquisition of the runway occurred at about 300 feet above the surface for most approaches. Two evaluation pilots each flew two approaches. Both pilots reported that there was never a usable runway image on the HUD. One of the pilots noted that the approach light stands provided a good radar signature at a range of about 1.2 nm. The ability to see the approach lights before the runway provides some evidence that radar reflectors may be effective as a means to overcome the inability of the MMW radar to image the runway surface in these conditions.

Approaches were made to Pueblo and Colorado Springs (COS) the next day, after the snow had stopped falling. The conditions consisted of damp runways, completely free of snow, and with about 4 to 5 inches of wet snow on the surrounding terrain. There was about a foot of snow on the sides of the plowed runways. The 35 GHz MMW did not produce a usable image of the runway in these conditions at either COS or PUB. Again, the approach light stands did provide a good radar signature at ranges between 1.2 and 1.5 nm. The visibility on these approaches was 3 miles at PUB increasing to 10 miles at COS. The cardboard shield was placed over the HUD to improve the chances of obtaining an image.

5.1.2. Subjective Pilot Ratings and Opinion

Subjective pilot ratings and commentary were obtained throughout the experiment. For runs in simulated IMC (cardboard shield in front of HUD), the ratings and commentary were obtained after the third repeat run. The protocol for runs in actual weather was to take ratings and commentary after every run. The ratings and commentary were dictated to the Test Director (in the jump seat) and also recorded on tape immediately following the landing or missed approach. The safety pilot was in control of the aircraft during the rating process. The pilot ratings and commentary were further discussed during the de-brief following each flight.

Two subjective rating scales and a questionnaire were used to quantify pilot opinion and guide the pilot commentary. These are shown in Figures 5.1-6, 7, and 8. A spreadsheet summarizing the pilot rating data and questionnaire results, as well as other conditions and results

for all the experimental runs is given in Appendix K. The Modified Cooper Harper (MCH) scale was used to obtain insight into the pilot workload associated with using the synthetic vision system. That scale was developed by two human factors specialists, Wierwille and Casali , and is patterned after the well known Cooper-Harper scale for handling qualities . It uses the Cooper-Harper decision tree process, but the semantics of the scale are oriented specifically toward workload. The Cooper-Harper scale was used in the SVS experiment because it also addresses pilot workload, and is considered to be quite reliable as a result of extensive use over the past 20 years. Experience has shown that the MCH workload ratings always track the Cooper Harper handling qualities ratings (HQRs). That proved to be the case in the present experiment (see Appendix K). For this reason, only the MCH workload ratings are plotted in this section. Separate ratings were assigned for the approach, the landing flare, and the rollout. The approach rating pertained only to the portion of the approach from 200 feet above the runway to the 50 foot flare point. It was reasoned that this is the area where SVS is an issue. All subjective pilot ratings must be referenced to some defined level of aggressiveness, hence performance standards must be established. The performance standards used in this program are summarized in the Table 5.1-4 below.

To put the workload ratings in context, they have been correlated with the first question on the questionnaire; "considering only these approaches, would you consider the system safe for commercial operations?". The results of this correlation are shown in the form of a cumulative distribution in Figure 5.1-9. Also shown are the results of another flight test program that studied the effect of various flight director and autopilot control laws on helicopter decelerating approaches to a 50 ft decision-height. The data for this program indicate that the pilots judged that even a moderate level of workload was excessive for the tasks associated with the synthetic vision system (usually a descent from Cat I to Cat IIIa minimums on Type I ILS guidance). This is in contrast with most handling qualities and display evaluations where a moderate level of workload (ratings of 5 to 7) are acceptable, if not desirable. Based on the SVS data in Figure 5.1-9, the context of the workload ratings discussed in the remainder of this section is that values of 4 have a reasonable chance of being judged as acceptable for normal operations, and values of 5 or greater are unacceptable.

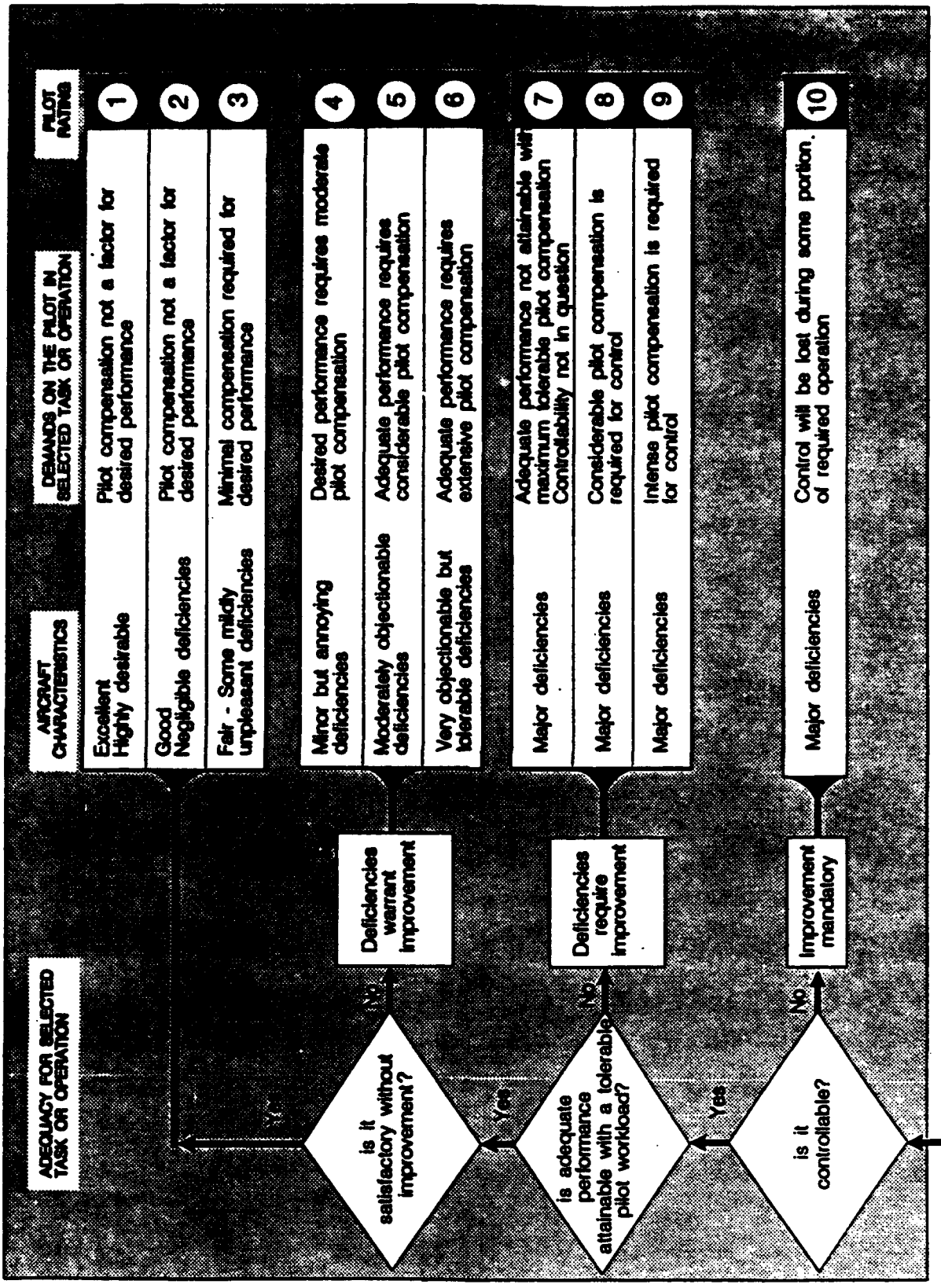

Figure 5.1-6. Cooper Harper Handling Qualities Rating (HQR) Scale

Figure 5.1-7. Modified Cooper Harper Workload Rating Scale (MCH)

Considering only these approaches, would you consider this system safe for commercial operations?

If the answer is no, discuss the primary shortcomings.

Give your overall impressions of the symbology and image for:

- Runway alignment
- Glidepath control
- Landing flare
- Rollout

Did your initial identification of the runway prove to be correct?

Did you ever feel it necessary to refer to head-down information? If yes, please discuss.

Did the quality of the image vary significantly with range? Please discuss.

Give separate Cooper Harper ratings for the approach task and for the landing task. Provide supporting commentary.

Give a Workload rating for the approach and landing task. Provide supporting commentary.

Figure 5.1-8. Pilot Questionnaire

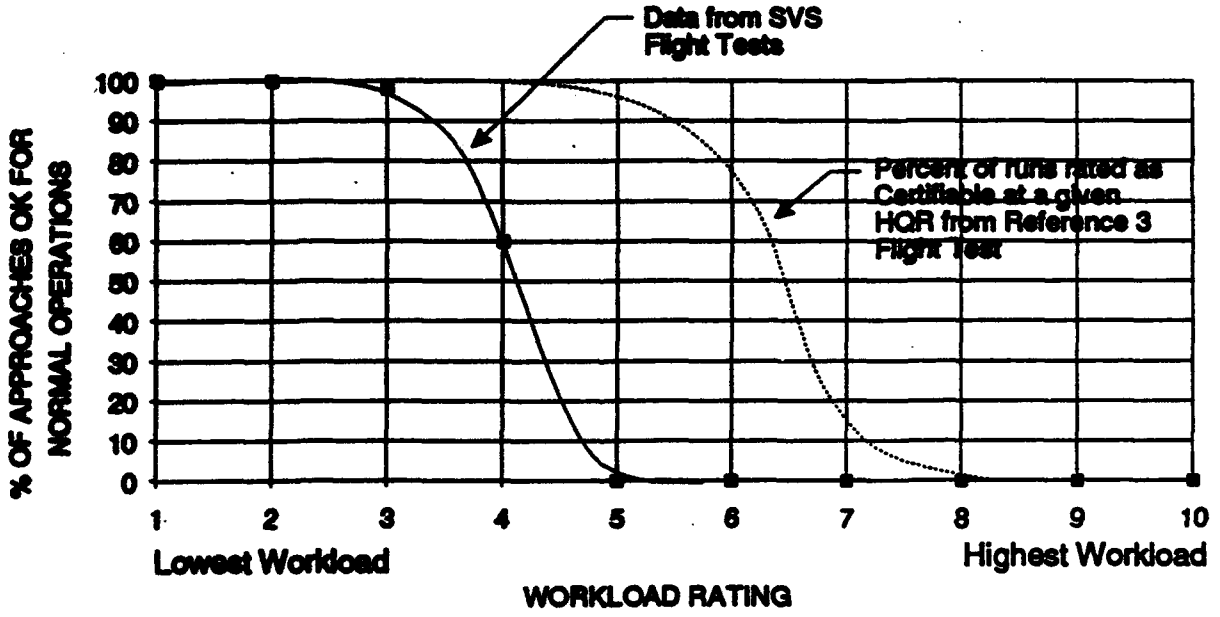

Figure 5.1-9. Correlation Between Workload Ratings and Acceptability for Normal Operations

Table 5.1-4 Performance Standards

	Desired Performance	Adequate Performance
Glideslope and localizer tracking above 200 ft. AGL.	± 1 dot	± 2 dot
Glideslope and localizer tracking between 200 and 50 ft AGL.	± 0.50 dots	± 1 dot
Airspeed control with respect to target speed.	± 5 knots	+ 10 knots - 5 knots
Flare performance	Touchdown between 1000 and 2000 feet of the runway threshold. Touchdown within 10 feet of centerline Sink rate subjectively smooth-to-firm	touchdown at greater than 500 feet and less than 3000 feet of the runway threshold. Touchdown on runway with at least 5 feet of margin from edge. Sink rate subjectively hard.
Takeoff roll	Maintain track within ± 10 feet of runway centerline. Achieve target climb attitude and speed with little or no bobbling or lateral directional problems.	Maintain aircraft on runway with at least 5 feet of margin from edge. Maintain positive control of pitch attitude and climb speed. No safety pilot takeover necessary.
Landing roll	Maintain track within ± 10 feet of runway centerline.	Maintain aircraft on runway with at least 5 feet of margin from edge

5.1.2.1 Subjective Pilot Ratings for Simulated IMC.

The frequency distributions of the subjective workload ratings for approaches and landing flares to simulated Cat IIIa and Cat IIIc conditions are shown in Figure 5.1-10 . This data indicates that the majority of the ratings were 3 (i.e., satisfactory without improvement). This should not be construed to imply that the SVS was acceptable as a certified system, but rather that it was acceptable for specific approaches in the specified test conditions; in this case simulated IMC. IMC was simulated by placing a cardboard shield in front of the HUD, and removing the shield at the appropriate time, e.g., 50 feet for simulated Cat IIIa. The cases rated as 4 or worse provide valuable insight into potential problems with an operational SVS and are discussed below.

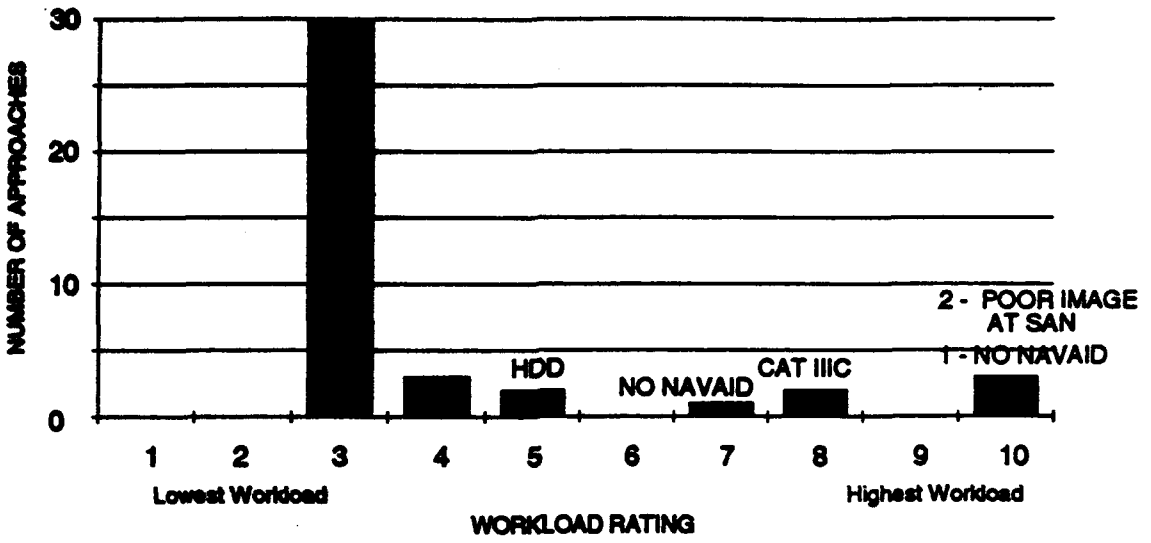

a) Workload Ratings for Approach Segment From an Altitude of 250 ft to 50 ft

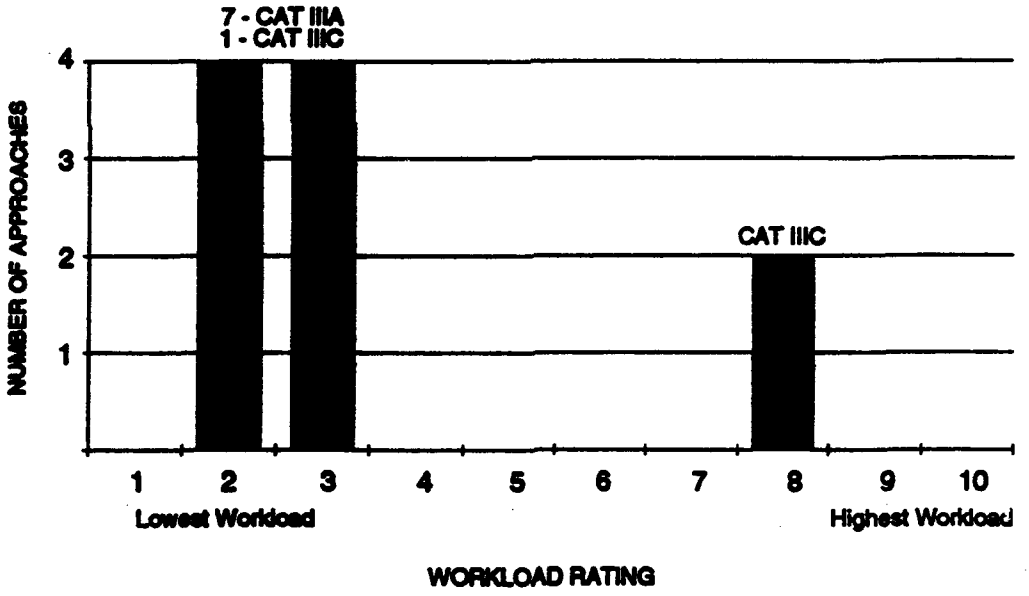

b) Workload Ratings for Flare

Figure 5.1-10. Frequency Distribution of Pilot Workload Rating Data for Simulated CAT IIIa and CAT IIIc Approaches

5.1.2.2 Runway Surface and Limited Range Problem at SAN.

Three of the runs shown in Figure 5.1-10A were assigned a workload rating of 10. Two of these cases were approaches to San Diego where the airport surface consists of a concrete runway on an asphalt surrounding. Because the approach has no glideslope, attempts were made to use the localizer approach and to descend below localizer minimums using the SVS image. Because of the poor differential radar reflectivity of the airport surfaces and relatively high minimums, the image quality was not good enough to initiate a descent below the minimum descent altitude. The system was rated as a 10 because improvement was judged to be mandatory for this task. The localizer minimum descent altitude (MDA) at San Diego is 500 feet above the runway. The geometry of a three degree glideslope is such that the descent from 500 feet would have to be started 1.6 nm from the touchdown zone (beyond the range of the tested MMW sensor). Non-precision approaches using steeper glideslopes were simulated during the SVS program, so the approach was theoretically possible (for example, the range to start the descent for a 4 degree glideslope would be 1.17 nm). However, the radar image proved to be very marginal, because of the unusual airport surface characteristics, resulting in a limiting condition for this experimental system.

5.1.2.3 Non-Precision and No-Navaid Approaches.

Seven approaches were made simulating a condition where localizer guidance was used until an image of the airport (Pt. Mugu) was achieved (runway image call). At this point the localizer was detuned from the evaluation pilots display, and the approach was completed using only HUD symbology and the SVS image. These are referred to as no-navaid final-segment approaches. Four of these approaches were rated as a 3, one was rated as 7 and one as 10 (see Figure 5.1-10A). There is good reason to believe that the SVS image was not properly aligned with the outside world for these approaches, and may have been off as much as one degree in the vertical axis. This error caused the initial portion of the approach to be made to a point in front of the actual runway, resulting in a tendency to be low on short final. For four of the approaches, this was notable, but not highly significant (rated 3). For two of the approaches (one for each of the two evaluation pilots) the final segment was excessively low, resulting in warnings from the safety pilot and ratings of 7 and 10. Because of this inconsistent performance, there is reason to suspect that there may be more to the problem than mis-registration. The possible scenario is shown in Figure 5.1-11.

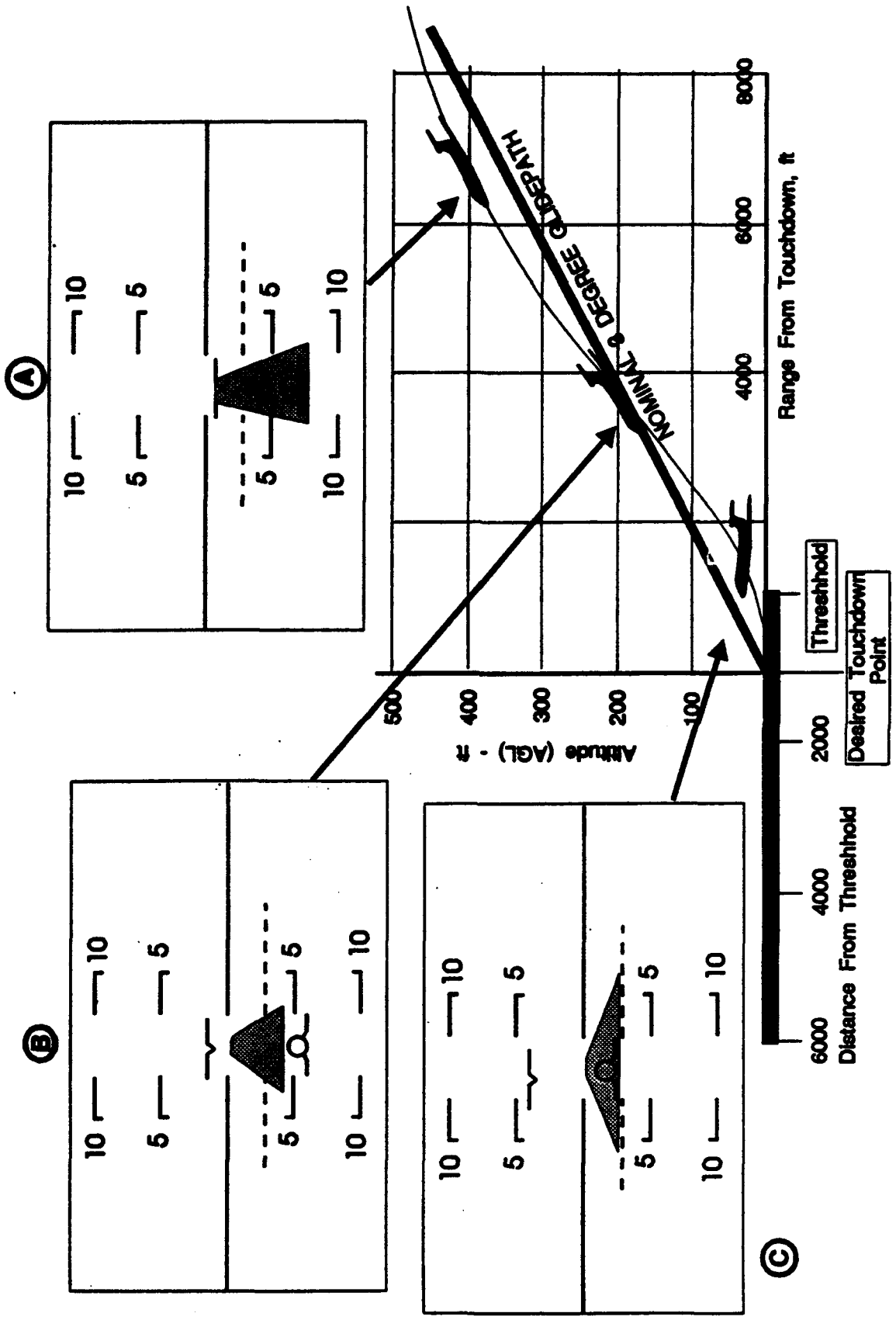

Figure 5.1-11. Observed Problem Descending to Low Minimums Without Vertical Guidance

In all cases the runway image call occurred well above the 3 degree glideslope. The pilot therefore commanded a descent angle steeper than -3 degrees (usually about -5 to -6 degrees) to capture the glidepath (HUD illustration A). For the two cases rated 7 and 10, the pilots passed through the glideslope without adjusting the flight path angle to -3 degrees (illustration B). This resulted in a condition where the aircraft completed the final segment of the approach at a very shallow angle, and hence excessively low (illustration C). This experience raises a number of questions. Does the use of the flight path symbol and -3 degree reference line to create a glideslope at altitudes down to 50 feet present a display to the pilot that is sufficiently compelling in terms of glideslope errors? This use of the flight path symbology on a HUD has become quite standard to create a glideslope in "black hole conditions", e.g., the Flight Dynamics Head-up Guidance System as used by Alaska Airlines. However, those approaches do not rely solely on symbology, especially at very low altitudes. Why did the pilots get excessively low for these no-navaid approaches, but not for non-precision approaches (localizer only) conducted during a different flight? Three pilots each flew three localizer approaches to simulated Cat IIIa (removed shield at 50 feet) and the assigned pilot ratings were all 3s for workload, and one 4 was assigned as an Cooper-Harper rating.. Perhaps the SVS image was better aligned during the non-precision approaches. The scope of the program did not allow further investigation into this problem. The following tentative conclusions are made, based on the limited experience described above.

> The SVS image must be perfectly aligned with the outside world if it is to be used as part of the primary guidance cue. This is especially critical for vertical guidance.
>
> The flight path symbol and -3 degree reference line may not be sufficiently compelling as the sole source of glideslope guidance below Cat I minimums.

Further work is required to identify the allowable mis-registration, and to investigate the use of symbology for non-precision approaches to very low minimums. It should be noted that lowering minimums from those typical of non-precision approaches (400 to 700 feet) to Cat I (200 feet) would provide a tremendous benefit. All of the pilots felt that this was well within the capability of the tested system. The only caveat is that the MDA must be low enough to allow a three degree descent after the image call is made. This is one of the more compelling arguments for increased MMW radar range. The required range as a function of MDA is given below in Table 5.1-5, assuming that .15 miles of pad is desirable (i.e., the pilot calls runway image .15 miles before initiating the descent). These numbers assume that a -3 degree glideslope reference is used and that approximately 1/2 mile of the runway is required in the scene for runway identification.

Table 5.1-5. Required Range From Runway Threshold for an MMW Radar Used for Non-Precision Approaches

Minimum Descent Altitude (ft)	Required Range for Runway Image Call (nm)
400	1.8
500	2.1
600	2.4
700	2.8

5.1.2.4 Approaches to Simulated Cat IIIC (0/0) Minimums.

Referring to Figures 5.1-10a and 10b, it is seen that two workload ratings of 8 were assigned for the simulated Cat IIIC approaches and landing flares. Each of the evaluation pilots flew three simulated Cat IIIC approaches in which the entire approach, touchdown, and rollout were conducted with the cardboard shield in front of the HUD. Two of the pilots assigned workload ratings of 8 for the approach, and for the flare and rollout. They indicated that the approaches could be safely conducted, but that the workload was excessive. One of the evaluation pilots felt that the Cat IIIC approaches were acceptable and rated them a 3. It should be noted that all of these approaches were flown at the Pt. Mugu Naval Air Station (NTD). The runway is 12000 feet long and 200 feet wide, leaving a significant margin for error. The deficiencies that led to ratings of 8 were taken from the pilot commentary and are summarized below.

- The minimum range of the image is not adequate in the flare. This comment stems from the fact that the minimum range of the 35 GHz MMW was between 150 and 200 feet. In the flare and during the rollout the near field was blanked out leaving only a small vertical band (about 3 degrees) of runway image. This is illustrated in Figure 5.1-12. Furthermore, at altitudes between 100 feet and 50 feet, the area that is marked as "blanked" in Figure 5.1-12, suffers from increasing noise that shows up a "blockiness" in the image.
- The edge definition of the runway was too coarse and was not straight.
- There was noise on the runway image and apparent spurious movements.
- The update rate of the display was inadequate for directional control during rollout. The display update rate varied between 200 and 400 milliseconds depending on the magnitude of the aircraft angular rates. The slow update rate also resulted in comments related to a tendency for pilot induced roll oscillations on very short final.

- The workload was increased considerably by light turbulence and an 8 knot crosswind component.

All of the pilots agreed that the flare was accomplished using only the flare cue, and that the image alone was inadequate for accomplishing the flare. The workload rating above 100 feet was a 4 (due to turbulence and crosswind), but degraded to 8 below 100 feet.

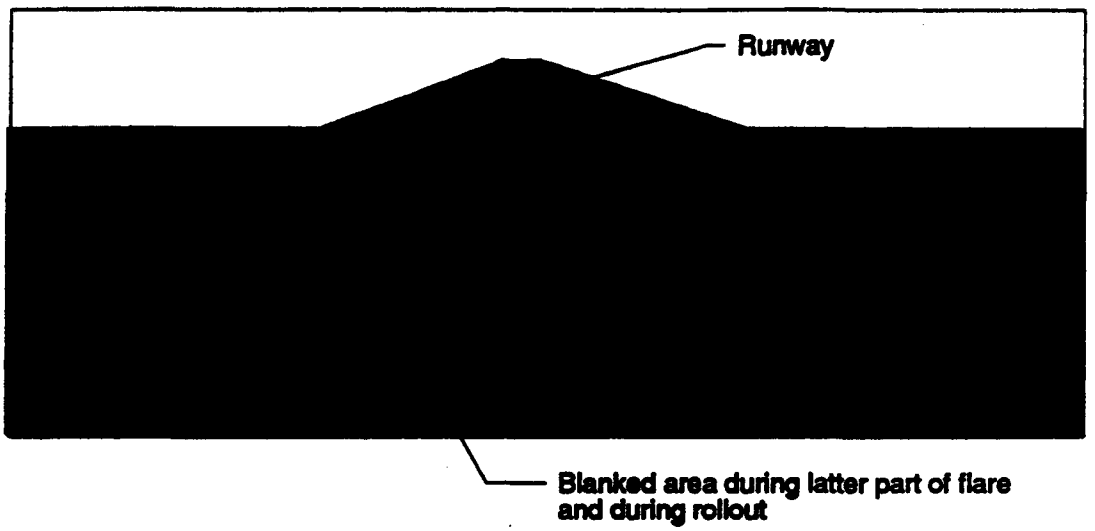

Figure 5.1-12. Illustration of Near-Range Problem experienced With 35-GHz MMW During Flare and Rollout

5.1.2.5 Takeoffs in Simulated Cat IIIc (0/0) Conditions.

Zero/zero takeoffs were simulated by completing an entire takeoff and climb-out with the HUD-shield in place. Several simulated 0/0 takeoffs were made using the 35 GHz MMW radar at the Pt. Mugu Naval Air Station (NTD) where the runway is 200 feet wide and 12000 feet long. The pilot commentary and workload ratings are summarized as follows.

Pilot CA

- Initially looked impossible, but turned out to be doable, but with a very high level of workload. Primary cue was heading. Workload rating = 6, Cooper-Harper rating = 7.
- Marginal maneuver - low confidence - probably would not be able to handle an engine failure
- Not acceptable for commercial operations

Pilot MN

- Image was felt to be useless on the first try, but helped a little on the second takeoff. Heading was the primary cue for both runs.
- Not acceptable for commercial operations. Workload and Cooper-Harper ratings were 3 based on use of heading and localizer symbology for instrument takeoff. Not acceptable for commercial operations because localizer accuracy for task may not be guaranteed.

5.1.2.6 Simulated Runway Intrusion Cases.

Several runs were made at Pt. Mugu wherein a truck was placed on the runway. The evaluation pilot was not aware which runs would involve a runway intrusion. Nine approaches were made and the pilot was able to identify the truck on the runway two out of two times. The truck appeared as a "dot" that should not be there. He noted that it was essential to be very familiar with the airport radar signature to identify an object on the runway. For example, the arresting wires at Pt. Mugu would appear as an obstruction to the unfamiliar pilot. The truck was also placed on the runway prior to a simulated 0/0 takeoff (HUD-shield in place). The pilot did not see the obstruction, and would have initiated the takeoff roll. It was felt that the reason that he did not see the radar image of the truck was because it was masked by the HUD symbology. The evaluation pilot felt that this experimental system was not adequate for reliably detecting a runway intrusion.

5.1.2.7 Approaches Using the Head-Down Display.

Four approaches were made using the head-down display (HDD). This display contained the same information that was displayed on the HUD, and it was mounted on the center of the instrument panel where the weather radar is usually located. The workload rating for the approach was a 5 and the deficiencies that drove this rating are summarized as follows.

- The display was not located in the pilot's primary field-of-view
- The symbology was too small resulting in insufficient display resolution for the required control inputs.
- There was no control over the contrast and brightness of the display.

The function of the HDD was to provide monitoring of the HUD information for the Test Director and the Safety Pilot. o be usable as a flight instrument, the HDD would have to be mounted directly in front of the pilot and must have brightness and contrast controls. The

comment related to the size of the symbology may be a fundamental limitation of using the head-up display format and symbology for a head-down display.

5.1.2.8 Approaches in Actual Cat II and Cat IIIa Conditions.

A frequency distribution of the pilot subjective workload ratings for approaches and landing flares in conditions below Cat I minimums is shown in Figures 5.1-13a and 13b respectively. Twenty-nine of the approaches received ratings of 2 and 3, two approaches were assigned a 4, and three approaches were rated 10 (Figure 5.1-13b). The runs rated 4 and 10 are discussed below as they provide insight into system deficiencies that must be addressed during the development of prototype hardware.

The workload ratings of 4 were assigned to two of four approaches made by pilot LO to ACV. One of the approaches was not rated, and the other was assigned a workload rating of 3, and a Cooper Harper rating of 5. All four approaches were rated as not acceptable for commercial operations. The RVR was reported as 1000 feet and there was a quartering tailwind of 7 knots (winds 180 degrees at 7 knots to runway 32). The pilot noted that the higher than desired workload was because of the short (6000 feet) wet runway, problems controlling airspeed (there was considerable hysteresis in the throttles), lateral lineup problems, and insufficient contrast on the raster scene on the HUD. He noted that the lower 20% of the HUD was in front of the glareshield. That portion had good contrast. The upper portion of the HUD was in front of the windscreen, and he felt that the raster contrast for this part of the HUD was too low. To compensate for this, the cardboard shield was placed in front of the HUD and removed at approximately 200 feet (only for pilot LO). The first approach resulted in a missed approach because it was de stabilized on short final. The second approach was stable, but the cardboard shield was inadvertently left in place, resulting in a second missed approach. The third and fourth approaches resulted in landings, but there was more than desired bank angle activity on short final (peak bank angle of 9 degrees). In contrast, pilot CA flew four approaches in the same conditions (same day) without any significant problems, and without using the cardboard shield (Cooper-Harper and workload ratings of 3, and no missed approaches). Pilot CA had considerably more recent experience with the HUD and the G-II aircraft than Pilot LO, so training was an important factor. This experience may indicate that recurrent training will be important for commercial SVS operations, especially in light of the fact that Cat II and Cat IIIa conditions occur very infrequently. All of the evaluation pilots noted that the learning effects were significant for approaches to actual Cat II and Cat IIIa conditions.

The three ratings of 10 in Figure 5.1-13a were also assigned by pilot LO. As noted above, training was an issue with this pilot as his schedule did not permit frequent participation in the program. The approaches were made to Santa Maria, California (SMX), which also had a 6000 foot runway, and there was a slight tailwind (290 degrees at 4 knots and runway 12). Three approaches were made, and all terminated in a missed approach. There were two other very important contributing factors; 1) the image quality at SMX was poor as evidenced by the late "runway image" calls, and 2) there was a consistent localizer beam bend between 0.50 and 1.2 nm from the runway threshold. This is illustrated in Figure 5.1-14. As shown in illustration A, the aircraft was displaced to the right of the runway centerline as the image came into view at altitudes of 275, 290, and 225 feet for each of the three consecutive approaches. The raw data localizer and the flight director were centered resulting in a conflict between the SVS image and HUD symbology at a critical point in the approach (illustration A in Figure 5.1-14). The pilot chose to follow the flight director, and as a result stayed to the right of the runway centerline. At about 0.50 nm, the beam rapidly returned to centerline, leaving the aircraft offset to the right, and showing a consistent error on the raw data localizer (illustration B). The flight director commanded a gentle return to course whereas an aggressive correction was required. Visual acquisition of the runway occurred at 100 feet, with the aircraft lined up with the right edge. It should be noted that the beam bend was very subtle and never exceeded 1/2 dot of localizer deflection. Such an aggressive correction would problably not be acceptable as a flight director control law as it would result in excessive guidance cue activity. In visual conditions, the pilot would ignore the raw data and flight director to accomplish the required "aggressive" sidestep to the runway center line. Such activity was observed for the other two evaluation pilots, using the SVS image. As noted, these pilots were able to accumulate significantly more recent experience with the system.

The pilot comments and discussions during the debrief are summarized as follows.

- Pilot LO was not willing to use the runway image when it conflicted with the guidance cue. The other evaluation pilots did not share that opinion.
- The pilot was not convinced that the image was good enough to abandon guidance at such low altitudes in IMC conditions. He kept asking himself "is that it?". It should be noted that the image at SMX was poor. Specific problems noted were poor runway edge definition, and a black stripe down the centerline of the image that was unique to the 35 GHz antenna mechanization for this program. That stripe is discussed elsewhere in the report and is referred to as the "centerline problem".
- The pilot had problems seeing the actual runway at 100 feet because he had to sit low to be in the HUD eye-box. This resulted in problems seeing over the glareshield, sometimes referred to as a low cockpit cutoff angle.

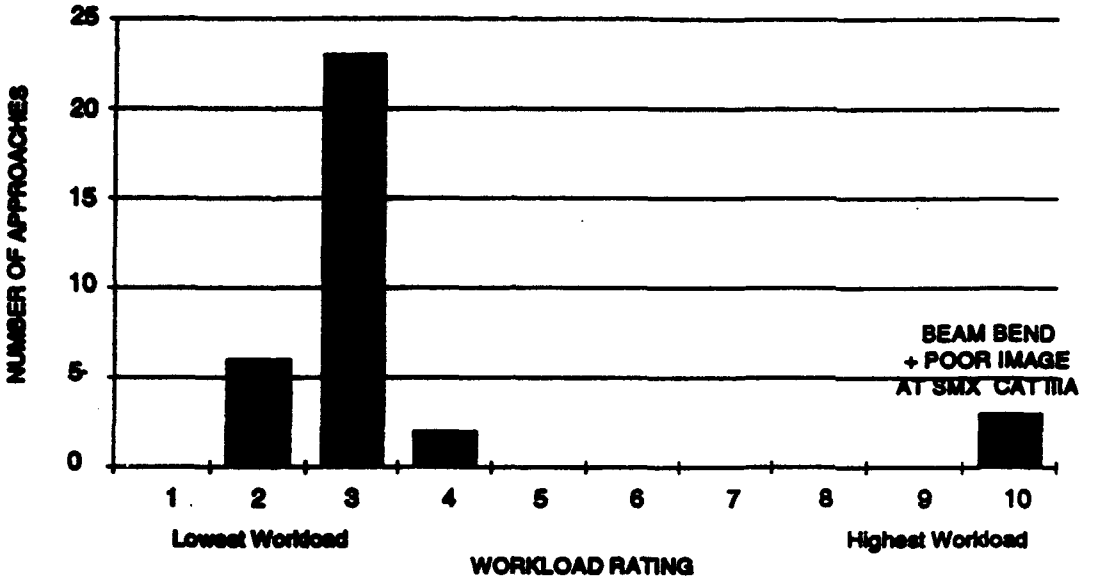

a) Workload Ratings for Approach Segment From an Altitude of 250 ft to 50 ft

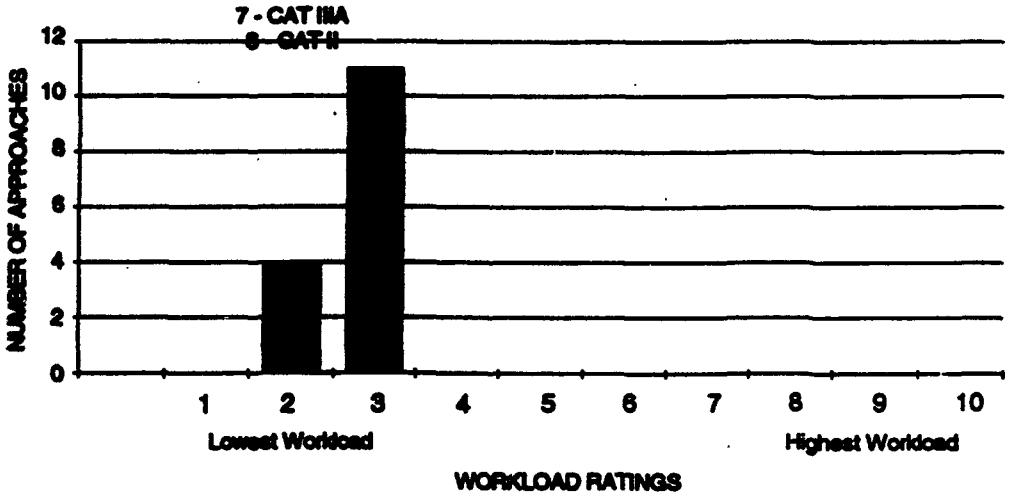

b) Workload Ratings for Flare

Figure 5.1-13. Frequency Distribution of Pilot Workload Rating Data for Actual Cat II and Cat IIIa Approaches

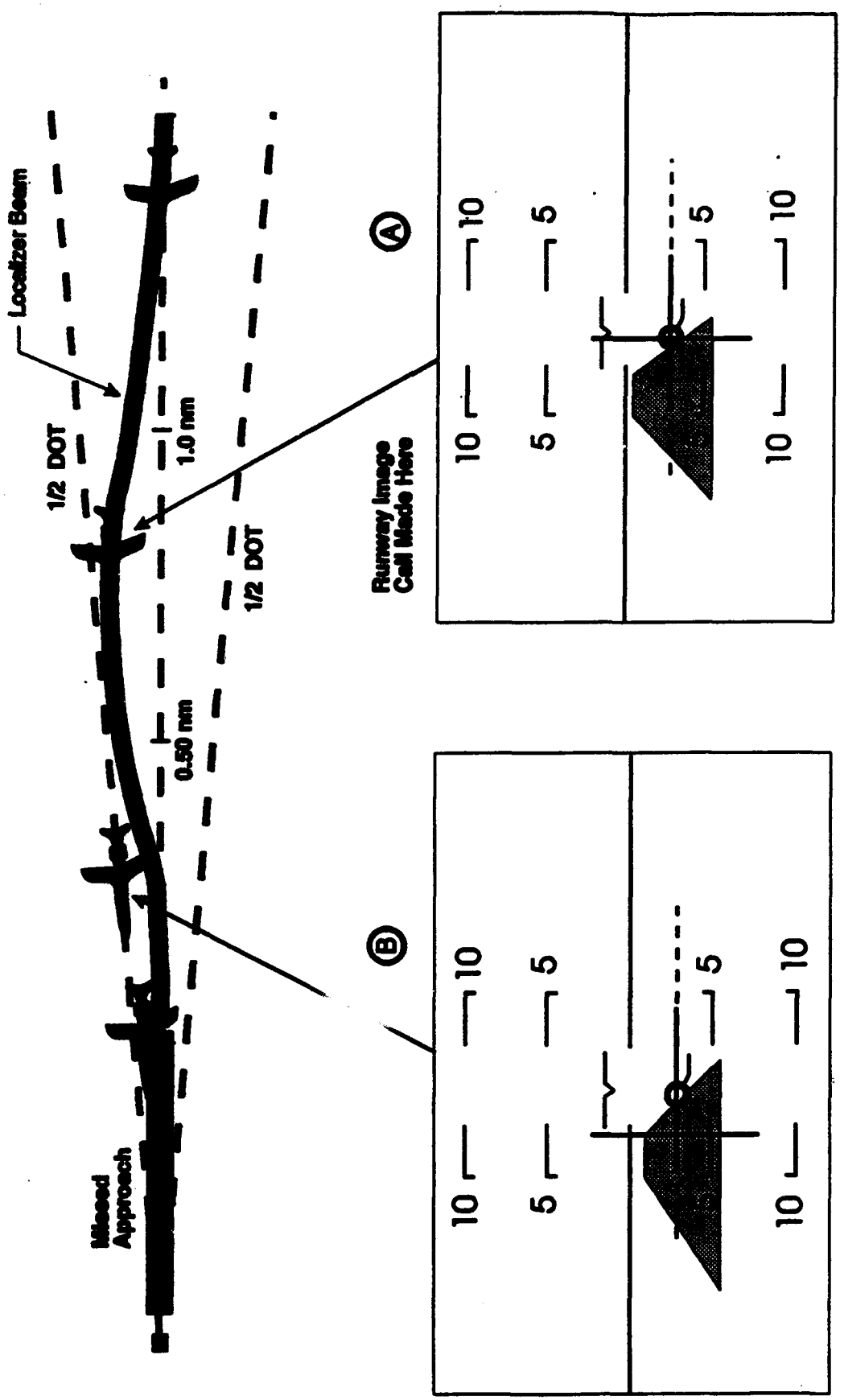

Figure 5.1-14.. Observed Beam Bend Problem at SMX - Actual Cat IIIA Conditions

5.1.3 Summary Comments Regarding Pilot Performance

All approaches made in actual or simulated Cat II or Cat IIIa conditions were acceptable at airports with long runways (e.g., Pt Mugu (NTD) and Vandenberg (VBG)). For approaches to shorter runways (6000 feet or less), issues such as beam bends, image quality, crosswinds, tailwinds, and pilot training became significant (e.g., Arcata (ACV) and Santa Maria (SMX)). The deficiencies associated with shorter runways were not apparent if an actual landing was not attempted, such as at Huntington WV (landing not attempted because the FAA below-minimums waiver was not valid at HTS). The workload associated with short runways tends to be less severe if the runway image is available well above the decision-height. Evidence of this is seen in Figure 5.1-15 where the workload ratings are plotted vs. the altitude and range where the pilots called "runway image". The ratings of 10 all occur for cases where the runway image call occurred below 300 feet, and less than 1 nm from the threshold. This would indicate that better MMW range is more important for short runways where the margin for error is less. An early runway image call gives the pilot more time to incorporate the image into his instrument scan and control strategy, so that beam anomalies and crosswinds are more easily handled. For example, the problems encountered at ACV resulted in workload ratings of 4, and the runway image call was made at about 500 feet. The only other rating worse than 3 (workload rating = 4) was assigned at Carlsbad/Palomar CA (CRQ), which is only 4700 feet long, and the runway image call was made at 490 feet. The approach speeds (135 to 150 knots depending on weight) and handling characteristics of the G-II are similar to transport aircraft so that these results are directly applicable to that class of aircraft.

The flare and landing data are summarized in Figures 5.1-10b and 5.1-13b. They indicate that there were no significant problems with that task for Cat II and Cat IIIa. The pilots all indicated that the flare cue on the HUD provided adequate guidance. The exception was for the simulated Cat IIIc (0/0) landings where the workload was judged to be very high by two of the three pilots. The deficiencies associated with the Cat IIIc landings are discussed above. One caveat to this data was that many of the Cat IIIa landings were touch-and-go landings where touchdown position was not a safety issue. Pilot CA's first landing was marginally long at Arcata, and there was a tendency to duck-under (using the SVS image) on the following two landings. This was never an issue for the longer runways. The flare cue used for this experimental system was not optimized to provide a landing footprint that would insure high probability safe landings on marginally short runways, and in varying wind and wind-shear conditions. It would be important to optimize the flare cue for a commercial system. The results of the pilot questionnaire in Figure 5.1-8 are summarized below in Table 5.1-6.

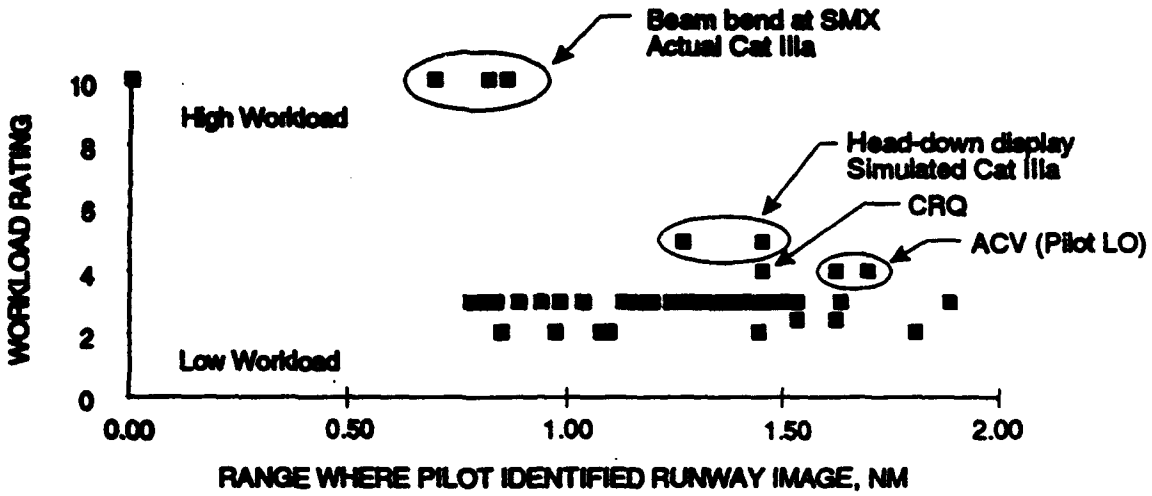

a) Workload Rating vs. Range Where Pilot Identified the Runway Image

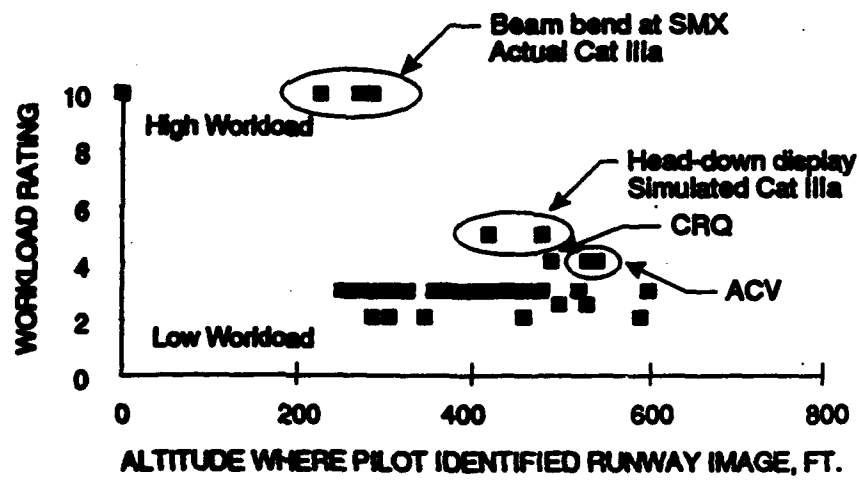

b) Workload Rating vs. Altitude Where Pilot Called Runway Image

Figure 5.1-15. Workload Ratings for All CAT I, Cat II, and Cat IIIa Approaches

Table 5.1-6 Results of Pilot Questionnaire

Question	Pilot Responses
Considering only these approaches, would you consider this system safe for commercial operations?	• Yes for the large majority of runs • "No" answers pinpoint deficiencies that have been discussed in detail in this section of the report. • The responses to this question (yes/no) are given for every run in Appendix K
Give your overall impressions of the symbology and image for: • Runway alignment • Glidepath control • Landing flare • Rollout	Runway Alignment: The pilots generally agreed that the image was adequate for runway alignment. The image transport delay resulted in a few comments related to a tendency towards a roll PIO on short final. This was overcome as experience was gained with the system, and the pilots learned to only use symbology for "inner-loop" aircraft control, and the image for "outer loop" guidance. Glidepath control: It was generally agreed that the image alone was not adequate for glidepath control. The combination of flight path symbology and image did provide for adequate glidepath control for most non-precision approaches, but there were problems as noted in the discussion related to Figure 5.2-6. Landing Flare: The image was not adequate for landing flare. The pilots relied 100% on the flare cue for flare management in simulated Cat IIIc landings and a combination of flare cue and outside world for landings in very low visibility. The primary deficiencies were lack of adequate resolution, poor edge definition, and the near range problem. Rollout: The image alone was not adequate to provide directional control for landing rollout or the takeoff roll. The pilots relied primarily on heading, second on raw localizer data, and to a much lesser extent on the image. The primary deficiencies were the lack of edge definition and the near range problem.
Did your initial identification of the runway prove to be correct?	The answer to this question was yes for all but four cases. One was at Arcata where the pilot initially mistook the ramp for the runway. This was corrected immediately. The other three cases occurred at Santa Maria where the image was poor and there was a beam bend. The pilot tended to mistake the ramp for the runway, but always realized the error before it affected his performance. The answers to this question (yes/no) for every run are given in Appendix K.
Did you ever feel it necessary to refer to head-down information?	The answer to this question was always no. The only exception was that the pilots sometimes looked at the fuel flow indicators to match the thrust on the right and left engines. The results of this question indicate that the information displayed on the HUD was sufficient and complete for the approach and landing task. It also indicates that the pilots had sufficient confidence in the data on the HUD that they did not feel that it was necessary to look down to verify. The other exception was for approaches in high crosswinds where the flight director disappeared from the display making it necessary to use the head-down flight director. This occurred during the rain runs where the visibility varied between 2 and 4 miles, so the loss of flight director was not critical to the experiment.
Did the quality of the image vary significantly with range.	The answer to this question was usually yes; the image improved with decreasing range. In a few cases the pilots noted that below 50 feet altitude, the image degraded rapidly due to blockiness in the near field. That problem existed for all runs, and the pilots did not choose to repeat the comment every time. For a few cases the image went from dim to very bright just above 200 feet altitude. This tended to happen in light rain and fog (e.g., Worcester MA (ORH)). For a few of the rain cases, the image degraded after the pilot called runway image. This was probably due to peaks in the rain-rate as the aircraft progressed down the glideslope (see Figure 5.1-5)

5.1.4. Summary of Pilot Commentary.

A summary of the pilot commentary related to strengths and shortcomings of the experimental SVS is presented below.

General Comments Related to Synthetic Vision System performance

- All of the evaluation pilots felt that the system was viable as a means to achieve Cat IIIa minimums on Type I ILS guidance, and to achieve lower minimum descent altitudes on non-precision approaches.
- All of the evaluation pilots were enthusiastic about the use of a head-up display to assist in the transition from use of the image to use of outside visual cues.

Comments Related to the 35 GHz MMW Radar and FLIR

- The FLIR image was excellent, or it was non-existent. Excellent images were observed in conditions of haze or at the bottoms of cloud bases. All pilots demonstrated Cat IIIc (0/0) landings using the FLIR image in simulated IMC conditions with workload ratings of 3 or better. When there was visible moisture (dense fog or rain) the FLIR did not produce a usable image.
- The MMW radar image was usable to identify the airport and the landing runway. The pilots commented that they relied heavily on airport runway/taxiway pattern recognition to insure that they did not mis-identify the runway as a road or other object.
- The pilots were able to learn radar signatures of the terrain approaching airports. For example certain roads, fields, and towns showed up very well on the radar. It was important to learn that some objects produce a radar return out of proportion to what that object produces in the normal visual field. For example the radar return of a chain-link fence along the side of the runway or arresting cables across the runway a Pt. Mugu were very bright. The radar return of approach light stands was very bright and was often seen well before the runway image (e.g. Worcester MA (ORH) in rain and fog, and Pueblo CO (COS) in snow conditions).
- The minimum range problem (see Figure 5.1-12) should be resolved for a commercial system.
- There was excessive noise in the near field below altitudes of about 75 feet. This showed up as blockiness down to about 25 feet at which time the near field was blanked due to the minimum range problem.
- The centerline problem should be resolved for a commercial system. This consisted of a black vertical stripe that occurred in the center of the image. This stripe could be nearly eliminated by tuning the proms in the Malibu antenna, as well as certain radar parameters.

This tuning was accomplished several times during the program. The primary problem was that the centerline sometimes interfered with the runway image.

- The image was excessively sensitive to the aircraft pitch attitude in the absence of antenna pitch stabilization. It was necessary to conduct all approaches with full flaps to maintain the proper nominal pitch attitude of zero. In turbulence the necessary changes in pitch attitude to maintain glideslope caused the image to fade in and out. It also caused the raster brightness to vary significantly so that it was not possible to set the proper value. Pitch attitudes of greater than 2 degrees had a noticeable degrading effect on the image.

- The raster brightness that was best for the approach, was too bright after breakout. In Cat II and Cat IIIa conditions, breakout consists of a dim view of the runway at best. The edges of the runway were obscured by the green raster because the radar image was not perfectly aligned with the runway and/or the radar image was more narrow than the runway. Some pilots compromised by using a less than desirable brightness on the approach, and others had the Test Director turn off the raster at breakout. One solution would be to install a "kill switch" on the column, but this could be a problem if the pilot encounters a fog bank on the runway.

- The latency in the image was too large, and was estimated to be approximately 200 ms. for gentle attitude changes and 400 ms. for large angular rates. It was particularly noticeable in roll.

- The radar image sometimes "jumped", especially a low altitudes. It is suspected that this is a result of the altitude data used as input to the B-to-C scope conversion. The altitude signal consisted of pure barometric data above 1000 feet and blended to pure radar data at touchdown. Significant variations in the terrain at low altitude would result in a discontinuity in the B-to-C conversion process.

- There was a tendency to get very low on short final when using the flight path symbology and MMW image to construct a -3 degree glideslope. This is believed to be a result of mis-registration of the radar image with the outside world. There is also reason to believe that the flight path symbology does not provide sufficiently compelling glideslope error data to the pilot at altitude below 200 feet.

Comments Related to the Head-Up Display Hardware and Symbology

- The pilot's head must be in a certain position to properly view the HUD, called the eyebox. For some pilots, it was necessary to make compromises to get into this position. For example, pilot LO could not use the toe-brakes. All of the pilots had to sit too low for an optimum view over the glareshield. It is well known that a high seat position is best when making approaches to very low minimums.

- Some type of auto brightness control is required for the raster.

- The flight director symbol was off the display in large (about 25 knot) crosswinds. The flight director should never leave the display, even at the expense of conformality with the outside world.
- The flight director algorithms were not optimized for the localizer and glideslope capture tasks. This was a minor issue as the SVS task did not occur until well after glideslope and localizer capture.

5.2. TRACKING PERFORMANCE

This section provides a brief examination of Localizer and Glideslope Deviations for approaches in clear, fog, rain, and of deviations from desired path in which no navaids where used in the final segment of the approach. A brief examination of sink rate in the flare maneuver is also provided.

There are two types of plots presented. The first is a 3-D bar plot of average values, maximum, minimum and standard deviation, and the second is a 3-D histogram . These plots are intended to show the distribution of the centerline and glideslope deviations during final approach under different weather conditions. The data plotted are RMS values of the ILS deviations. Localizer calculations are accomplished from the threshold to 9,000 ft out from the threshold. Glideslope is calculated from 2,000 ft out from the threshold to 9,000 ft out from threshold. The glideslope calculations were terminated 2,000 ft from threshold to eliminate data corruption from missed approaches.

The histogram presentation shows a clear cluster of deviations of 0.0° to 0.4° RMS for Localizer and 0.0° to 0.6° RMS for Glideslope (see Figures 5.2-1, 2, 3, and 4). This cluster is apparent for all approaches with the exception of the no-navaid approaches. For those cases, the data appear to have a much wider spread of 0.0° to 1.2° RMS for Localizer and 0.2° to 2.0° for the Glideslope. Looking at the bar plots, we also see a well behaved system for all but the no-navaid approaches.

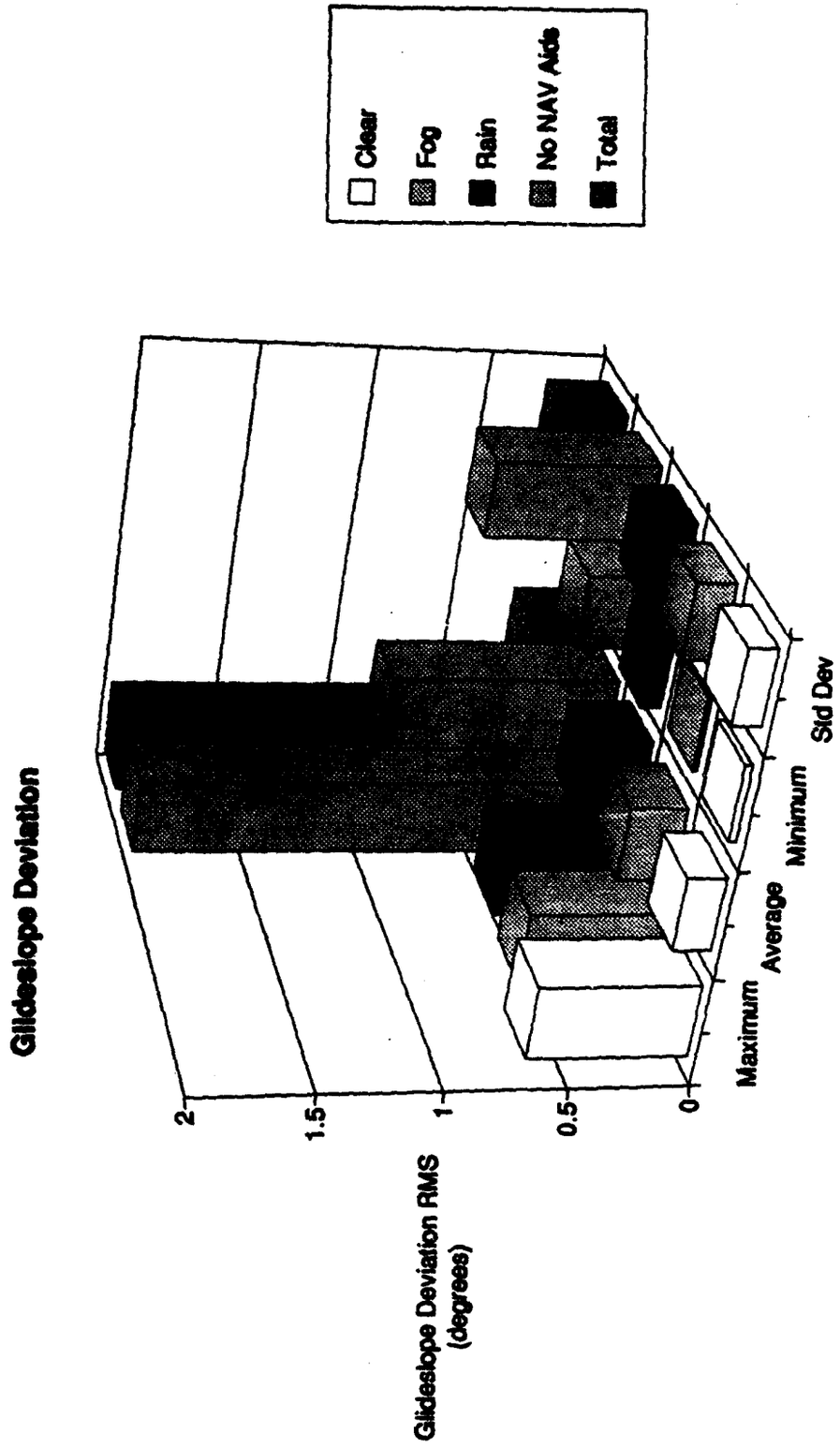

Figure 5.2-1. Glideslope Deviation Values

Figure 5.2-2. Glideslope Deviation Histogram

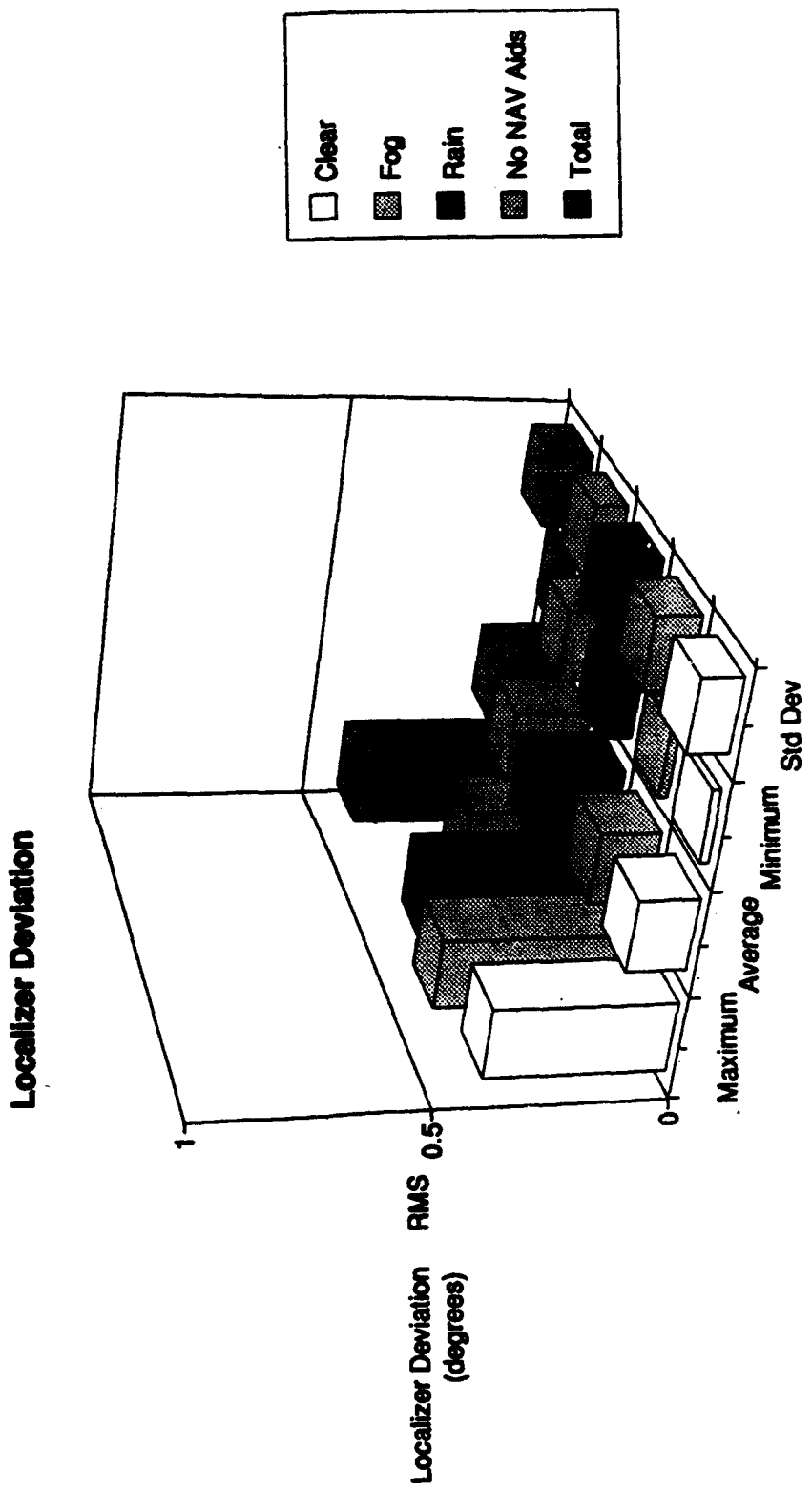

Figure 5.2-3. Localizer Deviation Values

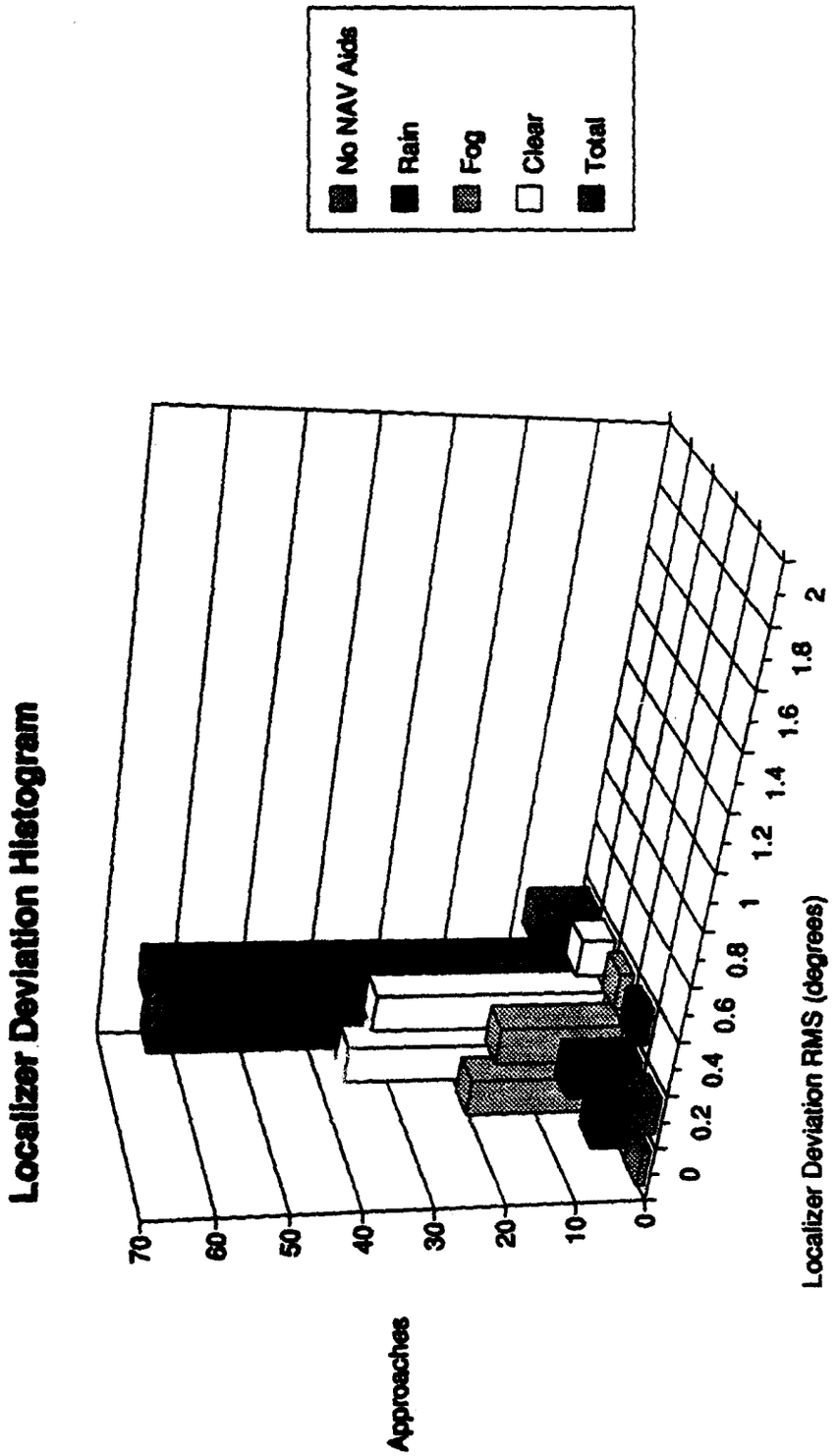

Figure 5.2-4. Localizer Deviation Histogram

Large glideslope deviations are expected for the no-navaid approaches since the electronic glideslope was not displayed to the pilot. The average values of RMS Deviations are consistently low for all approaches where the glideslope was displayed to the pilot. See Table 5.2-1 Localizer and Glideslope RMS Deviations.

Table 5.2-1 Localizer and Glideslope RMS Deviations

	Average	Max.	Minimum	Std. Dev.
Localizer (with ILS)	0.168°	0.431°	0.057°	0.092°
Glideslope (with ILS)	0.255°	0.626°	0.089°	0.174°
Localizer (w/o ILS)	0.170°	0.241°	0.088°	0.073°
Glideslope (w/o ILS)	0.980°	1.980°	0.218°	0.693°

For the limited number of no-navaid data points, there is a consistent trend of being high during acquisition (runway entering radar range at approximately 5,000 ft from threshold), and being well below glideslope at threshold (crossing over between 2,000 to 4,000 ft from threshold). We also see a significant difference in the glideslope deviation between the two pilots, see Table 5.2-2

Table 5.2-2 Localizer and Glideslope RMS Deviations Without ILS for Two Pilots

		Approach		
		1st	2nd	3rd
Pilot A	Localizer (w/o ILS)	0.088°	0.132°	*
	Glideslope (w/o ILS)	1.980°	1.099°	1.563°
Pilot B	Localizer (w/o ILS)	0.220°	0.241°	*
	Glideslope (w/o ILS)	0.399°	0.218°	0.619°

* Pilots were instructed to purposely fly 1 dot to the left of centerline.

Sink Rates for the flare maneuver are plotted for landings in clear, fog, rain, and for the no-navaid approaches.

The plots in this section were designed to show the values and distribution of the aircraft sink rates at touchdown under different weather conditions. The data has been cataloged and plotted in on two graphs. The first consists of the numerical values (maximum, average, minimum, and the standard distribution of the sink rates). The second plot is a histogram. This plot shows the distribution of data points.

The first graph, (Figure 5.2-5) Value Chart (max., avg., min., and std dev) shows that the sink rates are all within an acceptable range. The average sink rate was under 3 feet per second.

The histogram chart (Figure 5.2-6) shows clusters of sink rates. As seen, the clear weather landings have a good distribution with the most number of landings. The sink rates range from 0 to 6 ft/sec with the peak at 2 ft/sec. The rain landings exhibit similar peak (smaller deviations probably due to the lower number of approaches) and the no-navaid data is a very small sample. However, the sink rates while in fog clearly exhibit a peak that is centered at a higher sink rate, about 4.5 ft/sec. Further data points are required to determine if the distribution will continue to be centered at this higher value.

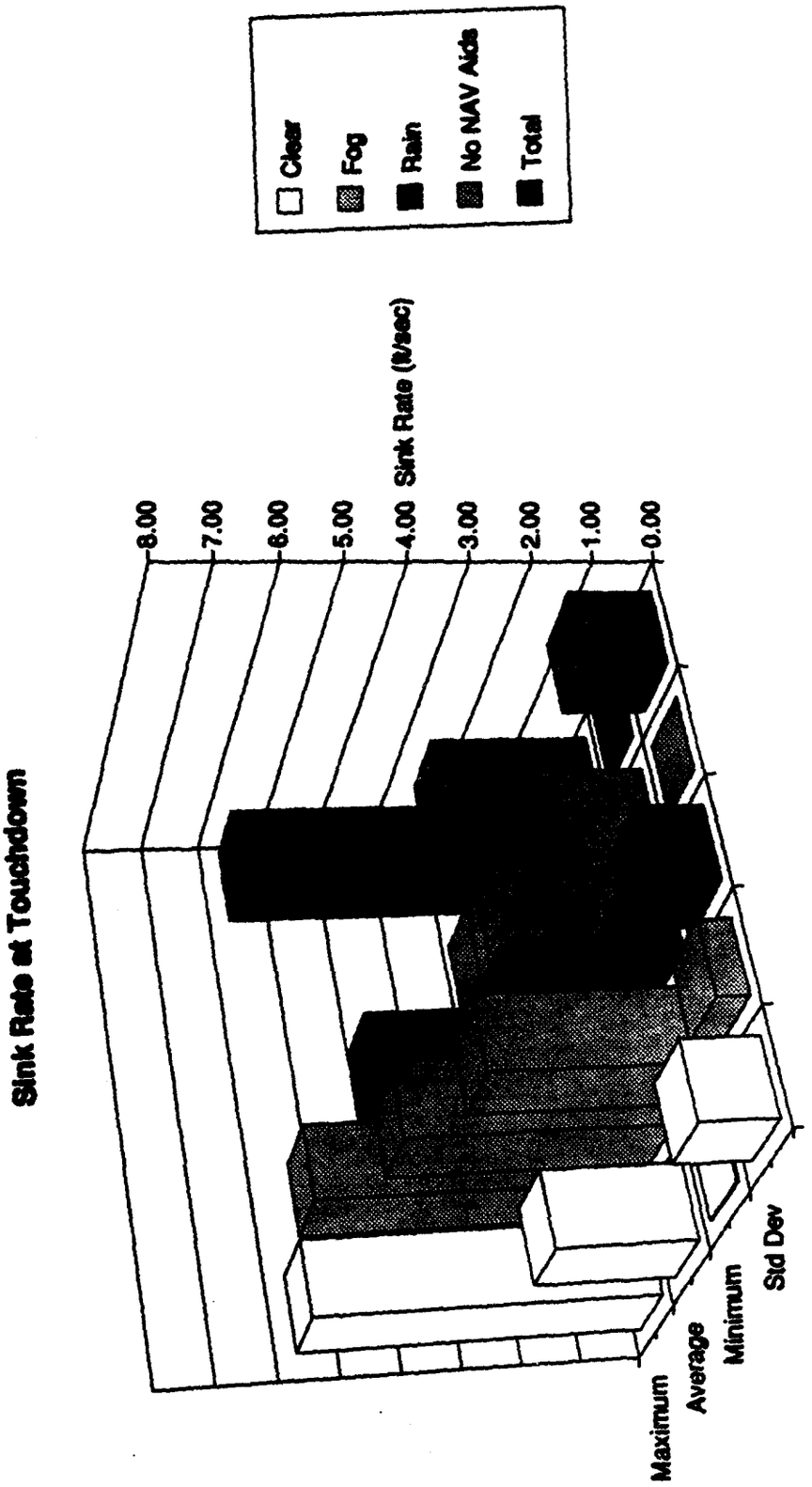

Figure 5.2-5. Sink Rate Values

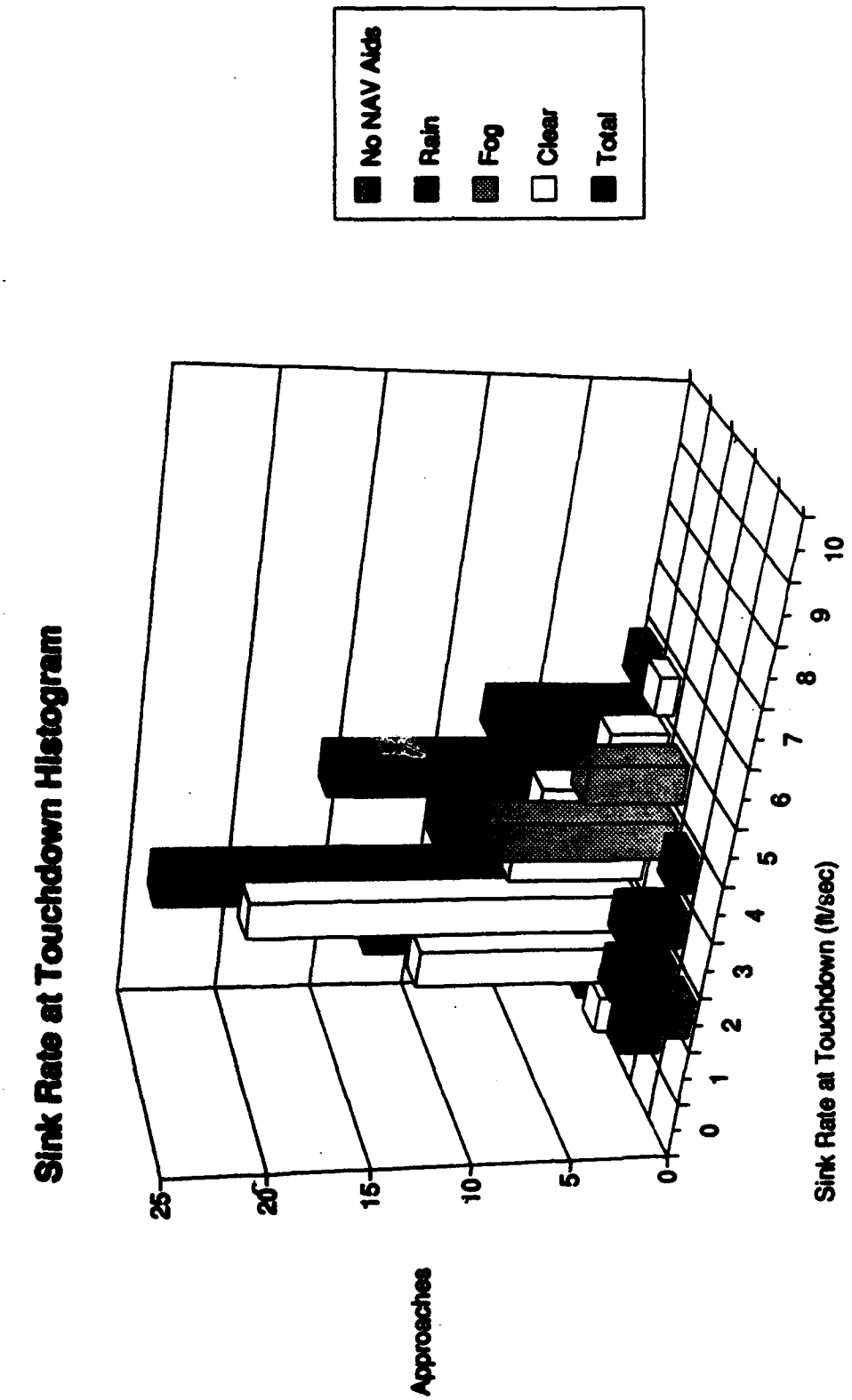

Figure 5.2-6. Sink Rate Histogram

SECTION 6

SENSOR PERFORMANCE RESULTS

6.1. RADAR PERFORMANCE

This discussion of results addresses those obtained from the flight test portion of the program. However, results from the tower tests are drawn upon where appropriate to complement or supplement the available flight test database. This report only discusses those tower test parameters measured during the flight tests as well. Parameters measured only during the tower tests are discussed in the tower test report (Volume 2 of this Final Report).

6.1.1 Basic Phenomenological Measures

The paragraphs which follow address basic phenomenological measurements made using the Honeywell radar system. These measurements include normalized radar cross sections as well as atmospheric attenuation and volumetric reflectivity. The term phenomenological is used to describe these measures since they quantify fundamental effects which will be encountered by any radar system radiating circularly polarized electromagnetic energy at 35 GHz. In a sense, then, these measures describe the physics of the synthetic vision scenario.

6.1.1.1 Surface Reflectivities

The basis for detection of a runway by a radar system is the difference between the electromagnetic properties of the runway surface and those of the surrounding terrain. The differences in the electromagnetic properties of these two regions result in a difference between the reflective properties of the two. The traditional measure of the magnitude of the radar reflectivity of a surface is radar cross section (RCS). This parameter quantifies the amount of radar energy scattered (reflected) back toward the radar by the surface of interest.

Radar cross section is measured in terms of area; thus, it is typically reported in units of meters-squared. The larger the RCS area, the greater the amount of energy reflected by the physical surface back toward the radar. The result is a larger radar target. Often, surface RCS values are normalized to isolate the inherent surface reflectivity, from the specific antenna parameters and viewing angle of the radar, which determine how large a portion of the target is

viewed at once. This normalized surface RCS is unitless, since it represents reflectivity expressed in area per unit area.

Since normalized RCS values for objects of interest span such a wide range, normalized RCS is typically reported in logarithmic units of decibels, symbolized by dB. Thus, all surface RCS values reported herein are reported in decibels.

The software described in Section 4.4.2.3.1.2.6 above was used to compute RCS values for four airport scenes. The measured RCS values for the respective runway surfaces and the surrounding terrain were plotted versus depression angle for each airport. In general, RCS for such surfaces is not a linear function of depression angle. However, over the limited depression angle range considered for this analysis (1 to 8 degrees), a linear fit to the data was deemed appropriate.

Figures 6.1-1 through 6.1-4 plot normalized RCS versus depression angle for both runway and terrain for Arcata, Vandenburg AFB, Santa Maria, and Santa Barbara, respectively. All sites are in California, and all data were acquired in August, 1992. For each plot, the raw measured RCS values were adjusted by the appropriate calibration factors. Each symbol in these plots represents a single measurement based on either a runway or terrain patch comprising six PPI pixels. Each line plotted represents the least-mean-square-error (LMSE) fit to the respective data set.

Figure 6.1-5 plots the normalized RCS for the terrain and the runway at Santa Barbara computed from the snapshot taken at an altitude of 47.95 meters (about 157 feet). The normalized RCS values for the terrain are denoted by open rectangles, and the runway normalized RCS values, by shaded rectangles.

Note the two plotted lines in Figure 6.1-5. These lines represent two estimates of the system noise floor for this particular data snapshot. Both lines are generated based on the data acquisition system transfer function. Consider the data acquisition system transfer function illustrated in Figure 6.1-6 below. The lower noise floor estimate in Figure 6.1-5 corresponds to the system noise floor based on the computed system transfer function denoted in Figure 6.1-6. Specifically, for the gain and bias settings corresponding to this snapshot, an analog-to-digital converter (ADC) output of 27 represents the noise floor based on previous Equations 4.4.2-4 through 4.4.2-7. Any measured ADC values of 27 or less are likely contaminated by noise and should be discarded.

Thus, the solid line in Figure 6.1-5 corresponds to this ADC output value converted to equivalent normalized RCS at various depression angles.

However, if Figure 6.1-6 is examined closely, the measured data acquisition system transfer function levels out at some ADC value just under 50. This same trend is observed in all of the measured transfer function curves available (see Appendix I). Thus, based on the measured data, the noise floor should actually be associated with an ADC value between 45 and 50. The more conservative value of 50 has been selected for Figure 6.1-5 and is denoted by the upper noise estimate curve.

In order to ensure that the measured RCS values were not contaminated by noise, data which fell on or below the noise floor were discarded. The actual noise floor for the system was felt to lie somewhere between the two noise floor estimates shown in Figure 6.1-5. However, the conservative approach was taken of discarding all data below the upper noise floor estimate. Figure 6.1-7 is identical to Figure 6.1-5, except that in it, the data values which were thus discarded are circled with a dashed line.

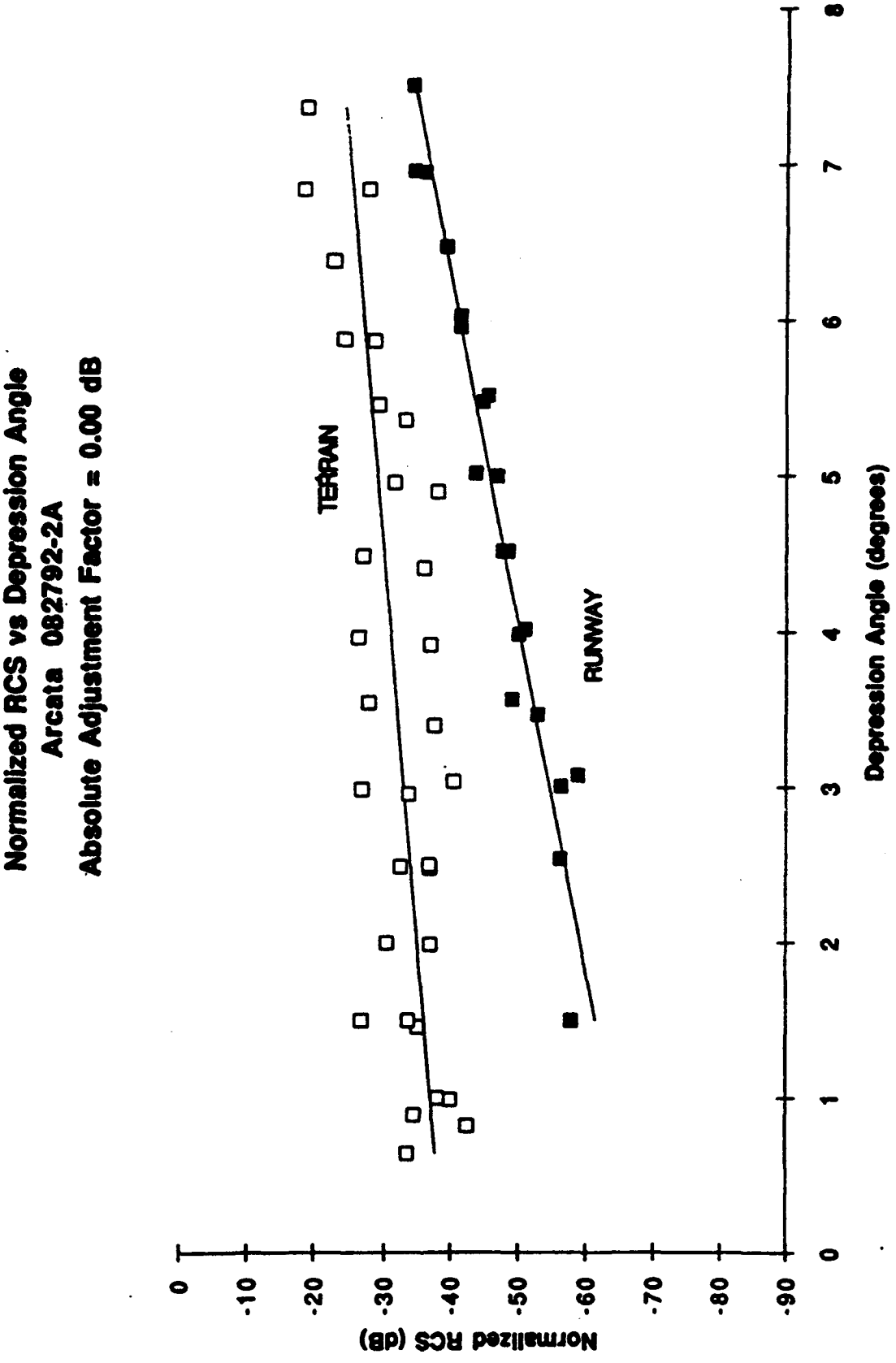

Figure 6.1-1. Plot of Normalized RCS Versus Depression Angle for Both Runway and Terrain At Arcata, CA, on August 27, 1992 (Approach 2A)

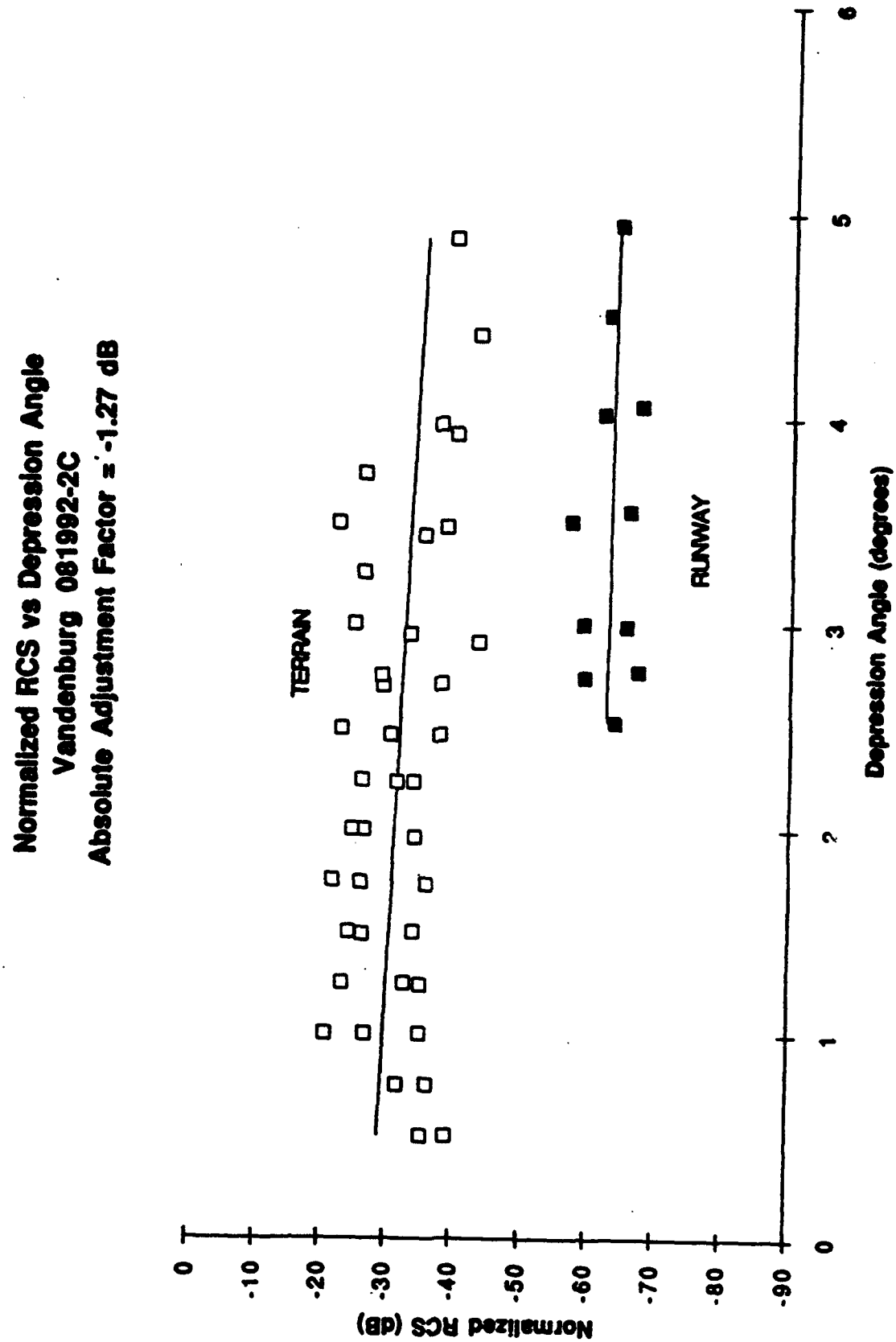

Figure 6.1-2. Plot of Normalized RCS Versus Depression Angle for Both Runway and Terrain At Vandenburg Air Force Base, CA, on August 19, 1992 (Approach 2C)

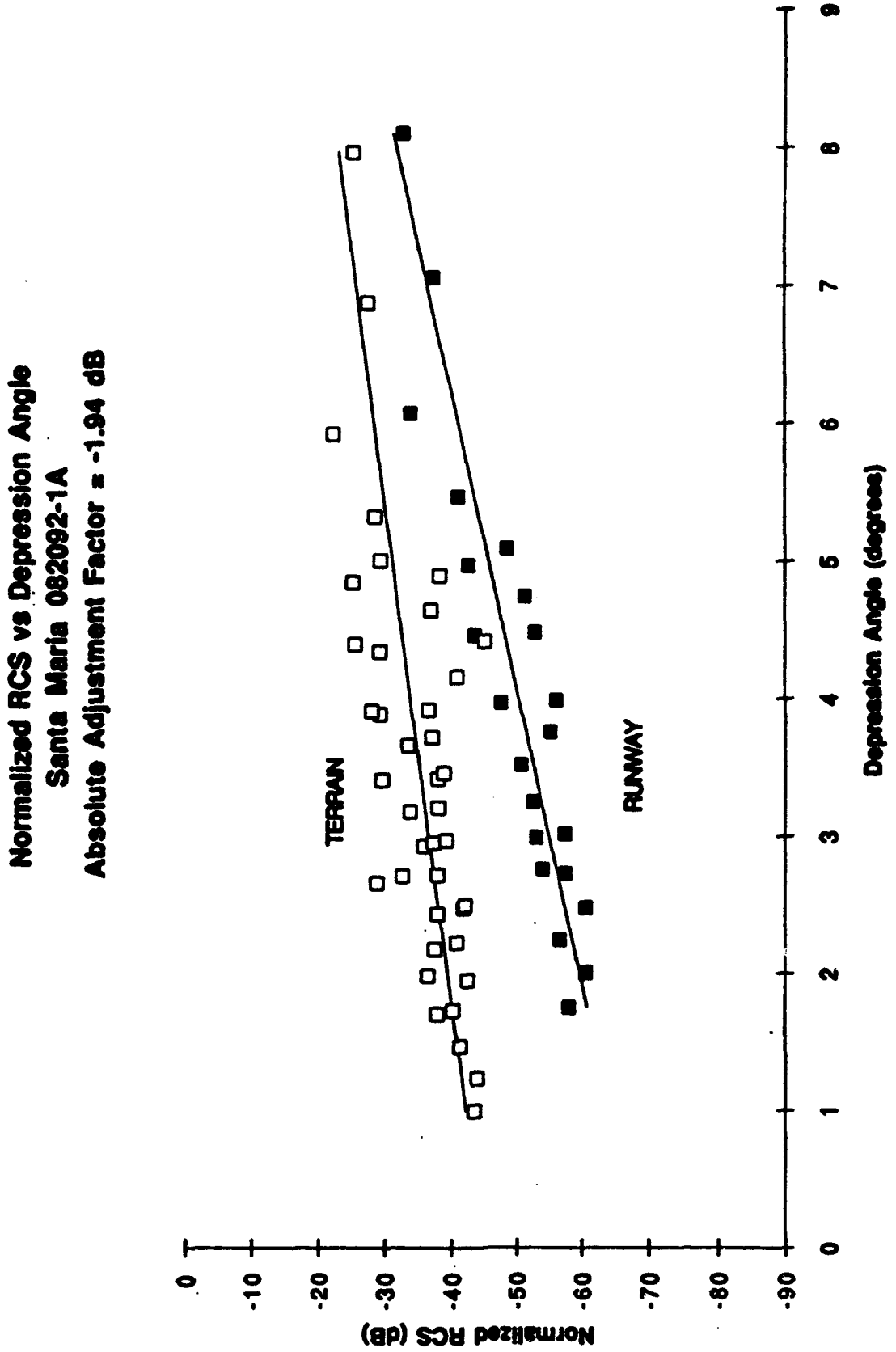

Figure 6.1-3. Plot of Normalized RCS Versus Depression Angle for Both Runway and Terrain At Santa Maria, CA, on August 20, 1992 (Approach 1A)

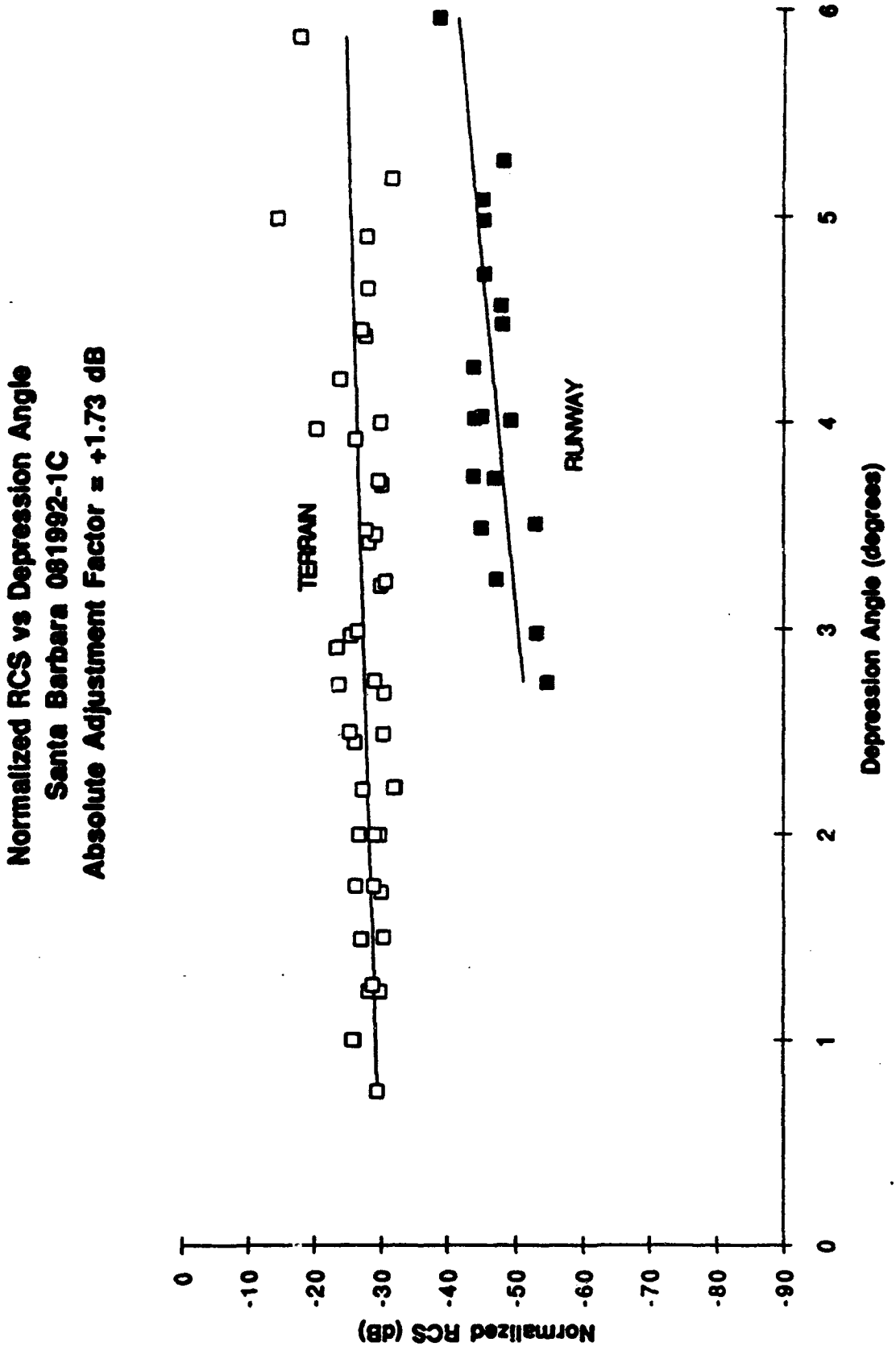

Figure 6.1-4 Plot of Normalized RCS Versus Depression Angle for Both Runway and Terrain At Santa Barbara, CA, on August 20, 1992 (Approach 1C)

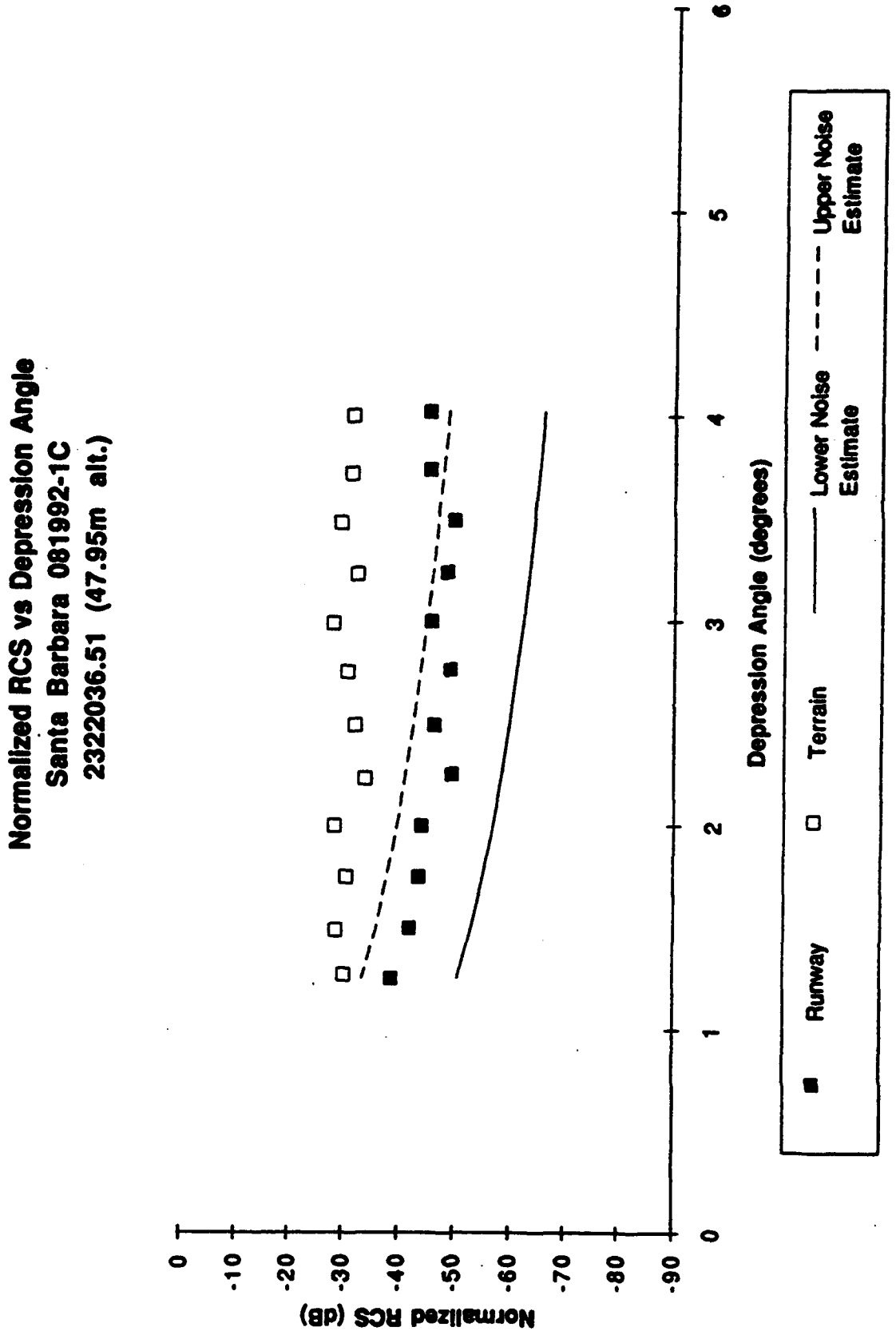

Figure 6.1-5. Plot of Normalized RCS Versus Depression Angle for Both Runway and Terrain and Noise Floor Estimates at Santa Barbara, CA.

Data Corresponds to an Altitude of 47.95m During Approach 1C on August 19, 1992.

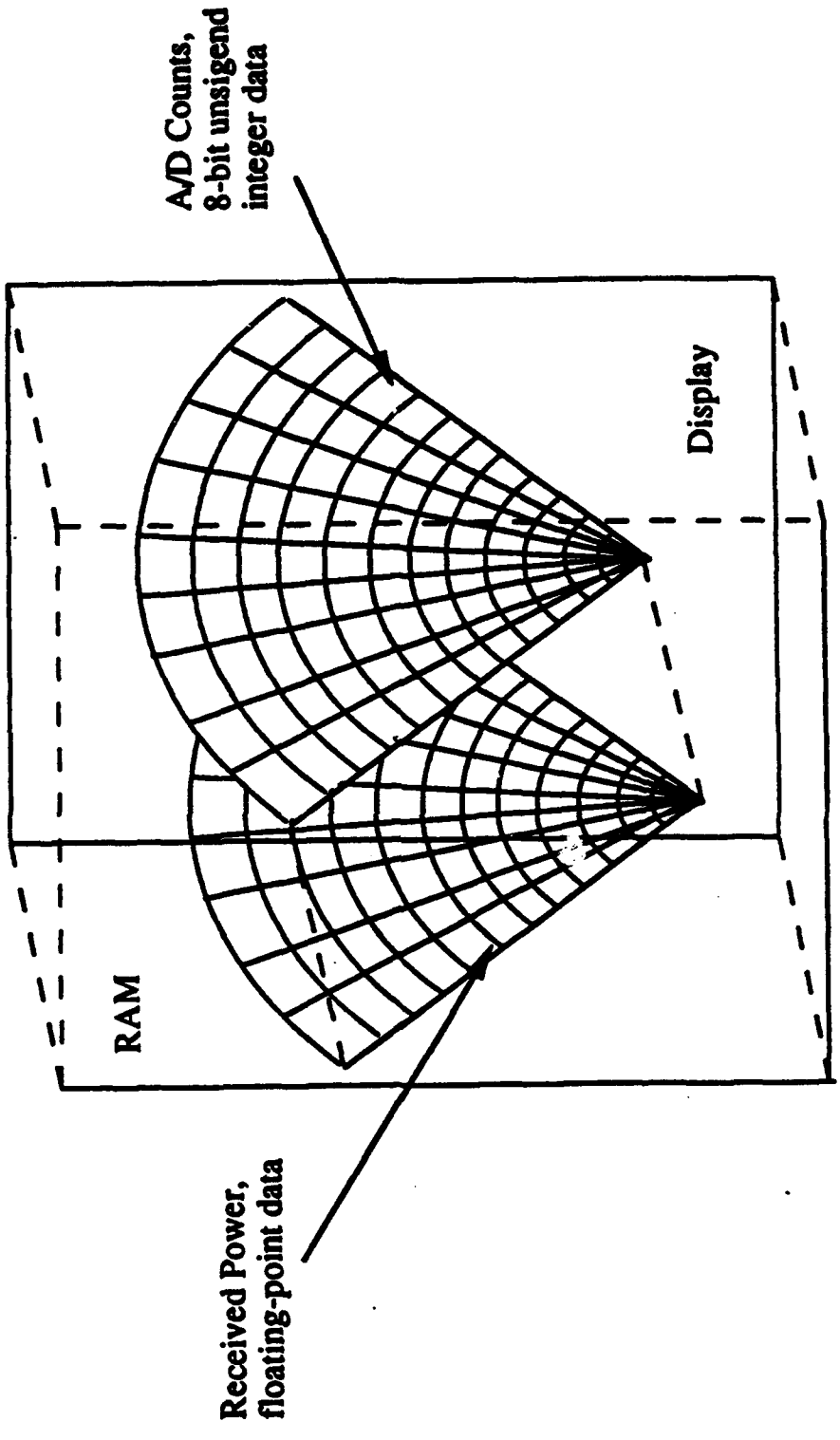

Figure 6.1-6. Image Displaying A/D Counts and Corresponding Received Power File in RAM

As can be seen from Figure 6.1-7, only two runway RCS values were not excluded by this noise-floor test. Fortunately, however, as the range to the runway decreased as the aircraft descended, the RCS of the runway became measurable above the noise floor. Figures 6.1-8 and 6.1-9 plot the measured RCS values for the 35.16 meter and 17.92 meter altitude snapshots, respectively. The data excluded via the conservative noise-floor test are again indicated via the dashed ovals.

If all the non-excluded data from Figures 6.1-7 through 6.1-9 are combined, Figure 6.1-10 is obtained. This is the same plot shown previously for Santa Barbara in Figure 6.1-4. However, in Figure 6.1-4 a common symbol is used for all terrain values, and another symbol for all runway values. In this case, designating the snapshot from which each RCS value was derived was not felt to be necessary. Also, all RCS values in Figure 6.1-4 have been adjusted upward by 1.73 with respect to Figure 6.1-10, since this is the calibration factor determined for Santa Barbara (see Section 6.2.4).

The process outlined above was used in creating the RCS plots for Arcata, Vandenburg, and Santa Maria, as well as for Santa Barbara. Thus, all of the data plotted in Figures 6.1-1 through 6.1-4 were created in a consistent manner.

In all cases there is considerable spread in these figures in the data. The spread in the Vandenburg data is the greatest of the four, with only four of the data point symbols actually touching the LMSE lines. The Vandenburg data is viewed more cautiously that the other data sets due the higher variability in aircraft attitude during the measurement approaches.

Figure 6.1-11 summarizes the LMSE lines for each of the four airports. Note that the three asphalt RCS lines are similar, whereas the single concrete line falls significantly below the asphalt lines. Also, there appears to be no great difference between the RCS of the PFC asphalt (Arcata and Santa Maria) and that of the grooved asphalt (Santa Barbara). That the RCS of the concrete would be lower than that of the asphalt is expected since the concrete surface appeared smoother than the asphalt based on observations and photographs and thus reflects more energy forward. And, when more energy is reflected forward, there is less energy that is scattered back toward the radar. The result is a lower RCS. The concrete line in Figure 6.1-11 must be viewed with caution, however, since the Vandenburg data set exhibited considerable spread.

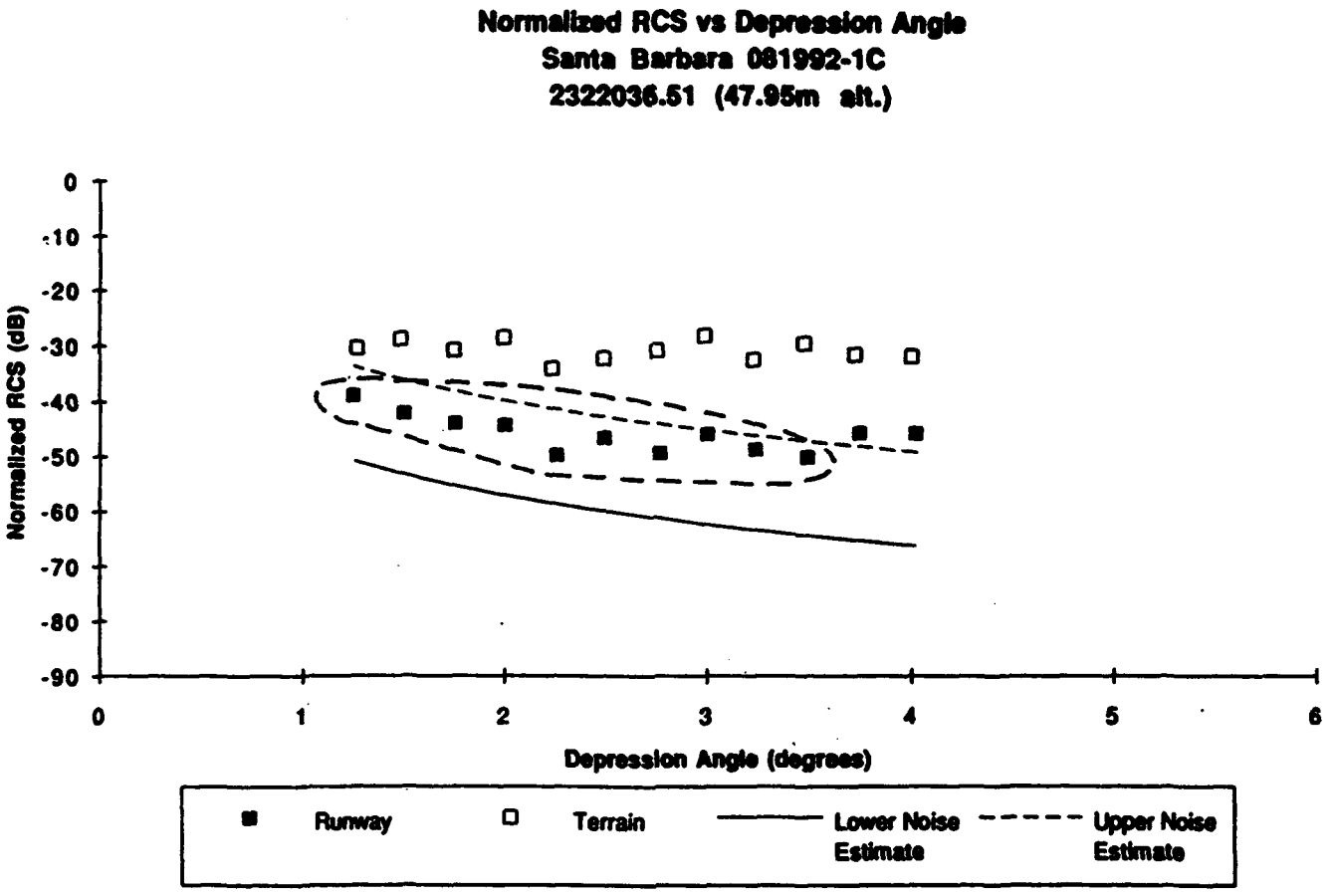

Figure 6.1-7, Plot of Normalized RCS Versus Depression Angle for Runway, Terrain, and Noise Floor Estimates at Santa Barbara, CA. Data Correspond to an Altitude of 47.95m During Approach 1C on August 19, 1992.

Data Excluded Due to Noise-Floor Limits Are Circled

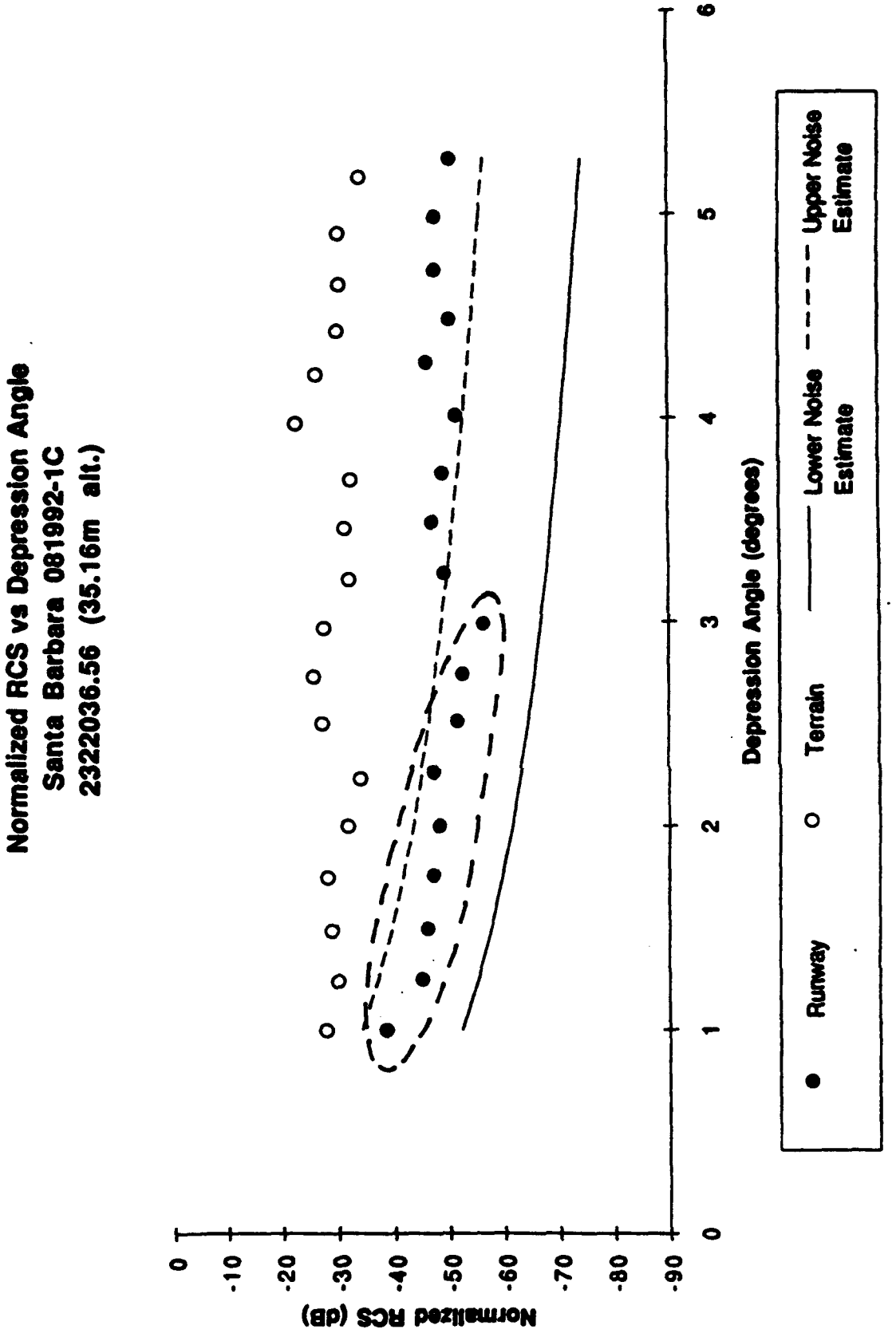

Figure 6.1-8, Plot of Normalized RCS Versus Depression Angle for Runway, Terrain, and Noise Floor Estimates at Santa Barbara, CA. Data Correspond to an Altitude of 35.16 m During Approach 1C on August 19, 1992.

Data Excluded Due to Noise-Floor Limits Are Circled

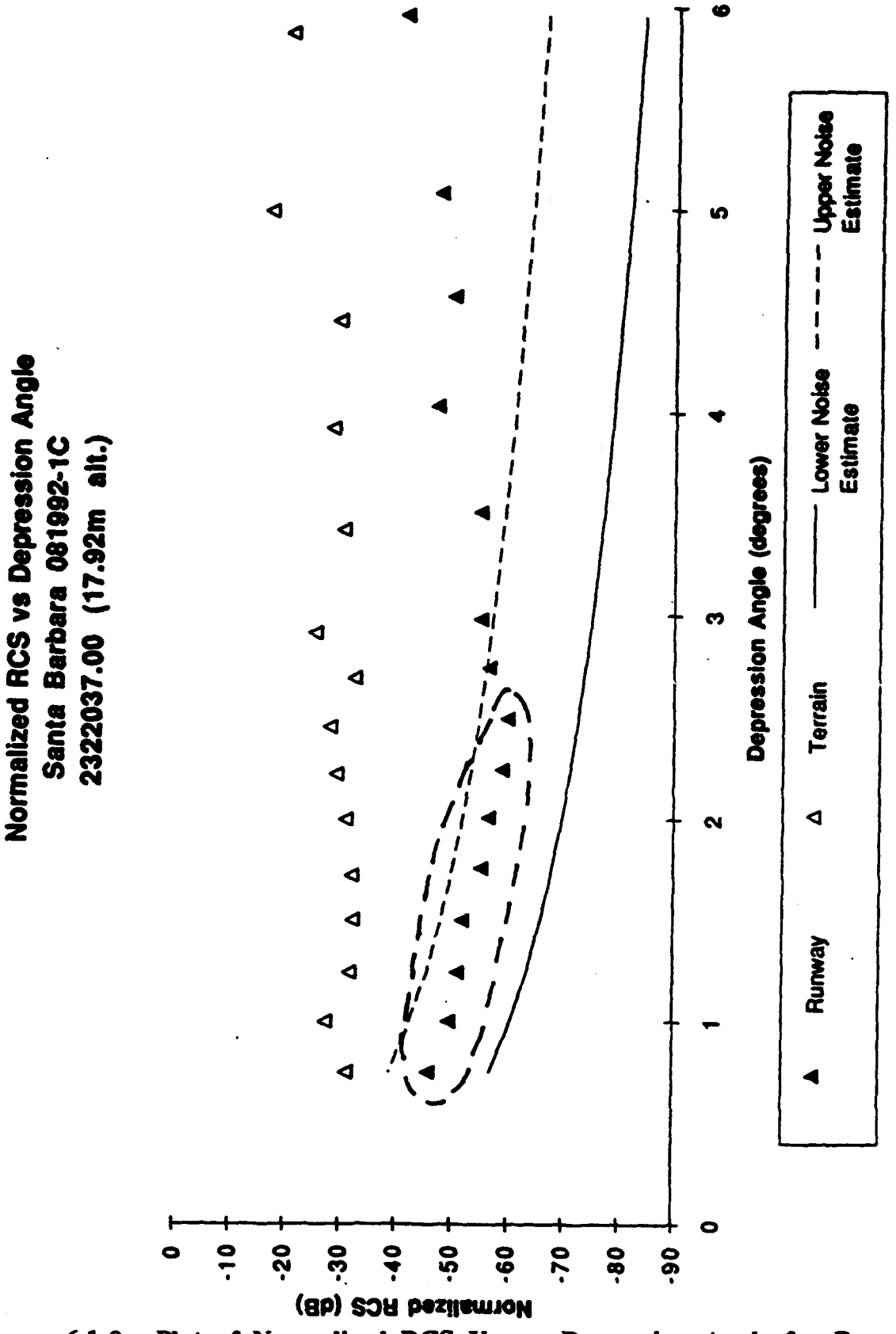

Figure 6.1-9, Plot of Normalized RCS Versus Depression Angle for Runway, Terrain, and Noise Floor Estimates at Santa Barbara, CA. Data Correspond to an Altitude of 17.92 m During Approach 1C on August 19, 1992.

Data Excluded Due to Noise-Floor Limits Are Circled

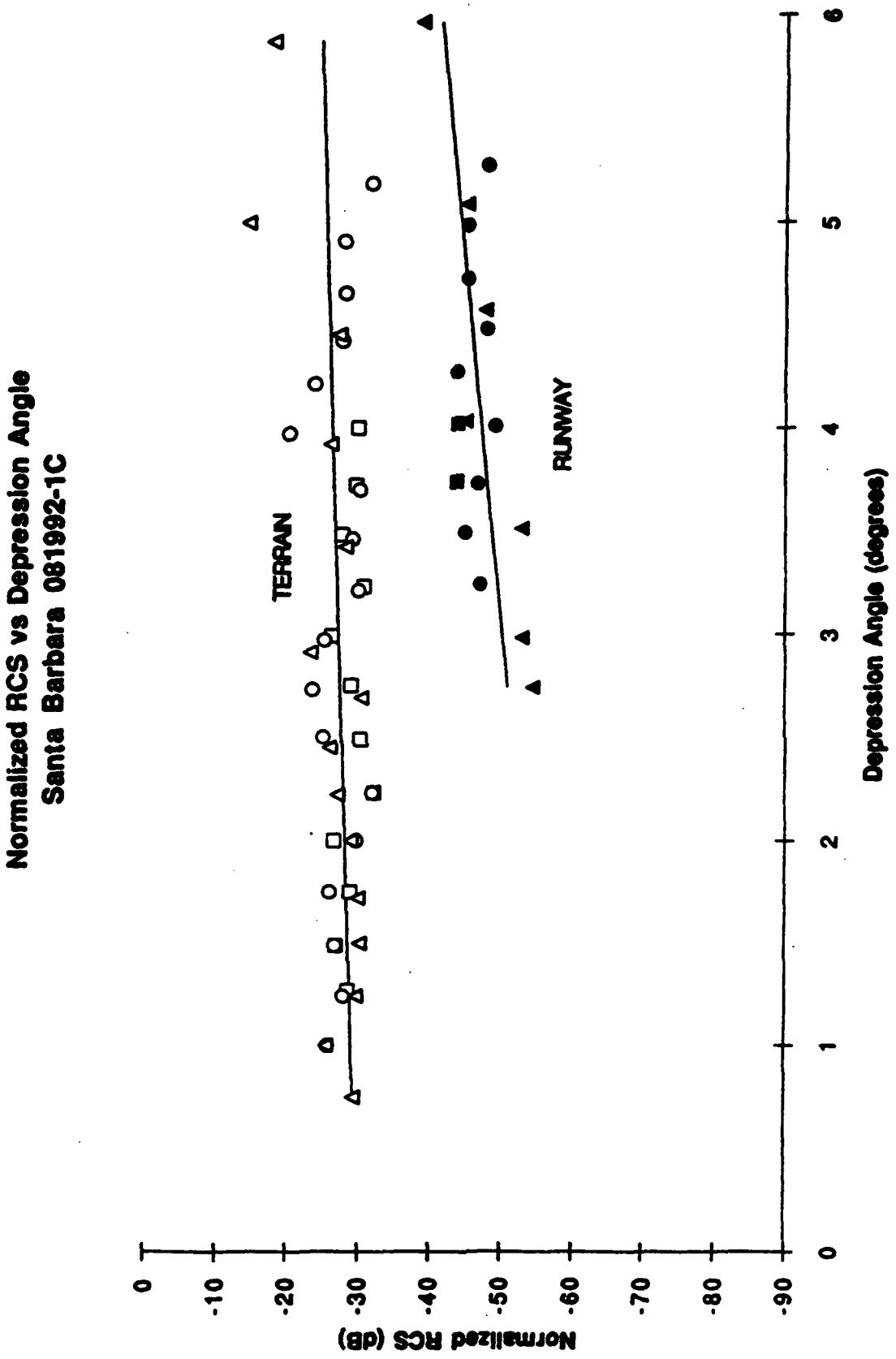

Figure 6.1-10, Plot of Normalized RCS Versus Depression Angle for Runway, Terrain, at Santa Barbara, CA. on August 19, 1992 (Approach 1C)

In addition to the RCS data analyzed during the flight tests, a measurement of normalized terrain RCS was made from the tower at Dayton, Ohio in April, 1992 using the Honeywell radar sensor. This single value is indicated by a "+" in Figure 6.1-11. Due to the geometry at the tower, the runway pavement RCS could not be measured due to noise-floor limitations. In any event, the single tower test terrain RCS measurement falls within the spread of values reported during the flight tests at the four noted airports.

The RCS of the terrain was significantly larger than that of the runway surfaces in all cases. This also is expected since the terrain is a considerably rougher surface than the pavement. The fact that there is a significant difference between the RCSs of the two surfaces is critical for the synthetic vision application since this difference is the fundamental basis for detection of the runway with radar.

The differences in RCS between the runways and the terrain tend to decrease with increasing depression angle. At a 90 degree depression angle (looking straight down), the RCS of the smoother surface (the pavement) would be expected to be greater than that of the rougher surface (the terrain). Thus, the increased RCS of the terrain with respect to the pavement would be expected to decrease with increasing depression angle, and at some cross-over point, the relationship will reverse. Then the RCS of the pavement will be greater than that of the terrain. The slopes of the respective lines in Figure 6.1-11 support this expectation.

For the current synthetic vision application, the difference between the normalized RCS of the terrain and that of the pavement for depression angles near 3 to 4 degrees is of most interest. Typical ILS approach glidepaths fall in the 3 - 4 degree regime, so that these are the angles from which the airport scene will typically be viewed by the radar on approach. It can be seen in Figure 6.1-11 that the terrain-to-pavement RCS ratios vary from about 18 to 23 dB for Arcata, Santa Barbara, and Santa Maria; to roughly 30 dB for Vandenburg.

RCS terrain-to-pavement ratios in this range are comfortably large, and provide a solid basis for expecting good contrast values for these airports in clear weather. Measured contrast values will be discussed in Section 6.1.2.1 below. Of course, in weather, the contrast observed by the radar is determined not only by the inherent contrast based on surface reflectivities, but also by the degrading effects introduced by the atmosphere lying between the radar and the scene being imaged. These weather effects are discussed in Section 6.1.1.3.

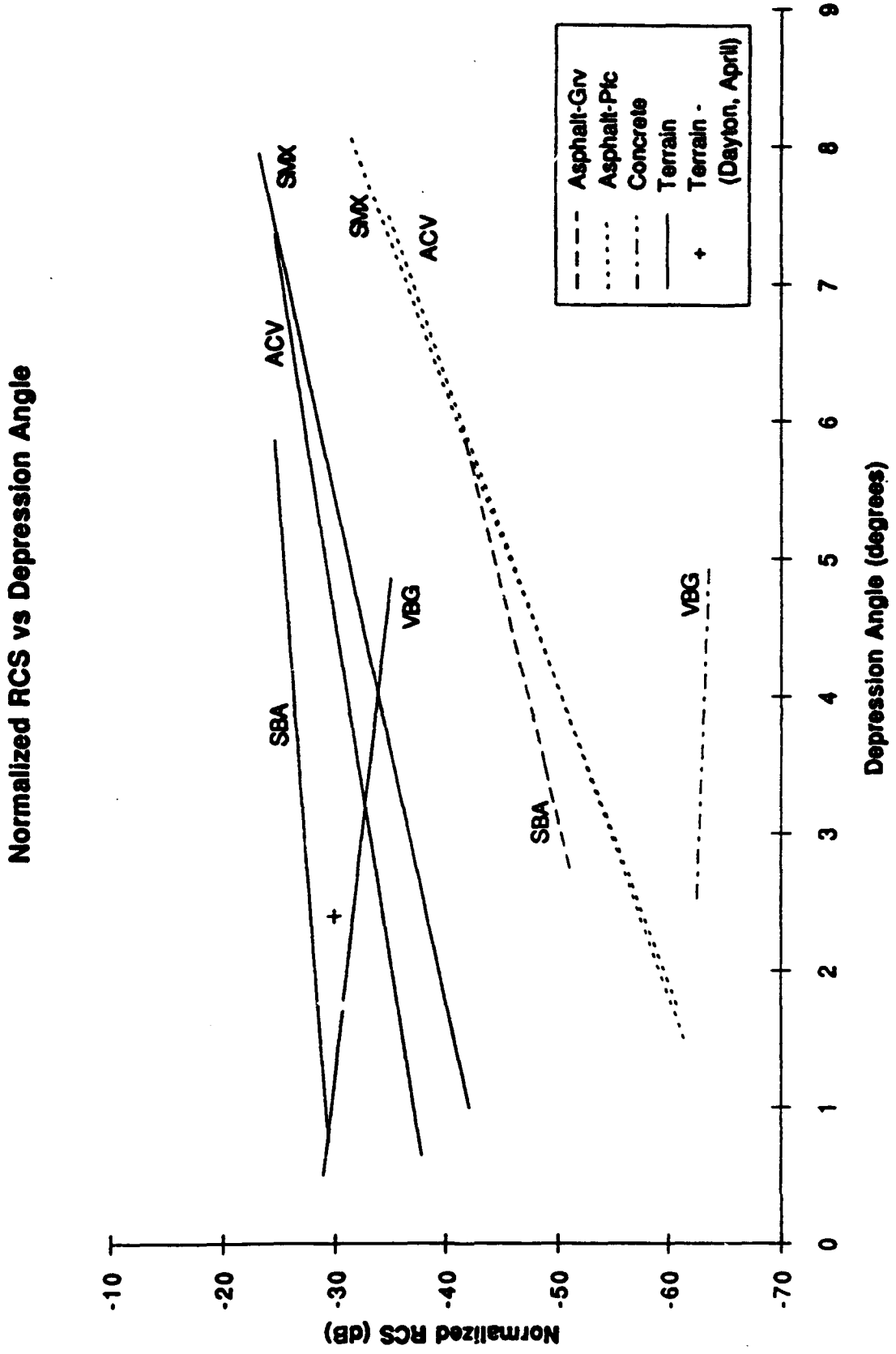

Figure 6.1-11. Summary of Normalized RCS Versus Depression Angle Plots For the Four Airports

6.1.1.2 Vehicle Reflectivity

A series of approaches were made at Point Mugu, CA on 8/18/92 to assess the ability of the test pilot to detect runway intrusions based on the MMW radar image. The ground vehicle used to create these test intrusions was a GMC Suburban four-passenger automobile. Pilot performance during these test approaches is documented in Section 5.

The radar return corresponding to this vehicle was examined in two sets of approaches from 8/18. These were approach 2C, during which the vehicle was parked broadside in the center of the runway at the threshold, and 2E, for which the vehicle was parked broadside in the center of a taxiway. In both cases, the test pilot detected the intrusion based on the MMW image.

The RCS of the GMC Suburban was computed for several snapshots along each of the two approaches. The resulting data are summarized in Table 6.1-1. For each snapshot, this table lists the snapshot number (file name), the reported altitude of the aircraft when the snapshot was acquired, and the measured RCS of the vehicle for that snapshot. In addition, for the highest-altitude snapshot from each approach, the corresponding slant range to the vehicle as well as the projected area of the radar beam on the ground from that point are listed.

Table 6.1-1. Measured RCS Values for GMC Suburban at Pt. Mugu, CA on 8/18/92

Approach	Snapshot Number	Altitude (m)	RCS (dBsm)	Range (m)	Area (m^2)
2C	2320046.02	176.86	-4.06	2985.10	36.48
	2320046.06	161.10	-2.64		
	2320046.10	145.25	-3.04		
	2320046.14	127.80	0.39		
	2320046.18	112.03	5.41		
	2320046.22	97.35	0.22		
	2320046.26	78.52	-4.66		
	2320046.30	68.10	-4.79		
2E	2320058.34	138.20	-9.91	2325.40	34.94
	2320058.38	121.02	-1.32		
	2320058.42	104.89	2.80		
	2320058.46	91.92	4.15		
	2320058.50	78.02	1.70		
	2320058.53	63.85	2.30		
	2320058.50	41.55	5.15		
	2320059.02	22.71	2.57		
	2320059.06	12.31	1.71		

As indicated in Table 6.1-1, the measured RCS of the GMC Suburban varied from about -10 dBsm to about 5 dBsm. This is quite a large target relative to the paved background against which

it is viewed. If it is assumed that the pavement reflectivity is roughly -50 dB (which is consistent with Figure 6.1-11), then even at the maximum snapshot range, where the projected antenna area is about 36 m^2, the corresponding pavement RCS is only about -34 dBsm (= -50 + 10log[36]). The corresponding target-to-clutter ratio is quite high (24 to 39 dB) and is consistent with reliable detection.

Consider a sample worse-case analysis. Assume the vehicle RCS is -10 dBsm (the lowest value measured) and that a 10 dB target-to-clutter ratio is required for detection of the runway intrusion. In this case, the intrusion would be detected so long as the illuminated patch of runway had an RCS less than -20 dBsm. For a 3-degree depression angle, this would not occur until the range to the target was over 7900 meters, more than twice the instrumented range of the Honeywell radar system.

However, long before runway clutter became a problem, detection of this vehicle would be prevented by system noise. As explained in the previous section, an upper bound for estimating the noise floor of the Honeywell radar system is the input power level corresponding to a measured A/D count of 50. The input power level corresponding to an RCS of -20 dBsm reaches 50 A/D counts at a range of about 3100 meters (depending on the specific gain and bias settings in use). Thus, based on our assumptions above, system noise would prevent detection of the GMC Suburban at ranges greater than about 3100 meters.

In summary, then, the Honeywell 35 GHz radar appears quite capable of detecting vehicles such as the Suburban at relatively long ranges. Of course, the radar return received from typical ground vehicles (and aircraft as well) is highly aspect-dependent. The return may be high when the vehicle is viewed from one angle and then may be tens of dBsm lower when viewed from a slightly different angle. The very limited intrusion detection test performed did not explore such viewing-aspect issues.

Finally, the vehicle RCS analysis addressed detection of ground vehicles on the basis of radar signal amplitude only. There is a spatial component of this human detection process which was not considered. Even though the vehicle produces a strong radar return, this return will be confined to a very few pixels in the data image. Thus, the pilot is faced with the task of detecting two or so very bright pixels against a dark background. The fact that there could be several other relatively bright pixels in the scene complicates this process, since these bright spots could occur in the vicinity of the runway as well. Example sources of such returns are the runway edge lights and the arresting wire at Point Mugu. There is also the issue of display clutter on the HUD. For

example, the flight guidance symbology could mask a couple of relatively bright pixels in the image data and thus prevent reliable detection of the intrusion. This phenomenon was experienced during a simulated 0/0 takeoff at Point Mugu, see Section 5.1-2.

6.1.1.3 Atmospheric Effects

Conditions in the intervening atmosphere between a MMW radar and a target can degrade the ability of the radar to detect and image that target. Airborne moisture due to fog and precipitation (rain, sleet, or snow) causes scattering and diffusion of the radar electromagnetic waves. Atmospheric effects are separated into attenuation and volumetric reflectivity. Appendix H described the atmospheric physics that cause attenuation and backscatter, and presented modeled values based on the size and density of airborne water droplets. This section presents values for attenuation and volumetric backscatter measured from Honeywell 35 GHz radar sensor data collected during tower and flight tests in instrumented meteorological conditions.

Since calculation of attenuation and volumetric reflectivity required data acquired in weather with a radar calibration reflector present, only a limited set of data were available for these analyses. The Bruderhedral reflectors were initially positioned at Vandenburg AFB on 8/19/92. Thus, the approaches in fog made on 8/27/92 were available for analysis of atmospheric effects. At Arcata, the reflectors were initially positioned on 8/27/92, so the Arcata fog approaches conducted on 8/28 were also available for analysis. No other approaches in weather were made against airports with reflectors in place during the flight test program.

6.1.1.3.1 Attenuation

Attenuation is the loss of apparent target RCS due to the intervening atmosphere, and is expressed in decibels per kilometer (dB/km). Atmospheric attenuation applies over the entire radar propagation path, from the radar to the target and back to the radar, or over twice the target slant range for a monostatic radar (transmitter and receiver co-located). Attenuation reduces the range at which a radar can resolve runways from bordering grass areas, mainly due to a reduction in apparent grass RCS.

6.1.1.3.1.1 Attenuation References

Attenuation through the atmosphere at millimeter wave (MMW) frequencies in "clear" weather conditions is very much a function of frequency,[15] as shown in Figure 6.1-12. The theoretical electromagnetic attenuation in dB/km is plotted for frequencies from 10 GHz to 100 GHz. Atmospheric absorption from water vapor peaks at 22 GHz, and atmospheric oxygen causes high attenuation at 60 GHz. Between 20 GHz and 100 GHz, there are two frequency "windows" of relatively low attenuation at 35 GHz and 95 GHz. These frequency bands (K_a-band and W-band) are, therefore, the best choices for medium-range MMW radars operating in the atmosphere. Note that attenuation in these bands increases with relative humidity, and that attenuation at 95 GHz is higher than at 35 GHz. At 50% relative humidity, the "clear air" attenuation at 95 GHz is about 0.14 dB/km, and at 35 GHz is 0.05 dB/km.

In meteorological conditions of fog and rain, the airborne water droplets increase the atmospheric attenuation above those values for clear weather conditions. Theoretical calculations supported by measurements have shown that attenuation in fog is directly related to the liquid water content (LWC) of the atmosphere,[16] as shown in Figure 6.1-13. Atmospheric attenuation in

---

15 C. L. Belcher, et al, "Millimeter Wave Clutter Reflectivity and Attenuation Handbook," Georgia Institute of Technology, Georgia Tech Research Institute Final Technical Report on Project A-4272, BOA DAAH01-84-D-A029, Delivery Order 0051, March 1987, pp. 60-64.

16 C. L. Belcher, et al, "Millimeter Wave Clutter Reflectivity and Attenuation Handbook," Georgia Institute of Technology, Georgia Tech Research Institute Final Technical Report on Project A-4272, BOA DAAH01-84-D-A029, Delivery Order 0051, March 1987, pp. 64-70.

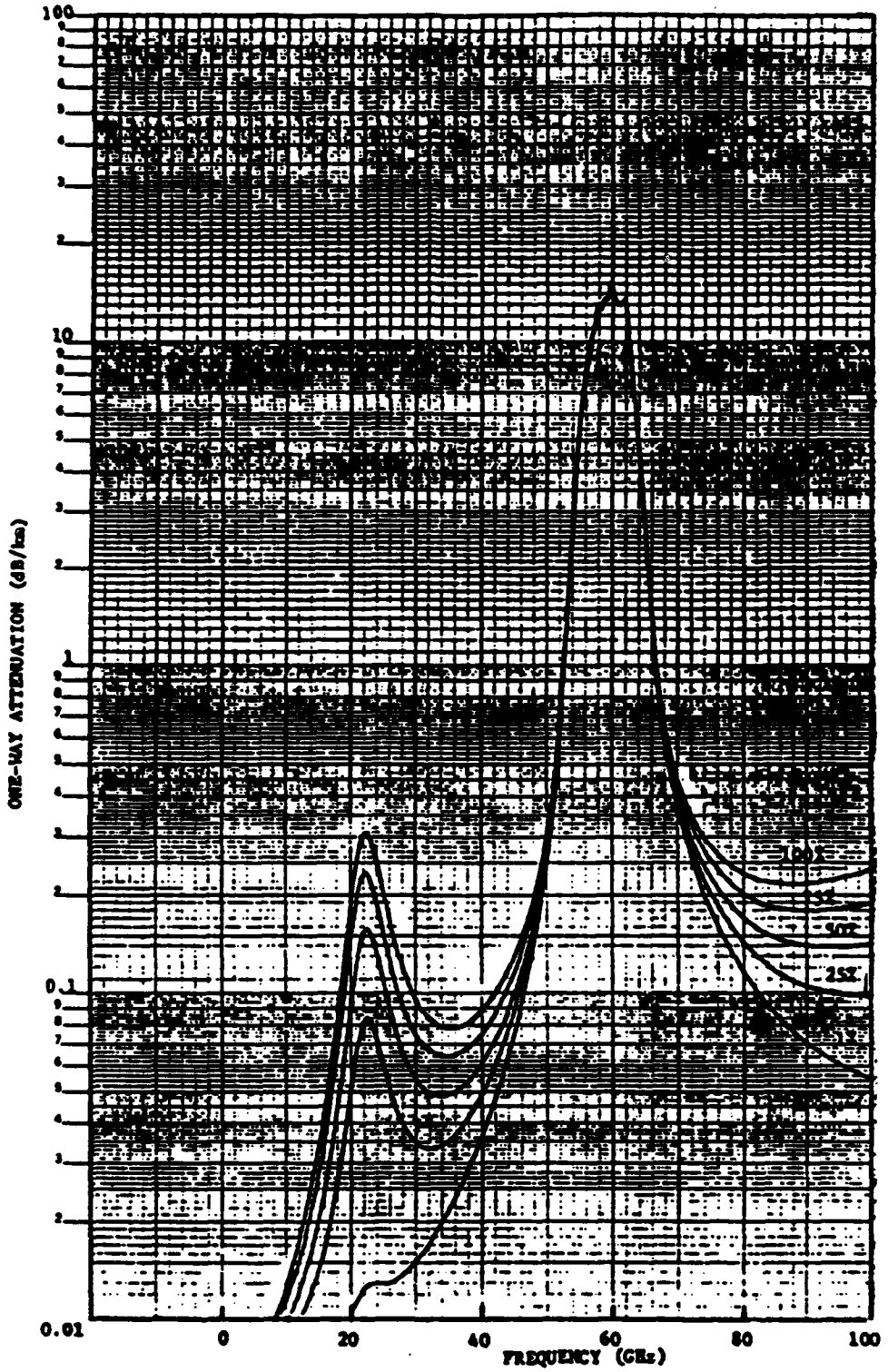

Figure 6.1-12. Total Atmospheric Attenuation Due To Both Water and Oxygen For Several Different Relative Humidities

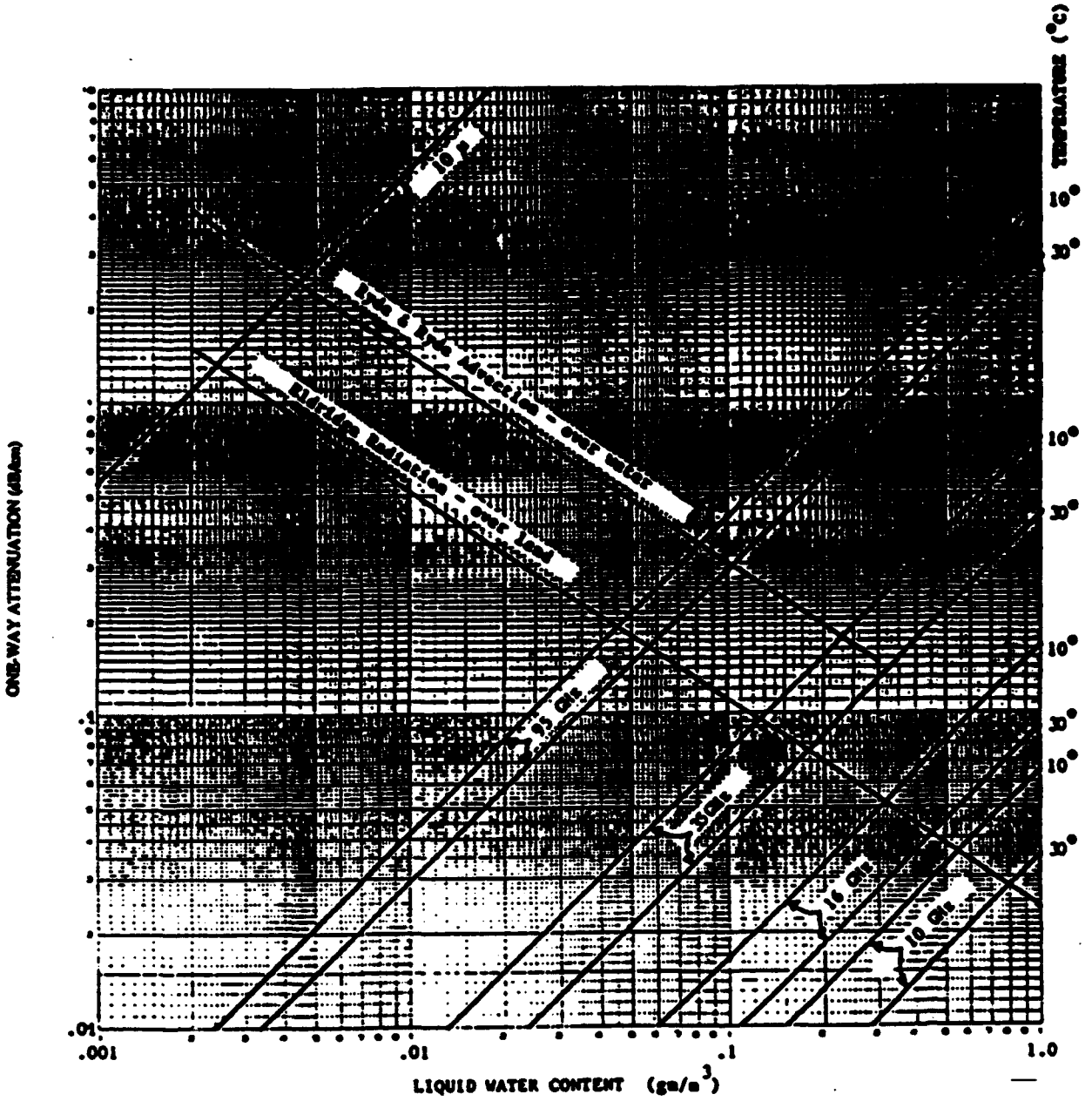

Figure 6.1-13. Atmospheric Attenuation in Fog at Four Different Radar Frequencies

dB/km is shown over three decades of LWC in grams per cubic meter. Attenuation values are plotted for two microwave frequencies of 10 and 16 GHz, and two MMW frequencies of 35 GHz and 95 GHz. Since the dielectric constant of water varies with temperature, the attenuation at each frequency is plotted for air temperatures of 10° and 30°C. For example, at 10°C the attenuation at 35 GHz for an LWC of 0.1 gm/m^3 is 0.075 dB/km. At 0.4 gm/m^3, the attenuation at 35 GHz increases to 0.3 dB/km. For a total path length of 6 km, attenuation values greater than about 0.5 dB/km become significant to the imaging performance of an SV radar sensor.

MMW attenuation in snow is a function of the accumulation rate and the wetness (LWC) of the snow. Snow accumulation rate is measured in equivalent rain rate by melting the snow. A rule of thumb is that 10 inches accumulation of snow is equivalent to one inch of rain. Previously reported data indicate that wet snow has approximately the same 35 GHz attenuation as rain with equivalent precipitation rate.[17] Dry snow, which falls at lower velocities, has significantly less attenuation per equivalent precipitation rate. A few MMW measurements were made at the tower during snow, but there were no meteorological instruments deployed to measure either the LWC or equivalent rain rate during measurements made with the Honeywell radar.

Attenuation in rain is related to the rain rate, but in a complex relationship based on the probability distributions of droplet sizes. Figure 6.1-14 is a typical raindrop size distribution plot from the ground-based precipitation probe (GBPP) used during the tower tests. There are 1,000 times more droplets of 0.2 mm (radius) size than of 2 mm size, but the 2 mm droplets have 1,000 times the volume. The corresponding rain rate measured by the NASA rapid-response gauge was 8 mm/hr. Rain rate is the integrated volume of all the raindrops that reach the ground per unit time. Attenuation, however, is based on the number and size of raindrops per unit volume of air. Larger rain drops fall more rapidly, so a higher percentage of them from a measured unit volume will accumulate on the ground per unit time. Droplet velocities were considered when calculating rain rate from drop size distribution data, as described in Appendix H. If the shape of the drop size distribution curve does not change significantly for different rain rates, as was the case during the 35 GHz sensor tower tests, then the measured attenuation can be directly related to the rain rate. Attenuation at 8 mm/hr rain rate has been previously measured at 35 GHz to be 2.4 dB/km.[18]

---

17 N. C. Currie and C. E. Brown, ed., *Principles and Applications of Millimeter-Wave Radar*, Artech House, Norwood, MA, 1987, p. 165.

18 N. C. Currie, F. B. Dyer, and R. D. Hayes, "Analysis of Radar Rain Return at Frequencies of 9.375, 35, 70, and 95 GHz," Georgia Institute of Technology, Atlanta, GA, Technical Report No. 2 under Contract DAAA25-73-C-0256, February 1975.

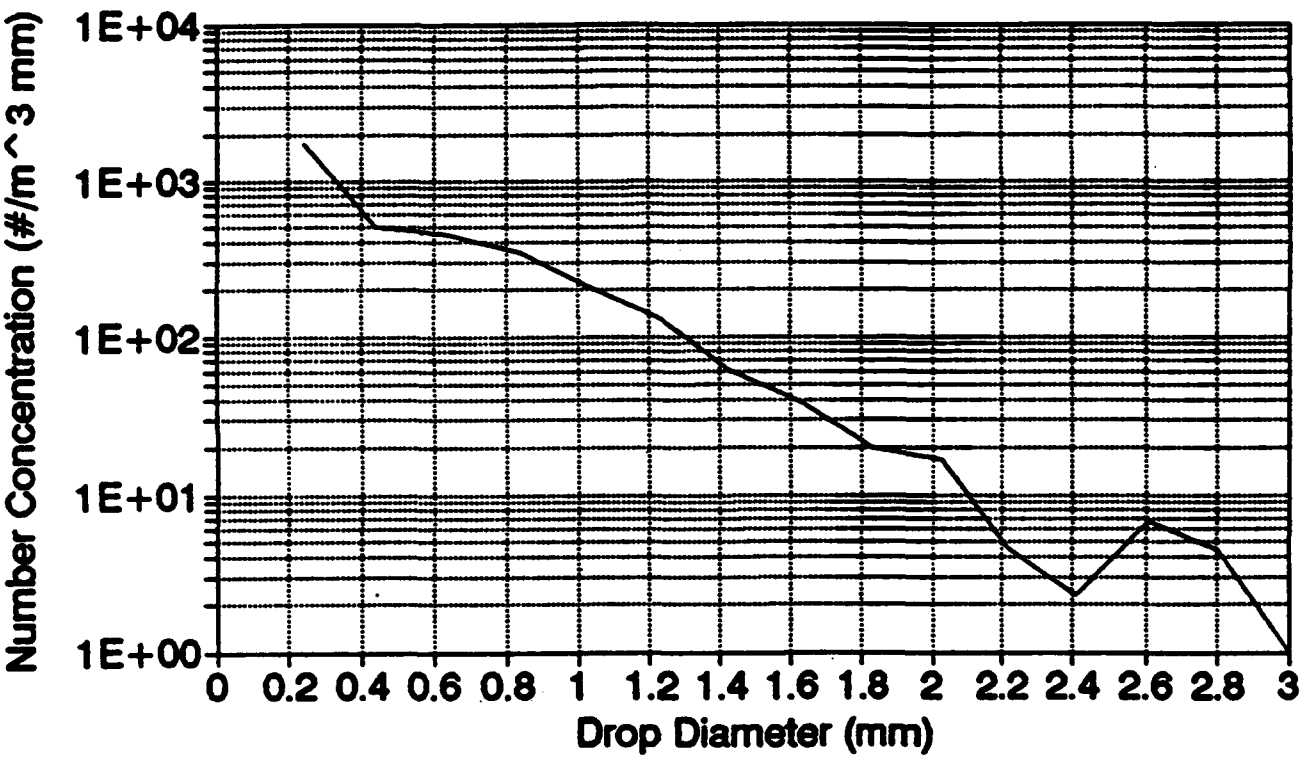

Figure 6.1-14. Typical Raindrop Size Distribution at 5.3 mm/hr Rain Rate, From Tower Measurements

6.1.1.3.1.2 Attenuation Measurements

Atmospheric attenuation is measured by comparing the apparent RCS of a reflector target in weather with the known RCS for that reflector. The radar sensor must be calibrated to permit absolute RCS measurements. The reduction in apparent RCS equals the total attenuation over a known path length. Total attenuation is divided by total path length in kilometers to yield the "one-way" attenuation per kilometer. For example, if a 23 dBsm reflector target at 2 km range were measured during rain as 15 dBsm, then the total attenuation is 8 dB, the total path is 4 km, and the attenuation is 2 dB/km. Multipath, antenna pattern, and reflector pattern effects must all be accounted for in the calculation so that the reduction in apparent reflector RCS due solely to atmospheric attenuation is isolated. The use of the radar scene modeling tool described in Section 6.2.1 enabled this to be done..

The same airborne water droplets that cause attenuation have a radar reflectivity that contributes to the RCS of all the range cells within the measurement scene, including those containing the reflector targets. If this volumetric reflectivity is significant, compared to the reflector RCS, then volumetric reflectivity must be included in the attenuation calculations. Section 4.4.2.3.1.2.7 describes the process for calculating attenuation and volumetric backscatter from two simultaneous equations (Equations 4.4.2-14 and 4.4.2-16). Volumetric reflectivity effects were, therefore, included in the attenuation calculations as well.

Attenuation values for 35 GHz in fog were extracted from the flight test data, and the results are presented for approach 1A on 8/28/92 into Arcata and for approach 1F into Vandenburg on 8/27/92. LWC values between 0.1 and 0.4 gm/m^3 were measured for these low-visibility fogs at Arcata and Vandenburg. Attenuation was calculated based on an 18.7 dBsm and a 23 dBsm Bruderhedral reflector located adjacent to the runway, with the larger reflector placed about 500 m further downrange. For the Arcata approaches, calculations were made using eight radar data snapshots taken between 216 and 116 m (709 - 381 ft) altitude along the approach. The results are tabulated in Table 6.1-2. For the Vandenburg approaches, calculations were made using four radar data snapshots taken between 197 and 126 m (646 - 413 ft) altitude along the approach. The results are tabulated in Table 6.1-3.

Table 6.1-2. Measured One-Way Fog Attenuation and Volumetric Reflectivity at 35 GHz for Approach 1A at Arcata on 8/28/92

Snapshot #	Altitude (m)	LWC (g/m^3)	Temp (°C)	Attenuation (dB/km) [23 dBsm Reflector]	Attenuation (dB/km) [18.7 dBsm Reflector]	Reflectivity ($dBsm/m^3$) [23 dBsm Reflector]	Reflectivity ($dBsm/m^3$) [18.7 dBsm Reflector]
2411519.45	215.98	0.16	13.4	n/a	0.19	n/a	-90.68
2411519.50	205.07	0.15	13.3	0.17	0.52	-91.22	-91.15
2411519.54	187.70	0.14	13.1	0.14	0.31	-90.15	-90.1
2411519.58	155.54	0.13	12.6	0.49	0	-83.17	-83.33
2411520.01	143.35	0.12	12.3	0.06	0	-89.02	-89.23
2411520.06	140.16	0.12	12.3	0.91	0.73	-98.03	-98.06
2411520.10	130.86	0.12	12.2	0	0	-93.89	-94.07
2411520.14	115.97	0.10	11.8	0.82	0	-92.64	-97.7
	Average	0.13	12.63	0.37	0.22	-90.91	-91.79

Table 6.1-3. Measured One-Way Fog Attenuation and Volumetric Reflectivity at 35 GHz for Approach 1F at VANDENBURG AFB, CA on 8/27/92

Snapshot #	Altitude (m)	LWC (g/m^3)	Temp (°C)	Attenuation (dB/km) [23 dBsm Reflector]	Attenuation (dB/km) [18.7 dBsm Reflector]	Reflectivity ($dBsm/m^3$) [23 dBsm Reflector]	Reflectivity ($dBsm/m^3$) [18.7 dBsm Reflector]
2401545.53	197.13	0.33	15.3	n/a	0.07	n/a	-89.77
2401545.57	173.18	0.31	14.8	0.16	0.73	-96.75	-96.64
2401546.01	158.54	0.30	14.6	1.16	0.51	-92.34	-92.45
2401546.05	125.87	0.28	14.2	0.58	0.068	-98.43	-98.61
	Average:	0.305	14.73	0.63	0.34	-95.84	-94.37

Within these tables, "Snapshot #" denotes the file name and includes the data frame IRIG date and time, "Altitude" is the reported height above the terrain in meters, "LWC" is the integrated liquid water content, and "Temp" is the measured air temperature. As indicated in these tables, attenuation is calculated for the larger (23 dBsm) and for the smaller (18.7 dBsm) reflectors, and volumetric reflectivity is shown based on both sets of calculations as well.

For altitudes between 216 and 116 m along the Arcata approach, the air temperature varied from 13.4° to 11.8° C, and the integrated LWC varied from 0.16 to 0.10 gm/m^3. The average attenuation reported based on the large reflector was 0.37 dB/km (one-way), and that reported based on the small reflector, was 0.22 dB/km. The overall linear average of these two values is 0.30 dB/km, which is significantly higher than to be expected for an average LWC of 0.13 based on Figure 6.1-13. This latter figure suggests an attenuation value a bit less than 0.1 dB/km corresponds to a 0.13 g/m^3 LWC. The average measured value of 0.30 dB/km is much more consistent, however, with the attenuation's computed based on the FSSP probe integrated drop-

size distributions in Appendix H. Table H-2 in this appendix reports an average computed attenuation of 0.199 dB/km and a maximum computed attenuation of 0.447 dB/km for all approaches during sortie 1 on 8/28/92.

The fog was somewhat heavier at Vandenburg on 8/27. For the four snapshots analyzed along this approach, the air temperature remained within 0.6 degree of 14.7°C, and the integrated LWC varied from 0.33 to 0.28 gm/m^3. The average attenuation reported based on the large reflector was 0.63 dB/km (one-way), and that reported based on the small reflector was 0.34 dB/km. The overall linear average of these two values is 0.48 dB/km, which again is higher than to be expected for an average LWC of 0.305 based on Figure 6.1-13. This latter figure suggests an attenuation value a bit less than 0.2 dB/km corresponds to this LWC.

In summary, then, the two sets of fog attenuation measurements from the flight tests yielded attenuation values considerably larger than to be expected according to previously reported data. Each of the two average attenuation measurements was about 2.4 times the expected value based on Figure 6.1-13. However, such a discrepancy is not severe as the values of attenuation are small. Over a 2 to 3 km slant range to the reflector, the 0.3 dB/km and 0.48 dB/km measured attenuation's correspond to total path attenuation's between 1.2 dB and 2.9 dB. These values are significant but not extremely large; expected measurement errors for a typical radar system could easily affect them substantially, resulting in a significant deviation in the measured attenuation value.

In addition, for the Honeywell system tested, there were data synchronization errors (as discussed in Section 4.4.2.2.3.3) which contributed to the apparent errors in measuring attenuation. The received signal amplitude errors caused by the synchronization problems could easily be 2 dB and are thus on the same order as the total path attenuation being measured. Changes in the data synchronization errors from one snapshot to the next are likely prime contributors to the great variability in the individual attenuation measurements. For example, in Table 6.1-2, attenuation's ranging from 0 to 0.91 dB/km are reported for nearly identical conditions. In Table 6.1-3, the spread among the individual measurements appears even greater. Again, such snapshot-to-snapshot variations are consistent with the nature of the data synchronization problems.

Snow attenuation measurements at 35 GHz are reported from three runs made at the tower on 4 April 1992. There are no associated meteorological data available other than visual observations of approximately 1 mile visibility. The measured value for attenuation in this wet falling snow was

about 0.5 dB/km. This attenuation is significantly higher than for fog conditions, and is equivalent to that for a rainfall rate of 1 mm/hr.

Rain attenuation values were extracted from the 35 GHz tower test data collected during April and May 1992. Radar data were collected during rain rates between 1 and 50 mm/hr, as measured with the NASA rapid-response rain gauge. Due to problems with measurement procedures, attenuation values were not extracted for rain rates above 22 mm/hr. Attenuation was calculated from two 18.7 dBsm Bruderhedral reflectors located near the runway, with one reflector placed 1000 m further downrange than the other. The 35 GHz attenuation values measured are plotted in Figure 6.1-15. These attenuation results are slightly higher than the values reported by Currie.[19]

6.1.1.3.2 Volumetric Reflectivity

Volumetric reflectivity is the RCS per unit volume of airborne particles within the radar beam. Volumetric reflectivity is expressed in decibels relative to one square meter RCS, per cubic meter of volume ($dBsm/m^3$). The atmospheric volume of a radar resolution cell increases with the square of range. The equivalent RCS of the precipitation can be computed at any range by adding the volume, in dB relative to one cubic meter, to the normalized volumetric RCS. Volumetric reflectivity at 35 GHz is very low for fog, relatively low for snow, but can be significant for high rain rates.

19 N. C. Currie and C. E. Brown, ed., *Principles and Applications of Millimeter-Wave Radar*, Artech House, Norwood, MA, 1987, p.151.

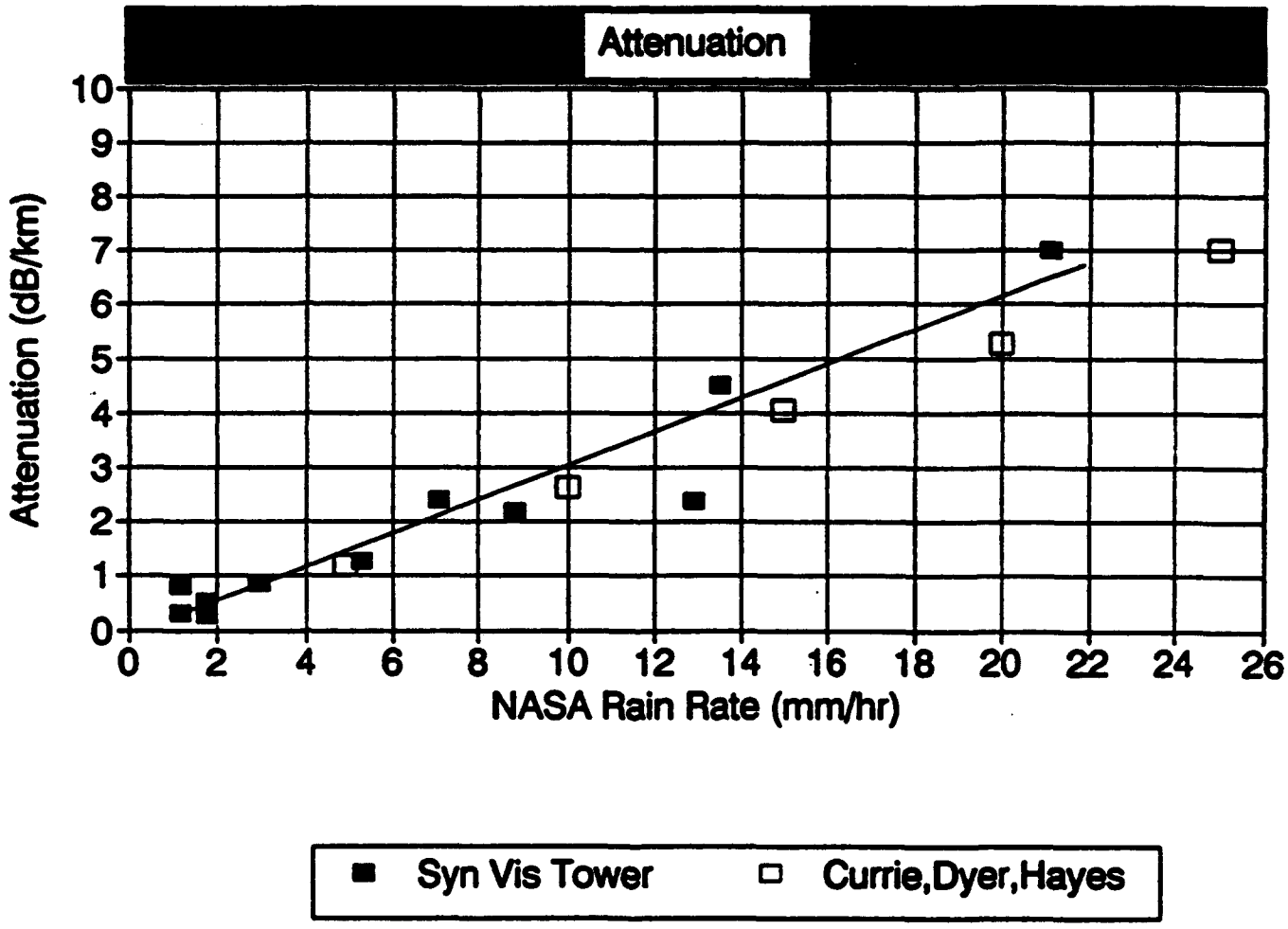

Figure 6.1-15. Measured Attenuation in Rain From 35 GHz Tower Tests

6.1.1.3.2.1 Volumetric Reflectivity References

Radar backscatter from precipitation of uniform distribution within the SV radar scene contributes to the measured RCS from all resolution cells, including those on the grass and those on the runway. This additive volumetric RCS from rain can make the runway becomes much less resolvable. Under these rain conditions, the atmospheric attenuation is also high, so there is a two-fold reduction in runway image quality. As described in an earlier section, the Honeywell radar uses circular polarization and thus can reject much more of the rain backscatter than can a system using a linear-polarized antenna. Previous measurements suggest that the use of circular polarization gives about a 10 dB reduction in rain clutter RCS as compared to linear polarization.

There are limited previous data available describing the volumetric reflectivity for precipitation at 35 GHz.[20] Sections H.2.3 and H.2.4 of Appendix H present volumetric backscatter values derived from a mathematical model of the dielectric scattering of the airborne droplets. These modeled values are compared with measured values from the tower and flight test data analyses in the following section.

6.1.1.3.2.2 Volumetric Reflectivity Measurements

Volumetric RCS was measured from a volume within the scanned antenna beam at a range less than the altitude of the aircraft, as described in Section 4.4.2.3.1.2.7. Volumetric RCS values were developed from the same two simultaneous equations used to extract attenuation values (Equation 4.4.2-14 and 4.4.2-16). Volume dimensions are defined by the antenna azimuth and elevation beamwidths, the range, and the range resolution. Volumetric RCS was extracted from the tower test data using range resolution cells at longer ranges, which normally contained very low clutter RCS. The flight test data provided volumetric RCS values for fog, and the tower test data provided volumetric RCS values for snow and rain.

Volumetric reflectivity values for 35 GHz in fog were extracted from the flight test data, using the same approach 1A on 8/28/92 into Arcata and approach 1F into Vandenburg on 8/27/92 as used for the attenuation analyses. LWC values between 0.1 and 0.4 gm/m^3 were measured for these low-visibility fogs at Arcata and Vandenburg. The measured volumetric reflectivity values are included in the rightmost columns of Tables 6.1-2 and 6.1-3 presented previously. Normalized

---

20 C. L. Belcher, et al, "Millimeter Wave Clutter Reflectivity and Attenuation Handbook," Georgia Institute of Technology, Georgia Tech Research Institute Final Technical Report on Project A-4272, BOA DAAH01-84-D-A029, Delivery Order 0051, March 1987, p. 38 ff.

volumetric reflectivity values were measured to be about -91 dBsm/m^3 for the Arcata fog, and about -94 dBsm/m^3 for the fog at Vandenburg. Expected radar backscatter from fog at 35 GHz is very low, even with an LWC as high as 0.2 gm/m^3. The average value computed for all Arcata sortie 1 fog snapshots on 8/28 (approaches 1A - 1H) based on the method described in Appendix H is -94 dBsm/m^3 based on the OAP probe, which is close to the average measured value of -91 dBsm/m^3 for approach A of sortie 1 (see Table H-3).

Measurement errors for such low reflectivity values are relatively large by comparison, especially in this case, given the data synchronization problems. The measured RCS of the fog volume is near the minimum RCS that can be measured above the radar receiver noise level. Typical RCS for the fog within a range cell at 105 m range was -69 dBsm, and the minimum resolvable RCS at the nose floor was -71 dBsm. The tabulated values indicate that normalized volumetric reflectivity at 35 GHz in these fog conditions was around -93 dBsm/m^3 for LWC ranging from about 0.1 to 0.3 gm/m^3. The measured data thus support the expectation that volumetric reflectivity for such fogs is quite small and in effect insignificant.

Snow volumetric RCS was extracted from two 35 GHz snow runs collected on 4 April, 1992, at the tower test facility. The normalized volumetric RCS for a moderate snowfall rate of wet snow was -61 dBsm/m^3. This value is comparable to the volumetric RCS for rain at 1 mm/hr.

Volumetric RCS for rain was measured at 35 GHz for more than 15 data runs from the tower tests at rain rates between 1 and 50 mm/hr. A subset of those data for rain rates less than 26 mm/hr are plotted in Figure 6.1-16. The normalized volumetric RCS values range from -60 dBsm/m^3 at 2 mm/hr rain to -45 dBsm/m^3 at 25 mm/hr. Since the radar resolution cell volume can become quite large at 3 km range, about 50 dB relative to one cubic meter, the RCS from the rain at more than 8 to 10 mm/hr should dominate the RCS from the grass at those ranges. In such cases, detection of the runway against a grass background is estimated to be very difficult. This, proved to be the case as is discussed in Section V.A (See Figure 5.1-4).

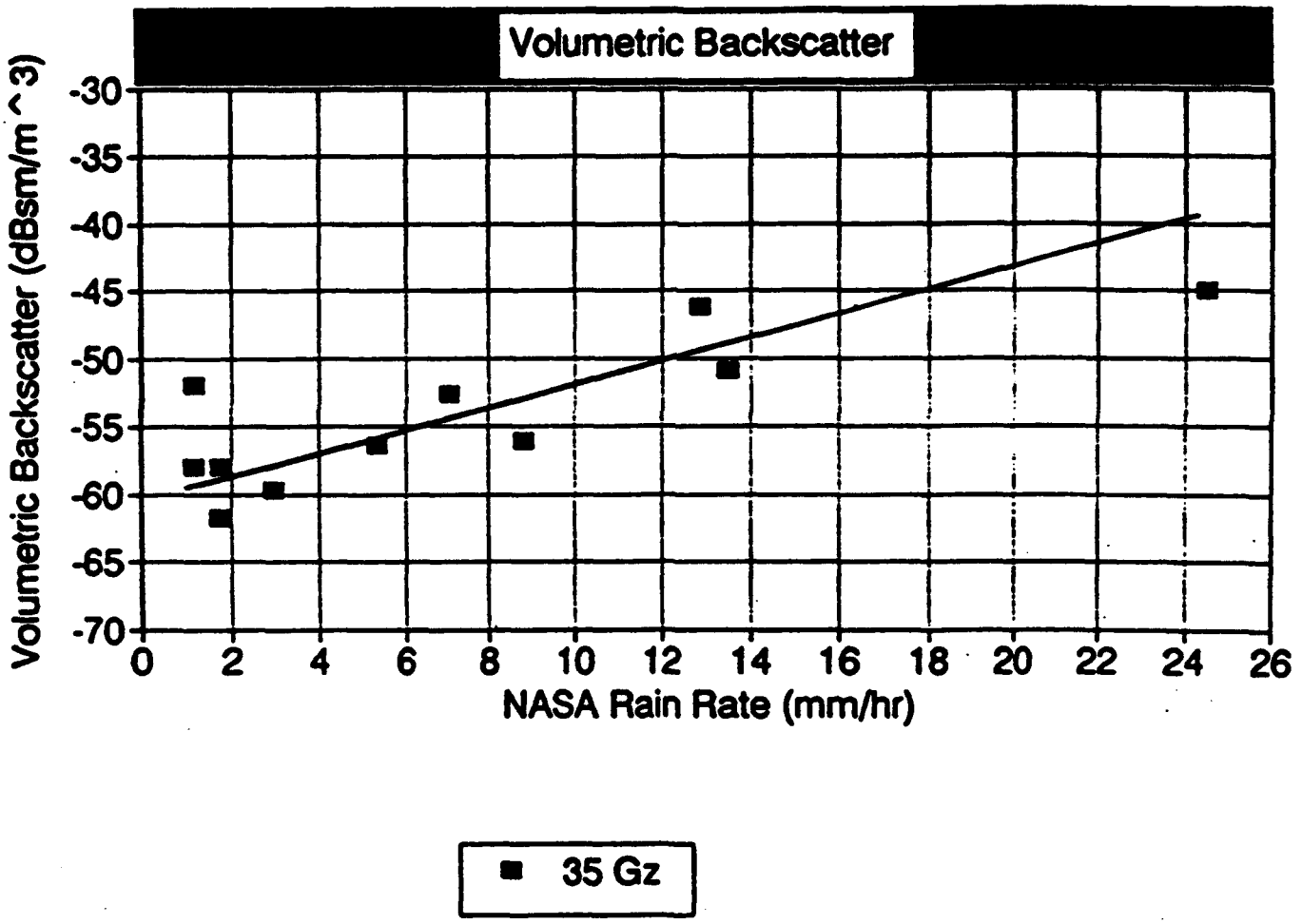

Figure 6.1-16. Measured Volumetric RCS in Rain From 35 GHz Tower Tests

6.1.2 Image Quality Metrics

The following sections present and discuss the image quality metrics measured for various weather conditions during flight testing of the Honeywell radar system. The software and techniques used to compute them were discussed in Sections 4.4.2.3.1.3 and 4.4.2.3.2.2, respectively.

6.1.2.1 Contrast Results

Contrast has been defined earlier, in Section 4.4.2.3.1.3.2, as the difference in the received radar returns from the runway surface and the surrounding terrain. This definition has the form

$$\text{Contrast} = \frac{\left(\frac{\beta_{\text{runway}} - \beta_{\text{terrain left}}}{\beta_{\text{terrain left}}}\right) + \left(\frac{\beta_{\text{runway}} - \beta_{\text{terrain right}}}{\beta_{\text{terrain right}}}\right)}{2} \qquad (6.1\text{-}1)$$

where

β_{runway} is the return from the runway area,

$\beta_{\text{terrain left}}$ is the return from the terrain area to the left of the runway, and

$\beta_{\text{terrain right}}$ is the return from the terrain area to the right of the runway.

The possible range of values of the contrast extends from -1 to $+\infty$. A value of -1 represents the highest contrast possible and indicates no measurable return from the runway surface. This absence of a return contrasts ideally with whatever measurable return exists from the surrounding terrain. Scenes in which the runway surface produces lower levels of return than does the terrain will result in contrasts between -1 and 0. This is the case with a radar sensor, since the backscatter from the smooth runway surfaces is generally much lower than the return expected from the surrounding terrain and vegetation. For a radar sensor, then, a contrast of -1 is ideal, whereas a contrast value of 0 indicates that the runway return is at the same level as the return from the terrain. Thus, there is no contrast in this case.

Contrast measurements were typically produced from at least three snapshots taken during each selected approach. These snapshots corresponded to a range of 2.5 km from the runway touchdown target, a 200-foot altitude above the runway (the decision height), and an altitude of 50 feet (the flare height). For each of these snapshots, the contrast was determined at three or four standard sampling areas. These areas were the runway threshold, the touchdown point, the

runway vanishing point, and the end of the runway pavement in the snapshot image. The measured contrast values were recorded along with the calculated range from the aircraft to each of these four possible regions of interest. Often multiple approaches were made to each airport during a single sortie so that many snapshots were available for computing contrast using this method.

Data suitable for the calculation of contrast were taken during the flight tests in clear weather, as well as during episodes of fog and snow. Raw radar data from a total of forty-six approaches made at thirteen different airports was used to establish the baseline clear-weather performance of the sensor. Data from forty-one approaches made in fog at three different airports are available to quantify performance in this weather condition. Finally, data from eight approaches to two airports were used to examine the effects on image quality of both falling snow and snow on the ground.

6.1.2.1.1 Measured Contrast as a Function of Weather

Numerous approaches were made in clear weather to establish a baseline against which comparisons could be made with data from approaches made during periods of degraded visibility. The baseline results from these clear weather approaches are illustrated and discussed in section 6.1.2.1.1.1 below. A large number of runs were made in fog, covering a range of fog liquid water contents and visibility's. The results from these fog runs illustrate a trend of steady or even improving MMW performance with increasing fog liquid water content. The results of these fog runs, and an interpretation of the phenomenology leading to this surprising effect will be discussed in section 6.1.2.1.1.2.

A series of approaches was made during rain along the east coast on September 25 and 26, 1992. Unfortunately, the raw radar data corresponding to these data runs were lost and are thus not available for analysis. Meteorological data from the flight tests and radar results from the tower test may, however, be combined to provide performance estimates for rain events. The extrapolation of the tower results to estimate performance in rain is examined in Section 6.1.2.1.1.3 Several approaches were also made both during and immediately after snowfalls. The effects of snowfall in the atmosphere, snow pack on the ground, and the effects of plowing the runway are examined in Section 6.1.2.1.1.4.

6.1.2.1.1.1 Contrast in Clear Weather

As stated above, a number of approaches were made during clear weather to establish the baseline sensor performance. In clear weather, attenuation and backscatter of MMW radiation is caused by water vapor and suspended aerosols. The effects of these factors are negligible over the operating range of the 35 GHz Honeywell synthetic vision radar sensor. Clear-weather approaches were made on both the east and west coasts of the U.S. from August through November of 1992. A few clear-weather approaches were made in November in Colorado with snow pack on the ground. Because the influence of the snow on the ground is significant, the Colorado runs will be considered later in Section 6.1.2.1.1.4.

The runways at these "clear-weather" airports were composed of a number of different materials including smooth asphalt, PFC-asphalt, grooved asphalt, concrete, and grooved concrete. The terrain surrounding these runways also differed from place to place. The terrain varied from mixed short and long grass with a relatively high moisture content, typically found at the airports along the east coast, to dry terrain covered with marginal, low-moisture grasses and shrubs typical of the west coast airfields.

Figure 6.1-17 plots the contrast measured at Vandenburg AFB for four approaches made on 8/19/92. Each symbol represents a contrast measurement made for a particular region of interest (ROI) from a selected snapshot. These contrast values are plotted versus slant range to that particular ROI when the corresponding snapshot was taken.

Different symbols are used for contrast values reported for each of the three different types of ROI. As expected, measurements of contrast at the runway threshold and the touchdown target tend to be closer in range than those made at the radar vanishing point. However, the gutter plots for the former two region types tend to be better defined than those corresponding to the vanishing point. By definition, the runway can barely be seen at the vanishing point.

Since the gutter plots for the vanishing points are less well-defined, the identification by the analyst of the six transition points (discussed in Section 4.4.2.3.2.2) in them is less straightforward than for the threshold and touchdown target regions. Consequently, the measurement of contrast at the vanishing point is more subjective and less repeatable. The conclusion drawn is that a lower confidence should be placed in the exact placement of the vanishing-point contrast symbols in Figure 6.1-17 than in the placement of the threshold and touchdown-target contrast symbols.

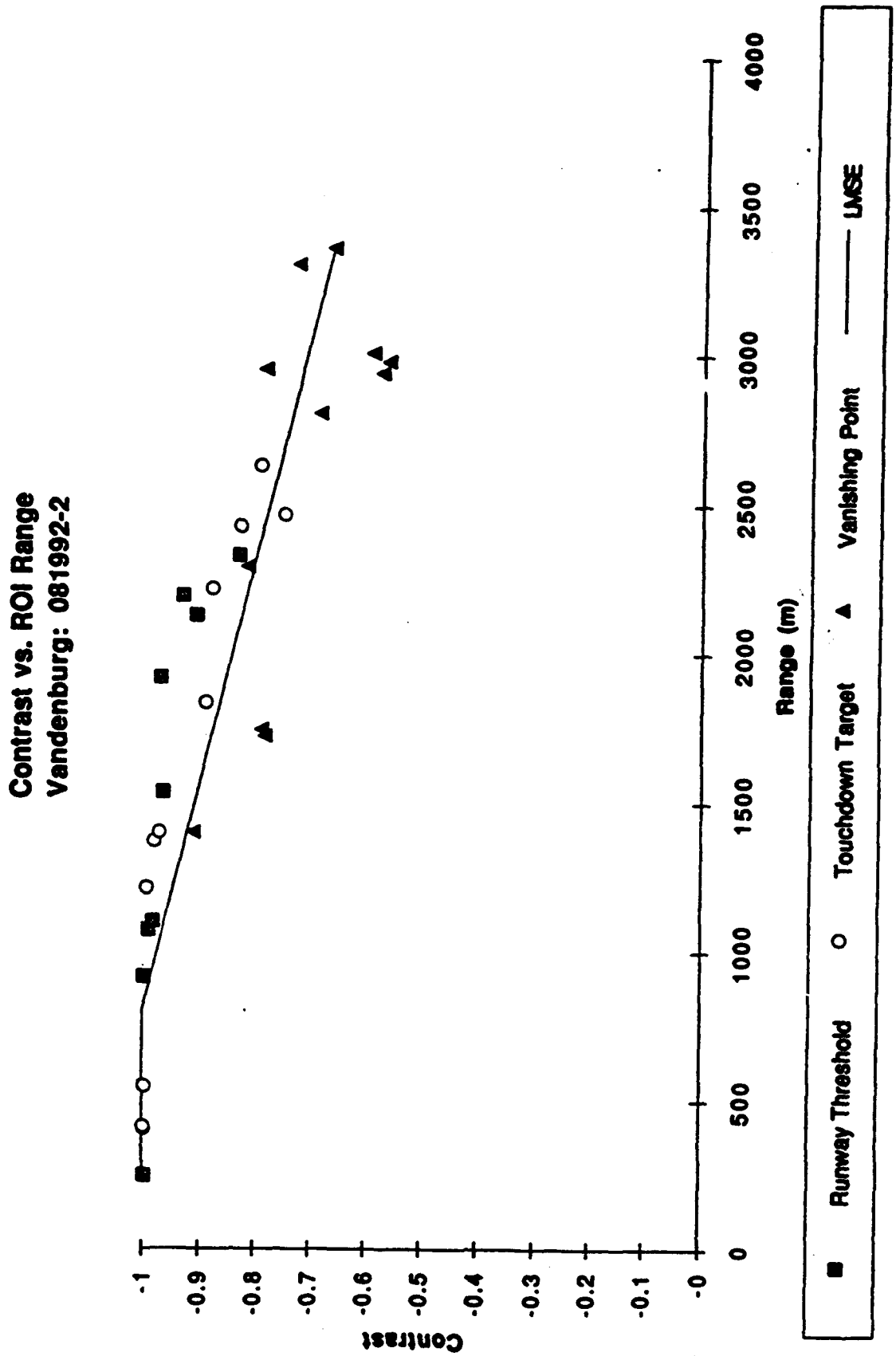

Figure 6.1-17. Plot of Contrast Versus Range to Region of Interest for Clear Weather at Vandenburg Air Force Base on August 19, 1992 (Approaches 2A-2D)

Along with the individual measured contrast values, Figure 6.1-17 also includes a two-segment linear fit applied to the data. This two-segment fit was created by first computing the least-mean-square-error (LMSE) line based on all the available data. If this line crossed the -1 contrast level (best contrast attainable), then the line was effectively clipped at the -1 level for all ranges for which it had originally been above the -1 level. In some cases, the LMSE line never reached -1, so that a single-segment linear fit was appropriate.

In addition to Vandenburg, clear weather contrast was computed for ten other airports as well. For one of these ten (Point Mugu, CA), contrast was measured on two separate days (8/18 and 11/27). The corresponding eleven clear-weather contrast plots are included in Appendix L for reference.

Figure 6.1-18 collects together all twelve of these two- or one-segment linear fits for contrast in clear weather. Note from this figure that no one runway surface provided significantly better contrast characteristics than another.

The RCS of the runway surfaces themselves generally lay close to, if not at, the noise level. At longer ranges the radar really senses this noise floor when aimed at the runway rather than the reflectivity of the runway itself. When this is the case, β_{runway} in Equation 6.1-1 above is determined by the noise floor of the radar, and is effectively independent of the physical runway composition. The contrast will therefore be determined by the return from the terrain (grass) which lays to either side of the runway. The type and nature of this terrain will in effect determine the contrast as it is against this background that the pilot judges the relative darkness of the runway (or of the noise floor of the radar).

The backscatter from these soil and vegetation areas is due to the type, height, and moisture content of the ground cover. Dew, standing water, or snow may cover the surface of the vegetation and further modify the backscatter. In addition, the moisture content, composition, and roughness of the underlying soil all affect the backscatter. Therefore, the contrast characteristics of a specific airport scene, at least at longer ranges, will be due more to the surrounding terrain than to the runway surface itself. Indeed, the contrast characteristics of a specific airport may even change from day to day, depending on the weather, whether the grass has been mowed, etc.

This phenomenon is illustrated in Figure 6.1-18. Note that there is no regular grouping of either the slopes or the levels of these line segments by runway type. The airport showing the best contrast at long range, Van Nuys (VNY), and the airport showing the worst contrast at long range,

Atlantic City (ACY), were both asphalt runways. Another pair of lines which show the lack of correlation among pavement types are those for the concrete runways at Vandenburg (VBG) and Millville, NJ (MIV). Though corresponding to the same surface type, this pair provides both the upper and lower bounds for contrast at relatively shorter ranges.

In addition to illustrating the relative independence of contrast with respect to runway type, the data in Figure 6.1-18 can also provide other insights. Figure 6.1-19 shows the same data plotted in Figure 6.1-18 with the addition of a set of limits defining the range at which the pilots reported identification of the runway on the synthetic vision display in clear weather. For all clear weather approaches, the mean range at which the pilots first declared runway detection was 1.5 nm, and the standard deviation was 0.26 nm. The two vertical edges of the box drawn in Figure 6.1-19 thus correspond to ranges of 1.24 nm (= 1.5 - 0.26) and 1.76 nm (= 1.5 + 0.26).

The horizontal bounds of the box in Figure 6.1-19 were drawn in a two-step process. First, the airports with the best (VNY) and worst (ACY) contrasts were eliminated. Then, the intercept of the right vertical line with the lowest contrast airport remaining (LAX or MIV) was projected onto the contrast axis. Likewise, the intercept of the left vertical line with the highest contrast airport remaining (NTD 8/18) was projected onto the contrast axis. This process should produce a reasonable estimate of the contrast levels required by the pilot for runway detection The approximate range of values is -0.6 to -0.8.

Care must be used in comparing such contrast values computed from the raw radar data with contrast computed based on the video display of the radar image data to the pilot. The raw data contrast values were determined using the received power in linear space; the power levels (β values) used in Equation 6.1-1 were expressed in power units such as watts. However, the data displayed on the HUD are presented in a log scale; the brightness varies roughly proportionally with the radar signal level expressed in dB units. Note that a raw-data contrast of -0.6 (computed in linear power space) corresponds to a 4 dB difference in received power. If it is assumed that the maximum dynamic range of the HUD data, in log space, is about 65 dB, and that the terrain return typically lay somewhere near the middle of this range, then this difference of 4 dB between the runway and the terrain would be perceived by the pilot as a contrast, on the logarithmic HUD display, of -0.125 (= -4 / 32).

The magnitude of this HUD-derived contrast value is larger than the 0.05 value corresponding to the FAA's operational definition of minimum visibility. However, the

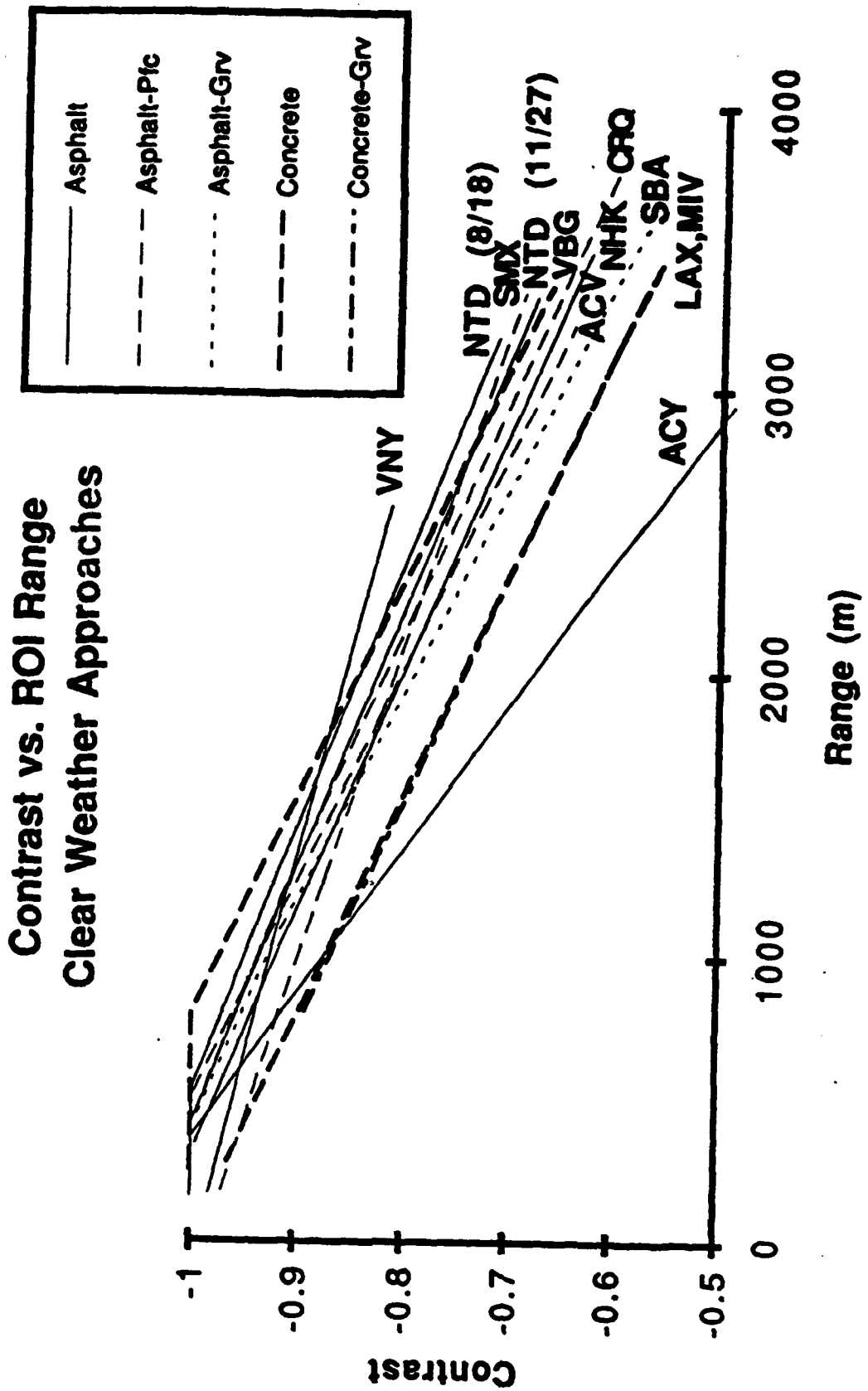

Figure 6.1-18. Plot of Contrast LMSE Linear Fit Versus Range to Region of Interest for Twelve Clear Weather Airports.

Different Line Symbols Are Used for Each Runway Composition Type

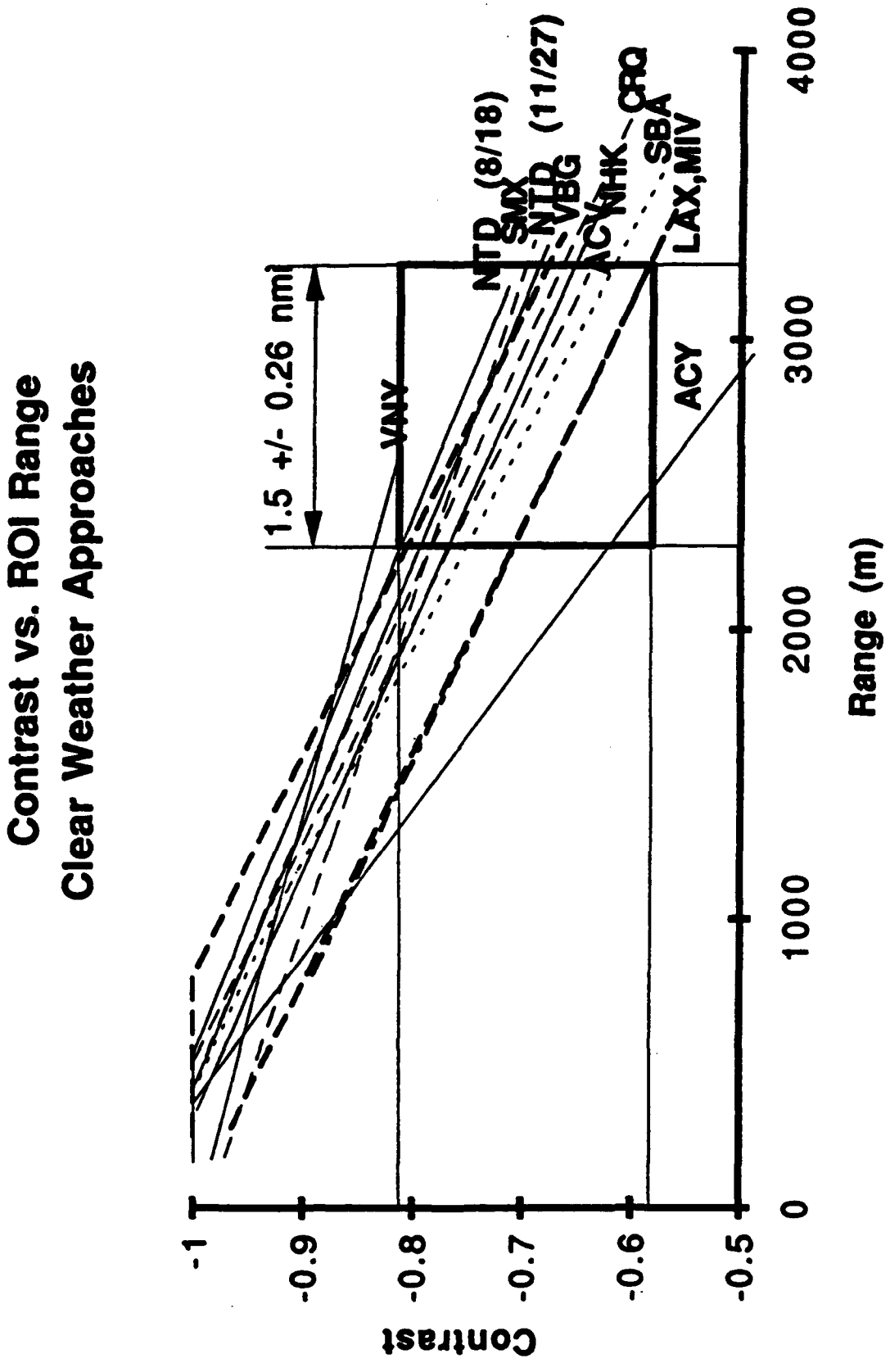

Figure 6.1-19. Plot of Contrast Versus Range to Region of Interest for Twelve Clear Weather Approaches. Approximate Contrast Levels Corresponding to Pilot Detection Ranges are Indicated

operational limit is based on the visibility of point sources of light against a uniformly dark background. The runway is a darker extended area, which must be perceived as a regular geometric area, surrounded by the lighter, but extremely non uniform terrain area. The non uniform nature of the surrounding area certainly contributes to the larger values of contrast needed for pilot identification of the runway. The pilot must also simultaneously handle the required workloads and be confident enough in the identification of the runway in the image to continue the approach. These requirements also effectively increase the contrast needed by the pilot for confident runway identification.

6.1.2.1.1.2 Contrast in Fog

A total of forty-one approaches involving data taken at three different locations were available for the analysis of contrast in fog. Observed ground level visibility's in the fogs ranged from 2 nm to less than 1/8 nm. The liquid water contents of the fogs, measured by the particle probes mounted on the aircraft, ranged from 0 to 0.47 g/m^3. The contrast produced by the MMW sensor was generally very good during all fog episodes. Data from Arcata, CA taken on August 28 are generally representative of the observed contrasts. Eight approaches were made during this fog episode, at which time the observed ground level visibility was 1/8 nm.

Plots of contrast as a function of ROI range for the Arcata data set are included as Figures 6.1-20, 6.1-21, and 6.1-22. These three plots separate the data from the eight approaches into groups according to the liquid water content of the fog, integrated from the aircraft altitude for each specific snapshot down to the ground. The two-segment LMSE fit for each data set is also superimposed on the plots.

The first plot, presenting data with liquid water contents from 0 to 0.09 g/m^3, represents the relatively lighter fogs during these approaches. The second plot, with liquid water contents ranging from 0.09 to 0.13 g/m^3, represents somewhat denser fogs. The third plot, containing measured data corresponding to liquid water contents ranging from 0.13 to over 0.20 g/m^3, represents the thickest fogs encountered that day. Visibility's within these overall fog conditions, as calculated from the number densities measured by the particle probes, would typically range from 0.04 to 0.2 km.

The most interesting feature of these plots is the relatively high contrast values measured for all these fog events. While the fogs contained large numbers of small fog particles, such droplets, because of their size relative to the wavelength of the radar, do not produce significant MMW attenuation. Calculations were made of the expected path attenuation's due to the observed drop densities for sortie 1 at Arcata on 8/28/92. (These calculations are described in detail in Section H.2.2 of Appendix H). The calculated attenuation along the slant path to the runway averaged about 0.2 dB/km based on the FSSP probe data (see Table H-2). The maximum calculated attenuation was found to be only 0.447 dB/km. The fog particles are simply too small, and lie too far down in the Rayleigh scattering region, to provide significant attenuation of the MMW energy.

A comparison of the various contrast levels measured for the three fog classes indicates that the presence of heavier fog tends to enhance the contrast. As the fog density increases, the measured contrast at Arcata also increases, as is illustrated in the composite plot of LMSE fits from all three classes of fog events shown in Figure 6.1-23. This effect could be due to the wetting of both the runway and the vegetation surfaces by these dense fogs. The increased dielectric constant of the moist blades of grass would tend to increase the backscatter from these surfaces, especially since these blades tend to be oriented perpendicularly to the radar line of sight.

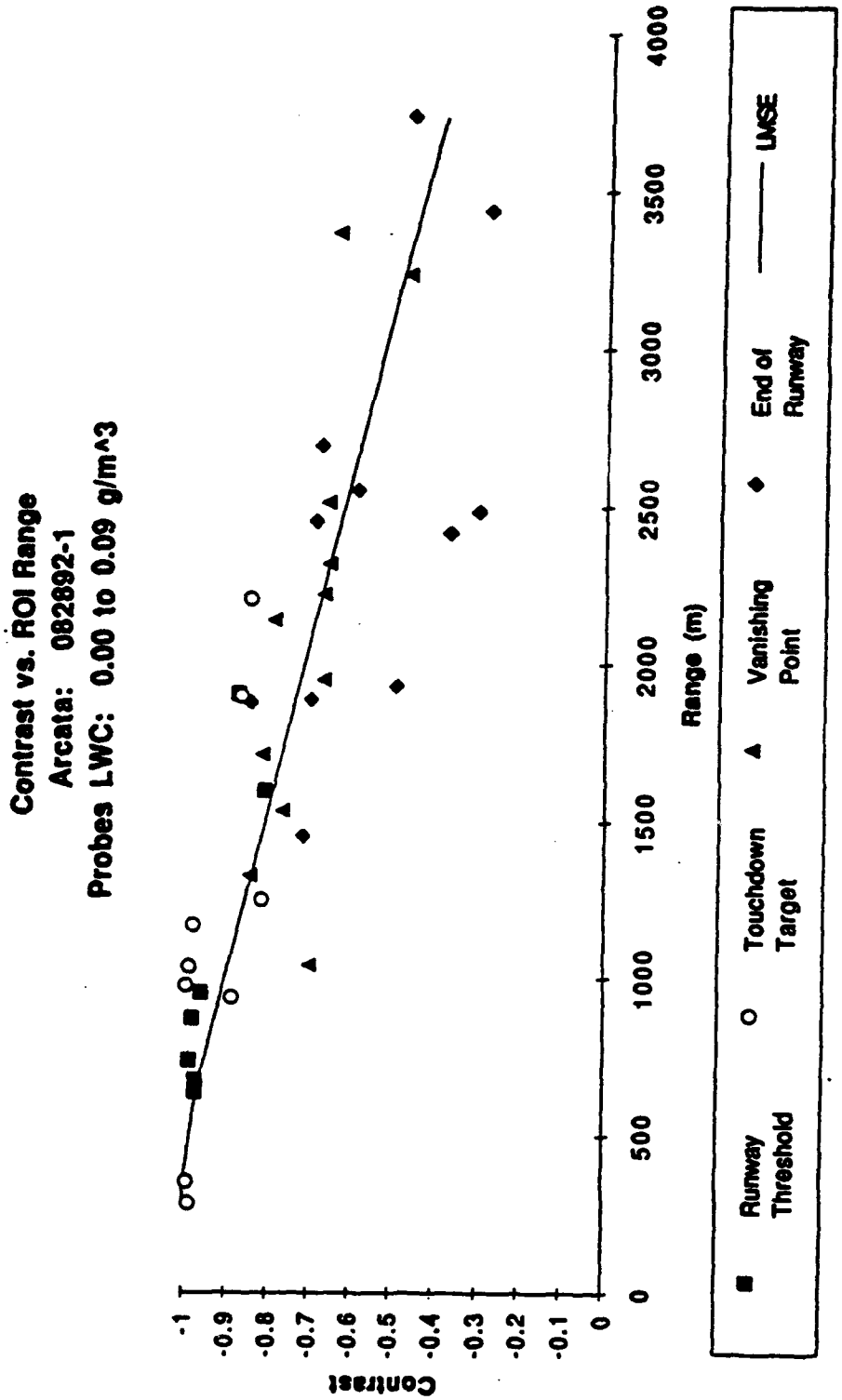

Figure 6.1-20. Plot of Contrast Versus Range to Region of Interest for Fog Approaches at Arcata, CA on August 28, 1992. Data are Taken From Snapshots with an Integrated LWC of 0.00 to 0.09 g/m^3

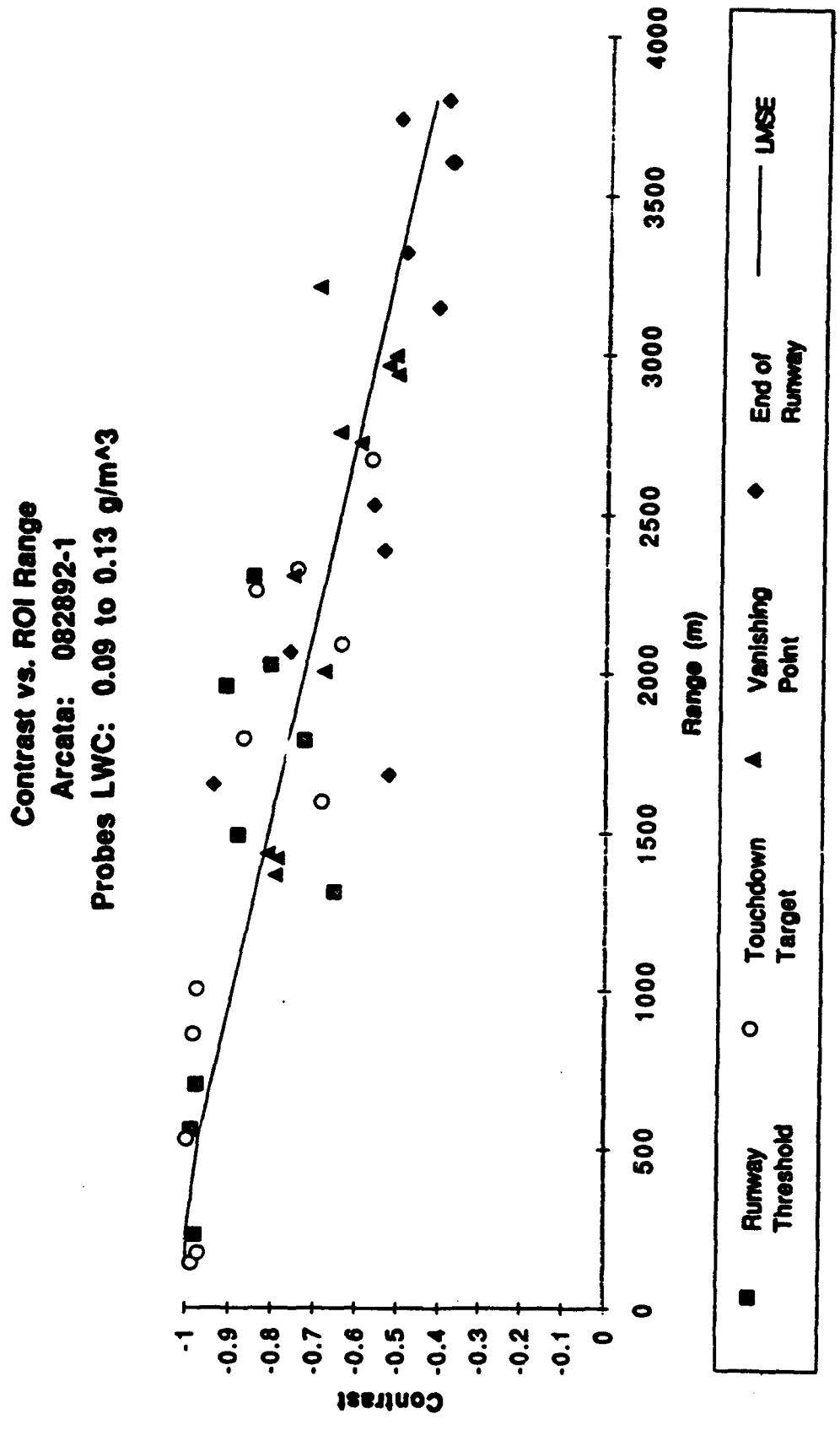

Figure 6.1-21. Plot of Contrast Versus Range to Region of Interest for Fog Approaches at Arcata, CA on August 28, 1992.
Data are Taken From Snapshots with an Integrated LWC of 0.09 to 0.13 g/m^3

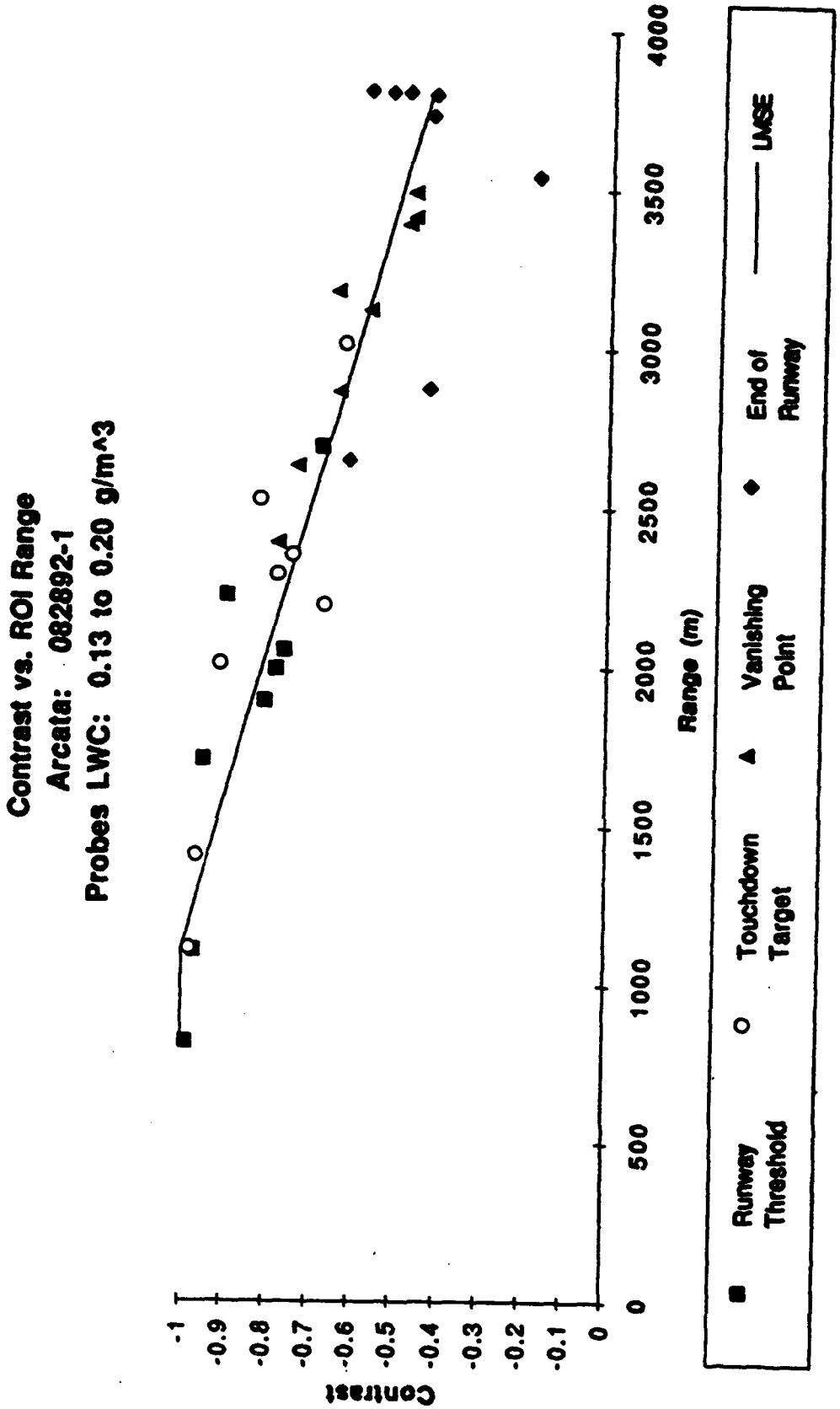

Figure 6.1-22. Plot of Contrast Versus Range to Region of Interest for Fog Approaches at Arcata, CA on August 28, 1992. Data are Taken From Snapshots with an Integrated LWC of 0.13 to 0.20 g/m^3

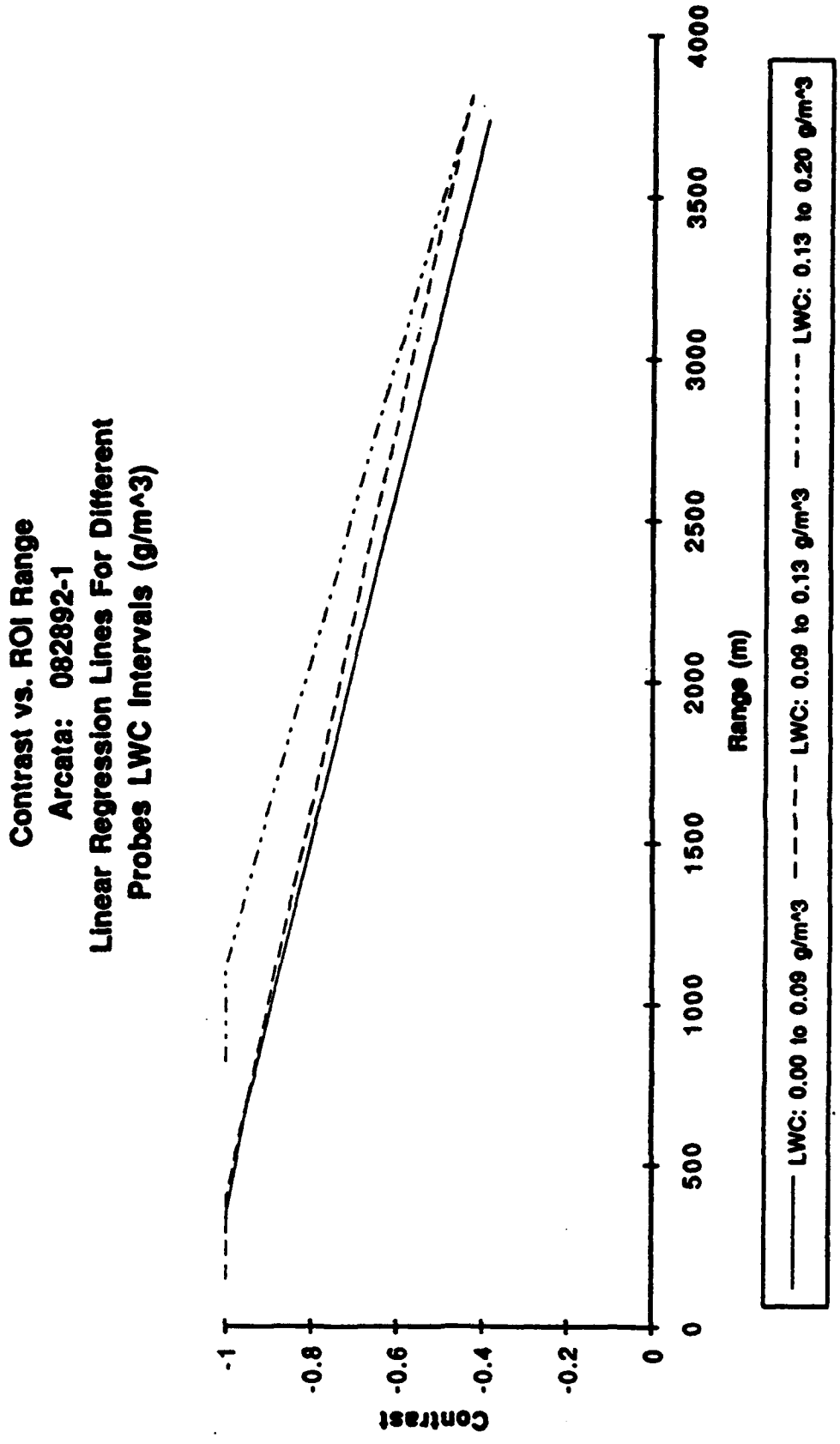

Figure 6.1-23. Plot of Contrast Versus Range to Region of Interest for Fog Approaches at Arcata, CA on August 28, 1992.

Data are Presented as the :MSE Lines Fitted to the Measured Values for each LWC Interval

On the other hand, the runway provides a much smoother surface than the blades of grass. The runway surface may become even smoother during these heavy fogs as the condensed water fills small irregularities in the paved surface. Thus, the moisture on the runway may tend to decrease the runway backscatter since the runway is viewed by the radar at a very shallow grazing angle. If $\beta_{terrain}$ in Equation 6.1-1 is increased, and β_{runway} is decreased or is left about the same, then the magnitude of the contrast will increase.

There is a potential competing mechanism in fog which will tend to reduce the perceived contrast if the runway return is near the noise floor of the receiver. This mechanism is due to the attenuation which decreases the radar signal level returned from both the terrain and the runway. But if the runway return level is already at the receiver noise floor, the perceived runway signal return level can go no lower. The end result is a decrease in contrast since the terrain return is attenuated while the perceived runway return remains fixed at the receiver noise floor.

However, attenuation in fog at 35 GHz is fairly small as noted earlier in Section 6.1.1.3.1.1 (And, as noted in Section 6.1.1.3.2.2, the volumetric reflectivity of fog at 35 GHz is insignificant, and thus is not addressed) The LMSE fits in Figure 6.1-23 indicate the perceived contrast is highest for the heaviest fog, and the contrast is lowest for the lightest fog. This result supports the assumption that the increase in inherent contrast due to moisture on the surfaces in fog more than compensates for the increased attenuation which tends to decrease the perceived scene contrast at the radar. The net effect is an increase in runway-terrain contrast as seen by the 35 GHz radar sensor.

Figure 6.1-24 presents the LMSE fits for measured contrast in fog for data taken during eight approaches to Vandenburg AFB on 8/11/92. Surface weather observations from the airport during these approaches reported an obscured ceiling with less than 100-foot vertical visibility and a runway visual range that varied between 1/8 and 1-1/8 nm. Again, note that the contrast levels are quite high for all three of the fog classes into which the data were divided. At closer ranges, the heavier fogs (0.14 to 0.31 g/m^3) yielded better contrast, while at longer ranges, the lightest fog (0 to 0.06 g/m^3 LWC) gave the best contrast. While no consistent trend is evident, the contrast in heavier fog appears about the same as that in lighter fog.

Figure 6.1-25 plots the LMSE fits for measured contrast in fog for data taken during five approaches to Vandenburg AFB on 8/27/92. Surface weather observations from the airport during these approaches reported an obscured ceiling with less than 100-foot vertical visibility and a runway visual range of 1/8 nm. Again, note that contrast levels are quite high for all three of the

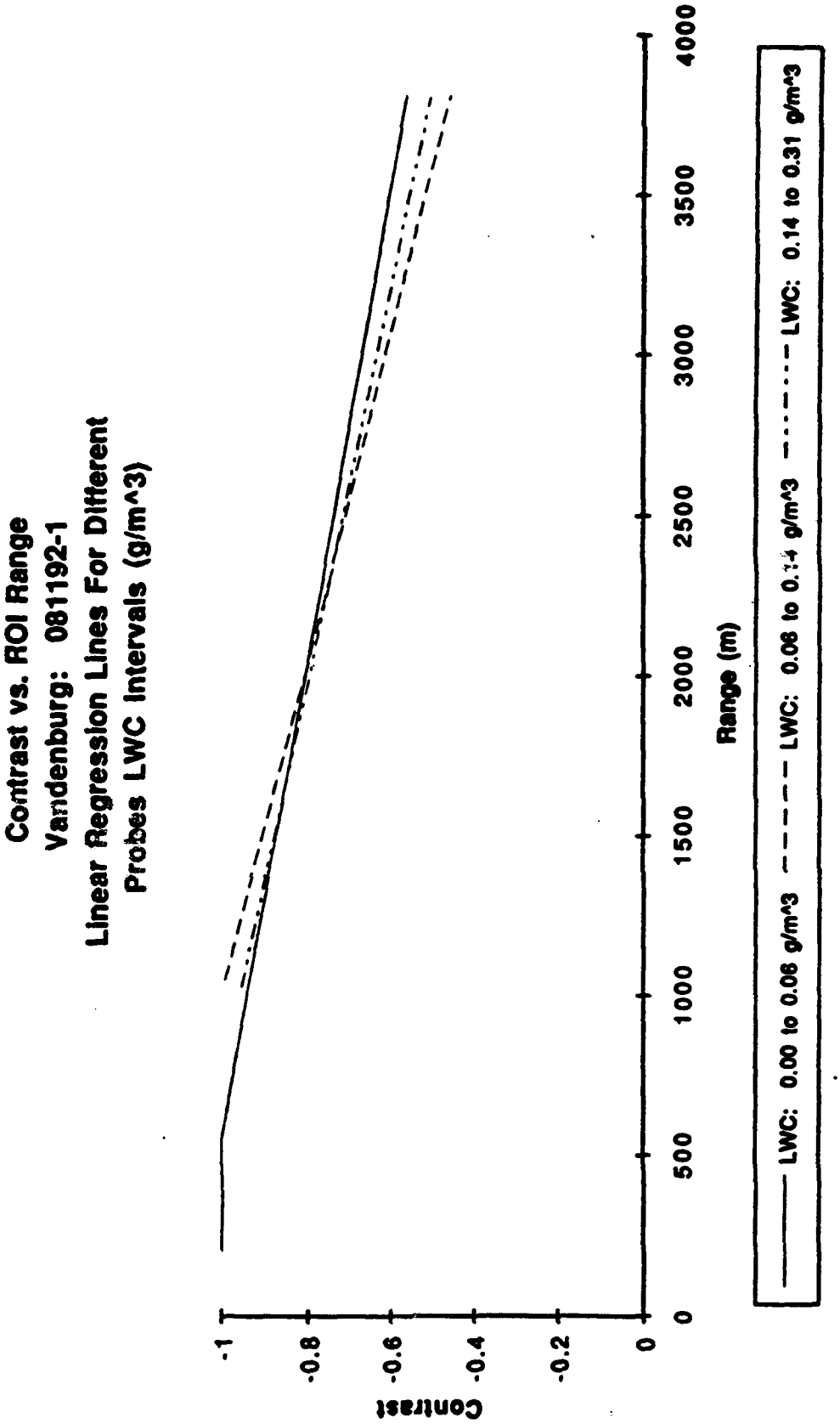

Figure 6.1-24. Plot of Contrast Versus Range to Region of Interest for Fog Approaches at Vandenburg Air Force Base, CA on August 11, 1992. Data are Presented as the LMSE Lines Fitted to the Measured Values for Each LWC Interval

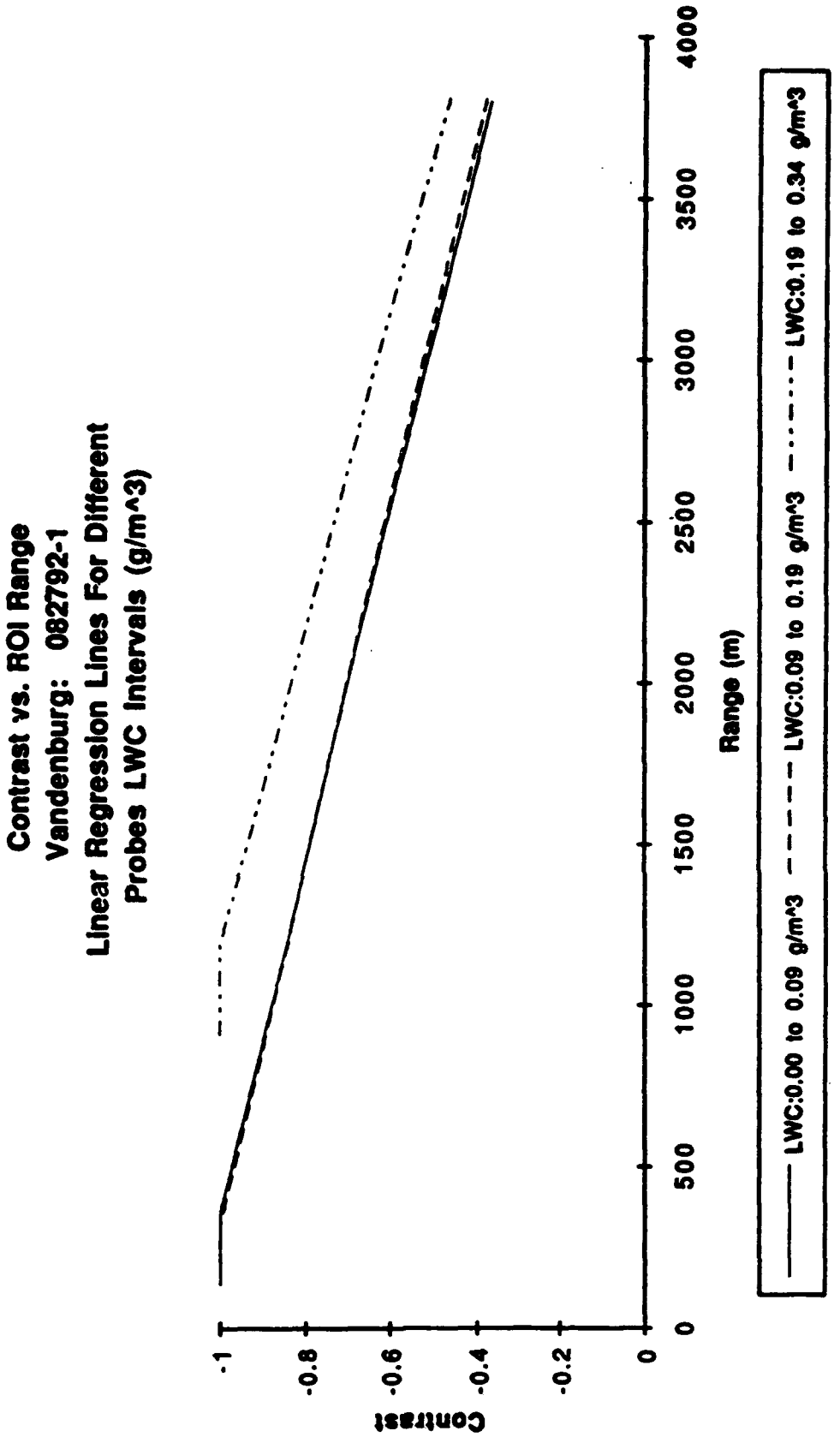

Figure 6.1-25. Plot of Contrast Versus Range to Region of Interest for Fog Approaches at Vandenburg Air Force Base, CA on August 27, 1992. Data are Presented as the LMSE Lines Fitted to the Measured Values for Each LWC Interval

fog classes into which the data were divided. In this case, the heaviest fog (0.19 to 0.34 g/m^3) yielded the best contrast. In summary, then, raw data contrast measured in fog is consistently quite high (based on the -0.6 to -0.8 rule-of-thumb), and there is a trend for contrast to be higher in heavier fogs.

6.1.2.1.1.3 Contrast in Rain

A number of approaches were made during rain events along the east coast on September 25 and 26, 1992. Unfortunately, the raw radar data for these runs are unavailable. The measured precipitation particle size distribution data can be used, however, to calculate MMW attenuation and backscatter estimates for these rain events. These values may then be evaluated and compared with the attenuation, backscatter, and contrast measurements made at the tower to provide some sense of expected contrast in these situations.

One particular rain event will be examined in detail in this section. These data were obtained on September 25 and represent approaches made to four different airports. Rain rates calculated from the drop size distributions averaged 10 mm/hr. The maximum estimated rain rate for these approaches was 29 mm/hr. Observed visibilities on the ground ranged from 1.3 to 1.7 nm. The average computed one-way MMW attenuation for these approaches was 2.56 dB/km (see Table H-2 of Appendix H). The maximum calculated one-way attenuation was 7.05 dB/km, corresponding to the maximum measured rain rate of 29 mm/hr. This is a much larger attenuation level than that observed in the fog events, due to the larger size of the raindrops. The raindrops have diameters comparable to the wavelength of the incident MMW radiation at 35 GHz and therefore scatter much more efficiently than the smaller fog particles.

A secondary effect of the rain is the effect of backscatter contributions by the precipitation present in the actively sensed volume. An estimation of the level of this effect may be made by calculating the backscatter due to the measured drop size distributions. For the runs made on September 25, this backscatter averaged -44 dBsm/m^3 (see Table H-3). The maximum calculated backscatter for these runs was -36 dBsm/m^3. The active volume sensed by the airborne radar at a slant range of 1200 m and an altitude of 200 feet is about 8240 cubic meters or 39 dBsm. This value was computed from Equation 4.4.2-15 under the assumption that 50% of the total volume is located above the ground surface. This would produce an average estimated backscatter contribution, due to the precipitation in the volume, of -5 dBsm (= -44 + 39), or an effective

scattering area of about 0.32 m^2. The maximum computed value of rain backscatter from this volume, corresponding to the 29 mm/hr. rain rate, is about 3 dBsm, or about 2 m^2.

Typical normalized RCS values for the terrain and the runway at this range and depression angle in clear weather are -33 and -53 dB, respectively. At this range and depression angle, the area of the radar pulse on the ground is calculated to be 428 m^2 (or 26 dBsm). The total expected return from a terrain area can then be estimated to be about -7 dBsm (= -33 +26), while the total return from a runway patch is expected to be about -27 dBsm. This represents an effective scattering area of 0.002 m^2 for the illuminated runway and 0.2 m^2 for the illuminated terrain. The difference, in log space, of these clear weather returns is 20 dBsm.

When the backscatter from the average (10 mm/hr) rain is added onto the backscatter from the illuminated areas, the terrain return increases from 0.2 to 0.52 m^2, or to about -2.8 dBsm. The return from the runway patch increases from 0.002 to 0.322 m^2, or to about -4.9 dBsm. The difference, in log space, between these two patches is now only 2.1 dB. The backscatter from the maximum rain rate encountered (29 mm/hr) increases the return from the terrain patch to 3.4 dBsm and the return from the runway patch to 3.0 dBsm. The difference in log space is then only about 0.4 dB.

The addition of rain backscatter can significantly reduce the difference, in term of dBsm, between the received power from the terrain and the runway. For reference, the computed 2.1 dB terrain-to-runway power ratio for the average 10 mm/hr rain rate corresponds to a raw data contrast of -0.38. The computed 0.4 dB terrain-to-runway ratio for the 29 mm/hr maximum observed rain rate corresponds to a raw data contrast of -0.09. In the first case, the contrast of -0.38 is not acceptable based on the -0.6 to -0.8 rule of thumb discussed for the clear weather case. The -0.09 contrast for the 29 mm/hr case represents effectively no contrast at all.

As was noted in Section 6.1.2.1.1.1, the contrast between the terrain and the runway is provided mainly by the backscatter from the surrounding terrain, since the return from the runway surface is close to or below the sensor noise floor. Attenuation of the returns will tend to reduce the perceived contrast by driving the terrain return towards this floor, while the level of the noise-limited return from the runway will remain unchanged. In this case, the average rain attenuation will reduce the signals about 8.2 dB along the path back to the receiver. If the runway backscatter is too close to the noise floor, the difference, in log space, between these the runway return and the return from the terrain could well end up being less than the already poor values calculated above.

Measurements made in the tower tests are generally consistent with these calculations. Figure 6.1-26 plots contrast measured at the tower with the Honeywell radar. As expected, contrast for the 12.9 mm/hr case is quite poor according to the predictions described above for a 10 mm/hr rate. The measured contrasts for the two lighter rain events were much better, but that for the 1.2 mm/hr rain appears better than that for the 5.3 mm/hr case. In all three cases, there is considerable spread in the measured values.

Clearly, additional data and further investigation are needed to better understand and reconcile these results. Perhaps the fairest tentative conclusion which can be offered at this point is that rain significantly impacts contrast, with rain rates greater than 8 to 10 mm/hr likely to produce poor contrasts. Undoubtedly, the actual contrast observed in a given rain event will be a strong function of the drop-size distributions as well as of the measured rain rate.

From another perspective, the reported pilot runway detection performances in rain varied from one rain event to another. For example, in a measured rain rate of 5.0 mm/hr, the Atlantic City, NJ airport was not detected at all on 9/25, while the Millville, NJ airport was detected at a range of about 0.45 nm (833 m) in a 17.5 mm/hr measured rain rate. Clearly, rain rate alone does not completely describe detection performance. Interestingly, Figure 6.1-18 indicates that Atlantic City (ACY) in general produced the poorest contrast of the eleven airports measured in clear weather. On the other hand, Millville in clear weather was not much better than Atlantic City.

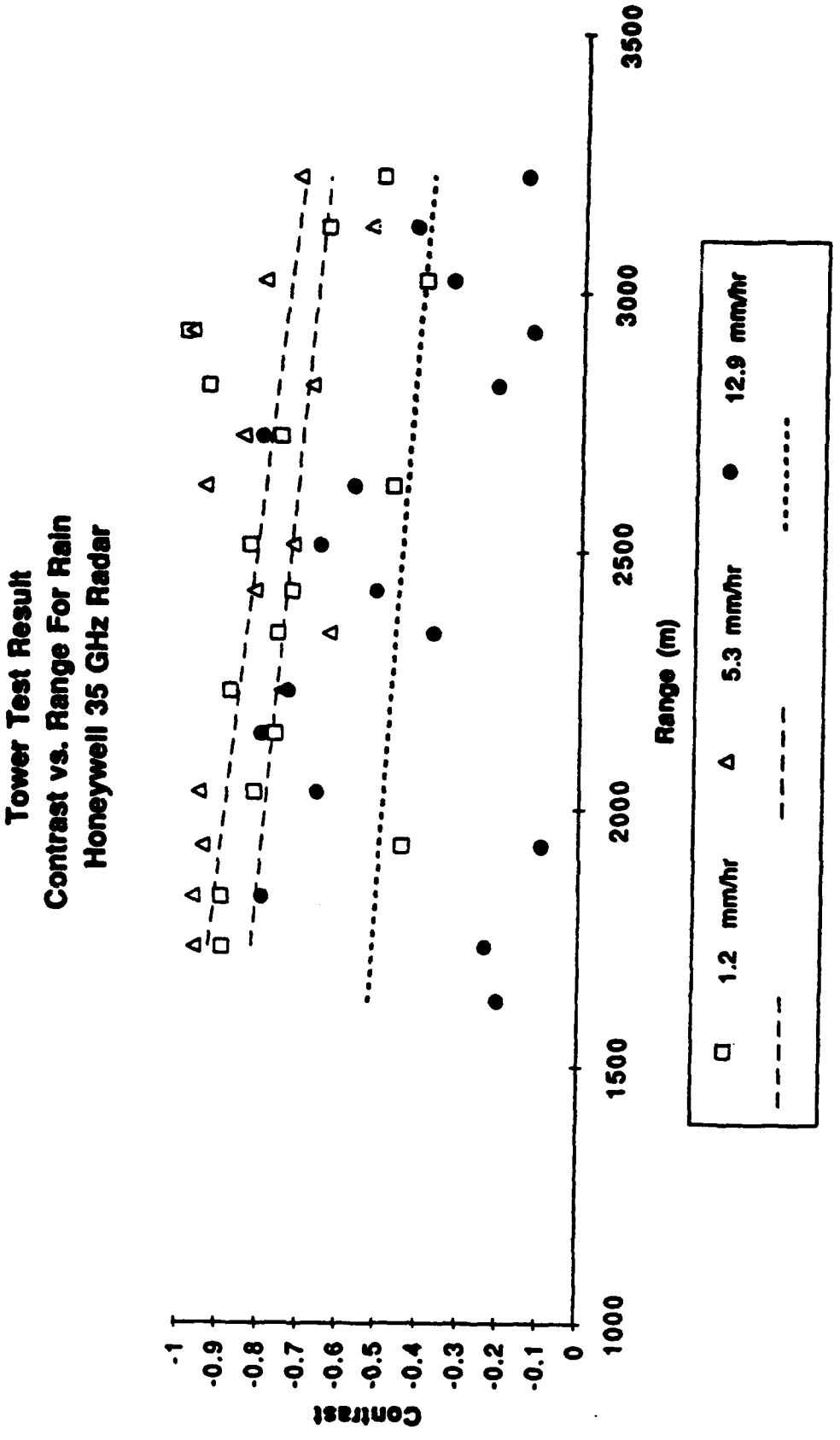

Figure 6.1-26. Plot of Measured Contrast Versus Range for the Honeywell Radar for Three Rain Rates at the Tower

6.1.2.1.1.4 Contrast in Snow

A limited set of data is available from the flight tests that helps quantify the performance of the Honeywell radar sensor in snow conditions. Flight test data are available which cover two general scenarios: (1) snow falling and both runway and terrain completely covered with accumulated snow, and (2) very little or no snow falling, complete snow cover on the terrain, with the runway plowed. In addition, the tower tests of the Honeywell radar system provide a third scenario, namely, moderate to heavy snow falling but no significant accumulation on either the terrain or the runway. Analyses of these data sets, as well as supporting calculations, have permitted some preliminary conclusions to be drawn regarding the effects of snow on radar performance at 35 GHz.

A set of four approaches were made to the airport at Pueblo, Colorado on November 20, 1992. The air temperature was at the freezing point and a light to moderate wet snow was falling. Surface observations from the airport reported a visibility of 3/4 nm, and about 3/4" of snow had accumulated on both the ground and the runway surfaces. However, the grass surrounding the runway was very short and the 3/4" snow cover completely covered the individual grass blades, based on reports from test personnel. This set of approaches produced very low contrast from the MMW sensor. Figure 6.1-27 plots the measured contrast values versus range to ROI for this set of approaches, with the standard LMSE linear fit also indicated. Note that the majority of the contrast values fall below the -0.6 level.

The falling snow in the air was not the cause of the dramatic reduction in contrast measured during this set of approaches. A table of expected attenuation at 35 GHz for various types and rates of snowfall is presented below as Table 6.1-4. This data has been extracted from a set of curves which combined the results of a number of studies regarding the attenuation of MMW radiation by falling snow.[11]

---

[11] C.L. Belcher, er al, "Millimeter Wave Clutter Reflectivity and Attenuation Handbook," Georgia Institute of Technology, Georgia Tech Research Institute Final Technical Report on Project A-4272, BOA DAAH01-84-D-A029, Delivery Order 0051, March 1987, p. 92ff.

Table 6.1-4. 35 GHz Attenuation in dB/km as a Function of Snow Concentration - g/m^3 (Equivalent Rain Rate - mm/hr)

Snow Type	0.2 (0.6)	0.4 (1.2)	0.8 (2.4)
Watery	0.45	0.94	1.88
Wet	0.31	0.59	1.19
Moist	0.13	0.19	0.38
Dry	0.03	0.06	0.13

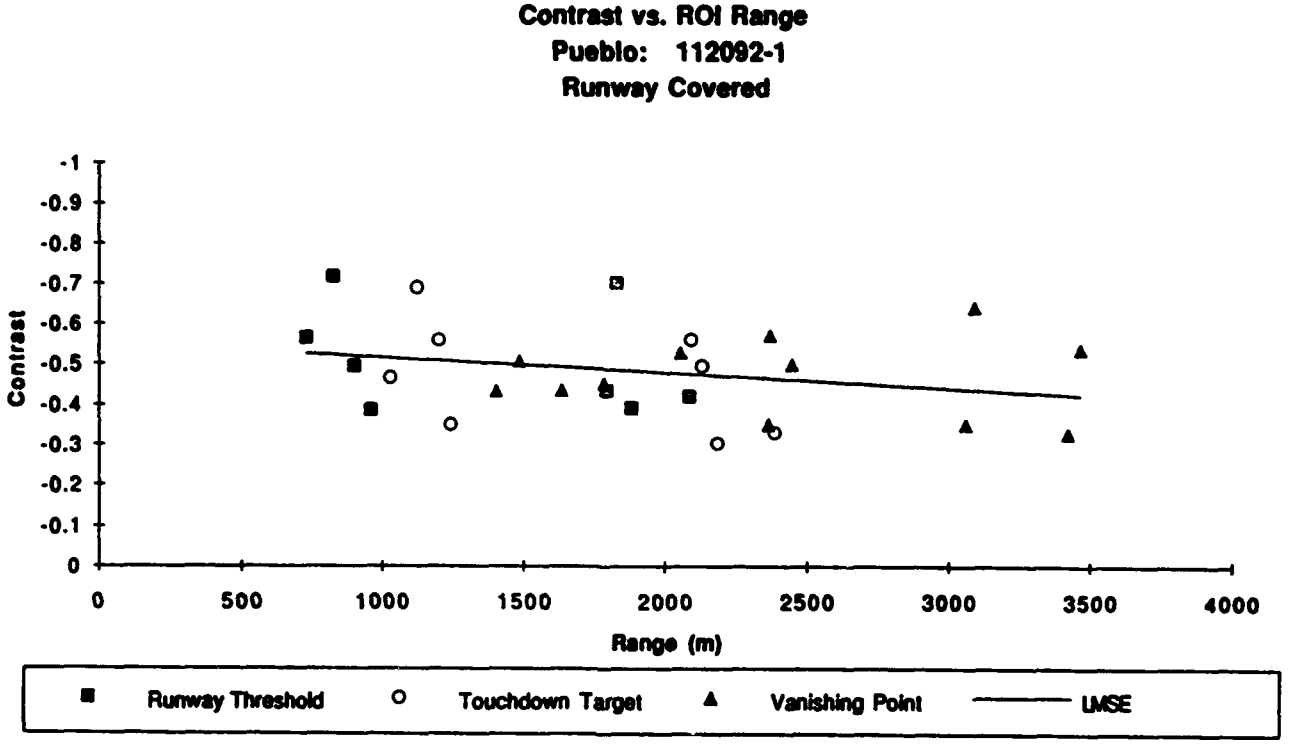

Figure 6.1-27. Plot of Contrast Versus Range to Region of Interest for Snow Approaches at Pueblo, CO on November 20, 1992. The Runway and Terrain Were Covered with Snow

Based on the JTD-supplied data, the radar snapshots analyzed for Pueblo on November 20 correspond to snow falls with equivalent rain rates between 0.12 and 1.03 mm/hr. If the average equivalent rain rate is assumed to be zero, and the value for "wet" snow type in Table 6.1-4 is used, the estimated attenuation due to the falling snow is 0.31 dB/km. Even at the maximum range of 3500 meters for which data are available in Figure 6.1-27, the corresponding round-trip attenuation would be less than 2.2 dB. Such a relatively small attenuation can not completely account for the severely degraded contrast observed in Figure 6.1-27.

This conclusion is consistent with data from the tower obtained with the Honeywell 35 GHz radar. Data from one run are available, during which moderate snow was falling, with an approximate 1 mile visibility reported. No significant snow accumulation was present on the runway or surrounding terrain. The measured contrast versus range is plotted in Figure 6.1-28 along with results in clear weather and in for comparison. Note that the contrast in snow, while not as high as that measured in clear weather or fog, is still fairly good. This leads to the conlusion that accumulated snow, rather than falling snow, is the the cause of the reduced contrast observed at Pueblo.

Thus, the greater influence on the contrast measurements made at Pueblo was due to the 3/4 inch of accumulated snow on the runway and surrounding terrain. Since the snow was wet, it is reasonable to assume that there was no significant backscatter from the underlying asphalt surface itself. The liquid water in the accumulated moist snow acted as an absorber of the MMW energy, reducing the amount of energy able to reach the runway surface as well as reducing the energy scattered from this surface back to the sensor. Since the backscatter from the runway surface is naturally very low under normal conditions, the backscatter from the runway area in this case can be considered to have been more characteristic of wet snow cover rather than of the pavement.

The grass at the sides of the runway was short and test personnel observed that the accumulated snow had covered the grass. Therefore, the return from the surrounding terrain was perhaps also typical of wet snow rather than of short grass. Since the normal backscatter from the terrain is significant, this dominating effect due to the snow cover would be smaller in this case than in the case of the snow-covered pavement. Nonetheless, the complete snow cover on both surfaces would tend to homogenize the scene and therefore reduce the differential contrast between the two areas.

The contrast data shown in Figure 6.1-27 are consistent with this analysis. Four approaches were made to Pueblo on November 20, and for none of these did the sensor provide an image

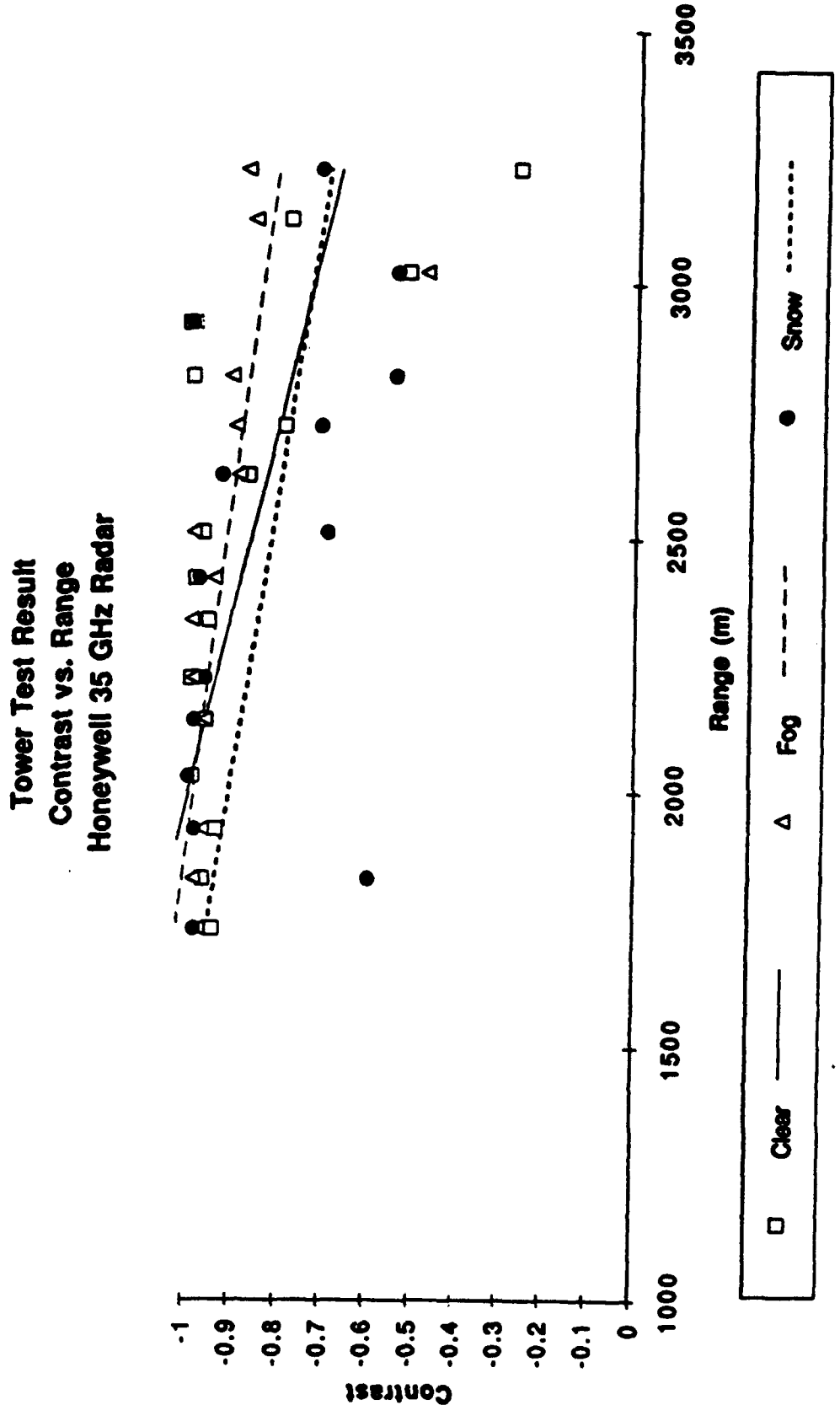

Figure 6.1-28. Plot of Measured Contrast Versus Range for the Honeywell Radar in Clear Weather, Fog, and Snow at the Tower

sufficient for the pilot to declare detection of the runway. This lack of apparent image quality is supported by the linear fit to the measured contrasts for these approaches, which indicates contrast values well below -0.6 for all ranges plotted.

Two more approaches were made at the Pueblo airport on the next day, November 21. The snowfall had accumulated overnight to a depth of five inches on the surrounding terrain. No snow was falling, and the observed visibility had risen to three miles. The runway had been plowed but was reported to still have patches of ice and snow on it. A clear runway should provide excellent contrast when viewed against snow-covered terrain. The runway surface should present very low backscatter and the snow cover will present backscatter at a level comparable to grassy areas when the snow is wet, and backscatter on the order of ten dB higher when the snow is dry and frozen.[12] [13]

The corresponding measured contrast for these two approaches is plotted in Figure 6.1-29. The data are sparse and there is considerable spread evident. Nonetheless, by comparing Figures VI.A-27 and 6.1-29, it can be seen that the two approaches on November 21 did not offer significantly greater contrast than the previous approaches when the runway was completely covered. Again, all the measured contrast values were below -0.6.

The probable reason for the lack of contrast in the Pueblo data on the second day was the presence of snow and ice in patches on the runway surface, in cracks and crevices, and as a glaze on the particles which make up the asphalt. The type of snow which produces the greatest backscatter is snow which has undergone melt-refreeze cycles, also known as "metamorphic" snow. Metamorphic snow may produce backscatter on the order of 10 dB higher than dry snow.[14,15] Thus, even a light covering of such metamorphic snow would significantly raise the backscatter from the pavement to a level closer to that of the surrounding snow-covered terrain.

---

[12] C.L. Belcher, et al, "Millimeter Wave Clutter Reflectivity and Attenuation Handbook," Georgia Institute of Technology, Georgia Tech Research Institute Final Technical Report on Project A-4272, BOA DAAH01-84-d-A029, Delivery Order 0051, March 1987, P15 ff.

[13] N.C. Currie, R.D. Hayes, and R.N. Trebits, *Millimeter-Wave Radar Clutter*, Artech House, Boston, 1992, pp. 145 ff.

[14] N.C. Currie, et al, "Millimeter-Wave Measurements and Analyses of Snow-Covered Ground," *IEEE Transactions on Geoscience and Romote Sensing*, Vol. 26, No. 3, May 1988, pp.307-318.

[15] N.C. Currie, R.D. Hayes, and R.N. Trebits, *Millimeter-Wave Radar Clutter*, Artech House, Boston, 1992, pp.145 ff.

Approaches were also made to a second airport, at Colorado Springs, Colorado, on November 21. The weather conditions present during these approaches were similar to those experienced that same day at Pueblo. No snow was falling and observed visibility's were good, being over ten miles. An accumulation of approximately four inches of snow covered the surrounding terrain. The runway at Colorado Springs had also been plowed and was reported to be completely free of snow. The corresponding measured contrast values are plotted in Figure 6.1-30. Again, the data exhibit considerable spread but the measured contrast is considerably better than for either Pueblo approach.

Figure 6.1-31 superimposes the LMSE linear fits for the three snow sorties. While the contrast observed at Colorado Springs was not comparable to the results obtained either in clear weather or during fog events at other locales, it was definitely better than the results seen in the

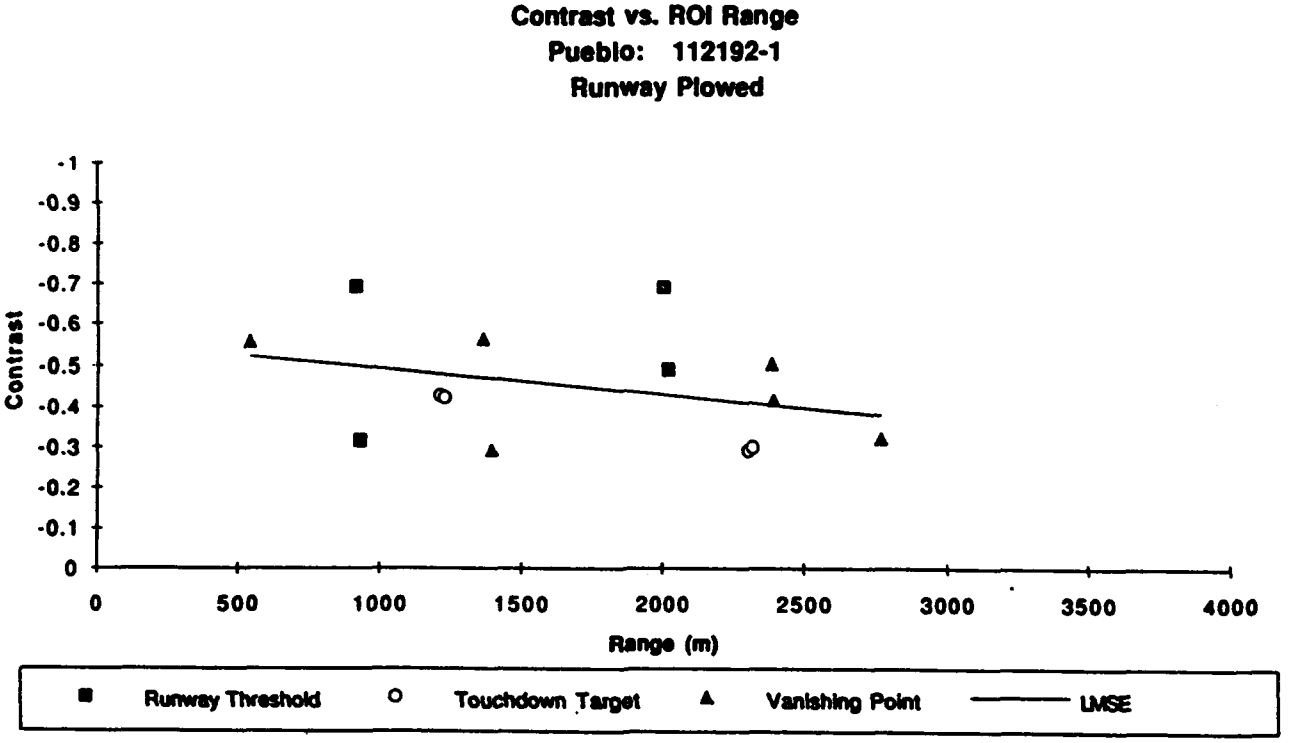

Figure 6.1-29. Plot of Contrast Versus Range to Region of Interest for Snow Approaches at Pueblo, CO , on November 21, 1992. The Runway had been Plowed, but Patches of Snow and Ice Remained

Pueblo data. However, the evaluation pilot noted that a usable image was not available for either of the approaches to Colorado Springs (COS).

The available measured data show that the effect of accumulated, rather than falling, snow is key for observed contrast. However, the exact effects of the accumulated snow are not fully understood. Unfortunately, information such as percent free water content, total water content, etc. is not available for the snow at any site. Thus, the conclusions drawn are based on the available qualitative observations such as "wet" snow and "dry" runway. More investigation is clearly needed in this area. Effects of dry, wet, and refrozen snow should all be explored. And the question of why the Colorado Springs contrast was not even better than observed should be

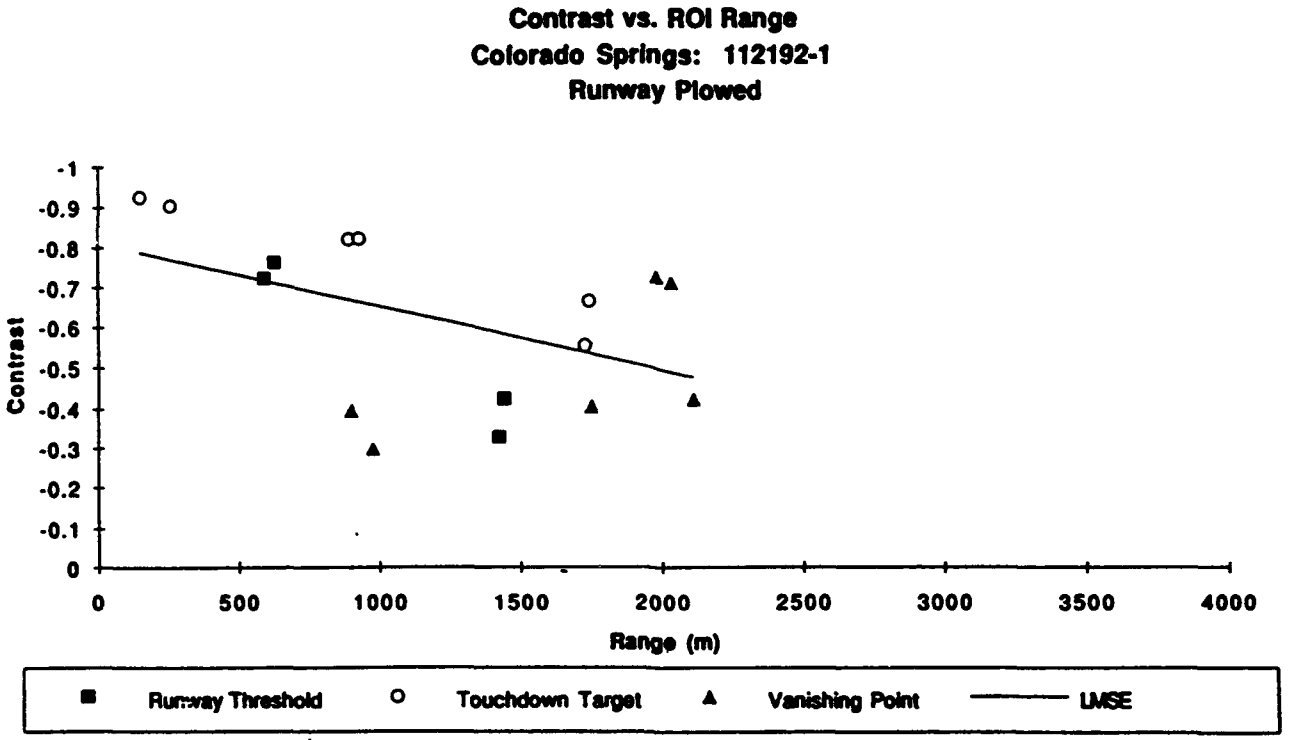

Figure 6.1-30. Plot of Contrast Versus Range to Region of Interest for Snow Approaches at Pueblo, CO , on November 21, 1992. The Runway had been Plowed

addressed. If the runway was really completely clean, and snow on the terrain had possibly experienced a melt-refreeze cycle, then why was the contrast not at least as good as in the typical clear-weather case? Recall that backscatter from wet snow is typically comparable to that of the terrain (about -30 dB at 3-degrees depression angle), and the backscatter from refrozen snow is even greater. Additional data and analyses are required to explore these issues

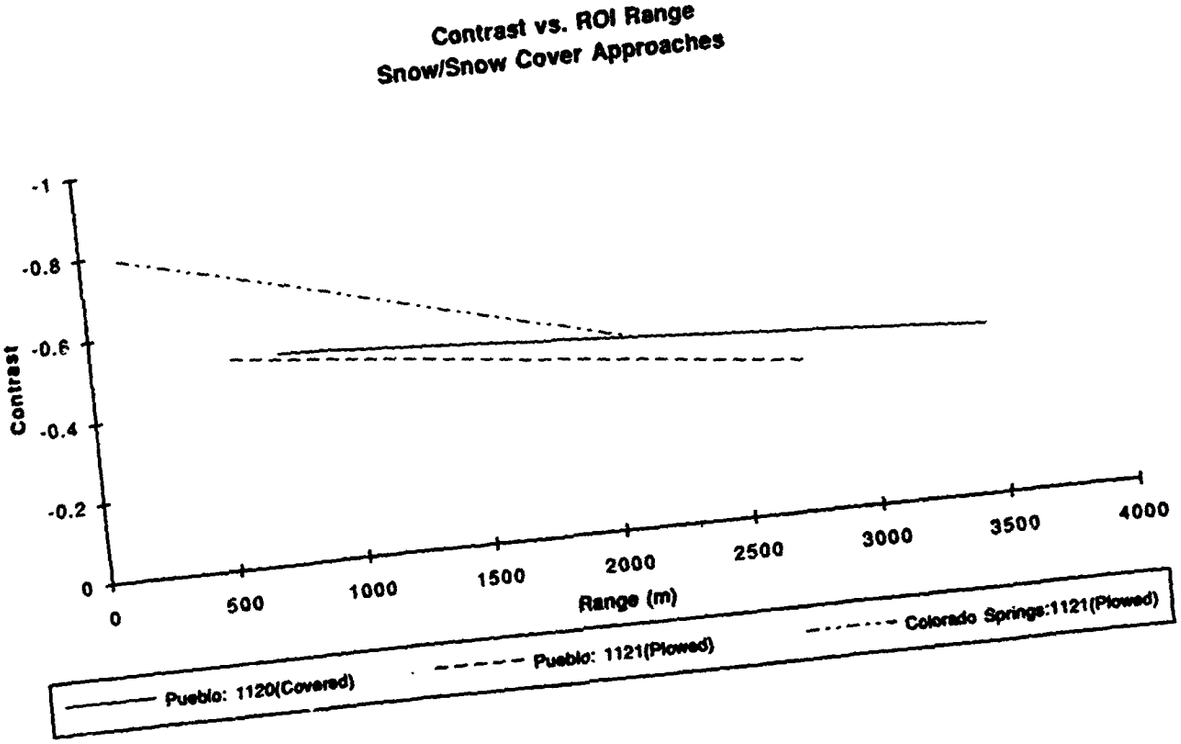

Figure 6.1-31. Plot of Contrast Versus Range to Region of Interest for Snow Approaches at Pueblo, CO , on November 20, 1992. Data are Presented as the LMSE Lines Fitted to the Measured Values for each Sortie

6.1.2.1.2 Summary of Contrast Results

The contrast values measured during the flight tests may naturally be separated into weather categories. The observed clear-weather performance is not critical in terms of the synthetic vision mission since in these cases, the pilot has a clear optical view of the runway and therefore does not need a synthetic vision sensor. These cases do, however, serve as a baseline against which to measure contrast during degraded weather when the pilot's vision may not be adequate to operate and land the aircraft unaided. The clear-weather measurements also demonstrated two important aspects of the observed contrast. The first is the relative independence of the measured contrast on the runway surface type, which indicates that the level of available contrast is primarily determined by the backscatter characteristics of the terrain clutter surrounding the runway. The runway backscatter is overwhelmed by the level of the terrain backscatter and in fact, the runway return level frequently lies close to or below the sensor noise floor.

A second important aspect, made apparent in the baseline clear weather measurements, is the influence of the airport-to-airport variability in the terrain radar returns. Just as the terrain varies from airport to airport, or even from month to month at the same airport, the observed contrast varied significantly from one facility to the next and even varied for two different approaches to Point Mugu. In addition, the somewhat random, non uniform nature of the terrain backscatter appears to lead to higher contrast than to be expected if the basis used is the FAA definition of visual threshold.

Measured contrast in clear weather was high, permitting the pilot to declare detection of the airport at a mean range of 1.5 nm, with a standard deviation of 0.26 nm. These detection ranges corresponded to measured contrast values between roughly -0.6 and -0.8.

The values of contrast measured during fog events were generally as high or higher than those measured during clear weather. Fog particles are too small to provide excessive attenuation of millimeter waves at the ranges important for these tests. The wetting action of the fog may also tend to enhance the backscatter from the surrounding terrain and thus increase the measured contrast. The test pilots were able to successfully detect the runway even in very dense fogs characterized by zero visibility or zero ceiling. Good contrast was observed in the measured data for heavy fogs characterized by 1/8 nm optical visibilities and vertical penetrations less than 100 feet.

The specific effects of rain on the available contrast are not well understood. An attempt was made to extrapolate from clear-weather contrast measurements with the aid of the particle size distributions measured in flight. The in-flight drop-size measurements, and the calculation of estimated attenuation's and rain rates from them, permitted estimates to be made of the reduction in signal levels due to the presence of this precipitation. These calculations indicate poor contrast at a 10 mm/hr rain rate and almost no contrast at a 29 mm/hr rain rate for the specific drop-size distributions measured. Results from the tower test indicate poor contrast at a 12.9 mm/hr rain rate but fairly good contrasts at 1.2 mm/hr and 5.3 mm/hr rain rates. Clearly, contrast tends to decrease with increasing rain rate. Contrast is also expected to be a function of the specific drop-size distributions encountered. Additional data are needed to better understand these relationships.

Accumulated snow was observed to greatly diminish the available contrast. When snow is present on both the runway and the terrain, this lowered contrast is due to homogenization of the scene by the roughly uniform snow layer. Plowing the runway enhanced the measured contrast, by lowering the backscatter from the runway, but improvement was not sufficient to produce a usable image. Falling snow, as opposed to accumulated snow, should not degrade the scene contrast significantly unless the snow is quite heavy. These conclusions for snow are preliminary since they are based on a small number of available snow scenes, for which quantitative physical data characterizing the snow (free water content, etc.) are not available.

6.1.2.2 Sharpness

Sharpness was defined under this program as an image quality metric to measure the distance over which the transitions from runway to terrain or from terrain to runway occurred in the image. Sharpness, as described previously in Section 4.4.2.3.1.3.3, was computed by partitioning the image into a runway plateau and a terrain plateau, with the region between the two defined as the transition region (see Figure 4.4.2-20). Since a transition region can be defined on either side of the runway, the overall image sharpness was computed as the average of the transition widths on each side of the runway (see Equation 4.4.2-21). From the combined tower and flight tests, image data were collected in clear weather, fog, rain, and snow. Data collected during the tower and flight tests were analyzed to determine the relationship between sharpness and the different conditions influencing image quality such as weather, distance from the aircraft to the runway, runway construction and pavement type, and terrain type.

6.1.2.2.1 Flight Tests

The flight test data offered a wide range of airport scenes for which sharpness could be measured. The flight tests included measurements made during clear weather as well as conditions of fog, rain, and snow. The flight tests included measurements taken at Vandenburg AFB, Arcata, and Huntington, WV during the presence of fog, and at Pueblo and Colorado Springs in the presence of snow.

Figure 6.1-32 plots measured sharpness (in inverse degrees) versus range to ROI for approaches made to Arcata in fog on 8/28/92. Only data for which the measured liquid water content was less than or equal to 0.09 g/m3 are included in the plot. Note the general increase in sharpness with range, which is quite surprising since larger sharpness values correspond to a sharper transition between the terrain and runway.

To probe this issue, data shown in Figure 6.1-32 was plotted in terms of PPI pixels rather than inverse degrees. The plot is included as Figure 6.1-33. Note that the sharpness values are reported in terms of the number of pixels in the PPI required for the transition between the terrain plateau and the runway valley to occur. The data are fairly randomly scattered between 1 and 5 pixels. However, in the PPI display, a single pixel at short range represents a larger angular extent in azimuth as does that same pixel at a longer range. This is reflected in the piece-of-pie shape of the PPI display. Relatively few pixels span the 30-degree instrumented azimuth window at close range, whereas many more pixels are required to span this same angular extent at longer ranges.

This phenomenon accounts for the apparent increase in sharpness with increasing range. The typical 1 to 5 pixel transition corresponds to a larger angle at shorter ranges than at longer ranges. Thus, the inverse of the corresponding angle at short range is smaller than the inverse of the angle at long range. Hence, the increasing trend seen in sharpness measured in inverse degrees as a function of range. Now the question arises: Why does sharpness measured in pixels behave so randomly and exhibit no clear trend with range?

GTRI has generated plots of sharpness in pixels for various approaches. Figures 6.1-34 and 6.1-35 complete the sharpness data set for sortie 1 to Arcata on 8/28. Whereas Figure 6.1-33 represented data from the lightest fog conditions, Figure 6.1-34 includes data from medium fog conditions, and Figure 6.1-35 plots data from the heaviest fog conditions encountered on that day. All three plots display the same random variation in sharpness between roughly 1 and 5 pixels.

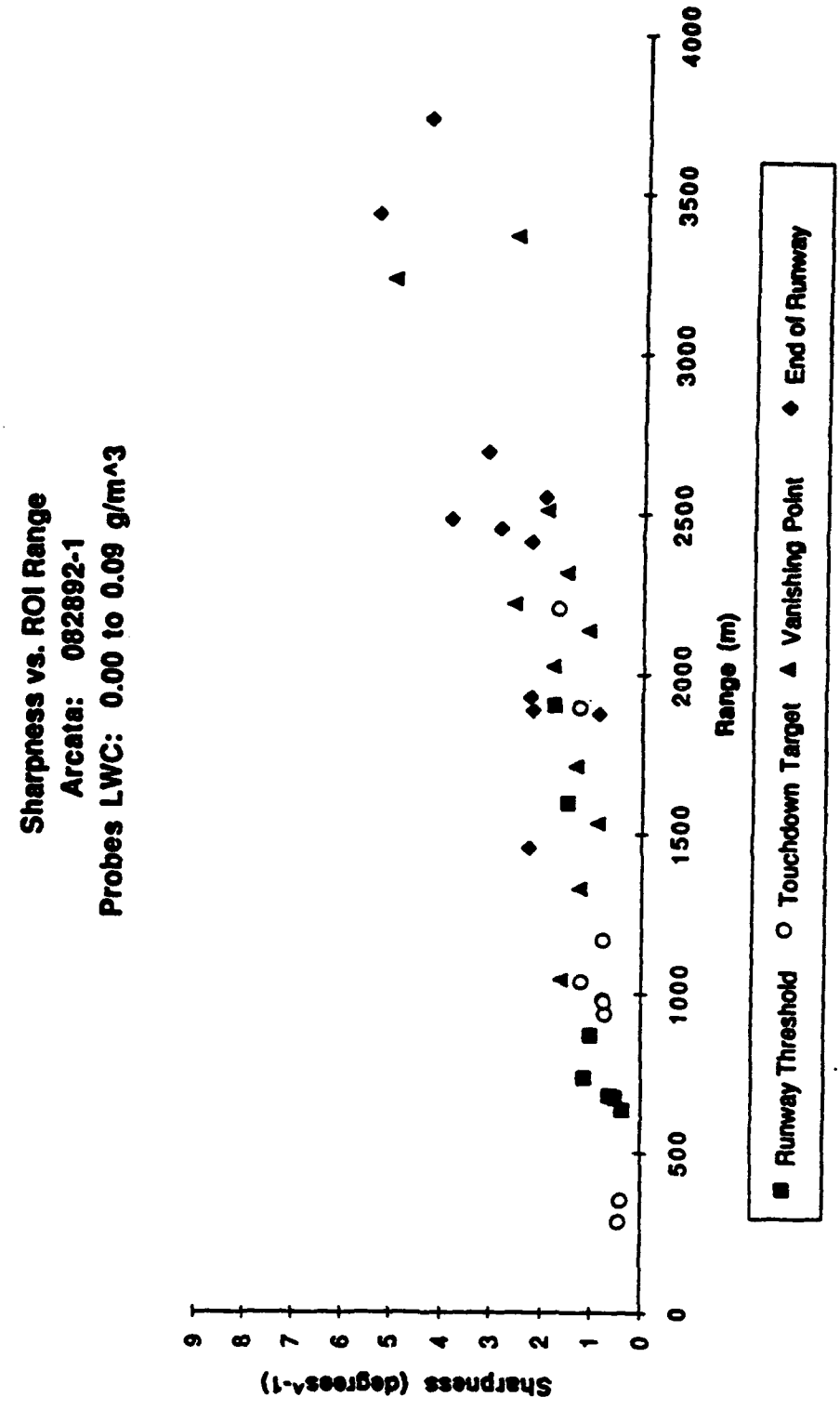

Figure 6.1-32. Plot of Sharpness (In Inverse Degrees) Versus Range to Region of Interest for Fog Approaches at Arcata, CA on August 28, 1992. Data are Taken from Snapshots with an Integrated LWC of 0.00 to 0.09 g/m^3.

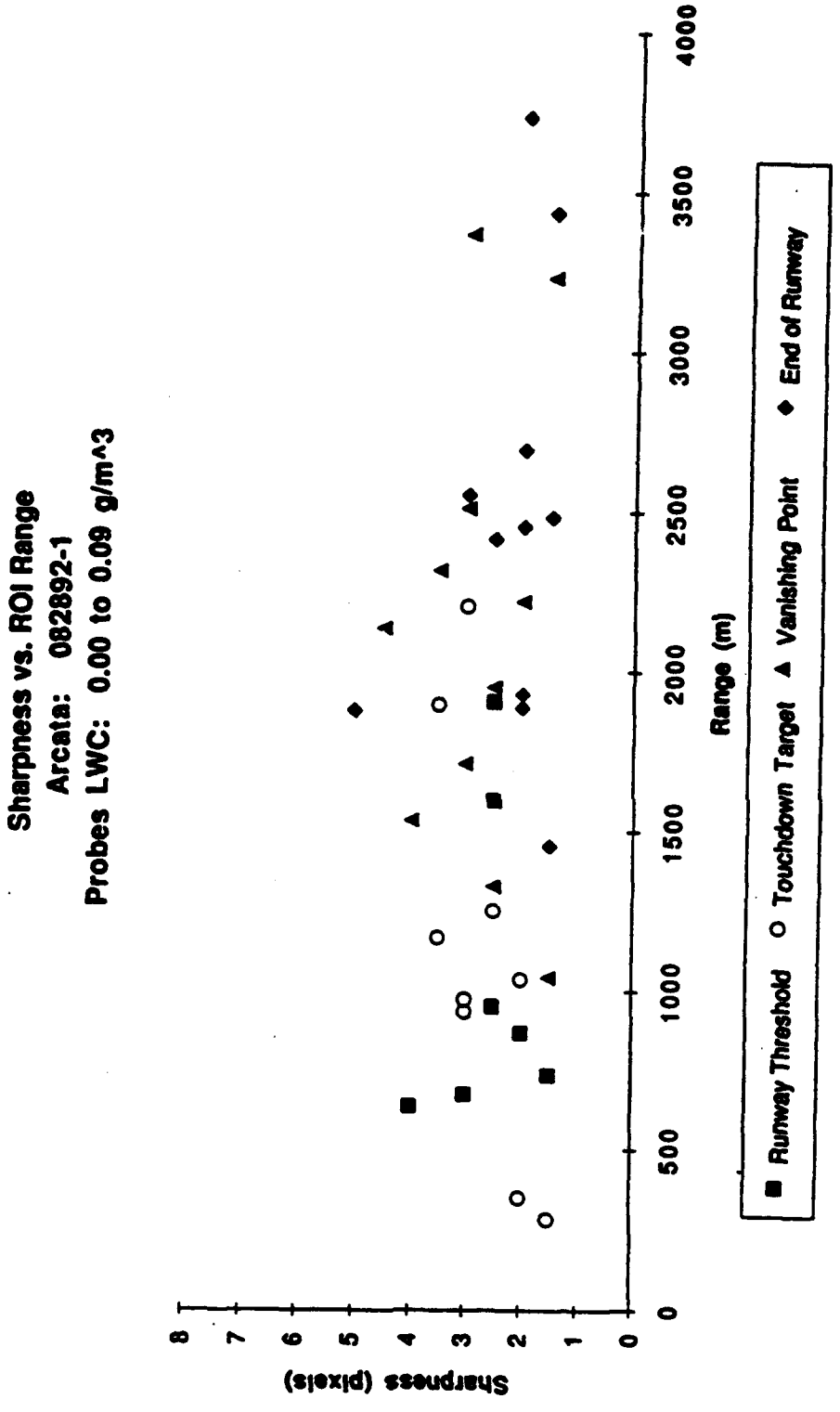

Figure 6.1-33. Plot of Sharpness (In Pixels) Versus Range to Region of Interest for Fog Approaches at Arcata, CA on August 28, 1992. Data are Taken from Snapshots with an Integrated LWC of 0.00 to 0.09 g/m^3.

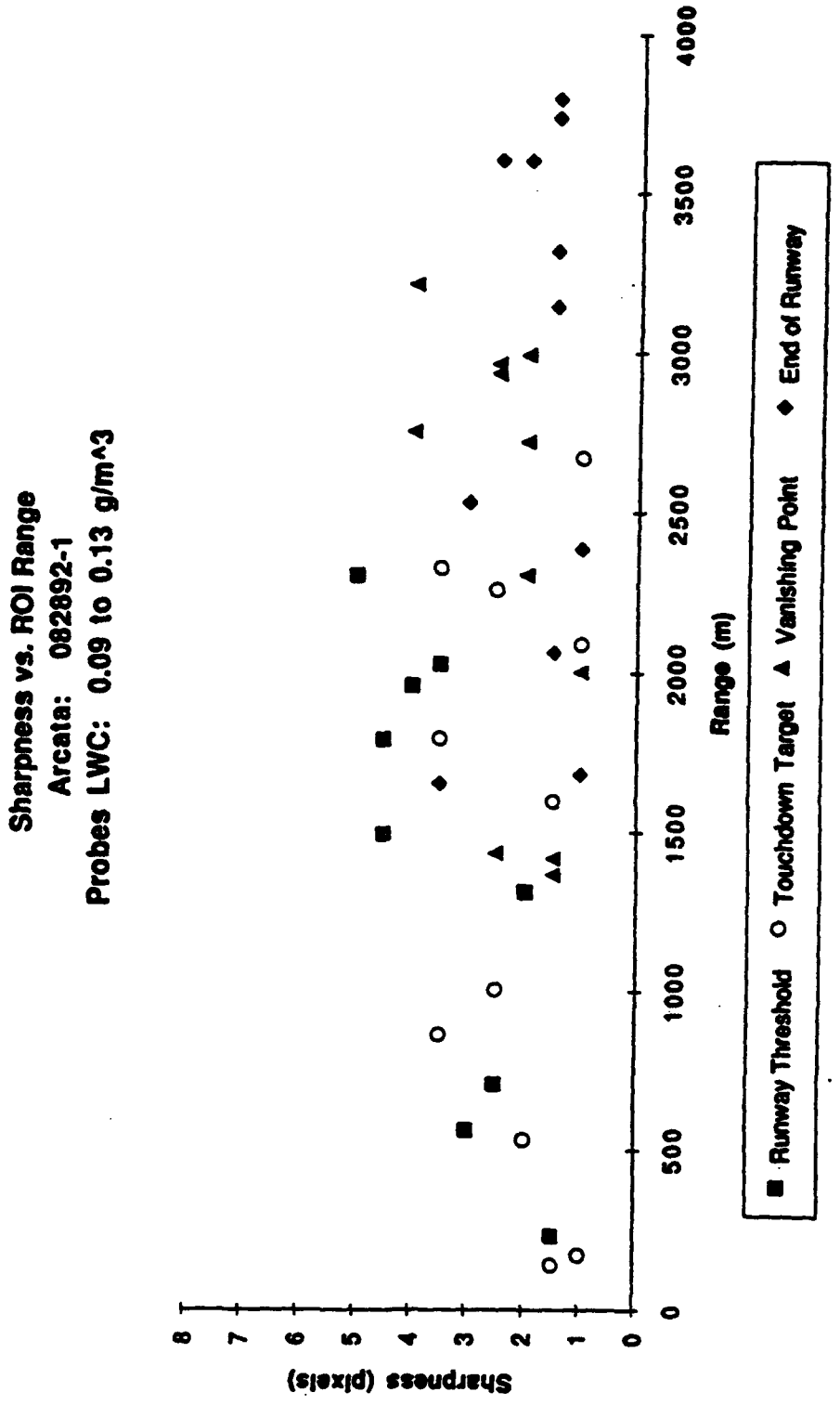

Figure 6.1-34 Plot of Sharpness (In Pixels) Versus Range to Region of Interest for Fog Approaches at Arcata, CA on August 28, 1992. Data are Taken from Snapshots with an Integrated LWC of 0.09 to 0.013 g/m^3.

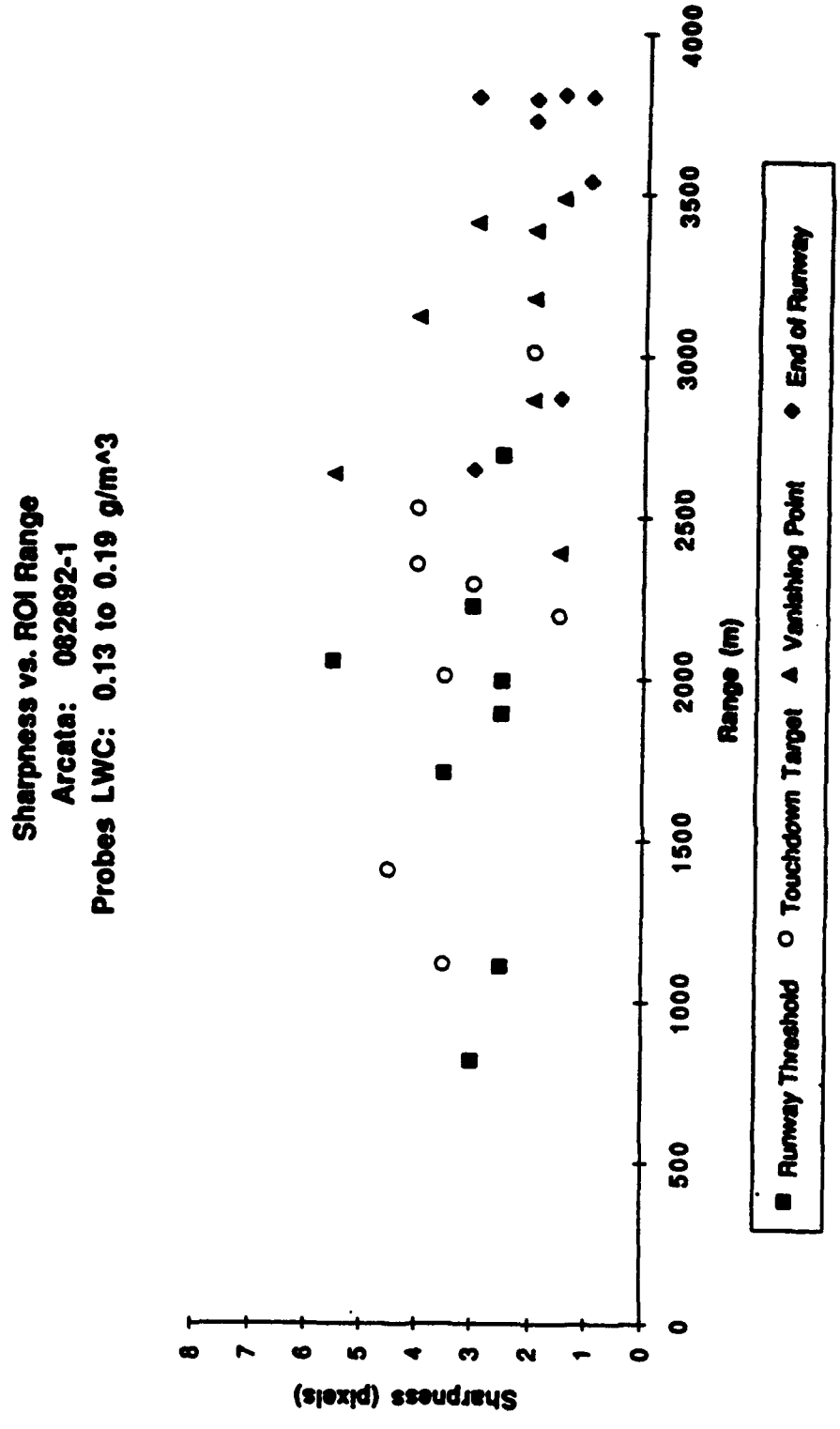

Figure 6.1-35 Plot of Sharpness (In Pixels) Versus Range to Region of Interest for Fog Approaches at Arcata, CA on August 28, 1992. Data are Taken from Snapshots with an Integrated LWC of 0.13 to 0.19 g/m^3.

Figure 6.1-36 plots sharpness in pixels for all data taken on 11/20 and 11/21 during the snow approaches into Pueblo and Colorado Springs. These plots are similar to those for the fog approaches at Arcata, with perhaps a slight decrease in the maximum pixel-value measured. The data in Figure 6.1-36 range from about 1 to 4 pixels, whereas the values in Figures 6.1-33 through VI.A-35 range from 1 to about 5 pixels. (Oddly enough, a smaller sharpness expressed in pixels corresponds to a sharper transition, so that if anything, the snow images are sharper than those in fog, according to this metric !) In any case, the same random variations are seen in both data sets. There is certainly no compelling distinction to be made between the representative sharpness values observed in fog at Arcata and those encountered in the snow at Pueblo and Colorado Springs.

However, there was certainly a difference in perceived image quality between the fog and snow approaches. It was postulated that, as an image quality metric, sharpness would correlate with the perceived image quality, much as contrast does. This is not the case based on the flight test measurements. In the presence of fog, the sharpness values were consistently within the range of 1 to 5 pixels, and for fog conditions, the runway detection performance of the test pilots was "good." In the presence of snow, however, the runway detection performance was poor, but the calculated sharpness values roughly tracked those seen in the presence of fog. Therefore, sharpness, as measured in the flight tests, does not appear to be a good indicator of runway detection performance or of image degradation due to weather effects. The possible explanation of this phenomenon will be addressed below.

6.1.2.2.2 Tower Tests

The tower tests were restricted to imaging a single runway from a fixed geometry, but these tests were conducted in similar weather conditions as those seen in the flight tests. A small number of sharpness measurements were taken at the tower for clear weather, fog, snow, and rain in order to compare with those taken during the flight tests. The results of these sharpness measurements, expressed in terms of PPI pixels, are listed in Table 6.1-5. The limited number of sharpness measurements made with the tower test data prevents any firm conclusions from being drawn concerning the relationship between sharpness and weather. However, the data in Table 6.1-5 are generally consistent with the sharpness ranges seen during the flight test (1 to 5 pixels).

Table 6.1-5. Sharpness in EQUIVALENT PPI Pixels Recorded at the Tower

Run	Sharpness	Conditions
HI2R11	1.4	clear
HI2R18	2.9	fog
HI2T09	2.8	snow
HI2R09	2.8	rain (1.2 mm/hr)
HI2R23	2.6	rain (5.3 mm/hr)
HI2R31	2.8	rain (2.9 mm/hr)

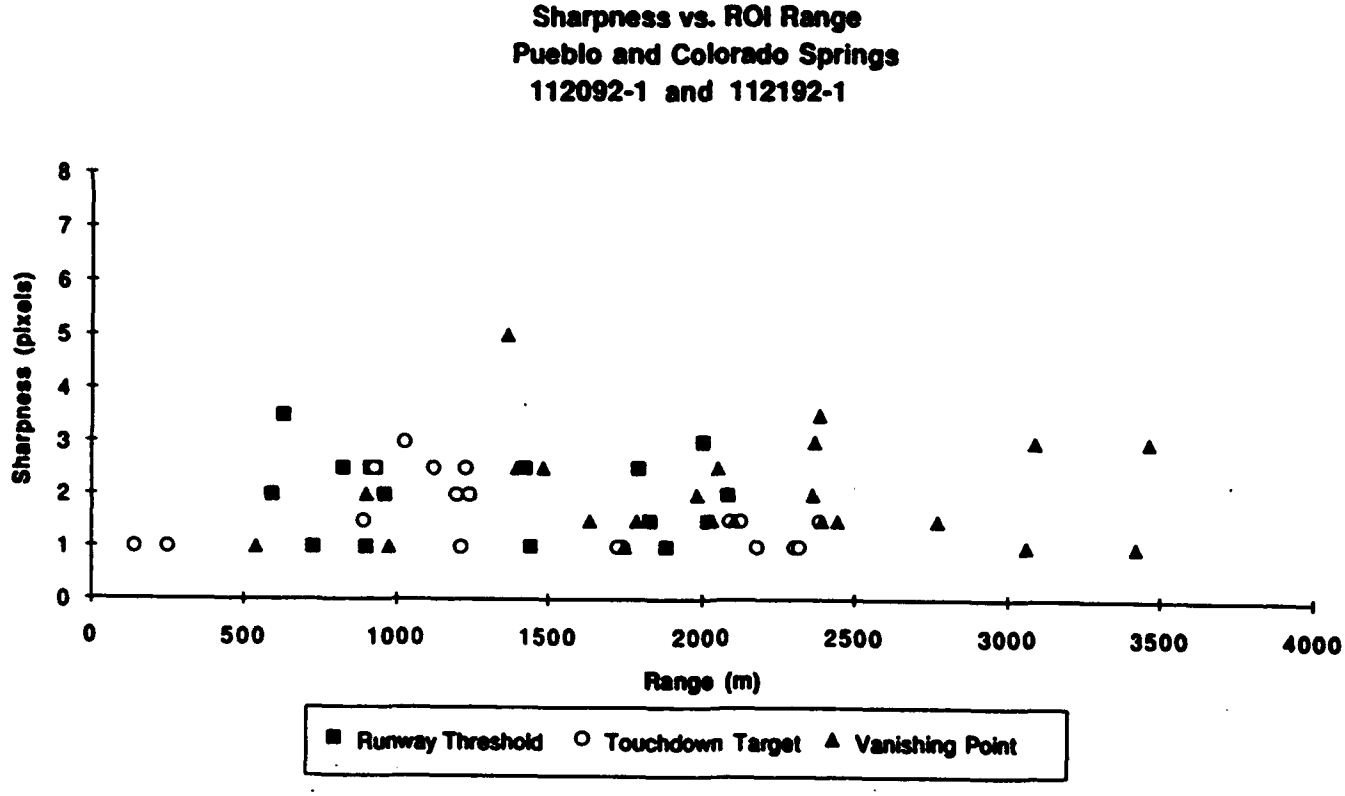

Figure 6.1-36 Plot of Sharpness (In Pixels) Versus Range to Region of Interest for Snow Approaches at Pueblo, CO and Colorado Springs, CO on November 20, 21, 1992

6.1.2.2.3 Conclusion

The data presented above indicate that the sharpness of the runway-terrain boundary varies between about 1 and 5 PPI pixels. This means that the transition between the terrain plateau and the runway valley occurs over a span of 1 to 5 pixels in the PPI image. Furthermore, variations in sharpness (reported in pixels) with range and different weather conditions appear random. One reason for these effects is the uncertainty inherent in the sharpness measurement technique employed. Figures 6.1-37 and 6.1-38 help illustrate this point.

As explained in Section 4.4.2.3.1.3.3 previously, the computation of sharpness is based on the identification of six transition points in each gutter plot. Figure 6.1-37 illustrates the selection of these points for a gutter plot taken from data acquired at Point Mugu on 11/27/92. The corresponding ROI is at a range of 2800 meters from the radar, and corresponds to the radar vanishing point in the image as determined by the analyst. As indicated in this figure, the left-hand terrain-to-runway transition occurs over a span of four pixels (pixels 11 to 15), and the right-hand runway-to-terrain transition occurs over four pixels as well (pixels 20 to 24). The overall sharpness is the average of these two values, or four pixels.

Figure 6.1-38 presents the same gutter plot, but this time the transition points have been selected a bit differently than before. The left-hand transition is now six pixels wide, and the right-hand transition occurs over six pixels as well. The overall sharpness in this case is thus measured to be six pixels. This represents an increase of 50% with respect to the previous value.

The measurement of sharpness is dependent on the subjective selection of these transition points. Even for a single gutter plot, some of these points might be adjusted to the left or right by a pixel or so. The spikes obvious in Figures 6.1-37 and 6.1-38 are characteristic of radar clutter data in general. A radar image of the scene a moment later or a few feet closer or further in range could produce different spikes in different pixel locations. In any gutter plot, modifying a few key pixel values would likely result in a different selection of the transition points. Consequently, a different sharpness measure would be produced.

The conclusion to be drawn from this observation is that the measurement error in determining sharpness in this fashion is roughly one or two pixels. However, since the measured values fall in the range of 1 to 5 pixels, the measurement error is substantial in relation to the value one is attempting to measure. For example, if the actual sharpness value were 3 pixels, and the measurement error was +/- 2 pixels, then the measured sharpness results would fall between 1 and 5 pixels. The magnitude of the measurement error is thus 67% of the true value to be measured.

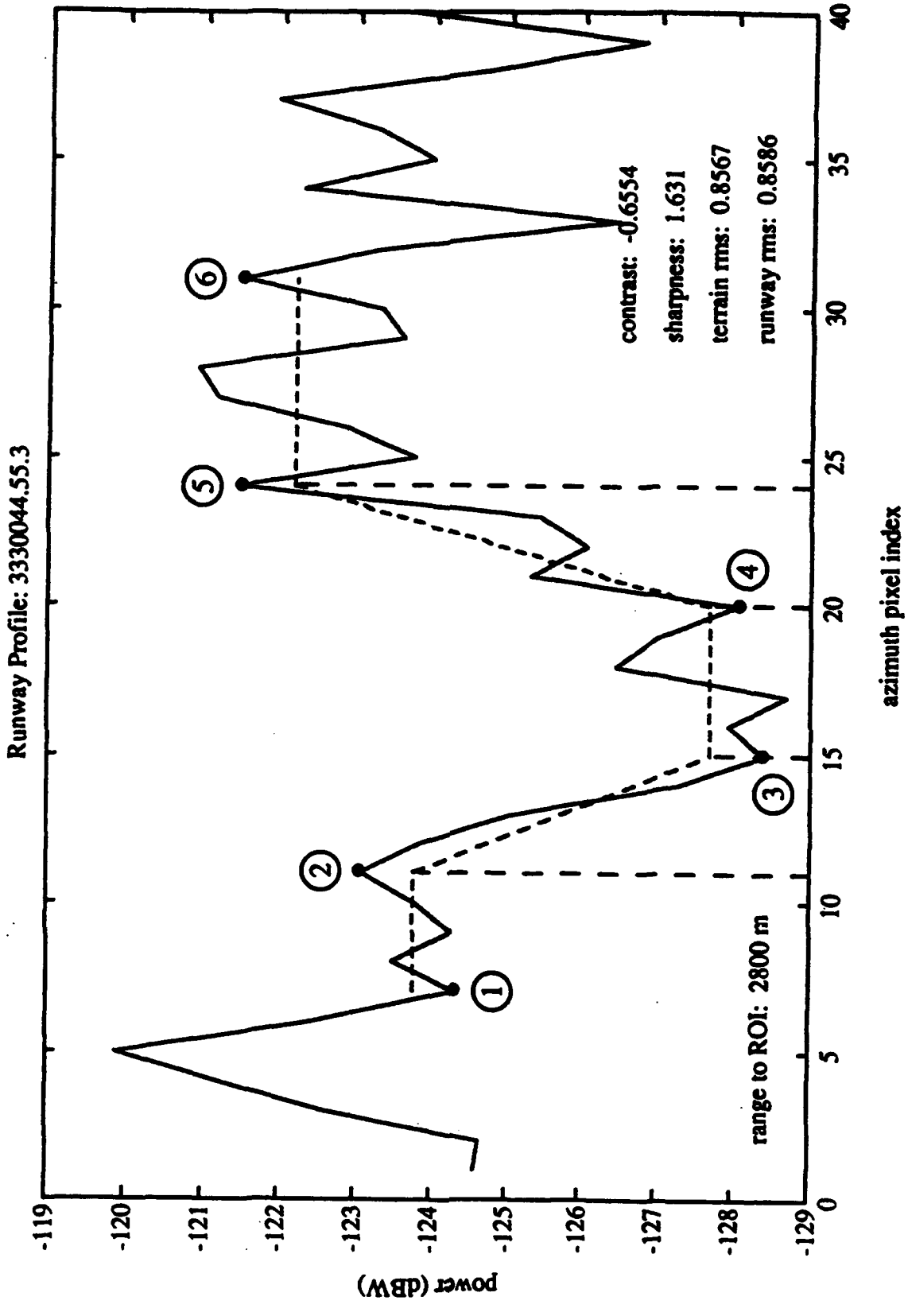

Figure 6.1-37. Illustration of Normal Transition-Point Selection in Sample Gutter Plot

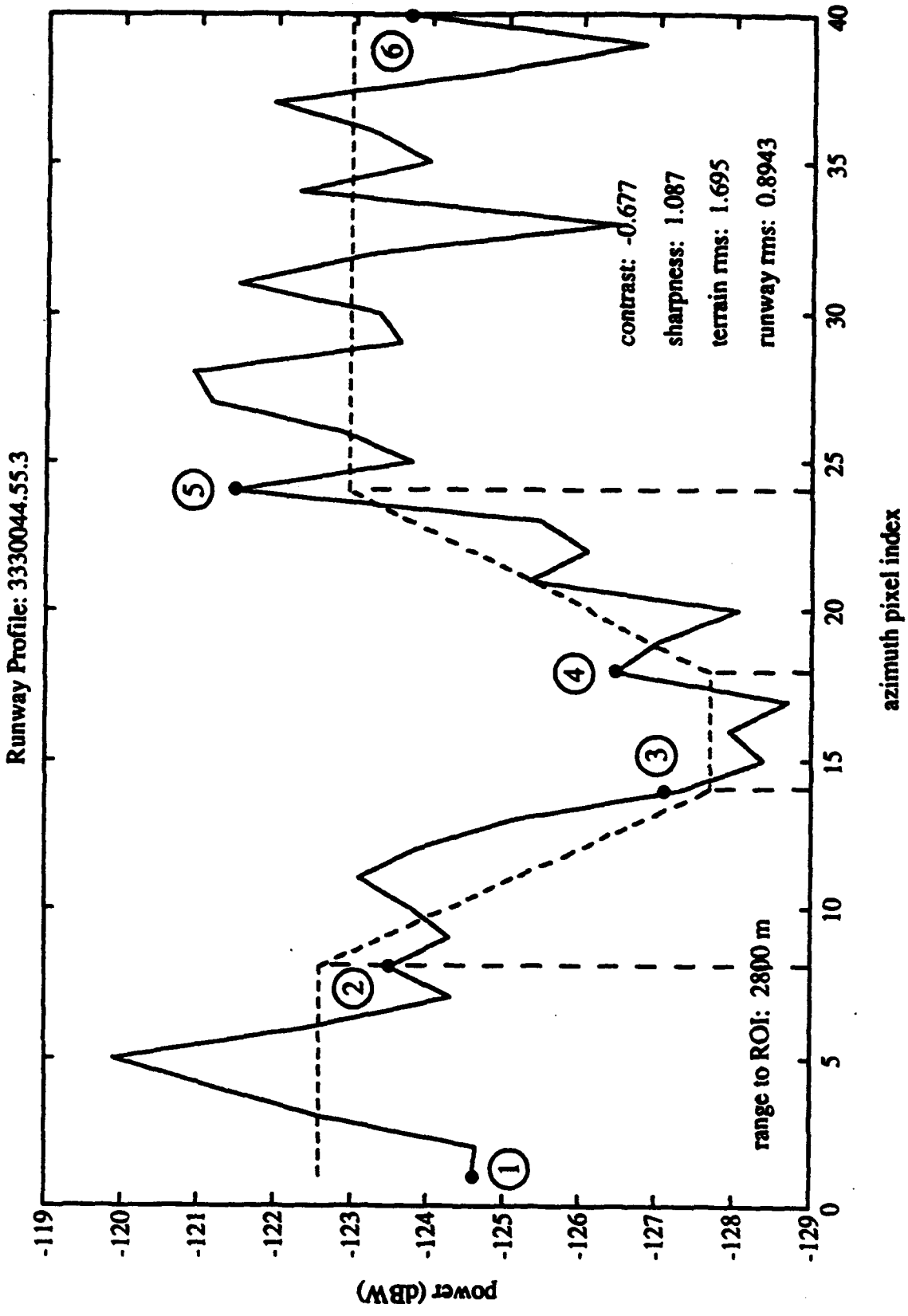

Figure 6.1-38. Illustration of Alternative Transition-Point Selection in Sample Gutter Plot

This hypothesis explains the observed random spread in the measured sharpness values, but what accounts for the apparent lack of correlation between measured sharpness and perceived visual image quality.

This phenomenon can be explained, at least to some extent, by considering the sharpness "penalty" associated with a high-contrast image. Figure 6.1-39 illustrates this point. A hypothetical antenna main beam pattern is shown in Figure 6.1-39(a), with the 3-dB beamwidth and the 10-dB beamwidths indicated. Figure 6.1-39(b) shows a low contrast scene (3 dB terrain-to-runway ratio) on the left and a high contrast scene (10 dB ratio) on the right. Now consider what happens when the antenna beam of Figure 6.1-39(a) scans across each of these scenes.

The result of this scanning process is illustrated in Figure 6.1-39(c). The beam effectively smears the transitions as indicated by the sloped lines Figure 6.1-39(c) versus the vertical transition lines in Figure 6.1-39(b). And the widths of these smeared transitions are determined by the shape of the main beam. At a range R, the lateral distance required for the transition from peak antenna gain to -3 dB with respect to the peak is approximately $R\theta_{3dB}/2$. Thus, the sharpness, which according to our definition is the width of the transition between terrain plateau and runway plateau, will be proportional to $R\theta_{3dB}/2$ for the low-contrast case. Similarly, for the high-contrast case, the measured sharpness will be proportional to $R\theta_{10dB}/2$. And, since θ_{3dB} is smaller than θ_{10dB}, the measured sharpness in the low-contrast case will be better than that in the high-contrast case, all other factors being equal. It was concluded that the sharpness measurement technique used in this case did not produce useful results as a means to measure describe image quality.

6.1.2.3 Signal-to-Variability Ratio

In the MMW radar synthetic vision application, the key to runway detection is the difference between the radar return from the runway and that from the surrounding terrain. Therefore, in a broad sense, this difference is the "signal" which the pilot is trying to detect. The signal-to-variability ratio (SVR) represents the ratio of the desired signal to this ubiquitous variability (see Section 4.4.2.3.1.3.4).

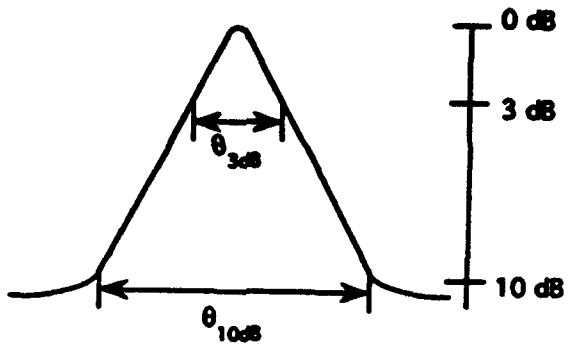

a). Antenna pattern

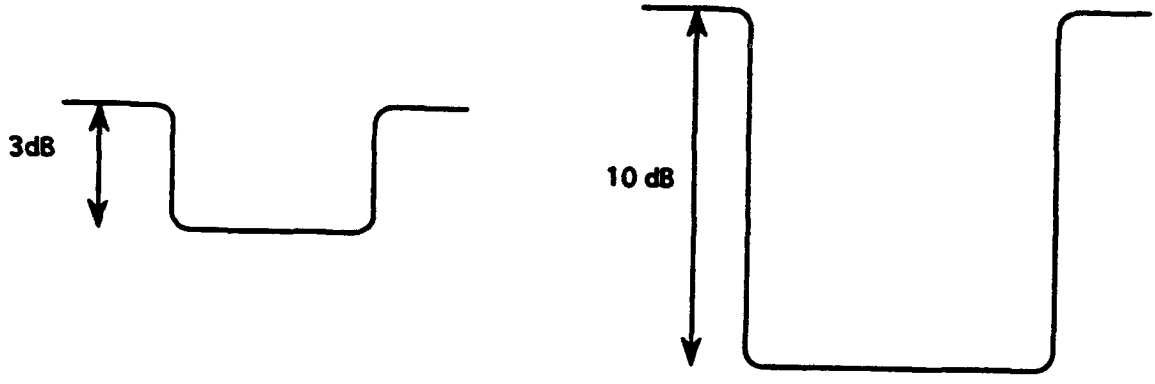

b). Actual gutter present for low and high contrast cases

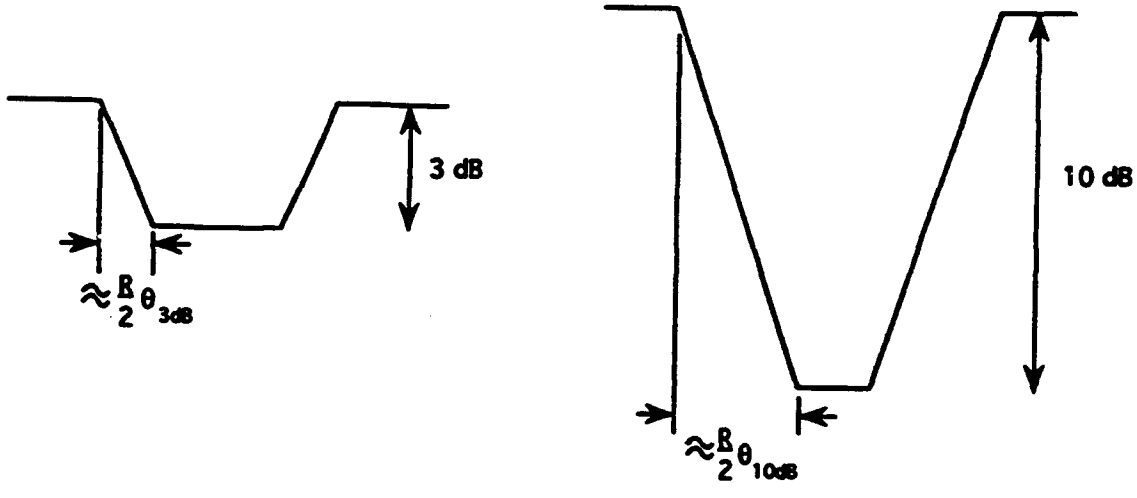

c). Measured sharpness for low and high contrast cases

Figure 6.1-39. Illustration of Sharpness "Penalty" For High-Contrast Scenes

Large SVR values indicate that the desired signal is much larger than the background variations so that signal detection and identification are relatively simple provided the signal exceeds some subjective detection threshold.

On the other hand, an SVR near unity, or even lower, indicates that the signal to be detected is "buried in" the inherent radar signal variations associated with nominally homogeneous regions in the scene. In this case, runway detection becomes a process of extracting the desired signal from the inherent variability within the scene, probably based on some type of temporal averaging. As a corollary, the pilot must be careful not to mistakenly identify a "transition-like" artifact due to the scene variability as the runway edge. Thus, measured SVR should indicate which type of runway detection environment the pilot must function within.

6.1.2.3.1 Flight Tests

Measurements of SVR from the flight test data revealed a general, consistent range dependency for clear weather, fog, and snow. Figures 6.1-40 through 6.1-42 plot measured SVR from data acquired during the first sortie in fog at Arcata on 8/28/92. As before, data are broken out according the integrated LWC of the fog for each snapshot.

The general trend with range as evidenced in these plots is representative of that seen for SVR analyses performed on other selected flight test data. This general trend takes the form of a roughly exponential decay in SVR values with increasing range. Values typically range between 2 and 15, with an occasional larger SVR value being encountered. In rough terms, the measured SVR tends to be greater than 5 for ranges less than about 1000 to 1500 km, and tends to vary fairly randomly between 2 and 8 at greater ranges.

Figure 6.1-43 plots measured SVR for all the snow approaches made on 11/20 and 11/21 to Pueblo and Colorado Springs combined. A dashed line corresponding to SVR = 2 is included for reference. Even for these relatively poorer images, the SVR follows the same general trend as seen for the fog case, except that perhaps fewer large amplitude SVR values at the closer ranges appear present. Nonetheless, there is no clear distinction to be made for the SVR data plotted in Figure VI.A-42 (a good image), for example, and that plotted in Figure 6.1-43 (a poor image). Note in Figure 6.1-43 that only three SVR measurements fell below 2.

The general trend seen in the SVR data can be accounted for by examining separately the signal level and variability parameters used in computing SVR. Figure 6.1-44 plots the signal

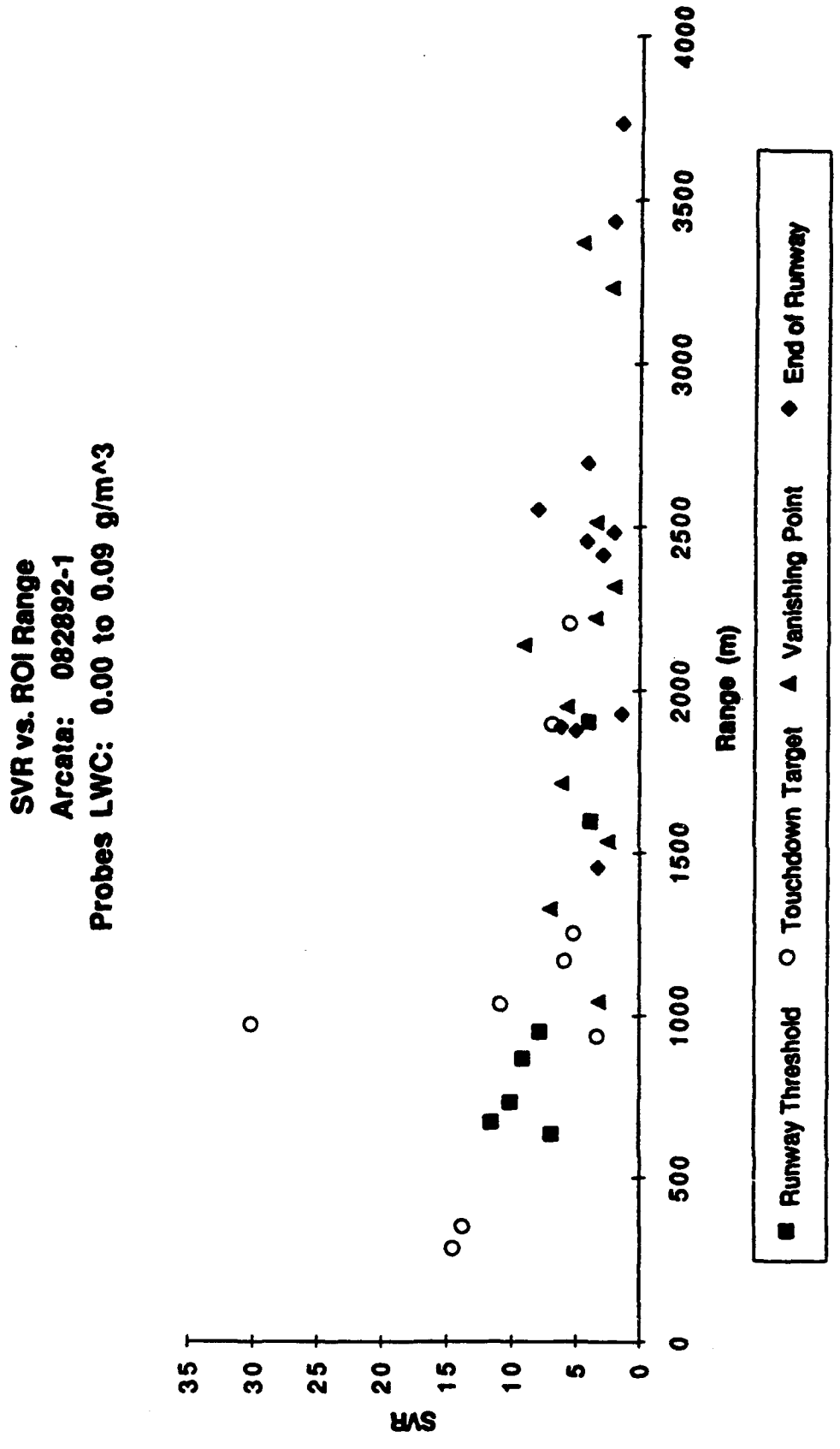

Figure 6.1-40. Plot of Signal-To-Variability Ratio Versus Range to Region of Interest for Fog Runs at Arcata, CA on August 28, 1992. Data are Taken From Snapshots With An Integrated LWC of 0.00 to 0.09 g/m^3

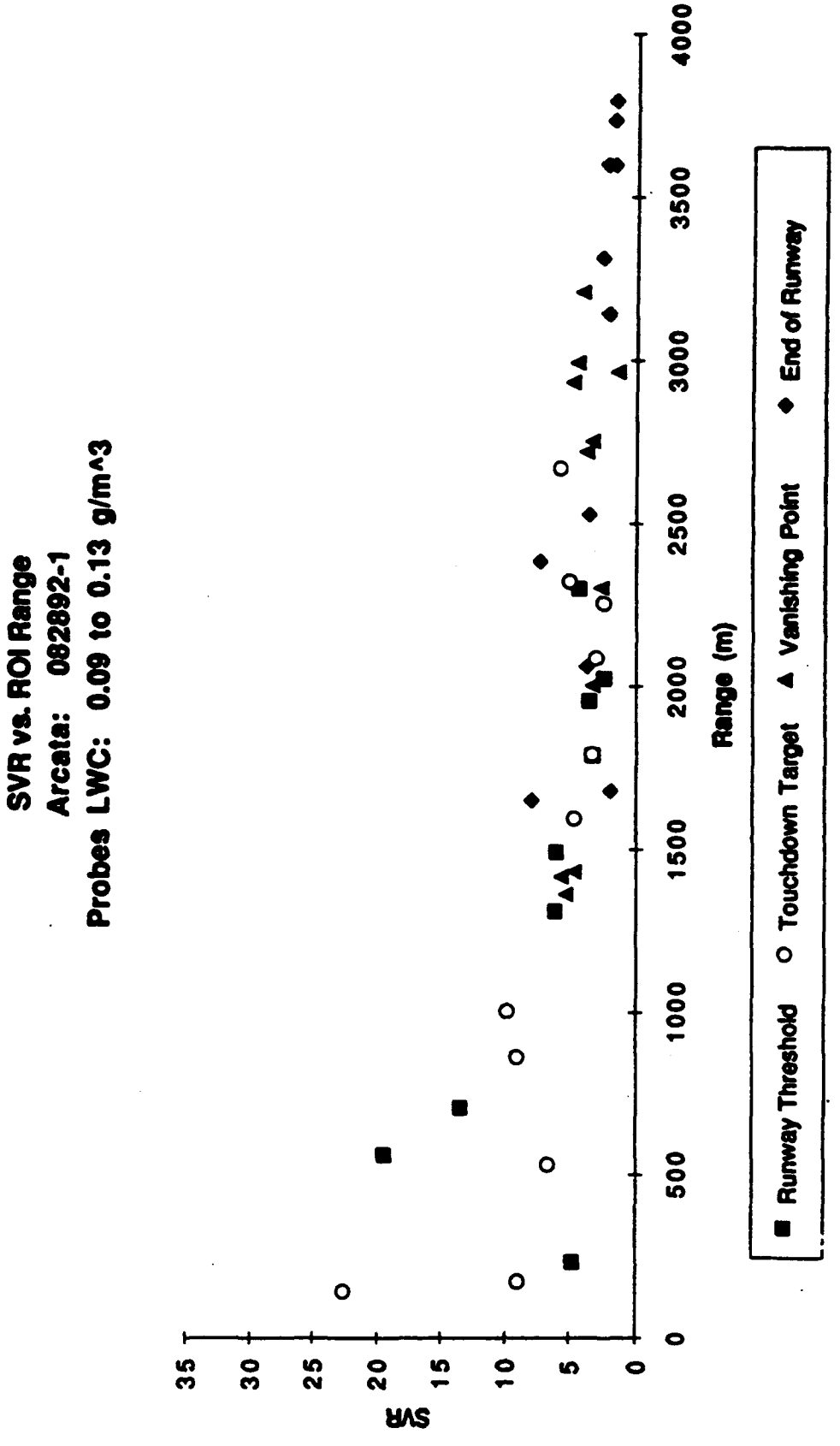

Figure 6.1-41. Plot of Signal-To-Variability Ratio Versus Range to Region of Interest for Fog Runs at Arcata, CA on August 28, 1992. Data are Taken From Snapshots With An Integrated LWC of 0.09 to 0.13g/m^3

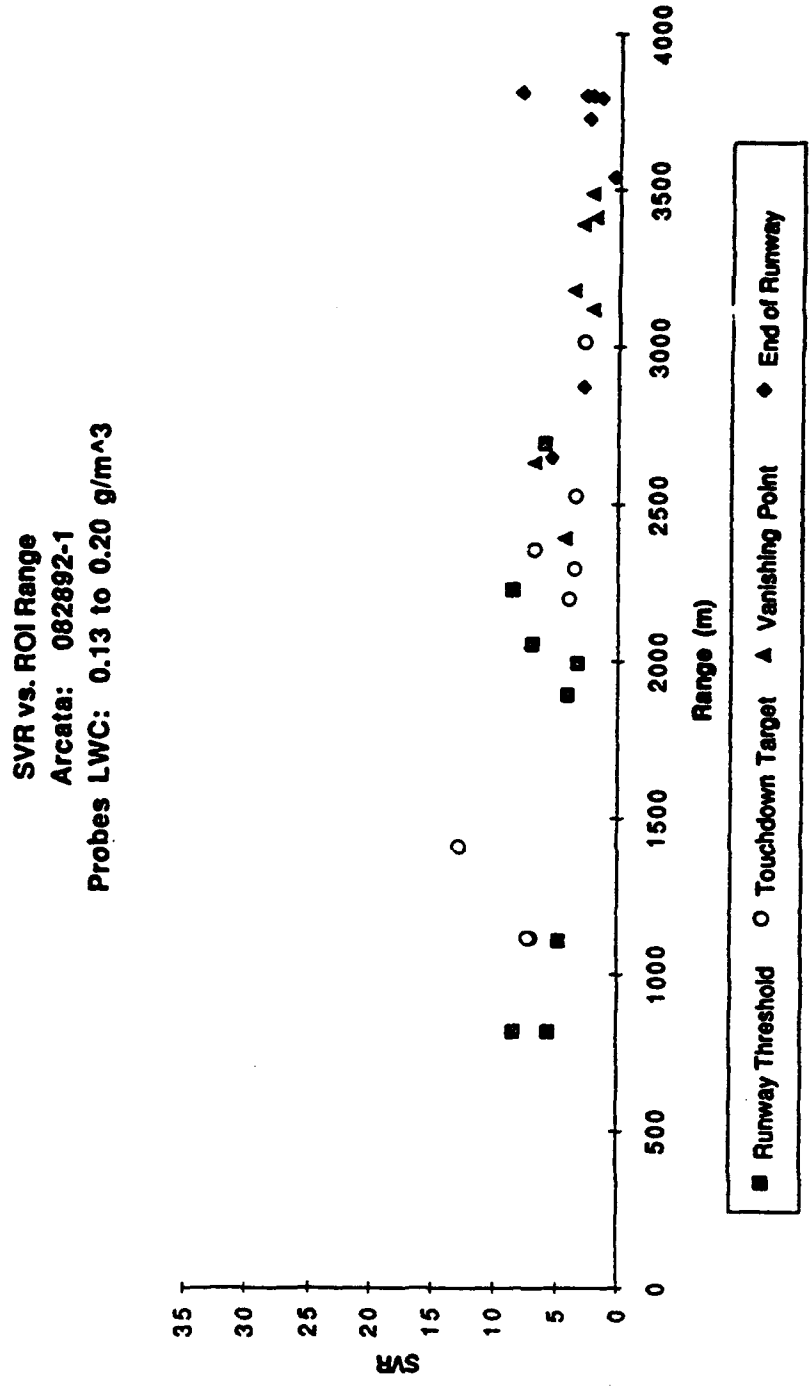

Figure 6.1-42. Plot of Signal-To-Variability Ratio Versus Range to Region of Interest for Fog Runs at Arcata, CA on August 28, 1992.

Data are Taken From Snapshots With An Integrated LWC of 0.13 to 0.20 g/m^3

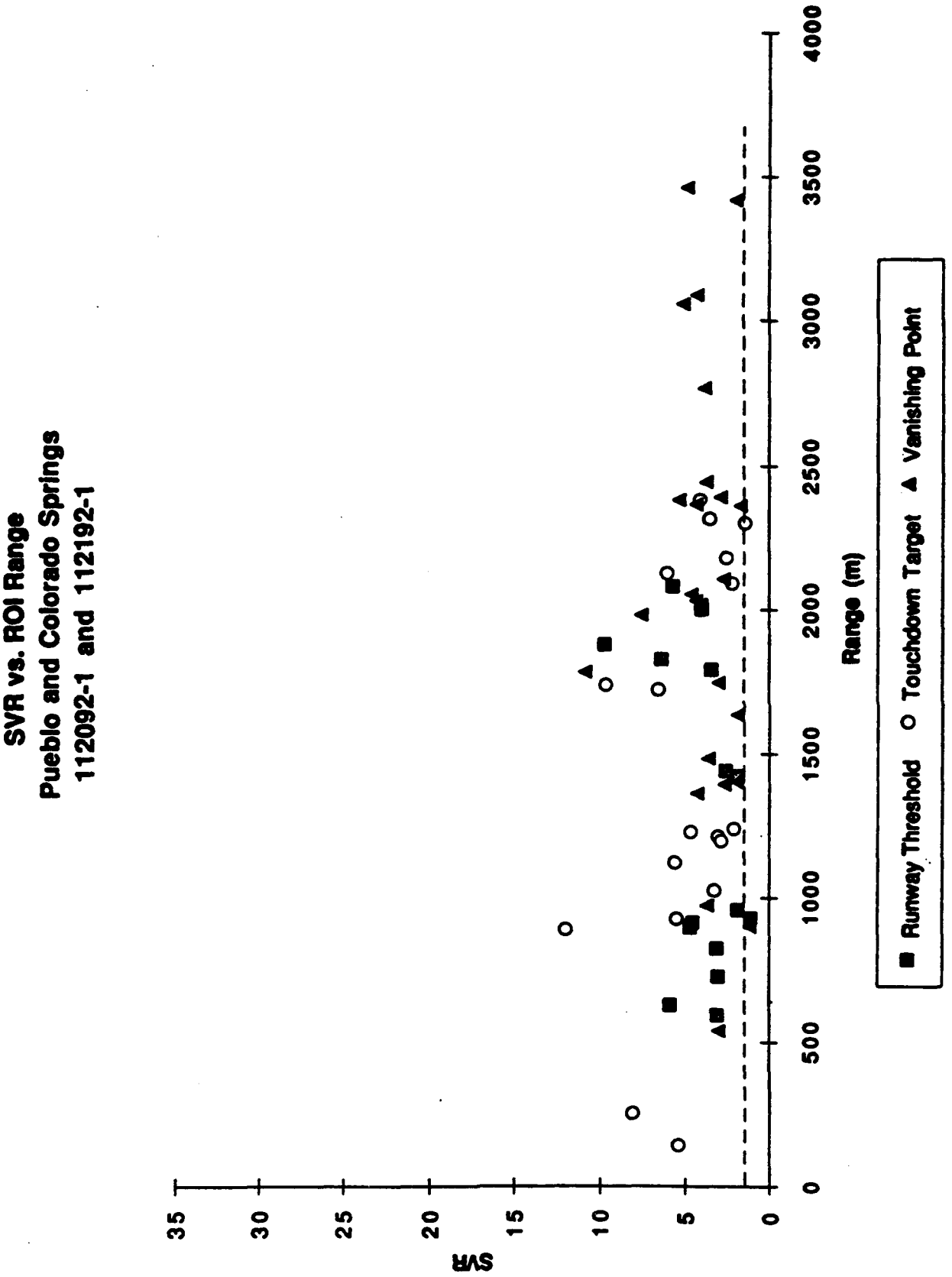

Figure 6.1-43. Plot of Signal-To-Variability Ratio Versus Range to Region of Interest for Snow Runs at Pueblo, CO and Colorado Springs, CO on August 20,21, 1992.

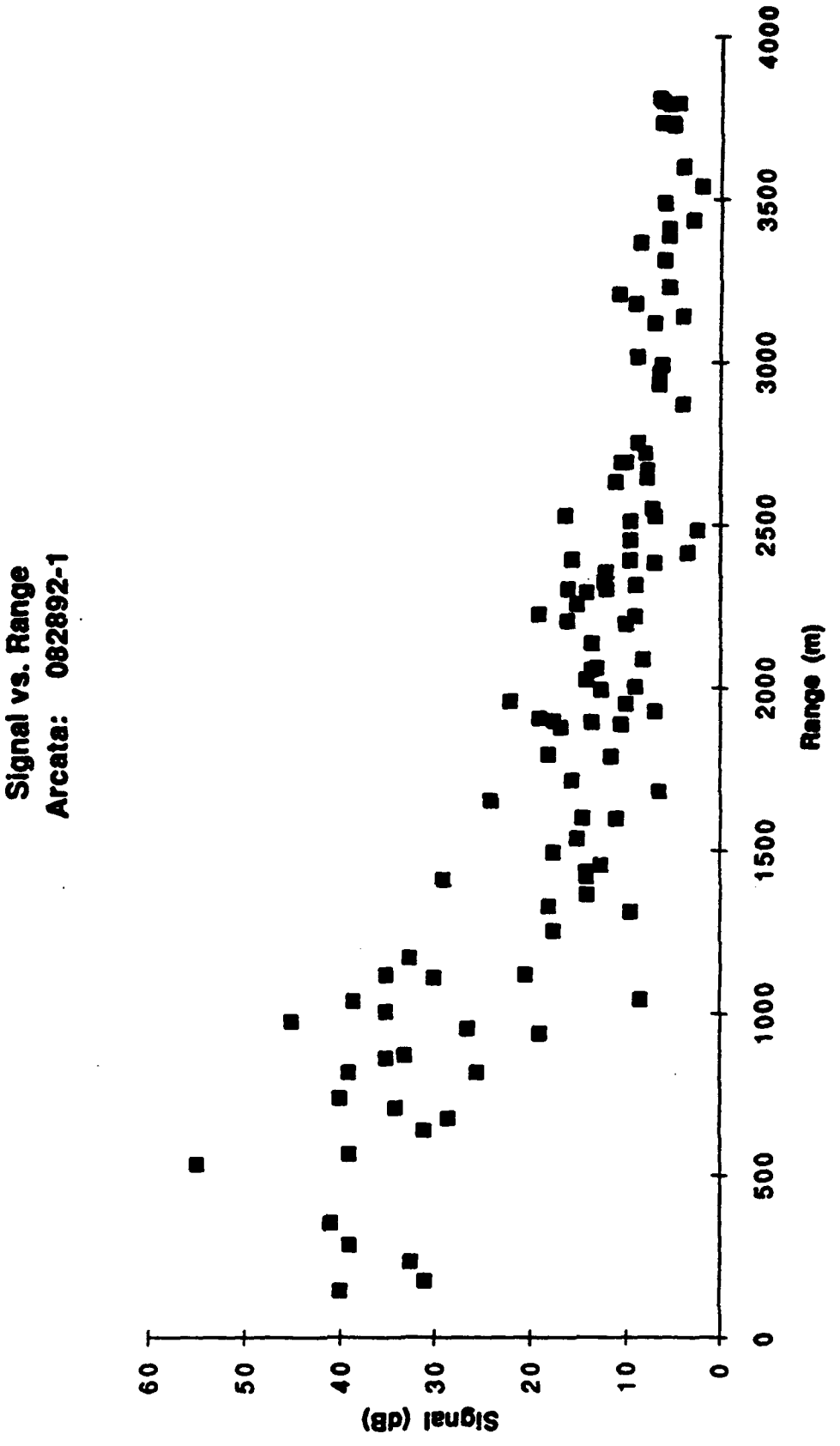

Figure 6.1-44. Plot of Signal Versus Range to Region of Interest for all Fog Runs at Arcata, CA on August 28, 1992

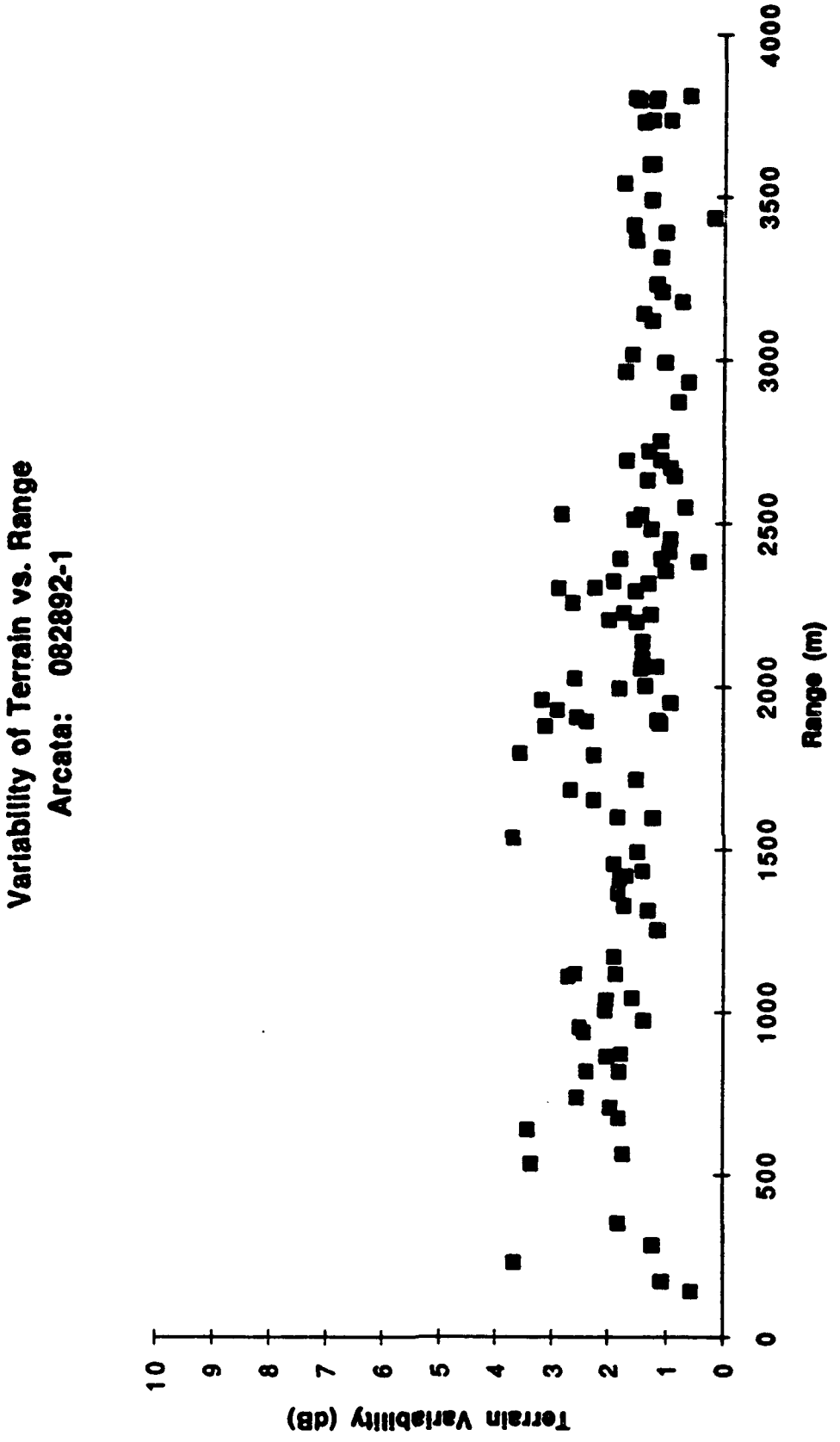

Figure 6.1-45. Plot of Terrain Variability Versus Range to Region of Interest for all Fog Runs at Arcata, CA on August 28, 1992

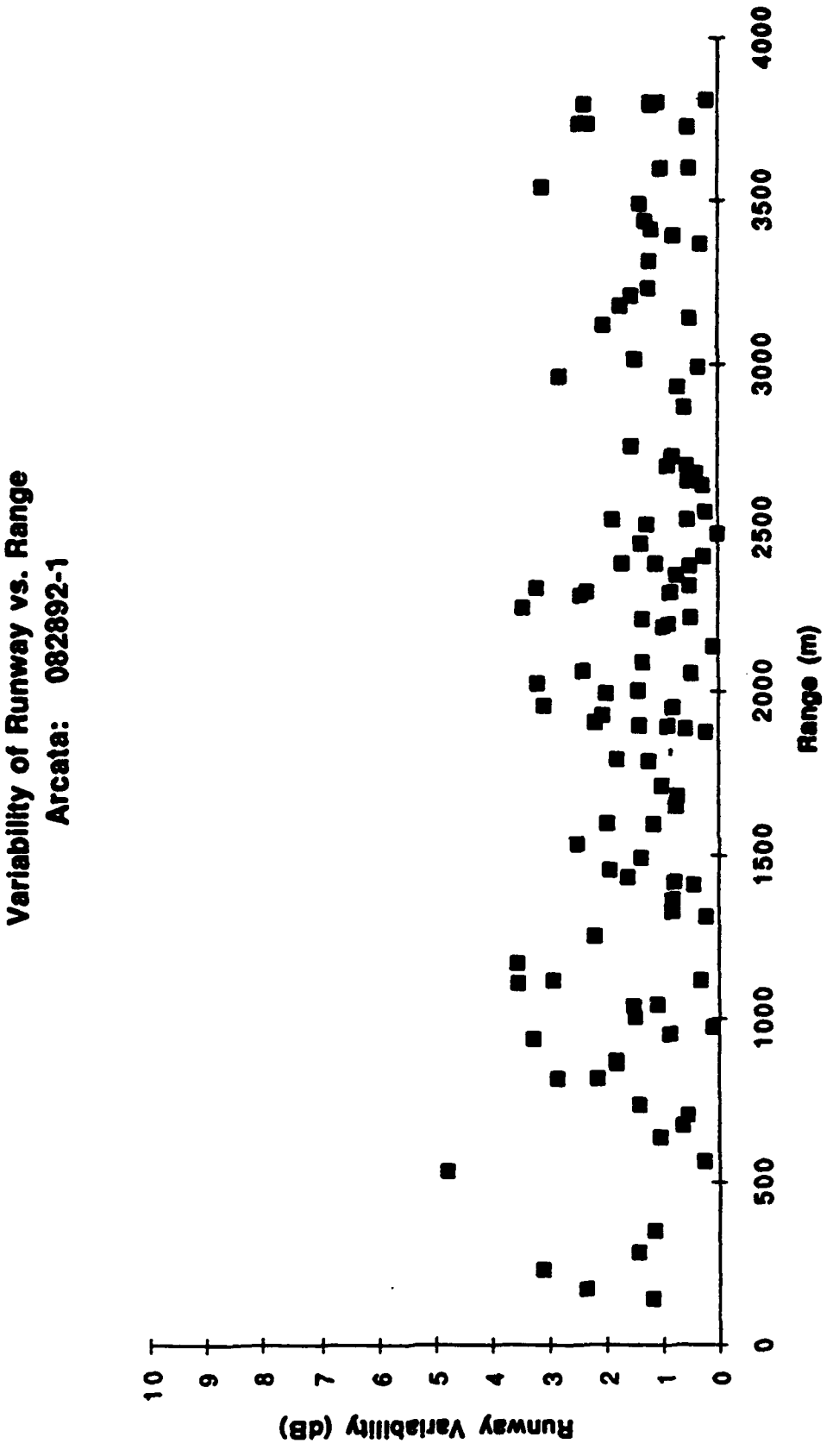

Figure 6.1-46. Plot of Runway Variability Versus Range to Region of Interest For All Fog Runs at Arcata, CA on August 28, 1992

component of the SVR metric for all data from Arcata on 8/28. Figures 6.1-45 and 6.1-46 plot the variability components of the SVR metric, with the terrain variability shown in the former, and the runway variability in the latter. Note that a different scale was used in Figure 6.1-44 (0 to 60 dB) than was used in Figures 6.1-45 and 6.1-46 (0 to 10 dB).

As can be seen from these figures, the measured variability appears fairly random when plotted versus range. There is perhaps a slight trend toward decreasing variability with increasing range, but in general, the data vary between 0 and 4 dB, virtually independent of range. There is also little distinction between the terrain and runway variabilities.

The measured signal levels, on the other hand, do display a clear trend with range. The roughly exponential decrease in the measured signal (expressed in dB) with increasing range gives the SVR plot this same general shape, since the variability's vary approximately randomly. Also note the magnitudes of the measured signal levels plotted in Figure 6.1-44. They vary from about 40 dB at the closest ranges down to about 15 dB at 1500 meters range. Beyond about 1500 meters, the signal varies between about 20 and roughly 4 dB. Thus, even at maximum range, the signal (minimum of about 4dB) is still typically larger than the variability (maximum of about 4 dB).

The SVR data from the flight tests indicate that the SVR rarely drops as low as 1, and typically is 2 or more. An SVR of 2 or more indicates that the signal the pilot is trying to detect in the image is at least twice as large as the inherent signal variations in the scene, when measured on a dB scale. This implies that the terrain-runway transition will typically be at least twice as bright on the HUD display as the typical background variations, provided it is assumed the HUD linearly maps received power levels in dB to its display gray scale.

This indicates that for synthetic vision applications of this MMW radar, the level of the radar return from the runway-terrain interface determines runway detection performance. Variations present in the radar return from nominally homogeneous clutter regions should not confuse the pilot or cause him to falsely identify a "noise" artifact as a runway boundary. In other words, the pilot should be able to detect the runway boundary the moment the contrast level is sufficient for him to discern it from the terrain. No significant "integration" time should be needed for him to extract the boundary return, once large enough to detect, from background radar variations. This is consistent with the pilot commentary discussed in Section 5.1.1.

The statements in the paragraph above are graphically illustrated in Figure 6.1-47. The left side of this figure shows the hypothetical gutter plot and PPI display that might be encountered for

a low SVR image. The corresponding plot and display for a relatively high SVR image are shown to the right. The large "spikes" in the low-SVR gutter plot are due to large variabilities. No matter where a runway detection threshold is set in the low SVR case, the return from some portions of the actual terrain would fall below it and would therefore appear to be associated with pavement. Likewise, the radar return from some portions of the pavement would be large enough to confuse these areas with terrain. In the corresponding PPI display, the runway boundary signal would be present but it would be embedded within the "noisy" background. This PPI display might have to be watched for some time before sufficient confidence could be gained to declare runway detection.

No such problem exists in the high-SVR case. A threshold can be drawn which consistently separates the runway returns from those of the terrain. The runway detection process based on the PPI display then becomes straightforward provided the signal to be extracted is sufficiently large. The flight test data indicate that this high-SVR scenario is consistent with the synthetic vision process using the Honeywell 35 GHz radar. This hypothesis is supported by the fact that the test pilots never mistakenly declared a runway detection when no runway was in fact present. Such "false alarms" are expected to be very rare in the high-SVR case, but potentially more of a problem in the low-SVR scenario.

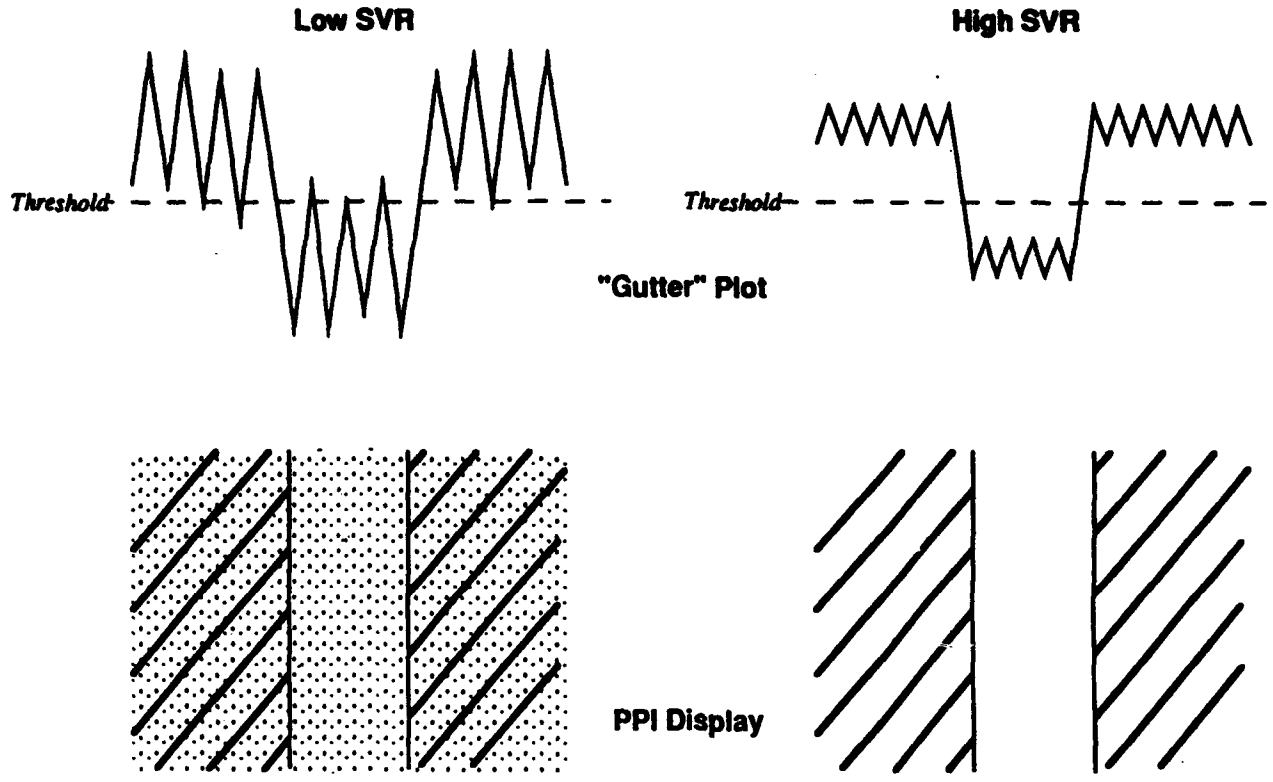

Figure 6.1-47. Conceptual Illustration of Gutter Plot and PPI Display for Low and High SVR Scenarios

6.1.2.3.2 Tower Tests

During the tower tests, SVR was measured for selected runs in clear weather, fog, snow, and rain. The SVR measurement technique was slightly different than that used for the flight test data and was based on a B-scope presentation of the data. In the tower tests, the radar returns from two-dimensional "patches" of terrain and "patches" of runway were isolated at various ranges. The mean and standard deviation were then computed for each of these patches. The SVR was computed for a given range by computing the difference between corresponding patch means, and then dividing this difference by the average of the measured standard deviations for the two patches. The technique used for the flight test data, as explained in Section 4.4.2.3.2.2, was based on gutter plots. Although different techniques were used for the two data sets, the results are comparable.

Figure 6.1-48 plots SVR values calculated from the tower data in clear weather, fog, and snow at ranges between 1500 and 3000 meters. The general trend, as observed in the flight test

data, is that at these ranges, the majority of the SVR values fall between 2 and 8. The tower data do appear to exhibit more spread than the flight test data, with several values larger than 8 and smaller than 2 reported. There is also perhaps a trend toward lower SVR values in the case of snow for the tower data, compared to clear weather or fog, but this trend is not dominant. A similar possible tendency was noted above for the flight test data. Since tower test SVR values are not available for ranges significantly less than 1500 meters, the general exponential shape of the SVR curve, observed in the flight test data, cannot be confirmed based on these data.

The SVR values calculated for rain events at the tower are clearly lower than those computed for clear weather, fog, or snow. These rain data are of special interest since there are no rain data from the flight tests. Figure 6.1-49 is a plot of SVR values for three different rain rates. The SVR values are lower than in Figure 6.1-48, with over half the measured rain SVR values falling below 2. The lowest SVR values typically correspond to the 12.9 mm/hr rain, for which the 35 GHz Honeywell radar produced poor contrast. In this case, an appreciable-amplitude "signal" would not be expected in the image at all so that the relative effects of the speckle noise are quite noticeable. If the 12.9 mm/hr data are deleted from Figure 6.1-49, then all but two of the remaining data points are above 1 (signal = variability), and roughly half are above 2 (signal = twice variability).

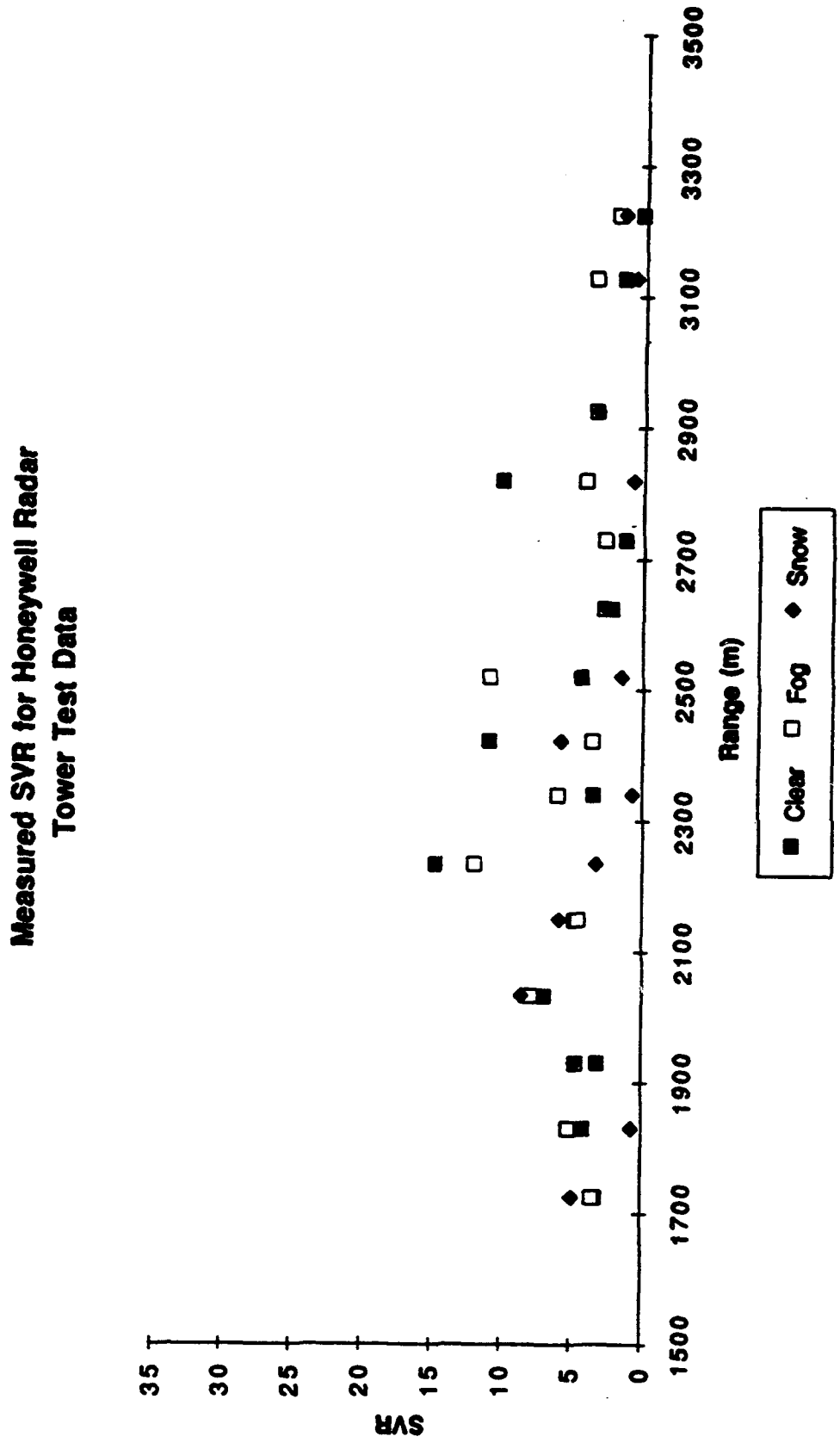

Figure 6.1-48. Plot of Signal-To-Variability Ratio Versus Range for Honeywell Tower Test Data in Clear Weather, Fog, and Snow

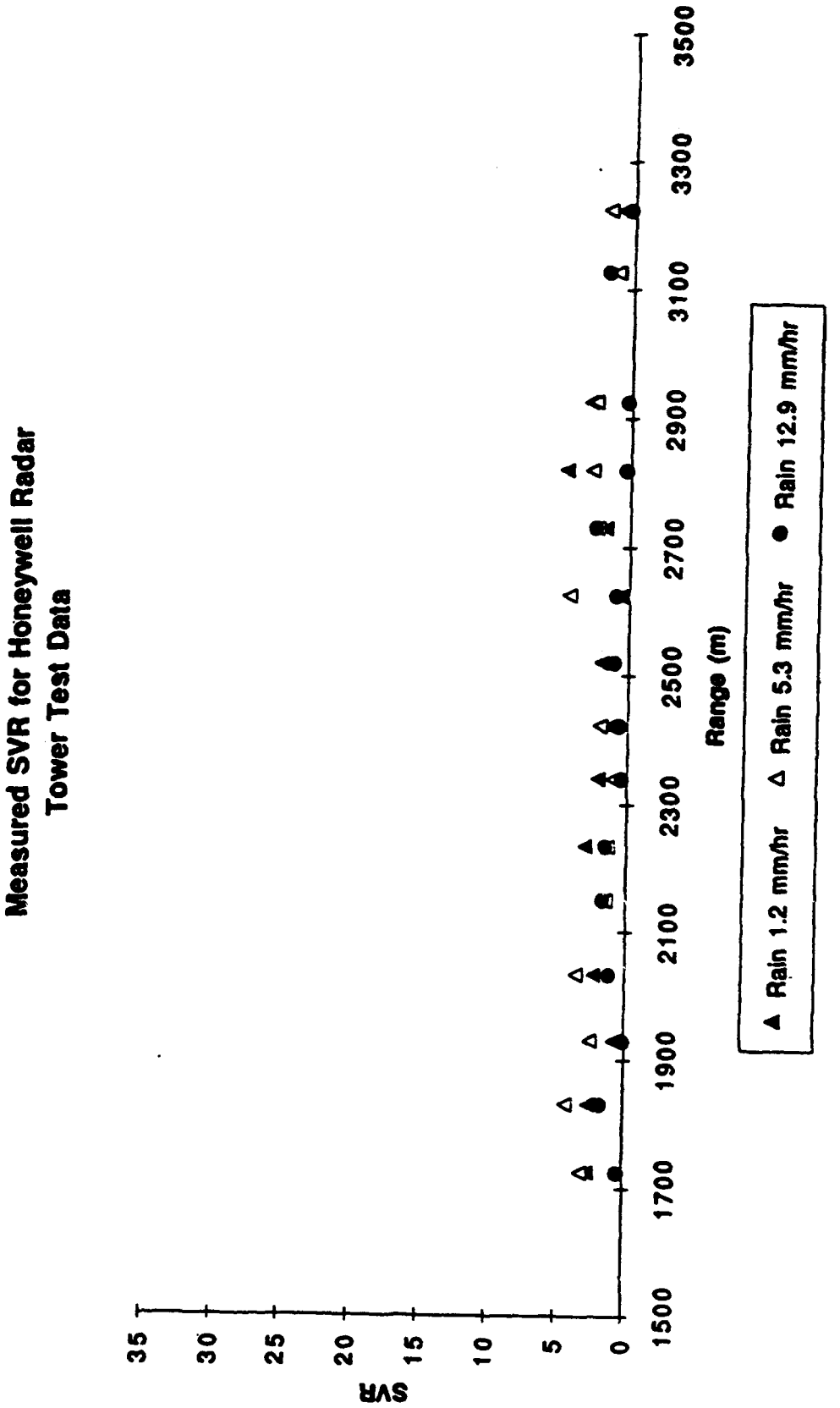

Figure 6.1-49. Plot of Signal-To-Variability Ratio Versus Range for Honeywell Tower Test Data for Rain Rates of 1.2, 5.3, and 12.9 mm/hr

6.1.2.3.3 Summary

Measured signal-to-variability ratios exhibited a roughly exponential decay with increasing range. Values measured in clear weather, fog, or snow typically range between 2 and 15, with an occasional larger or smaller SVR value being encountered. In rough terms, the measured SVR tends to be greater than 5 for ranges less than about 1 to 1.5 km, and tends to vary fairly randomly between 2 and 8 at greater ranges. Measured data from the tower in clear weather, fog, or snow deviated a little from this general trend in that they exhibited greater spread at the ranges greater than 1500 meters examined. SVR values greater than 8 and less than 2 were reported about 40 % of the time in the tower data.

The SVR values measured in rain from the tower data tended to be significantly lower than those measured for clear weather, fog, or snow conditions. If the SVR values corresponding to the heaviest rain (12.9 mm/hr) for which the radar could not produce a good image of the runway are neglected, about half the remaining SVR values fall between 1 and 2, and half are above 2.

Examining the two components of the SVR metric separately provides insight into the trends seen in the overall metric. The measured variability's in clear, fog, and snow from the flight tests appear fairly random when plotted versus range, and, in general, vary between 0 and 4 dB, virtually independent of range. There is also little distinction between the terrain and runway variability's. The corresponding signal levels vary from about 40 dB at the closest ranges down to about 15 dB at 1500 meters range. Beyond about 1500 meters, the signal varies between about 20 and roughly 4 dB. Thus, even at maximum range, the signal (minimum of about 4dB) is still typically larger than the variability (maximum of about 4 dB).

The lower SVR values observed for rain are assumed to be due to the absence of a strong runway-terrain interface return (the "signal") rather than the presence of excess variability. The SVR data generally support the hypothesis that the level of the radar return from the runway-terrain interface determines runway detection performance, at least for clear weather, fog, and snow. Variations present in the radar return from nominally homogeneous clutter regions should not confuse the pilot or cause him to falsely identify a "noise" artifact as a runway boundary. This high-SVR scenario is conducive to reliable runway detection within the image. Scene variabilitys severe enough to cause false detections of a runway which is in fact not present were not observed. Of course, when insufficient "signal" (pavement-terrain interface return) is present, such as for heavy rain events, the runway will not be detected. But this lack of detection should be due to lack of signal rather than excessive variability.

The relative dominance of the signal component in the SVR metric reinforces the importance of the contrast metric. As noted previously, contrast is a good indicator of runway detection performance. The observations above regarding SVR support this. If the "signal" is large, which implies the contrast is high, then detection performance should be good. If the signal is weak (poor contrast), then detecting the runway will be very difficult if not impossible. The variability component of the SVR metric is really a secondary factor when viewed from this perspective.

6.1.2.4 Other Potential Image Quality Metrics

The analyses described above indicate that of the three image quality metrics, contrast is the most important in predicting when the runway can be recognized in the image. The sharpness metric was difficult to accurately quantify based on the measurement technique employed. Measured sharpness values were typically about 1 to 5 pixels but varied in an apparently random fashion within this range as a function of distance to region of interest. There were also no clear trends in measured sharpness as a function of weather conditions.

Signal-to-variability results were somewhat more consistent. For slant ranges of about 1500 meters or less, the measured SVR values for clear weather, fog, and snow were typically greater than five. For slant ranges greater than 1500 meters or so, the SVR typically fell in the range of 2 to 8. A SVR of 5 indicates that the signal the pilot is trying to detect (namely, the transition between the runway pavement and the surrounding terrain) is five times larger than the background variability from which this signal must be extracted.

This ratio is computed based on the logarithm of the signal and that of the variability since the brightness levels presented to the pilot via the HUD are roughly proportional to the logarithms of the corresponding received power levels. The SVR values measured indicate that in general for clear weather, fog, and snow, the signal to be detected is significantly larger than the background variability in the scene. These relatively large SVR values lend insight into the runway detection process that faces a human. Namely, this process is best viewed as acquiring a signal (runway-terrain transition) which has grown large enough to cross some detection threshold, rather than as a process whereby the signal (transition) must be extracted over time from a highly variable background which tends to mask the desired signal.

In this view, detection of the runway is largely determined by the absolute signal itself, rather than the signal compared to the background variability. And the most direct measurement of this

signal alone is contrast. Thus, the relatively large signal-to-variability ratios tend to reinforce the importance of contrast in runway detection.

In addition to this indirect evidence, there is also considerable direct evidence supporting the importance of contrast. Throughout the flight test program, contrast was found to correlate well with the subjective image quality perceived by the pilot as well as by the radar analyst. In general, the measured contrast fell between -0.6 and -0.8 when initial detection of the runway was reported by the pilot in clear weather. Thus, the contrast at pilot detection was fairly consistent.

The contrast at the radar vanishing point selected by the raw data analyst typically fell between -0.4 and -0.8. The tolerance of lower contrast values by the analyst is consistent with the work loads the pilot must deal with in flying the aircraft and also detecting the runway, as well as with the fact that the pilot must be "comfortable" with the image before declaring a detection. The analyst, on the other hand, can concentrate exclusively on the image when looking for the runway.

However, as important as contrast appears to be in determining when the runway is detected, it is certainly not a complete descriptor of the detection process. Detection of the runway by the pilot is a very complex action in which at least a portion of the airport complex pattern (including runways, taxiways, building lines, approach lights, etc.) is *recognized* in the image. The simple image quality metrics used in this analysis effort do not fully represent this complicated pattern recognition task. The purpose of the paragraphs which follow is to briefly outline some observations regarding other "image quality" metrics which might prove useful in the synthetic vision application.

One limitation of the image quality metrics used in this effort is their essential two-dimensional nature. The gutter plots introduced in Section 4.4.1.3 above are basically a plot of radar return amplitude versus cross-range pixel count (which represents azimuth). There is no range dimension.

As pointed out in Section 4.4.1.3, seven sequential gutter plots were averaged in range to produce the composite gutter plot from which contrast, sharpness, and signal-to-variability ratio were computed. This averaging process does introduce range dependence; if the azimuthal positions of the runway-terrain transition did not line up well in each of these seven individual gutter waveforms, then the final gutter plot, based on the average of these seven, would not have a clear transition. The result, in general, would be degraded contrast, sharpness, and signal-to-variability ratio.

Nonetheless, this seven-range-cell averaging technique does not fully reflect the three-dimensional edge definition the pilot surely wishes to see before he or she can recognize the runway. Consider Figure 6.1-50, which shows a magnified portion of a PPI display from Vandenburg AFB, CA with the runway clearly evident as the dark stripe in the middle of the image. If an integrated gutter plot at any point along the runway were to be analyzed, the contrast would be good. However, the fact that one can readily detect the runway in this image is due not only to the strong signal level transition across an azimuth swath at each range, but is also due to the fact that these transitions line up vertically as one moves out in range within the image. In other words, a linear edge is present. Specifically, the runway is detected because a parallel pair of edges are present.

Another figure of merit that could be defined based on Figure 6.1-50 is the vertical straightness of the detected edges. Roughly one-third of the way up the image, the right edge (black line) shifts to the left by one pixel. Since such a one-pixel shift appears relatively minor to the eye and detracts very little from the overall observation that this line represents the edge of the runway, the "edge straightness" metric for this particular image would be very good. However, many such breaks in the edge lines, positioned randomly, would create uncertainty in declaring this the pavement edge. The proposed straightness metric would quantify this effect.

When performing analyses based on PPI data displays, edge-based figures of merit appear very attractive. One key reason for this is the fact that the runway edges appear as parallel vertical lines in the PPI image. However, this is not the case in the corresponding B-scope display, in which the runway edges are curved, or in the C-scope display, where the runway edges are straight but not parallel .

One of the important goals of the synthetic vision program was to use consistent image quality metrics in the tower test raw data analysis, the flight test raw radar data analysis, and the flight test RS-170 video data analysis. Such consistency allows direct comparison of reported results. However, the flight test RS-170 video data analysis naturally used the C-scope presentation format since this is the format in which the data were presented on the HUD. The tower test raw data analyses were based on B-scope presentations; the PPI format was not as attractive in this case since the runway slanted across the field of view and was therefore not viewed down the center-line.

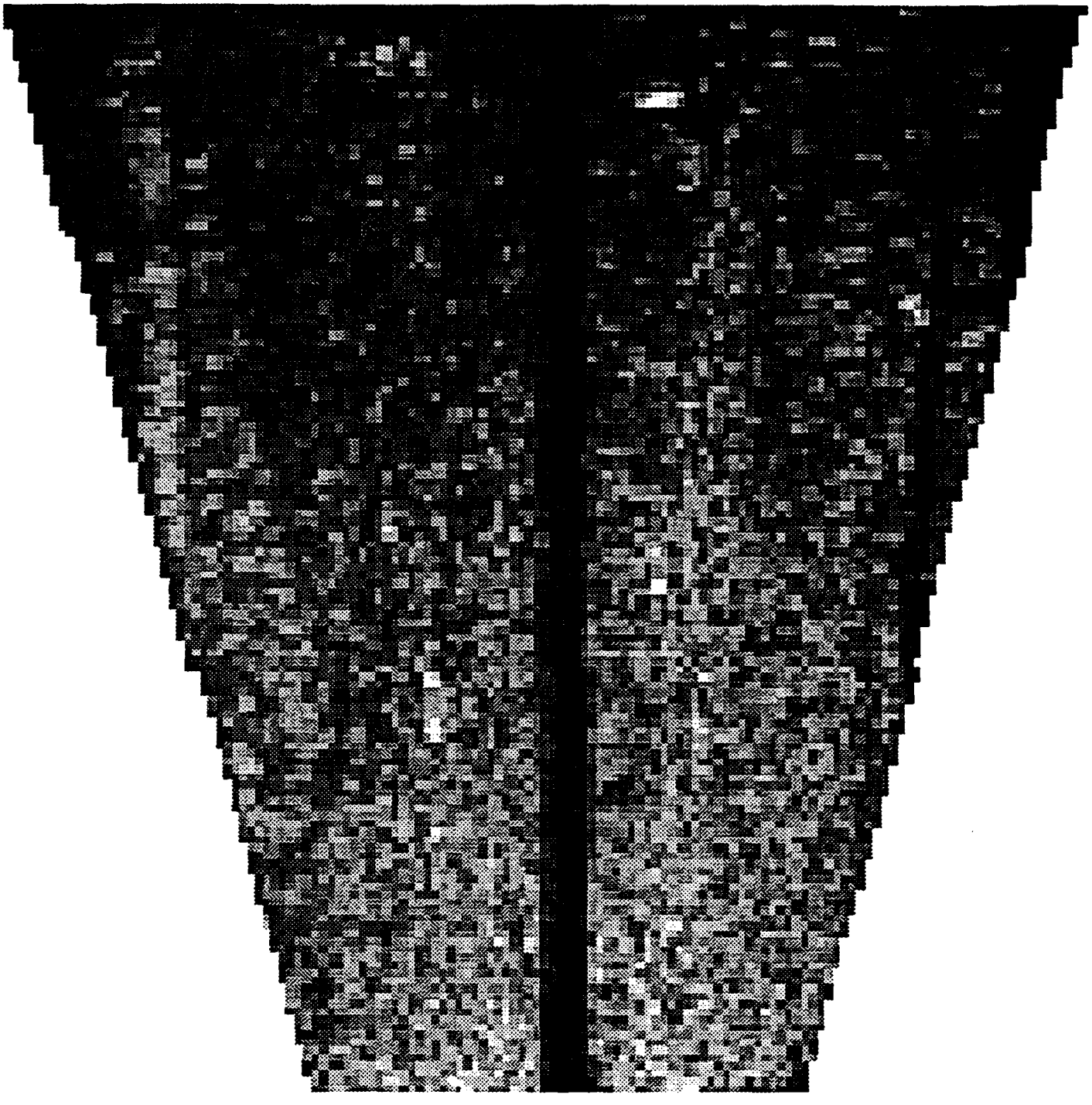

Figure 6.1-50. Magnified Portion of PPI Image from Vandenburg Air Force Base, CA

Consequently, the SVSTD program pursued simpler image quality metrics which could be conveniently applied to various data presentation formats. Thus, the definitions of contrast, sharpness, and SVR described previously were agreed upon early in the program. The transfer of the edge-based image quality analysis technique described in this section from one format to another is not straightforward and would require thought in any subsequent analysis effort.

While the edge-based image quality metrics may be more comprehensive than the simple gutter-plot-based set used for the current analyses, even they are far from comprehensive. For example, they take no account of the relationship between the runway and parallel or cross taxiways, information which the pilot uses in detecting the runway. Clearly, the issue of defining comprehensive image quality metrics for the synthetic vision application is still worthy of investigation. Hopefully, the results obtained during this program will provide valuable insight for future researchers.

SECTION 7

7. IMAGE QUALITY PERFORMANCE

During each approach, the pilot was instructed to give a verbal callout when he could confirm that the runway image had been identified. Using the time of those callouts, the image quality was examined to determine if metrics commonly used in other imaging applications correlated to the detection of airport features in the MMW raster images.

It was planned that this work would be done using a through-the-HUD video camera, permitting the analyst to use the same scene used by the pilot. When the through-the-HUD camera capability was not achieved with sufficient quality in time to support image analyses, a secondary approach using the recorded sensor video output was used. This video output does not reflect the settings of the HUD raster brightness and contrast controls, nor does it suffer degradation from the outside scene brightness . However, since the pilots used a repetitive technique in adjusting the HUD controls, it was felt that the metrics would reflect with a relatively constant difference between the measured values and those actually seen by the pilots.

The digitized image used for the analysis was made up of 480 horizontal image scan lines, each of which could have 640 pixels or dots of varying brightness along its length. Actual images from the sensors often did not incorporate all of these lines or pixels, averaging 463 image scan lines and 631 pixels per scan line. The convention for locating a point number (479) at the bottom of the image, and to count pixels as 0 on the left and increasing to a maximum of 639 at the right edge. The digitized scene covers a full 30 Hz field of the NTSC interlaced video. The field is made up of two separate 60 Hz frames which are offset by one image scan line. Since the imaging sensors produce their video data at the frame rate (1/60 second), the interlacing causes the two adjoining even/odd scan lines to have the same or very close data values. This accounts for the characteristic pairing of data points seen in the plotted contrast data for adjacent even/odd image scan lines.

CONTRAST

Based on the GTRI work with raw radar data, the contrast between the runway and the surrounding terrain appeared to have the most promise as a correlation factor. This analysis of

image quality is consistent with GTRI raw radar data analyses in the formulation of contrast. Zero implies no contrast; larger negative numbers imply increasing contrast with the runway darker than the surrounding terrain; and larger positive numbers imply increasing contrast with the runway brighter than the surrounding terrain.

The data plots used for the analysis provide the "runway to terrain" contrast for each video scan line of the image which passed through the runway. The image counts scan lines from the top to the bottom, so scan lines with smaller numbers represent the far end of the runway and scan lines with larger numbers represent the near or approach end of the runway.

Figures 7-1 through 7-3 show the typical evolution of the runway scene during the approach.

- Figure 7-1 presents the runway-to-terrain contrast at 2.5 Km from touchdown. Notice that contrast increases fairly linearly from the far end of the runway to about mid-field (scan lines 121 - 135) and then becomes a relatively constant value (about -0.75) for the near end of the runway (scan lines 136-152).
- Figure 7-2 presents the runway-to-terrain contrast for the same runway when the aircraft is approximately 200' above the airport's surface and nominally 1.2 km from the touchdown zone. The constant contrast continues to be seen, the deviations are due primarily to interference of other objects such as intersecting taxiways or reflective objects along the runway.
- Figure 7-3 again presents the runway-to-terrain contrast for the same runway, but now at a point 50' above the threshold area. The decreasing contrast as the near end of the runway is partially due to the build up of "blockiness" in the radar's near field view. The effects of intersections and/or reflecting items are even more pronounced.

Figures 7-4 through 7-28 at the end of this section present the contrast plots for 25 approaches covering much of the weather experienced by the SVSTD/SIED flight test and representative airports and terrain features.

The results are summarized in Table 7-1. Note that there are two columns for contrast: one labeled *Average* and the other *Best*, representing two ways of looking at the runway data.

- Average Contrast is the average over all of the scan lines going through the runway (i.e., all of those shown on the plot).
- Best Contrast assumes that the pilot only needs a few vertically aligned pixels to recognize the edges of the runway, and thus considers only the best contiguous scan lines (usually 4 or more) for averaging.

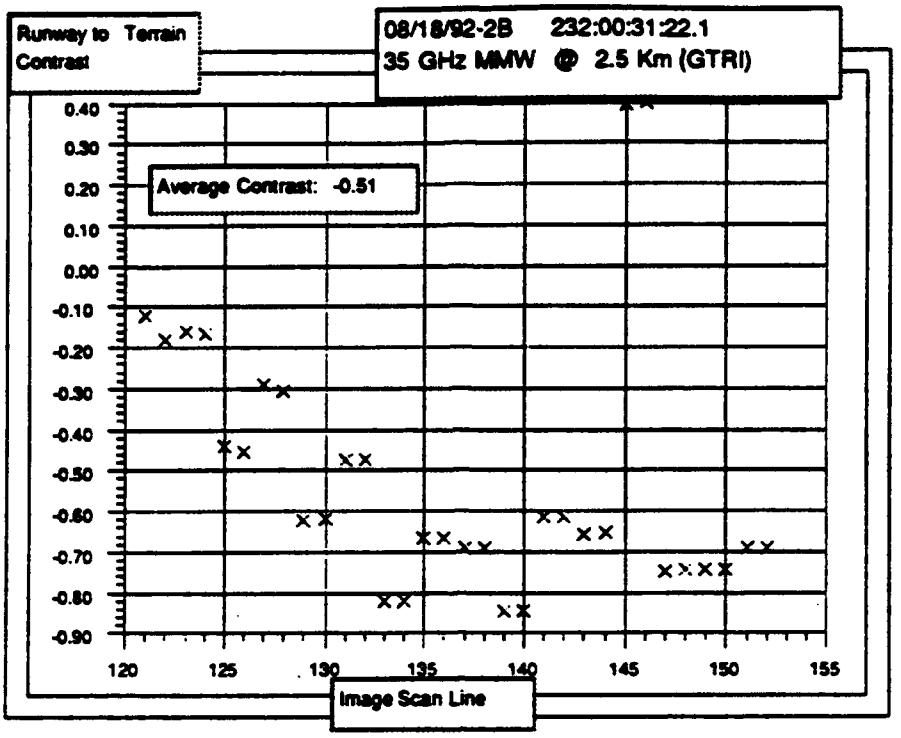

Figure 7-1. Contrast - August 18, 1992-2B (NTD at 2.5 KM)

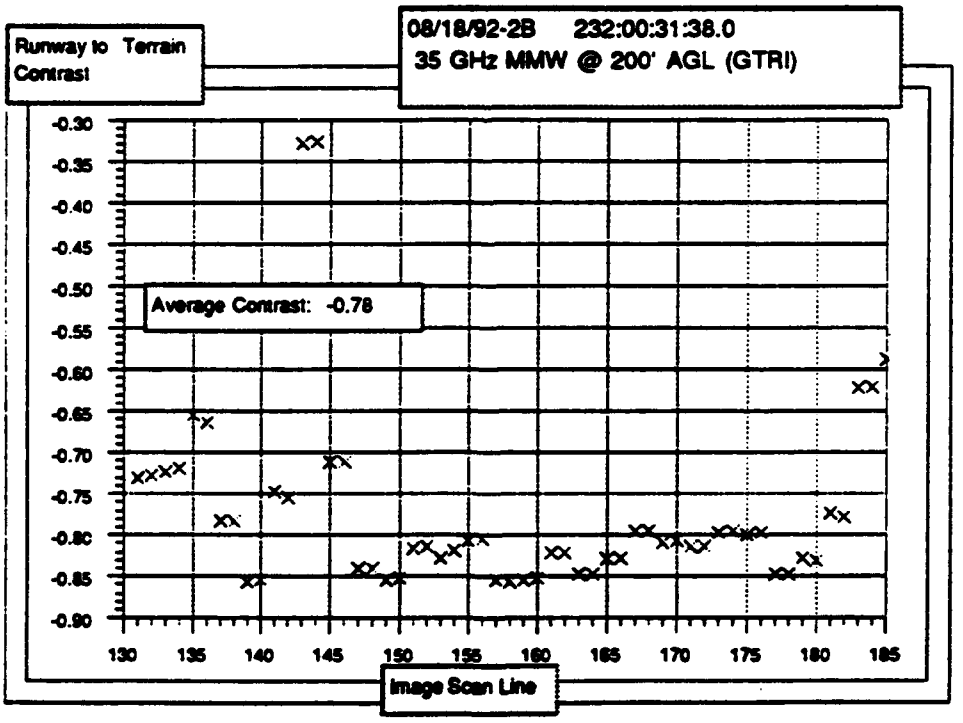

Figure 7-2. Contrast - August 18, 1992-2B (NTD at 200' AGL)

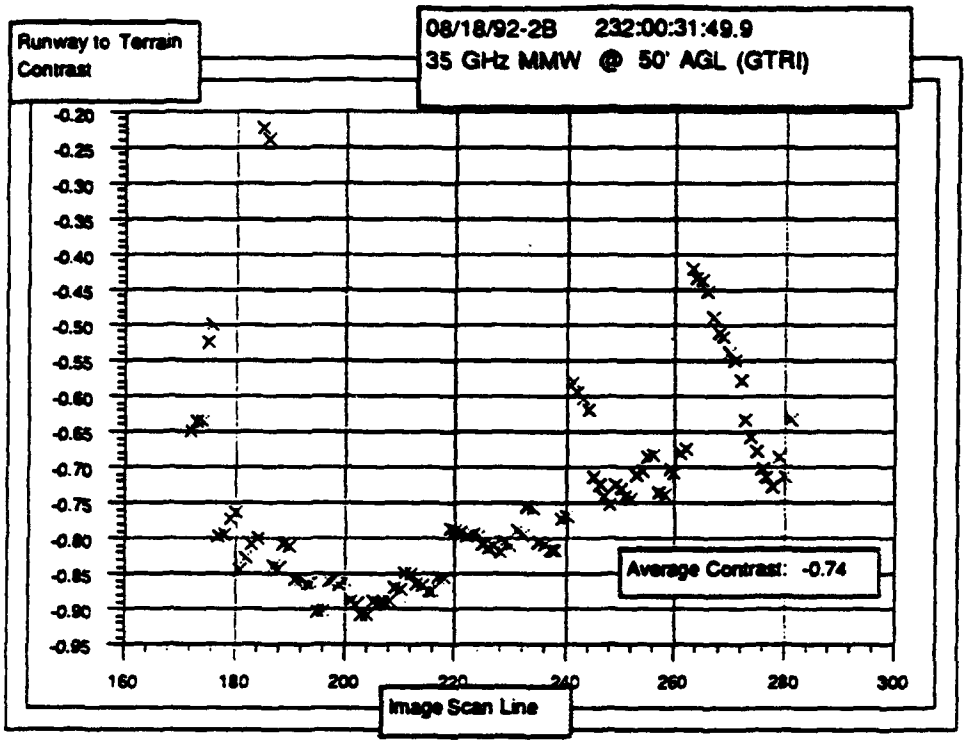

Figure 7-3. Contrast - August 18, 1992-2B (NTD at 50' AGL)

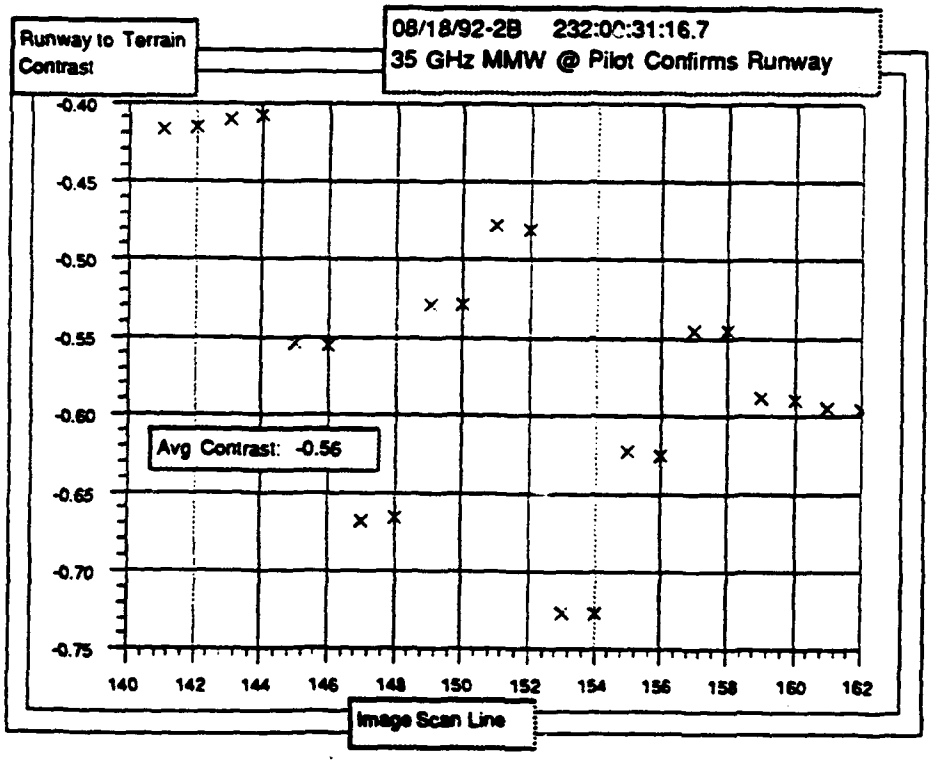

Figure 7-4. Contrast - August 18, 1992-2B (NTD at Pilot Confirms Runway)

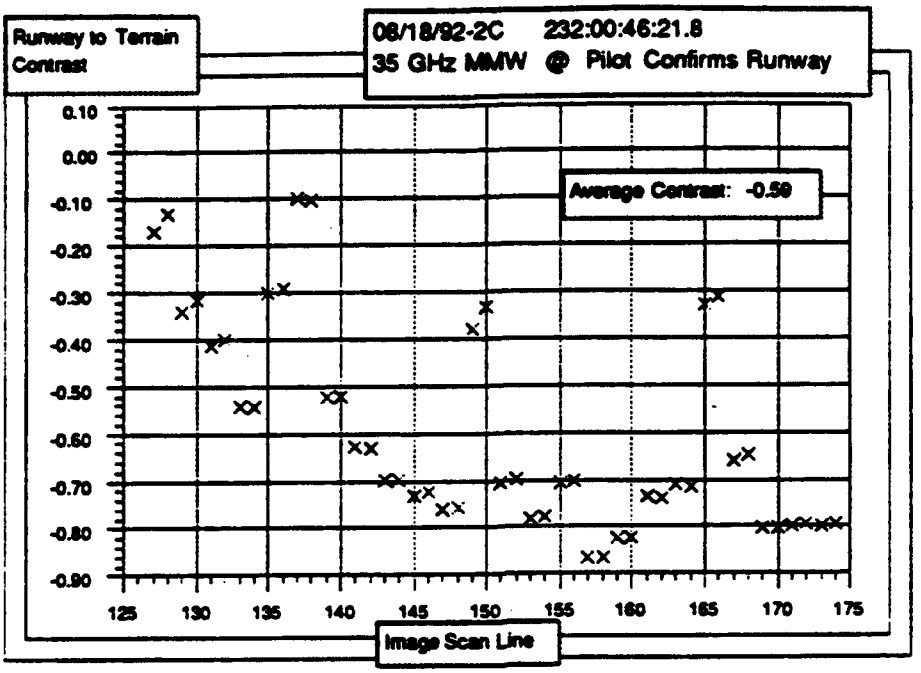

Figure 7-5. Contrast - August 18, 1992-2C (NTD at Pilot Confirms Runway)

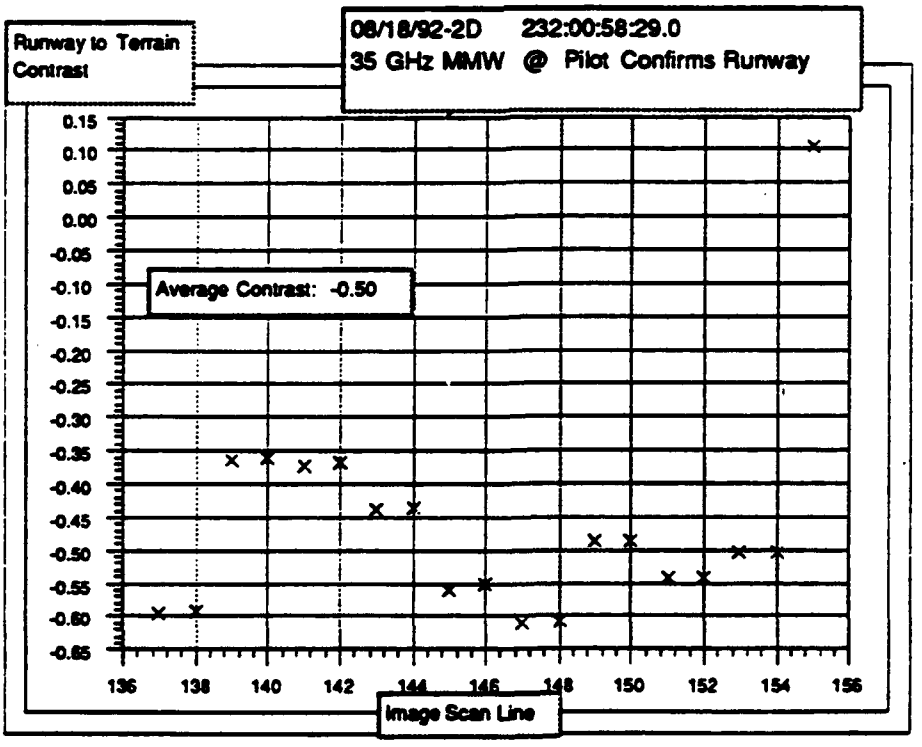

Figure 7-6. Contrast - August 18, 1992-2D (NTD at Pilot Confirms Runway)

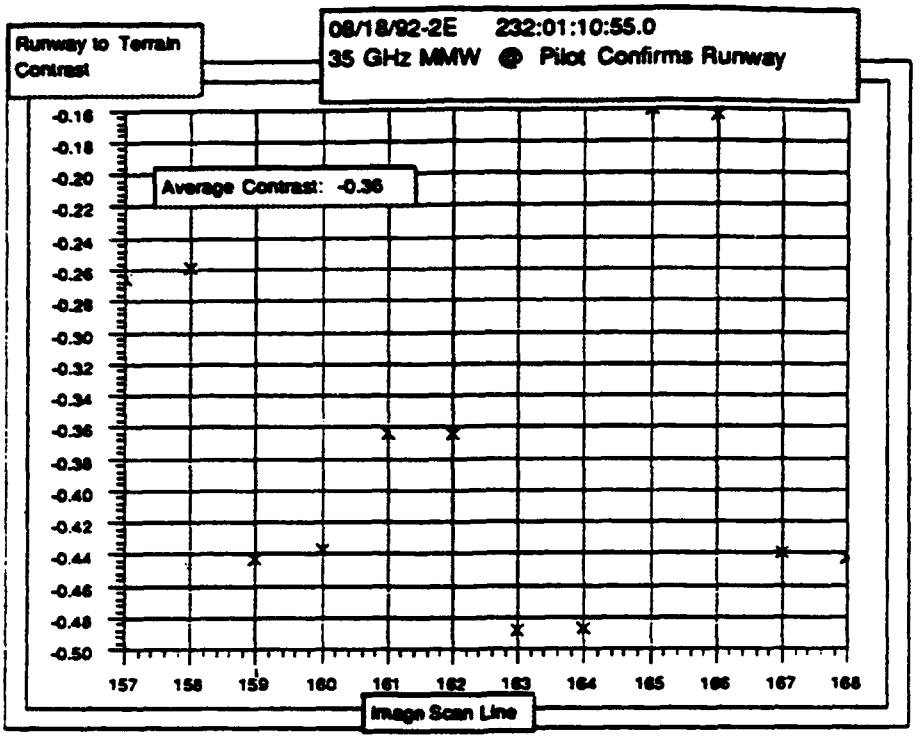

Figure 7-7. Contrast - August 18, 1992-2E (NTD at Pilot Confirms Runway)

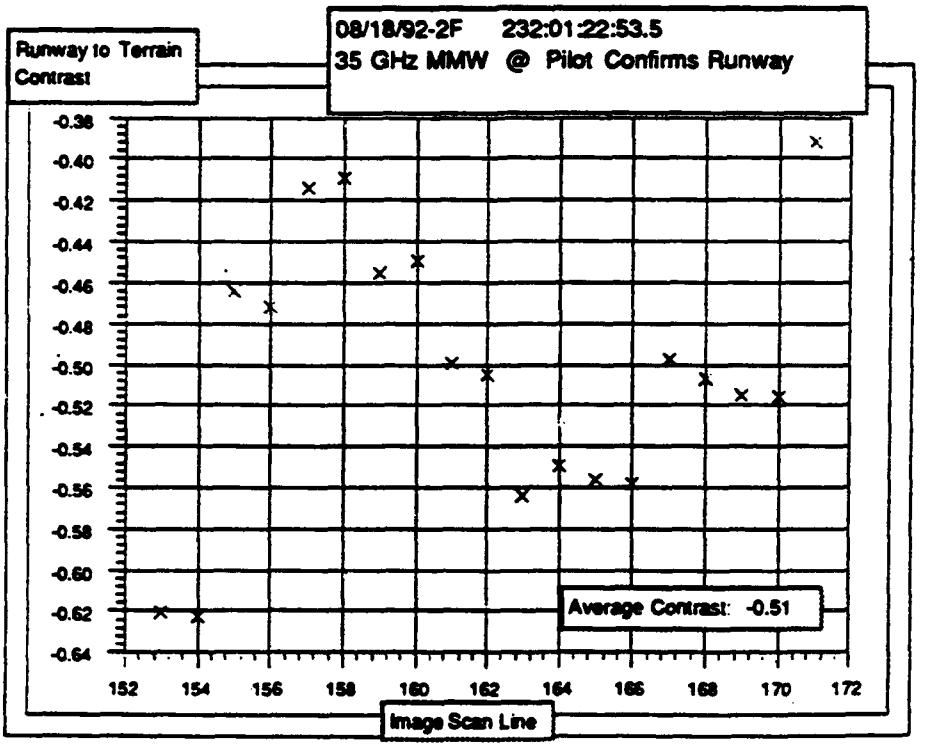

Figure 7-8. Contrast - August 18, 1992-2F (NTD at Pilot Confirms Runway)

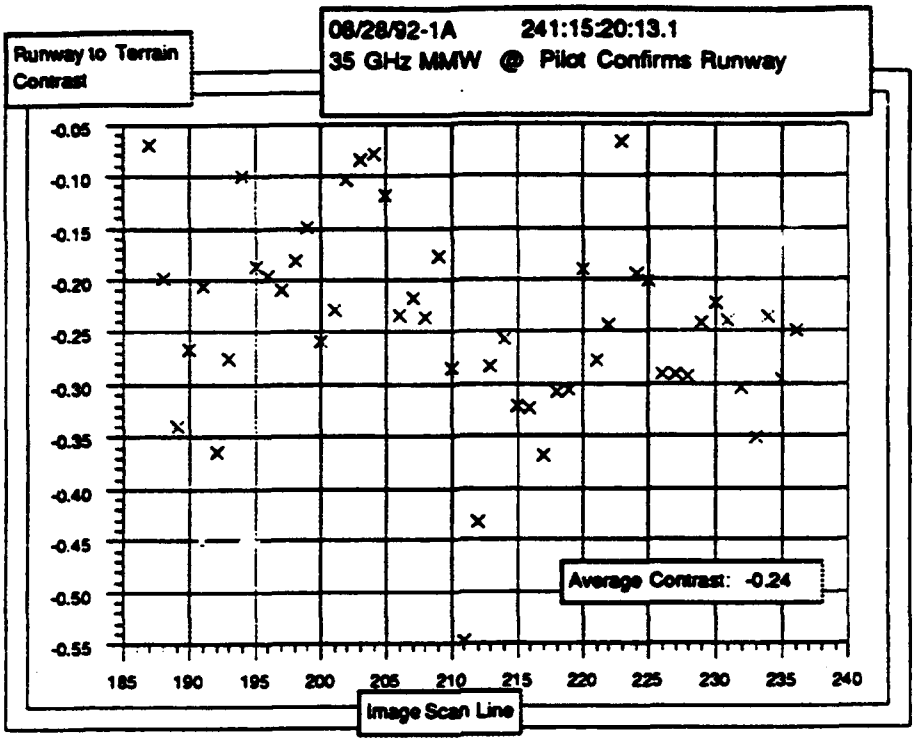

Figure 7-9. Contrast - August 28, 1992-1A (ACV at Pilot Confirms Runway)

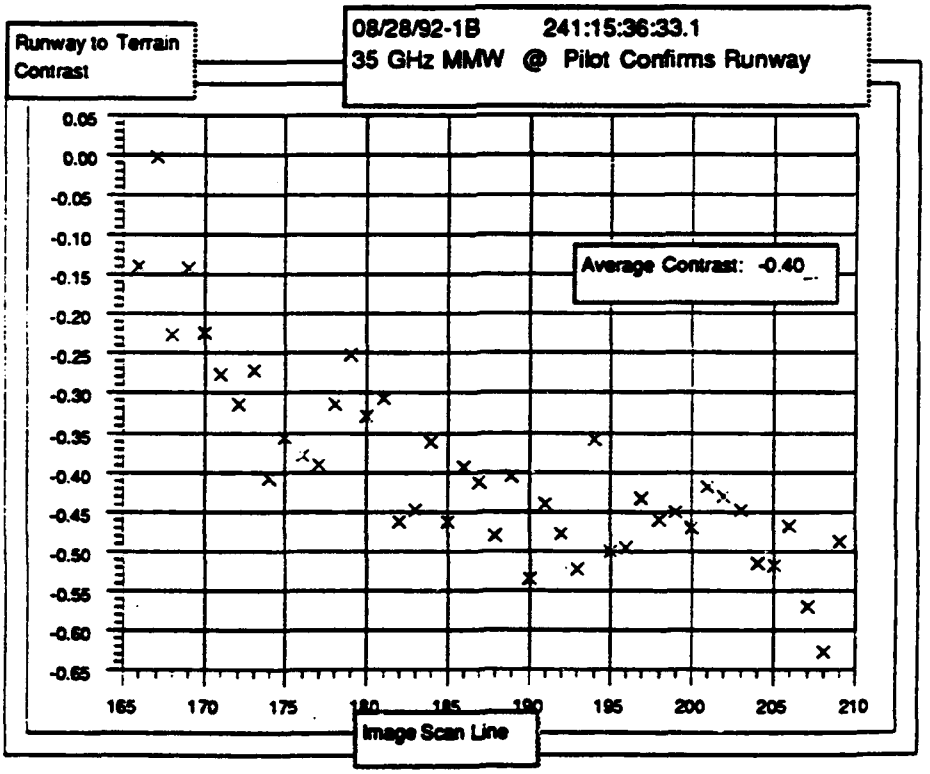

Figure 7-10. Contrast - August 28, 1992-1A (ACV at Pilot Confirms Runway)

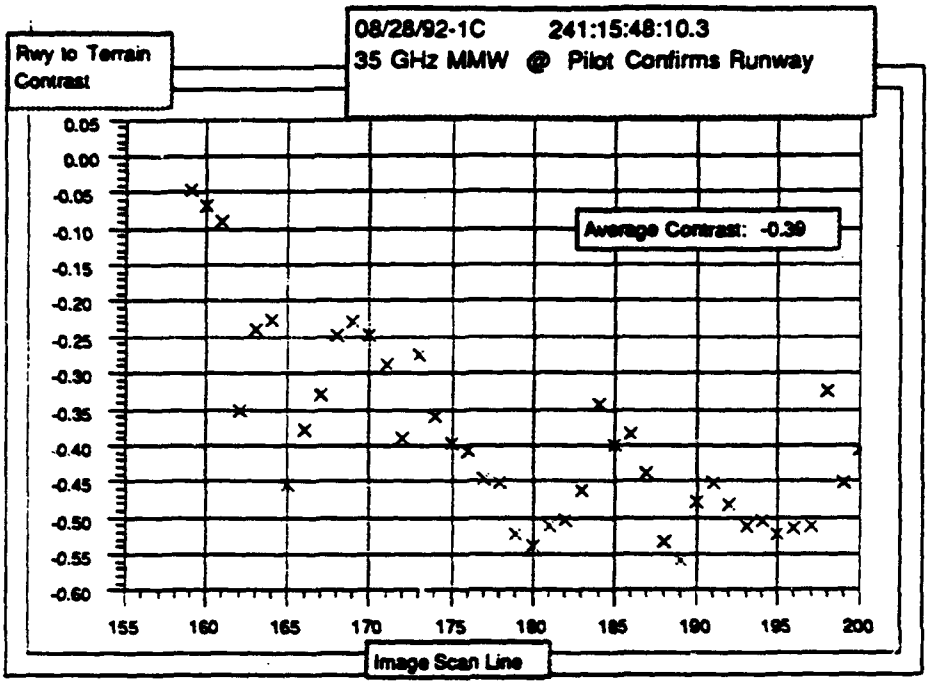

Figure 7-11. Contrast - August 28, 1992-1C (ACV at Pilot Confirms Runway)

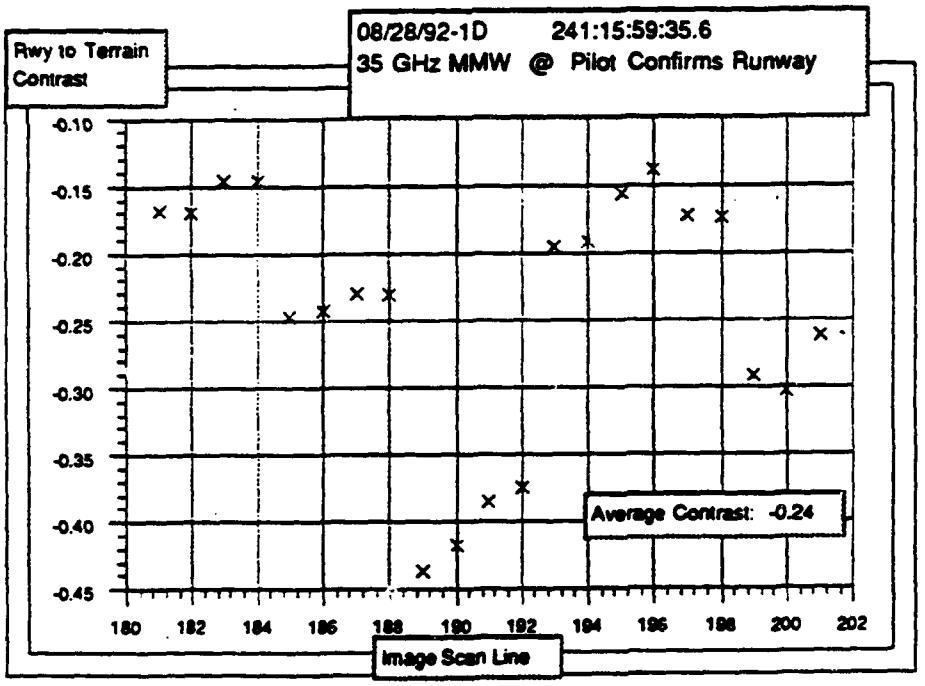

Figure 7-12. Contrast - August 28, 1992-1D (ACV at Pilot Confirms Runway)

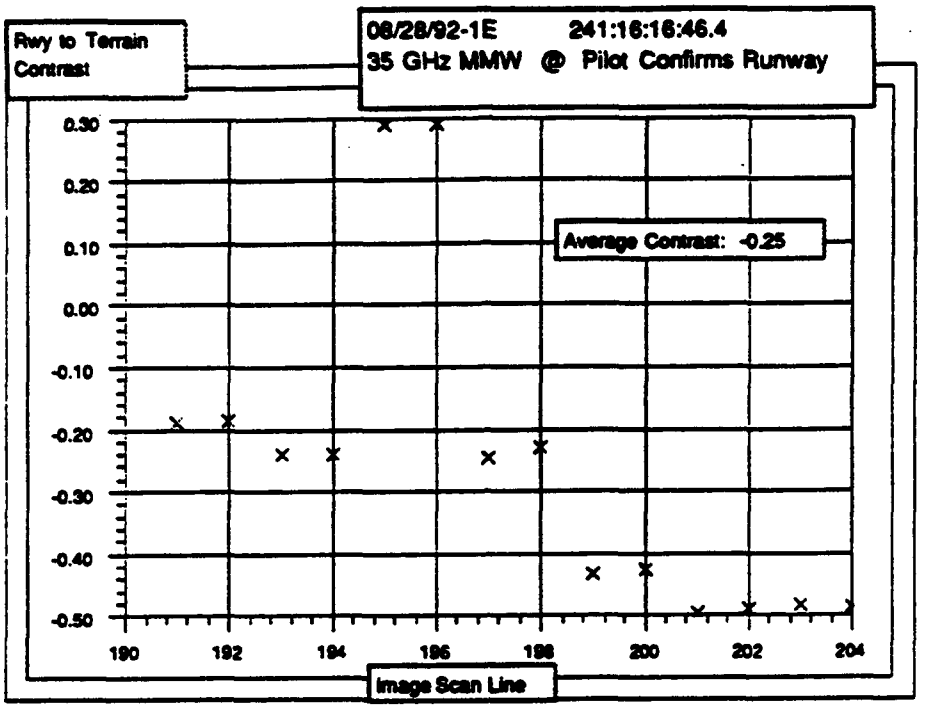

Figure 7-13. Contrast - August 28, 1992-1E (ACV at Pilot Confirms Runway)

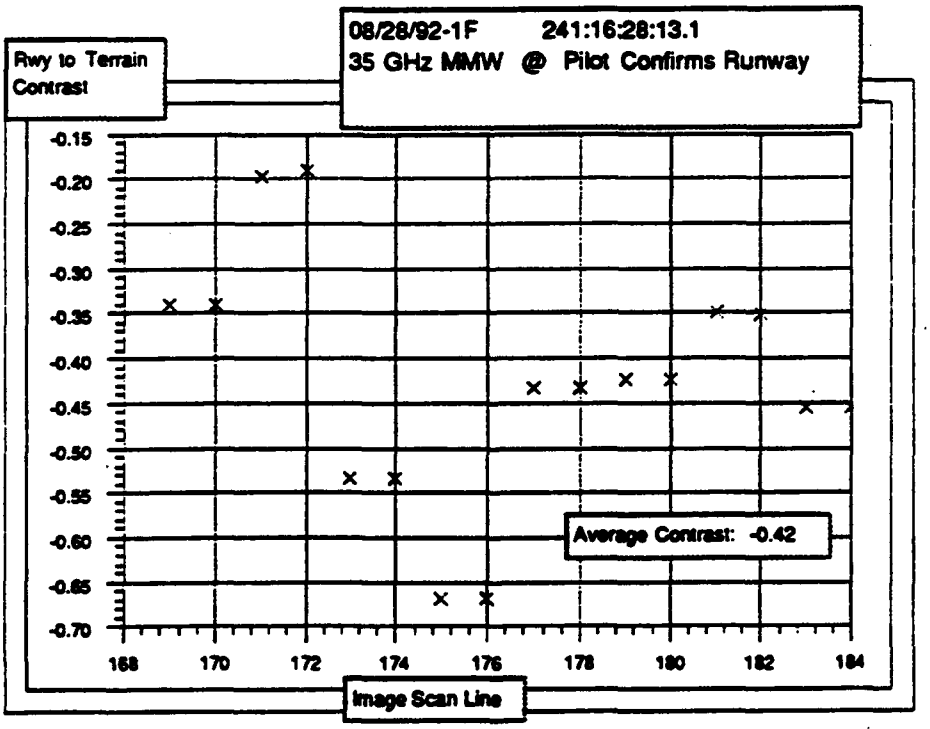

Figure 7-14. Contrast - August 28, 1992-1F (ACV at Pilot Confirms Runway)

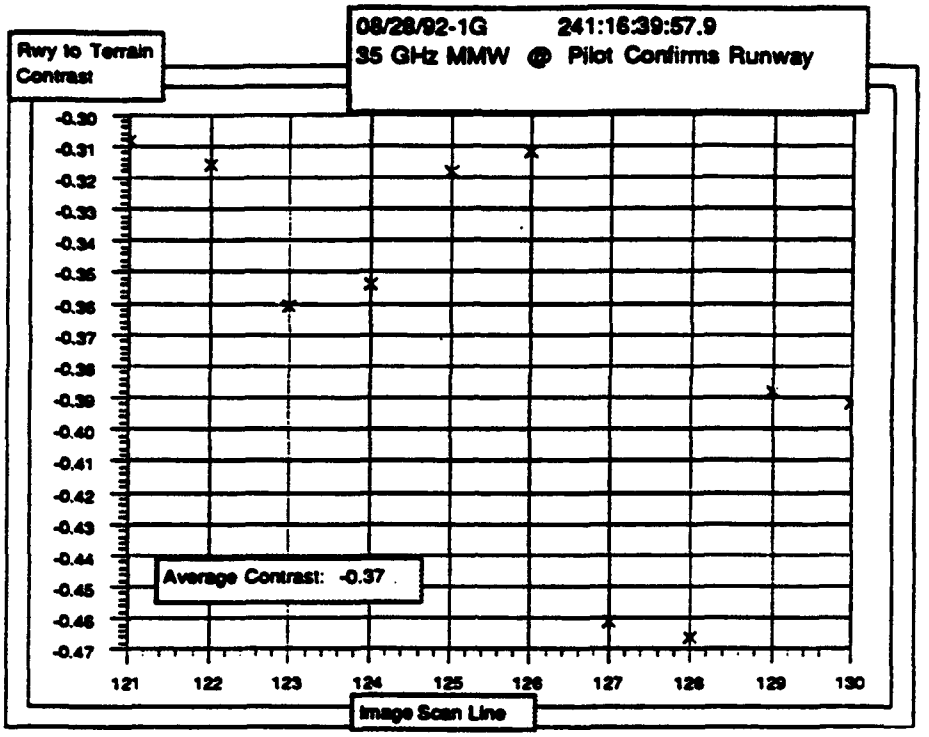

Figure 7-15. Contrast - August 28, 1992-1G (ACV at Pilot Confirms Runway)

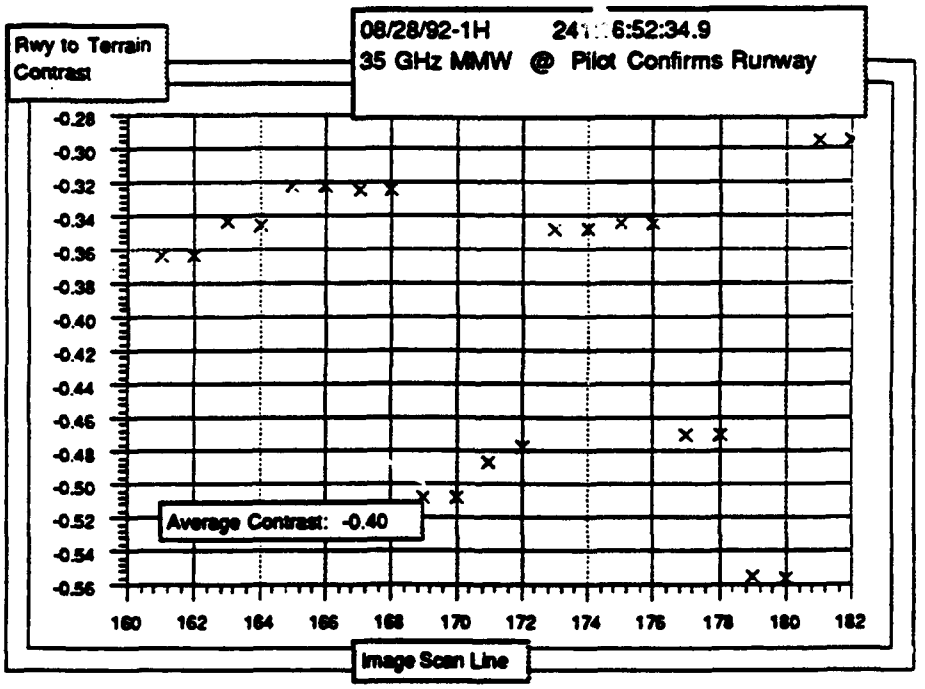

Figure 7-16. Contrast - August 28, 1992-1H (ACV at Pilot Confirms Runway)

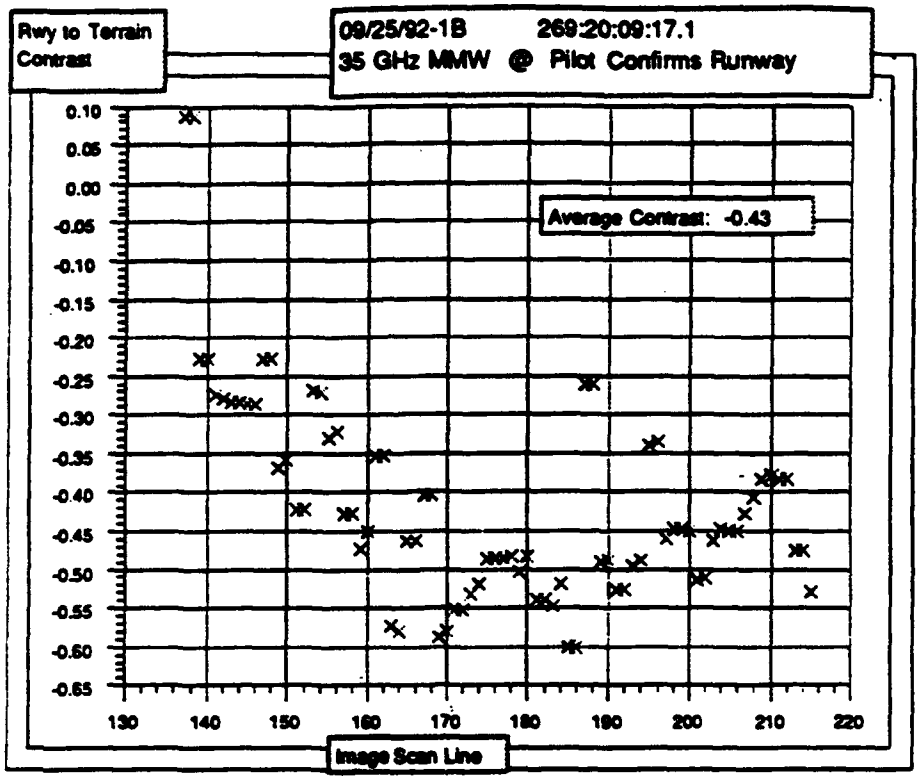

Figure 7-17. Contrast - September 25, 1992 - 1B (LFI at Pilot Confirms

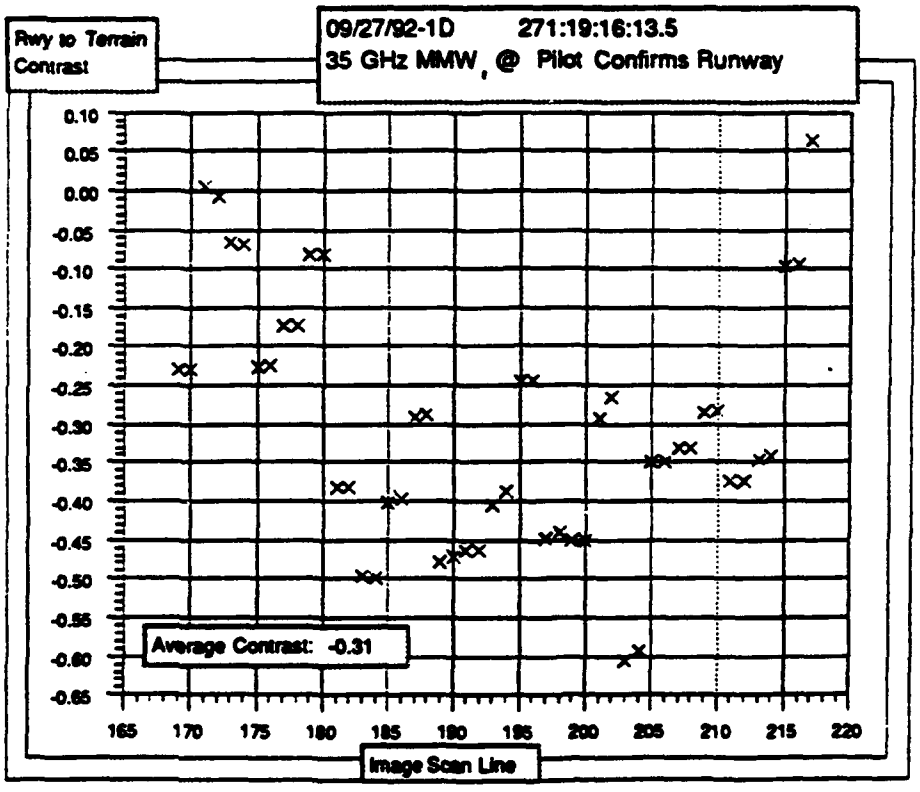

Figure 7-18. Contrast - September 25, 1992 - 1B (LFI at Pilot Confirms Runway)

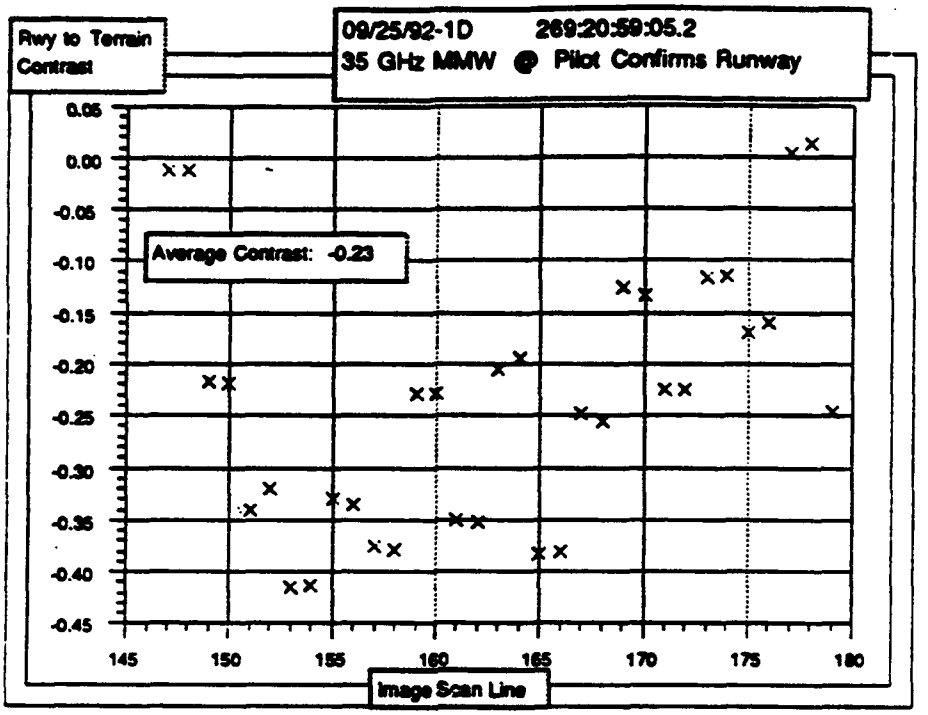

Figure 7-19. Contrast - September 25, 1992 - 1D (NHK at Pilot Confirms Runway)

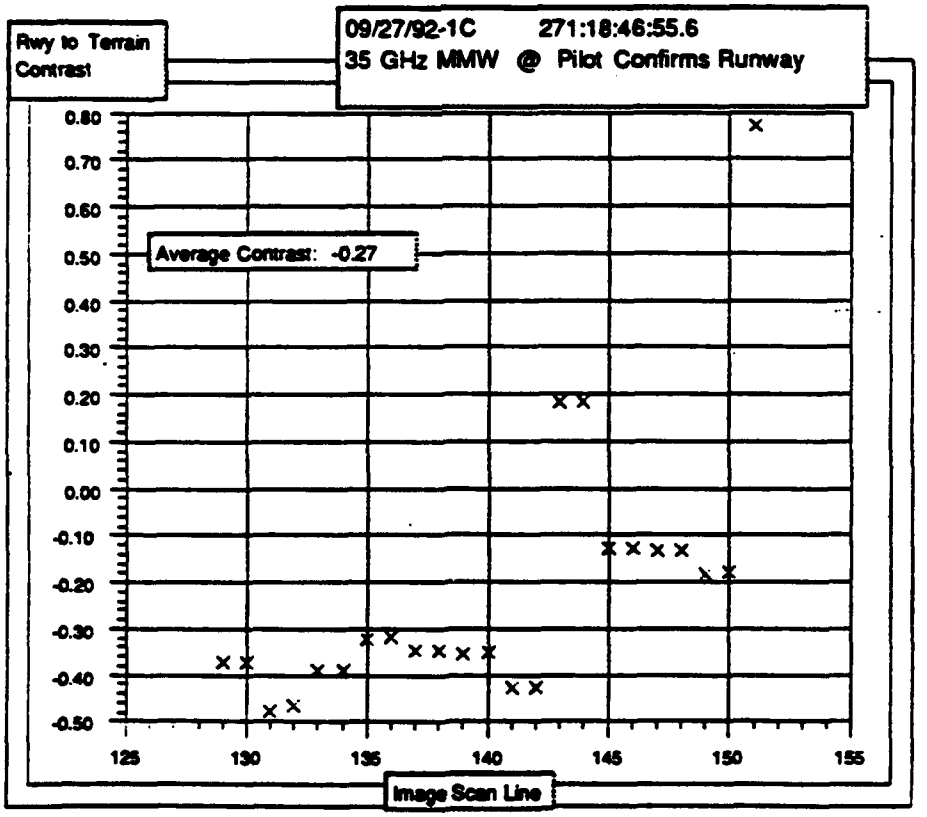

Figure 7-20. Contrast - September 27, 1992 - 1C (NHK at Pilot Confirms Runway)

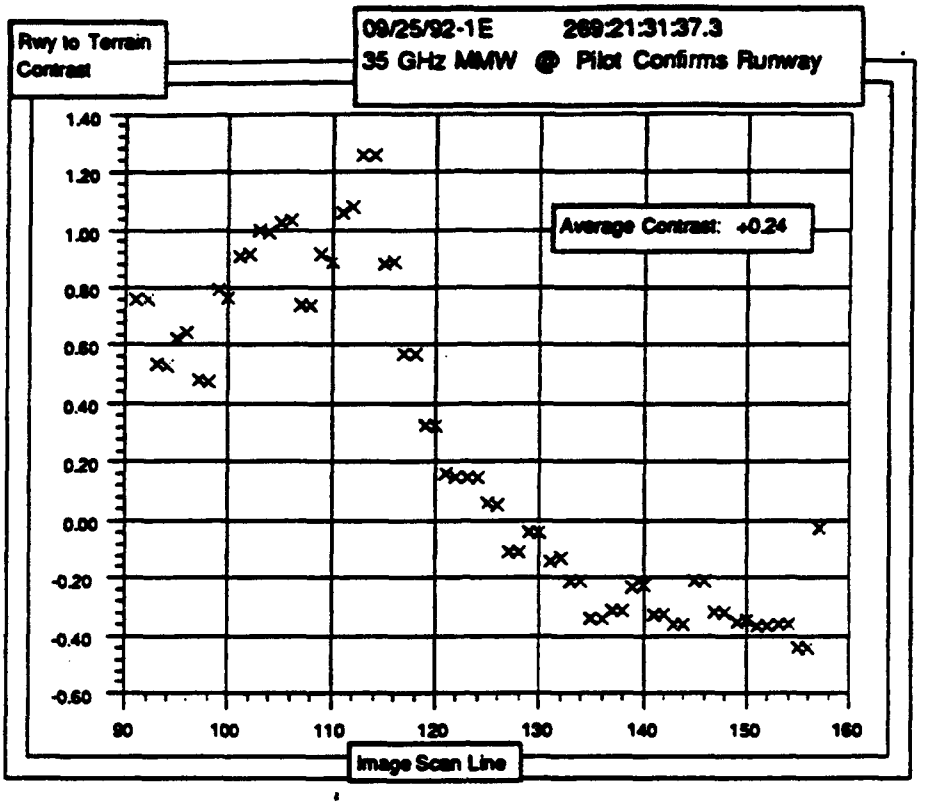

Figure 7-21. Contrast - September 25, 1992 - 1E (MIV at Pilot Confirms Runway)

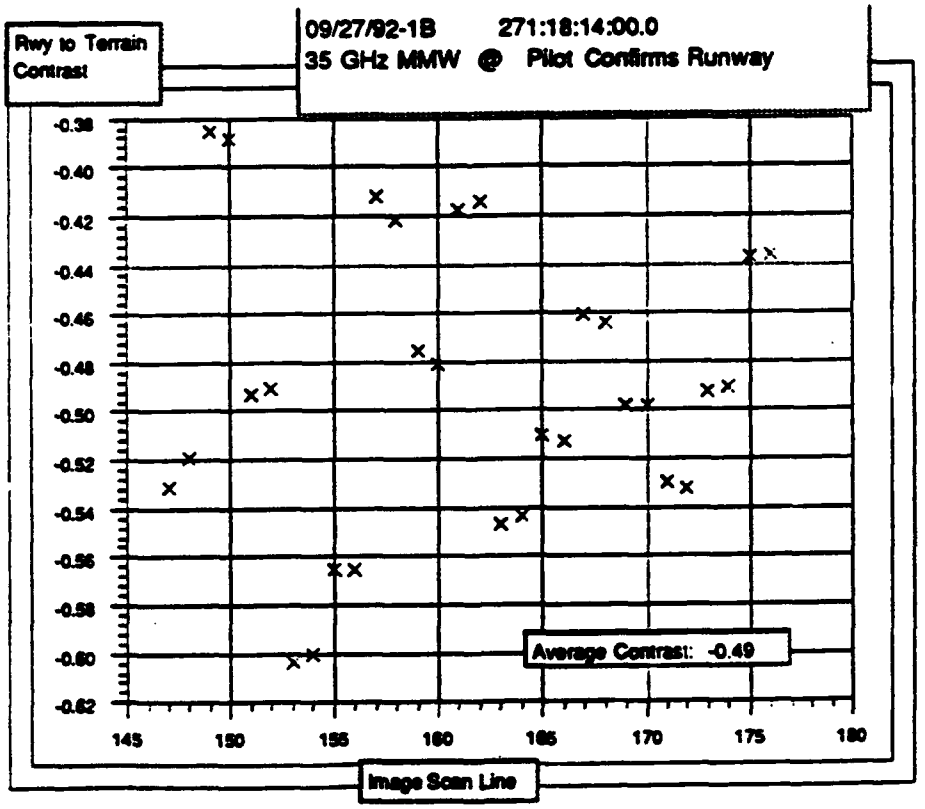

Figure 7-22. Contrast - September 27, 1992 - 1B (MIV at Pilot Confirms Runway)

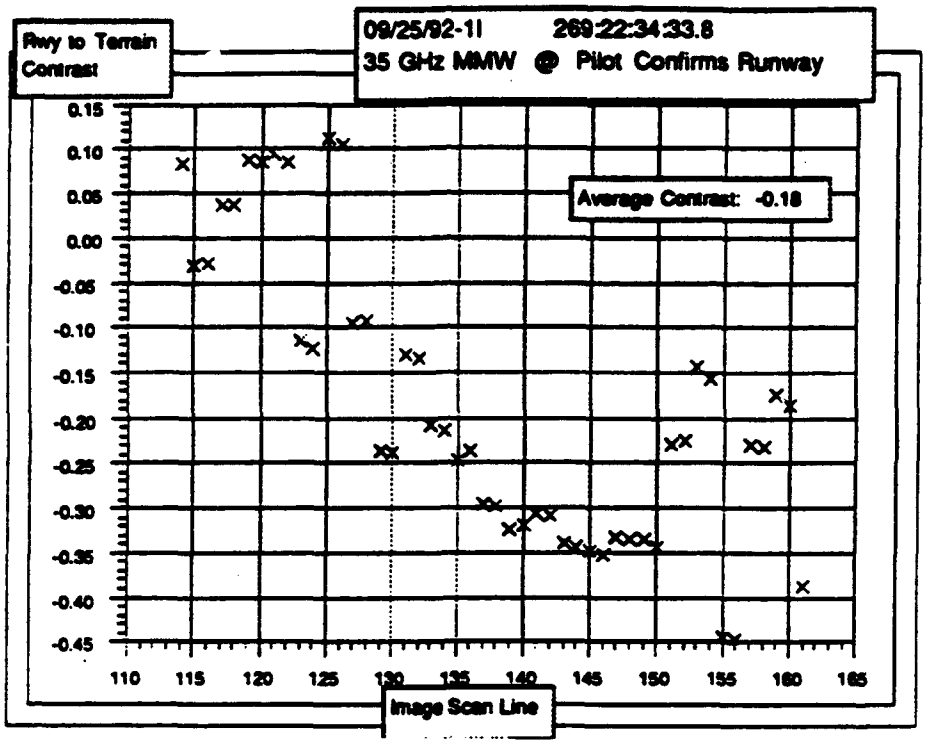

Figure 7-23. Contrast - September 25, 1992 - 1I (ACY at Pilot Confirms Runway)

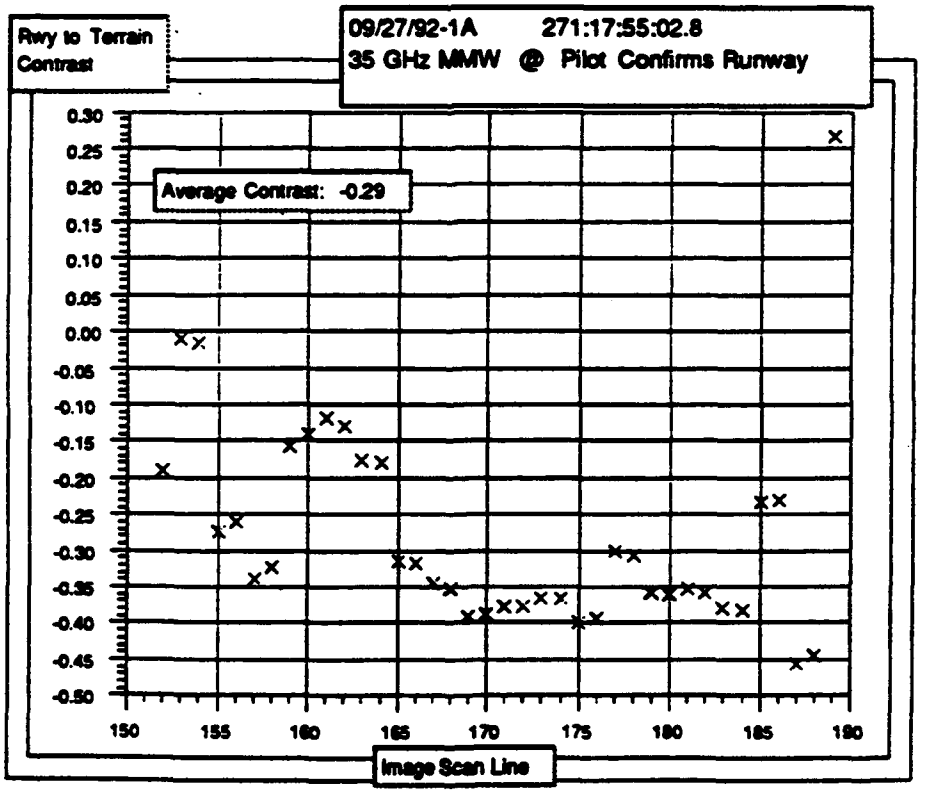

Figure 7-24. Contrast - September 27, 1992 - 1A (ACY at Pilot Confirms Runway)

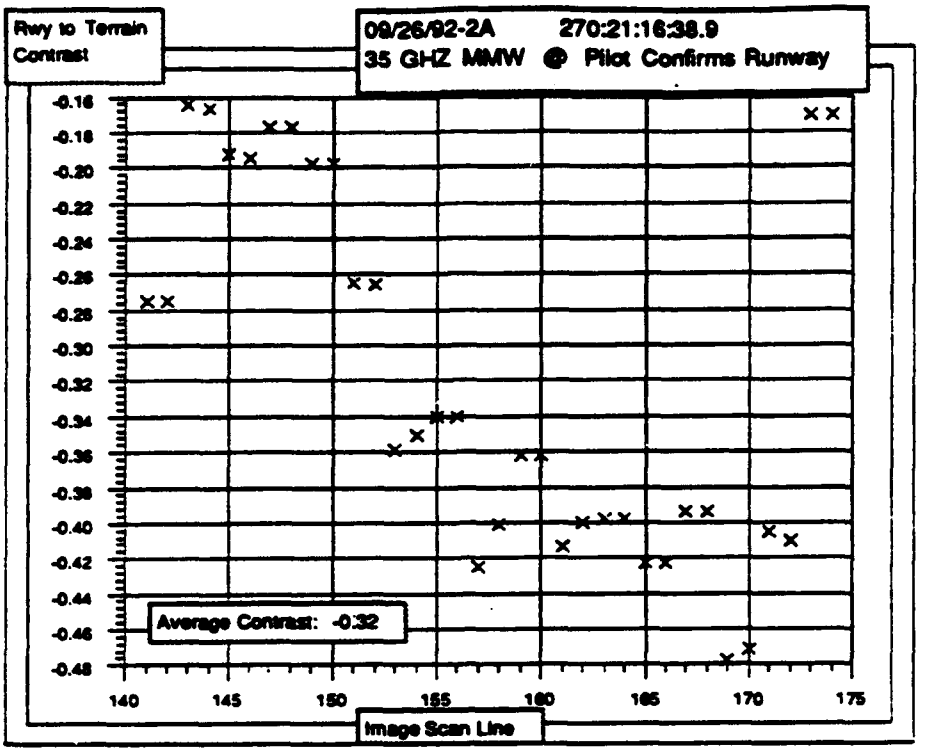

Figure 7-25. Contrast - September 26, 1992 - 2A (ORH at Pilot Confirms Runway)

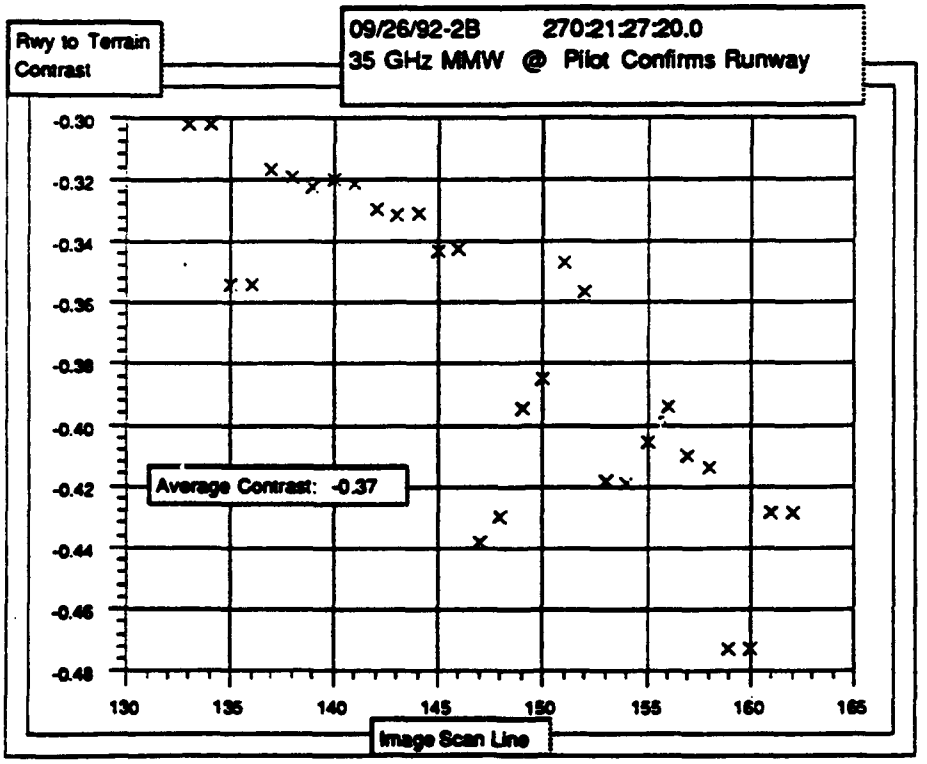

Figure 7-26. Contrast - September 26, 1992 - 2B (ORH at Pilot Confirms Runway)

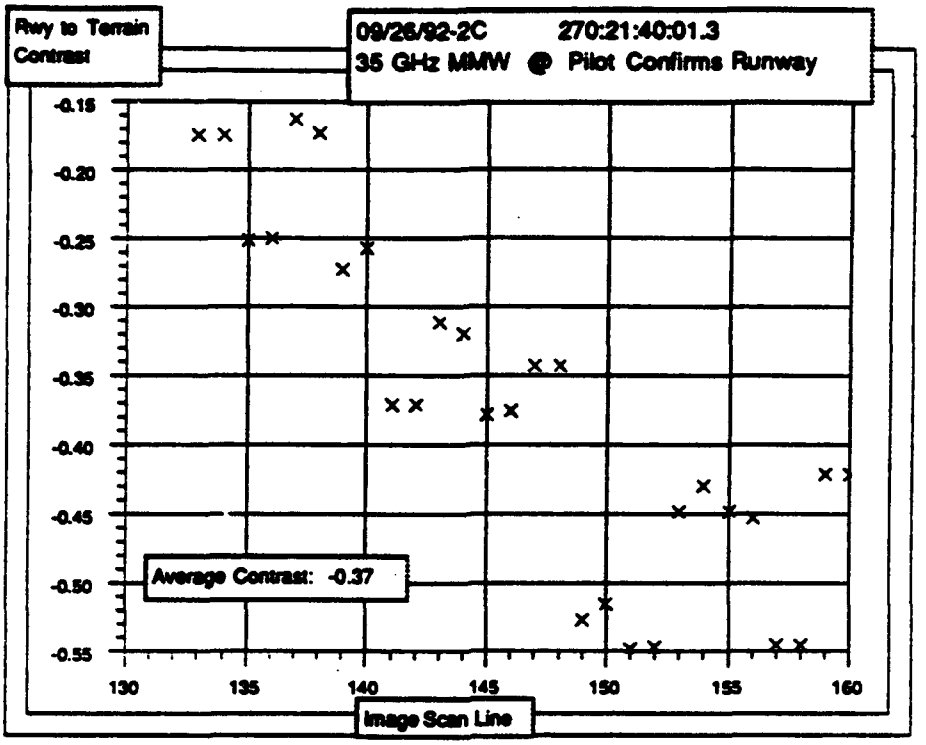

Figure 7-27. Contrast - September 26, 1992 - 2C (ORH at Pilot Confirms Runway)

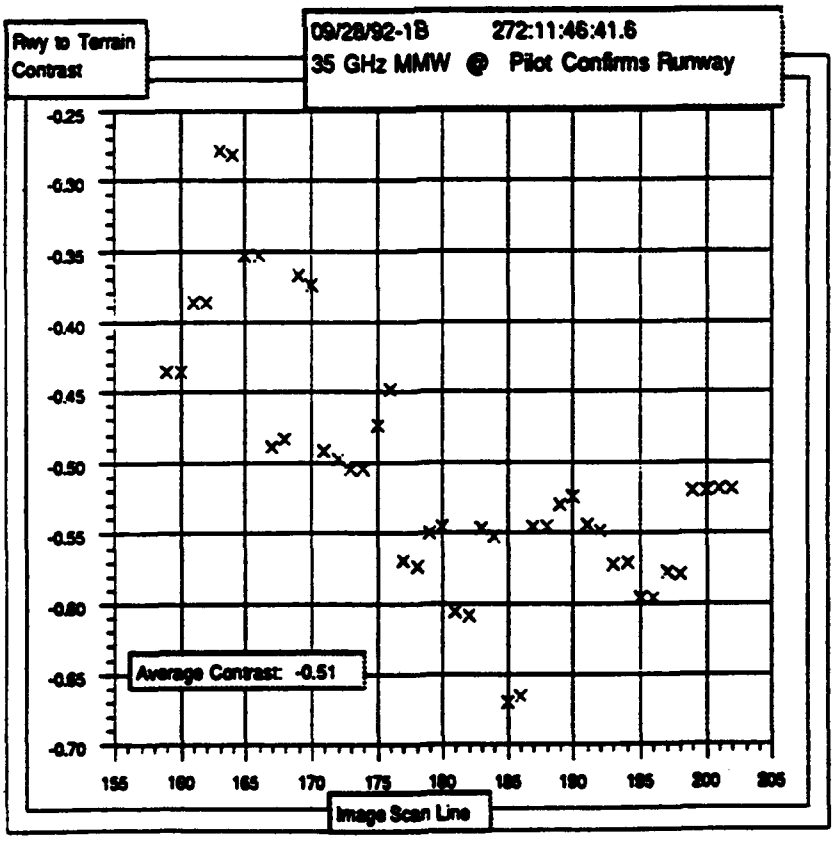

Figure 7-28. Contrast - September 28, 1992 - 1B (HTS at Pilot Confirms Runway)

Table 7-1 Summary of Contrast Metric Correlation to Runway Detection

PILOT CONFIRMS RUNWAY CONTRAST METRIC CORRELATION					
Figure Number	Airport	Flight ID	Contrast Average	Contrast Best	Weather
4	NTD	08/18/92-2B	-0.56	-0.59	VMC
5	NTD	08/18/92-2C	-0.59	-0.75	VMC
6	NTD	08/18/92-2D	-0.50	-0.55	VMC
7	NTD	08/18/92-2E	-0.36	-0.44	VMC
8	NTD	08/18/92-2F	-0.51	-0.52	VMC
9	ACV	08/28/92-1A	-0.24	-0.27	W 0 X 1/8 Fog
10	ACV	08/28/92-1B	-0.40	-0.45	W 0 X 1/8 Fog
11	ACV	08/28/92-1C	-0.39	-0.50	W 0 X 1/8 Fog
12	ACV	08/28/92-1D	-0.24	-0.24	W 0 X 1/8 Fog
13	ACV	08/28/92-1E	-0.25	-0.48	W 0 X 1/8 Fog
14	ACV	08/28/92-1F	-0.42	-0.45	W 0 X 1/8 Fog
15	ACV	08/28/92-1G	-0.37	-0.37	W 1 X 3/8 Fog
16	ACV	08/28/92-1H	-0.40	-0.50	W 1 X 3/8 Fog
17	LFI	09/25/92-1B	-0.43	-0.50	6 SCT M9 BKN 12 OVC, 1 1/2 L-F
18	LFI	09/27/92-1D	-0.31	-0.35	VMC
19	NHK	09/25/92-1D	-0.23	-0.36	-X 3 SCT M7 BKN 10 OVC, 2 R-F
20	NHK	09/27/92-1C	-0.27	-0.38	VMC
21	MIV	09/25/92-1E	+0.24	-0.32	M5 BKN 10 OVC, 2 R-F
22	MIV	09/27/92-1B	-0.49	-0.50	VMC
23	ACY	09/25/92-1I	-0.18	-0.33	M5 BKN 12 OVC, 2 R-F
24	ACY	09/27/92-1A	-0.29	-0.37	VMC
25	ORH	09/26/92-2A	-0.32	-0.41	W 1 X, 1/4 L-F
26	ORH	09/26/92-2B	-0.37	-0.42	W 1 X, 1/4 L-F
27	ORH	09/26/92-2C	-0.37	-0.49	W 1 X, 1/4 L-F
28	HTS	09/28/92-1B	-0.51	-0.57	-X, 1/16 Fog
Average Values:			-0.34	-0.44	
Standard Deviation:			0.16	0.11	

With the common band of recognition extending from -0.2 to -0.6 contrast, the data does not support a clear correlation of contrast to the pilot's ability to detect the runway. Much of this dispersion may be due to the use of the runway contrast without a means to include other objects which aid in pattern recognition. Primary among these are the distinct and repeatable patterns from reflectors in the scene such as light bars, runway arresting wires, VASI installations, and structures near the runway. A secondary aid to recognition may have been repeatable patterns in the ground terrain returns just prior to reaching runway recognition point. These usually include roads, fences, and other cultural features.

Note should be taken of the approach 09/25/92-1E where the average runway contrast at identification was +0.24. This was due to an unusual scene where the far end of the runway was *brighter* than the surrounding terrain, with the scene reversing in the near portion of the runway.

7.2. VARIABILITY

Variability was considered as a possible metric for image recognition. However, analysis of variability in the video data was not done when the GTRI studies showed that it had a very low correlation in the raw radar data which forms the video data.

7.3 SHARPNESS

Sharpness was considered as a possible metric for image recognition. Again, no correlation was found in the GTRI work with the raw radar data so it was not repeated in the video.

SECTION 8

LESSONS LEARNED SUMMARY

Early in the formulation of the SVS Technology Demonstration, a survey was performed of the status of the technologies needed to demonstrate the SVS concept and the key issues were identified that would have to be resolved in the course of successfully implementing the SVS concept as an operational capability. As the Technology Demonstration program progressed, these issues began to be thought of in terms of operational, systems and technology issues with a great deal of overlap between these three general categories of issues.[31] Summarized briefly below are the more significant lessons learned in the flight test phase of the SVS Technology Demonstration.

- The quality of the image produced by the experimental 35 GHz radar system was sufficient to support approaches and landings in Cat IIIa conditions on Type I ILS guidance. A majority of the approaches were flown using ILS approach procedures and guidance. Terrain imagery cues were verified on the display early in the approach (typically 1200-1500 ft AGL). At about 450-550 ft. AGL a runway image could be seen on the display of sufficient quality to use as a reference for flight path control. At 200 ft. AGL, the flight test minimums required the presence of a good raster image to continue the approach. At 50 ft AGL a vision-obstructing cardboard shield was manually removed, if previously put up, to permit the evaluation pilot to transition to outside references. The flare and landing rollout were flown visually for most of the approaches. Other than in conditions of moderate to heavy rain or snow covered terrain, runway and adjacent taxiway image quality were good with lateral, near, and far runway and taxiway edges relatively well defined. During ground rollout, small artifacts could occasionally be seen moving laterally across the field-of-view of the raster image. These artifacts were attributed by the Honeywell team to sidelobe returns (no sidelobe rejection hardware or software was installed) caused perhaps by such objects as taxiway markers or distance remaining signs along the edges of the runway. These images, though anomalous, were not overly objectionable to the pilots.

- Performance of the 35 GHz system in fog was excellent, providing good images in the presence of all advection or radiation fog in which flight tests were conducted right down to zero ceiling and visibility conditions.

- Performance of the 35 GHz system in light rain (less than 6-8 mm per hour) was adequate. In moderate (8-10 mm per hour) to heavy (22-26mm per hour) rain, image degradation consisted of a pronounced reduction in maximum range. The existence of pooled water on and beside the runway coupled with heavy rain further reduced the

usefulness of the image. In all rain conditions encountered, however, runway visibility always exceeded that required for existing ILS minimums.

- Performance of the 35 GHz system through falling snow was excellent. In the very few snow conditions available during the test period, however, snow cover of the terrain surrounding the runway dramatically reduced the range at which a useful image could be attained. Although the runway approach lights could be clearly seen in the images on all approaches, contrast between the runway surface and surrounding terrain was nonexistent until very low (below 200 ft.) on the approaches. These effects were apparently the same whether or not the runway surface was plowed and even in the presence of piled snow along the runway edges.

- MMW sensor range is key to the identification of the airport runway prior to reaching the decision height (DH) or minimum decent altitude (MDA)/visual descent point (VDP) in an IMC approach where visual identification is normally required to continue the approach. The synthetic vision system must provide a synthetic visual image of sufficient quality prior to that point in the approach to permit the decision to be made to continue with the approach using the sensor image. Unlike today's instrument approach in which the performance of the human eye and brain permit an almost instantaneous decision upon reaching the DH or MDA/VDP, the poorer resolution and hence fewer cues in the SVS image will require a greater period of time for the pilot to assimilate the needed information and make the decision. The experimental system 35 GHz radar range was adequate for use in extending the capability of the test aircraft and crew from CAT I minimums to CAT IIIa minimums on Type I ILS guidance.

- A requirement for image enhancement is highly dependent on the intended operational use of the SVS system Surprisingly, system resolution was not the limiting factor for runway detection and identification or for accomplishing the approach to the initiation of the flare maneuver. On the other hand, the somewhat coarse resolution of the 35 GHz system (approximately 0.8 degrees in azimuth and 12-15 meters in range), and the rather jagged runway and taxiway edges in the video display during the latter phases of the flare, landing rollout and taxi contributed to the very limited usefulness of the experimental system to the pilots for those operations. Although simulated (cardboard shield up) zero visibility landings were made, pilot comfort in lateral aircraft control in the flare and for taxi or rollout was degraded significantly by the lack of adequate runway edge definition and by the limited vertical field of view of the image when the aircraft was on the ground

- Antenna pitch stabilization is necessary to keep the antenna elevation pattern pointed at the runway surface as aircraft pitch attitudes vary during the approach and for ground operations. The usefulness of a runway radar image depends on consistency in the difference between radar energy forward scatter on the runway and taxiway surfaces (dark image areas) and back scatter from the runway surroundings (bright image areas). In the Technology Demonstration the antenna elevation angle of the 35 GHz radar system could be varied on the ground through adjustments inside the radome, but could not be

varied in flight. Significant changes in image quality were observed on occasion with relatively small (1 to 2 degree) changes in pitch attitude on approach.

- The specified maximum transport delay for the experimental system image of 200 milliseconds was exceeded in some circumstances with the 35 GHz sensor system by an approximate factor of two, reaching an estimated 400 milliseconds in periods of high roll rates. An image system latency of about 200 milliseconds did appear to be the value beyond which pilot workload and pilot acceptance rapidly degraded when the image was used as an element of the primary guidance system with the pilot in the loop.

- In addition to precision ILS approaches, localizer-only ILS approaches and a few no-navaid (for the final segment of the approach) were flown with the 35 GHz system. During the limited tests performed, the vertical path was managed by the pilot primarily through the combined use of the raster image of the runway, the HUD flight path marker (velocity vector) and the flight path reference symbols. It became clear in these tests that precise registration must be achieved between the raster image, the HUD symbology and the outside scene. Errors in registration of less than 1/2 degree seriously affected the pilots' workload and vertical path management performance.

- Further development and testing is required to establish the minimum requirements for SVS technology to support detection and avoidance of runway and taxiway intrusions and to support pilot situation awareness on the airport surface. The ability of the experimental 35 GHz MMW system to provide runway intrusion information was tested briefly by intentionally placing a runway intruder (pickup truck) at various locations on the runway and taxiways during approaches and a takeoff without the pilot's knowledge and with the pilot's external vision restricted by a cardboard shield in front of the HUD. The pilot quite successfully detected the intrusions in each instance during the approach and accomplished the missed approach in a timely manner. The pilot did not detect the intrusion on the takeoff roll due to the obscuration of the obstacle in the image by the HUD symbology. The pilots were unable to detect and identify obstacles in other tests while on the airport surface with the experimental SVS because of the limitations in resolution, minimum range and limited vertical field of view.

- Millimeter wave approaches flown using the 94 GHz radar resulted in significantly different image characteristics than the 35 GHz system. While image resolution was visibly improved, image quality was degraded by random speckle frequently interfering with image content. Maximum ranges using the 94 GHz radar were considerably less than required for operations below CAT I minimums; adequate runway images were achieved at 150 ft AGL or below. The significant factors thought to affect the performance of the 94 GHz sensor were the limited transmitter power, limitations in processing of the radar data, transmissivity of the radome material selected, and problems with reflections within the radome. The limited performance of this system permitted only limited flight test and no exposure to weather conditions other than dry VMC.

- Performance of the Kodak 3-5 micron infrared sensor system was excellent in moderate (less than 80 degrees Fahrenheit) temperatures and in the absence of any measurable moisture in the air. Image contrast was markedly better than visual contrast in haze conditions and where the moisture was visible but not measurable. In high (greater than 80 degree Fahrenheit) temperatures, image thermal blooming caused a general washout of surface terrain features and reduced operational usefulness. In dry moderate temperature conditions the performance permitted simulated (cardboard shield in place to block outside scene) zero visibility landings and supported good lateral control during rollout and taxi operations. No image was obtained during any of the fog, rain or snow conditions tested. Infrared sensor approaches were flown in day and night conditions, in temperatures from below freezing to above 100 degrees Fahrenheit, and in other weather conditions as specified for the MMW sensor using procedures identical to those used in testing the MMW sensor.

- The HUD itself, even without runway imagery, reduced workload in the approach and landing.

- HUD conformality and image registration are critical issues. The pilot depends on accurately registered image and symbology to provide cues for flight path control. The methodology must be developed and used in future SVS operations to ensure that hardware and software installation features provide the pilot a conformal, accurately registered image.

- Increased brightness of the stroke and raster information displayed on the Head-Up Display is definitely needed in future systems. Improved control of the relative brightness of the stroke and raster information is needed. Also, control of the brightness of the raster image relative to the brightness of the outside scene is definitely needed when the outside scene appears during the approach. In the Technology Demonstration, high levels of cockpit ambient light sometimes caused the evaluation pilot to be unable to effectively see and use the raster image on the HUD In some cases the stroke symbology was also difficult to see and use. To resolve the problem for the purposes of the flight test program, a sunshade was used over the windshield behind the HUD combiner glass. When in clouds the cockpit ambient light was much reduced and the pilot could view the HUD without the sunshade most of the time. Auto-brightness for stroke only was implemented in the HUD for the SVS flight test program and was only partially successful.

- The flare control laws and display were adequate to ensure a smooth and safe touchdown virtually every time, and with minimal required training. Flare cues were adequate using the display and symbology cues alone (horizon, airspeed, radio altimeter height, flight director), in low visibility conditions. The flare cue consisted of a cross that filled the center of the circular flight director symbol, and flashed at about 1.5 Hz. Flashing of the flare cue began at about 50 ft. AGL. during ILS approaches, and continued to touchdown. The flare cue did not, of course, compensate for lateral or vertical beam bends in the ILS guidance.

- Coding the HUD symbology to annunciate when the display is no longer conformal is acceptable but the flight director should never be removed from the display. The HUD field of view (FOV) was 30 degrees laterally. During SVSTD approaches to landings with high crosswinds (up to 35 knots at 90 degrees) the velocity vector became a dotted circle at the edge of the display, and the flight director vanished from the display.
- HUD control laws were tailored for the flight tests using a fixed base engineering simulator at Douglas Aircraft Company. The ability to set the gains in the simulator and then fly them in the aircraft the same day was invaluable and undoubtedly saved much time in preparation for flight test.

- There are as many different operational applications of synthetic vision system technologies as there are users. Each operational scenario will have its unique functional requirements of the technologies and will lead to variations in the systems derived to satisfy those requirements. Images of the runway and surrounding area complemented with aircraft performance and navigation data can be synthesized from a number of differenct sources, only some of which were investigated in the SVTD Program described in this report.

At one end of the spectrum of applications of the synthetic vision capability, and the most easily certificated and implemented, will be its use as an independent monitor of other components of approach and landing guidance systems. At the other end of the spectrum will be applications in which the pilot's cognitive skills will be incorporated as an integral part of the implementation of the synthetic vision concept as a low visibility landing system. While likely to provide greater operational flexibility, this application will require greater certification effort because criteria for its certification do not presently exist. With sufficient development, synthetic vision technologies will substantially contribute to increased aircrew situation awareness and to the detection and avoidance of runway intrusions in any implement-ation within these two philosophies.

SECTION 9.

CONCLUSIONS

Potential applications of Synthetic Vision System Technologies are extensive and there appear to be no insurmountable obstacles to their implementation from an operational perspective. These applications promise dramatic improvements to the economics and safety of flight operations in low visibility conditions.

While this Technology Demonstration Program did not identify nor respond to any specific operational requirement, a carefully selected set of scenarios and associated flight test experiments were established in conjunction with the Program's Certification Issues Study Team to ensure that a reasonably complete cross section of potential users' interests were addressed. These operational scenarios included precision guidance approach and landing operations down to and through Category IIIc operations on Type I and Type II landing guidance systems, nonprecision approach and landing operations, no-navaid approach and landing operations, and airport surface operations including low visibility takeoff. While this joint government/industry SVS Program demonstrated the performance of selected *existing* technologies only and did not investigate any aspect of the costs of developing and implementing those technologies, the Program's participants identified and investigated all technical and certification issues in sufficient depth to conclude that there are no insurmountable operational or technical or certification obstacles to implementation of the SVS capability.

It remains for potential users to establish carefully validated operational requirements for low visibility operations from which cost effective functional and system requirements can be established.

The SVS Technology Demonstration Program has caused the user industry, the manufacturing industry and the regulators to become aware of the potential of SVS technologies for substantial operational, economic and safety improvements. Substantial research is now required to establish adequate models of low visibility conditions and sensor phenomenology with which to examine alternative sensor technologies, to examine alternative system concepts with which to satisfy the user's operational requirements in the most cost effective manner, and to establish the relationship of those SVS technologies that were investigated to other technologies such as GPS and stored digital map data in meeting those operational requirements. Probably the most difficult challenge to industry is in performing the necessary economic studies with sufficient depth to fully understand the true costs and benefits of the many technology options.